

**UNIVERSIDAD DE CONCEPCIÓN**  
**DIRECCIÓN DE POSTGRADO**  
**CONCEPCIÓN - CHILE**

**ON MATHEMATICAL MODELS AND NUMERICAL METHODS FOR  
KINEMATIC FLOWS WITH DISCONTINUOUS FLUX**

*Tesis para optar al grado de  
Doctor en Ciencias Aplicadas con mención en Ingeniería Matemática*

**Antonio Iván García Alvear**

**FACULTAD DE CIENCIAS FÍSICAS Y MATEMÁTICAS**  
**DEPARTAMENTO DE INGENIERÍA MATEMÁTICA**  
**2007**



**ON MATHEMATICAL MODELS AND NUMERICAL METHODS FOR  
KINEMATIC FLOWS WITH DISCONTINUOUS FLUX**

**Antonio Iván García Alvear**

**Director de Tesis:** Dr. Raimund Bürger

**Director de Programa:** Dr. Raimund Bürger

**COMISION EVALUADORA**

Dr. Kenneth H. Karlsen, Universidad de Oslo, Oslo, Noruega.

Dr. John D. Towers, MiraCosta College, Cardiff-by-the-Sea, California, E.U.A.

Dr. Stefan Diehl, Instituto de Tecnología de Lund, Lund, Suecia.

Dr. Eleuterio F. Toro, Universidad de Trento, Trento, Italia.

**COMISION EXAMINADORA**

Firma: \_\_\_\_\_

Dr. Mostafa Bendahmane, Universidad de Concepción, Chile.

Firma: \_\_\_\_\_

Dr. Juan Carlos Muñoz, Pontificia Universidad Católica de Chile.

Firma: \_\_\_\_\_

Dr. Mauricio Sepúlveda, Universidad de Concepción, Chile.

Firma: \_\_\_\_\_

Dr. Raimund Bürger, Universidad de Concepción, Chile.

**Fecha Examen de Grado:** \_\_\_\_\_

**Calificación:** \_\_\_\_\_

*Concepción - Agosto 2007*



# Agradecimientos

A los profesores y al personal del Departamento de Ingeniería Matemática, de la Universidad de Concepción, por haberme aceptado en su programa de doctorado y, por todos los conocimientos y el apoyo otorgados.

A mi director de tesis, Dr. Raimund Bürger, por su constante disposición, preocupación y generosidad.

A los académicos Dr. Kenneth Karlsen de la Universidad de Oslo y Dr. John Towers de MiraCosta College, por su muy importante colaboración en el desarrollo de esta tesis.

Al académico Dr. Matthias Kunik de la Universidad de Magdeburg, por su valiosa colaboración en uno de los artículos que forman esta tesis.

Al profesor Dr. Fernando Concha de la Universidad de Concepción, por haberme guiado, por medio de los seminarios, en los primeros pasos del tema de esta tesis.

A la Dirección de Postgrado de la Universidad de Concepción, por la beca otorgada durante el año 2003.

Al Proyecto Mecesus UCO-9907, por la beca otorgada durante el periodo 2004-2006 y la beca de estadía en el extranjero.

A CONICYT, por las becas de asistencia a congresos y de término de tesis.

Al Centro de Matemáticas para las Aplicaciones (CMA) de la Universidad de Oslo, por haberme permitido y facilitado realizar mi estadía de investigación en ese lugar.



# Resumen

Los flujos de suspensiones y emulsiones polidispersas son aproximados frecuentemente por modelos cinemáticos unidimensionales, en los cuales la velocidad de cada especie de la fase dispersa es una función explícita del vector de concentraciones de todas las especies. Las ecuaciones de balance de masa para todas las especies forman entonces un sistema de leyes de conservación que describe la segregación espacial y la creación de áreas de diferente composición. Este tipo de modelos incluye también el flujo vehicular multi-clase, donde los vehículos pertenecen a clases diferentes de acuerdo a sus velocidades preferenciales. Estos modelos también han sido extendidos a flujos que dependen discontinuamente de la coordenada espacial, los cuales aparecen en modelos de clarificador-espesador, flujos en ductos con variación abrupta del área de sección transversal, y flujo vehicular con condiciones variables de la superficie del camino. Por otro lado, suspensiones polidispersas con partículas de  $N$  clases distintas de tamaño se han utilizado principalmente en experimentos de laboratorio, pero, en la mayoría de las aplicaciones reales, por ejemplo en procesamiento de minerales, los tamaños de las partículas están distribuidos continuamente.

Primero, se presenta un modelo cinemático de separación y clasificación continua de suspensiones polidispersas (separación continua de suspensiones monodispersas). Para este fin, el montaje del clarificador-espesador (CT) es extendido a un clarificador-espesador generalizado (GCT). Los flujos de descarga son descritos por nuevos términos de sumidero singulares. Combinando el montaje GCT con el modelo para la velocidad relativa sólido-fluido (modelo de Masliyah-Lockett-Bassoon (MLB), para suspensiones polidispersas) genera un sistema de leyes de conservación no-lineales con una función de flujo discontinua y un nuevo término de transporte no-conservativo que describe los sumideros. El análisis del caso escalar (para suspensiones monodispersas) con un sumidero singular y área de sección transversal constante está enfocado en las nuevas dificultades analíticas que surgen debido

a este término no-conservativo. Para este fin, se formula un problema reducido, el cual contiene el nuevo término de sumidero del modelo de clarificador-espesador generalizado, pero no el término de fuente y las discontinuidades de la función flujo. Para el problema reducido, se proporciona una definición de soluciones de entropía, basada en funciones y flujos de entropía de tipo Kružkov. Se derivan condiciones de salto y se demuestra la unicidad de la solución de entropía. La existencia de una solución de entropía se demuestra probando la convergencia de un esquema monótono de diferencias finitas. En el caso escalar, los ejemplos numéricos ilustran que el esquema y dos variantes convergen a la solución de entropía, pero introducen cantidades diferentes de difusión numérica. En el caso de sistemas, se presenta un algoritmo numérico para la solución de este modelo junto con ejemplos numéricos, adoptando en parte datos de la literatura. El análisis relacionado a la presencia de términos de sumidero conduce a dos publicaciones.

Esta tesis presenta también dos trabajos que están relacionados por el estudio de ecuaciones conservativas con función de flujo discontinua. En el primero, se presenta una nueva familia de esquemas numéricos para flujos cinemáticos con una función de flujo discontinua. Se demuestra como un esquema muy simple para el caso escalar, el cual es adaptado a la estructura “concentración  $\times$  velocidad” de la función de flujo, puede extenderse a modelos cinemáticos con velocidades de fase que cambian de signo, flujos con dos o más especies (el caso de sistemas), y funciones de flujo discontinuas. Se prueba que dos esquemas particulares dentro de la familia, que se aplican a sistema de leyes de conservación, preservan una región invariante de vectores admisibles de concentración, siempre que todas las velocidades tengan el mismo signo. Además, se prueba que para el caso relevante de una discontinuidad multiplicativa de la función de flujo y una densidad máxima constante, una versión escalar converge a una solución de entropía  $BV_t$  del modelo. En el otro trabajo, el conocido modelo cinemático de tránsito vehicular de Lighthill-Whitham-Richards (LWR) es extendido a un modelo de flujo unidireccional en el cual la densidad máxima  $a(x)$  representa las heterogeneidades del camino (modelo LWR heterogéneo), tales como número variable de pistas, y que puede variar en forma discontinua. Entonces, este modelo LWR heterogéneo es una ley de conservación escalar con una función de flujo discontinua espacialmente. Además, el diseño y análisis del esquema descrito anteriormente es mejorado, mientras su simplicidad es mantenida. En particular, se reducen las pequeñas desviaciones espurias que pueden ocurrir con la versión original. Se propone también una novedosa versión del

---

esquema de Engquist-Osher que se aplica al modelo LWR heterogéneo. Además, se propone un concepto de solución que incluye desigualdades de entropía de tipo Kružkov, y se prueba que estas desigualdades de entropía implican la unicidad de la solución. Este concepto incluye una entropía adaptada similar al tipo recientemente propuesto por Audusse y Perthame en [Proc. Royal Soc. Edinburgh Sect. A, **135**, 253–265, 2005]. Se prueba que ambos esquemas de diferencia y el esquema de Godunov mejorado usado por Daganzo en [Transp. Res. B, **29**, 79–93, 1995] convergen a la única solución de entropía. En ambos trabajos, para las demostraciones de compacidad, se utiliza una novedosa estimación uniforme pero local de la variación total espacial de las soluciones aproximadas. Además, puede idearse un mejoramiento tipo MUSCL en combinación con una discretización del tiempo tipo Runge-Kutta para alcanzar precisión de segundo orden. Ejemplos numéricos y estudios de error  $L^1$  ilustran el desempeño de los esquemas de primer y segundo orden.

Finalmente, el modelo cinemático unidimensional para sedimentación batch de suspensiones polidispersas de esferas pequeñas es extendido a suspensiones con distribución continua de tamaño de partículas. Para este propósito, se introduce la llamada función de densidad de fase  $\Phi = \Phi(t, x, \xi)$ , donde  $\xi \in [0, 1]$  es el tamaño normalizado al cuadrado de las partículas, cuya integral con respecto a  $\xi$  en un intervalo  $[\xi_1, \xi_2]$ , equivale a la fracción volumétrica en  $(t, x)$  ocupada por las partículas en ese rango de tamaño. El nuevo modelo matemático se obtiene combinando el modelo Masliyah-Lockett-Bassoon (MLB) para la velocidad relativa sólido-fluido para cada especie sólida con el concepto de función de densidad de fase, el cual es una ecuación cinética escalar de primer orden para  $\Phi$ . Se presentan tres esquemas numéricos para la solución de esta ecuación. Se observa de un ejemplo numérico y de un estudio del error  $L^1$  que uno de estos esquemas introduce poca difusión numérica y sin oscilaciones espurias cerca de las discontinuidades. Varios ejemplos numéricos ilustran el comportamiento simulado de este tipo de suspensiones.



# Abstract

Flows of polydisperse suspensions and emulsions are frequently approximated by spatially one-dimensional kinematic models, in which the velocity of each species of the disperse phase is an explicitly given function of the vector of concentrations of all species. The mass balance equations for all species then form a system of conservation laws, which describes spatial segregation and the creation of areas of different composition. This type of models also includes multi-class traffic flow, where vehicles belong to different classes according to their preferential velocities. These models have also been extended to fluxes that depend discontinuously on the spatial coordinate, which appear in clarifier-thickener models, flows in ducts with abruptly varying cross-sectional area, and traffic flow with variable road surface conditions. On the other hand, polydisperse suspensions with particles of  $N$  distinct size classes have been mainly utilized in laboratory experiments, but, in most real-world applications, for example in mineral processing, the sizes of particles are continuously distributed.

First, a kinematic model of continuous separation and classification of polydisperse suspensions (separation of monodisperse suspensions) is presented. To this end, the clarifier-thickener (CT) setup for the continuous separation of suspensions is extended to a generalized clarifier-thickener (GCT). Discharge streams are described by new singular sink terms. Combining the GCT setup with the model for the solid-fluid relative velocity (Masliyah-Lockett-Bassoon (MLB) model, for polydisperse suspensions) yields a system of nonlinear conservation laws with a discontinuous flux and a new non-conservative transport term describing the sinks. The analysis of the scalar case (for monodisperse suspensions) with one singular sink and constant cross-sectional area is focused on the new analytical difficulties arising due to this non-conservative term. To this end, a reduced problem is formulated, which contains the new sink term of the generalized clarifier-thickener model, but not the

source term and flux discontinuities. For the reduced problem, a definition of entropy solutions, based on Kruřkov-type entropy functions and fluxes, is provided. Jump conditions are derived and uniqueness of the entropy solution is shown. Existence of an entropy solution is shown by proving convergence of a monotone difference scheme. In the scalar case, numerical examples illustrate that the scheme and two variants converge to the entropy solution, but introduce different amounts of numerical diffusion. In the system case, a numerical algorithm for the solution of this model is presented along with numerical examples, in part adopting data from the literature. The analysis related to the presence of sink terms leads to two papers.

This thesis also presents two works, which are related by the study of conservative equations with discontinuous flux. In the first one, a new family of numerical schemes for kinematic flows with a discontinuous flux is presented. It is shown how a very simple scheme for the scalar case, which is adapted to the “concentration times velocity” structure of the flux, can be extended to kinematic models with phase velocities that change sign, flows with two or more species (the system case), and discontinuous fluxes. It is proved that two particular schemes within the family, which apply to systems of conservation laws, preserve an invariant region of admissible concentration vectors, provided that all velocities have the same sign. Moreover, for the relevant case of a multiplicative flux discontinuity and a constant maximum density, it is proved that one scalar version converges to a  $BV_t$  entropy solution of the model. In the other work, the well-known Lighthill-Whitham-Richards (LWR) kinematic traffic model is extended to a unidirectional road on which the maximum density  $a(x)$  represents road inhomogeneities (inhomogeneous LWR model), such as variable numbers of lanes, and is allowed to vary discontinuously. Then, this inhomogeneous LWR model is a scalar conservation law with a spatially discontinuous flux. Furthermore, the design and analysis of the scheme described above is improved, while its simplicity is maintained. In particular, small spurious overshoots that can occur with the original version are reduced. A novel version of the Engquist-Osher scheme that applies to the inhomogeneous LWR model is also proposed. Furthermore, a solution concept involving Kruřkov-type entropy inequalities is proposed, and it is proved that these entropy inequalities imply uniqueness. This concept includes an adapted entropy similar to the type recently proposed by Audusse and Perthame in [Proc. Royal Soc. Edinburgh Sect. A, **135**, 253–265, 2005]. It is proved that both difference schemes and the improved Godunov scheme used by Daganzo in [Transp. Res. B,

---

29, 79–93, 1995] converge to the unique entropy solution. In both works, for the compactness proofs, a novel uniform but local estimate of the spatial total variation of the approximate solutions is utilized. In addition, a MUSCL-type upgrade in combination with a Runge-Kutta type time discretization can be devised to attain second-order accuracy. Numerical examples and  $L^1$  error studies illustrate the performance of both the first order and the second order schemes.

Finally, the one-dimensional kinematic model for batch sedimentation of polydisperse suspensions of small equal-density spheres is extended to suspensions with a continuous particle size distribution. For this purpose, the so-called phase density function  $\Phi = \Phi(t, x, \xi)$ , where  $\xi \in [0, 1]$  is the normalized squared size of the particles, is introduced, whose integral with respect to  $\xi$  on an interval  $[\xi_1, \xi_2]$ , is equivalent to the volume fraction at  $(t, x)$  occupied by the particles in that size range. The resulting mathematical model, obtained by combining the MLB model for the solid-fluid relative velocity for each solids species with the concept of phase density function, is a scalar first-order kinetic equation for  $\Phi$ . Three numerical schemes for the solution of this equation are introduced, and a numerical example and an  $L^1$  error study show that one of these schemes introduces not much numerical diffusion and without spurious oscillations near discontinuities. Several numerical examples illustrate the simulated behaviour of this kind of suspensions.



# Contents

<b>Resumen</b>	<b>vii</b>
<b>Abstract</b>	<b>xi</b>
<b>1 Motivación, Asuntos Preliminares y Conclusiones</b>	<b>1</b>
1.1 <b>Ámbito del trabajo</b> . . . . .	1
1.2 <b>Novedad de este trabajo</b> . . . . .	3
1.3 <b>Modelos cinemáticos para flujo multi-especie</b> . . . . .	6
1.4 <b>Análisis de modelos cinemáticos</b> . . . . .	7
1.5 <b>Ingredientes no-estándar de los modelos</b> . . . . .	8
1.6 <b>Discretizaciones</b> . . . . .	9
1.7 <b>Perfil de este trabajo</b> . . . . .	11
1.8 <b>Perspectivas y problemas abiertos</b> . . . . .	16
1.9 <b>Conclusiones</b> . . . . .	17
<b>2 Motivation and Preliminaries</b>	<b>25</b>
2.1 <b>Scope</b> . . . . .	25
2.2 <b>Novelty of this work</b> . . . . .	27
2.3 <b>Kinematic models for multi-species flow</b> . . . . .	30
2.4 <b>Analysis of kinematic models</b> . . . . .	31
2.5 <b>Non-standard model ingredients</b> . . . . .	32
2.6 <b>Discretizations</b> . . . . .	33
2.7 <b>Outline of this work</b> . . . . .	35

---

2.8	Outlook and open problems . . . . .	40
<b>3</b>	<b>Extended Clarifier-Thickener Model</b>	<b>43</b>
3.1	Introduction . . . . .	44
3.1.1	Scope . . . . .	44
3.1.2	Reduced problem and full model . . . . .	46
3.1.3	Outline of the paper . . . . .	48
3.2	The extended clarifier-thickener model . . . . .	49
3.2.1	Clarifier-thickener models, singular sources, and singular sinks	49
3.2.2	Bulk flow variables . . . . .	52
3.2.3	Solids feed and sink terms . . . . .	53
3.2.4	Reduced problem . . . . .	55
3.3	Entropy solution and uniqueness analysis of the reduced problem . .	55
3.4	Numerical scheme and some properties . . . . .	64
3.5	Convergence to an entropy solution for the reduced problem . . . . .	67
3.6	Variants of the difference scheme . . . . .	73
3.7	Numerical results . . . . .	75
3.7.1	Numerical solutions of the reduced problem . . . . .	75
3.7.2	Numerical solutions of the full problem . . . . .	76
3.7.3	Error study . . . . .	77
3.8	Conclusion . . . . .	78
3.8.1	Discussion of the numerical results . . . . .	78
3.8.2	Discussion of the entropy condition. . . . .	85
3.8.3	An open problem. . . . .	85
<b>4</b>	<b>Classification of Polydisperse Suspensions</b>	<b>87</b>
4.1	Introduction . . . . .	88
4.2	Motivation . . . . .	90
4.2.1	Kinematic sedimentation models . . . . .	90
4.2.2	Clarifier-thickener models . . . . .	91
4.2.3	Related work . . . . .	93

---

4.3	Mathematical model of polydisperse sedimentation . . . . .	95
4.3.1	Model equations . . . . .	95
4.3.2	Stability of the MLB model . . . . .	98
4.4	The generalized clarifier-thickener (GCT) model . . . . .	100
4.4.1	Suspension bulk flows . . . . .	100
4.4.2	Solids feed and sink terms . . . . .	101
4.4.3	Final form of the mathematical model . . . . .	103
4.5	Numerical scheme . . . . .	104
4.5.1	Discretization of the interior of the GCT . . . . .	104
4.5.2	Calculation of the sink concentrations . . . . .	107
4.6	Numerical examples . . . . .	109
4.6.1	Preliminary remarks . . . . .	109
4.6.2	Example 4.1 . . . . .	113
4.6.3	Example 4.2 . . . . .	115
4.6.4	Example 4.3 . . . . .	119
4.7	Conclusions . . . . .	125
<b>5</b>	<b>Numerical Schemes for Kinematic Flows</b>	<b>127</b>
5.1	Introduction . . . . .	128
5.1.1	Scope of the paper . . . . .	128
5.1.2	Multi-species kinematic models . . . . .	130
5.1.3	Limitations of kinematic models . . . . .	132
5.1.4	Numerical schemes for kinematic models . . . . .	134
5.1.5	Well-posedness analysis and numerical schemes for conserva- tion laws with discontinuous flux . . . . .	135
5.1.6	Contents of the paper . . . . .	136
5.2	Examples of kinematic flow models . . . . .	138
5.2.1	Traffic flow models . . . . .	138
5.2.2	Sedimentation of polydisperse suspensions . . . . .	140
5.2.3	Separation of oil-in-water dispersions . . . . .	141

5.3	Numerical schemes . . . . .	142
5.3.1	Discretizations . . . . .	142
5.3.2	The scalar case . . . . .	144
5.3.3	Numerical flux for systems of conservation laws . . . . .	147
5.3.4	Invariant regions and CFL conditions for systems . . . . .	149
5.3.5	Higher-order versions (Schemes 9 and 10) . . . . .	155
5.4	Convergence analysis . . . . .	158
5.5	Numerical examples . . . . .	165
5.5.1	Example 5.1: Scalar equation without spatially varying parameters . . . . .	165
5.5.2	Example 5.2: Scalar equation with spatially varying coefficients . . . . .	167
5.5.3	Example 5.3: Clarifier-thickener model . . . . .	167
5.5.4	Example 5.4: Multi-species traffic model . . . . .	170
5.5.5	Example 5.5: Multiclass traffic model with spatially varying $\phi_{\max}$ . . . . .	174
5.5.6	Example 5.6: Settling of a bidisperse suspension of equal-density spheres . . . . .	174
5.5.7	Example 5.7: Settling of a suspension with particles of 11 different sizes . . . . .	178
5.5.8	Example 5.8: Oil-in-water dispersion model: Creaming of a dispersion with 10 different droplet sizes . . . . .	181
5.6	Conclusions . . . . .	185
<b>6</b>	<b>Inhomogeneous Kinematic Traffic Model</b>	<b>191</b>
6.1	Introduction . . . . .	192
6.1.1	Scope . . . . .	192
6.1.2	Outline of the paper . . . . .	195
6.2	Preliminaries . . . . .	198
6.2.1	Assumptions on the flux function . . . . .	198
6.2.2	Connections . . . . .	199
6.2.3	The entropy solution concept . . . . .	201

6.3	Uniqueness . . . . .	202
6.4	Relationship between interface entropy conditions and traffic flow . . . . .	205
6.5	Definition of difference schemes . . . . .	211
6.5.1	Numerical fluxes and first-order schemes . . . . .	213
6.5.2	A MUSCL/Runge-Kutta extension of the schemes . . . . .	218
6.6	Convergence analysis . . . . .	220
6.7	Numerical Examples . . . . .	227
6.7.1	Example 6.1 (Riemann problem: HW flux) . . . . .	227
6.7.2	Example 6.2 (Riemann problem: comparison of schemes) . . . . .	227
6.7.3	Example 6.3 (bottleneck problem, after Jin & Zhang [101]) . . . . .	228
6.7.4	Example 6.4 (bottleneck problem: comparison of schemes, after Garavello & Piccoli [75]) . . . . .	230
6.7.5	Example 6.5 (bottleneck problem with zero initial condition, after Garavello & Piccoli [75]) . . . . .	233
<b>7</b>	<b>Continuous Particle Size Distribution</b>	<b>239</b>
7.1	Introduction . . . . .	240
7.2	The mathematical model . . . . .	241
7.2.1	Polydisperse suspensions with a discrete particle size distribution . . . . .	241
7.2.2	Properties of the model for a finite number of particle species . . . . .	243
7.2.3	Polydisperse suspensions with a continuous particle size distribution . . . . .	243
7.2.4	Kinetic problem in final form . . . . .	244
7.2.5	Cumulative quantities for the conservation of mass . . . . .	245
7.3	The eigenvalue problem for the kinetic equation . . . . .	246
7.3.1	Introduction to the eigenvalue problem and formulation of the basic integral equation . . . . .	246
7.3.2	Solution of the eigenvalue problem . . . . .	251
7.4	Numerical scheme . . . . .	254

7.4.1	Discretization parameters and boundary conditions . . . . .	254
7.4.2	Discretization of the kinetic equation . . . . .	256
7.4.3	Numerical test of mass conservation . . . . .	259
7.5	Numerical examples . . . . .	260
7.5.1	Examples with zero-flux boundary conditions . . . . .	260
7.5.2	Example 7.4: Sedimentation of a suspension with periodic boundary conditions . . . . .	272
7.5.3	Examples 7.5 and 7.6: Sedimentation of a suspension with Rie- mann initial data . . . . .	275
<b>8</b>	<b>Conclusions</b>	<b>285</b>
<b>A</b>	<b>Additional numerical examples</b>	<b>291</b>
A.1	Additional numerical examples of Chapter 4 . . . . .	291
A.1.1	Preliminary remarks . . . . .	291
A.1.2	Example A.1: Continuous separation of a bidisperse suspen- sion in a closed-bottom CT with sink . . . . .	292
A.1.3	Example A.2: Separation of a bidisperse suspension in a con- tinuous CT with sink . . . . .	298
A.1.4	Example A.3: Continuous separation of a bidisperse suspen- sion in a liquid fluidized bed classifier with variable control functions . . . . .	303
A.1.5	Example A.4: Continuous separation of a tridisperse suspen- sion in a liquid fluidized bed classifier . . . . .	307
	<b>Bibliography</b>	<b>313</b>

# Chapter 1

## Motivación, Asuntos Preliminares y Conclusiones

### 1.1 **Ámbito del trabajo**

Muchos flujos multifásicos en el campo de la ingeniería suponen el flujo de una sustancia dispersa, por ejemplo partículas minerales sólidas o gotas de aceite, a través de una fase continua, digamos un líquido o gas. En numerosos casos, la sustancia dispersa consiste de pequeñas partículas que pertenecen a diferentes especies que difieren en alguna cantidad característica tal como tamaño o densidad. Como consecuencia, la sustancia dispersa no se mueve como una sola fase; más bien, las especies diferentes se segregan y crean áreas de diferente composición, lo cual es la propiedad más interesante en varias aplicaciones. Este movimiento diferencial de las especies se describe frecuentemente por modelos espacialmente unidimensionales, y en la mayoría de los casos, el diámetro de las partículas es muy pequeño comparado con el del ducto o recipiente, lo que justifica identificar cada especie con una fase continua. Modelos similares incluyen también ciertas aproximaciones continuas de tránsito vehicular en una autopista, si los automóviles con conductores que tienen velocidades preferenciales diferentes son identificados como especies diferentes.

## 2 CHAPTER 1. MOTIVACIÓN, ASUNTOS PRELIMINARES Y CONCLUSIONES

En general, distinguimos  $N$  especies diferentes que originan  $N$  fases continuas sobrepuestas asociadas con fracciones volumétricas o concentraciones (en flujos multifásicos, o, en el caso de flujo vehicular, densidades)  $\phi_1, \dots, \phi_N$ . Si  $v_i$  es la velocidad unidimensional de la especie  $i$ , entonces las ecuaciones de continuidad de las  $N$  especies en forma diferencial son

$$\partial_t \phi_i + \partial_x(\phi_i v_i) = 0, \quad i = 1, \dots, N, \quad (1.1.1)$$

donde  $t$  es el tiempo y  $x$  es la posición espacial. Se asume que las velocidades  $v_1, \dots, v_N$  son funciones dadas del vector  $\Phi := (\phi_1(x, t), \dots, \phi_N(x, t))^T$  de concentraciones locales. Esto produce sistemas de leyes de conservación del tipo

$$\partial_t \phi_i + \partial_x(\phi_i v_i(\Phi)) = 0, \quad i = 1, \dots, N. \quad (1.1.2)$$

Los modelos de flujo unidimensional multi-especie dados por (1.1.2), que involucran a las concentraciones como únicas variables de flujo, se llaman *cinemáticos*. Estamos interesados especialmente en dos modelos específicos que han atraído interés reciente: uno de tránsito vehicular multi-especie [10, 168, 169, 176, 177, 178], y uno de sedimentación de suspensiones polidispersas [12, 32, 149, 158, 170, 175].

En numerosas aplicaciones, el número  $N$  de especies puede ser grande. Además, las especies diferentes son competitivas. Por tanto, es conveniente asumir una densidad máxima  $\phi_{\max}$  (por ejemplo, una densidad máxima de automóviles en modelos de tránsito o la densidad máxima de empaquetamiento de esferas en modelos de sedimentación), tal que el espacio de fase para (1.1.2) es

$$\mathcal{D}_{\phi_{\max}} := \left\{ \Phi = (\phi_1, \dots, \phi_N)^T \in \mathbb{R}^N : \right. \\ \left. \phi_1 \geq 0, \dots, \phi_N \geq 0, \phi := \phi_1 + \dots + \phi_N \leq \phi_{\max} \right\}. \quad (1.1.3)$$

Introduciendo el vector flujo

$$\mathbf{f}(\Phi) = (f_1(\Phi), \dots, f_N(\Phi))^T := (\phi_1 v_1(\Phi), \dots, \phi_N v_N(\Phi))^T, \quad (1.1.4)$$

podemos reescribir (1.1.2) como el sistema no-lineal de leyes de conservación

$$\partial_t \Phi + \partial_x \mathbf{f}(\Phi) = 0. \quad (1.1.5)$$

Soluciones de (1.1.5) son en general discontinuas, y la velocidad de propagación  $\sigma(\Phi^+, \Phi^-)$  de una discontinuidad en el campo de concentraciones  $\phi_i$  que separa los estados  $\Phi^+$  y  $\Phi^-$  satisface la bien conocida condición de Rankine-Hugoniot

$$\sigma = \frac{f_i(\Phi^+) - f_i(\Phi^-)}{\phi_i^+ - \phi_i^-}.$$

Esta tesis trata de modelos cinemáticos de ecuaciones de continuidad (o balance) de diferentes especies, con funciones de flujo que son discontinuas con respecto a la variable espacial, es decir, ecuaciones del tipo  $\Phi_t + \mathbf{f}(\boldsymbol{\gamma}(x), \Phi)_x = \eta(x)\Phi_x$ , donde  $\boldsymbol{\gamma}$  es un vector de parámetros que es función discontinua de la posición espacial  $x, y$ , la función posiblemente discontinua  $\eta(x)$  es el coeficiente de transporte del término no conservativo  $\eta(x)\Phi_x$ . El vector  $\boldsymbol{\gamma}(x)$  puede describir, por ejemplo, en el modelo de tránsito vehicular, condiciones de cambio abrupto de la superficie del camino, y cambios en el número de pistas. El término  $\eta(x)\Phi_x$  puede representar, por ejemplo, un sumidero singular que modela la extracción continua de material desde un clarificador-espesador. Esta tesis se preocupa del análisis de buen planteamiento y, de los métodos numéricos para la solución de problemas de valor inicial y problemas de valores inicial y de contorno basados en estos modelos.

## 1.2 Novedad de este trabajo

Los nuevos temas introducidos y/o analizados en esta tesis incluyen los siguientes

en el Capítulo 3:

- Una extensión del modelo de clarificador-espesador estudiado en [31] mediante un sumidero singular a través del cual se extrae material de la unidad (modelo completo)
- Formulación de un problema reducido a partir del modelo completo

#### 4 CHAPTER 1. MOTIVACIÓN, ASUNTOS PRELIMINARES Y CONCLUSIONES

- Una definición de soluciones de entropía para el problema reducido
- Demostraciones de unicidad y existencia de una solución de entropía del problema reducido
- Un esquema de diferencias finitas explícito para los modelos completo y reducido
- Dos variantes del esquema, los cuales varían en su facilidad de implementación y nivel de resolución no-difusiva

en el Capítulo 4:

- Un nuevo modelo para la clasificación y separación continuas de suspensiones polidispersas, el cual extiende el modelo de clarificador-espesador por medio de sumideros singulares que describen la descarga continua de productos en varios puntos
- Un esquema numérico para su simulación y un método para calcular las concentraciones en los sumideros
- Ejemplos numéricos con datos de experimentos publicados en la literatura, y comparación entre las simulaciones y los resultados experimentales

en el Capítulo 5:

- Una nueva familia de esquemas numéricos para modelos cinemáticos con función de flujo discontinua, en los cuales el flujo numérico está basado explícitamente en la estructura “concentración  $\times$  velocidad” de cada componente del flujo. Además, estos esquemas no requieren ningún cálculo de valores propios (a parte de una estimación del radio espectral para la condición CFL de estabilidad), vectores propios, descomposición campo-a-campo, partición del vector flujo, etc.

- Demostración que dos esquemas particulares dentro de la familia, que se aplican a sistemas de leyes de conservación, preservan una región invariante de concentraciones o densidades admisibles, siempre que todas las velocidades tengan el mismo signo
- Demostración de convergencia de un esquema de diferencias monótono a una solución de entropía  $BV_t$  para el caso escalar de función de flujo discontinua y densidad máxima constante
- Una nueva estimación uniforme pero local de la variación total espacial de soluciones aproximadas generadas por esquemas monótonos para leyes de conservación con función de flujo discontinua

en el Capítulo 6:

- Una extensión del conocido modelo cinemático de tránsito vehicular de Lighthill-Witham-Richards a un modelo de flujo unidireccional en el cual la densidad máxima  $a(x)$  representa las inhomogeneidades del camino, tales como número variable de pistas, y que puede variar en forma discontinua
- Mejora del diseño y el análisis del esquema propuesto por Bürger et al. in [25], manteniendo su simplicidad. En particular, se reducen pequeñas desviaciones espurias que pueden ocurrir con la versión original
- Una novedosa versión del esquema de Engquist-Osher que se aplica al mismo modelo
- Un concepto de solución que incluye desigualdades de entropía de tipo Kružkov, el cual incluye una entropía adaptada similar al tipo recientemente propuesto por Audusse y Perthame [6]
- Demostración de unicidad de una solución de entropía del modelo

- Demostración de convergencia a la única solución de entropía de ambos esquemas de diferencias finitas y del esquema mejorado de Godunov usado por Daganzo en [49]

en el Capítulo 7:

- Un nuevo modelo matemático para la sedimentación de suspensiones con distribución continua de tamaño de partículas, el cual extiende el modelo cinemático unidimensional para la sedimentación batch de suspensiones polidispersas de esferas pequeñas de igual densidad
- Una función de densidad de fase  $\Phi = \Phi(t, x, \xi)$ , donde  $\xi \in [0, 1]$  es el tamaño normalizado al cuadrado de las partículas
- Tres esquemas numéricos para la solución de problemas basados en esta ecuación

Para insertar más este trabajo en el marco de la literatura, recordaremos brevemente en las Secciones 1.3-1.6 algunos hechos conocidos acerca de modelos cinemáticos, ingredientes no-estándar, y discretizaciones.

### **1.3 Modelos cinemáticos para flujo multi-especie**

El modelo cinemático de tránsito para  $N = 1$  se remonta a Lighthill y Whitham [125], y Richards [146]; para la sedimentación de suspensiones, la referencia clásica es Kynch [120]. La extensión del modelo de Lighthill-Whitham-Richards (LWR) al tránsito multi-clase fue propuesto independientemente por Wong y Wong [168] y, Benzoni-Gavage y Colombo [10], mientras extensiones análogas del modelo de sedimentación han sido sugeridas por varias décadas (ver reseñas en [20, 175]), principalmente en la literatura de ingeniería química. Aunque los modelos cinemáticos caen dentro del área de investigación establecida de leyes de conservación [48, 124],

la aplicación de herramientas disponibles de análisis numérico y matemático es difícil. Esto se debe en gran parte a la dependencia de las funciones  $v_i(\Phi)$  de todas las variables  $\phi_1, \dots, \phi_N$ , la cual es en general no-lineal. Para  $\Phi$  en el interior de  $\mathcal{D}_{\phi_{\max}}$ , el Jacobiano  $\mathcal{J}_f(\Phi) := (\partial f_i / \partial \phi_k)_{1 \leq i, k \leq N}$  tiene usualmente solo componentes distintas de cero, tal que fórmulas cerradas para sus valores propios y vectores propios son al menos complicadas, y en general no disponibles para  $N \geq 5$ . Por lo tanto, es en general imposible resolver en forma cerrada el problema de Riemann para (1.1.2).

## 1.4 Análisis de modelos cinemáticos

Recordemos que el sistema (1.1.5) se llama *hiperbólico* en un estado  $\Phi$ , si  $\mathcal{J}_f(\Phi)$  solo tiene valores propios reales, y *estrictamente hiperbólico* si además éstos son distintos entre sí. Para  $N = 2$ , un sistema con un par de valores propios complejos conjugados es *elíptico*. En algunas circunstancias, el tipo es *mixto*, lo cual significa que el sistema es no-hiperbólico (o elíptico) para todo  $\Phi \in E \subset \mathcal{D}_{\phi_{\max}}$ , y  $\mathcal{D}_{\phi_{\max}} \setminus E \neq \emptyset$ . Para  $N \leq 3$ , el criterio de elipticidad puede ser evaluado mediante el cálculo conveniente de un discriminante [32].

Mientras las construcciones de soluciones exactas continúan siendo difíciles, grandes avances se han hecho recientemente en el análisis de hiperbolicidad y caracterización de valores propios de modelos cinemáticos multi-especie. Para un modelo de asentamiento de dispersiones aceite-en-agua, el cual es similar a los modelos de sedimentación y tránsito, Rosso y Sona [149] probaron para  $N$  arbitrario hiperbolicidad estricta en el interior de  $\mathcal{D}_{\phi_{\max}}$ . La demostración se basa en derivar una fórmula cerrada explícita del polinomio característico  $p(\lambda; \Phi) = \det(\mathcal{J}_f(\Phi) - \lambda I)$  mediante posibilidades de eliminación en el determinante. Luego,  $p(\lambda; \Phi)$  es evaluado en  $N$  argumentos  $\lambda$  apropiados que producen valores de signo alternado, lo cual junto con una discusión de  $p(\lambda; \Phi)$  para  $\lambda \rightarrow \pm\infty$  implica que  $p(\lambda; \Phi)$  debe tener  $N$  distintos ceros. Después de análisis preliminares para  $N \leq 3$  [32], Berres et al. [12] probaron en una forma similar que el modelo de Masliyah-Lockett-Bassoon (MLB) [12, 128, 129] para la sedimentación de suspensiones polidispersas con partículas

de igual densidad es estrictamente hiperbólico para un número arbitrario  $N$  de especies (clases de tamaño). La idea básica fue también usada por Zhang et al. [178] para probar hiperbolicidad estricta del modelo de tránsito multi-clase propuesto en [10, 168].

## 1.5 Ingredientes no-estándar de los modelos

Las aplicaciones en que estamos interesados originan también flujos espacialmente no-homogéneos, en los cuales la velocidad  $v_i$  no solo depende de  $\Phi$ , sino también de un vector de parámetros  $\gamma_i$  que es una función de la posición espacial  $x$ ,  $\gamma_i = \gamma_i(x)$ . Mientras que modelos para los cuales  $\gamma_i$  depende, por ejemplo, en forma Lipschitz continua de  $x$  llevan a leyes de conservación que pueden ser tratadas con métodos analíticos y numéricos estándar, aquí estamos interesados en el caso que  $\gamma_i$  depende discontinuamente de  $x$ ; más precisamente, asumimos que  $\gamma_i$  es suave por tramos con un número finito de discontinuidades. El vector  $\gamma_i(x)$  puede describir, por ejemplo, en el modelo de tránsito vehicular, condiciones de cambio abrupto de la superficie del camino, como fue hecho en [27, 132] para un modelo de especie única, y cambios en el número de pistas [75]; fuentes de alimentación singular y flujos volumétricos divergentes en modelos de clarificador-espesador [23, 31]; y cambios abruptos de área de sección transversal en recipientes para el asentamiento de suspensiones y emulsiones.

Algunos modelos pueden incluir también términos de fuente y sumidero singulares, los cuales pueden depender de la posición espacial  $x$ , del tiempo  $t$ , o ambos. El término fuente puede representar, por ejemplo, la inyección de suspensión de alimentación en clarificadores-espesadores, como fue hecho en [31], en el cual este término no depende de  $x$ , y por consiguiente el modelo puede expresarse como una ley de conservación homogénea con función de flujo discontinua. Mientras que, el término de sumidero puede modelar, por ejemplo, la extracción de material desde recipientes de clarificación-espesamiento, como se vió en [24], en el cual el término de sumidero depende de  $x$  y  $t$ , debido a que depende de la solución del problema.

Por otro lado, en la mayoría de las aplicaciones, por ejemplo en procesamiento de minerales, las partículas no son de un número finito de distintas clases de tamaño, sino que el tamaño de las partículas están distribuidas continuamente [40, 170].

## 1.6 Discretizaciones

Para modelos cinemáticos escalares ( $N = 1$ ) con función de flujo continua, diversos esquemas numéricos ya han sido propuestos y analizados en la literatura (ver por ejemplo LeVeque [124]). Para leyes de conservación escalares con función de flujo discontinua, varios métodos numéricos se han desarrollado y analizado. Mencionaremos por ejemplo, el método front tracking y el esquema de diferencias finitas upwind de Engquist-Osher.

El método front tracking se basa en los trabajos de Dafermos [47] y Holden et al. [94]. Variantes del método han sido usados por muchos autores, ver Holden y Risebro [96] para la historia y varias referencias del método. Por ejemplo, Gimse y Risebro en [82] usaron este método para estudiar la ecuación de flujo bifásico. Algunas variantes de la técnica front tracking también han sido usadas previamente para calcular soluciones aproximadas de problemas de sedimentación batch, ver Kunik [116, 117], Kunik et al. [118] y, Bustos y Concha [37]. Una demostración de convergencia del método front tracking para el modelo de clarificador-espesador es dado por Bürger et al. en [28].

El esquema de Engquist-Osher para problemas con función de flujo discontinua se deriva modificando ligeramente el esquema upwind estándar de Engquist-Osher [64]. Con el flujo numérico de Engquist-Osher, el algoritmo resultante es un bien llamado esquema upwind, lo cual significa que la diferenciación de la función de flujo es predispuesta en la dirección de las ondas entrantes, haciendo posible resolver los choques sin difuminación excesiva. Para el caso de un único parámetro discontinuo, Towers en [159] probó que el esquema modificado de Engquist-Osher converge para el caso de una función de flujo cóncava, y en [160] para una función de flujo con cualquier número finito de puntos críticos. Karlsen et al. en [104] ex-

tendieron el esquema, tal que pueda aplicarse a ecuaciones parabólicas degeneradas con discontinuidades en la función de flujo convectiva, y estableció la convergencia a una solución débil. Bürger et al. en [31] probaron convergencia del esquema de Engquist-Osher para el modelo de clarificador-espesador, es decir, el caso de dos parámetros discontinuos.

A pesar de los nuevos resultados de hiperbolicidad, conocimientos más profundos en cualquier modelo cinemático específico de  $N$  especies con  $N \geq 3$  pueden ser obtenidos de manera realista solamente a través de simulación numérica. Esquemas de alta resolución para sistemas de leyes de conservación, que aproximan las discontinuidades marcadamente y sin oscilaciones espurias y que son al menos de segundo orden en precisión en regiones suaves, son candidatos naturales para la solución numérica de (1.1.2). Por ejemplo, Wong, Shu y sus colaboradores [176, 178] aplicaron los esquemas esencialmente no-oscilatorios con peso (WENO) al modelo de tránsito, mientras que Bürger, Karlsen y colaboradores [12, 20, 22, 145] emplearon esquemas de diferencias centrales [119, 138] para el modelo de sedimentación. Mientras tanto, esquemas centrales también han sido aplicados a un número de problemas reales de sedimentación polidispersa, ver por ejemplo Xue y Sun [170], Simura y Ozawa [153], y Wang et al. [167]. Recientemente [36], los esquemas WENO fueron combinados con una técnica de multiresolución para producir un método para modelos cinemáticos que concentran en forma adaptiva el esfuerzo computacional en zonas de variación fuerte.

Todo estos métodos están basados en esquemas que pueden aplicarse universalmente a sistemas de leyes de conservación, y que no están adaptados a una estructura algebraica particular de la función vectorial de flujo. Los esquemas que son de primer orden en precisión, pueden ser mejorados a un orden más alto de precisión empleando técnicas de tipo MUSCL [124].

## 1.7 Perfil de este trabajo

Los Capítulos 3 a 7 de este trabajo están basados en artículos de investigación originales que han sido publicados, aceptados o están en diferentes etapas de revisión, o en preparación. Se han aplicado ligeras correcciones a las versiones de las revistas para lograr un estilo uniforme de citas y referencias, y de diseño dentro de este trabajo.

En el **Capítulo 3**, extendemos el modelo de clarificador-espesador estudiado en [31] por un sumidero singular a través del cual se extrae material desde la unidad. Una dificultad es que en contraste a la fuente singular, el término de sumidero no puede ser incorporado en la función de flujo; más bien, el sumidero es representado por un nuevo término de transporte no-conservativo. Para centrarse en las nuevas dificultades analíticas que surgen debido a este término no-conservativo, formulamos un problema reducido, el cual contiene el nuevo término de sumidero del modelo de clarificador-espesador extendido (modelo completo), pero no el término de fuente y las discontinuidades de la función de flujo. Para el análisis de buen planteamiento del problema reducido, proporcionamos una definición de soluciones de entropía, basada en funciones y flujos de entropía de tipo Kružkov, derivamos condiciones de salto y mostramos la unicidad de la solución de entropía. Demostramos la existencia de una solución de entropía probando la convergencia de un esquema de diferencias monótono. Introducimos dos variantes del esquema numérico para ambos modelos (completo y reducido). Observamos de los resultados numéricos y de los estudios de error  $L^1$  que las tres variantes convergen a la solución de entropía, pero introducen diferentes cantidades de difusión numérica.

El **Capítulo 3** ha sido publicado como:

- Bürger, R., García, A., Karlsen, K.H. & Towers, J.D. On an extended clarifier-thickener model with singular source and sink terms. *European Journal of Applied Mathematics* **17** (2006), 257–292.

En el **Capítulo 4**, empleamos el modelo cinemático para suspensiones polidispersas de Masliyah-Lockett-Bassoon (MLB) para simular separación y clasificación continua de este tipo de suspensiones. Para este fin, extendemos el montaje del clarificador-espesador (CT) para separación continua de suspensiones a un clarificador-espesador generalizado (GCT), adicionando flujos de descarga (de productos) en varios puntos, los cuales son descritos mediante nuevos términos de sumidero singulares. Combinando el montaje GCT con el modelo MLB, se genera un sistema de leyes de conservación no-lineales con una función de flujo discontinua y un nuevo término de transporte no-conservativo que describe los sumideros. Definimos un algoritmo numérico para la solución de esta ecuación, y un método para calcular las concentraciones en los sumideros. Presentamos ejemplos numéricos, adoptando en parte datos de la literatura. Concluimos que el modelo describe la unidad GCT con todos los parámetros de diseño críticos, y predice las composiciones del rebalse, descarga y sumideros, y la evolución espacio-temporal de las concentraciones de las especies sólidas dentro de la unidad.

El **Capítulo 4** ha sido aceptado para publicación como:

- Bürger, R., García, A., Karlsen, K.H. & Towers, J.D. (2007) A kinematic model of continuous separation and classification of polydisperse suspensions. *Computers & Chemical Engineering*, por aparecer.

En el **Capítulo 5**, presentamos una nueva familia de esquemas numéricos para modelos cinemáticos con funciones de flujo que dependen discontinuamente de la variable espacial. Extendemos un esquema muy simple para el caso escalar, el cual se adapta a la estructura “concentración  $\times$  velocidad” de la función de flujo, a modelos cinemáticos con velocidades de fase que cambian de signo, flujos con dos o más especies, y funciones de flujo discontinuas. Además, puede idearse un mejoramiento tipo MUSCL en combinación con una discretización del tiempo tipo Runge-Kutta para alcanzar precisión de segundo orden. Probamos que dos esquemas particulares dentro de la familia, que se aplican a sistema de leyes de conser-

vación, preservan una región invariante de vectores admisibles de concentración, siempre que todas las velocidades tengan el mismo signo. Además, probamos que para el caso relevante de una discontinuidad multiplicativa de la función de flujo y una densidad máxima constante, una versión escalar converge a una solución de entropía  $BV_t$  del modelo. En el último caso, la demostración de compacidad incluye una novedosa estimación uniforme pero local de la variación total espacial de las soluciones aproximadas. Presentamos ejemplos numéricos y estudios del error  $L^1$  para dos de los ejemplos, para ilustrar el desempeño de todas las variantes dentro de la nueva familia de esquemas, incluyendo aplicaciones a problemas de sedimentación, tránsito vehicular, y asentamiento de emulsiones aceite-en-agua.

El **Capítulo 5** ha sido aceptado para publicación como:

- Bürger, R., García, A., Karlsen, K.H. & Towers, J.D. (2007) A family of schemes for kinematic flows with discontinuous flux. *Journal of Engineering Mathematics*, por aparecer.

En el **Capítulo 6**, extendemos el conocido modelo cinemático de tránsito vehicular de Lighthill-Witham-Richards a un modelo de flujo unidireccional en el cual la densidad máxima  $a(x)$  representa las inhomogeneidades del camino, tales como número variable de pistas, y que puede variar en forma discontinua. La evolución de la densidad de automóviles  $\phi = \phi(x, t)$  puede ser descrita por el problema de valor inicial

$$\phi_t + (\phi v(\phi/a(x)))_x = 0, \quad (x, t) \in \mathbb{R} \times (0, T); \quad \phi(x, 0) = \phi_0(x), \quad x \in \mathbb{R}. \quad (1.7.1)$$

Aquí  $z \mapsto v(z)$  es la función velocidad, donde se asume que  $v(z) \geq 0$ , y  $z \mapsto v(z)$  es no-creciente. Ya que  $a(x)$  puede tener una discontinuidad de salto, (1.7.1) es una ley de conservación escalar con una función de flujo discontinua espacialmente. Leyes de conservación que tienen discontinuidades de flujo han recibido mucha atención en los años recientes. Propusimos en el Capítulo 5 [25] un esquema de diferencias

finitas simple para leyes de conservación como (1.7.1). En esta contribución, mejoramos el diseño y el análisis de ese esquema, mientras mantenemos su simplicidad. En particular, se reducen pequeñas desviaciones espurias que pueden ocurrir con la versión original. También proponemos una novedosa versión del esquema de Engquist-Osher que se aplica al problema (1.7.1). Además, proponemos un concepto de solución incluyendo desigualdades de entropía tipo Kružkov, y probamos que estas desigualdades de entropía implican la unicidad de la solución. Este concepto incluye una entropía adaptada similar al tipo propuesto recientemente por Audusse y Perthame [6]. Probamos que ambos esquemas de diferencias finitas y el esquema mejorado de Godunov usado por Daganzo en [49], convergen a la única solución de entropía. Para establecer compacidad de la sucesión aproximante, utilizamos una nueva cota local de la variación espacial [25] [Capítulo 5 de esta tesis). El concepto de solución concuerda necesariamente con el que se deduce al considerar el problema presente como un sistema hiperbólico resonante. Esto se deduce del teorema de unicidad presentado aquí, junto con el teorema de convergencia que se aplica a su esquema de Godunov. Presentamos resultados de experimentos numéricos y un estudio del error  $L^1$  para los esquemas de primer orden, y para las versiones MUSCL/Runge-Kutta que son formalmente de precisión de segundo orden.

El **Capítulo 6** corresponde al siguiente artículo en preparación:

- Bürger, R., García, A., Karlsen, K.H. & Towers, J.D. A difference scheme and entropy solutions for an inhomogeneous kinematic traffic flow model.

En el **Capítulo 7**, extendemos el modelo cinemático unidimensional para sedimentación batch de suspensiones polidispersas de esferas pequeñas a suspensiones con distribución continua de tamaño de partículas. Para este propósito, introducimos la llamada función de densidad de fase  $\Phi = \Phi(t, x, \xi)$ , donde  $\xi \in [0, 1]$  es el tamaño normalizado al cuadrado de las partículas, cuya integral con respecto a  $\xi$  en un intervalo  $[\xi_1, \xi_2]$ , equivale a la fracción volumétrica en  $(t, x)$  ocupada por las partículas en ese rango de tamaño. Obtenemos el nuevo modelo matemático combi-

nando el modelo Masliyah-Lockett-Bassoon (MLB) para la velocidad relativa sólido-fluido para cada especie sólida con el concepto de función de densidad de fase, el cual es una ecuación cinética escalar de primer orden para  $\Phi$ . Presentamos tres esquemas numéricos para la solución de esta ecuación. Observamos de un ejemplo numérico y de un estudio del error  $L^1$  que uno de estos esquemas introduce poca difusión numérica y sin oscilaciones espurias cerca de las discontinuidades. Finalizamos con varios ejemplos numéricos que ilustran el comportamiento simulado de este tipo de suspensiones.

El **Capítulo 7** es parte de un trabajo más completo en preparación, el cual incluirá un análisis de los valores propios de la ecuación del modelo. Los autores y el título del artículo son:

- Bürger, R., García, A. & Kunik, M. Sedimentation of polydisperse suspensions with a continuous particle size distribution.

## Apéndice

En el Apéndice, presentamos ejemplos numéricos que fueron parte de versiones anteriores del artículo “A kinematic model of continuous separation and classification of polydisperse suspensions” (Capítulo 4 de este trabajo). La elección de ejemplos de la versión final de ese artículo está basada en los comentarios que recibimos en las revisiones del mismo. No obstante, decidimos incluir los ejemplos previos en esta tesis, ya que representan otros casos interesantes, tales como clasificación continua en recipientes con área de sección transversal rectangular, clasificadores operados en modo clarificador-espesador (es decir, el flujo de alimentación se divide en flujos ascendente y descendente), y clasificación continua con cambios en las variables de control.

## 1.8 Perspectivas y problemas abiertos

En el Capítulo 3, nos hemos centrado en el modelo reducido y su esquema numérico asociado para destacar los aspectos del problema que son más o menos únicos a la porción de sumidero del modelo. Dejamos como un problema abierto la tarea de combinar la definición de solución de entropía y los resultados de este capítulo (buen planteamiento del problema reducido) con aquellos de [31] (buen planteamiento del modelo de clarificador-espesador). El objetivo sería probar que el problema completo está bien planteado. Por otro lado, debido a que es posible la formación de un salto de concentración a través del nivel del sumidero  $x = x_D$ , el valor  $u(x_D, t)$  se vuelve indeterminado, y en consecuencia, es necesario desarrollar un método para calcular la concentración de sólidos de la suspensión que se extrae por el sumidero. Dejamos el diseño y análisis de ese método como otro problema abierto.

En el Capítulo 4, un problema abierto sería el análisis de buen planteamiento del modelo de clarificador-espesador generalizado. Además, es posible mejorar este modelo por medio de otros modelos de velocidad relativa sólido-fluido, modelos parabólicos, ecuaciones adicionales de balance (momento lineal, energía), tratamiento multidimensional, etc. Por otra parte, se propuso un método numérico para calcular la concentración de sólidos en los sumideros, a partir de balances de masa de los sólidos y basados en la velocidad finita de propagación de las ondas de concentración. Dejamos el análisis de este método como otro problema abierto.

En el Capítulo 5, los problemas abiertos serían probar que para el modelo de sedimentación polidispersa, los esquemas 6, 7 y 8 generan aproximaciones que asumen valores en el dominio de las concentraciones físicamente relevantes; y estudiar las oscilaciones en la solución usando el esquema 9 (de segundo orden) en la ubicación de un salto grande en  $\phi$ .

En el Capítulo 6, si la función de flujo no es estrictamente cóncava, nuestra teoría de entropía producirá saltos que pueden no estar completamente de acuerdo con nuestra motivación en términos de flujo vehicular. La pregunta de cómo modificar

la definición de solución de entropía, y también los esquemas de diferencias finitas, tal que la teoría de entropía concuerde completamente con nuestra noción de comportamiento del conductor es un interesante problema abierto.

En el Capítulo 7, un problema abierto es el análisis de valores propios de la ecuación del modelo.

## 1.9 Conclusiones

En el **Capítulo 3**, el modelo de clarificador-espesador estudiado en [31] fue extendido por un sumidero singular a través del cual se extrae material desde la unidad.

La inyección de material de una concentración dada en un lugar fijo lleva a una ley de conservación homogénea con función de flujo discontinua. Por otra parte, la extracción de suspensión en un lugar fijo lleva a una ecuación de balance con función de flujo discontinua, y que tiene un nuevo término de transporte no conservativo. Esta diferencia justificó estudiar el problema con término de sumidero por derecho propio.

Los Esquemas 2 y 3 propuestos para el problema completo tienen el leve inconveniente que para evaluar el flujo numérico de Engquist-Osher, uno tiene que determinar numéricamente los extremos de la función de flujo compuesta, que para el Esquema 2 es  $q(u - u_F) + b(u)$  para  $q \in \{q_L, \tilde{q}_R\}$ . Esto es una desventaja para el desarrollo de metodologías de control.

Los ejemplos numéricos ilustran que el término de sumidero puede originar una variedad de discontinuidades estacionarias a través del nivel del sumidero  $x = x_D$  (decreciente o creciente en la dirección de  $x$  creciente). Los parámetros pueden ser escogidos de manera tal que el material sólido que fluye dentro de la zona de clarificación sea completamente absorbido por el sumidero singular, o que el material sea extraído a través del sumidero sin afectar la solución (concentración) en la zona de clarificación. La existencia de una discontinuidad a través del nivel del sumidero en algunos casos puede determinarse si miramos la condición de salto (3.3.9) del problema reducido asociado para los parámetros dados en esos casos.

Debido a que es posible la formación de un salto de concentración a través del nivel del sumidero  $x = x_D$ , el valor  $u(x_D, t)$  se vuelve indeterminado, y en consecuencia, es necesario el desarrollo de un método para calcular la concentración de sólidos de la suspensión que se extrae por el sumidero. Dejamos el diseño y análisis de ese método como un problema abierto.

En el **Capítulo 4**, se presenta un nuevo modelo para la separación y clasificación de suspensiones polidispersas. Para este propósito, se extendió el modelo del clarificador-espesador (CT) para separación continua de suspensiones a un modelo de clarificador-espesador generalizado (GCT), en el cual un número arbitrario de flujos de descarga son descritos mediante términos de sumidero singulares. Esta característica nos permite describir la extracción continua de productos de composición diferente.

Algunas simplificaciones son hechas en la formulación de las funciones de flujo con el propósito de facilitar el cálculo, y ser consistente con los trabajos previos, en particular, con el análisis de estabilidad de Bürger et al. [32]. Por ejemplo, se derivó una fórmula explícita para la velocidad relativa sólido-fluido de cada especie a partir de la formulación implícita definida por Masliyah [129], y se usó un exponente de Richardson-Zaki promedio para todas las especies en el factor de asentamiento obstaculizado  $V(\phi)$ .

En el Capítulo 3 [23] probamos que, para el caso de una suspensión monodispersa en un recipiente con área de sección transversal constante y un sumidero, el modelo está bien planteado, y mostramos que un esquema numérico monótono converge a la solución de entropía. Estos resultados junto con aquellos de [31] fueron una motivación para formular nuestro modelo GCT.

Se propuso un método numérico para calcular la concentración de sólidos en los sumideros, a partir de balances de masa de los sólidos y basados en la velocidad finita de propagación de las ondas de concentración. Dejamos el análisis de este método como un problema abierto.

En los Ejemplos 4.2 y 4.3 adoptamos datos experimentales dados por Chen et al.

en [40], y nuestras simulaciones se ajustan razonablemente a los resultados de sus experimentos.

Es claro que el modelo GCT está sujeto a limitaciones. Primero, el modelo se aplica solamente a unidades que son (al menos aproximadamente) unidimensionales, y donde los gradientes laterales de concentración o velocidad son despreciables. Esto significa, por ejemplo, que las partículas debieran ser razonablemente pequeñas, tal que los efectos de pared no sean importantes, y que cambios fuertes en el área de sección transversal deben ser excluidos. Se presume también que los parámetros del modelo MLB son conocidos, por ejemplo de un experimento de sedimentación batch. El modelo MLB supone de hecho que las partículas son pequeñas esferas rígidas. Mientras la esfericidad puede considerarse como una aproximación conveniente para partículas de geometría ligeramente más general, la rigidez de las partículas es esencial.

En el **Capítulo 5**, se presentó una familia de esquemas numéricos aplicables a flujos cinemáticos con función de flujo discontinua. El principio de diseño básico de los esquemas, y el análisis de algunos de ellos, se basa en la estructura explícita “concentración  $\times$  velocidad” de la función de flujo de cada especie.

Una de las principales ventajas de estos nuevos esquemas es que no requieren ningún cálculo de valores propios (a parte de una estimación del radio espectral para la condición CFL de estabilidad), vectores propios, descomposición campo-a-campo, partición del vector flujo, etc., que son requeridos usualmente para un esquema upwind. En este sentido son como un esquema central.

Los modelos cinemáticos estudiados son algebraicamente muy similares, pero pertenecen a dos grupos, uno formado por los modelos de tránsito vehicular y de dispersión aceite-en-agua, para los cuales todas las velocidades son no negativas, y otro incluyendo el modelo de sedimentación polidispersa, el cual para  $N \geq 2$  incluye velocidades de ambos signos.

Formalmente, casi todo sistema de leyes de conservación  $\partial_t \phi_i + \partial_x (f_i(\Phi)) = 0$ ,  $i = 1, \dots, N$ , puede escribirse como un “sistema cinemático”  $\partial_t \phi_i + \partial_x (\phi_i v_i(\Phi)) = 0$ ,

$i = 1, \dots, N$ , si definimos  $v_i(\Phi) = f_i(\Phi)/\phi_i$  (presumiendo que este cociente permanece acotado cuando  $\phi_i \rightarrow 0$ ). En consecuencia, los esquemas podrían ser aplicados a casi cualquier sistema de leyes de conservación. Sin embargo, las propiedades que son específicas a los modelos cinemáticos escalares y esenciales para nuestro análisis son que la velocidad  $v(\phi)$  está dada por una coeficiente positivo preestablecido multiplicando una función de obstaculización, tal que  $v(\phi) \geq 0$  y  $v'(\phi) \leq 0$ . Por otro lado, algunas de las propiedades deseables, por ejemplo, que  $\Phi$  pertenezca a un espacio de fase acotado  $\mathcal{D}_{\phi_{\max}}$ , son típicas de los modelos multi-especie, pero por supuesto, no tiene sentido para sistemas que representan balances de cantidades físicas diferentes tales como masa, momento lineal y energía.

Aunque el esquema básico, Esquema 1, puede ser adaptado para resolver numéricamente modelos multi-especie de ambos grupos (Esquemas 4–8), sólo en el caso de velocidades no negativas fue posible establecer un deseable principio de región invariante (Teoremas 5.3.1 y 5.3.2). No es claro si este principio también puede ser establecido para el modelo de sedimentación polidispersa.

Además, nuestro Ejemplo 5.8.1, por ejemplo (ver Figura 5.12 (d) y (f)), ilustra que para  $N \geq 2$  nuestros esquemas de segundo orden no parecen obedecer un principio de invarianza. No obstante, nuestras Figuras 5.5 and 5.8 ilustran que todos los esquemas de segundo orden convergen con errores consistentemente más pequeños en el sentido  $L^1$ , y a tasas ligeramente mejores que sus versiones de primer orden, aún en el caso de sistemas que no está respaldado por un análisis de convergencia.

En cuanto a los aspectos que están mas relacionados a la discontinuidad del flujo numérico, el principal desafío técnico para establecer la convergencia de una sucesión aproximante para leyes de conservación con coeficientes discontinuos es de algún modo controlar la variación espacial de la solución. La cota de variación local desarrollada aquí se aplica solamente a las discontinuidades espaciales, no se vuelve más complicada si el flujo es no convexo, y no requiere suposiciones acerca de la no linealidad genuina.

Finalmente, nuestra definición (5.3.25) y el principio de invarianza para el Esquema 5, Teorema 5.3.1, incluye explícitamente el caso de una densidad máxima

variable (y posiblemente discontinua)  $\phi_{\max} = \phi_{\max}(x)$ , el cual aparece en los Ejemplos 5.2 y 5.5, pero el análisis de convergencia de la Sección 5.4 está limitado al caso de  $\phi_{\max}$  constante. Mientras tanto, en el Capítulo 6 hemos hecho nuevos avances en el análisis del problema donde permitimos a  $\phi_{\max}(x)$  variar en forma discontinua.

En el **Capítulo 6**, el conocido modelo cinemático de tránsito vehicular de Lighthill-Witham-Richards (LWR) fue extendido a un modelo de flujo unidireccional en el cual la densidad máxima  $a(x)$  representa las inhomogeneidades del camino, tales como número variable de pistas, y que puede variar en forma discontinua.

En el caso donde  $a(x)$  es constante (sin interfaz), nuestra motivación para discontinuidades admisibles entrega las mismas condiciones de salto del llamado impulso de viaje del conductor de Ansorge [5], que establece que los conductores suavizan una solución discontinua si  $\phi_L > \phi_R$ , pero no si  $\phi_L < \phi_R$ . Este criterio también coincide con la teoría clásica de Lax/Oleinik/Kružkov si la función de flujo  $f$  es estrictamente cóncava. Si la función de flujo no es estrictamente cóncava, el impulso de viaje del conductor y nuestro razonamiento dan una condición de salto que es diferente de aquella dictada por la teoría clásica de Lax/Oleinik/Kružkov. En el caso del impulso de viaje del conductor, esto fue señalado por Gasser [76].

En la situación más general considerada en el Capítulo 6, el impulso de viaje del conductor no se aplica al salto en la discontinuidad de  $a$ . Esto se debe a que no es posible suavizar la discontinuidad en  $x = 0$ , es decir, siempre habrá una discontinuidad ahí a menos que  $\phi_L = \phi_R = 0$ . Esta es la razón de por qué hemos propuesto nuestro razonamiento aquí, es decir, que el/la conductor(a) tratará de acelerar cuando detecte que la velocidad inmediatamente adelante es mayor que su propia velocidad (cuando la distancia entre su automóvil y el del frente está creciendo). Esto también parece más directamente relacionado al comportamiento del conductor que el impulso de viaje del conductor, puesto que los conductores pueden detectar más fácilmente una diferencia en velocidad que una diferencia en densidad.

En el **Capítulo 7**, se extendió el modelo cinemático unidimensional para sedimentación batch de suspensiones polidispersas de esferas pequeñas a suspensiones con distribución continua de tamaño de partículas. El modelo matemático resultante, obtenido combinando el modelo Masliyah-Lockett-Bassoon (MLB) para la velocidad relativa sólido-fluido para cada especie sólida con el concepto de función de densidad de fase  $\Phi$ , es una ecuación cinética escalar de primer orden para  $\Phi$ .

De acuerdo a lo expuesto en el Capítulo 5 [25], no hay una demostración de estabilidad para el esquema numérico utilizado (Esquema 3), pero se entrega una condición CFL basada en el análisis de un modelo con velocidades no negativas. No obstante, las Figuras 7.1 y 7.2, y las Tablas 5.1 y 5.2 indican la superioridad del Esquema 3 sobre los Esquemas 1 y 2. En particular, la Figura 7.1 muestra que el Esquema 2 introduce oscilaciones espurias cerca de las discontinuidades, y la Figura 7.2 (a) ilustra la creciente viscosidad numérica del Esquema 1 cuando avanza el tiempo.

Varios ejemplos numéricos nos permiten conocer más acerca del comportamiento de este tipo de suspensiones. En particular:

En el Ejemplo 7.1 (sedimentación de una suspensión con equi-distribución de tamaño de partículas), la Figura 7.3 ilustra que las partículas más grandes sedimentan más rápido que las pequeñas, y por lo tanto las más grandes ocupan las capas inferiores del recipiente y forman capas gruesas de sedimento, y, las partículas más pequeñas son parcialmente removidas del fondo y junto a las que están en suspensión forman capas de sedimento muy delgadas sobre las más grandes.

En el Ejemplo 7.3 (comparación entre sedimentación de suspensiones con equi-distribución y distribución Rosin-Rammler de tamaño de partículas), la Figura 7.12 indica que la suspensión con distribución Rosin-Rammler sedimenta más lentamente que la suspensión con equi-distribución de tamaño de partículas, debido a la mayor razón de partículas pequeñas a partículas grandes de la distribución Rosin-Rammler con respecto a la equi-distribución.

En el Ejemplo 7.5 (sedimentación de una suspensión con dato inicial de Riemann), la Figura 7.18 ilustra que hay una acumulación considerable de partículas

de tamaño medio en la parte posterior de la onda de partículas sólidas.



# Chapter 2

## Motivation and Preliminaries

### 2.1 Scope

Many multiphase flows in engineering applications involve the flow of one disperse substance, for example solid mineral particles or oil droplets, through a continuous phase, say a liquid or gas. In numerous cases, the disperse substance consists of small particles that belong to different species which differ in some characteristic quantity such as size or density. As a consequence, the disperse substance does not move as one phase; rather, the different species segregate and create areas of different composition, which is the most interesting property in many applications. This differential movement of the species is frequently described by spatially one-dimensional models, and in most circumstances, the particles diameter is very small compared to that of the flow duct or vessel, which justifies identifying each species with a continuous phase. Similar models also include certain continuum approximations of traffic flow of vehicles on a highway if cars with drivers having different preferential velocities are identified as different species.

In general, we distinguish  $N$  different species that give rise to  $N$  superimposed continuous phases associated with volume fractions or concentrations (in multiphase flows; or, in the case of traffic flow, densities)  $\phi_1, \dots, \phi_N$ . If  $v_i$  is the one-dimensional velocity of species  $i$ , then the continuity equations of the  $N$  species

in differential form are

$$\partial_t \phi_i + \partial_x(\phi_i v_i) = 0, \quad i = 1, \dots, N, \quad (2.1.1)$$

where  $t$  is time and  $x$  is the spatial position. The velocities  $v_1, \dots, v_N$  are assumed to be given functions of the vector  $\Phi := (\phi_1(x, t), \dots, \phi_N(x, t))^T$  of local concentrations. This yields systems of conservation laws of the type

$$\partial_t \phi_i + \partial_x(\phi_i v_i(\Phi)) = 0, \quad i = 1, \dots, N. \quad (2.1.2)$$

One-dimensional multi-species flow models given by (2.1.2), which involve no unknown flow variables other than the concentrations, are called *kinematic*. We are especially interested in two specific models that have attracted recent interest: one of multi-species traffic flow [10, 168, 169, 176, 177, 178], and one of sedimentation of polydisperse suspensions [12, 32, 149, 158, 170, 175].

In many applications, the number  $N$  of species may be large. On the other hand, the different species in these applications are competitive. It is therefore convenient to assume a maximal density  $\phi_{\max}$  (for example, a maximal 'bumper-to-bumper' car density in traffic models or the maximal sphere packing density  $\phi_{\max}$  in sedimentation models), such that the phase space for (2.1.2) is

$$\begin{aligned} \mathcal{D}_{\phi_{\max}} := \{ \Phi = (\phi_1, \dots, \phi_N)^T \in \mathbb{R}^N : \\ \phi_1 \geq 0, \dots, \phi_N \geq 0, \phi := \phi_1 + \dots + \phi_N \leq \phi_{\max} \}. \end{aligned} \quad (2.1.3)$$

Introducing the flux vector

$$\mathbf{f}(\Phi) = (f_1(\Phi), \dots, f_N(\Phi))^T := (\phi_1 v_1(\Phi), \dots, \phi_N v_N(\Phi))^T, \quad (2.1.4)$$

we can rewrite (2.1.2) as the nonlinear system of conservation laws

$$\partial_t \Phi + \partial_x \mathbf{f}(\Phi) = 0. \quad (2.1.5)$$

Solutions of (2.1.5) are discontinuous in general, and the propagation speed  $\sigma(\Phi^+, \Phi^-)$  of a discontinuity in the concentration field  $\phi_i$  separating the states  $\Phi^+$  and  $\Phi^-$  satisfies the well-known Rankine-Hugoniot condition

$$\sigma = \frac{f_i(\Phi^+) - f_i(\Phi^-)}{\phi_i^+ - \phi_i^-}.$$

This thesis deals with kinematic models consisting of continuity (or balance) equations of different species, with flux functions that are discontinuous with respect to the spatial variable, that is, we consider systems of equations of the type  $\Phi_t + \mathbf{f}(\boldsymbol{\gamma}(x), \Phi)_x = \eta(x)\Phi_x$ , where  $\boldsymbol{\gamma}$  is a vector of parameters, which is a discontinuous function of the spatial position  $x$ , and, the possibly discontinuous function  $\eta(x)$  is the transport coefficient of the non-conservative term  $\eta(x)\Phi_x$ . The vector  $\boldsymbol{\gamma}(x)$  may describe, for instance, in the traffic flow model, abruptly changing road surface conditions, and changes in number of lanes. The term  $\eta(x)\Phi_x$  may represent, for example, singular sinks that model the continuous extraction of material from a clarifier-thickener. This thesis is concerned with the well-posedness analysis and, the numerical methods for the solution of initial value problems and initial and boundary value problems based on these models.

## 2.2 Novelty of this work

The new subjects introduced and/or analyzed in this thesis include the following

in Chapter 3:

- An extension of the clarifier-thickener model studied in [31] by a singular sink through which material is extracted from the unit (full model)
- Formulation of a reduced problem from the full model
- A definition of entropy solutions for the reduced problem
- Proofs of uniqueness and existence of an entropy solution of the reduced problem
- An explicit finite difference scheme for the full and reduced models,

- Two variants of the scheme, which vary in their ease of implementation and level of non-diffusive resolution

in Chapter 4:

- A new model for continuous separation and classification of polydisperse suspensions, which extends the clarifier-thickener setup by means of singular sinks describing the continuous discharge of products at several points
- A numerical scheme for its simulation and a method to calculate the sinks concentrations
- Numerical examples with experimental data published in the literature, and comparison between simulations and experimental results.

in Chapter 5:

- A new family of numerical schemes for kinematic models with discontinuous flux, in which the numerical flux is explicitly based on the “concentration times velocity” structure of each flux component. Moreover, these schemes do not require any calculation of eigenvalues (other than an estimate of the spectral radius for the CFL condition), eigenvectors, field-by-field decomposition, flux vector splitting, etc.
- Proof that two particular schemes within the family, which apply to systems of conservation laws, preserve an invariant region of admissible concentration vectors, provided that all velocities have the same sign
- Proof of convergence of a monotone difference scheme to a  $BV_t$  entropy solution for the scalar case ( $N = 1$ ) of a discontinuous flux and a constant maximum density

- A novel uniform but local estimate of the spatial total variation of approximate solutions generated by monotone schemes for conservation laws with discontinuous flux

in Chapter 6:

- An extension of the well-known Lighthill-Whitham-Richards kinematic traffic model to a unidirectional road on which the maximum density  $a(x)$  represents road inhomogeneities, such as variable numbers of lanes, and is allowed to vary discontinuously
- Improvement of the design and analysis of the scheme proposed in Chapter 5 [25], maintaining its simplicity. In particular, small spurious overshoots that can occur with the original version are reduced
- A novel version of the Engquist-Osher scheme that applies to the same model
- A solution concept involving Kružkov-type entropy inequalities, which includes an adapted entropy similar to the type recently proposed by Audusse and Perthame [6]
- Proof of uniqueness of an entropy solution of the model
- Proof of convergence of both difference schemes and the improved Godunov scheme used by Daganzo in [49], to the unique entropy solution

in Chapter 7:

- A new mathematical model for sedimentation of suspensions with continuous particle size distribution, which extends the one-dimensional kinematic model for batch sedimentation of polydisperse suspensions of small equal-density spheres

- A phase density function  $\Phi = \Phi(t, x, \xi)$ , where  $\xi \in [0, 1]$  is the normalized squared size of the particles
- Three numerical schemes for the solution of problems based on this equation

To further embed this work in the framework of literature, we briefly recall in Sections 2.3-2.6 some known facts about kinematic models, non-standard ingredients, and discretizations.

## 2.3 Kinematic models for multi-species flow

The kinematic traffic model for  $N = 1$  goes back to Lighthill and Whitham [125] and Richards [146]; for the sedimentation of suspensions, the classic reference is Kynch [120]. The extension of the Lighthill-Whitham-Richards (LWR) model to multi-class traffic flow was proposed independently by Wong and Wong [168] and Benzoni-Gavage and Colombo [10], while analogous extensions of the sedimentation model have been suggested for several decades (see [20, 175] for reviews), mainly in the chemical engineering literature. Though the kinematic models fall within the mainstream research area of systems of conservation laws [48, 124], the application of available tools of mathematical and numerical analysis is difficult. This is largely due to the dependence of the functions  $v_i(\Phi)$  on all variables  $\phi_1, \dots, \phi_N$ , which in general is nonlinear. For  $\Phi$  from the interior of  $\mathcal{D}_{\phi_{\max}}$ , the Jacobian  $\mathcal{J}_{\mathbf{f}}(\Phi) := (\partial f_i / \partial \phi_k)_{1 \leq i, k \leq N}$  usually has nonzero entries only, such that closed formulas for its eigenvalues and eigenvectors are at least complicated, and in general unavailable for  $N \geq 5$ . It is therefore in general not possible to solve the Riemann problem for (2.1.2) in closed form. This contrasts with what is known for many systems of conservation laws representing balances of different variables (for example, mass, linear momentum and energy) of a single-phase flow, such as the Euler equations of gas dynamics. Moreover, for multi-species kinematic flow models eigenvalues lack a direct physical interpretation, and in particular do not coincide with any of the phase velocities  $v_1, \dots, v_N$ . (In contrast to this, the eigenvalues for the Euler

equations of gas dynamics are the velocity of the gas, and the velocity plus or minus sound speed.)

Most published solution constructions for multi-species kinematic flow models are based on simplifications. For example, Greenspan and Ungarish [85] and Schneider et al. [151] solve the problem of settling of an  $N$ -disperse, initially homogeneous suspension with equal-density particle species under the assumption that solutions exclusively consist of areas of constant composition that are separated by straight, possibly intersecting kinematic shocks whose speeds are determined by the Rankine-Hugoniot condition. Unfortunately, this construction violates Liu's entropy condition (see [48]). In fact, some of the kinematic shocks constructed in [85, 151] should be replaced by rarefaction waves. For the case  $N = 2$ , correct solutions including rarefaction waves were constructed by Fried and Roy [69]. The simplification applied in [69] is the choice of the functions  $v_i(\Phi) = c_i(1 - \phi)$  for  $i = 1, 2$ , where  $c_i > 0$  are constants. A full solution construction of the case where the factor  $(1 - \phi)$  is replaced by  $(1 - \phi)^n$  with  $n > 1$ , for  $N = 2$ , which obeys Liu's entropy principle, is given in [11]. However, the result does not appear in closed or implicit form; rather, certain trajectories have to be determined by numerical integration of ordinary differential equations.

## 2.4 Analysis of kinematic models

We recall that the system (2.1.5) is called *hyperbolic* at a state  $\Phi$  if  $\mathcal{J}_f(\Phi)$  only has real eigenvalues, and *strictly hyperbolic* if these are moreover pairwise distinct. For  $N = 2$ , a system with a pair of complex conjugate eigenvalues is *elliptic*. In some circumstances, the type is *mixed*, which means that the system is non-hyperbolic (or elliptic) for all  $\Phi \in E \subset \mathcal{D}_{\phi_{\max}}$ , and  $\mathcal{D}_{\phi_{\max}} \setminus E \neq \emptyset$ . For  $N \leq 3$ , the ellipticity criterion can be evaluated by a convenient calculation of a discriminant [32].

While exact solution constructions remain difficult, great advances were made recently in the hyperbolicity analysis and characterization of eigenvalues of multi-species kinematic models. For a model of settling of oil-in-water dispersions, which

is similar to the sedimentation and traffic models, Rosso and Sona [149] proved for arbitrary  $N$  strict hyperbolicity in the interior of  $\mathcal{D}_{\phi_{\max}}$ . The proof is based on deriving an explicit closed formula of the characteristic polynomial  $p(\lambda; \Phi) = \det(\mathcal{J}_f(\Phi) - \lambda I)$  by exploiting elimination possibilities in the determinant. Then  $p(\lambda; \Phi)$  is evaluated at  $N$  suitable  $\lambda$ -arguments that produce values of alternating sign, which along with a discussion of  $p(\lambda; \Phi)$  for  $\lambda \rightarrow \pm\infty$  implies that  $p(\lambda; \Phi)$  must have  $N$  distinct zeros. After preliminary analyses for  $N \leq 3$  [32], Berres et al. [12] proved in a similar way that the Masliyah-Lockett-Bassoon (MLB) model [12, 128, 129] for sedimentation of polydisperse suspensions with equal-density particles is strictly hyperbolic for an arbitrary number  $N$  of species (size classes). The basic idea was also used by Zhang et al. [178] to prove strict hyperbolicity of the multi-class traffic model proposed in [10, 168].

## 2.5 Non-standard model ingredients

The applications which we are interested in also give rise to spatially non-homogeneous flows, in which the velocity  $v_i$  not only depends on  $\Phi$ , but also on a vector of parameters  $\gamma_i$  that is a function of the spatial position  $x$ ,  $\gamma_i = \gamma_i(x)$ . While models for which  $\gamma_i$  depends, for example, Lipschitz continuously on  $x$  lead to conservation laws that can be treated with standard analytical and numerical methods, we are here interested in the case that  $\gamma_i$  depends discontinuously on  $x$ ; more precisely, we assume that  $\gamma_i$  is piecewise smooth with a finite number of discontinuities. The vector  $\gamma_i(x)$  may describe, for instance, in the traffic flow model, abruptly changing road surface conditions, as was done in [27, 132] for a single-species model, and changes in number of lanes [75]; singular feed sources and diverging bulk flows in clarifier-thickener models [23] (Chapter 3 of this thesis), [31]; and abruptly changing cross-sectional areas in vessels for the settling of suspensions and emulsions.

Some models can also include singular source and sink terms, where the function multiplying the Dirac delta function may depend on either the spatial position  $x$ , or

the time  $t$ , or both. The source term can represent, for example, the injection of feed suspension in clarifier-thickener units, as was done in [31], in which the function multiplying  $\delta(\cdot)$  does not depend on  $x$ , and consequently the model can be expressed as a homogeneous conservation law with discontinuous flux. While, the sink term can model, for instance, the extraction of material from clarifier-thickener vessels, as is seen in Chapter 4 [24], in which the multiplicative function depends on both  $x$  and  $t$ , because it involves the solution of the problem.

On the other hand, in most real-world applications, for example in mineral processing, the particles are not of a finite number of distinct size classes, but the size of particles are continuously distributed [40, 170].

## 2.6 Discretizations

For scalar kinematic models ( $N = 1$ ) with continuous flux, many numerical schemes have been proposed and analysed already in the literature (see for example LeVeque [124]). For scalar conservation laws with discontinuous flux, several numerical methods have been developed and analysed. Let us mention for instance, the front tracking method and the Engquist-Osher upwind finite difference scheme.

The front tracking method is based on the works of Dafermos [47] and Holden et al. [94]. Variants of the method have been used by many authors, see Holden & Risebro [96] for the history and many references. For example, Gimse & Risebro in [82] used this method to study the two phase flow equation. Some variants of the front tracking technique have also been used earlier to compute approximate solutions to batch sedimentation problems, see Kunik [116, 117], Kunik et al. [118] and, Bustos and Concha [37]. A convergence proof for the front tracking method for the clarifier-thickener model is given by Bürger et al. in [28].

The Engquist-Osher scheme for problems with discontinuous flux is derived by slightly modifying the standard Engquist and Osher upwind scheme [64]. With the Engquist-Osher flux, the resulting algorithm is a so-called upwind scheme, meaning that the flux differencing is biased in the direction of incoming waves, making

it possible to resolve shocks without excessive smearing. For the case of a single discontinuous parameter, the modified Engquist-Osher scheme was proven to converge for the case of a concave flux by Towers in [159] and for a flux with any finite number of critical points by Towers in [160]. Karlsen et al. in [104] extended the scheme so that it would apply to degenerate parabolic equations with discontinuities in the convective flux, and established convergence to a weak solution. Bürger et al. in [31] proved convergence for the Engquist-Osher scheme for the clarifier-thickener model, i.e., the case of two discontinuous parameters.

Despite the new hyperbolicity results, insight into any specific  $N$ -species kinematic model with  $N \geq 3$  can realistically be gained through numerical simulation only. High resolution schemes for systems of conservation laws, which approximate discontinuities sharply and without spurious oscillations and are at least second-order accurate in smooth regions, are natural candidates for the numerical solution of (2.1.2). For example, Wong, Shu and their collaborators [176, 178] applied weighted essentially non-oscillatory (WENO) schemes to the traffic model, while Bürger, Karlsen and collaborators [12, 20, 22, 145] employed central difference schemes [119, 138] for the sedimentation model. Meanwhile, central schemes have also been applied to a number of real-world problems of polydisperse sedimentation, see for example Xue and Sun [170], Simura and Ozawa [153] and Wang et al. [167]. Recently [36], WENO schemes were combined with a multiresolution technique to yield a numerical method for kinematic models that adaptively concentrates computational effort on zones of strong variation.

All these methods are based on schemes that can be applied universally to systems of conservation laws, and that are not tailored to a particular algebraic structure of the flux vector. The schemes, which are first-order accurate, can be upgraded to higher order accuracy by employing MUSCL-type techniques [124].

## 2.7 Outline of this work

Chapters 3 to 7 of this work are based on original research papers that have been published or are in different stages of review. Slight edits of the journal versions have been applied to attain a uniform reference and citation style, and layout within this work.

In **Chapter 3**, we study an extended clarifier-thickener model given by the equation

$$u_t + f(\gamma(x), u)_x = \gamma^3(x)u_x, \quad (x, t) \in \Pi_T := \mathbb{R} \times (0, T), \quad (2.7.1)$$

where  $\gamma(x) = (\gamma^1(x), \gamma^2(x))$  is a vector of discontinuous parameters which correspond to singular feed sources and flux discontinuities. The discontinuous function  $\gamma^3(x)$  is the transport coefficient of the non-conservative term  $\gamma^3(x)u_x$ , which represents a new singular sink that models the continuous extraction of material from the clarifier-thickener. The function  $\gamma^3$  is a Heaviside-type function whose jump is located at the position of the sink. On the other hand, the functions  $\gamma^1$  and  $\gamma^2$  are continuous across the sink position. Since their discontinuities do not interfere with the sink, and we already know from [31] how to deal with them, we concentrate in Chapter 3 on an initial-value problem for the reduced equation

$$u_t + \varphi(u)_x - \gamma(x)u_x = 0, \quad (x, t) \in \Pi_T. \quad (2.7.2)$$

Roughly speaking, the nonlinear function  $\varphi$  arises from evaluating  $f(\gamma(x), u)$  at a fixed point of continuity of  $\gamma$ , and the remaining discontinuous coefficient  $\gamma$  represents  $\gamma^3$  after the sink has been shifted to  $x = 0$ . We refer to (2.7.1) and (2.7.2) as the *full equation* and the *reduced equation*, respectively. Together with an initial condition and further assumptions on the nonlinearity of the flux and on the discontinuous coefficients, these equations form the *full extended clarifier-thickener model* (or, in short, *full model*) and the *reduced problem*, respectively. We introduce a definition of entropy solutions for the reduced problem, which consists of two separate Kruřkov-type

[114] integral inequalities for the two half-spaces on either side of  $x = 0$ . The solutions on both sides are coupled by a series of jump conditions. We then prove that these jump conditions ensure an  $L^1$  stability property, which implies uniqueness of an entropy solution. We introduce an explicit finite difference scheme for the full model, which is the scheme analyzed in [31] extended by an upwind discretization of  $\gamma^3(x)u_x$ . We prove that the numerical solution remains in the interval  $[0, 1]$ , that the scheme is monotone, that it satisfies a time continuity property, and that for the reduced problem, it converges to an entropy solution. Thus, the reduced problem is well posed. Numerical examples and  $L^1$  error studies demonstrate that several variants of the scheme, which vary in their ease of implementation and level of non-diffusive resolution, converge to entropy solutions of both the reduced problem and the full model.

**Chapter 3** has been published as:

- Bürger, R., García, A., Karlsen, K.H. & Towers, J.D. On an extended clarifier-thickener model with singular source and sink terms. *European Journal of Applied Mathematics* **17** (2006), 257–292.

In **Chapter 4**, we present a new model for continuous separation and classification of polydisperse suspensions, which extends the CT setup (Berres et al. [13], Bürger et al. [31], Diehl [59], Zeidan et al. [174]). The new feature are singular sinks describing the continuous discharge of products at several points, whose composition will vary during a transient startup procedure. The mathematical treatment and discretization of a singular sink is not entirely analogous to that of a singular feed source, since the composition of the sink stream is part of the solution. The singular sinks give rise to a novel so-called non-conservative transport term. The well-posedness of the resulting model and the convergence of a numerical scheme for  $N = 1$  and for sinks located above the feed level or when the whole device is operated as a fluidization column, are proved by Bürger et al. in [23] (Chapter 3 of this thesis). We herein formulate an analogous model for a generalized clarifier-

thickener (GCT) setup, which may include several sinks, can also be operated as a fluidization column, and is allowed to have a varying cross-sectional area. We define a numerical scheme for its simulation and a method to calculate the sinks concentrations, and present numerical examples, in part adopting data from the literature.

**Chapter 4** has been accepted for publication as:

- Bürger, R., García, A., Karlsen, K.H. & Towers, J.D. (2007) A kinematic model of continuous separation and classification of polydisperse suspensions. *Computers & Chemical Engineering*, to appear.

In **Chapter 5**, we formulate, in part analyze, and present numerical experiments for easy-to-implement numerical schemes for kinematic models, in which the numerical flux is explicitly based on the “concentration times velocity” structure of each flux component. The starting point is a simple two-point monotone numerical flux for scalar ( $N = 1$ ) kinematic flows with a non-negative velocity function  $v = v(\phi)$ . We develop extensions of the scheme defined by this numerical flux to equations with a velocity of variable sign, to equations with a discontinuous flux, to systems of conservation laws ( $N \geq 2$  species), and finally to schemes with second-order accuracy. All these variants form the family of new schemes under study. It is proved that for  $N \geq 1$  flows with non-negative velocities, the schemes preserve an invariant region, i.e. generate approximations that assume values in the domain of physically relevant concentrations only. For the scalar case ( $N = 1$ ) and a discontinuous flux, we prove convergence to a  $BV_t$  entropy solution. The proof is based on a new uniform but local estimate of the spatial total variation of approximate solutions. Numerical experiments and  $L^1$  error studies demonstrate the performance of the new family of schemes. What is intriguing about the new schemes is that (other than an estimate of the spectral radius for the CFL condition) they do not require any calculation of eigenvalues, eigenvectors, field-by-field decomposition, flux vector splitting, etc., that are usually required for an upwind scheme. In this sense they are like a central scheme. However, in many cases the first-order accurate version of

the new schemes is much less dissipative than the first-order version of the central scheme (the Lax-Friedrichs scheme).

**Chapter 5** has been accepted for publication as:

- Bürger, R., García, A., Karlsen, K.H. & Towers, J.D. (2007) A family of schemes for kinematic flows with discontinuous flux. *Journal of Engineering Mathematics*, to appear.

In **Chapter 6**, we first extend the well-known Lighthill-Witham-Richards kinematic traffic model to a unidirectional road on which the maximum density  $a(x)$  represents road inhomogeneities, such as variable numbers of lanes, and is allowed to vary discontinuously. The new model can then be described by the initial value problem

$$\phi_t + (\phi v(\phi/a(x)))_x = 0, \quad (x, t) \in \mathbb{R} \times (0, T); \quad \phi(x, 0) = \phi_0(x), \quad x \in \mathbb{R}. \quad (2.7.3)$$

Here  $z \mapsto v(z)$  is the velocity function, where it is assumed that  $v(z) \geq 0$ , and  $z \mapsto v(z)$  is nonincreasing. Since  $a(x)$  is allowed to have a jump discontinuity, (2.7.3) is a scalar conservation law with a spatially discontinuous flux. Moreover, we advance a well-posedness and numerical analysis for the initial value problem (2.7.3). In particular, we present an entropy solution concept, a new uniqueness result including jump conditions, a convergence result for the adaptation of three known schemes for the case with constant  $a$  to the conservation law (2.7.3), and numerical experiments. For each scheme, this adaptation consists the definition of a numerical interface flux that handles the flux discontinuities. For two of the schemes, these interface versions are new. A further novelty of our approach is the application of so-called connections between fluxes adjacent to a flux discontinuity, see e.g. Adimurthi *et al.* [2], in combination with the recent, related concept of adapted entropies for discontinuous flux problems due to Audusse and Perthame [6]. Results of numerical experiments and an  $L^1$  error study are presented both for the first order schemes, and for the MUSCL/Runge-Kutta versions that are formally second order accurate.

**Chapter 6** corresponds to the following article under preparation:

- Bürger, R., García, A., Karlsen, K.H. & Towers, J.D. A difference scheme and entropy solutions for an inhomogeneous kinematic traffic flow model.

In **Chapter 7**, we present a new mathematical model for sedimentation of suspensions with continuous particle size distribution, which extends the one-dimensional kinematic model for batch sedimentation of polydisperse suspensions of small equal-density spheres [12, 32, 158, 170, 175]. We know that polydisperse suspensions with particles of  $N$  distinct size classes have been mainly utilized in laboratory experiments [40, 41, 134, 135, 136]. However, in most real-world applications, for example in mineral processing, the sizes of particles are continuously distributed [40, 170]. To develop the new model, we introduce the so-called phase density function  $\Phi = \Phi(t, x, \xi)$ , where  $\xi \in [0, 1]$  is the normalized squared size of the particles, whose integral with respect to  $\xi$  on an interval  $[\xi_1, \xi_2]$ , is equivalent to the volume fraction at  $(t, x)$  occupied by the particles in that size range. The resulting mathematical model, obtained by using the Masliyah-Lockett-Bassoon (MLB) model [128, 129] for the solid-fluid relative velocity for each solids species and replacing the concept of volume fraction for that of phase density function, is a scalar first-order kinetic equation for  $\Phi$ . We introduce three numerical schemes for the solution of this equation, and a numerical example and an  $L^1$  error study show that one of these schemes introduces not much numerical diffusion and without spurious oscillations near discontinuities. Several numerical examples illustrate the simulated behaviour of this kind of suspensions.

**Chapter 7** corresponds to the following article under preparation:

- Bürger, R., García, A. & Kunik, M. Sedimentation of polydisperse suspensions with a continuous particle size distribution.

In the **Appendix**, we present numerical examples that were part of earlier versions of the article “A kinematic model of continuous separation and classification

of polydisperse suspensions” (Chapter 4 of this work). The choice of examples of the final version of that paper is based on comments we received in the reviews of that. Nevertheless, we decided to include the earlier examples in this thesis, since they represent other interesting cases, such as continuous classification in vessels with rectangular cross-sectional area, classifier operated in clarifier-thickener mode (i.e., the feed flow is divided into upwards- and downwards-directed bulk flows), and continuous classification with changes in the control variables.

## 2.8 Outlook and open problems

In Chapter 3, we have focused on the reduced model and its associated scheme in order to highlight the aspects of the problem that are more or less unique to the sink portion of the model. We leave as an open problem the task of combining the definition of entropy solution and the results of this chapter (well-posedness of reduced problem) with those of [31] (well-posedness of clarifier-thickener model). The goal would be to prove that the full problem is well-posed. On the other hand, due to that the formation of a jump of concentration across the sink level  $x = x_D$  is possible, the value  $u(x_D, t)$  becomes indeterminate, and therefore, it is necessary to develop a method to calculate the solids concentration of the suspension extracted through the sink. We leave the devise and analysis of that method as other open problem.

In Chapter 4, an open problem would be the well-posedness analysis of the generalized clarifier-thickener model. Moreover, it is possible to improve this model by means of others slip velocity models, diffusive-like models, additional balance equations (of lineal momentum, energy), multidimensional treatment, etc. On the other hand, we propose a numerical method to calculate the solids concentration in the sinks, from mass balances of solids and based on the finite speed of propagation of the concentration waves. We leave the analysis of this method as other open problem.

In Chapter 5, open problems would be proving that for the polydisperse sedimentation model, Schemes 6, 7 and 8 generate approximations that assume values

in the domain of physically relevant concentrations; and studying the oscillations in the solution using Scheme 9 (of second order) at the location of a large jump in  $\phi$ .

In Chapter 6, if the flux is not strictly concave, our entropy theory will give jumps that may not be completely in agreement with our motivation in terms of traffic flow. The question of how to modify the definition of entropy solution, and also the difference schemes, so that the entropy theory completely agrees with our notion of driver behavior is an interesting open problem.

In Chapter 7, an open problem is the eigenvalue analysis of the model equation.



## Chapter 3

# On an Extended Clarifier-Thickener Model with Singular Source and Sink Terms

A one-dimensional model of clarifier-thickener units in engineering applications can be expressed as a conservation law with a flux that is discontinuous with respect to the spatial variable. This model also includes a singular feed source. In this paper, the clarifier-thickener model studied in the paper Numer. Math. **97** (2004) 25–65, is extended by a singular sink through which material is extracted from the unit. A difficulty is that in contrast to the singular source, the sink term cannot be incorporated into the flux function; rather, the sink is represented by a new non-conservative transport term. To focus on the new analytical difficulties arising due to this non-conservative term, a reduced problem is formulated, which contains the new sink term of the extended clarifier-thickener model, but not the source term and flux discontinuities. The paper is concerned with numerical methods for both models (extended and reduced) and with the well-posedness analysis for the reduced problem. For the reduced problem, a definition of entropy solutions, based on Kružkov-type entropy functions and fluxes, is provided. Jump conditions are derived and uniqueness of the entropy

solution is shown. Existence of an entropy solution is shown by proving convergence of a monotone difference scheme. Two variants of the numerical scheme are introduced. Numerical examples illustrate that all three variants converge to the entropy solution, but introduce different amounts of numerical diffusion.

## 3.1 Introduction

### 3.1.1 Scope

In recent years there has been an increased interest in the analysis and numerics of conservation laws of the type  $u_t + f(\gamma(x), u)_x = 0$ , where  $\gamma(x)$  is a vector of parameters that depend discontinuously on the spatial position  $x$ . This equation is the main ingredient of a clarifier-thickener model (see e.g. [28, 31, 34, 53]), but also appears in other applications [27, 33, 39, 102, 132, 141, 148, 164]. We herein study an extended clarifier-thickener model given by the equation

$$u_t + f(\gamma(x), u)_x = \gamma^3(x)u_x, \quad (x, t) \in \Pi_T := \mathbb{R} \times (0, T), \quad (3.1.1)$$

where  $\gamma(x) = (\gamma^1(x), \gamma^2(x))$  is a vector of discontinuous parameters which correspond to singular feed sources and flux discontinuities. The discontinuous function  $\gamma^3(x)$  is the transport coefficient of the non-conservative term  $\gamma^3(x)u_x$ , which represents a new singular sink that models the continuous extraction of material from the clarifier-thickener. The function  $\gamma^3$  is a Heaviside-type function whose jump is located at the position of the sink. On the other hand, the functions  $\gamma^1$  and  $\gamma^2$  are continuous across the sink position. Since their discontinuities do not interfere with the sink, and we already know from [31] how to deal with them, we concentrate in this paper on an initial-value problem for the reduced equation

$$u_t + \varphi(u)_x - \gamma(x)u_x = 0, \quad (x, t) \in \Pi_T. \quad (3.1.2)$$

Roughly speaking, the nonlinear function  $\varphi$  arises from evaluating  $f(\gamma(x), u)$  at a fixed point of continuity of  $\gamma$ , and the remaining discontinuous coefficient  $\gamma$  represents  $\gamma^3$  after the sink has been shifted to  $x = 0$ . We refer to (3.1.1) and (3.1.2) as the

*full equation* and the *reduced equation*, respectively. Together with an initial condition and further assumptions on the nonlinearity of the flux and on the discontinuous coefficients, these equations form the *full extended clarifier-thickener model* (or, in short, *full model*) and the *reduced problem*, respectively.

In this paper, we introduce a definition of entropy solutions for the reduced problem, which consists of two separate Kružkov-type [114] integral inequalities for the two half-spaces on either side of  $x = 0$ . The solutions on both sides are coupled by a series of jump conditions. We then prove that these jump conditions ensure an  $L^1$  stability property, which implies uniqueness of an entropy solution. We introduce an explicit finite difference scheme for the full model, which is the scheme analyzed in [31] extended by an upwind discretization of  $\gamma^3(x)u_x$ . We prove that the numerical solution remains in the interval  $[0, 1]$ , that the scheme is monotone, that it satisfies a time continuity property, and that for the reduced problem, it converges to an entropy solution. Thus, the reduced problem is well posed. Numerical examples demonstrate that several variants of the scheme, which vary in their ease of implementation and level of non-diffusive resolution, converge to entropy solutions of both the reduced problem and the full model.

To put the treatment in the proper perspective, let us first recall some known results for the equation  $u_t + f(\gamma(x), u)_x = 0$ . The basic difficulty is that its well-posedness is not a straightforward limit case of the standard theory for conservation laws with a flux that depends smoothly on  $x$ . In fact, several extensions of the Kružkov entropy solution concept [114] to conservation laws with a discontinuous flux were proposed in recent years [3, 6, 7, 80, 82, 103, 106, 112, 113, 130, 150, 159, 160]. Each of these concepts is supported by a convergence analysis of a numerical scheme; the differences between them appear in the respective admissibility conditions for stationary jumps of the solution across the discontinuities of  $\gamma$  [29].

The choice of the entropy solution concept depends on the regularizing viscous physical model. For clarifier-thickener models, the appropriate concept emerges from the limit  $\varepsilon \rightarrow 0$  of a viscous regularization  $\varepsilon u_{xx}$  with a diffusion constant  $\varepsilon > 0$  [34]. Thorough analyses of and construction of exact entropy solutions for

clarifier-thickener models were advanced by Diehl [52, 53, 54, 55, 56, 57]. On the other hand, the authors with collaborators made a series of contributions (including [13, 28, 30, 31, 34, 35]) to the well-posedness and numerical analysis for these models, whose basic non-standard ingredient is a singular feed source that produces diverging bulk flows, which causes the discontinuous  $x$ -dependence of the flux.

We may also write the reduced equation (3.1.2) as a non-strictly hyperbolic system

$$\begin{aligned} a_t = 0, \quad u_t + F(a, u)_x - G(a, u)a_x = 0, \quad x \in \mathbb{R}, \quad t \geq 0; \\ (a, u)(0, x) = (a_0(x), u_0(x)), \quad x \in \mathbb{R}, \end{aligned} \quad (3.1.3)$$

where we define  $a_0(x) := H(x)$ ,  $G(a, u) := u$  and  $F(a, u) := (q + a)u + b(u)$ . In passing, we note that for  $F(a, u) := f(a, u)$ ,  $G \equiv 0$ , and  $a_0(x) := \gamma(x)$ , (3.1.3) is equivalent to the Cauchy problem for  $u_t + f(\gamma(x), u)_x = 0$  with a scalar discontinuous parameter  $\gamma(x)$ . The resulting triangular hyperbolic system has been the starting point of several analyses of this Cauchy problem [28, 54, 61, 80, 82, 112, 113].

Systems of the type (3.1.3) with  $G \not\equiv 0$  were recently analyzed by Amadori et al. [4]. They solve the Riemann problem for (3.1.3), prove convergence of a Godunov scheme, and address uniqueness by a Kružkov-type technique. However, our reduced model is not a sub-case included in their analysis, since some of their structural assumptions are not satisfied in our case. For example, their requirement (P<sub>4</sub>), stating that  $F_a - G \neq 0$  for all  $(a, u)$  with  $F_u(a, u) = 0$ , is not satisfied, since  $F_a - G \equiv 0$  in our case. Let us point out that their uniqueness result does not hold for a discontinuous coefficient  $a$ , while our approach does include uniqueness.

### 3.1.2 Reduced problem and full model

The novel feature of our new extended clarifier-thickener model is a singular sink through which material may be extracted. The reduced problem emerges from the new model if the “unit” is assumed to have a sink only, but no sources, and is defined by the reduced equation (3.1.2) along with

$$u(x, 0) = u_0(x), \quad x \in \mathbb{R}, \quad u_0 \in [0, u_{\max}], \quad u_{\max} \in (0, 1], \quad (3.1.4)$$

$$\varphi(u) = qu + b(u), \quad \gamma(x) = \begin{cases} 0 & \text{for } x < 0, \\ \gamma_+ & \text{for } x > 0, \end{cases} \quad q \leq 0, \gamma_+ > 0. \quad (3.1.5)$$

Here, the function  $b(u)$  is assumed to be Lipschitz continuous, positive for  $u \in (0, 1)$ , and to vanish for  $u \notin (0, 1)$ . We assume that  $b(u)$  is twice differentiable in  $(0, 1)$ , that  $b'(u) = 0$  at exactly one location  $u = u_b^* \in (0, 1)$ , where  $b(u)$  has a maximum, and that  $b''(u) = 0$  at no more than one inflection point  $u_{\text{infl}} \in (0, 1)$ ; if such a point is present, we assume that  $u_{\text{infl}} \in (u_b^*, 1)$ . The restriction  $q \leq 0$  is required in the stability and uniqueness analysis. See Section 3.2 for a detailed derivation.

If we set  $u_{\text{max}} = 1$ , then the assumptions on  $b(u)$  are satisfied by the frequently used Richardson-Zaki [147] type function

$$b(u) = \begin{cases} v_\infty u(1-u)^n & \text{for } u \in [0, u_{\text{max}}], \\ 0 & \text{otherwise,} \end{cases} \quad n > 1, \quad v_\infty > 0, \quad (3.1.6)$$

where  $v_\infty$  is the settling velocity of a single particle in an unbounded medium. With the assumptions on  $b(u)$  and the sign of  $q$ , the flux  $\varphi(u)$  has a single maximum at  $u^* \in [0, 1]$ , and  $\varphi$  is non-decreasing on  $[0, u^*]$  and non-increasing on  $[u^*, 1]$ .

The full model is defined by (3.1.1) along with the initial condition (3.1.4) and

$$f(\gamma(x), u) := \gamma^1(x)b(u) + \gamma^2(x)(u - u_F), \quad \gamma(x) := (\gamma^1(x), \gamma^2(x)), \quad (3.1.7)$$

$$\gamma^1(x) := \begin{cases} 0 & \text{for } x \notin [x_L, x_R], \\ 1 & \text{for } x \in [x_L, x_R], \end{cases} \quad \gamma^2(x) := \begin{cases} \tilde{q}_R - q_F & \text{for } x < 0, \\ \tilde{q}_R & \text{for } x > 0, \end{cases} \quad (3.1.8)$$

where  $u_F$  denotes the feed concentration,  $x_L < x_D < 0 < x_R$  are the overflow, sink, and discharge levels, respectively, reflecting the design of the unit, and  $\tilde{q}_R < 0$  and  $q_F > 0$  are given bulk flow velocities describing operating conditions. Thus,  $f(\gamma(x), u)$  incorporates the batch flux, the source term, and the discontinuities at the discharge and overflow levels. (The precise meaning of all variables is given in Section 3.2.) Finally, the discontinuous transport coefficient  $\gamma^3(x)$  is given by

$$\gamma^3(x) := \begin{cases} 0 & \text{for } x < x_D, \\ -q_D > 0 & \text{for } x > x_D, \end{cases} \quad (3.1.9)$$

where  $q_D < 0$  is another velocity related to sink control (see Section 3.2). Observe that the full model is defined by a conservation law with a flux that is discontinuous at the source and transition points, but *not* at the location of the singular sink.

### 3.1.3 Outline of the paper

The remainder of this paper is organized as follows. The full extended clarifier-thickener model and the reduced problem are derived in Section 3.2. For the reduced problem, we present in Section 3.3 the definition of entropy solutions and, using the jump conditions, establish an  $L^1$  stability property, which implies uniqueness of an entropy solution.

In Section 3.4, we introduce an explicit finite difference scheme for the full model, and prove that the numerical solution remains in the interval  $[0, 1]$ , that the scheme is monotone, and that it satisfies a time continuity property. In Section 3.5 we focus on the reduced problem and prove that the scheme satisfies a spatial variation bound. Starting from a discrete entropy inequality, using the monotonicity and proceeding as in the proof of the Lax-Wendroff theorem, we then show that the scheme converges to an entropy solution of the reduced problem. The analysis is summarized in Theorem 3.5.1 stating the well-posedness of the reduced problem.

Several suitable schemes for the reduced or full equation can be formulated by combining upwind discretizations for the linear terms with an Engquist-Osher type numerical flux for the remaining nonlinear portion. Based on this observation, we introduce in Section 3.6 two different variants of our scheme, which are referred to as “Scheme 1” and “Scheme 3”, respectively, while the scheme analyzed so far is called “Scheme 2”. (This nomenclature anticipates the observed ranking in performance.) The analysis of Scheme 2 in Sections 3.4 and 3.5 also fully holds for Scheme 1. The convergence result also applies to Scheme 3, while the entropy analysis may require different arguments. Numerical examples for the three schemes are presented in Section 3.7 for both the reduced problem and the complete model.

Section 3.8 collects some conclusions that can be drawn from our well-posedness

and numerical analysis. Moreover, we comment on the numerical results of Section 3.7. It turns out that although all three schemes converge to the entropy solution, they significantly differ in the degree of numerical diffusion introduced. Scheme 1 is very easy to implement, but turns out to be very diffusive, especially for steady-state, while Scheme 3 produces sharp resolution.

## 3.2 The extended clarifier-thickener model

### 3.2.1 Clarifier-thickener models, singular sources, and singular sinks

Clarifier-thickener units are widely used in chemical engineering, wastewater treatment, mineral processing and other applications to separate a suspension of finely divided solid particles dispersed in a viscous fluid into its solid and liquid components. The basic clarifier-thickener model can be derived from the scalar conservation law

$$u_t + b(u)_x = 0, \quad x \in [0, L], \quad t > 0; \quad u(x, 0) = u_0(x), \quad x \in [0, L] \quad (3.2.1)$$

of the kinematic sedimentation model [38, 120], which describes the settling of a suspension of initial concentration  $u_0(x)$  in a settling vessel of height  $L$ . Here,  $u$  is the sought concentration as a function of depth  $x$  and time  $t$ , and  $b(u)$  is the hindered settling function or batch flux density function, which is a material-dependent function. A typical example is the function (3.1.6).

Suppose now that we pump the suspension into a vertical tube that is filled with water at a feed level  $x = 0$ , and that part of the mixture flows upwards at velocity  $q_L < 0$ , while the remainder flows downwards at velocity  $q_R > 0$ , as in the left diagram of Figure 3.1. Consequently, if  $\mathcal{S}$  is the cross-sectional area of the tube, then  $Q_F = (q_R - q_L)\mathcal{S}$ . Assuming for a moment that we inject only clear water at  $x = 0$ ,

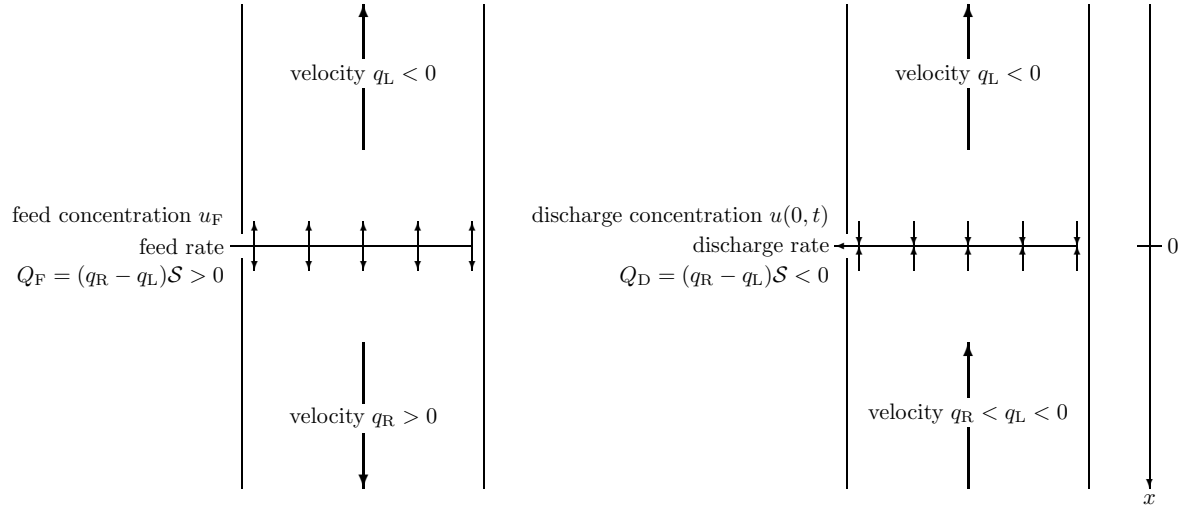


Figure 3.1: Basic flow variables for a singular source term (left) and a singular sink term (right).

we obtain the conservation law with discontinuous flux

$$u_t + (q(x)u + b(u))_x = 0, \quad q(x) := \begin{cases} q_L < 0 & \text{for } x < 0, \\ q_R > 0 & \text{for } x > 0. \end{cases} \quad (3.2.2)$$

Now let us inject feed suspension of a given concentration  $u_F$  at a volume rate  $Q_F$ . Since the feed source is concentrated at  $x = 0$ , we need to add the singular source term  $\delta(x)(q_R - q_L)u_F$  to the right-hand side of the equation in (3.2.2), obtaining

$$u_t + (q(x)u + b(u))_x = \delta(x)(q_R - q_L)u_F. \quad (3.2.3)$$

However, using the Heaviside function  $H(x)$ , we may formally write

$$\delta(x)(q_R - q_L)u_F = (H(x)(q_R - q_L)u_F)_x.$$

Then (3.2.3) assumes the form

$$u_t + \left( q(x)u + b(u) - (H(x)(q_R - q_L)u_F) \right)_x = 0, \quad (3.2.4)$$

so that the singular source is expressed as a discontinuity of the flux function. This is possible since  $u_F$  is a *given* constant (or possibly a given (control) function of  $t$ ). Thus, the governing conservation law can be written as

$$u_t + g(u, x)_x = 0, \quad g(u, x) := \begin{cases} q_L(u - u_F) + b(u) & \text{for } x < 0, \\ q_R(u - u_F) + b(u) & \text{for } x \geq 0. \end{cases} \quad (3.2.5)$$

Note that the *injection* of material of given concentration and at given rate leads to a homogeneous conservation law with discontinuous flux. This property has made the clarifier-thickener model tractable.

In the present work, we extend the clarifier-thickener model to the case that we also extract material at a fixed location. To elucidate the problem, consider a column with an upwards directed bulk flow of  $Q_R < 0$ . At depth  $x = 0$ , we divide the flow into a discharge flow  $Q_D < 0$  and the remaining upwards directed bulk flow  $Q_L$  with  $Q_R < Q_L < 0$ , see the right diagram of Figure 3.1. Considering that the concentration  $u(0, t)$  of the suspension extracted is unknown beforehand and defining  $q_R := Q_R/S$  and  $q_L := Q_L/S$ , we obtain instead of (3.2.5) the equation

$$u_t + h(u, x)_x = \delta(x)(q_R - q_L)u(x, t), \quad h(u, x) = \begin{cases} q_L u + b(u) & \text{for } x < 0, \\ q_R u + b(u) & \text{for } x > 0. \end{cases} \quad (3.2.6)$$

Note that we cannot use the Heaviside function in the same way as in (3.2.4), since now the solution value  $u(x, t)$  replaces the constant  $u_F$  in the singular term. This difference justifies studying the sink term problem in its own right, rather than claiming that it is just analogous to the source term problem.

Finally, let us mention that several researchers in chemical engineering and mineral processing have reported experiments with separation devices that can be modeled by the extended clarifier-thickener concept by possibly considering several discharge sink terms located at different depths. (It is clear that if we know how to properly handle one sink term, then we can also deal with any array of them.) References to experimental information include [71, 72, 73, 134, 135, 136, 139, 154].

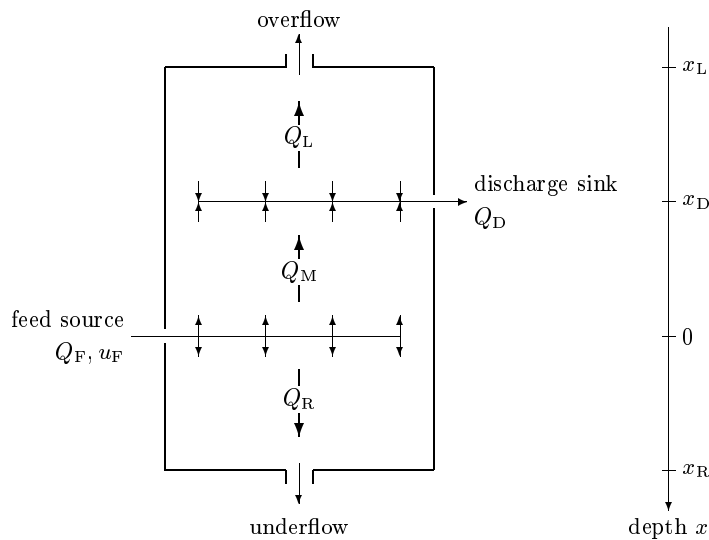


Figure 3.2: The extended clarifier-thickener setup showing the known bulk flows and control variables.

### 3.2.2 Bulk flow variables

Consider the extended clarifier-thickener drawn in Figure 3.2, which is supposed to have a constant cross-sectional area  $\mathcal{S}$ . This setup is similar to that considered in [28, 30, 31], but is equipped with an additional sink located at depth  $x_D$ . This (of course, idealized) unit is operated as follows.

At  $x = 0$ , suspension is fed into the unit at a volume rate  $Q_F(t) \geq 0$ . The feed suspension is loaded with solids of the volume fraction  $u_F(t) \in [0, u_{\max}]$ , where  $u_{\max}$  is a maximum solids concentration. At  $x = 0$ , the feed flow divides into an upwards-directed and a downwards-directed bulk flow. We also prescribe the underflow volume rate  $Q_R(t) \geq 0$  with  $Q_R(t) \leq Q_F(t)$ . Thus, the signed volume rate of the upwards-directed bulk flow immediately above the feed source is

$$Q_M(t) = Q_R(t) - Q_F(t) \leq 0. \quad (3.2.7)$$

At depth  $x = x_D$ ,  $x_L < x_D < 0$ , a discharge sink is located. Suspension is extracted from the column at a signed volume rate  $Q_D(t) \leq 0$ , where we assume  $Q_D(t) \geq Q_M(t)$ . Above the discharge sink, for  $x_L \leq x \leq x_D$ , there is an upwards directed bulk

flow with the volume rate

$$Q_L(t) = Q_M(t) - Q_D(t) = Q_R(t) - Q_F(t) - Q_D(t) \leq 0. \quad (3.2.8)$$

Summarizing, we prescribe the volume rates  $Q_F(t)$ ,  $Q_R(t)$  and  $Q_D(t)$  and the feed concentration  $u_F(t)$  as independent control variables. From these we calculate the dependent control variables  $Q_M(t)$  and  $Q_L(t)$  by (3.2.7) and (3.2.8), respectively.

For the remainder of the paper, we assume that all control variables are constant, and introduce the velocities  $q_c := Q_c/\mathcal{S}$ ,  $c \in \{D, F, L, M, R\}$ . Disregarding for a moment the solids sources and sinks but taking into account the bulk flows and utilizing independent control variables only, we can write the flux function as

$$\tilde{g}(u, x) = \begin{cases} (q_R - q_F - q_D)u & \text{for } x \leq x_L, \\ (q_R - q_F - q_D)u + b(u) & \text{for } x_L < x \leq x_D, \\ (q_R - q_F)u + b(u) & \text{for } x_D < x \leq 0, \\ q_R u + b(u) & \text{for } 0 < x \leq x_R, \\ q_R u & \text{for } x > x_R. \end{cases} \quad (3.2.9)$$

### 3.2.3 Solids feed and sink terms

Including now the solids feed and sink mechanisms, we obtain the conservation law with source terms

$$\begin{aligned} u_t + \tilde{g}(u, x)_x &= q_F u_F \delta(x) + q_D u(x, t) \delta(x - x_D) \\ &= q_F u_F H'(x) + q_D (H(x - x_D) u(x, t))_x - q_D H(x - x_D) u_x(x, t), \end{aligned} \quad (3.2.10)$$

where  $\delta(\cdot)$  denotes the Dirac delta mass. Observe that the differentiation by parts used here,

$$u(x, t) \delta(x - x_D) = (H(x - x_D) u(x, t))_x - H(x - x_D) u_x(x, t),$$

is not defined in the sense of distributions. However, we continue to use the second equality in (3.2.10) as the defining equation of the extended clarifier-thickener

model. This is supported by the integral version of the balance law, and the desired effect of the singular sink. Namely, if we fix  $a \in (x_L, x_D)$  and  $b \in (x_D, 0)$ , so that  $x_D \in [a, b]$  and define the total amount of solids

$$U_{[a,b]}(t) := \int_a^b u(x, t) dx,$$

then the rate of change of  $U_{[a,b]}(t)$  should be given by the solids flux through  $x = a$  minus the flux through  $x = b$  minus the rate at which solids are extracted through  $x = x_D$ . However, integrating the second equality in (3.2.10) over  $[a, b]$ , taking into account the definition of  $g(x, u)$  and assuming that the solution is smooth, we obtain

$$\begin{aligned} U'_{[a,b]}(t) &= -(\tilde{g}(u(b, t), b) - \tilde{g}(u(a, t), a)) + q_D H(b - x_D)u(b, t) - q_D H(a - x_D)u(a, t) \\ &\quad - q_D \int_a^b H(x - x_D)u_x(x, t) dx \\ &= -(\tilde{g}(u(b, t), b) - \tilde{g}(u(a, t), a)) + q_D u(b, t) - q_D \int_{x_D}^b u_x(x, t) dx \\ &= \tilde{g}(u(a, t), b) - \tilde{g}(u(b, t), b) + q_D u(x_D, t), \end{aligned}$$

which ensures equivalence at least at the level of smooth solutions between the first equation of (3.2.10) and the full extended clarifier-thickener model (3.1.1).

Next, absorbing the term  $q_F u_F H'(x) + q_D (H(x - x_D)u(x, t))_x$  into the convective flux yields the equation

$$u_t + g(u, x)_x = -q_D H(x - x_D)u_x(x, t), \quad (3.2.11)$$

where, after defining  $\tilde{q}_R := q_R - q_D$  and adding  $-q_L u_F$ , we obtain the flux function

$$g(u, x) = \begin{cases} (\tilde{q}_R - q_F)(u - u_F) & \text{for } x \leq x_L, \\ (\tilde{q}_R - q_F)(u - u_F) + b(u) & \text{for } x_L < x \leq 0, \\ \tilde{q}_R(u - u_F) + b(u) & \text{for } 0 < x \leq x_R, \\ \tilde{q}_R(u - u_F) & \text{for } x > x_R, \end{cases} \quad (3.2.12)$$

which is continuous across  $x = x_D$ . Defining the discontinuous parameters  $\gamma^1(x)$ ,  $\gamma^2(x)$  and  $\gamma^3(x)$  via (3.1.8) and (3.1.9) yields  $g(u, x) = f(\gamma(x), u)$ , where  $f(\gamma(x), u)$

is defined by (3.1.7), so that the governing balance law (3.2.11) takes the final form (3.1.1).

### 3.2.4 Reduced problem

The analysis in this paper is focused on the reduced problem (3.1.2), (3.1.4), (3.1.5), which emerges from the model derived above if we consider only the vicinity of the sink term and assume that the velocities have been normalized such that  $q_D$  (in the original problem description) equals  $-\gamma_+$ , and that  $q \leq 0$ . Recall that we refer to (3.1.2), (3.1.4), (3.1.5) as *reduced problem*, while (3.1.1), (3.1.4), and (3.1.7)–(3.1.9) form the *full extended clarifier-thickener model* (in short, *full model*).

## 3.3 Entropy solution and uniqueness analysis of the reduced problem

Before stating the definition of entropy solution, we recall the notation  $a \vee b := \max\{a, b\}$ ,  $a \wedge b := \min\{a, b\}$ . Also, we use the notation  $\mathcal{D}(\Pi_T)$  to denote the set of test functions;  $\mathcal{D}(\Pi_T) = C_c^\infty(\Pi_T)$ .

**Definition 3.3.1 (Entropy solution)** *A function  $u : \Pi_T \mapsto \mathbb{R}$  is an entropy solution of the initial value problem (3.1.2), (3.1.4), (3.1.5) if it satisfies the following conditions:*

(D.1)  $u \in L^1(\Pi_T) \cap BV(\Pi_T)$  and  $u(x, t) \in [0, 1]$  for a.e.  $(x, t) \in \Pi_T$ .

(D.2) If  $0 \leq \psi \in \mathcal{D}(\Pi_T)$  vanishes for  $x > 0$ , then

$$\iint_{\Pi_T} \left( |u - c| \psi_t + \operatorname{sgn}(u - c) (\varphi(u) - \varphi(c)) \psi_x \right) dt dx \geq 0 \quad \forall c \in \mathbb{R}, \quad (3.3.1)$$

and if  $0 \leq \psi \in \mathcal{D}(\Pi_T)$  vanishes for  $x < 0$ , then

$$\iint_{\Pi_T} \left( |u - c| \psi_t + \operatorname{sgn}(u - c) (\varphi(u) - \varphi(c) - \gamma_+(u - c)) \psi_x \right) dt dx \geq 0 \quad (3.3.2)$$

$\forall c \in \mathbb{R}.$

(D.3) With the abbreviation  $u_{\pm} = u(0\pm, t)$ , the following jump conditions hold at  $x = 0$  for a.e.  $t \in (0, T)$ : if  $u_- \leq c \leq u_+$ , then

$$\varphi(u_+) - \varphi(c) \leq \gamma_+(u_+ - c), \quad (3.3.3)$$

$$\varphi(u_-) - \varphi(c) \leq 0, \quad (3.3.4)$$

and if  $u_- \geq c \geq u_+$ , then

$$\varphi(u_+) - \varphi(c) \geq \gamma_+(u_+ - c), \quad (3.3.5)$$

$$\varphi(u_-) - \varphi(c) \geq 0. \quad (3.3.6)$$

(D.4) The initial condition is satisfied in the following strong  $L^1$  sense:

$$\operatorname{ess\,lim}_{t \downarrow 0} \int_{\mathbb{R}} |u(x, t) - u_0(x)| dx = 0. \quad (3.3.7)$$

**Remark 3.3.1** For the full extended clarifier-thickener model captured by equation (3.1.1), we would have to replace the condition  $u \in BV(\Pi_T)$  by the weaker condition  $u \in BV_t(\Pi_T)$ . Here  $BV_t(\Pi_T)$  is the class of functions  $W(x, t)$  with  $\partial_t W$  being a finite measure. The presence of the discontinuities in the parameter vector  $\gamma$  makes it difficult (in the case of the extended model (3.1.1)) to get global control of the spatial variation of the solution  $u$ .

**Remark 3.3.2** It is clear from (3.3.1), (3.3.2) that if  $u$  is an entropy solution in the sense of Definition 3.3.1, then for  $x < 0$ ,  $u$  is an entropy solution in the usual Kružkov sense of the conservation law  $u_t + \varphi(u)_x = 0$ , while for  $x > 0$ ,  $u$  is an entropy solution (in the usual Kružkov sense) of the conservation law  $u_t + (\varphi(u) - \gamma_+ u)_x = 0$ .

**Remark 3.3.3** The reduced equation (3.1.2) has a so-called non-conservative product. More specifically, we have what amounts to a  $\delta$  function,  $u_x$ , multiplied by a discontinuous function  $\gamma(x)$ . We expect a jump condition of the form

$$\varphi(u_+) - \varphi(u_-) = \bar{\gamma}(u_+ - u_-), \quad (3.3.8)$$

where  $\bar{\gamma}$  is some intermediate value of  $\gamma$ , i.e.  $0 = \gamma_- \leq \bar{\gamma} \leq \gamma_+$ . In fact, when  $u_- \leq u_+$ , we can take  $c = u_-$  in (3.3.3) and then  $c = u_+$  in (3.3.4) to get

$$0 \leq \varphi(u_+) - \varphi(u_-) \leq \gamma_+(u_+ - u_-),$$

which implies (3.3.8). Similarly, when  $u_- \geq u_+$ , we can take  $c = u_-$  in (3.3.5) and then  $c = u_+$  in (3.3.6) to get

$$\gamma_+(u_+ - u_-) \leq \varphi(u_+) - \varphi(u_-) \leq 0,$$

which again implies (3.3.8).

From the jump conditions in Definition 3.3.1 we derive the following additional jump conditions.

**Lemma 3.3.1** *Let  $u$  be an entropy solution of the reduced problem in the sense of Definition 3.3.1. The following jump conditions hold at  $x = 0$  for a.e.  $t \in (0, T)$  for which  $u_-(t) \neq u_+(t)$ :*

$$0 \leq \frac{\varphi(u_+) - \varphi(u_-)}{u_+ - u_-} \leq \gamma_+, \quad (3.3.9)$$

$$u_+ < u_- \Rightarrow u_+ < u_- \leq u^*, \quad (3.3.10)$$

where  $u^*$  is the single maximum of  $\varphi(u)$  (see Subsection 3.1.2).

**Proof.** To prove (3.3.9), first take the case where  $u_- < u_+$ . Letting  $c = u_-$  in (3.3.3), and then  $c = u_+$  in (3.3.4), yields the inequalities

$$\varphi(u_+) - \varphi(u_-) \leq \gamma_+(u_+ - u_-), \quad \varphi(u_+) - \varphi(u_-) \geq 0,$$

which imply inequality (3.3.9). If  $u_+ < u_-$ , we arrive at (3.3.9) by a similar calculation, this time taking  $c = u_-$  in (3.3.5), and then  $c = u_+$  in (3.3.6).

To prove (3.3.10), it suffices to show that neither of the orderings  $u_+ \leq u^* < u_-$ ,  $u^* < u_+ < u_-$  is possible. If  $u_+ \leq u^* < u_-$ , letting  $c = u^*$  in (3.3.6) results in  $\varphi(u^*) - \varphi(u_-) \leq 0$ , which contradicts our assumptions about the shape of the graph of  $u \mapsto \varphi(u)$ . If  $u^* < u_+ < u_-$ , letting  $c = u^+$  in (3.3.6) yields  $\varphi(u_+) - \varphi(u_-) \leq 0$ . Since  $\varphi$  is strictly decreasing on  $[u^*, 1]$ , this is a contradiction.  $\square$

**Remark 3.3.4** In the absence of the sink term ( $\gamma_+ = 0$ ), the jump condition (3.3.9) becomes

$$\frac{\varphi(u_+) - \varphi(u_-)}{u_+ - u_-} = 0,$$

which is the usual Rankine-Hugoniot condition satisfied by a zero-speed discontinuity for the conservation law  $u_t + \varphi(u)_x = 0$ . Based on this observation, it seems that (3.3.9) is playing the role of a Rankine-Hugoniot condition for a steady jump located at  $x = 0$  where the delta-function due to the sink term is concentrated. Maintaining for the moment our focus on the situation where  $\gamma_+ = 0$ , the shape of the flux function  $u \mapsto \varphi(u)$ , along with the Rankine-Hugoniot condition,  $\varphi(u_+) = \varphi(u_-)$ , requires that  $u^*$  lies between  $u_-$  and  $u_+$ . It follows from (3.3.10) that in this situation  $u_- < u^* < u_+$  if  $u_- \neq u_+$ . Thus when  $\gamma_+ = 0$ , the local entropy condition implied by the jump conditions (D.3) is the classical Lax condition for a steady shock.

**Remark 3.3.5** If we set  $\varphi \equiv 0$ , the partial differential equation (3.1.2) reduces to

$$u_t - \gamma(x)u_x = 0, \tag{3.3.11}$$

a simple transport equation. Note that due to the form of the coefficient  $\gamma(x)$ , the interface values  $u(0_-, t)$  and  $u(0_+, t)$  are determined by the initial data alone, i.e., no interface conditions are required. Indeed, in the limiting case where  $\varphi$  vanishes, our jump conditions at  $x = 0$  are satisfied trivially, i.e., they impose no restrictions on  $u_-$  and  $u_+$ . Using (3.3.1), (3.3.2) and (3.3.7), we find that the solution to (3.3.11) that is dictated by our definition of entropy solution is

$$u(x, t) = \begin{cases} u_0(x) & \text{for } x < 0, \\ u_0(x + \gamma_+ t) & \text{for } x > 0, \end{cases} \tag{3.3.12}$$

as expected from the form of (3.3.11) and the definition of  $\gamma$ . We refer the reader to the work of Bouchut and James [17] for a detailed study of linear transport equations with discontinuous coefficients such as (3.3.11). Note that (3.3.11) can be written in the form of [17, Eq. (1.1)],  $u_t + a(x)u_x = 0$ , if we define  $a(x) = -\gamma(x)$ . In view of our definition of  $\gamma(x)$ , (3.1.5), the function  $a(x)$  is then piecewise constant with

one decreasing jump. Thus, the one-sided Lipschitz condition [17, (1.8)] is trivially satisfied, and our solution (3.3.12) of (3.3.11) is also a solution in the sense of [17].

We are now ready to prove that entropy solutions are  $L^1$  stable and hence unique.

**Theorem 3.3.2 ( $L^1$  stability and uniqueness)** *Let  $u$  and  $v$  be two entropy solutions in the sense of Definition 3.3.1 of the initial value problem (3.1.2), (3.1.4), (3.1.5) with initial data  $u_0$  and  $v_0$ , respectively. Then, for a.e.  $t \in (0, T)$ ,*

$$\int_{\mathbb{R}} |u(x, t) - v(x, t)| dx \leq \int_{\mathbb{R}} |u_0(x) - v_0(x)| dx.$$

*In particular, there exists at most one entropy solution of the reduced model (3.1.2), (3.1.4), (3.1.5).*

**Proof.** Using standard methods and in particular the doubling of variables technique [114], one can derive from (3.3.1) and (3.3.2) the following pair of integral inequalities for  $u$  and  $v$ :

$$\begin{aligned} \forall \psi^1 \in \mathcal{D}(\Pi_T), \quad \psi^1(x, t) = 0 \text{ for } x > 0: \\ \iint_{\Pi_T} \left( |u - v| \psi_t^1 + \operatorname{sgn}(u - v) (\varphi(u) - \varphi(v)) \psi_x^1 \right) dt dx \geq 0, \end{aligned} \quad (3.3.13)$$

$$\begin{aligned} \forall \psi^2 \in \mathcal{D}(\Pi_T), \quad \psi^2(x, t) = 0 \text{ for } x < 0: \\ \iint_{\Pi_T} \left( |u - v| \psi_t^2 + \operatorname{sgn}(u - v) (\varphi(u) - \varphi(v) - \gamma_+(u - v)) \psi_x^2 \right) dt dx \geq 0. \end{aligned} \quad (3.3.14)$$

An approximation argument reveals that we may choose  $\psi^1(x, t) = \Phi(t) \nu_h(x)$  and  $\psi^2(x, t) = \Phi(t) \mu_h(x)$ , where  $\Phi \in C_0^2(0, T)$ ,  $\Phi(\cdot) \geq 0$ , and  $\{\mu_h\}_{h>0}$  and  $\{\nu_h\}_{h>0}$  are standard boundary layer sequences that are assumed to satisfy  $\mu_h \in C^1(\mathbb{R})$ ,  $\mu_h(x) = 0$  for  $x \leq 0$ ,  $0 \leq \mu_h(\cdot) \leq 1$ ,  $\mu_h(x) = 1$  for  $x > h$ ,  $|\mu_h'(\cdot)| \leq C/h$ , where  $C$  is a constant independent of  $h$ , and  $\nu_h(x) := 1 - \mu_h(x + h)$ . Since the solutions  $u$  and  $v$  possess traces with respect to  $x \rightarrow 0$ , we obtain by inserting  $\psi^1$  and  $\psi^2$  in (3.3.13) and (3.3.14), letting  $h \rightarrow 0$ , and using that for all  $h$ ,  $\psi^1$  vanishes for  $x \geq 0$ , while  $\psi^2$  vanishes for  $x \leq 0$ , the inequalities

$$\int_{-\infty}^0 \int_0^T |u - v| \Phi'(t) dt dx \geq \int_0^T \operatorname{sgn}(v_- - u_-) (\varphi(v_-) - \varphi(u_-)) \Phi(t) dt, \quad (3.3.15)$$

$$\begin{aligned}
& \int_0^\infty \int_0^T |u - v| \Phi'(t) dt dx \\
& \geq - \int_0^T \operatorname{sgn}(v_+ - u_+) (\varphi(v_+) - \varphi(u_+) - \gamma_+(v_+ - u_+)) \Phi(t) dt.
\end{aligned} \tag{3.3.16}$$

In a standard fashion, let now  $\omega_h$  be a non-negative  $C^\infty$  mollifier with support on  $(-h, h)$  and  $\|\omega_h\|_{L^1(\mathbb{R})} = 1$ . Then let  $\varrho_h(x) := \int_0^x \omega_h(\xi) d\xi$  and take  $\Phi(t) := \varrho_h(t - t_1) - \varrho_h(t - t_2)$ , where  $0 \leq t_1 < t_2 \leq T$ . Taking  $h \rightarrow 0$ , we obtain

$$\begin{aligned}
& \int_{\mathbb{R}} |u(\cdot, t_2) - v(\cdot, t_2)| dx - \int_{\mathbb{R}} |u(\cdot, t_1) - v(\cdot, t_1)| dx \leq E, \\
E := & \int_{t_1}^{t_2} \left\{ \operatorname{sgn}(v_+ - u_+) (\varphi(v_+) - \varphi(u_+) - \gamma_+(v_+ - u_+)) \right. \\
& \left. - \operatorname{sgn}(v_- - u_-) (\varphi(v_-) - \varphi(u_-)) \right\} dt.
\end{aligned} \tag{3.3.17}$$

To prove the  $L^1$  contraction property, we verify that  $E \leq 0$  by showing that the jump conditions ensure that the integrand in (3.3.17) is non-positive for almost all  $t \in (0, T)$ . To this end, we give a name to this integrand:

$$S := \operatorname{sgn}(v_+ - u_+) (\varphi(v_+) - \gamma_+ v_+ - \varphi(u_+) + \gamma_+ u_+) - \operatorname{sgn}(v_- - u_-) (\varphi(v_-) - \varphi(u_-)).$$

Our goal now is to show that  $S \leq 0$ . We prove this by examining the cases corresponding to the ordering among the four numbers  $u_-, u_+, v_-, v_+$ . There are 24 such cases, but we can eliminate half of them, since interchanging  $u_-$  with  $v_-$  and  $u_+$  with  $v_+$  leads to the same proofs, only with different labels.

**Case 1.**  $u_- \leq v_- \leq u_+ \leq v_+$ . In this case

$$S = \varphi(v_+) - \gamma_+ v_+ - \varphi(u_+) + \gamma_+ u_+ - (\varphi(v_-) - \varphi(u_-)).$$

Taking  $c = v_-$  in (3.3.4), we get

$$\varphi(u_-) - \varphi(v_-) \leq 0.$$

Interchanging  $u$  and  $v$  and setting  $c = u_+$  in (3.3.3), we obtain  $\varphi(v_+) - \varphi(u_+) - \gamma_+(v_+ - u_+) \leq 0$ , which makes it clear that  $S \leq 0$ .

**Case 2.**  $u_- \leq v_- \leq v_+ \leq u_+$ . In this case

$$\begin{aligned} S &= \varphi(u_+) - \gamma_+ u_+ - \varphi(v_+) + \gamma_+ v_+ - (\varphi(v_-) - \varphi(u_-)) \\ &\leq \varphi(u_+) - \gamma_+ u_+ - \varphi(v_+) + \gamma_+ v_+. \end{aligned}$$

Here we have used that  $\varphi(v_-) - \varphi(u_-) \geq 0$ , which results by taking  $c = v_-$  in (3.3.4). Now letting  $c = v_+$  in (3.3.3), we get  $\varphi(u_+) - \varphi(v_+) \leq \gamma_+(u_+ - v_+)$ , which implies  $S \leq 0$ .

**Case 3.**  $u_- \leq u_+ \leq v_- \leq v_+$ . In this case

$$S = \varphi(v_+) - \gamma_+ v_+ - \varphi(u_+) + \gamma_+ u_+ - (\varphi(v_-) - \varphi(u_-)).$$

From (3.3.9),  $\varphi(u_-) - \varphi(u_+) \leq 0$ , and so

$$S \leq \varphi(v_+) - \varphi(v_-) - \gamma_+(v_+ - u_+) \leq \varphi(v_+) - \varphi(v_-) - \gamma_+(v_+ - v_-).$$

Taking  $c = v_-$  in (3.3.3), it is now clear that  $S \leq 0$ .

**Case 4.**  $u_- \leq u_+ \leq v_+ \leq v_-$ . In this case

$$S = \varphi(v_+) - \gamma_+ v_+ - \varphi(u_+) + \gamma_+ u_+ - (\varphi(v_-) - \varphi(u_-)).$$

From (3.3.9),  $\varphi(u_-) - \varphi(u_+) \leq 0$ ,  $\varphi(v_+) - \varphi(v_-) \leq 0$  and so

$$S \leq -\gamma_+(v_+ - u_+) \leq 0.$$

**Case 5.**  $u_- \leq v_+ \leq v_- \leq u_+$ . In this case

$$S = \varphi(u_+) - \gamma_+ u_+ - \varphi(v_+) + \gamma_+ v_+ - (\varphi(v_-) - \varphi(u_-)).$$

Taking  $c = v_+$  in (3.3.3), and then  $c = v_-$  in (3.3.4), we find that

$$\varphi(u_+) - \varphi(v_+) - \gamma_+(u_+ - v_+) \leq 0, \quad \varphi(v_-) - \varphi(u_-) \geq 0,$$

which clearly yields  $S \leq 0$ .

**Case 6.**  $u_- \leq v_+ \leq u_+ \leq v_-$ . In this case

$$S = \varphi(u_+) - \gamma_+ u_+ - \varphi(v_+) + \gamma_+ v_+ - (\varphi(v_-) - \varphi(u_-)).$$

Letting  $c = v_+$  in (3.3.3) results in

$$\varphi(u_+) - \varphi(v_+) \leq \gamma_+(u_+ - v_+),$$

and so

$$S \leq -(\varphi(v_-) - \varphi(u_-)).$$

Taking  $c = v_+$  in (3.3.4) gives  $\varphi(v_+) - \varphi(u_-) \geq 0$ . Also, from (3.3.9), we see that  $\varphi(v_-) \geq \varphi(v_+)$ . Combining these inequalities gives  $\varphi(v_-) - \varphi(u_-) \geq 0$ , and thus  $S \leq 0$ .

**Case 7.**  $u_+ \leq u_- \leq v_- \leq v_+$ . In this case

$$\begin{aligned} S &= \varphi(v_+) - \gamma_+v_+ - \varphi(u_+) + \gamma_+u_+ - (\varphi(v_-) - \varphi(u_-)) \\ &\leq \varphi(v_+) - \gamma_+v_+ - \varphi(u_+) + \gamma_+u_+ - (\varphi(v_-) - \varphi(u_-)) + \gamma_+v_- - \gamma_+u_- \\ &= \varphi(v_+) - \varphi(v_-) - \gamma_+(v_+ - v_-) - (\varphi(u_+) - \varphi(u_-) - \gamma_+(u_+ - u_-)). \end{aligned}$$

By (3.3.9), we have the inequalities

$$\varphi(v_+) - \varphi(v_-) - \gamma_+(v_+ - v_-) \leq 0, \quad \varphi(u_+) - \varphi(u_-) - \gamma_+(u_+ - u_-) \geq 0,$$

yielding  $S \leq 0$ .

**Case 8.**  $u_+ \leq u_- \leq v_+ \leq v_-$ . In this case

$$S = \varphi(v_+) - \gamma_+v_+ - \varphi(u_+) + \gamma_+u_+ - (\varphi(v_-) - \varphi(u_-)).$$

By (3.3.9),  $\varphi(v_+) \leq \varphi(v_-)$ , which results in the inequality

$$S \leq \varphi(u_-) - \varphi(u_+) - \gamma_+(v_+ - u_+) \leq \varphi(u_-) - \varphi(u_+) - \gamma_+(u_- - u_+).$$

Taking  $c = u_-$  in (3.3.5), we find that  $\varphi(u_-) - \varphi(u_+) - \gamma_+(u_- - u_+) \leq 0$ , yielding  $S \leq 0$ .

**Case 9.**  $v_+ \leq u_- \leq v_- \leq u_+$ . In this case

$$S = \varphi(u_+) - \gamma_+u_+ - \varphi(v_+) + \gamma_+v_+ - (\varphi(v_-) - \varphi(u_-)).$$

Taking  $c = u_-$  in (3.3.5) gives  $\varphi(v_+) - \varphi(u_-) \geq \gamma_+(v_+ - u_-)$ , which we can rearrange as  $-\varphi(v_+) + \varphi(u_-) + \gamma_+v_+ \leq \gamma_+u_-$ . From this it follows that

$$S \leq \varphi(u_+) - \varphi(v_-) - \gamma_+u_+ + \gamma_+u_-.$$

Now (3.3.10) tells us that  $v_+ \leq v_- \leq u^*$ . Recalling that  $u \mapsto \varphi(u)$  is non-decreasing on  $[0, u^*]$ , and that  $v_+ \leq u_- \leq v_-$ , we find that  $\varphi(u_-) \leq \varphi(v_-)$ , and so

$$S \leq \varphi(u_+) - \varphi(u_-) - \gamma_+u_+ + \gamma_+u_-.$$

The right side of this last inequality is non-positive due to (3.3.9), and so  $S \leq 0$ .

**Case 10.**  $v_+ \leq u_- \leq u_+ \leq v_-$ . In this case

$$S = \varphi(u_+) - \gamma_+u_+ - \varphi(v_+) + \gamma_+v_+ - (\varphi(v_-) - \varphi(u_-)).$$

Taking  $c = u_+$  in (3.3.5) gives  $\varphi(v_+) - \varphi(u_+) \geq \gamma_+(v_+ - u_+)$ , from which we derive  $S \leq \varphi(u_-) - \varphi(v_-)$ . From (3.3.10) we have that  $v_+ \leq v_- \leq u^*$ . Since also  $u_- \leq v_- \leq u^*$ , we see that  $\varphi(u_-) \leq \varphi(v_-)$ , yielding  $S \leq 0$ .

**Case 11.**  $u_+ \leq v_- \leq u_- \leq v_+$ . In this case

$$S = \varphi(v_+) - \gamma_+v_+ - \varphi(u_+) + \gamma_+u_+ - (\varphi(u_-) - \varphi(v_-)).$$

Taking  $c = u_-$  in (3.3.3) results in

$$\varphi(v_+) - \varphi(u_-) - \gamma_+v_+ \leq -\gamma_+u_-,$$

which in turn gives us

$$S \leq -\varphi(u_+) + \gamma_+u_+ + \varphi(v_-) - \gamma_+u_-.$$

From (3.3.10) we have that  $u_+ \leq u_- \leq u^*$ . Since also  $v_- \leq u_- \leq u^*$ , we have  $\varphi(v_-) \leq \varphi(u_-)$ , and so

$$S \leq -\varphi(u_+) + \gamma_+u_+ + \varphi(u_-) - \gamma_+u_- = \varphi(u_-) - \varphi(u_+) - \gamma_+(u_- - u_+).$$

This last quantity is non-positive, due to (3.3.9), resulting in  $S \leq 0$ .

**Case 12.**  $u_+ \leq v_+ \leq u_- \leq v_-$ . In this case

$$S = \varphi(v_+) - \gamma_+ v_+ - \varphi(u_+) + \gamma_+ u_+ - (\varphi(v_-) - \varphi(u_-)).$$

Taking  $c = v_+$  in (3.3.5) results in

$$\varphi(v_+) - \varphi(u_+) - \gamma_+(v_+ - u_+) \leq 0,$$

which in turn gives us  $S \leq \varphi(u_-) - \varphi(v_-)$ . From (3.3.10) we have that  $v_+ \leq v_- \leq u^*$ . Since also  $u_- \leq v_- \leq u^*$ , we have  $\varphi(u_-) \leq \varphi(v_-)$ , making it clear that  $S \leq 0$ .  $\square$

### 3.4 Numerical scheme and some properties

In this section we discuss a difference scheme that applies to the full model (3.1.1). We begin the definition of the algorithm by discretizing the spatial domain  $\mathbb{R}$  into cells  $I_j := [x_{j-1/2}, x_{j+1/2})$ ,  $j \in \mathbb{Z}$ , where  $x_k = k\Delta x$  for  $k = 0, \pm 1/2, \pm 1, \pm 3/2, \dots$ . Similarly, the time interval  $(0, T)$  is discretized via  $t_n = n\Delta t$  for  $n = 0, \dots, N$ , where  $N = \lfloor T/\Delta t \rfloor + 1$ , which results in the time strips  $I^n := [t_n, t_{n+1})$ ,  $n = 0, \dots, N - 1$ . Here  $\Delta x > 0$  and  $\Delta t > 0$  denote the spatial and temporal discretization parameters, respectively. These parameters are chosen so that the following CFL condition holds:

$$\lambda \max_{u \in [0,1], x \in \mathbb{R}} |f_u(\gamma(x), u)| + \lambda \max_{x \in \mathbb{R}} \gamma^3(x) \leq \frac{1}{2}, \quad \lambda := \frac{\Delta t}{\Delta x}. \quad (3.4.1)$$

When sending  $\Delta \downarrow 0$  we will do so with the ratio  $\lambda$  kept constant. We use the symbol  $\Delta$  to refer to the discretization parameters collectively:  $\Delta = (\Delta x, \Delta t)$ .

We propose a scheme that is a direct modification of the one described in [31]. Let  $U_j^n$  denote our approximation to  $u(x_j, t^n)$ . Then the marching formula for our new scheme is

$$U_j^{n+1} = U_j^n - \lambda \Delta_- h(\gamma_{j+1/2}, U_{j+1}^n, U_j^n) + \lambda \gamma_j^3 \Delta_+ U_j^n. \quad (3.4.2)$$

Here  $\gamma_{j+1/2} = \gamma(x_{j+1/2-})$ , and  $\gamma_j^3 := \gamma^3(x_{j-})$ . In (3.4.2) the symbols  $\Delta_{\pm}$  are spatial difference operators:

$$\Delta_- h(\gamma_{j+1/2}, U_{j+1}^n, U_j^n) = h(\gamma_{j+1/2}, U_{j+1}^n, U_j^n) - h(\gamma_{j-1/2}, U_j^n, U_{j-1}^n),$$

and  $\Delta_+ U_j^n = U_{j+1}^n - U_j^n$ .

The main difference between (3.4.2) and the scheme defined in [31] is the new term  $\lambda \gamma_j^3 \Delta_+ U_j^n$  that incorporates the sink feature. The use of the forward difference  $\Delta_+$  in this new sink term is deliberate; we bias this difference to preserve the upwind nature of the scheme. Here we are explicitly using the assumption that  $\gamma^3(x) \geq 0$ . The function  $h(\gamma, v, u)$  is the Engquist-Osher (EO henceforth) numerical flux [65]

$$h(\gamma, v, u) := \frac{1}{2}(f(\gamma, u) + f(\gamma, v)) - \frac{1}{2} \int_u^v |f_u(\gamma, w)| dw. \quad (3.4.3)$$

To define an approximate solution not just at the mesh points, but on all of  $\Pi_T$ , we let  $\chi_j^n$  denote the indicator for the rectangle  $I_j \times I^n$  and introduce

$$u^\Delta(x, t) := \sum_{n=0}^N \sum_{j \in \mathbb{Z}} \chi_j^n(x, t) U_j^n.$$

Although the scheme is not conservative, several important properties of monotonicity are preserved. The following lemma is adapted from Lemma 3.1 of [31].

**Lemma 3.4.1** *The computed solution  $U_j^n$  belongs to the interval  $[0, 1]$ . Moreover, the difference scheme (3.4.2) is monotone.*

**Proof.** We start by noting that the marching formula (3.4.2) defines  $U_j^{n+1}$  as a function of the three independent variables  $U_{j-1}^n, U_j^n, U_{j+1}^n$ . Using (3.4.2), we compute the partial derivatives of  $U_j^{n+1}$  with respect to these variables:

$$\begin{aligned} \frac{\partial U_j^{n+1}}{\partial U_{j+1}^n} &= -\lambda f_u^-(\gamma_{j+1/2}, U_{j+1}^n) + \lambda \gamma_j^3 \geq 0, & \frac{\partial U_j^{n+1}}{\partial U_{j-1}^n} &= \lambda f_u^+(\gamma_{j-1/2}, U_{j-1}^n) \geq 0, \\ \frac{\partial U_j^{n+1}}{\partial U_j^n} &= 1 + \lambda f_u^-(\gamma_{j-1/2}, U_j^n) - \lambda f_u^+(\gamma_{j+1/2}, U_j^n) - \lambda \gamma_j^3. \end{aligned}$$

Thus  $U_j^{n+1}$  is a non-decreasing function of the conserved variables at  $t_n$  if

$$1 + \lambda f_u^-(\gamma_{j-1/2}, U_j^n) - \lambda f_u^+(\gamma_{j+1/2}, U_j^n) - \lambda \gamma_j^3 \geq 0.$$

This will hold if  $U_j^n \in [0, 1]$  for all  $j$  and the CFL condition (3.4.1) is satisfied. The rest of the proof is similar to the proof of Lemma 3.1 of [31], and is omitted.  $\square$

Next we establish a fundamental time-continuity estimate.

**Lemma 3.4.2** *There exists a constant  $C$ , independent of  $\Delta$  and  $n$ , such that*

$$\Delta x \sum_{j \in \mathbb{Z}} |U_j^{n+1} - U_j^n| \leq \Delta x \sum_{j \in \mathbb{Z}} |U_j^1 - U_j^0| \leq C \Delta t. \quad (3.4.4)$$

**Proof.** Starting from the marching formula (3.4.2), we can express the time differences as follows:

$$\begin{aligned} U_j^{n+1} - U_j^n &= U_j^n - U_j^{n-1} - \lambda \Delta_- [h(\gamma_{j+1/2}, U_{j+1}^n, U_j^n) - h(\gamma_{j+1/2}, U_{j+1}^{n-1}, U_j^{n-1})] \\ &\quad + \lambda \gamma_j^3 \Delta_+ U_j^n - \lambda \gamma_j^3 \Delta_+ U_j^{n-1} \\ &= (1 - \lambda C_{j+1/2}^{n-\frac{1}{2}} + \lambda B_{j-1/2}^{n-\frac{1}{2}} - \lambda \gamma_j^3) (U_j^n - U_j^{n-1}) \\ &\quad - \lambda B_{j+1/2}^{n-\frac{1}{2}} (U_{j+1}^n - U_{j+1}^{n-1}) + \lambda C_{j-1/2}^{n-\frac{1}{2}} (U_{j-1}^n - U_{j-1}^{n-1}) + \lambda \gamma_j^3 (U_{j+1}^n - U_{j+1}^{n-1}), \end{aligned}$$

where we define

$$\begin{aligned} B_{j+1/2}^{n-\frac{1}{2}} &:= \int_0^1 f_u^- (\gamma_{j+1/2}, \theta U_{j+1}^n + (1-\theta) U_{j+1}^{n-1}) d\theta \leq 0, \\ C_{j+1/2}^{n-\frac{1}{2}} &:= \int_0^1 f_u^+ (\gamma_{j+1/2}, \theta U_j^n + (1-\theta) U_j^{n-1}) d\theta \geq 0. \end{aligned}$$

Due to the CFL condition (3.4.1),

$$1 - \lambda C_{j+1/2}^{n-\frac{1}{2}} + \lambda B_{j-1/2}^{n-\frac{1}{2}} - \lambda \gamma_j^3 \geq 0.$$

Thus, we conclude that

$$\begin{aligned} |U_j^{n+1} - U_j^n| &\leq (1 - \lambda C_{j+1/2}^{n-\frac{1}{2}} + \lambda B_{j-1/2}^{n-\frac{1}{2}} - \lambda \gamma_j^3) |U_j^n - U_j^{n-1}| \\ &\quad - \lambda B_{j+1/2}^{n-\frac{1}{2}} |U_{j+1}^n - U_{j+1}^{n-1}| + \lambda C_{j-1/2}^{n-\frac{1}{2}} |U_{j-1}^n - U_{j-1}^{n-1}| + \lambda \gamma_j^3 |U_{j+1}^n - U_{j+1}^{n-1}| \\ &\leq (1 - \lambda C_{j+1/2}^{n-\frac{1}{2}} + \lambda B_{j-1/2}^{n-\frac{1}{2}} - \lambda \gamma_j^3) |U_j^n - U_j^{n-1}| \\ &\quad - \lambda B_{j+1/2}^{n-\frac{1}{2}} |U_{j+1}^n - U_{j+1}^{n-1}| + \lambda C_{j-1/2}^{n-\frac{1}{2}} |U_{j-1}^n - U_{j-1}^{n-1}| + \lambda \gamma_{j+1}^3 |U_{j+1}^n - U_{j+1}^{n-1}|. \end{aligned}$$

Here we have used the fact that  $x \mapsto \gamma^3(x)$  is non-decreasing when replacing  $\gamma_j^3$  by  $\gamma_{j+1}^3$ . Summing this inequality over  $j$  and multiplying by  $\Delta x$  gives

$$\Delta x \sum_{j \in \mathbb{Z}} |U_j^{n+1} - U_j^n| \leq \Delta x \sum_{j \in \mathbb{Z}} |U_j^n - U_j^{n-1}|.$$

Applying this last inequality inductively, we arrive at

$$\Delta x \sum_{j \in \mathbb{Z}} |U_j^{n+1} - U_j^n| \leq \Delta x \sum_{j \in \mathbb{Z}} |U_j^1 - U_j^0|.$$

The rest of the proof is similar to the proof of Lemma 3.2 of [31] and is omitted.  $\square$

Lemmas 3.4.1 and 3.4.2 provide several important stability properties of our new difference scheme. We will not pursue the analysis for the full model (3.1.1), but focus on the reduced problem described in Section 3.2.4.

### 3.5 Convergence to an entropy solution for the reduced problem

We can write the scheme for the reduced problem (3.1.2) as

$$U_j^{n+1} = U_j^n - \lambda \Delta_- h(U_{j+1}^n, U_j^n) + \lambda \gamma_j \Delta_+ U_j^n. \quad (3.5.1)$$

Here we are abusing the notation slightly by continuing to use the symbol  $h$  of Section 3.4 for the numerical flux, i.e.

$$h(v, u) = \frac{1}{2}(\varphi(v) + \varphi(u)) - \frac{1}{2} \int_u^v |\varphi'(w)| dw.$$

The appropriate CFL condition for our reduced problem is

$$\lambda \max_{u \in [0,1], x \in \mathbb{R}} |\varphi'(u)| + \lambda \max_{x \in \mathbb{R}} \gamma(x) \leq \frac{1}{2}, \quad \lambda := \frac{\Delta t}{\Delta x}. \quad (3.5.2)$$

Lemmas 3.4.1 and 3.4.2 remain valid in this setting, and need not be repeated. In order to establish compactness, we will also need a spatial variation bound, which is provided by the following lemma. Let  $TV(z)$  denote the total variation of a function  $z \in L^1_{\text{loc}}(\mathbb{R})$ .

**Lemma 3.5.1** *For any  $t \in [0, T]$  we have the spatial variation bound*

$$TV(u^\Delta(\cdot, t)) \leq C, \quad (3.5.3)$$

where  $C$  is independent of  $\Delta$  and  $t$  for  $t \in [0, T]$ .

**Proof.** We start by writing the scheme (3.5.1) in incremental form

$$U_j^{n+1} = U_j^n + C_{j+1/2}^n \Delta_+ U_j^n - D_{j-1/2}^n \Delta_- U_j^n,$$

where

$$C_{j+1/2}^n = \lambda \left( \frac{\varphi(U_j^n) - h(U_{j+1}^n, U_j^n)}{\Delta_+ U_j^n} + \gamma_j \right), \quad D_{j-1/2}^n = \lambda \frac{\varphi(U_j^n) - h(U_j^n, U_{j-1}^n)}{\Delta_- U_j^n}.$$

Using the monotonicity of the numerical flux  $h$ , that  $\gamma_j \geq 0$ , and the CFL condition (3.5.2), one can easily check that

$$C_{j+1/2}^n \geq 0, \quad D_{j+1/2}^n \geq 0, \quad C_{j+1/2}^n + D_{j+1/2}^n \leq 1.$$

It now follows from Harten's lemma (Lemma 2.2 of [88]) that

$$\sum_{j \in \mathbb{Z}} |U_{j+1}^{n+1} - U_j^{n+1}| \leq \sum_{j \in \mathbb{Z}} |U_{j+1}^n - U_j^n|.$$

Continuing by induction, we conclude that

$$TV(u^\Delta(\cdot, t)) \leq TV(u^\Delta(\cdot, 0)) \leq TV(u_0),$$

and the proof is complete.  $\square$

In what follows, we will employ the following regularizations of the function  $\gamma(x)$ .

$$\bar{\gamma}^\epsilon(x) := \begin{cases} 0 & \text{for } x \leq -\epsilon, \\ ((x + \epsilon)/\epsilon)\gamma_+ & \text{for } -\epsilon \leq x \leq 0, \\ \gamma_+ & \text{for } x \geq 0, \end{cases}$$

$$\underline{\gamma}^\epsilon(x) := \begin{cases} 0 & \text{for } x \leq 0, \\ (x/\epsilon)\gamma_+ & \text{for } 0 \leq x \leq \epsilon, \\ \gamma_+ & \text{for } x \geq \epsilon. \end{cases}$$

Observe that  $\underline{\gamma}^\epsilon(x) \leq \gamma(x) \leq \bar{\gamma}^\epsilon(x)$  for all  $x \in \mathbb{R}$ . When discretizing  $\underline{\gamma}^\epsilon$  and  $\bar{\gamma}^\epsilon$ , we do so in the same manner as  $\gamma$ , thus preserving the ordering  $\underline{\gamma}_j^\epsilon \leq \gamma_j \leq \bar{\gamma}_j^\epsilon$ .

One more preliminary issue before we discuss entropy conditions is the existence of traces along the line  $x = 0, t \in [0, T]$ . Our spatial  $BV$  bounds carry over to the limit solution  $u$ , guaranteeing that we have limits from both the left and right, denoted  $u_-(t), u_+(t)$  or simply  $u_-, u_+$ , for a.e  $t \in [0, T]$ .

**Lemma 3.5.2** *Any (subsequential) limit  $u$  of the scheme (3.5.1) satisfies the entropy conditions (3.3.1)–(3.3.6).*

**Proof.** The proof of the Kružkov-type entropy inequalities (3.3.1), (3.3.2) is standard [45], and is omitted.

We now turn to the proof of (3.3.3). The following discrete entropy inequality holds for any  $c \in \mathbb{R}$ ; this follows from the monotonicity of the scheme:

$$U_j^{n+1} \vee c \leq U_j^n \vee c - \lambda \Delta_+ h(U_j^n \vee c, U_{j-1}^n \vee c) + \lambda \gamma_j \Delta_+(U_j^n \vee c). \quad (3.5.4)$$

Now let

$$V_j^n := \begin{cases} c & \text{for } j \leq 0, \\ U_j^n \vee c & \text{for } j > 0, \end{cases} \quad v(x, t) := \begin{cases} c & \text{for } x < 0, \\ u(x, t) \vee c & \text{for } x > 0. \end{cases}$$

Note that

$$\Delta_+ V_0^n = U_1^n \vee c - c \geq 0. \quad (3.5.5)$$

Since  $\gamma_j = 0$  for  $j \leq 0$ , and  $\Delta_+ V_j^n = \Delta_+(U_j^n \vee c)$  for  $j > 0$ , we can replace inequality (3.5.4) by

$$U_j^{n+1} \vee c \leq U_j^n \vee c - \lambda \Delta_+ h(U_j^n \vee c, U_{j-1}^n \vee c) + \lambda \gamma_j \Delta_+ V_j^n. \quad (3.5.6)$$

Since  $\bar{\gamma}_j^\epsilon \geq \gamma_j = 0$  for  $j \leq 0$  and  $\bar{\gamma}_j^\epsilon = \gamma_j = \gamma_+$  for  $j > 0$ , in view of (3.5.5) we can replace inequality (3.5.6) by

$$U_j^{n+1} \vee c \leq U_j^n \vee c - \lambda \Delta_+ h(U_j^n \vee c, U_{j-1}^n \vee c) + \lambda \bar{\gamma}_j^\epsilon \Delta_+ V_j^n. \quad (3.5.7)$$

Employing the identity

$$A_j \Delta_+ B_j = \Delta_+(A_j B_j) - B_{j+1} \Delta_+ A_j, \quad (3.5.8)$$

we can rewrite (3.5.7) in the form

$$U_j^{n+1} \vee c \leq U_j^n \vee c - \lambda \Delta_+ (h(U_j^n \vee c, U_{j-1}^n \vee c) - \bar{\gamma}_j^\epsilon V_j^n) - \lambda V_{j+1}^n \Delta_+ \bar{\gamma}_j^\epsilon. \quad (3.5.9)$$

Let  $0 \leq \psi \in \mathcal{D}(\Pi_T)$ , and  $\psi_j^n = \psi(x_j, t^n)$ . Proceeding as in the proof of the Lax-Wendroff theorem, we move all terms in (3.5.9) to the left-hand side of the inequality, multiply by  $\psi_j^n \Delta x$ , and sum over  $j \in \mathbb{Z}, n \geq 0$ , and finally sum by parts to get

$$\begin{aligned} \Delta x \Delta t \sum_{j \in \mathbb{Z}} \sum_{n \geq 0} (U_j^n \vee c) \frac{\psi_j^{n+1} - \psi_j^n}{\Delta t} \\ + \Delta x \Delta t \sum_{j \in \mathbb{Z}} \sum_{n \geq 0} [h(U_j^n \vee c, U_{j-1}^n \vee c) - \bar{\gamma}_j^\epsilon V_j^n] \frac{\Delta_+ \psi_j^n}{\Delta x} \\ - \Delta x \Delta t \sum_{j \in \mathbb{Z}} \sum_{n \geq 0} \frac{\Delta_+ \bar{\gamma}_j^\epsilon}{\Delta x} V_{j+1}^n \psi_j^n \geq 0. \end{aligned} \quad (3.5.10)$$

When  $\Delta \downarrow 0$ , the bounded convergence theorem yields

$$\iint_{\Pi_T} \left( (u \vee c) \psi_t + (\varphi(u \vee c) - \bar{\gamma}^\epsilon(x) v) \psi_x \right) dx dt - \iint_{\Pi_T} (\bar{\gamma}^\epsilon)'(x) v \psi dx dt \geq 0. \quad (3.5.11)$$

With the observation that

$$(\bar{\gamma}^\epsilon)'(x) = \begin{cases} \gamma_+/\epsilon & \text{for } x \in (-\epsilon, 0), \\ 0 & \text{for } x \notin (-\epsilon, 0), \end{cases}$$

when  $\epsilon \downarrow 0$  we obtain

$$\iint_{\Pi_T} (\bar{\gamma}^\epsilon)'(x) v \psi dx dt \rightarrow \gamma_+ c \int_0^T \psi(0, t) dt.$$

Combining this with an application of the bounded convergence theorem, when  $\epsilon \downarrow 0$ , (3.5.11) yields the inequality

$$\iint_{\Pi_T} \left( (u \vee c) \psi_t + (\varphi(u \vee c) - \gamma(x) v) \psi_x \right) dx dt - \gamma_+ c \int_0^T \psi(0, t) dt \geq 0. \quad (3.5.12)$$

By applying a standard test function argument to (3.5.12), we find that for a.e.  $t \in (0, T)$ ,

$$\varphi(u_-(t) \vee c) - \gamma_- c - (\varphi(u_+(t) \vee c) - \gamma_+(u_+(t) \vee c)) - \gamma_+ c \geq 0.$$

Recalling that  $\gamma_- = 0$ ,  $u_- \leq c \leq u_+$ , dropping the dependence on  $t$ , and rearranging, this inequality becomes

$$\varphi(u_+) - \varphi(c) \leq \gamma_+(u_+ - c),$$

and the proof of (3.3.3) is complete.

For the proof of (3.3.4) we use the monotonicity of the scheme to derive the discrete entropy inequality

$$U_j^{n+1} \wedge c \geq U_j^n \wedge c - \lambda \Delta_+ h(U_j^n \wedge c, U_{j-1}^n \wedge c) + \lambda \gamma_j \Delta_+ (U_j^n \wedge c). \quad (3.5.13)$$

Let

$$W_j^n := \begin{cases} c & \text{for } j \leq 0, \\ U_j^n \wedge c & \text{for } j > 0, \end{cases}, \quad w(x, t) := \begin{cases} c & \text{for } x < 0, \\ u(x, t) \wedge c & \text{for } x > 0. \end{cases}$$

Observing that

$$\Delta_+(U_0^n \wedge c) = U_1^n \wedge c - U_0^n \wedge c \geq \Delta_+ W_0^n = U_1^n \wedge c - c \leq 0,$$

we find that the following inequality holds:

$$U_j^{n+1} \wedge c \geq U_j^n \wedge c - \lambda \Delta_+ h(U_j^n \wedge c, U_{j-1}^n \wedge c) + \lambda \gamma_j \Delta_+ W_j^n.$$

Using  $0 \leq \gamma_j \leq \bar{\gamma}_j^\epsilon$  and  $\Delta_+ W_0^n \leq 0$ , we also have

$$U_j^{n+1} \wedge c \geq U_j^n \wedge c - \lambda \Delta_+ h(U_j^n \wedge c, U_{j-1}^n \wedge c) + \lambda \bar{\gamma}_j^\epsilon \Delta_+ W_j^n.$$

Proceeding as in the proof of (3.3.3), we find that

$$\iint_{\Pi_T} \left( (u \wedge c) \psi_t + (\varphi(u \wedge c) - \bar{\gamma}^\epsilon(x) w) \psi_x \right) dx dt - \iint_{\Pi_T} (\bar{\gamma}^\epsilon)'(x) w \psi dx dt \leq 0,$$

from which it follows that

$$\varphi(u_-(t) \wedge c) - \gamma_- c - (\varphi(u_+(t) \wedge c) - \gamma_+(u_+(t) \wedge c)) - \gamma_+ c \leq 0,$$

and this holds for a.e.  $t \in [0, T]$ . Recalling that  $\gamma_- = 0$ , and then observing that the terms involving  $\gamma_+(u_+(t) \wedge c)$  and  $\gamma_+ c$  cancel, the proof of (3.3.4) is complete.

For the proof of (3.3.6), we start from the discrete entropy inequality (3.5.4), and then apply the identity (3.5.8) to get

$$\begin{aligned} U_j^{n+1} \vee c &\leq U_j^n \vee c - \lambda \Delta_+ (h(U_j^n \vee c, U_{j-1}^n \vee c) - \gamma_j (U_j^n \vee c)) \\ &\quad - \lambda (U_{j+1}^n \vee c) \Delta_+ \gamma_j. \end{aligned} \quad (3.5.14)$$

We then define

$$\tilde{V}_j^n := \begin{cases} U_j^n \vee c & \text{for } j \leq 0, \\ c & \text{for } j > 0, \end{cases} \quad \tilde{v}(x, t) := \begin{cases} u(x, t) \vee c & \text{for } x < 0, \\ c & \text{for } x > 0, \end{cases}$$

and observe that it is possible to replace the inequality (3.5.14) by

$$U_j^{n+1} \vee c \leq U_j^n \vee c - \lambda \Delta_+ (h(U_j^n \vee c, U_{j-1}^n \vee c) - \gamma_j (U_j^n \vee c)) - \lambda \tilde{V}_{j+1}^n \Delta_+ \gamma_j.$$

More specifically, this inequality holds because  $\Delta_+ \gamma_j = 0$ , except at  $j = 0$ , and  $U_1^n \vee c \geq \tilde{V}_1 = c$ . Another application of the identity (3.5.8) yields

$$\begin{aligned} U_j^{n+1} \vee c &\leq U_j^n \vee c - \lambda \Delta_+ (h(U_j^n \vee c, U_{j-1}^n \vee c) - \gamma_j (U_j^n \vee c) + \gamma_j \tilde{V}_j^n) \\ &\quad + \lambda \gamma_j \Delta_+ \tilde{V}_j^n. \end{aligned} \quad (3.5.15)$$

Since  $\Delta_+ \tilde{V}_j^n = 0$  for  $j > 0$ ,  $\Delta_+ \tilde{V}_0^n \leq 0$ ,  $\underline{\gamma}_j^\epsilon = \gamma_j$  for  $j < 0$ , and  $\underline{\gamma}_j^\epsilon \leq \gamma_j$  for  $j \geq 0$ , we can replace (3.5.15) by

$$U_j^{n+1} \vee c \leq U_j^n \vee c - \lambda \Delta_+ (h(U_j^n \vee c, U_{j-1}^n \vee c) - \gamma_j (U_j^n \vee c) + \gamma_j \tilde{V}_j^n) + \lambda \underline{\gamma}_j^\epsilon \Delta_+ \tilde{V}_j^n.$$

A final application of (3.5.8) results in

$$\begin{aligned} U_j^{n+1} \vee c &\leq U_j^n \vee c - \lambda \Delta_+ (h(U_j^n \vee c, U_{j-1}^n \vee c) - \gamma_j (U_j^n \vee c) + (\gamma_j - \underline{\gamma}_j^\epsilon) \tilde{V}_j^n) \\ &\quad - \lambda \tilde{V}_{j+1}^n \Delta_+ \underline{\gamma}_j^\epsilon. \end{aligned}$$

The rest of the proof of (3.3.6) is similar to the proofs of (3.3.3) and (3.3.4), and so we omit the details.

The proof of (3.3.5) is similar to that of (3.3.6), the main difference being that one starts from the discrete entropy inequality (3.5.13) and uses the modified functions

$$\tilde{W}_j^n := \begin{cases} U_j^n \wedge c & \text{for } j \leq 0, \\ c & \text{for } j > 0, \end{cases}, \quad \tilde{w}(x, t) := \begin{cases} u(x, t) \wedge c & \text{for } x < 0, \\ c & \text{for } x > 0. \end{cases}$$

We omit the details. □

We can now state and prove our main theorem.

**Theorem 3.5.1** *As  $\Delta \downarrow 0$ , the approximations  $u^\Delta$  generated by the scheme (3.5.1) converge in  $L^1(\Pi_T)$  and a.e. in  $\Pi_T$  to the unique entropy solution  $u$  of the initial value problem (3.1.2), (3.1.4), (3.1.5).*

**Proof.** For the approximations  $u^\Delta$ , we have an  $L^\infty$  bound (Lemma 3.4.1), a time continuity bound (Lemma 3.4.2), and a spatial variation bound (Lemma 3.5.1). In addition, it is a straightforward exercise using the time continuity bound provided by Lemma 3.4.2 to derive a bound for the approximations  $u^\Delta$  in the  $L^1(\Pi_T)$  norm. Moreover, these bounds are independent of  $\Delta$ , for  $(x, t) \in \Pi_T$ . It follows from standard compactness arguments that there is a subsequential limit, converging in  $L^1(\Pi_T)$ , and a.e. in  $\Pi_T$ , which we will denote  $u$ . A proof of (3.3.7), i.e., that the initial values are assumed in the strong  $L^1$  sense is standard and is thus omitted. The proof is completed with an application of our Lemma 3.5.2, which guarantees that the subsequential limit  $u$  is an entropy solution. By our uniqueness result (Theorem 3.3.2), the entire sequence converges to  $u$ . □

Theorem 3.5.1 shows that there exists a unique entropy solution to the initial value problem (3.1.2), (3.1.4), (3.1.5), i.e., that this problem is well-posed.

## 3.6 Variants of the difference scheme

The scheme described herein for the full problem has the slight inconvenience that to evaluate the Engquist-Osher flux function, one has to determine the extrema of the composite flux function  $q(u - u_F) + b(u)$  for  $q \in \{q_L, \tilde{q}_R\}$  numerically. This can be avoided if we determine the Engquist-Osher flux function for the function  $b(u)$  only, and discretize the linear portion  $q(u - u_F)$  by a properly oriented upwind stencil. The resulting scheme, to which we shall refer as “Scheme 1”, then reads

$$U_j^{n+1} = U_j^n - \lambda \Delta_- h^1(\gamma_{j+1/2}^1, U_{j+1}^n, U_j^n)$$

$$- \lambda w(\gamma_{j-1/2}^2, \gamma_{j+1/2}^2, U_{j-1}^n, U_j^n, U_{j+1}^n) + \lambda \gamma_j^3 \Delta_+ U_j^n,$$

where  $\gamma^1, \gamma^2, \gamma^3$  are defined in (3.1.8) and (3.1.9), and the function  $h^1$  is the EO flux applied to the function  $\gamma^1 b(u)$ , i.e.,

$$h^1(\gamma^1, v, u) = \frac{\gamma^1}{2} \left( b(u) + b(v) - \int_u^v |b'(s)| ds \right),$$

and the function  $w$  arises from determining the EO flux for the linear term  $\gamma^2(x)(u - u_F)$ , followed by differencing with respect to  $x$ , i.e.,

$$w(\gamma_{j-1/2}^2, \gamma_{j+1/2}^2, U_{j-1}^n, U_j^n, U_{j+1}^n) := \Delta_- \tilde{h}(\gamma_{j+1/2}^2, U_{j+1}^n - u_F, U_j - u_F),$$

where we define

$$\tilde{h}(\gamma^2, v, u) := \frac{1}{2} \left( \gamma^2(u + v) - \int_u^v |\gamma^2| ds \right).$$

This yields the upwind formula

$$\begin{aligned} & w(\gamma_{j-1/2}^2, \gamma_{j+1/2}^2, U_{j-1}^n, U_j^n, U_{j+1}^n) \\ &= \begin{cases} \gamma_{j+1/2}^2 (U_j^n - u_F) - \gamma_{j-1/2}^2 (U_{j-1}^n - u_F) & \text{if } \gamma_{j-1/2}^2 \geq 0 \text{ and } \gamma_{j+1/2}^2 \geq 0, \\ \gamma_{j+1/2}^2 (U_{j+1}^n - u_F) - \gamma_{j-1/2}^2 (U_j^n - u_F) & \text{if } \gamma_{j-1/2}^2 < 0 \text{ and } \gamma_{j+1/2}^2 < 0, \\ (\gamma_{j+1/2}^2 - \gamma_{j-1/2}^2) (U_j^n - u_F) & \text{if } \gamma_{j+1/2}^2 \geq 0 \text{ and } \gamma_{j-1/2}^2 < 0. \end{cases} \end{aligned}$$

For easy reference, let us refer to the scheme (3.4.2), (3.4.3), which is analyzed in this paper, as ‘‘Scheme 2’’. Clearly, Scheme 1 emerges from Scheme 2 by applying a direct upwind linearization, and avoiding the EO formula, for as many terms as possible. As we shall see, the performance of Scheme 1 is much inferior to that of Scheme 2 in terms of numerical viscosity. On the other hand, this observation suggests that an even better scheme can possibly be produced if we replace Scheme 2 by a new scheme, called Scheme 3, if we avoid any explicit linear upwind differences at all, and express the numerical flux on all segments as one EO flux. Thus, the marching formula for Scheme 3 is

$$U_j^{n+1} = \begin{cases} U_j^n - \lambda \Delta_- h^3(\tilde{\gamma}_{j+1/2}, \gamma_{j+1/2}^3, U_{j+1}^n, U_j^n) & \text{for } j > 0, \\ U_j^n - \lambda \Delta_- h^2(\tilde{\gamma}_{j+1/2}, U_{j+1}^n, U_j^n) & \text{for } j \leq 0, \end{cases}$$

Case	$q$	$-\gamma_+$	$u_0(x)$	$\lambda$
1	-4.9	-4.3	$0.1\chi_{[-2,2]}(x)$	0.03125
2	-2.8	-2.6	$0.1\chi_{[-1,1]}(x)$	0.04
3	-4.9	0	$0.1\chi_{[-2,-0.4]}(x)$	0.04
4	-4.9	-4.9	$0.1\chi_{[-2,-0.4]}(x)$	0.025

Table 3.1: Parameters for the numerical examples for the reduced problem shown in Figure 3.3.

where we define  $\tilde{\gamma} := (\gamma^1, \gamma^2)$  and

$$h^2(\tilde{\gamma}, v, u) := \frac{1}{2} \left( f(\tilde{\gamma}, u) + f(\tilde{\gamma}, v) - \int_u^v |f_u(\tilde{\gamma}, w)| dw \right),$$

$$h^3(\tilde{\gamma}, \gamma^3, v, u) := \frac{1}{2} \left( f(\tilde{\gamma}, u) + f(\tilde{\gamma}, v) - \gamma^3(u + v) - \int_u^v |f_u(\tilde{\gamma}, w) - \gamma^3| dw \right).$$

For the simplified version of Scheme 1 that applies to the reduced problem (3.1.2), (3.1.4), (3.1.5), it is possible to prove convergence to an entropy solution by repeating the analysis in Section 3.5. For Scheme 3, the convergence proof still goes through, but it is not clear that our proof of convergence to an entropy solution (Lemma 3.5.2) is directly applicable. However, our numerical experiments seem to indicate that approximations generated by Scheme 3 converge to the same (entropy) solutions as provided by Schemes 1 and 2.

## 3.7 Numerical results

### 3.7.1 Numerical solutions of the reduced problem

In the first series of examples, Cases 1 to 4, we consider the reduced problem (3.1.2), (3.1.4), (3.1.5). We assume that the function  $b(u)$  is given by (3.1.6) with  $v_\infty = 6.75$ ,  $u_{\max} = 1$  and  $n = 2$ . The plots of Figure 3.3 correspond to the parameters given in Table 3.1. The simulations have been made with Scheme 3,  $\Delta x = 1/80$ , and

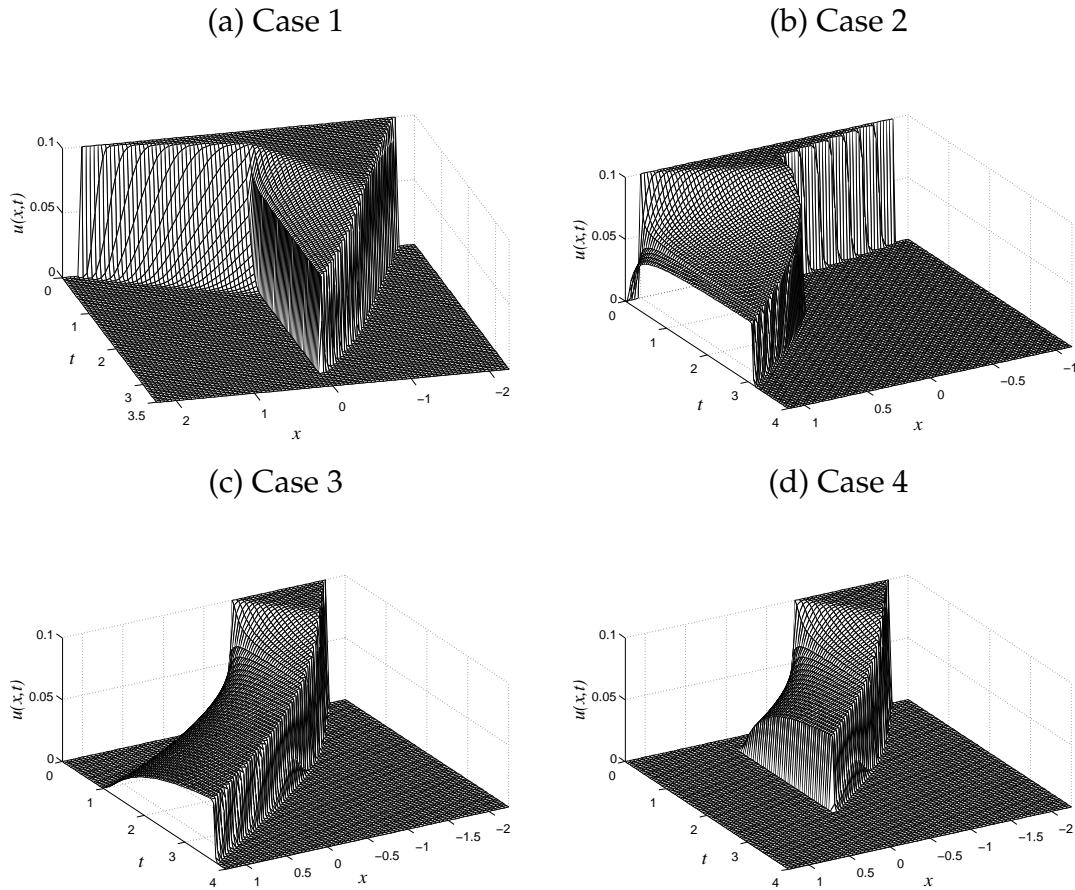


Figure 3.3: Numerical examples with  $\Delta x = 0.0125$  for the reduced problem.

the values of  $\lambda = \Delta t / \Delta x$  indicated in Table 3.1. Note that the sink term in Case 3 is switched off. This solution of a standard nonlinear conservation law has been included to illustrate the difference to Case 4, where the sink term is included, but all other parameters are the same.

### 3.7.2 Numerical solutions of the full problem

Next, we consider the full extended clarifier-thickener model (3.1.1), (3.1.4), (3.1.7)–(3.1.9). The parameters of four different simulations shown in Figure 3.4,

Case	$q_L$	$q_D$	$q_R$	$u_F$	$\lambda$
5	0.0	-1.0	0.6	0.7	0.05333
6	-0.7	-0.3	0.6	0.7	0.06250
7	-2.25	-2.25	1.35	0.3	0.03922
8	-3.6	-2.25	1.35	0.3	0.03968

Table 3.2: Parameters for the numerical examples for the full model shown in Figure 3.4.

Cases 5 to 8, are shown in Table 3.2. In all cases, we start from an initially empty clarifier-thickener unit ( $u_0 \equiv 0$ ), and consider the same function  $b(u)$  as for Cases 1 to 4. The simulations have been made with  $\Delta x = 1/80$  and the values of  $\lambda$  given in Table 3.2.

### 3.7.3 Error study

We consider first Case 1, which corresponds to the reduced problem. Figure 3.5 shows the numerical solution produced by Schemes 1, 2 and 3 for  $t = 0.5$  and  $t = 2$ , while Table 3.3 displays the approximate  $L^1$  error for this case, measured over the interval  $[-1, 1]$ .

Next, we consider Case 5, which corresponds to the full problem. Figure 3.6 shows the numerical solution produced by Schemes 1, 2 and 3 for  $t = 1$ ,  $t = 2$  and  $t = 4$ , respectively, while Table 3.4 displays the approximate  $L^1$  error for this case, measured over the interval  $[-2.1, 1.1]$  (so that all flux discontinuities are included). Finally, we present in Figure 3.7 numerical solutions generated by all three schemes for Case 7 and  $t = 0.3$  and  $t = 10$ . The corresponding approximate  $L^1$  errors are shown in Table 3.5.

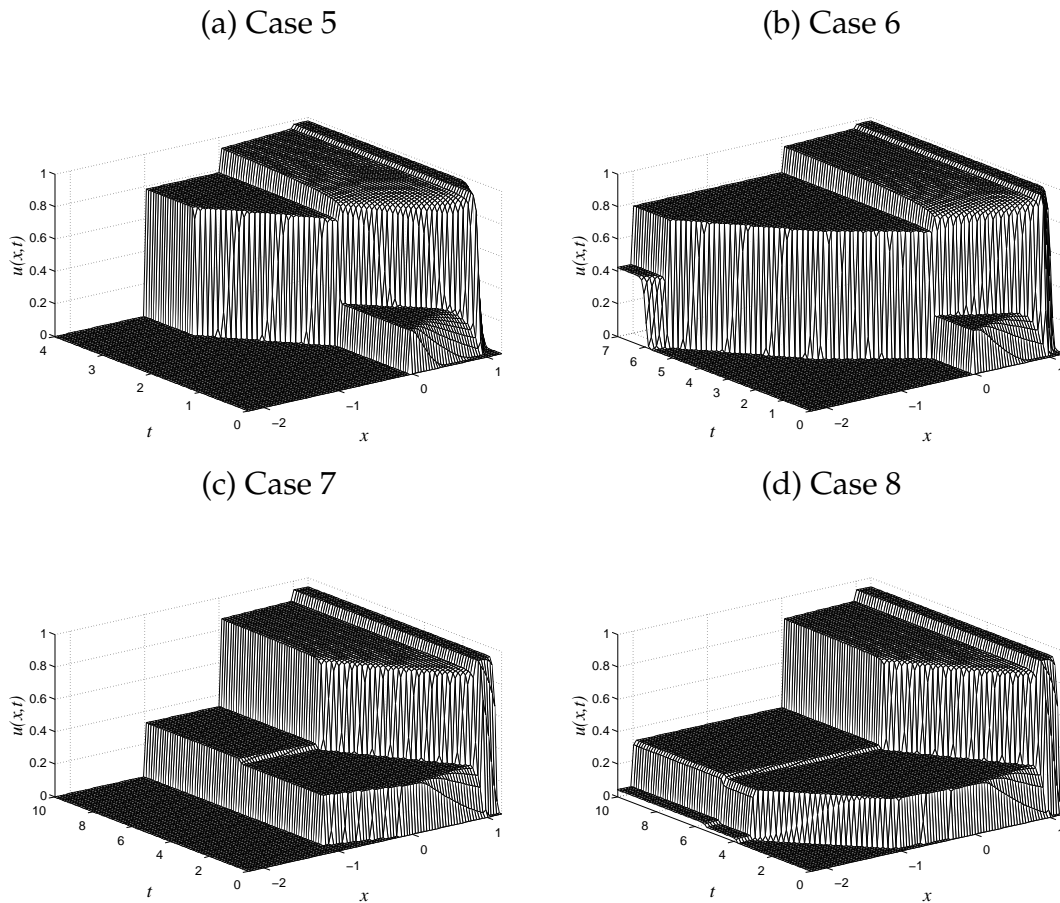


Figure 3.4: Numerical examples with  $\Delta x = 0.0125$  for the full extended clarifier-thickener model.

## 3.8 Conclusion

### 3.8.1 Discussion of the numerical results

Figure 3.3 illustrates that the sink term gives rise to a variety of stationary discontinuities. In fact, the reduced problem models how material whose flow is otherwise governed by the conservation law  $u_t + \varphi(u)_x = 0$  is absorbed by a singular sink. In Cases 1 and 4, the sink produces a decreasing step (in the direction of increasing  $x$ ),

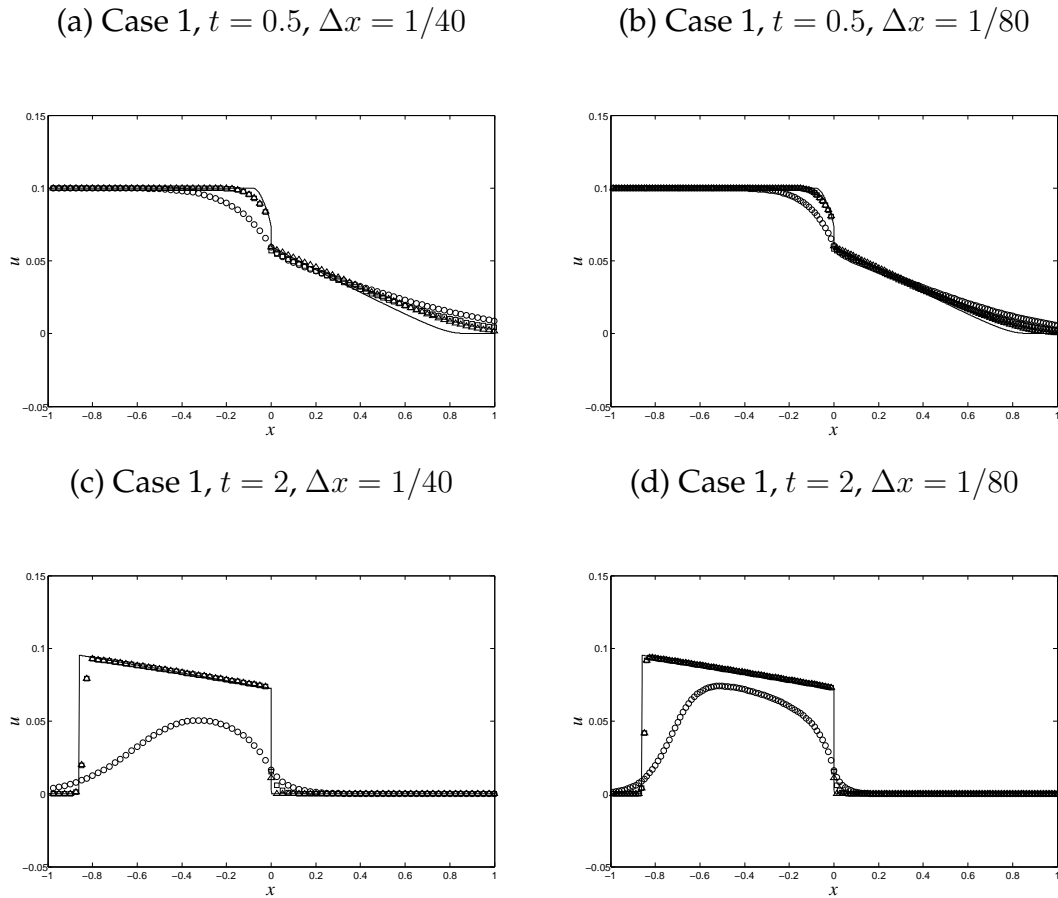


Figure 3.5: Comparison of Scheme 1 ( $\circ$ ), Scheme 2 ( $\square$ ) and Scheme 3 ( $\triangle$ ) applied to Case 1. The solid line is a reference solution with  $\Delta x = 1/1600$ .

while in Case 2, an increasing step is generated. Observe that in Case 2, roughly at  $t = 2$ , the stationary discontinuity at  $x = 0$  ceases to exist, and is followed by a curved shock moving in direction of  $x > 0$ .

The parameters in Figure 3.4 have been chosen in such a way that either the solid material flowing into the clarifier zone is fully absorbed by the singular sink term (Cases 5 and 7), or material is extracted through the sink without affecting the solution in the clarifier zone (Cases 6 and 8). The absence of a discontinuity across  $x = x_D = -1$  in these cases can be made plausible if we look at the associated

$J = 1/\Delta x$	$t = 0.5$		$t = 2$	
	approx. $L^1$ error	conv. rate	approx. $L^1$ error	conv. rate
	Scheme 1			
20	1.715e-2		6.214e-2	
40	1.195e-2	0.522	4.418e-2	0.492
80	8.363e-3	0.515	2.616e-2	0.756
160	5.610e-3	0.576	1.510e-2	0.793
320	3.571e-3	0.652	8.573e-3	0.817
	Scheme 2			
20	7.785e-3		8.310e-3	
40	5.285e-3	0.559	4.332e-3	0.940
80	3.422e-3	0.627	2.221e-3	0.963
160	2.081e-3	0.718	1.107e-3	1.005
320	1.174e-3	0.826	5.171e-4	1.098
	Scheme 3			
20	8.067e-3		7.033e-3	
40	5.045e-3	0.677	3.694e-3	0.929
80	3.003e-3	0.749	1.903e-3	0.957
160	1.674e-3	0.843	9.476e-4	1.006
320	8.487e-4	0.980	4.379e-4	1.114

Table 3.3: Approximate  $L^1$  errors for Case 1.

reduced problem for the parameters given in these cases. For instance, Case 6 corresponds to  $q = q_L = -0.7$ . We observe in Figure 3.4 (b) that the solution in the clarification zone after the solids break through the feed level assumes at least a value of 0.78. However, inspecting the shape of  $u \mapsto b(u)$  it is easy to see that we

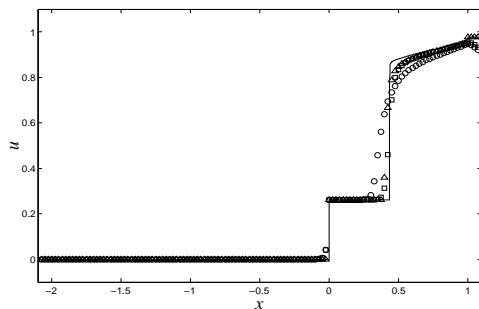
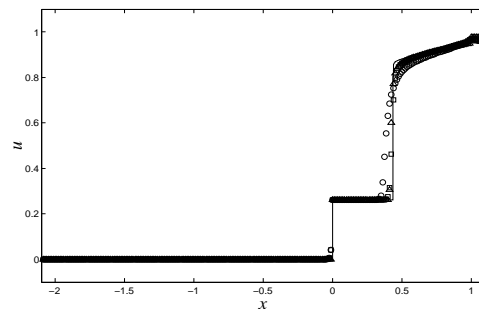
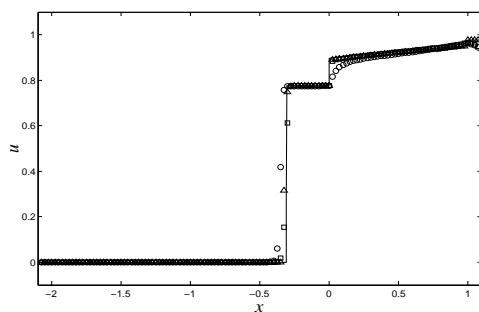
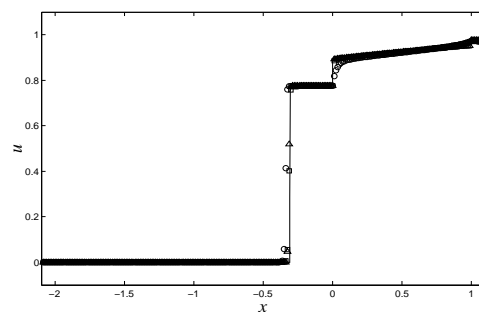
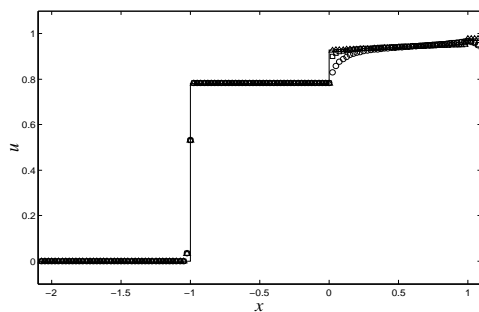
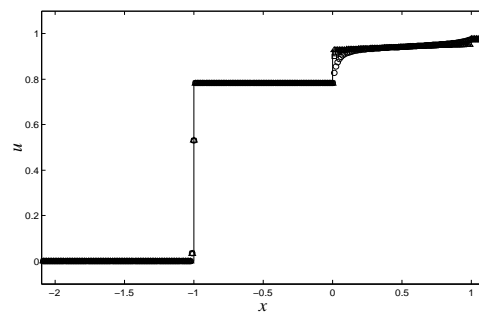
(a) Case 5,  $t = 1$ ,  $\Delta x = 1/40$ (b) Case 5,  $t = 1$ ,  $\Delta x = 1/80$ (c) Case 5,  $t = 2$ ,  $\Delta x = 1/40$ (d) Case 5,  $t = 2$ ,  $\Delta x = 1/80$ (e) Case 5,  $t = 4$ ,  $\Delta x = 1/40$ (f) Case 5,  $t = 4$ ,  $\Delta x = 1/80$ 

Figure 3.6: Comparison of Scheme 1 ( $\circ$ ), Scheme 2 ( $\square$ ) and Scheme 3 ( $\triangle$ ) applied to Case 5. The solid line is a reference solution with  $\Delta x = 1/1600$ .

$J = 1/\Delta x$	$t = 1$		$t = 2$		$t = 4$	
	approx. $L^1$ error	conv. rate	approx. $L^1$ error	conv. rate	approx. $L^1$ error	conv. rate
	Scheme 1					
20	1.139e-1		9.123e-2		7.228e-2	
40	6.561e-2	0.796	4.836e-2	0.916	2.739e-2	1.400
80	4.000e-2	0.714	3.178e-2	0.605	1.488e-2	0.880
160	2.587e-2	0.628	2.123e-2	0.582	8.269e-2	0.848
320	1.665e-2	0.636	1.383e-2	0.619	4.521e-3	0.871
	Scheme 2					
20	7.118e-2		6.616e-2		5.614e-2	
40	2.876e-2	1.308	2.201e-2	1.588	1.856e-2	1.597
80	1.268e-2	1.182	1.106e-2	0.994	1.001e-2	0.891
160	7.428e-3	0.771	5.740e-3	0.946	5.577e-3	0.844
320	4.713e-3	0.656	4.111e-3	0.482	3.025e-3	0.882
	Scheme 3					
20	3.483e-2		3.151e-2		2.466e-2	
40	1.990e-2	0.808	1.753e-2	0.846	1.241e-2	0.991
80	1.101e-2	0.854	9.637e-3	0.863	6.164e-3	1.009
160	6.118e-3	0.847	3.984e-3	1.274	2.979e-3	1.049
320	3.128e-3	0.968	1.906e-3	1.064	1.352e-3	1.140

Table 3.4: Approximate  $L^1$  errors for Case 5.

have

$$\begin{aligned}
\sup_{u^+ \in [0.78, 1]} \max_{u^- \in [0, 1]} \frac{\varphi(u^+) - \varphi(u^-)}{u^+ - u^-} &= q + \sup_{u^+ \in [0.78, 1]} \max_{u^- \in [0, 1]} \frac{b(u^+) - b(u^-)}{u^+ - u^-} \\
&\leq q + \frac{b(0.78) - b(0)}{0.78} = -0.7 + 6.75 \times 0.22^2 = -0.3733,
\end{aligned}$$

so for this value and  $u_+ \geq 0.78$  (in fact, we may choose this lower bound even

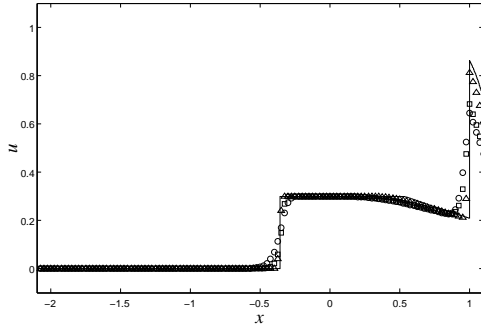
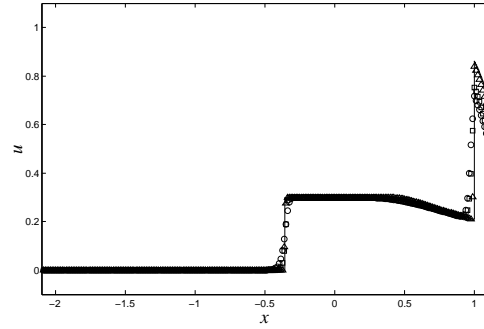
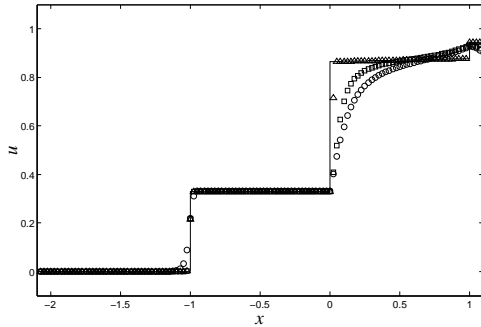
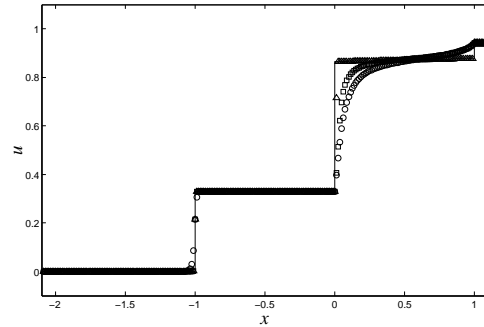
(a) Case 7,  $t = 0.3$ ,  $\Delta x = 1/40$ (b) Case 7,  $t = 0.3$ ,  $\Delta x = 1/80$ (c) Case 7,  $t = 10$ ,  $\Delta x = 1/40$ (d) Case 7,  $t = 10$ ,  $\Delta x = 1/80$ 

Figure 3.7: Comparison of Scheme 1 ( $\circ$ ), Scheme 2 ( $\square$ ) and Scheme 3 ( $\triangle$ ) applied to Case 7. The solid line is a reference solution with  $\Delta x = 1/1600$ .

smaller), the left-hand inequality in jump condition (3.3.9) is never satisfied. In other words, from an engineering point of view, jump condition (3.3.9) helps to predict under which flow conditions extracting material from a sink affects the bulk concentration (i.e., causes a concentration jump) and under which conditions this does not happen (as in our Cases 6 and 8).

Figures 3.5 to 3.7 and Tables 3.3 to 3.5 illustrate that all schemes converge to the unique entropy solution of the reduced problem or the full extended clarifier-thickener model. However, all these results also show that Scheme 1, though it

$J = 1/\Delta x$	$t = 0.3$		$t = 10$	
	approx. $L^1$ error	conv. rate	approx. $L^1$ error	conv. rate
Scheme 1				
20	9.406e-2		1.946e-1	
40	6.394e-2	0.557	1.069e-1	0.864
80	4.255e-2	0.588	6.332e-2	0.756
160	2.685e-2	0.664	3.694e-2	0.778
320	1.609e-2	0.739	2.084e-2	0.826
Scheme 2				
20	7.619e-2		1.365e-1	
40	5.023e-2	0.601	7.423e-2	0.879
80	3.176e-2	0.661	4.303e-2	0.787
160	1.888e-2	0.751	2.465e-2	0.804
320	1.069e-2	0.821	1.358e-2	0.860
Scheme 3				
20	3.092e-2		4.109e-2	
40	1.738e-2	0.831	2.041e-2	1.010
80	9.185e-3	0.920	1.000e-2	1.029
160	4.420e-3	1.055	4.766e-3	1.069
320	2.134e-3	1.051	2.131e-3	1.161

Table 3.5: Approximate  $L^1$  errors for Case 7.

has the convenience of being easy to implement, suffers from excessive numerical viscosity, which becomes apparent in smearing of transient shocks travelling at nonzero speed (for example, near  $x = 0.5$  in Figures 3.6 (a) and (b)) and the formation of one-sided boundary layers near discontinuities of the flux function (for example, near  $x = 0$  in Figures 3.7 (c) and (d)). Scheme 2 exhibits smaller numerical

viscosity, while Scheme 3 sharply resolves all flux discontinuities. Both Schemes 2 and 3 sharply resolve the solution near  $x_D = -1$ . Let us comment that the superiority of Scheme 3 is in part balanced by the slightly increased effort needed to evaluate the flux functions  $h^2$  and  $h^3$ , which need to be calculated anew (by a discussion of extrema) for each value of the control variables  $q_R, q_F, q_D$  and  $u_F$ .

### 3.8.2 Discussion of the entropy condition.

From the proof of Lemma 3.5.2, it is evident that the entropy jump conditions (D.3) that hold at the interface ultimately result from the dissipation built into the monotone difference scheme described in Section 3.4. To be more specific, in the proof of Lemma 3.5.2 we employ two different Lipschitz-continuous regularizations,  $\bar{\gamma}^\epsilon(x) \geq \gamma(x)$  and  $\underline{\gamma}^\epsilon(x) \leq \gamma(x)$ , which approximate the parameter function  $\gamma(x)$ . Examining that proof, it is clear that the entropy conditions (D.3) can be derived by employing monotone schemes for each of the two regularized conservation laws that result by replacing  $\gamma$  by  $\bar{\gamma}^\epsilon$  and  $\underline{\gamma}^\epsilon$ . This yields  $\epsilon$ -dependent entropy conditions. The entropy conditions (D.3) then result by letting the regularization parameter  $\epsilon \rightarrow 0$ .

### 3.8.3 An open problem.

Using the monotone difference scheme (3.5.1), we have established well-posedness of the reduced model. Our ultimate interest is the more complicated scheme (3.4.2) which we use to construct approximate solutions of the full model. We have focused on the reduced model and its associated scheme in order to highlight the aspects of the problem that are more or less unique to the sink portion of the model. We leave as an open problem the task of combining the definition of entropy solution and the results of the present paper with those of [31]. The goal would be to prove that the version of Theorem 3.5.1 that applies to the full problem is also true.



## Chapter 4

# A Kinematic Model of Continuous Separation and Classification of Polydisperse Suspensions

Kinematic models for polydisperse suspensions are based on specifying the solid-fluid relative velocity for each solids species as a function of the local solids concentrations. One such model, the Masliyah-Lockett-Bassoon (MLB) model, is employed herein to simulate continuous separation and classification of polydisperse suspensions. To this end, the clarifier-thickener (CT) setup for the continuous separation of suspensions is extended to a generalized clarifier-thickener (GCT). Discharge streams (or products) are described by new singular sink terms. Combining the GCT setup with the MLB model yields a system of nonlinear conservation laws with a discontinuous flux and a new non-conservative transport term describing the sinks. A numerical algorithm for the solution of this equation is presented along with numerical examples. The model describes the GCT unit with all critical design parameters, and predicts the composition of the overflow, underflow and discharge streams and the spatio-temporal evolution of the solids species concentrations inside the unit.

## 4.1 Introduction

Kinematic models are common approximate descriptions for multiphase flows that are essentially one-dimensional, for example in columns and ducts that are aligned with the driving body force. Usually, in these applications the relative (differential) movement of the phases is more important than are lateral flow components, and one continuous phase (for solid-liquid suspensions, the fluid), and  $N$  disperse phases (species) are distinguished. We here consider polydisperse suspensions with a finite number  $N$  of solid particle species, where particles of species  $i$  have diameter  $d_i$  and density  $\rho_i$ , and  $d_i \neq d_j$  or  $\rho_i \neq \rho_j$  for  $i \neq j$ . To be consistent with previous works of the authors we assume here  $d_1 \geq d_2 \geq \dots \geq d_N$ .

Kinematic models are based on the specification of the velocity of each species relative to that of the fluid as a function of the local concentrations of all species. For batch settling, this leads to a strongly coupled system of  $N$  nonlinear and spatially one-dimensional scalar conservation laws for the volume fractions  $\phi_1, \dots, \phi_N$  of all species. The extension to a continuously operated clarifier-thickener (CT) unit with a singular feed source leads to a system with an additional transport flux whose velocity is a discontinuous function of the spatial position.

We are aware of the progress has been made over the past 10 years concerning the two- and three-dimensional modelling of the flow of particles in fluidized beds, including, for example, the works of Tsuji and co-workers [77, 107, 108, 161, 162, 171] and Glowinski, Joseph, Pan and their collaborators [83, 142] for gas-solid and liquid-solid fluidized beds, respectively. Results of fluidized bed modelling are also well documented in the monographs by Crowe et al. [46], Jackson [97] and Gibilaro [78] and in the slightly older book by Gidaspow [79]; for the alternative two-phase flow and discrete particle modelling approaches, we also refer to the reviews by Enwald et al. [66] and Deen et al. [51]. Most of the cited works are biased towards providing insight into the interaction between the fluid and individual particles, or between individual particles. They consider relatively small numbers of particles, which in turn are relatively large compared with the vessel interior diame-

ter so that wall effects are dominant. Moreover, these models are associated with considerable computational effort. In contrast to this, our model is motivated by industrial applications, in which the particles are small with respect to the vessel diameter and computational effort in calculating each of them would be excessive. A one-dimensional description is adequate, since for small particles in liquid-solid fluidized beds, velocities and compositions are mostly horizontal in the lateral direction. In addition, the model presented herein is supposed to form the basis of design and control calculations, for which low computational cost is desirable. This view is implicitly adapted in many engineering treatments of fluidized beds, see for example [40, 41, 85, 110, 134, 135, 136, 174, 175], and other work cited herein.

In this paper, we present a new model for continuous separation and classification of polydisperse suspensions, which extends the CT setup [13, 31, 59, 174]. The new feature are singular sinks describing the continuous discharge of products at several points, whose composition will vary during a transient startup procedure. The mathematical treatment and discretization of a singular sink is not entirely analogous to that of a singular feed source, since the composition of the sink stream is part of the solution. The singular sinks give rise to a novel so-called non-conservative transport term. The well-posedness of the resulting model and the convergence of a numerical scheme for  $N = 1$  and for sinks located above the feed level or when the whole device is operated as a fluidization column, are proved by Bürger et al. in [23] (Chapter 3 of this thesis). We herein formulate an analogous model for a generalized clarifier-thickener (GCT) setup, which may include several sinks, can also be operated as a fluidization column, and is allowed to have a varying cross-sectional area. We define a numerical scheme for its simulation and present numerical examples, in part adopting data from the literature.

The remainder of the paper is organized as follows. We briefly outline in Section 4.2.1 kinematic models for polydisperse suspensions, recall in Section 4.2.2 recent advances in the analysis and simulation of CT models, and review in Section 4.2.3 related work from the literature. In Section 4.3 we outline the kinematic model of polydisperse suspensions due to Masliyah [129] and Lockett and Bassoon

[128] (MLB model), and recall its stability properties. In Section 4.4 we describe the GCT setup by balancing feed, sink, discharge and overflow bulk flows, and combine it with the MLB model to obtain the final model, which is a system of balance laws, where the nonlinear flux vector depends discontinuously on the space variable and a non-conservative transport term models the new sink feature. The numerical scheme proposed in Section 4.5 for the final model is based on a scheme by Kurganov and Tadmor [119]. In Section 4.5.1, we describe the scheme for the spatio-temporal evolution of the solids concentrations in the interior of the GCT, while Section 4.5.2 provides a method to calculate the sink concentrations. Section 4.6 presents three different numerical examples, and Section 4.7 collects some conclusions.

## 4.2 Motivation

### 4.2.1 Kinematic sedimentation models

The basic postulate of the kinematic model by Kynch [120] states that the settling velocity  $v_s$  of a particle in a monodisperse suspension of solids concentration  $\phi$  is given by  $v_s = v_\infty(1 - \phi)^2V(\phi)$ , where  $v_\infty$  is the settling velocity of a single particle in an unbounded fluid, and  $V(\phi)$  is a hindered settling factor that takes into account the presence of other particles. This function can for example, be chosen as (Richardson and Zaki [147])

$$V(\phi) = \begin{cases} (1 - \phi)^{n-2} & \text{for } \phi \in [0, \phi_{\max}], \\ 0 & \text{otherwise,} \end{cases} \quad n > 2, \quad (4.2.1)$$

where  $0 < \phi_{\max} \leq 1$  is a maximum concentration, and  $n$  is specified later. The one-dimensional solids continuity equation then turns into the following conservation law, where  $t$  is time and  $x$  is depth:

$$\partial_t \phi + \partial_x f(\phi) = 0, \quad f(\phi) = \phi v_s = v_\infty \phi (1 - \phi)^2 V(\phi),$$

which describes the settling of a suspension in a column. Due to the nonlinearity of  $f(\phi)$ , its solutions are in general discontinuous.

For polydisperse suspensions, the sought quantity is the vector  $\Phi := (\phi_1, \dots, \phi_N)^\top$  as a function of  $x$  and  $t$ , where  $\phi_i$  is the concentration of species  $i$  having diameter  $d_i$  and density  $\rho_i$ . For batch settling of an  $N$ -disperse suspension with initial concentration  $\Phi_0(z)$  in a column of height  $L$ , the kinematic model can be expressed as the initial-boundary value problem of a system of conservation laws

$$\begin{aligned} \partial_t \Phi + \partial_x \mathbf{f}(\Phi) &= 0, \\ \Phi(x, 0) &= \Phi_0(x), \quad 0 \leq x \leq L; \quad \mathbf{f}|_{x=0} = \mathbf{f}|_{x=L} = 0, \quad t > 0, \end{aligned} \tag{4.2.2}$$

where  $\mathbf{f}(\Phi) = (f_1(\Phi), \dots, f_N(\Phi))^\top$  is the vector of flux densities  $f_i(\Phi) = \phi_i v_i$ , where  $v_i$  is the velocity of particle species  $i$ ,  $i = 1, \dots, N$ . Choices of  $\mathbf{f}(\Phi)$  proposed in the literature are compared by Ha and Liu [86], Bürger et al. [20, 32] and Zeidan et al. [175]. In this paper, we adopt the MLB model [129, 128]. Our preference of this model is based on the experimental study by Law et al. [122] and analyses of global stability [32, 12]. Since each function  $f_i(\Phi)$  depends nonlinearly on all concentrations  $\phi_1, \dots, \phi_N$ , and exact solution constructions are at least complicated [85, 69], numerical methods are needed for the solution of (4.2.2). Clearly, its solutions are also in general discontinuous.

### 4.2.2 Clarifier-thickener models

The model (4.2.2) can be extended to continuous flow if a linear transport term  $q(x, t)\Phi$  is added to the flux  $\mathbf{f}(\Phi)$ , which describes the differential motion of the species. The velocity  $q(x, t)$  is controlled externally. We then obtain the system

$$\partial_t \Phi + \partial_x (q(x, t)\Phi + \mathbf{f}(\Phi)) = 0. \tag{4.2.3}$$

Models of continuously operated CT units have a clarification zone, corresponding to depth  $x < 0$ , adjacent to a thickening zone with  $x > 0$ . The feed mechanism is represented as a singular source sitting at  $x = 0$ . Usually, part of the feed bulk flow is directed into the thickening zone (this can be controlled by a discharge valve),

while the remainder flows upwards into the clarification zone. This means that

$$q(x, t) = \begin{cases} q_L(t) < 0 & \text{for } x < 0, \\ q_R(t) > 0 & \text{for } x > 0, \end{cases} \quad (4.2.4)$$

so that the total flux  $q(x, t)\Phi + \mathbf{f}(\Phi)$  is discontinuous across  $x = 0$ . If the unit is operated as a fluidization column, then we have  $q(x, t) < 0$  throughout, but this quantity is equally discontinuous across  $x = 0$ . We continue to refer to “clarifier-thickener” units for polydisperse suspensions, even if in the latter case they are used for classification.

The basic difficulty is that the discontinuous flux model (4.2.3), (4.2.4) is not well posed a priori, and that numerical methods need to be tailored for its simulation. In fact, even in the scalar (monodisperse) case, the well-posedness of (4.2.3), (4.2.4) (i.e., existence and uniqueness of a properly defined solution) is not a straightforward limit case of the standard theory for conservation laws with a flux that depends smoothly on  $x$ . Even when  $q$  is constant, and  $N = 1$ , solutions of (4.2.3) are in general discontinuous, and require an entropy condition to select the physically relevant solution. In addition, they are also discontinuous across the stationary jumps of  $q(x, t)$ , which calls for the application of a further entropy condition. The design of entropy conditions in order to single out a unique admissible solution for a conservation law with discontinuous flux is a topic of current research. The extension of findings of mathematical analysis for  $N = 1$  to  $N \geq 2$  is strongly based on numerical experimentation. We refer to [174] and [21] for details and references.

The new ingredient of the GCT setup are one or several singular sinks, which affect the continuity equation in two ways: first, the deviation of part of the bulk flow through a sink causes a new discontinuity of  $q(x, t)$ , and second, the extraction of solids through a sink gives rise to an additional solution-dependent singular term. Combining both ingredients admits to replace the new flux discontinuity and the singular term by a non-conservative transport term. For  $N = 1$  and for sinks located above the feed level or when the whole device is operated as a fluidization column, we proved that the model is well posed [23] (Chapter 3 of this thesis).

### 4.2.3 Related work

Several groups of researchers have proposed mathematical models and numerical techniques for, and conducted experiments with separation devices that are special cases of our GCT setup. Nasr-el-Din et al. [134, 135, 136] study vertical columns for the gravity separation and classification of polydisperse suspensions that have a feed source at a central depth level, and which are tapped near the top and bottom ends. They also present a mathematical model which, however, handles the steady-state case only. Experimental results for a similar setup are also presented by Spannenberg et al. [154].

A shortcoming of the model outlined in [134, 135, 136] is their source zone of finite depth, in which the composition of the mixture is supposed to be uniform and which acts as a buffer between the downwards- and upwards-directed bulk flows (if the unit is operated as the CT mode, that is, with a co-gravity bulk flow in the thickening zone), so that these flows take place in spatially separated regions. Moreover, Nasr-el-Din et al. [135] require that “the solids and the carrier fluid are allowed to exit through the overflow or the underflow boundaries, but they are not allowed to enter the source zone through the feed stream”. However, a CT model in which the clarification and thickening zones are disconnected does not capture interesting cases such as solids breaking through into the clarification zone due to overload, and it cannot be easily modified to accommodate the fluidization column mode of operation (in which the thickening zone is fluidized by a counter-gravity bulk flow).

Chen et al. [40, 41] develop a model of a liquid fluidized-bed classifier, first for steady state [40] and then for the transient case [41]. (A closely related experimental study is that of Mitsutani et al. [131].) The model is similar to ours in the fluidization column mode of operation, but differs in the detailed treatment of sources, sinks, overflows and boundary conditions. It is based on both the continuity equation and the linear momentum balance for each particle species, and includes several regularizing elements, in particular an axial dispersion (in mathematical terms, diffusion) coefficient, by which, as the authors write, “turbulence and non-uniformities are

[...] taken into account indirectly”. Mathematically, this term acts as a regularizing diffusion term. Moreover, the feed source and discharge sink are blended in over a finite depth interval (by means of the parameter  $\alpha$  in Table 1 of [41]), and the imposed boundary condition is equivalent to stating that the concentrations are continuous across the overflow and underflow levels. The latter condition is consistent with the global diffusion assumed by Chen et al. [41], but is incompatible with the condition of equality of fluxes for a kinematic model. Our approach shows that regularizing ingredients, which tend to blur features of a “true” solution such as sharp interfaces, are unnecessary, and that a complete GCT model can be based on a kinematic approach with singular sources, sinks, and flux transitions at overflow and underflow or fluidization levels.

A similar model of a so-called hindered-settling column was proposed by Kim and Klima [110], see also [173] for experimental findings. Kim and Klima [110] solve a scalar convection-diffusion equation for each species, which represents the continuity equation. Again, positive diffusivity is introduced, this time called a “mixing coefficient”. The setup considered by Kim and Klima [110] is that of a clarifier-thickener. One remarkable feature of the discretization chosen by Kim and Klima [110] is that the overflow, underflow and feed mechanisms are assigned to one cell each, of the same width  $\Delta z$  as that of the discretization, so that their sinks and sources become singular in the limit  $\Delta z \rightarrow 0$ . Unfortunately, Kim and Klima [110] do not indicate the precise algebraic treatment of these mechanisms.

The model of Zeidan et al. [174] is equivalent to ours in the special case that there are no sinks, and a cylindrical vessel is considered. Thus, our GCT setup and its numerical treatment can be viewed as a direct extension of the model by Zeidan et al. [174]. Moreover, they use Godunov’s method for discretization of the governing equations. This method is sound, but only first-order accurate, while our method is second-order accurate both in time and space. (Of course, the formal order of accuracy is recovered on smooth portions of the solution only.) The discretization chosen by Zeidan et al. [174] is extremely coarse; the entire CT unit is subdivided into 8 cells only.

## 4.3 Mathematical model of polydisperse sedimentation

### 4.3.1 Model equations

Model equations for the three-dimensional motion of a polydisperse suspension were derived from the mass and linear momentum balances for the fluid and each solid species, considered as  $N + 1$  separate phases, by introducing constitutive assumptions and simplifying the equations through a dimensional analysis [12]. The result is a particular expression of the solid-fluid relative velocity of each species as a function of  $\Phi$ , which in one space dimension is equivalent to expressions stated by Masliyah [129] and Lockett and Bassoon [128], see (4.3.5) below.

We denote by  $\phi := \phi_1 + \dots + \phi_N$  the total solids concentration. If  $v_f$  is the fluid phase velocity, and  $S(x)$  is the cross-sectional area of the vessel at depth  $x$ , then the one-dimensional continuity equations for the  $N$  solids phases and the fluid can be written as

$$S(x)\partial_t\phi_i + \partial_x(S(x)\phi_i v_i) = 0, \quad i = 1, \dots, N, \quad (4.3.1)$$

$$-S(x)\partial_t\phi + \partial_x(S(x)(1 - \phi)v_f) = 0. \quad (4.3.2)$$

Introducing the volume average flow velocity weighted with  $S(x)$ ,

$$Q(x, t) := S(x)(\phi_1 v_1 + \dots + \phi_N v_N + (1 - \phi)v_f), \quad (4.3.3)$$

we obtain by adding (4.3.1) and (4.3.2) the mixture continuity equation  $\partial_x Q(x, t) = 0$ . Since a constitutive equation will be introduced for the solid-fluid relative velocities or slip velocities  $u_i := v_i - v_f$ ,  $i = 1, \dots, N$ , we use (4.3.3) and  $\partial_x Q(x, t) = 0$  to rewrite (4.3.1) as

$$S(x)\partial_t\phi_i + \partial_x \left( Q(x, t)\phi_i + S(x)\phi_i \left[ u_i - \sum_{j=1}^N \phi_j u_j \right] \right) = 0, \quad i = 1, \dots, N. \quad (4.3.4)$$

We define the parameters  $\delta_i := d_i^2/d_1^2$  and  $\bar{\rho}_i := \rho_i - \rho_f$  for  $i = 1, \dots, N$ , and  $\mu := gd_1^2/(18\mu_f)$ , where  $\rho_f$  and  $\mu_f$  are the density and the viscosity of the fluid, respectively, and  $g$  is the acceleration of gravity.

Within the MLB model,  $u_i$  is specified as

$$u_i = u_i(\Phi) = \frac{\mu\delta_i}{1 + 0.15\text{Re}_i^{0.687}} V(\phi)(\bar{\rho}_i - \bar{\rho}^T\Phi), \quad i = 1, \dots, N, \quad (4.3.5)$$

for  $\text{Re}_i < 1000$ ,

where  $\bar{\rho} := (\bar{\rho}_1, \dots, \bar{\rho}_N)^T$ , the hindered settling factor  $V(\phi)$  may be chosen as (4.2.1), and  $\text{Re}_i$  is the particle Reynolds number for species  $i$ ,

$$\text{Re}_i := |u_i|(1 - \phi) \frac{d_i \rho_f}{\mu_f}. \quad (4.3.6)$$

The pair of equations (4.3.5) and (4.3.6) (see e.g. [129]) defines  $u_i$  implicitly. To avoid this implicit form and to be consistent with previous work, in particular, with the stability analysis of Bürger et al. [32], we approximate  $\text{Re}_i$  by

$$\text{Re}_i \approx \widetilde{\text{Re}}_i := \mu\delta_i |\rho_i - \rho_f| (1 - \beta\phi_{\max})^n \frac{d_i \rho_f}{\mu_f}, \quad (4.3.7)$$

where  $\beta \in [0, 1]$  is a constant parameter that has to be adjusted, and the exponent  $n$  is specified below.

For sufficiently small Reynolds numbers, namely less than 0.1, we may set the denominator in (4.3.5) to one. To be definite, we utilize

$$u_i = \mu\tilde{\delta}_i V(\phi)(\bar{\rho}_i - \bar{\rho}^T\Phi),$$

$$\tilde{\delta}_i := \begin{cases} \delta_i & \text{if } \widetilde{\text{Re}}_i < 0.1, \\ \delta_i / (1 + 0.15\widetilde{\text{Re}}_i^{0.687}) & \text{if } 0.1 < \widetilde{\text{Re}}_i < 1000, \end{cases} \quad i = 1, \dots, N. \quad (4.3.8)$$

The specific property of the MLB model is the appearance of the factor  $V(\phi)(\bar{\rho}_i - \bar{\rho}^T\Phi)$  in (4.3.5), which in a reduced form reflects the linear momentum balances.

For spherical particles and in the monodisperse case, the exponent  $n$  depends on the particle Reynolds number at infinite dilution and the particle to vessel diameter

ratio, and may be given by

$$n = \begin{cases} 4.65 + 19.5d/W & \text{for } \text{Re}_\infty \leq 0.2, \\ (4.35 + 17.5d/W)\text{Re}_\infty^{-0.03} & \text{for } 0.2 < \text{Re}_\infty \leq 1, \\ (4.45 + 18d/W)\text{Re}_\infty^{-0.1} & \text{for } 1 < \text{Re}_\infty \leq 200, \\ 4.45\text{Re}_\infty^{-0.1} & \text{for } 200 < \text{Re}_\infty \leq 500, \\ 2.39 & \text{for } \text{Re}_\infty > 500, \end{cases} \quad (4.3.9)$$

according to Richardson and Zaki [147]. Here,  $d$  is the diameter of the particles,  $W$  is the vessel diameter (of the cylindrical section of its interior), and  $\text{Re}_\infty := \rho_f v_\infty d / \mu_f$  is the particle Reynolds number based on the particle settling velocity at infinite dilution,  $v_\infty$ , which we calculate as follows [115]:

$$v_\infty = \frac{(\mu_f(\rho_s - \rho_f)g)^{1/3}}{\rho_f^{2/3} \left( \frac{18}{(d^*)^2} + \frac{0.591}{(d^*)^{0.5}} \right)}, \quad d^* := d \left( \frac{\rho_f(\rho_s - \rho_f)g}{\mu_f^2} \right)^{1/3}. \quad (4.3.10)$$

In our examples, we calculate  $N$  exponents  $n_1, \dots, n_N$  using (4.3.9) and (4.3.10) with  $d$  and  $\rho_s$  replaced by  $d_i$  and  $\rho_i$ , respectively, for  $i = 1, \dots, N$ , and finally use  $n = (n_1 + \dots + n_N)/N$  in the hindered settling factor.

Inserting (4.3.5) into (4.3.4) yields the system of conservation laws

$$S(x)\partial_t \Phi + \partial_x(Q(x, t)\Phi + S(x)\mathbf{f}^M(\Phi)) = 0, \quad (4.3.11)$$

where the components of the vector

$$\mathbf{f}^M(\Phi) := (f_1^M(\Phi), \dots, f_N^M(\Phi))^T \quad (4.3.12)$$

are the MLB flux functions  $f_1^M(\Phi), \dots, f_N^M(\Phi)$  given by

$$f_i^M(\Phi) := \mu V(\phi)\phi_i \left[ \tilde{\delta}_i(\bar{\rho}_i - \bar{\rho}^T \Phi) - \sum_{k=1}^N \tilde{\delta}_k \phi_k (\bar{\rho}_k - \bar{\rho}^T \Phi) \right], \quad i = 1, \dots, N. \quad (4.3.13)$$

### 4.3.2 Stability of the MLB model

The system (4.2.2) is called *hyperbolic* if the eigenvalues of the Jacobian  $\mathcal{J}_f(\Phi) := (\partial f_i / \partial \phi_k)_{1 \leq i, k \leq N}$  are real, and *strictly hyperbolic* if these are also pairwise distinct. For  $N = 2$ , a system with a pair of complex conjugate eigenvalues is *elliptic*. Some of the flux density vectors  $\mathbf{f}(\Phi)$  proposed in the literature cause (4.2.2) to be of mixed type, depending on the size and density parameters, where the type is called *mixed* if the system is non-hyperbolic for certain choices of  $\Phi$ .

The criterion for ellipticity is equivalent to the instability criterion by Batchelor and Janse van Rensburg [8]. Bürger et al. [32] showed that loss of hyperbolicity, that is the occurrence of complex eigenvalues of  $\mathcal{J}_f(\Phi)$ , provides an instability criterion for polydisperse suspensions for arbitrary  $N$ . For  $N = 3$ , this criterion can be evaluated by a convenient calculation of a discriminant, which is an explicit algebraic function of pointwise values of the partial derivatives  $\partial f_i / \partial \phi_j$ . Biesheuvel et al. [15] and Bürger et al. [32] determine instability regions for  $N = 2, 3$  and different choices of  $\mathbf{f}(\Phi)$ . Berres et al. [12] proved that for equal-density particles ( $\bar{\rho}_1 = \dots = \bar{\rho}_N = \rho_s - \rho_f$ ) and arbitrary particle size distributions with  $\tilde{\delta}_i \neq \tilde{\delta}_j$  for  $i \neq j$ , the system (4.2.2) with the flux vector  $\mathbf{f}(\Phi)$  given by (4.3.12), (4.3.13) is strictly hyperbolic for all  $\Phi \in \mathcal{D}_1$  with  $\phi_1 > 0, \dots, \phi_N > 0$  and  $\phi < 1$ .

The instability criterion for one-dimensional batch settling is the same as for the full two- or three-dimensional model, in which the corresponding first-order system of conservation laws is coupled with additional equations of motion for the mixture. Likewise, for a given vector  $\Phi$  the equation (4.3.11) and the final governing equation for the GCT developed herein (see Section 4.4.3) is unstable if and only if the system (4.2.2) with (4.3.12), (4.3.13) is.

Biesheuvel et al. [15] provide a vivid description of the consequences of lack of stability, which include the formation of blobs and “fingers” in bidisperse sedimentation, increased sedimentation rates, decreased separation quality of hydraulic classifiers, and non-homogeneous sediments in material manufacturing by suspension processing. These phenomena have indeed been observed in experiments (e.g. by Weiland et al. [166]) under the circumstances predicted by the instability crite-

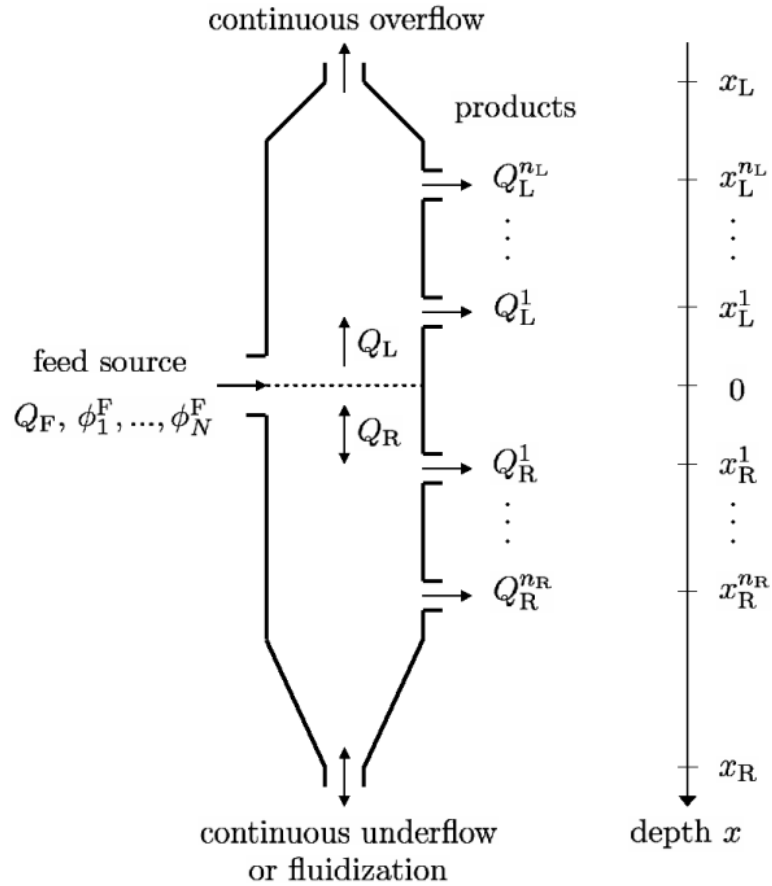


Figure 4.1: Generalized clarifier-thickener (GCT).

tion. On the other hand, the hyperbolicity, and thus stability result for equal-density spheres agrees with experimental evidence, since instabilities never have been observed with this type of mixtures, but always involve particles of different densities [166].

For one-dimensional kinematic models, such as ours, lack of stability may lead to anomalous behaviour of the numerical solution, for example to oscillations or a “locking” effect, i.e., heavy and buoyant particles block each other within the vessel; such an example is presented by Berres et al. ([13], Figure 10). These phenomena do, however, not appear in the examples of this paper.

## 4.4 The generalized clarifier-thickener (GCT) model

We consider a vessel with axisymmetric circular interior cross-sectional area and circular cylindrical outer pipes, see Figure 4.1. This unit can be operated continuously in two modes, the clarifier-thickener (CT) mode and the fluidization column (FC) mode. In the CT mode, the feed flow is divided into upwards- and downwards-directed bulk flows, and the upper and lower ends of the unit are identified as overflow and underflow levels, respectively, whereas in the FC mode, there is an additional counter-gravity bulk inflow of liquid from  $x = x_R$ . Our numerical examples are limited to the FC mode; for examples of the CT mode, we refer to [13] and [23] (Chapter 3 of this thesis).

We subdivide the unit into four different zones: the overflow zone ( $x < x_L$ ), the clarification zone ( $x_L < x < 0$ ), the settling zone ( $0 < x < x_R$ ), and the underflow (in CT mode) or fluidization (in FC mode) zone ( $x > x_R$ ). The vessel is continuously fed at depth  $x = 0$ , the feed level, with fresh feed suspension, and it has discharge outlets for products at different depths located above and below the feed point.

### 4.4.1 Suspension bulk flows

If  $Q_F(t) \geq 0$  is the volume feed rate of suspension, and assuming for a moment that the discharge outlets are not active, we require that the global suspension continuity equation

$$Q_F(t) = Q_R(t) - Q_L(t) \quad (4.4.1)$$

be always satisfied, where  $Q_R(t) > 0$  and  $Q_R(t) \leq 0$  in the CT and FC modes, respectively, and  $Q_L(t) \leq 0$ .

Now let us include discharge openings located at  $0 > x_L^1 > \dots > x_L^{n_L} > x_L$  and  $0 < x_R^1 < \dots < x_R^{n_R} < x_R$  associated with the respective discharge rates  $Q_L^1(t) \leq 0, \dots, Q_L^{n_L}(t) \leq 0$  and  $Q_R^1(t) \leq 0, \dots, Q_R^{n_R}(t) \leq 0$ . We now denote by  $Q_L(t)$  and  $Q_R(t)$  the volume bulk flows adjacent to  $x = 0$ , so that (4.4.1) remains valid. Using the

Heaviside function

$$H(\xi) := \begin{cases} 1 & \text{if } \xi \geq 0, \\ 0 & \text{if } \xi < 0, \end{cases}$$

we can write the piecewise constant (with respect to  $x$ ) bulk flow as

$$Q(x, t) = \begin{cases} Q_L(t) - \sum_{m=1}^{n_L} Q_L^m(t) H(x_L^m - x) & \text{for } x < 0, \\ Q_R(t) + \sum_{m=1}^{n_R} Q_R^m(t) H(x - x_R^m) & \text{for } x > 0. \end{cases} \quad (4.4.2)$$

#### 4.4.2 Solids feed and sink terms

As in [21], we assume that for  $x > x_R$  and  $x < x_L$ , the cross-sectional area shrinks to a very small value, so that these zones actually correspond to transport pipes in which all solids (if any) move with the velocity of the fluid. Consequently, the slip velocities  $u_1, \dots, u_N$  are “switched off” outside the vessel interior  $(x_L, x_R)$  by the discontinuous function

$$\gamma^1(x) := \begin{cases} S(x) & \text{if } x_L < x < x_R, \\ 0 & \text{otherwise.} \end{cases}$$

The next step is to replace (4.3.11) by the equation

$$S(x) \partial_t \Phi + \partial_x (Q(x, t) \Phi + \gamma^1(x) \mathbf{f}^M(\Phi)) = 0, \quad (4.4.3)$$

where  $Q(x, t)$  is given by (4.4.2). Next, we consider that at  $x = 0$ , the unit is fed at a volume rate  $Q_F(t) \geq 0$  with feed suspension that contains solids of species 1 to  $N$  at the volume fractions  $\phi_1^F(t)$  to  $\phi_N^F(t)$ . Specifying the phase space of physically relevant concentrations

$$\mathcal{D}_{\phi_{\max}} := \{(\phi_1, \dots, \phi_N)^T : \phi_1 \geq 0, \dots, \phi_N \geq 0, \phi \leq \phi_{\max}\},$$

where  $\phi_{\max}$  is the maximal solids concentration, we assume that

$$\Phi^F(t) := (\phi_1^F(t), \dots, \phi_N^F(t))^T \in \mathcal{D}_{\phi_{\max}} \quad \text{for all } t > 0.$$

The feed mechanism gives rise to an additional singular source term to (4.4.3), so that we now consider the equation

$$S(x)\partial_t\Phi + \partial_x(Q(x,t)\Phi + \gamma^1(x)\mathbf{f}^M(\Phi)) = \delta(x)Q_F(t)\Phi^F(t), \quad (4.4.4)$$

where  $\delta(x)$  is the Dirac delta function centered at  $x = 0$ . Using the Heaviside function and  $Q_R(t)$  and  $Q_L(t)$  as control variables, we may absorb the right-hand side of (4.4.4) into the flux function. Furthermore, we take into account that the *sink* terms model the discharge of suspension of *unknown* concentration. This leads to the equation

$$\begin{aligned} & S(x)\partial_t\Phi + \partial_x\left(Q(x,t)\Phi + \gamma^1(x)\mathbf{f}^M(\Phi) - H(x)(Q_R(t) - Q_L(t))\Phi^F(t)\right) \\ &= \sum_{m=1}^{n_L} \delta(x - x_L^m)Q_L^m(t)\Phi(x,t) + \sum_{l=1}^{n_R} \delta(x - x_R^l)Q_R^l(t)\Phi(x,t). \end{aligned} \quad (4.4.5)$$

Finally, we define the piecewise constant (with respect to  $x$ ) function

$$\mathcal{H}(x,t) := -\sum_{m=1}^{n_L} H(x - x_L^m)Q_L^m(t) - \sum_{l=1}^{n_R} H(x - x_R^l)Q_R^l(t),$$

and we may rewrite the right-hand side of (4.4.5) as

$$-\Phi(x,t)\partial_x\mathcal{H}(x,t) = -\partial_x(\mathcal{H}(x,t)\Phi(x,t)) + \mathcal{H}(x,t)\partial_x\Phi(x,t),$$

so that we obtain from (4.4.5) the following equation:

$$\begin{aligned} & S(x)\partial_t\Phi + \partial_x\left(Q(x,t)\Phi + \gamma^1(x)\mathbf{f}^M(\Phi) + \mathcal{H}(x,t)\Phi\right. \\ & \quad \left. - H(x)(Q_R(t) - Q_L(t))\Phi^F(t)\right) = \mathcal{H}(x,t)\partial_x\Phi(x,t). \end{aligned} \quad (4.4.6)$$

**Remark 4.4.1** The motivation for writing this way the model equation comes from that expound in the section 3.2.3 of the Chapter 3.

### 4.4.3 Final form of the mathematical model

We assume that the control variables  $Q_F(t)$ ,  $Q_R(t)$  and  $Q_L(t)$  as well as the discharge fluxes controlling the sink terms are constant. Then, in view of (4.4.2), and defining  $\tilde{Q}_L := Q_L - (Q_L^1 + \dots + Q_L^{n_L})$ , we can rewrite (4.4.6) as

$$S(x)\partial_t\Phi + \partial_x\tilde{\mathbf{g}}(x, \Phi) = \mathcal{H}(x)\partial_x\Phi,$$

where we define

$$\tilde{\mathbf{g}}(x, \Phi) := \begin{cases} \tilde{Q}_L\Phi + \gamma^1(x)\mathbf{f}^M(\Phi) & \text{for } x < 0, \\ Q_R\Phi - (Q_R - Q_L)\Phi^F + (\tilde{Q}_L - Q_L)\Phi + \gamma^1(x)\mathbf{f}^M(\Phi) & \text{for } x \geq 0, \end{cases}$$

and  $\mathcal{H}(x)$  is the time-independent version of  $\mathcal{H}(x, t)$ . Adding the constant vector  $-\tilde{Q}_L\Phi^F$  to  $\tilde{\mathbf{g}}(x, \Phi)$ , and defining  $\tilde{Q}_R := Q_R - (Q_L^1 + \dots + Q_L^{n_L})$ , we obtain the flux vector

$$\mathbf{g}(x, \Phi) := \begin{cases} \tilde{Q}_L(\Phi - \Phi^F) + \gamma^1(x)\mathbf{f}^M(\Phi) & \text{for } x < 0, \\ \tilde{Q}_R(\Phi - \Phi^F) + \gamma^1(x)\mathbf{f}^M(\Phi) & \text{for } x \geq 0. \end{cases}$$

Defining the discontinuous parameter

$$\gamma^2(x) := \begin{cases} \tilde{Q}_L & \text{for } x < 0, \\ \tilde{Q}_R & \text{for } x \geq 0 \end{cases}$$

and the vector  $\boldsymbol{\gamma}(x) := (\gamma^1(x), \gamma^2(x))$ , we obtain

$$\mathbf{g}(x, \Phi) = \mathbf{f}(\boldsymbol{\gamma}(x), \Phi) := \gamma^1(x)\mathbf{f}^M(\Phi) + \gamma^2(x)(\Phi - \Phi^F).$$

This yields the governing equation

$$S(x)\partial_t\Phi + \partial_x\mathbf{f}(\boldsymbol{\gamma}(x), \Phi) = \mathcal{H}(x)\partial_x\Phi. \quad (4.4.7)$$

This system is solved together with the initial condition

$$\Phi(x, 0) = \Phi^0(x) := (\phi_1^0(x), \dots, \phi_N^0(x))^T \in \mathcal{D}_{\phi_{\max}}. \quad (4.4.8)$$

Note that the decisive new feature of (4.4.7) is the non-conservative transport term  $\mathcal{H}(x)\partial_x\Phi$ , which models the singular sinks.

## 4.5 Numerical scheme

### 4.5.1 Discretization of the interior of the GCT

We discretize the spatial domain into cells  $I_j := [x_{j-1/2}, x_{j+1/2})$ ,  $j = 0, \pm 1, \pm 2, \dots$ , where  $x_k = k\Delta x$  for  $k = 0, \pm 1/2, \pm 1, \pm 3/2, \dots$ . Similarly, the time interval  $(0, T)$  is discretized via  $t_n = n\Delta t$  for  $n = 0, \dots, \mathcal{N}$ , where  $\mathcal{N} = \lfloor T/\Delta t \rfloor + 1$ , which results in the time strips  $I^n := [t_n, t_{n+1})$ ,  $n = 0, \dots, \mathcal{N} - 1$ . Here  $\Delta x > 0$  and  $\Delta t > 0$  denote the spatial and temporal discretization parameters, respectively. These parameters are chosen so that the following stability condition (CFL condition) holds:

$$\frac{\Delta t}{\Delta x S_{\min}} \left( \max \rho(J_f(\gamma, \Phi)) + \max_{x \in (-\infty, \infty)} \mathcal{H}(x) \right) \leq \frac{1}{8},$$

where  $\rho(\cdot)$  denotes the spectral radius,  $J_f(\gamma, \Phi)$  the  $N \times N$  Jacobian of  $\mathbf{f}(\gamma, \Phi)$ , and  $S_{\min} = \min_{x \in (-\infty, \infty)} S(x)$ .

In the numerical scheme, we approximate  $\max \rho(J_f(\gamma, \Phi))$  by

$$\alpha := \max_{x \in (-\infty, \infty)} |\gamma^2(x)| + S_{\max} \max_{1 \leq i \leq N} \{ |v_\infty^i| \},$$

where  $S_{\max} = \max_{x \in (-\infty, \infty)} S(x)$ , and  $v_\infty^i$  is given by (4.3.10) with  $d$  and  $\rho_s$  replaced by  $d_i$  and  $\rho_i$ , respectively.

Our scheme is a direct modification of the one described by Kurganov and Tadmor in [119] and the CFL condition is the extension to our system of that stated there for scalar equations. Let  $\mathbf{U}_j^n := (U_{1,j}^n, \dots, U_{N,j}^n)^\top$  denote our approximation to  $\Phi(x_j, t_n)$ . Expressed in terms of the forward Euler solver, we consider the one-parameter family of Runge-Kutta schemes

$$\begin{aligned} \mathbf{U}_j^{(1)} &= \mathbf{U}_j^n - \lambda_j \Delta_- \mathbf{h}(\gamma_{j+1/2}, \mathbf{U}_{j-1}^n, \dots, \mathbf{U}_{j+2}^n) + \lambda_j \mathcal{H}_j \Delta_+ \mathbf{U}_j^n, \\ \mathbf{U}_j^{(k+1)} &= (1 - \eta_k) (\mathbf{U}_j^{(k)} - \lambda_j \Delta_- \mathbf{h}(\gamma_{j+1/2}, \mathbf{U}_{j-1}^{(k)}, \dots, \mathbf{U}_{j+2}^{(k)}) \\ &\quad + \lambda_j \mathcal{H}_j \Delta_+ \mathbf{U}_j^{(k)}) + \eta_k \mathbf{U}_j^n, \quad k = 1, 2, \dots, s-1, \\ \mathbf{U}_j^{n+1} &:= \mathbf{U}_j^{(s)}, \end{aligned} \tag{4.5.1}$$

where we denote by  $G(x^-)$  the limit of a function  $G(\xi)$  for  $\xi \rightarrow x$ ,  $\xi < x$ , introduce the difference operators  $\Delta_- V_j := V_j - V_{j-1}$  and  $\Delta_+ V_j := V_{j+1} - V_j$ , and define  $\gamma_{j+1/2} :=$

$\gamma(x_{j+1/2}^-)$ ,  $\lambda_j := \Delta t / (S_j \Delta x)$  with  $S_j := S(x_j^-)$ ,  $\mathcal{H}_j := \mathcal{H}(x_j^-)$ , and  $\mathbf{U}_j^0 := \Phi_0(x_j^-)$ . We employ second-order time differencing ( $s = 2$ ), for which  $\eta_1 = 1/2$ ; for third-order time differencing ( $s = 3$ ), the appropriate values are  $\eta_1 = 3/4$  and  $\eta_2 = 1/3$ .

Before describing the computation of the numerical flux vector  $\mathbf{h}$ , we briefly justify the scheme. The main differences between (4.5.1) and the scheme originally defined by Kurganov and Tadmor [119] (KT scheme) and adapted to the CT setup by Berres et al. [13] are the coefficient  $\lambda_j$  and the term  $\lambda_j \mathcal{H}_j \Delta_+ \mathbf{U}_j^n$ . The original KT scheme is a high-resolution central difference scheme for the approximation of first-order systems of conservation laws with a flux that depends continuously on  $\Phi$ , such as our system (4.2.2). High-resolution schemes approximate smooth parts of solutions with at least second order of accuracy, and resolve discontinuities sharply and without spurious oscillations. The main advantage of the KT scheme for our model is that as a central scheme, and unlike upwind schemes, it avoids approximate Riemann solvers, projections along characteristic directions, and splittings of the flux vector in upwind and downwind directions. It shares these properties with the previous central scheme due to Nessyahu and Tadmor [138] (NT scheme), but the KT scheme has a smaller numerical viscosity than the NT scheme, is better suited for near-steady-state solutions, and admits a convergent semi-discrete variant. Berres et al. [13] applied this scheme to a CT model for polydisperse suspensions, compared it with alternative discretizations and demonstrated that these advantages persist when the scheme is applied to a system of conservation laws with discontinuous flux.

The new ingredient is the term  $\lambda_j \mathcal{H}_j \Delta_+ \mathbf{U}_j^n$  that has been added to incorporate the sink feature of the model, and which discretizes the transport term  $\mathcal{H}(x) \partial_x \Phi$  in the right-hand side of (4.4.7). Since this term is non-conservative, its discretization cannot simply be made part of the KT scheme. For the scalar case, several possibilities to discretize this term are compared by Bürger et al. [23] (Chapter 3 of this thesis); the simplest one is the difference  $\lambda_j \mathcal{H}_j \Delta_+ \mathbf{U}_j^n$  that has been chosen here. The orientation of the stencil is deliberate; in view of  $\mathcal{H}(x) \geq 0$ , we chose here the forward difference  $\Delta_+$  as a discretization that has an upwind property. Moreover, this

is the discretization to which the convergence analysis for the scalar scheme introduced by Bürger et al. [23] (Chapter 3 of this thesis) directly applies.

The numerical flux vector  $\mathbf{h}$  appearing in (4.5.1) is given by

$$\begin{aligned} \mathbf{h}(\gamma_{j+1/2}, \mathbf{U}_{j-1}^n, \dots, \mathbf{U}_{j+2}^n) &:= \frac{1}{2} [\mathbf{f}(\gamma_{j+1/2}, \mathbf{U}_{j+1/2}^+(t_n)) + \mathbf{f}(\gamma_{j+1/2}, \mathbf{U}_{j+1/2}^-(t_n))] \\ &\quad - \frac{1}{2} a_{j+1/2}^n [\mathbf{U}_{j+1/2}^+(t_n) - \mathbf{U}_{j+1/2}^-(t_n)], \end{aligned}$$

which is expressed in terms of the intermediate values

$$\mathbf{U}_{j+1/2}^+(t_n) := \mathbf{U}_{j+1}^n - \frac{\Delta x}{2} (\Phi_x)_{j+1}^n, \quad \mathbf{U}_{j+1/2}^-(t_n) := \mathbf{U}_j^n + \frac{\Delta x}{2} (\Phi_x)_j^n,$$

and the local speeds of propagation  $a_{j+1/2}^n$ , which we estimate by

$$a_{j+1/2} = \gamma^1(x_{j+1/2}^-) \max\{|v_\infty^1|, \dots, |v_\infty^N|\} + |\gamma^2(x_{j+1/2}^-)|.$$

The numerical derivatives are determined by

$$(\Phi_x)_j^n := \frac{1}{\Delta x} \text{MM} \left\{ \theta(\mathbf{U}_j^n - \mathbf{U}_{j-1}^n), \frac{1}{2}(\mathbf{U}_{j+1}^n - \mathbf{U}_{j-1}^n), \theta(\mathbf{U}_{j+1}^n - \mathbf{U}_j^n) \right\},$$

where  $\theta \in [1, 2]$  is a parameter and  $\text{MM}(\cdot, \cdot, \cdot)$  is the minmod function:

$$\text{MM}(a, b, c) := \begin{cases} \min\{a, b, c\} & \text{if } a, b, c > 0, \\ \max\{a, b, c\} & \text{if } a, b, c < 0, \\ 0 & \text{otherwise.} \end{cases}$$

As stated by Kurganov and Tadmor [119], in the scalar case ( $N = 1$ ) the value  $\theta = 2$  corresponds to the least dissipative limiter, while  $\theta = 1$  ensures the non-oscillatory nature of the approximate solution. The best choice of  $\theta$  depends on the model considered. For systems, the optimal values of  $\theta$  vary between 1.1 and 1.5 (see [119]). As a compromise, and following previous works [13, 145], we choose  $\theta = 1.3$  in all examples.

### 4.5.2 Calculation of the sink concentrations

The concentrations of each species in the GCT sinks can be computed a posteriori from the concentration distribution in the interior, for example after every time interval whose length is a fixed multiple of  $\Delta t$ .

For a GCT with exactly one sink, the sink concentrations follow from the overall mass balance of each particle species. To specify this balance, let  $\tilde{x}_L := M_L \Delta x$  and  $\tilde{x}_R := M_R \Delta x$  be chosen such that  $\tilde{x}_L < x_L$  and  $\tilde{x}_R > x_R$ , and assume that the approximate solution of the problem between these two positions has been stored. The difference between the total flow rate into and out of the vessel for particle species  $i$  must equal the accumulation rate of that particle species in it, i.e.

$$\begin{aligned} & Q(\tilde{x}_L, t)\phi_i(\tilde{x}_L, t) + Q_F(t)\phi_i^F(t) + Q_S(t)\phi_i^S(t) - Q(\tilde{x}_R, t)\phi_i(\tilde{x}_R, t) \\ &= \frac{d}{dt} \int_{\tilde{x}_L}^{\tilde{x}_R} \phi_i(\xi, t) S(\xi) d\xi, \end{aligned} \quad (4.5.2)$$

where  $Q_S(t)$  and  $\phi_i^S(t)$  are the volume flow rate and the volume fraction of the species  $i$  in the sink located at  $x = x_S$  at time  $t$ , respectively.

For  $t = t_n$ , we approximate the right-hand side of (4.5.2) by

$$I_i(\tilde{x}_L, \tilde{x}_R, t_n) := \sum_{k=M_L+1}^{M_R-1} \frac{U_{i,k}^{n+1} - U_{i,k}^n}{\lambda_k} + \frac{U_{i,M_L}^{n+1} - U_{i,M_L}^n}{2\lambda_{M_L}} + \frac{U_{i,M_R}^{n+1} - U_{i,M_R}^n}{2\lambda_{M_R}}. \quad (4.5.3)$$

We approximate  $\phi_i^S(t_n)$  by the following formula, which follows from replacing the right-hand side of (4.5.2) by (4.5.3), and the exact solution  $\phi_i$  by the approximate solution  $U_{i,k}^n$ :

$$\phi_i^S(t_n) \approx \frac{1}{Q_S(t_n)} \left( I_i(\tilde{x}_L, \tilde{x}_R, t_n) - Q(\tilde{x}_L, t_n)U_{i,M_L}^n - Q_F(t_n)\phi_i^F(t_n) + Q(\tilde{x}_R, t_n)U_{i,M_R}^n \right).$$

Now we consider a GCT with two or more sinks. First we explain the method for calculating the concentrations of the sinks located from  $x_L^1$  to  $x_L^{n_L}$ , i.e. above the feed level. For a sink located at  $x_L^\mu$ , we solve in the order  $\mu = n_L, n_L - 1, \dots, 1$ , with our numerical scheme, a set of auxiliary problems with the initial condition  $\tilde{\Phi}(x, 0) = \Phi(x, t_n)$ . These auxiliary problems are based on the original problem

(4.4.7), (4.4.8), but we turn off the sinks located at  $x_L^\mu$  to  $x_L^{n_L}$  and add their discharge rates to the bulk flow  $Q(x, t)$  in  $x < x_L^\mu$ . Then, for each  $t_n$  we write the overall mass balances of each particle species for the original problem and for the corresponding auxiliary problem. Due to the finite speed of propagation and the smallness of the time interval  $[t_n, t_{n+1})$ , we may assume that the concentrations of the sinks located below  $x_L^\mu$  and of the underflow are the same for both problems. Then, the difference between both mass balances of each particle species gives

$$\begin{aligned} Q(\tilde{x}_L, t)(\phi_i(\tilde{x}_L, t) - \tilde{\phi}_i(\tilde{x}_L, t - t_n)) + \sum_{j=\mu}^{n_L} Q_L^j(t)(\phi_{i,L}^j(t) - \tilde{\phi}_i(\tilde{x}_L, t - t_n)) \\ = \frac{d}{dt} \int_{\tilde{x}_L}^{\tilde{x}_R} (\phi_i(\xi, t) - \tilde{\phi}_i(\xi, t - t_n)) S(\xi) d\xi, \end{aligned} \quad (4.5.4)$$

where  $\tilde{\phi}_i(x, t - t_n)$  is the volume fraction of species  $i$  for the auxiliary problem, and  $\tilde{\phi}_{i,L}^j(t)$  is the volume fraction of species  $i$  in the sink located in  $x_L^j$ ,  $j = \mu, \dots, n_L$ , at time  $t$ . As in the case with one sink, we denote the numerical approximation of the right hand side of (4.5.4) as  $I_{i,L}^\mu(\tilde{x}_L, \tilde{x}_R, t)$  and replace the exact solutions  $\phi_i$  and  $\tilde{\phi}_i$  by the approximate solutions  $U_{i,k}^n$  and  $\tilde{U}_{i,k}^n$ , respectively. Then we obtain

$$\begin{aligned} \phi_{i,L}^\mu(t_n) \approx \tilde{U}_{i,M_L}^n + \frac{1}{Q_L^\mu(t_n)} \left\{ I_{i,L}^\mu(\tilde{x}_L, \tilde{x}_R, t_n) - Q(\tilde{x}_L, t_n)(U_{i,M_L}^n - \tilde{U}_{i,M_L}^n) \right. \\ \left. - \sum_{j=\mu+1}^{n_L} Q_L^j(t_n)(\phi_i^j(t_n) - \tilde{U}_{i,M_L}^n) \right\}. \end{aligned}$$

Note that the initial condition of the auxiliary problems implies that  $U_{i,k}^n = \tilde{U}_{i,k}^n$ . The value of  $I_{i,L}^\mu(\tilde{x}_L, \tilde{x}_R, t_n)$  is then calculated by

$$I_{i,L}^\mu(\tilde{x}_L, \tilde{x}_R, t_n) := \sum_{k=M_L+1}^{M_R-1} \frac{U_{i,k}^{n+1} - \tilde{U}_{i,k}^{n+1}}{\lambda_k} + \frac{U_{i,M_L}^{n+1} - \tilde{U}_{i,M_L}^{n+1}}{2\lambda_{M_L}} + \frac{U_{i,M_R}^{n+1} - \tilde{U}_{i,M_R}^{n+1}}{2\lambda_{M_R}}.$$

For the sinks located at  $x_R^2$  to  $x_R^{n_R}$  we follow the same method as for those located at  $x_L^1$  to  $x_L^{n_L}$ . For the sink at  $x_R^1$  we only use the overall mass balance of each particle species. Then we have

$$\phi_{i,R}^1(t_n) \approx \frac{1}{Q_R^1(t_n)} \left\{ I_{i,R}^1(\tilde{x}_L, \tilde{x}_R, t_n) - Q(\tilde{x}_L, t_n)U_{i,M_L}^n - Q_F(t_n)\phi_i^F(t_n) \right\}$$

$$+ Q(\tilde{x}_R, t_n) U_{i, M_R}^n - \left. \left\{ \sum_{j=1}^{n_L} Q_L^j(t_n) \phi_{i, L}^j(t_n) - \sum_{j=2}^{n_R} Q_R^j(t_n) \phi_{i, R}^j(t_n) \right\}, \right.$$

where  $I_{i, R}^1(\tilde{x}_L, \tilde{x}_R, t_n)$  is calculated by (4.5.3).

**Remark 4.5.1** For the general case with two or more sinks, we first had calculated the sink concentrations with mass balances around each sink, but we observed that such a method introduced oscillations in these values, so we prefer the method expound here.

## 4.6 Numerical examples

### 4.6.1 Preliminary remarks

We consider three GCT vessels, which are operated in FC mode and have varying cross-sectional area, see Figures 4.2, 4.6 and 4.11. Associated to Vessels 1, 2, and 3 are Examples 4.1, 4.2, and 4.3, respectively, whose parameters are given in Table 4.1. In all cases, the fluid is water at 20 °C with  $\rho_f = 998.2 \text{ kg/m}^3$  and  $\mu_f = 1.005 \times 10^{-3} \text{ Pa s}$

Example 4.1 is “virtual” and has been included to study the behaviour of particles differing both in size and density, while Examples 4.2 and 4.3 are based on, and in part compared with, experimental data by Chen et al. [40] for equal-density particles. Published data on classifier-type experiments with particles having different densities is scarce; for comparisons of experiments with such suspensions with numerical simulations in the (simpler) cases of batch settling and a CT setup (without sinks), we refer to [20] and [13].

To ensure that the solution assumes values in  $\mathcal{D}_{\phi_{\max}}$ , we replace (4.2.1) by the following function, which continuously goes to zero as  $\phi \rightarrow \phi_{\max}$  and where  $0 <$

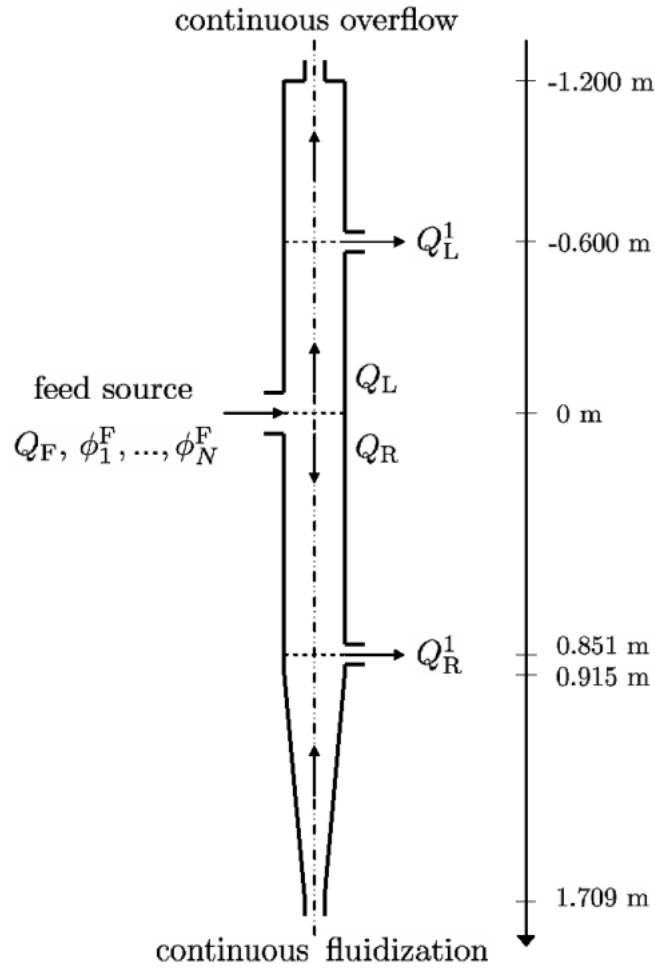


Figure 4.2: Vessel 1 with varying interior area and two sinks.

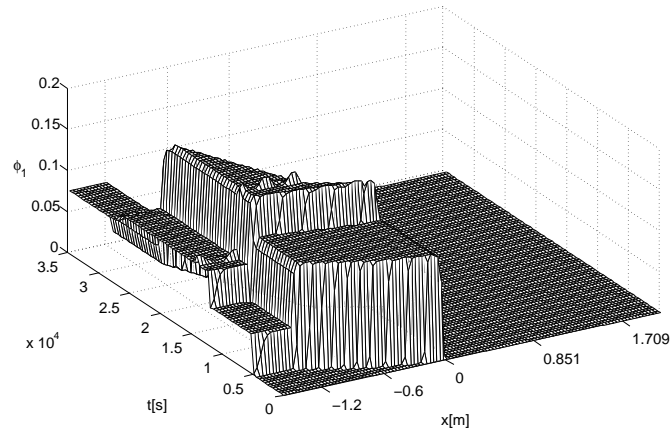
$\phi_q < \phi_{\max}$  is a parameter:

$$V(\phi) = \begin{cases} (1 - \phi)^{n-2} & \text{for } \phi \in [0, \phi_q), \\ (1 - \phi_q)^{n-2} \frac{\phi_{\max} - \phi}{\phi_{\max} - \phi_q} & \text{for } \phi \in [\phi_q, \phi_{\max}], \quad n > 2. \\ 0 & \text{otherwise,} \end{cases} \quad (4.6.1)$$

	Example 4.1	Example 4.2	Example 4.3
$N$	3	2	6
$d_1$ [m]	$1.5 \times 10^{-4}$	$9.0 \times 10^{-4}$	$2.3 \times 10^{-3}$
$d_2$ [m]	$5.0 \times 10^{-5}$	$5.5 \times 10^{-5}$	$1.7 \times 10^{-3}$
$d_3$ [m]	$3.5 \times 10^{-5}$	—	$1.2 \times 10^{-3}$
$d_4$ [m]	—	—	$8.6 \times 10^{-4}$
$d_5$ [m]	—	—	$6.1 \times 10^{-4}$
$d_6$ [m]	—	—	$4.0 \times 10^{-4}$
$\rho_1$ [kg/m <sup>3</sup> ]	1050	2470*	2470*
$\rho_2$ [kg/m <sup>3</sup> ]	2403	—	—
$\rho_3$ [kg/m <sup>3</sup> ]	2850	—	—
$n$	4.66	2.91	2.74
$\phi_1^F$	0.0728	0.0676	0.00787
$\phi_2^F$	0.0676	0.0624	0.02616
$\phi_3^F$	0.0624	—	0.03485
$\phi_4^F$	—	—	0.02484
$\phi_5^F$	—	—	0.01480
$\phi_6^F$	—	—	0.01147
$Q_F$ [m <sup>3</sup> /s]	$1.78 \times 10^{-5}$	$5.9596 \times 10^{-3}$	$6.074 \times 10^{-3}$
$Q_R$ [m <sup>3</sup> /s]	$2.1 \times 10^{-6}$	$-1.444 \times 10^{-3}$	$-1.378 \times 10^{-3}$
$Q_L^1$ [m <sup>3</sup> /s]	$-4.2 \times 10^{-6}$	0	0
$Q_L$ [m <sup>3</sup> /s]	$-1.99 \times 10^{-5}$	$-7.404 \times 10^{-3}$	$-7.452 \times 10^{-3}$
$Q_R^1$ [m <sup>3</sup> /s]	$-3.5 \times 10^{-6}$	$-3.668 \times 10^{-4}$	$-4.183 \times 10^{-4}$
$\Delta x$ [ $10^{-3}$ m]	8.081	5.206	5.693
$\Delta t$ [ $10^{-3}$ s]	105.0	0.1096	0.05315

Table 4.1: Parameters for the numerical simulations. \*: species of equal density.

(a)



(b)

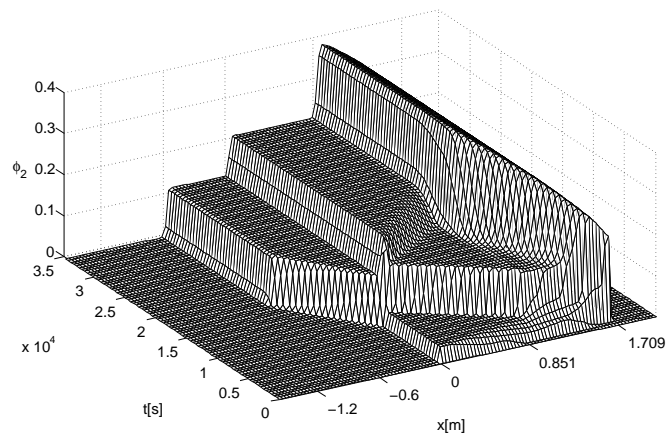
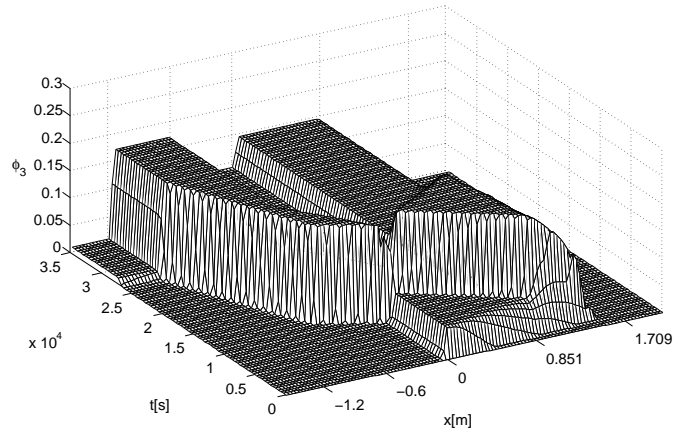


Figure 4.3: Example 4.1: Simulated concentrations (a)  $\phi_1$  (species 1), (b)  $\phi_2$  (species 2).

(a)



(b)

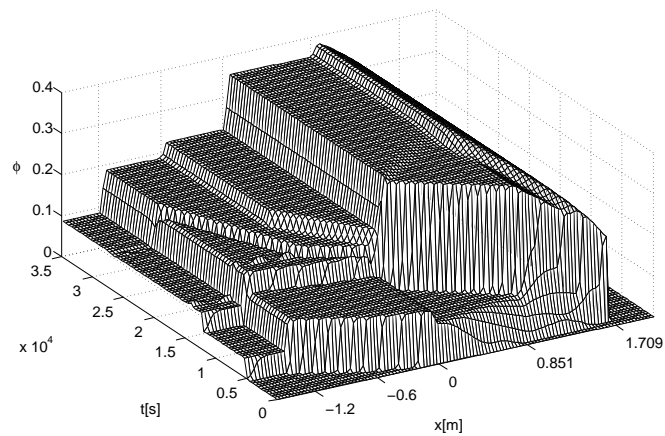


Figure 4.4: Example 4.1: (a) Simulated concentration  $\phi_3$  (species 3), (b) simulated total concentration  $\phi$ .

#### 4.6.2 Example 4.1

We consider Vessel 1 with the function

$$S(x) = \begin{cases} 0.01815 \text{ m}^2 & \text{for } x \leq -1.200 \text{ m,} \\ 0.0287 \text{ m}^2 & \text{for } -1.200 \text{ m} < x \leq 0.915 \text{ m,} \\ S_1(x) & \text{for } 0.915 \text{ m} < x \leq 1.709 \text{ m,} \\ 8.17 \times 10^{-3} \text{ m}^2 & \text{for } x > 1.709 \text{ m,} \end{cases}$$

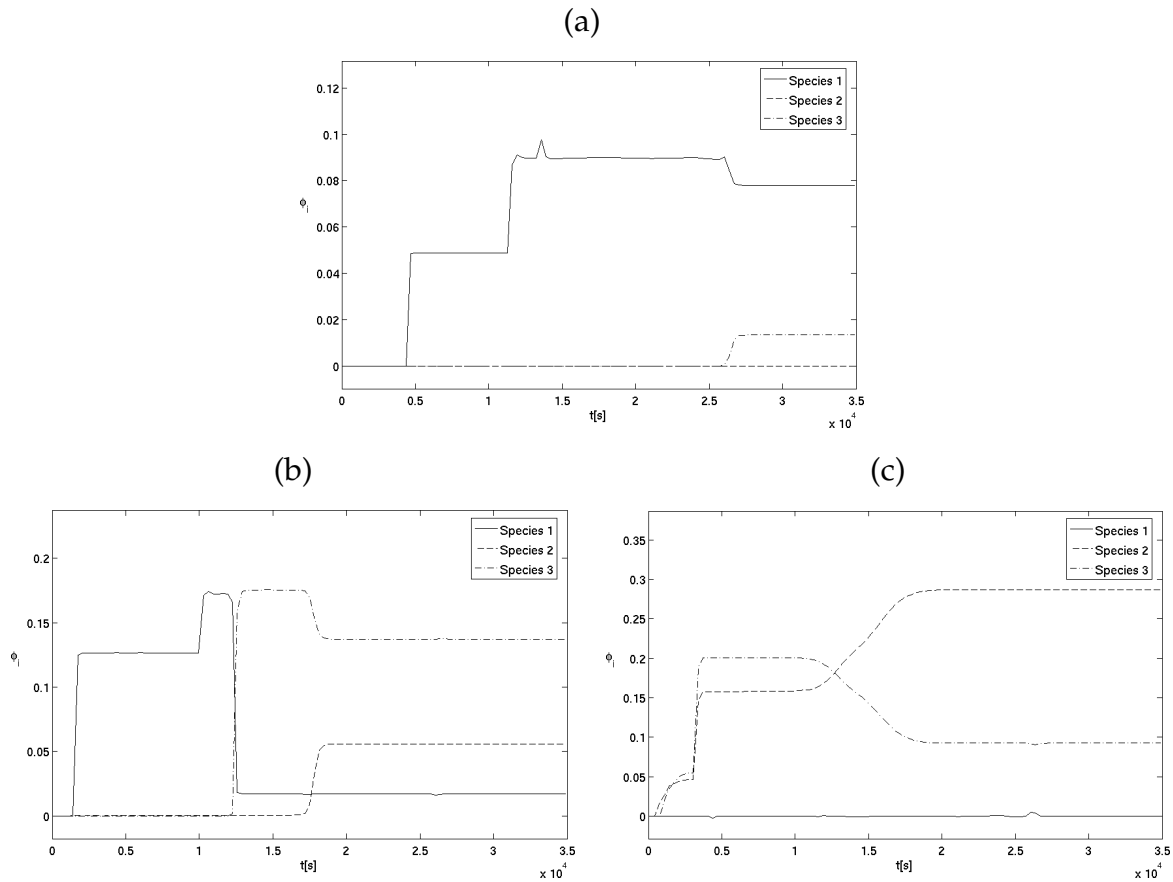


Figure 4.5: Example 4.1: (a) Overflow, (b) upper sink, (c) lower sink concentrations.

where the conical segment is described by

$$S_1(x) := 0.7854(0.191 \text{ m} - 0.1121(x - 0.915 \text{ m}))^2.$$

The solids are supposed to be spheres made of polystyrene (species 1), glass (species 2) and ballotini (species 3). We here obtain  $n = 4.66$ , and utilize (4.6.1) with  $\phi_q = 0.63$  and  $\phi_{\max} = 0.68$ . In light of the low particle Reynolds numbers, we employ the first alternative in (4.3.8).

Since different densities are involved here, the equations are possibly unstable for certain concentration vectors  $\Phi$ . However, we evaluated the instability criterion for the numerical solution obtained here, with the result that the solution completely

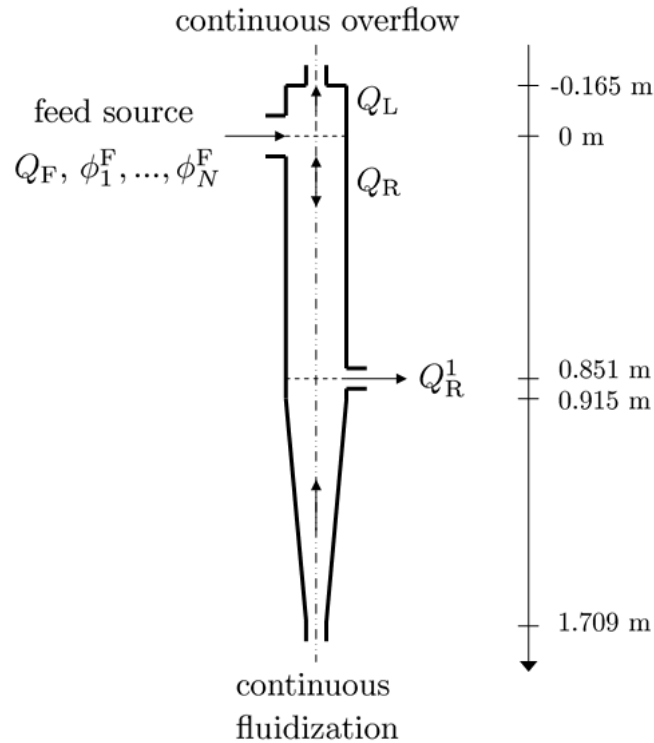


Figure 4.6: Vessel 2 with varying interior area and one sink.

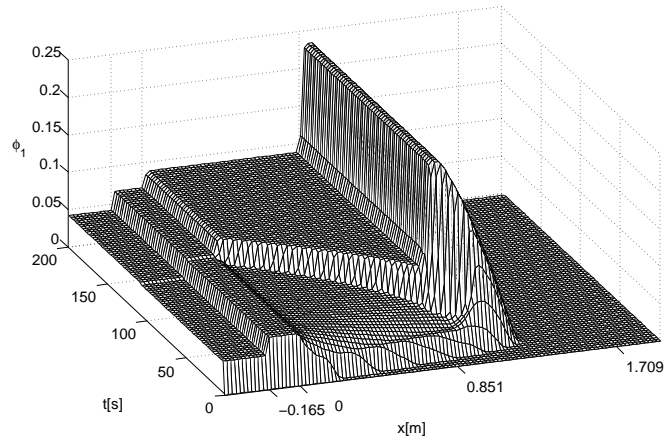
sojourns in the stability region. In other words, instability phenomena do not occur here.

Figures 4.3 (a) and (b) and Figure 4.4 (a) show the simulated concentrations  $\phi_1$ ,  $\phi_2$  and  $\phi_3$  until a steady state is attained. We observe in Figure 4.5 that the overflow, upper sink, and lower sink streams are mainly composed by species 1, 3, and 2, respectively. Figure 4.4 (b) shows the total volume fraction of solids for this example.

### 4.6.3 Example 4.2

We here adopt experimental data by Chen et al. ([40], Figure 3) for the steady-state separation of a bidisperse suspension in a liquid fluidized bed classifier. Ves-

(a)



(b)

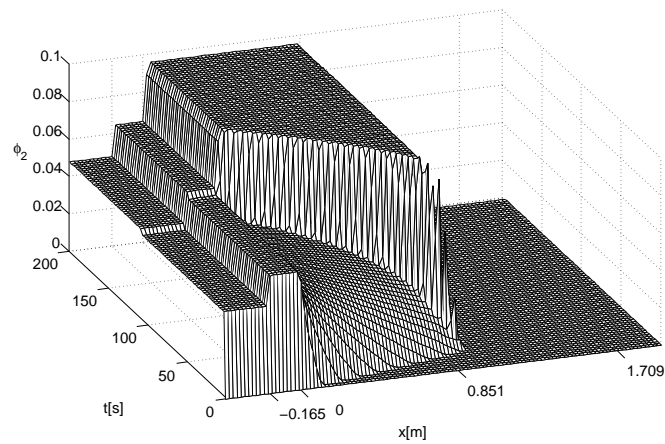


Figure 4.7: Example 4.2: Simulated concentrations (a)  $\phi_1$  (large particles), (b)  $\phi_2$  (small particles).

sel 2 corresponds to equipment “T-2” of [40], and is described by

$$S(x) = \begin{cases} 4.54 \times 10^{-3} \text{ m}^2 & \text{for } x \leq -0.165 \text{ m,} \\ 0.0287 \text{ m}^2 & \text{for } -0.165 \text{ m} < x \leq 0.915 \text{ m,} \\ S_2(x) & \text{for } 0.915 \text{ m} < x \leq 1.709 \text{ m,} \\ 2.04 \times 10^{-3} \text{ m}^2 & \text{for } x > 1.709 \text{ m,} \end{cases}$$

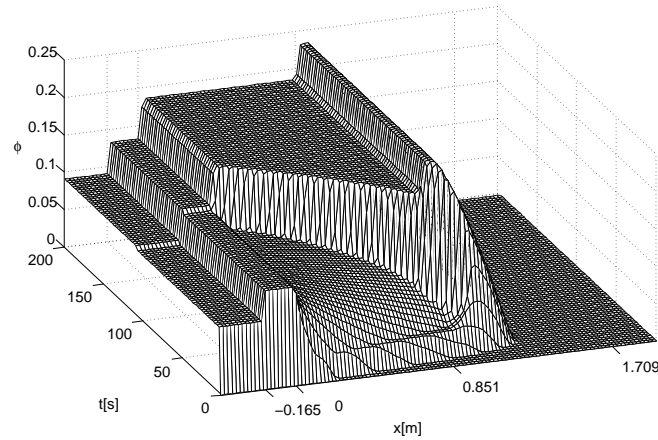


Figure 4.8: Example 4.2: Simulated total concentration  $\phi$ .

including a conical segment defined by

$$S_2(x) := 0.7854(0.191 \text{ m} - 0.1763(x - 0.915 \text{ m}))^2.$$

The solids parameters correspond to glass beads of two sizes. For this suspension, we obtain  $n = 2.91$  and use (4.6.1) with  $\phi_q = 0.63$  and  $\phi_{\max} = 0.68$ , and use the second alternative of (4.3.8) with  $\beta = 0.65$ .

Figure 4.7 shows the simulated concentrations  $\phi_1$  and  $\phi_2$  until a steady state is attained. Figure 4.8 presents the total concentration of solids. We observe in Figure 4.9 that at steady state, species 1 and 2 leave the vessel by the sink stream and overflow, with an increase of the concentration of species 1 and a decrease of that of species 2 with respect to the feed concentration, whereas in the overflow, concentrations of both species are smaller in relation to feed. Figure 4.10 indicates that the model fits reasonably well the experimental data; here, we use those data reported in Figure 3 of [40] that have been obtained by sampling, plus the recorded overflow and underflow concentrations.

Of course, our Figure 4.10 displays some discrepancy between the fourth experimental data point and our numerical solution (roughly, near  $x = 0.25 \text{ m}$ ). This

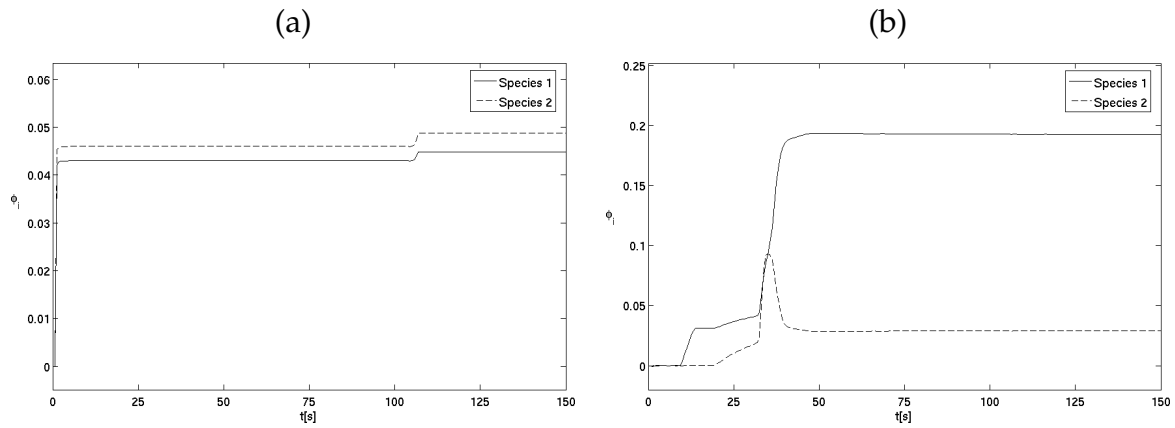


Figure 4.9: Example 4.2: (a) Overflow, (b) sink concentrations.

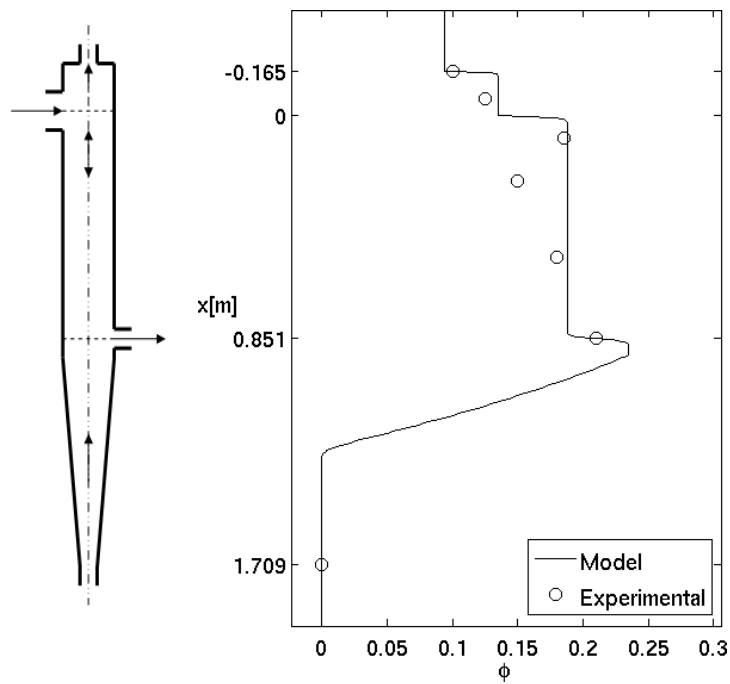


Figure 4.10: Example 4.2: Comparison of total concentration  $\phi$  in steady state predicted by the model with experimental data extracted from [40].

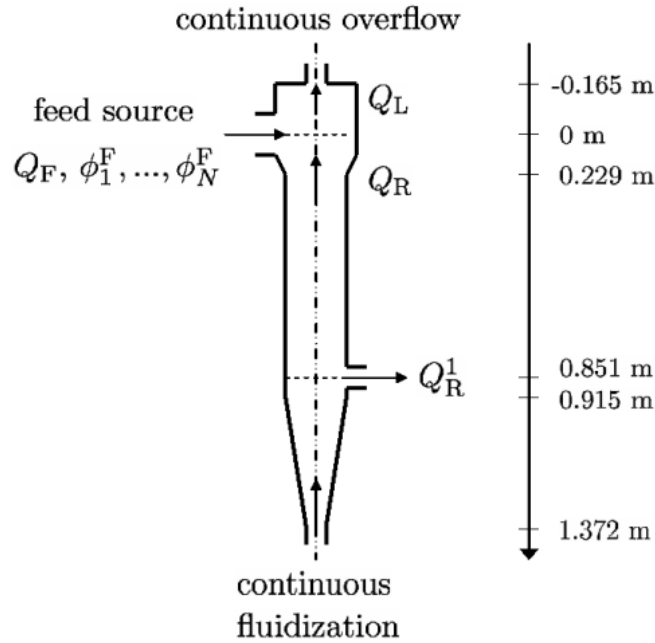


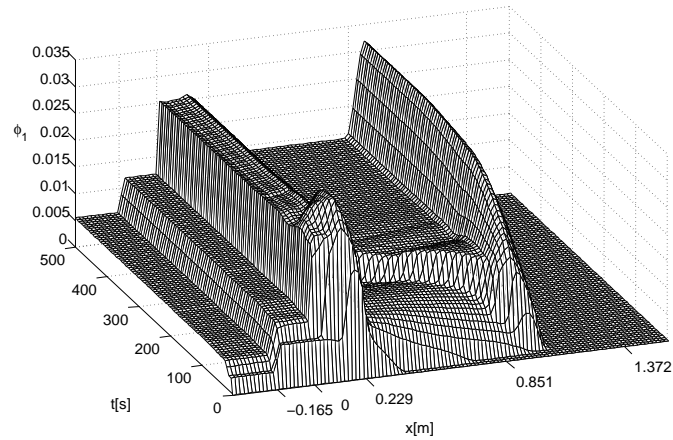
Figure 4.11: Vessel 3 with varying interior area and one sink.

difference is possibly due to voidage fluctuations in the radial direction, which are particularly likely to occur near the feed inlet. This reveals a limitation of the one-dimensional model used herein. On the other hand, experimental uncertainty is present in the data recorded by Chen et al. [40], which is indicated by the different values, and the error bars, associated with different types of measurement, see Figure 3 of and the authors' discussion in [40].

#### 4.6.4 Example 4.3

Chen et al. [40] also study the steady-state separation of a suspension with a continuous particle size distribution fitted by the Rosin-Rammler equation, showing results for six representative species. We here apply our model to a suspension composed of  $N = 6$  species, adopting the experimental data in [40]. Vessel 3 corre-

(a)



(b)

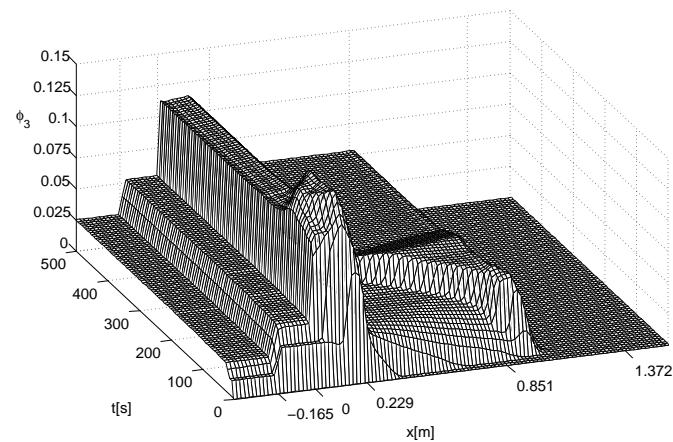
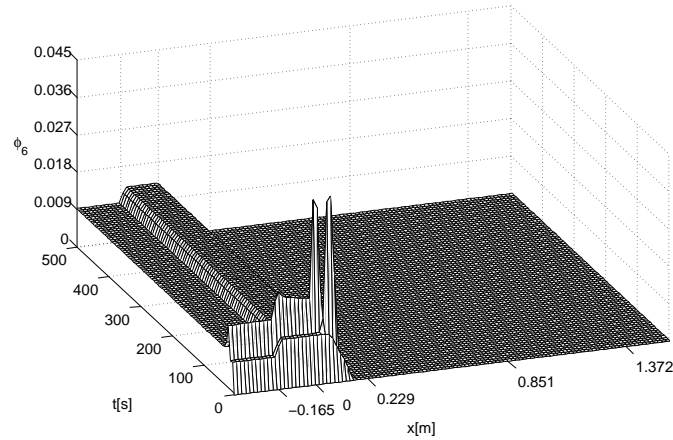


Figure 4.12: Example 4.3: Simulated concentrations (a)  $\phi_1$  (largest species), (b)  $\phi_3$  (medium species).

sponds to their equipment "C-0", and is described by

$$S(x) = \begin{cases} 4.54 \times 10^{-3} \text{ m}^2 & \text{for } x \leq -0.165 \text{ m,} \\ 0.0670 \text{ m}^2 & \text{for } -0.165 \text{ m} < x \leq 0.127 \text{ m,} \\ S_3(x) & \text{for } 0.127 \text{ m} < x \leq 0.229 \text{ m,} \\ 0.0287 \text{ m}^2 & \text{for } 0.229 \text{ m} < x \leq 0.915 \text{ m,} \\ S_4(x) & \text{for } 0.915 \text{ m} < x \leq 1.372 \text{ m,} \\ 2.04 \times 10^{-3} \text{ m}^2 & \text{for } x > 1.372 \text{ m,} \end{cases}$$

(a)



(b)

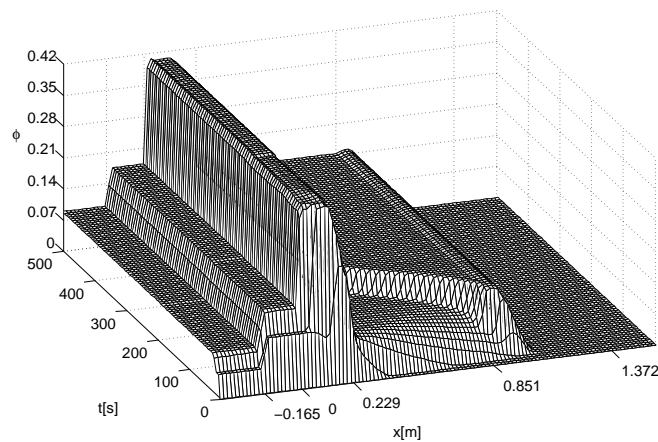


Figure 4.13: Example 4.3: (a) Simulated concentration  $\phi_6$  (smallest species), (b) simulated total concentration  $\phi$ .

including conical segments defined by

$$S_3(x) := 0.7854(0.292 \text{ m} - 0.9902(x - 0.127 \text{ m}))^2,$$

$$S_4(x) := 0.7854(0.191 \text{ m} - 0.3063(x - 0.915 \text{ m}))^2.$$

The solids parameters correspond to glass beads of six different sizes. We here

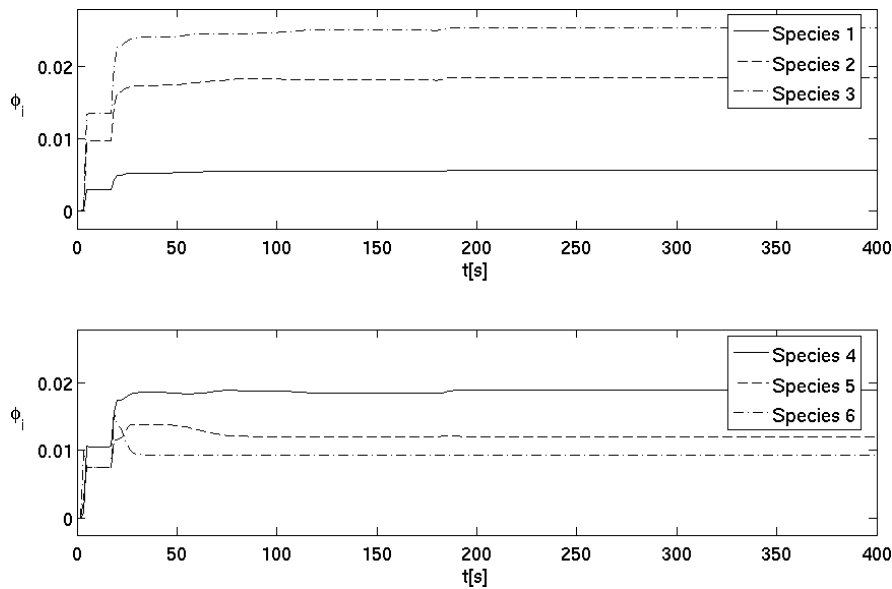


Figure 4.14: Example 4.3: Overflow concentrations.

obtain  $n = 2.74$ , and use (4.6.1) with  $\phi_q = 0.95$  and  $\phi_{\max} = 1.0$ , along with the second alternative of (4.3.8) with  $\beta = 0.3$ . Figures 4.12 (a) and (b) and Figure 4.13 (a) shows the simulated concentrations  $\phi_1$ ,  $\phi_3$  and  $\phi_6$  until a steady state is attained. In Figure 4.13 (b) we show the total concentration  $\phi$  for this simulation. We observe in Figure 4.14 that at steady state, all species leave the vessel by the overflow, whereas in Figure 4.15 we see that only species 1, 2, 3 and 4 leave the vessel by the sink stream.

Figure 4.16 displays the relative volume fraction  $C_i := \phi_i/\phi$ ,  $i = 1, \dots, N$ , at steady state, i.e., after a simulated time of  $t = 500$  s, within the unit. Thus, we can compare numerical results with measurements displayed in Figure 5 of [40]. Our Figure 4.16 shows that for this example our model agrees well with the experimental data.

However, some discrepancy becomes visible in the “bump” of the profile of normalized solids volume fraction of species 4 (see Figure 4.16 (b)) in the zone below the feed inlet. The concentrations of species 1 to 3 also experience a kind of “bump”

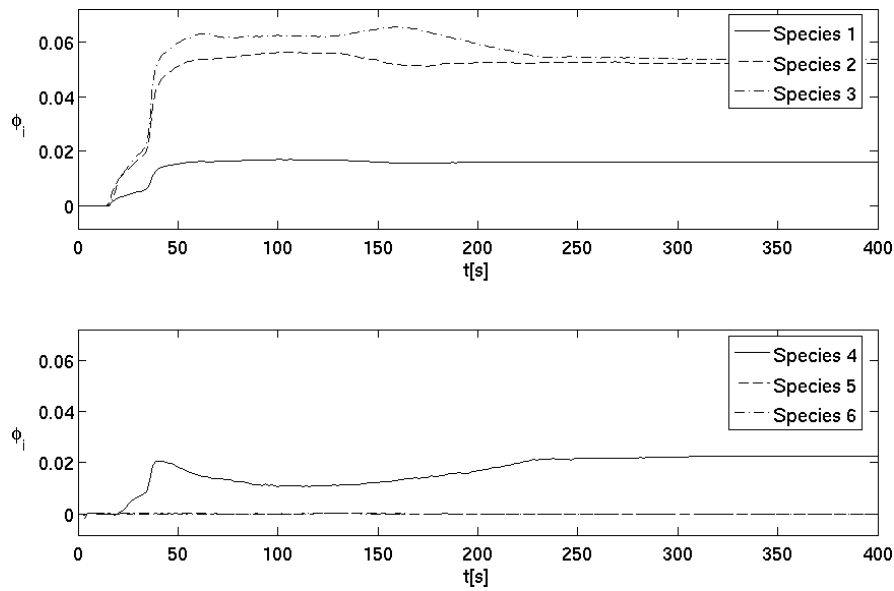


Figure 4.15: Example 4.3: Sink concentrations.

in that zone; this does not become apparent in Figure 4.16 (a) since the *normalized* concentration  $\phi_i/\phi$  of these species seems not to change significantly. The obvious model ingredient that is responsible for this behaviour is the sudden change of cross-sectional area. If seen from downwards, in the direction of the fluidization bulk flow, the vessel widens rapidly for  $x \leq 0.229$  m. As a consequence, and considering the system at steady state, the relative importance of the particle entrainment by counter-gravity bulk flow compared to that of gravity settling (associated with the flux vector  $\mathbf{f}^M(\Phi)$ ) diminishes, which explains the overall enrichment of solids concentrations in  $[0 \text{ m}, 0.229 \text{ m}]$  (see also Figure 4.13 (b)). On the other hand, the vector  $\mathbf{f}^M(\Phi)$  depends nonlinearly on  $\Phi$ , so the *normalized* concentrations  $\phi_i/\phi$  may change when the vessel widens. In fact, in several terms of  $\mathbf{f}^M(\Phi)$ , the concentration  $\phi_i$  is associated with the coefficient  $\tilde{\delta}_i$ . Roughly speaking, we can therefore expect that the concentrations of smaller species are more sensitive to changes of vessel diameter at equilibrium, since the equilibrium composition is algebraically determined by equating  $S(x)\mathbf{f}^M(\Phi)$  to some linear bulk flow  $Q\Phi$ , and possibly other terms, that

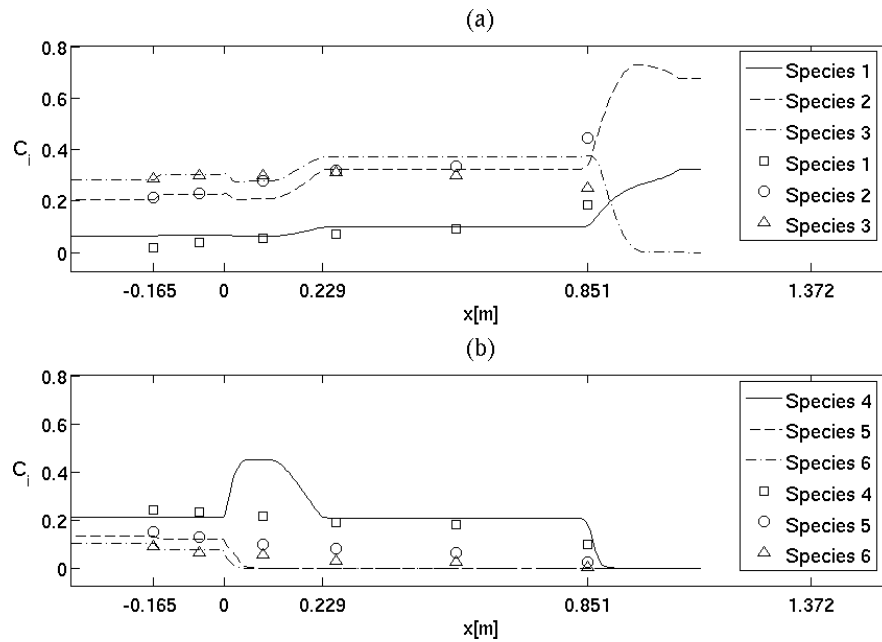


Figure 4.16: Example 4.3: Comparison of simulated normalized solids volume fractions  $C_i = \phi_i/\phi$  with experimental data by Chen et al. ([40], Figure 5).

do not depend on  $S(x)$ , nor on  $\tilde{\delta}_1, \dots, \tilde{\delta}_N$ . This makes it ultimately plausible that the proportion of species 4, the smallest of those that enter the settling zone, increases in  $[0 \text{ m}, 0.229 \text{ m}]$ . Finally, it should be commented that the simulated sudden increase of  $\phi_4/\phi$  is observed in a relatively small sub-zone of the vessel, whereas below or above that agreement with experimental values is acceptable. It seems that our simulated behaviour in that sub-zone, though explicable within our model, is not observed in the experimental data, nor in the numerical simulation by Chen et al. [40], since both in the real-world system and their numerical simulation diffusive mechanisms that tend to diminish extremal concentrations are active. The proximity of the feed inlet to this sub-zone may also have caused radial voidage fluctuations, and again question the appropriateness of the one-dimensional model used for that zone.

## 4.7 Conclusions

The discontinuous-flux CT model for the continuous solid-liquid separation of suspensions has been extended to a generalized clarifier-thickener model (GCT), in which an arbitrary number of discharge streams (or products) is described by singular sink terms. This feature allows us to describe the continuous extraction of products of different composition. A GCT can be operated either in the CT mode or in the FC mode, depending on whether the feed bulk flow is split into diverging bulk flows or not. Such a unit can be employed for continuous solid-liquid separation or classification of suspensions. To this end, the GCT setup is combined with a kinematic model of sedimentation of polydisperse suspensions. The governing equation of the resulting model is a strongly coupled system of nonlinear conservation laws that has a discontinuous flux and a non-conservative transport term describing the sinks. A numerical algorithm for the solution of this system has been presented, along with three numerical examples. The model provides a complete description of the GCT unit including all critical design parameters, and predicts the composition of the overflow, underflow and discharge streams as well as the spatio-temporal evolution of the composition inside the unit.

Clearly, the model presented herein is subject to limitations that already appear in the assumptions stated in Sections 4.2–4.4. Obviously, the model applies only to units that are (at least approximately) one-dimensional, and where lateral concentration or velocity gradients are negligible. This means, for example, that particles should be reasonably small, so that wall effects are unimportant, and that inclined settlers are at present excluded. It is also presumed that the model parameters for the MLB framework are known, for example from batch settling experiment. The MLB framework actually presumes that particles are small rigid spheres. While sphericality can be considered as a useful approximation for particles of slightly more general geometry, the rigidity of particles is essential. For example, soft particles, such as flocs, form compressible sediments with curved iso-concentration lines, which cannot be captured by a purely kinematic model; rather, dynamic effects such as

effective solids stress have to be taken into account. This can be achieved by a degenerate hyperbolic-parabolic system of equations, which is slightly more involved than (4.4.7), see [12].

## Chapter 5

# A Family of Numerical Schemes for Kinematic Flows with Discontinuous Flux

Multiphase flows of suspensions and emulsions are frequently approximated by spatially one-dimensional kinematic models, in which the velocity of each species of the disperse phase is an explicitly given function of the vector of concentrations of all species. The continuity equations for all species then form a system of conservation laws which describes spatial segregation and the creation of areas of different composition. This class of models also includes multi-class traffic flow, where vehicles belong to different classes according to their preferential velocities. Recently, these models were extended to fluxes that depend discontinuously on the spatial coordinate, which appear in clarifier-thickener models, in duct flows with abruptly varying cross-sectional area, and in traffic flow with variable road surface conditions.

This paper presents a new family of numerical schemes for such kinematic flows with a discontinuous flux. It is shown how a very simple scheme for the scalar case, which is adapted to the “concentration times velocity” structure of the flux, can be extended to kinematic models with phase velocities that change sign, flows with two or more species (the system case), and discontinu-

ous fluxes. In addition, a MUSCL-type upgrade in combination with a Runge-Kutta type time discretization can be devised to attain second-order accuracy. It is proved that two particular schemes within the family, which apply to systems of conservation laws, preserve an invariant region of admissible concentration vectors, provided that all velocities have the same sign. Moreover, for the relevant case of a multiplicative flux discontinuity and a constant maximum density, it is proved that one scalar version converges to a  $BV_t$  entropy solution of the model. In the latter case, the compactness proof involves a novel uniform but local estimate of the spatial total variation of the approximate solutions.

Numerical examples illustrate the performance of all variants within the new family of schemes, including applications to problems of sedimentation, traffic flow, and the settling of oil-in-water emulsions.

## 5.1 Introduction

### 5.1.1 Scope of the paper

Numerous multiphase flows involve the flow of one disperse substance, for example solid mineral particles or oil droplets in an emulsion, through a continuous phase, say a liquid or gas. In many cases, the disperse substance consists of small particles that belong to different species which differ in some characteristic quantity such as size or density. The different species will segregate and create areas of different composition, which is the most interesting property in many applications. Similar models also include certain continuum approximations of traffic flow of vehicles on a highway if cars with drivers having different preferential velocities are identified as different species.

In general, we distinguish between  $N$  different species that give rise to  $N$  superimposed continuous phases associated with volume fractions (or densities)  $\phi_1, \dots, \phi_N$ . If  $v_i$  is the one-dimensional velocity of species  $i$ , then the continuity equa-

tions of the  $N$  species in differential form are

$$\partial_t \phi_i + \partial_x(\phi_i v_i) = 0, \quad i = 1, \dots, N, \quad (5.1.1)$$

where  $t$  is time and  $x$  is the spatial position. The basic assumption of kinematic models is that the velocities  $v_1, \dots, v_N$  are given functions of the vector  $\Phi := (\phi_1, \dots, \phi_N)^T$  of local concentrations of all species,  $v_i = v_i(\Phi)$ . This yields systems of conservation laws of the type

$$\partial_t \phi_i + \partial_x(\phi_i v_i(\Phi)) = 0, \quad i = 1, \dots, N. \quad (5.1.2)$$

We focus on three specific kinematic models that recently attracted interest: one of multi-species traffic flow [10, 168, 169, 176, 177, 178], one of sedimentation of polydisperse suspensions [12, 32, 158, 170, 175], and one of separation of oil-in-water dispersions [149].

All these applications also give rise to spatially non-homogeneous flows, in which the velocity  $v_i$  not only depends on  $\Phi$ , but also on a vector of parameters  $\gamma_i$  that is a function of the spatial position  $x$ ,  $\gamma_i = \gamma_i(x)$ . While models for which  $\gamma_i$  depends, for example, Lipschitz continuously on  $x$  lead to conservation laws that can be treated with standard analytical and numerical methods, we are here interested in the case that  $\gamma_i$  depends discontinuously on  $x$ ; more precisely, we assume that  $\gamma_i$  is piecewise smooth with a finite number of discontinuities. The vector  $\gamma_i(x)$  may describe, for instance, abruptly changing road surface conditions in the traffic flow model, as was done in [27, 132] for a single-species model; singular feed sources and diverging bulk flows in clarifier-thickener models [23] (Chapter 3 of this thesis), [31]; and abruptly changing cross-sectional areas in vessels for the settling of suspensions and emulsions.

It is the purpose of this contribution to formulate, in part analyze, and present numerical experiments for easy-to-implement numerical schemes for kinematic models, in which the numerical flux is explicitly based on the “concentration times velocity” structure of each flux component. The starting point is a simple two-point monotone numerical flux for scalar ( $N = 1$ ) kinematic flows with a non-negative

velocity function  $v = v(\phi)$ . We develop extensions of the scheme defined by this numerical flux to equations with a velocity of variable sign, to equations with a discontinuous flux, to systems of conservation laws ( $N \geq 2$  species), and finally to schemes with second-order accuracy. All these variants form the family of new schemes under study. It is proved that for  $N \geq 1$  flows with non-negative velocities, the schemes preserve an invariant region, i.e. generate approximations that assume values in the domain of physically relevant concentrations only. For the scalar case ( $N = 1$ ) and a discontinuous flux, we prove convergence to a  $BV_t$  entropy solution. The proof is based on a new uniform but local estimate of the spatial total variation of approximate solutions. Numerical experiments demonstrate the performance of the new family of schemes.

What is intriguing about the new schemes is that (other than an estimate of the spectral radius for the CFL condition) they do not require any calculation of eigenvalues, eigenvectors, field-by-field decomposition, flux vector splitting etc. that are usually required for an upwind scheme. In this sense they are like a central scheme. However, in many cases the first-order accurate version of the new schemes is much less dissipative than the first-order version of the central scheme (the Lax-Friedrichs scheme).

### 5.1.2 Multi-species kinematic models

In this and the following section, we recall some known properties and discretizations of kinematic models of the type (5.1.2), while some results related to conservation laws with discontinuous flux are reviewed in Section 5.1.5.

In many applications, the number  $N$  of species may be large, and the different species in these applications are competitive. It is therefore convenient to assume a maximal density  $\phi_{\max}$  (for example, a maximal 'bumper-to-bumper' car density in traffic models or the maximal sphere packing density  $\phi_{\max} \approx 0.66$  in sedimentation

models), such that the phase space for (5.1.2) is

$$\mathcal{D}_{\phi_{\max}} := \left\{ \Phi = (\phi_1, \dots, \phi_N)^T \in \mathbb{R}^N : \phi_1 \geq 0, \dots, \phi_N \geq 0, \right. \\ \left. \phi := \phi_1 + \dots + \phi_N \leq \phi_{\max} \right\}. \quad (5.1.3)$$

Introducing the flux vector

$$\mathbf{f}(\Phi) = (f_1(\Phi), \dots, f_N(\Phi))^T := (\phi_1 v_1(\Phi), \dots, \phi_N v_N(\Phi))^T, \quad (5.1.4)$$

we can rewrite (5.1.2) as the nonlinear system of conservation laws

$$\partial_t \Phi + \partial_x \mathbf{f}(\Phi) = 0. \quad (5.1.5)$$

It is well known that solutions of (5.1.5) are discontinuous in general, and that the propagation speed  $\sigma(\Phi^+, \Phi^-)$  of a discontinuity in the concentration field  $\phi_i$  separating the states  $\Phi^+$  and  $\Phi^-$  is given by the Rankine-Hugoniot condition

$$\sigma = \frac{f_i(\Phi^+) - f_i(\Phi^-)}{\phi_i^+ - \phi_i^-}.$$

We recall that the system (5.1.5) is called *hyperbolic* at a state  $\Phi$  if the Jacobian  $\mathcal{J}_{\mathbf{f}}(\Phi) := (\partial f_i / \partial \phi_k)_{1 \leq i, k \leq N}$  only has real eigenvalues, and *strictly hyperbolic* if these are moreover pairwise distinct.

The kinematic traffic model for  $N = 1$  goes back to Lighthill and Whitham [125] and Richards [146] (“LWR model”); for the sedimentation of suspensions, the classic reference is Kynch [120]. The extension of the LWR model to multi-class traffic flow was proposed by Benzoni-Gavage and Colombo [10] and Wong and Wong [168], while extensions of the sedimentation model to several species have been suggested for several decades (see [20, 175] for reviews), mainly in the chemical engineering literature. The application of available tools of mathematical and numerical analysis to kinematic flow models is difficult due to the dependence of the functions  $v_i(\Phi)$  on all variables  $\phi_1, \dots, \phi_N$ , which in general is nonlinear. Closed formulas for the eigenvalues and eigenvectors of  $\mathcal{J}_{\mathbf{f}}(\Phi)$  are at least complicated, if not unavailable for  $N \geq 5$ . It is therefore in general not possible to solve the Riemann problem for

(5.1.2) in closed form. Moreover, for multi-species kinematic models eigenvalues lack a direct physical interpretation, and in particular do not coincide with any of the phase velocities  $v_1, \dots, v_N$ .

Advances were made recently in the hyperbolicity analysis and characterization of eigenvalues of kinematic models. For the model of settling of oil-in-water dispersions, Rosso and Sona [149] proved for arbitrary  $N$  strict hyperbolicity in  $\mathcal{D}_{\phi_{\max}}$ . The proof is based on deriving an explicit closed formula of the characteristic polynomial of  $\mathcal{J}_f(\Phi)$ , and discussing its zeros. Berres et al. [12] proved in a similar way that the model [12, 128, 129] for the sedimentation of polydisperse suspensions utilized herein is strictly hyperbolic for arbitrary  $N$ , provided that all particles have the same density. The basic idea was also used by Zhang et al. [177] to prove strict hyperbolicity of the multi-class traffic model proposed in [10, 168].

### 5.1.3 Limitations of kinematic models

Before proceeding with the discussion, we comment on the limitations of our class of kinematic models. The one-dimensional setting may be adequate for traffic models, but certainly presents a strong simplification for multiphase flows of real materials such as suspensions and emulsions. Nevertheless, one-dimensional multiphase flow models are widely used in engineering applications under well-controlled flow conditions, especially for separation processes in ducts (e.g., settling columns or hydraulic classifiers) that are aligned with the body force (gravity or centrifugal force) that drives the separation. If one assumes that the sizes of particles or droplets are small compared with the diameter of the vessel, then wall effects become negligible, and in many circumstances one-dimensional approximation is acceptable. Experimental support for one-dimensional kinematic models is provided in [14, 63, 68, 70, 86, 89, 90, 98, 99, 100, 122, 128, 133, 143, 144, 151, 170, 172, 175] (this list is not complete). Of course, multiphase flows under more general circumstances, for example in equipments with more complicated geometry, in natural ducts or under a combination of various body forces require a truly multidimensional treat-

ment, which is also necessary for the description of the formation of structures like plumes and eddies that are not easily modeled in one dimension. Monographs dealing with multi-dimensional multiphase flow models include [19, 46, 62, 97, 163].

The dimensionality of a multiphase flow model is intimately related with the number and structure of balance equations that describe its evolution. For example, in more than one space dimension, the flux appearing in the solids continuity equations of sedimentation models has a linear contribution involving the bulk velocity of the mixture [12, 32]. This quantity is then not just a controllable constant, as in one space dimension, but a flow variable with its own equations of evolution, for example a variant of the Navier-Stokes equation which is strongly coupled with the continuity equations. On the other hand, independently from the number of space dimensions, a physically more accurate description (than kinematic modelling) of traffic and multiphase flows requires that we take into account further balance equations, for example for the linear momentum and energy of each species. As a consequence, the flow velocity  $v_i$  of a particular species is no longer an explicitly prescribed function of  $\Phi$ , but is governed by its own equation of evolution. In traffic modeling, this leads to so-called second-order traffic models, which include elements such as anticipation length, and reaction time. For the more involved physics of non-kinematic multiphase flow models, we refer again to [19, 46, 62, 97, 163]; for traffic models, see [9, 75, 91, 111].

Frequently, the flux of a species is assumed to depend not only on  $\Phi$ , but also on  $\nabla\Phi$  (in one space dimension,  $\partial_x\Phi$ ), which results in diffusive-like models. These gradient-type terms either emerge from simplified versions of additional balance equations, as in sedimentation models, where they reflect sediment compressibility [12]; accrue from truncated expansions of velocities with displaced arguments reflecting anticipation length, reaction time, and relaxation to equilibrium in traffic modelling [27, 91, 137]; or are postulated a priori as a formal generalization  $v_i = v_i(\Phi, \nabla\Phi)$  of the dependency  $v_i = v_i(\Phi)$  of kinematic models [16, 18, 43, 67]. In traffic modelling, the last assumption has the behavioristic interpretation that drivers are not only sensitive to the local density, but to the gradient of density.

Some diffusive models are actually strongly degenerate, which means that diffusion is present only wherever the density exceeds a critical value. The governing equations are of mixed parabolic-hyperbolic type, where the location of the type-change interface is unknown beforehand. Sedimentation and traffic models of this kind are discussed in [12] and [27, 137], respectively.

#### 5.1.4 Numerical schemes for kinematic models

Despite the new hyperbolicity results, insight into any specific  $N$ -species kinematic model with  $N \geq 3$  can realistically be gained through numerical simulation only. High resolution schemes for systems of conservation laws, which approximate discontinuities sharply and without spurious oscillations and are at least second-order accurate in smooth regions, are natural candidates for the numerical solution of (5.1.2). For example, Wong, Shu and their collaborators [176, 178] applied weighted essentially non-oscillatory (WENO) schemes to the traffic model, while Bürger, Karlsen and collaborators [12, 20, 22, 145] employed central difference schemes [119, 138] for the sedimentation model. Meanwhile, central schemes have also been applied to a number of real-world problems of polydisperse sedimentation, see for example Xue and Sun [170], Simura and Ozawa [153] and Wang et al. [167]. Recently [36], WENO schemes were combined with a multiresolution technique to yield a numerical method for kinematic models that adaptively concentrates computational effort on zones of strong variation.

All these methods are based on schemes that can be applied universally to systems of conservation laws, and that are not tailored to a particular algebraic structure of the flux vector. Our new family of schemes does, however, explicitly make use of the structure of fluxes for kinematic models. The schemes, which are first-order accurate, can be upgraded to higher order accuracy by employing MUSCL-type techniques.

### 5.1.5 Well-posedness analysis and numerical schemes for conservation laws with discontinuous flux

To put the treatment in the proper perspective, we first recall some known results for the equation  $u_t + f(\gamma(x), u)_x = 0$ . The basic difficulty is that its well-posedness is not a straightforward limit case of the standard theory for conservation laws with a flux that depends smoothly on  $x$ . In fact, several extensions of the Kruřkov entropy solution concept [114] to conservation laws with a flux that is discontinuous with respect to  $x$  were proposed in recent years [3, 6, 7, 82, 103, 104, 105, 106, 112, 113, 130, 150, 159, 160]. Each of these concepts is supported by a convergence analysis of a numerical scheme; the differences between them appear in the respective admissibility conditions for stationary jumps of the solution across the discontinuities of  $\gamma$  [29].

The choice of the entropy solution concept depends on the regularizing viscous physical model. For clarifier-thickener models, the appropriate concept emerges from the limit  $\varepsilon \rightarrow 0$  of a viscous regularization  $\varepsilon u_{xx}$  with a diffusion constant  $\varepsilon > 0$  [34]. Diehl advanced thorough analyses and construction of exact entropy solutions for clarifier-thickener models, which are culminating in his series of papers “Operating charts for continuous sedimentation” [57, 58, 59, 60]. On the other hand, the authors with collaborators made a series of contributions (including [23] (Chapter 3 of this thesis), [31, 34, 28]) to the well-posedness and numerical analysis for these models, whose basic non-standard ingredient is a singular feed source that produces diverging bulk flows, which causes the discontinuous  $x$ -dependence of the flux. The same entropy solution concept has also been applied to establish well-posedness, and to construct a working numerical scheme, for a model of single-species traffic flow with abruptly changing road surface conditions [27].

The rigorous analysis is limited to the scalar case, but the numerical schemes that have been used to constructively establish existence of weak solutions to the scalar clarifier-thickener model also possess working versions for systems with discontinuous flux. In the context of clarifier-thickener models, such systems model fluidiza-

tion and classification units for polydisperse suspensions, see [13],[24] (Chapter 4 of this thesis).

### 5.1.6 Contents of the paper

The remainder of the paper is organized as follows. In Section 5.2, three specific kinematic models are presented. Section 5.2.1 presents the multi-class kinematic traffic model, which gives rise to an initial-value problem with periodic boundary conditions. Next, in Section 5.2.2, we outline the polydisperse sedimentation model, for which the zero-flux boundary condition is relevant. A similar model for the separation of oil-in-water dispersions is mentioned in Section 5.2.3. The distinctive property of the sedimentation model is that the phase velocities of the particle species may be positive, zero or negative, due to buoyancy effects, while in the two other models, these velocities are always non-negative.

Section 5.3 is devoted to the presentation of the family of schemes. To this end, we first introduce in Section 5.3.1 the basic time and space discretizations. In Section 5.3.2, the scalar versions (i.e., for  $N = 1$ ) of the schemes are introduced, starting with Schemes 1 and 2 for fluxes with non-negative velocity and a velocity of variable sign, respectively. It is shown that both schemes are monotone provided that a CFL condition is satisfied. Furthermore, we extend Scheme 1 to an equation with discontinuous flux (Scheme 3). In Section 5.3.3, we formulate schemes for multi-species kinematic models, that is, for systems of conservation laws ( $N \geq 1$ ). The systems variants of the scalar Schemes 1 and 3 for models with non-negative velocities only are Schemes 4 and 5. For models with velocities of variable sign, the direct extension of the scalar Scheme 2 is Scheme 6. However, as is detailed in Section 5.3.3, this scheme produces sharply resolved interfaces, but overshoots in certain situations. An analysis of the viscosity coefficients of Scheme 6 leads to the improved Scheme 7. It turns out that for the sedimentation model, this scheme still produces overshoots near stationary discontinuities; for this reason, the final scheme advocated for systems with velocities of variable sign is Scheme 8, which is slightly more viscous than

Scheme 7. One desirable property of schemes for kinematic models consists in the preservation of an invariant region, i.e. under a suitable CFL condition, the scheme should produce approximations that assume values within the physically relevant phase space only (i.e., concentrations should be non-negative and sum up at most to the maximal concentration). We show in Section 5.3.4 that Scheme 5, applied to the traffic model, and Scheme 4, applied to the oil-in-water dispersion model, indeed do have these properties. Experience with the traffic and oil-in-water dispersion model leads us to propose a working CFL condition also for the sedimentation model. In Section 5.3.5 we demonstrate how the schemes developed so far can be improved to second-order accuracy both in space and time by combining Runge-Kutta temporal differencing with MUSCL-type spatial differencing. The latter involves the use of slope limiter functions; we refer to the variants with the minmod and Van Leer limiter functions as Scheme 9 and 10, respectively. We show that if applied to scalar problems with a flux that does not depend on  $x$ , these schemes preserve the maximum principle and the TVD property of the first-order version under the same CFL condition.

In Section 5.4, we consider a scalar initial-boundary value problem with periodic boundary conditions and a discontinuous flux, and prove that Scheme 3 generates a sequence of approximate solutions that converge to the unique  $BV_t$  entropy solution of the problem as the mesh parameters tend to zero. One basic ingredient of the compactness argument involved here is a new type of local but uniform estimate of the total spatial variation of approximate solutions. This type of argument (see Lemma 5.4.2 in Section 5.4 and its proof) is new, and has not been used in any previous work on discontinuous flux problems.

In Section 5.5, we present eight numerical examples to demonstrate the performance of the schemes of the family, especially compared to variants of the Lax-Friedrichs scheme. Examples 5.1 and 5.2 refer to scalar equations that do not represent a particular application. Example 5.3 presents a simulation of a scalar clarifier-thickener model, and allows comparison with a numerical result published in [31]. In Example 5.4, we study the multi-species traffic model with  $N = 9$ , but with-

out flux discontinuities, and choose parameters in such a way that results can be compared with those presented in [176]. In addition, for this example (and for Example 5.6) we present a history of approximate  $L^1$  numerical errors. This is done for the first- and second-order variants of the scheme, as well as for the corresponding variants of the LxF scheme. Example 5.5 corresponds to the traffic model with a discontinuously varying parameter, and the numerical results can be compared those of Zhang et al. [178]. In Example 5.6, we simulate the settling of a suspension with  $N = 2$  species in a column using parameters from a well-documented experiment by Schneider et al. [151]. These results, as those of Example 5.7, where we consider a suspension with  $N = 11$  species, can also be compared with those of [36]. Finally, Example 5.8 presents a simulation of the settling of an oil-in-water dispersion with  $N = 10$  species.

Section 5.6 collects some conclusions of this paper.

## 5.2 Examples of kinematic flow models

### 5.2.1 Traffic flow models

The classical LWR kinematic wave model [125, 146] for unidirectional traffic flow on a single-lane highway starts from the principle of “conservation of cars”, where  $\phi$  is the density of cars as a function of distance  $x$  and time  $t$  and  $v = v(x, t)$  is the velocity of the car located at position  $x$  at time  $t$ :

$$\partial_t \phi + \partial_x(\phi v) = 0, \quad x \in \mathbb{R}, \quad t > 0, \quad (5.2.1)$$

The original LWR model (5.2.1) is a single-species model ( $N = 1$ ), whose basic assumption  $v = v(\phi)$  states that each driver instantaneously adjusts his velocity to the local car density. A common choice is  $v(\phi) = v_{\max} V(\phi)$ , where  $v_{\max}$  is a preferential velocity assumed on a free highway, and  $V(\phi)$  is a hindrance function taking into account that the presence of other cars urges each driver to adjust his speed. Thus,

the flux is

$$f(\phi) := \phi v(\phi) = \begin{cases} v_{\max} \phi V(\phi/\phi_{\max}) & \text{for } 0 \leq \phi \leq \phi_{\max}, \\ 0 & \text{otherwise,} \end{cases} \quad (5.2.2)$$

where  $\phi_{\max}$  is the maximum “bumper-to-bumper” car density.

Recently, Benzoni-Gavage and Colombo [10] and Wong and Wong [168] independently formulated an extension of the LWR model to multi-class traffic flow, considering that cars belong to a finite number  $N$  of classes (species), each associated with a function  $v = v_i(\Phi)$ . It is assumed that drivers of each species adjust their velocity to the global car density  $\phi = \phi_1 + \dots + \phi_N$  seen at a point  $(x, t)$ , which means that  $v_i(\Phi(x, t)) = v_i(\phi(x, t))$  for  $i = 1, \dots, N$ , and that all drivers adjust their velocity in the same way, such that

$$v_i(\Phi) = v_{\max}^i V(\phi/\phi_{\max}), \quad i = 1, \dots, N. \quad (5.2.3)$$

Here,  $v_{\max}^i$  is the preferential (maximum) of species  $i$  and the function  $V : [0, \phi_{\max}] \rightarrow [0, 1]$  describes the attitude of drivers [10], that is, represents the same hindrance function as in the single-class case.

Also of interest are models where we replace (5.2.3) by

$$v_i = v_i(x, \Phi) = v_{\max}^i(x) V(\phi/\phi_{\max}(x)), \quad v_{\max}^i(x) > 0, \quad i = 1, \dots, N. \quad (5.2.4)$$

By allowing  $v_i$  to vary spatially through the coefficients  $v_{\max}^i(x)$  and  $\phi_{\max}(x)$ , it is possible to model road conditions that change from location to location.

For the traffic model, we assume a circular road of length  $L$  and assume an initial traffic density

$$\Phi(x, 0) = \Phi^0(x) = (\phi_1^0(x), \dots, \phi_N^0(x))^T \in \mathcal{D}_{\phi_{\max}}, \quad 0 \leq x \leq L. \quad (5.2.5)$$

The periodicity condition is

$$\phi_i(0, t) = \phi_i(L, t), \quad t > 0, \quad i = 1, \dots, N.$$

## 5.2.2 Sedimentation of polydisperse suspensions

We consider a polydisperse suspension of rigid spherical particles which are dispersed in a viscous fluid of density  $\varrho_f$  and of dynamic viscosity  $\mu_f$ . The solid particles belong to  $N$  different species having sizes (diameters)  $d_1 \geq d_2 \geq \dots \geq d_N$  and densities  $\varrho_1, \dots, \varrho_N$ , where  $d_i \neq d_j$  or  $\varrho_i \neq \varrho_j$  for  $i \neq j$ . Model equations for the three-dimensional motion of such a mixture were derived in [32], based on earlier work by Masliyah [129] and Lockett and Bassoon [128]. We consider here the kinematic model obtained by reducing these equations to one space dimension, see [32] for details. The relevant parameters are  $\delta_i := d_i^2/d_1^2$  and  $\bar{\varrho}_i := \varrho_i - \varrho_f$  for  $i = 1, \dots, N$ . Here,  $\phi_{\max}$  denotes a maximum solids volume fraction, which we here assume to be constant. Moreover, we introduce the vector  $\bar{\varrho} := (\bar{\varrho}_1, \dots, \bar{\varrho}_N)^T$ , the cumulative solids fraction  $\phi := \phi_1 + \dots + \phi_N$ , the viscosity parameter  $\mu := gd_1^2/(18\mu_f) > 0$ , where  $g$  is the acceleration of gravity, and the hindered settling factor  $V = V(\phi)$ , which may be chosen as

$$V(\phi) = \begin{cases} (1 - \phi)^{n-2} & \text{if } \Phi \in \mathcal{D}_{\phi_{\max}}, \\ 0 & \text{otherwise,} \end{cases} \quad n > 2. \quad (5.2.6)$$

The phase velocity of particle species  $i$  is then given by

$$v_i(\Phi) = \mu V(\phi) \left[ \delta_i (\bar{\varrho}_i - \bar{\varrho}^T \Phi) - \sum_{m=1}^N \delta_m \phi_m (\bar{\varrho}_m - \bar{\varrho}^T \Phi) \right], \quad i = 1, \dots, N. \quad (5.2.7)$$

For one-dimensional batch settling of a suspension in a closed vessel of depth  $L$ , the initial condition is again (5.2.5), while the zero-flux boundary conditions are

$$\mathbf{f}|_{x=0} = \mathbf{f}|_{x=L} = 0. \quad (5.2.8)$$

If the particles differ in size only (i.e.,  $\varrho_1 = \varrho_2 = \dots = \varrho_N =: \varrho_s$ ), then (5.2.7) simplifies to the following expression, where  $v_\infty = \mu(\varrho_s - \varrho_f)$  is the settling velocity of a single particle of the largest species in an unbounded medium (the so-called Stokes velocity of the largest species):

$$v_i(\Phi) = v_\infty (1 - \phi) V(\phi) (\delta_i - (\delta_1 \phi_1 + \dots + \delta_N \phi_N)), \quad i = 1, \dots, N. \quad (5.2.9)$$

In [12] it is proved that for equal-density particles ( $\bar{\rho} = \dots = \bar{\rho}_N = \rho_s - \rho_f$ ), arbitrary  $N$  and particle size distributions, the system (5.1.5) is strictly hyperbolic for all  $\Phi \in \mathcal{D}$  with  $\phi_1 > 0, \dots, \phi_N > 0$  and  $\phi < 1$  if the flux vector (5.2.7) is chosen. As mentioned in Section 5.1.2, the proof proceeds in a similar fashion to that of Rosso and Sona [149] outlined in Section 5.1.2.

### 5.2.3 Separation of oil-in-water dispersions

Kinematic models have also been proposed for the sedimentation of small oil droplets in liquid-liquid dispersions. The separation process is similar to the settling of a polydisperse suspension, the major difference being that since the density of oil is smaller than that of water, the oil droplets move upwards, a process called *creaming*; however, to make results comparable with the sedimentation model, we assume that the separation takes place in the direction of the positive  $x$ -axis, so  $x$  is considered here to be a height variable. Numerous contributions to kinematic models for liquid-liquid dispersions have been made by Hartland, Jeelani, and their collaborators, see for example [89, 90, 98, 99, 100]. The analogy between suspension and dispersion models is also emphasized by Nadiv et al. [133] and Frising et al. [70]. The model utilized herein is due to Rosso and Sona [149], who consider the separation of small oil droplets in an oil-in-water dispersion. (It is worth mentioning that Rosso and Sona explicitly refer to [143], a doctoral thesis prepared under Hartland's guidance.)

The model outlined in [149] can be written in the form (5.1.2) if we consider oil droplets of  $N$  different volumes  $\mathcal{V}_1 > \mathcal{V}_2 > \dots > \mathcal{V}_N > 0$ , where  $x$  is the upward-increasing height variable and  $\phi_i = \phi_i(x, t)$  is the volume fraction occupied by droplets of volume  $\mathcal{V}_i$ . The model is similar to that of sedimentation, but as the authors argue, the differential motion of the particle species is not driven by the dispersion-water density difference, which actually can be considered constant, but rather by differences in viscosity. The basic nonlinearity is introduced by a viscosity function  $\mu_d = \mu_d(\Phi) = \mu_d(\phi_1, \dots, \phi_N)$ . If we denote again by  $\mu_f$  the viscosity of pure

water (without oil), then  $\mu_d(\Phi)$  is assumed to satisfy

$$\mu_d \in C^1(\mathcal{D}); \quad \mu_d(\Phi) > 0, \quad \frac{\partial \mu_d}{\partial \phi_1} > 0, \dots, \frac{\partial \mu_d}{\partial \phi_N} > 0 \quad \forall \Phi \in \mathcal{D}; \quad \mu_d(0, \dots, 0) = \mu_f.$$

The velocity functions  $v_1(\Phi), \dots, v_N(\Phi)$  are then given by

$$v_i(\Phi) = c \frac{\mathcal{V}_i^{2/3}}{\mu_d(\Phi)} (1 - \phi), \quad i = 1, \dots, N, \quad c := \frac{2g(\rho_f - \rho_{oil})}{9(4\pi/3)^{2/3}}, \quad (5.2.10)$$

where  $g$ ,  $\rho_f$  and  $\rho_{oil}$  denote the acceleration of gravity, the density of pure water and density of pure oil, respectively. For separation of a dispersion in a column of height  $L$ , we may again employ the initial and boundary conditions (5.2.5) and (5.2.8).

### 5.3 Numerical schemes

Section 5.2 shows that we are interested in schemes for kinematic models with a flux that possibly depends discontinuously on the spatial position  $x$ . Thus, seek weak solutions to the initial value problem

$$\begin{aligned} \partial_t \phi_i + \partial_x f_i(x, \Phi) &= 0, \quad (x, t) \in (0, L) \times (0, T) =: \Pi_T, \quad i = 1, \dots, N, \\ f_i(x, \Phi) &= \phi_i v_i(\gamma_i(x), \Phi), \quad \Phi(x, 0) = \Phi^0(x), \quad x \in (0, L), \end{aligned} \quad (5.3.1)$$

which may be supplemented by periodic boundary conditions

$$\Phi(0, t) = \Phi(L, t), \quad t > 0,$$

or zero-flux boundary conditions

$$f_i(0, \Phi) = f_i(L, \Phi) = 0, \quad i = 1, \dots, N.$$

This setup is general enough to include the models discussed in the previous section.

#### 5.3.1 Discretizations

We start by discretizing the domain  $[0, L] \times [0, T]$ . To discretize the spatial interval  $[0, L]$ , we choose a mesh width  $\Delta x$  and an integer  $\mathcal{J}$  such that  $(\mathcal{J} + 1)\Delta x = L$ , and

set

$$x_j = (j + 1/2)\Delta x, \quad j = -1/2, 0, 1/2, 1, 3/2, \dots, \mathcal{J} - 1, \mathcal{J} + 1/2.$$

With this setup,  $x_{-1/2} = 0$ ,  $x_{\mathcal{J}+1/2} = L$ . We discretize the time interval  $[0, T]$  by selecting an integer  $\mathcal{N}$  and a sequence of temporal mesh widths  $\Delta t_n$ , and defining  $t_0 := 0$  and  $t_{n+1} := t_n + \Delta t_n$  for  $n = 0, 1, \dots, \mathcal{N}$  subject to the condition  $\Delta t_0 + \dots + \Delta t_{\mathcal{N}-1} = T$ . The ratio  $\lambda_n := \Delta t_n / \Delta x$  is always assumed to satisfy a CFL condition, which will be specified below. Our numerical schemes will generate an approximation  $\Phi_j^n \approx \Phi(x_j, t_n)$  defined at the mesh points  $(x_j, t_n)$  for  $j \in \{0, 1, \dots, \mathcal{J}\} =: \mathbb{Z}_{\mathcal{J}}$  and  $n = 0, 1, \dots, \mathcal{N}$ . For our first-order accurate scheme, we start by discretizing the initial data and the parameter vectors

$$\Phi_j^0 = \Phi_0(x_j^+) := \lim_{x \downarrow x_j} \Phi_0(x), \quad \gamma_{i,j} := \gamma_i(x_j^+), \quad i = 1, \dots, N.$$

Here we have arbitrarily chosen the limit from above to resolve the ambiguities at possible jump discontinuities in the data. This is somewhat arbitrary; we could also use the limit from below, or any average of the two. We then march the solution forward in time according to

$$\Phi_j^{n+1} = \Phi_j^n - \lambda_n (\mathbf{h}_{j+1/2}^n - \mathbf{h}_{j-1/2}^n), \quad j \in \mathbb{Z}_{\mathcal{J}}, \quad n = 0, 1, \dots, \mathcal{N}. \quad (5.3.2)$$

The numerical flux vector  $\mathbf{h}_{j+1/2}^n$  is

$$\mathbf{h}_{j+1/2}^n := (h_1(\gamma_{1,j+1}, \Phi_{j+1}^n, \Phi_j^n), \dots, h_N(\gamma_{N,j+1}, \Phi_{j+1}^n, \Phi_j^n))^T. \quad (5.3.3)$$

Recall that we are considering two types of boundary conditions. When dealing with zero flux boundary conditions, we always set

$$\mathbf{h}_{-1/2}^n = \mathbf{h}_{\mathcal{J}+1/2}^n = 0, \quad n = 0, 1, 2, \dots \quad (5.3.4)$$

When dealing with periodic boundary conditions, we may have formulas where  $j < -1/2$  or  $j > \mathcal{J} + 1/2$ . In such cases we simply interpret  $j$  modulo  $(\mathcal{J} + 1)$ , in such a way that it lies within the proper range. For periodic boundary conditions, we will always have

$$\mathbf{h}_{-1/2}^n = \mathbf{h}_{\mathcal{J}+1/2}^n, \quad n = 0, \dots, \mathcal{N}. \quad (5.3.5)$$

With these observations, we can deal with both types of boundary conditions simultaneously, and mostly avoid discussing special processing at the boundaries.

### 5.3.2 The scalar case

To discuss our new numerical flux in the simplest possible setting, we start with scalar kinematic wave models, where no spatially dependent parameter vector occurs:

$$\phi_t + f(\phi)_x = 0, \quad (5.3.6)$$

where the flux takes the special form for kinematic flow models

$$f(\phi) = \phi v(\phi). \quad (5.3.7)$$

The assumptions are that  $\phi \geq 0$ , and that  $v(\phi)$  is given by a positive default velocity multiplying a hindrance function. Since the hindrance increases with  $\phi$ , the assumptions  $v(\phi) \geq 0$  and  $v'(\phi) \leq 0$  are very natural, and clearly satisfied for all examples of kinematic models considered herein. For traffic flow,  $\phi$  is the traffic density, and  $v$  is the velocity of cars as a function of density, while for sedimentation,  $\phi$  is the solids volume fraction and  $v$  is the solids phase velocity.

#### Scheme 1 for scalar equations ( $N = 1$ ) with non-negative velocity

The following is a two-point numerical flux consistent with the actual flux (5.3.7):

$$h(\phi_{j+1}, \phi_j) := \phi_j v(\phi_{j+1}). \quad (5.3.8)$$

For easy reference, we refer to the scheme (5.3.2), (5.3.3) with  $N = 1$ ,  $\gamma \equiv \text{const.}$  and the flux (5.3.8) as Scheme 1. Due to the special structure of this problem ( $\phi \geq 0$ ,  $v(\phi) \geq 0$ ,  $v'(\phi) \leq 0$ ), Scheme 1 is monotone [45], meaning that the function  $h(\phi_{j+1}, \phi_j)$  is non-increasing with respect to  $\phi_{j+1}$  and nondecreasing with respect to  $\phi_j$ . Therefore, Scheme 1 produces approximations that converge to the correct entropy solution to the conservation law (5.3.6). However, these approximations will

be at best first order accurate. What makes the flux (5.3.8) interesting is that like the Lax-Friedrichs numerical flux, it is very simple (there is no Riemann solver involved), but in many cases it is less dissipative than the Lax-Friedrichs numerical flux. This motivates us to use (5.3.8), and various extensions to deal with systems and discontinuous coefficients, as a starting point to build a second-order scheme.

### Scheme 2 for scalar equations ( $N = 1$ ) with a velocity of variable sign

Motivated by the polydisperse settling model, where the velocities may become negative, we next consider the scalar case where the velocity  $v$  may become negative. It is easy to check that the following modification of (5.3.8) is a flux that retains the monotonicity property in this more general situation:

$$h(\phi_{j+1}, \phi_j) = \phi_j \max\{0, v(\phi_{j+1})\} + \phi_{j+1} \min\{0, v(\phi_{j+1})\}. \quad (5.3.9)$$

We refer to the scheme (5.3.2), (5.3.3) for  $N = 1$  and  $\gamma \equiv \text{const.}$  with the flux (5.3.9) as Scheme 2. Another formulation of (5.3.9) that will be useful in what follows is the so-called viscous form:

$$h(\phi_{j+1}, \phi_j) = \frac{1}{2}(f(\phi_{j+1}) + f(\phi_j)) - \frac{1}{2\lambda}Q(\phi_{j+1}, \phi_j)(\phi_{j+1} - \phi_j), \quad (5.3.10)$$

where the numerical viscosity coefficient  $Q(\phi_{j+1}, \phi_j)$  is defined by

$$Q(\phi_{j+1}, \phi_j) := \lambda|v(\phi_{j+1})| + \lambda\phi_j \frac{v(\phi_j) - v(\phi_{j+1})}{\phi_{j+1} - \phi_j}. \quad (5.3.11)$$

To derive CFL conditions, let us concentrate for now on the case where the boundary conditions are periodic. If we write Scheme 2 in incremental form

$$\phi_j^{n+1} = \phi_j^n + C_{j+1/2} \Delta_+ \phi_j^n - D_{j-1/2} \Delta_- \phi_j^n,$$

where we define the spatial difference operators  $\Delta_- V_j := V_j - V_{j-1}$  and  $\Delta_+ V_j := V_{j+1} - V_j$ , the incremental coefficients are given by

$$\begin{aligned} C_{j+1/2} &= \lambda\phi_j \frac{v(\phi_j^n) - v(\phi_{j+1}^n)}{\phi_{j+1}^n - \phi_j^n} - \lambda \min\{0, v(\phi_{j+1}^n)\}, \\ D_{j+1/2} &= \lambda \max\{0, v(\phi_{j+1}^n)\}. \end{aligned} \quad (5.3.12)$$

To have a maximum principle

$$\min\{\phi_{j-1}^n, \phi_j^n, \phi_{j+1}^n\} \leq \phi_j^{n+1} \leq \max\{\phi_{j-1}^n, \phi_j^n, \phi_{j+1}^n\} \quad (5.3.13)$$

and the Total Variation Decreasing (TVD) property

$$\sum_{j=0}^{\mathcal{J}} |\phi_{j+1}^{n+1} - \phi_j^{n+1}| \leq \sum_{j=0}^{\mathcal{J}} |\phi_{j+1}^n - \phi_j^n|, \quad (5.3.14)$$

sufficient conditions are [88, 156]

$$C_{j+1/2} + D_{j+1/2} \leq 1, \quad C_{j+1/2} + D_{j-1/2} \leq 1, \quad C_{j+1/2} \geq 0, \quad D_{j+1/2} \geq 0.$$

It is clear from (5.3.12) that  $C_{j+1/2} \geq 0$  and  $D_{j+1/2} \geq 0$  are already satisfied. To enforce the first two inequalities, we impose the CFL conditions

$$\lambda \max_{j \in \mathbb{Z}_{\mathcal{J}}} |v(\phi_j)| \leq \alpha, \quad \alpha = 1/4, \quad \lambda \max_{j \in \mathbb{Z}_{\mathcal{J}}} \phi_j \cdot \max_{j \in \mathbb{Z}_{\mathcal{J}}} |v'(\phi_j)| \leq \alpha, \quad \alpha = 1/2. \quad (5.3.15)$$

In this paper we state a CFL condition, like those in (5.3.15), in terms of the number  $\alpha$  for ease of comparison with other CFL conditions (with different values of  $\alpha$ ) that will appear elsewhere.

If the speed  $v$  is nonnegative, the second term on the right-hand side of the equation for  $C_{j+1/2}$  in (5.3.12) is not present, and we can replace (5.3.15) by the less restrictive CFL conditions

$$\lambda \max_{j \in \mathbb{Z}_{\mathcal{J}}} v(\phi_j) \leq \alpha, \quad \lambda \max_{j \in \mathbb{Z}_{\mathcal{J}}} \phi_j \cdot \max_{j \in \mathbb{Z}_{\mathcal{J}}} |v'(\phi_j)| \leq \alpha, \quad \alpha = 1/2. \quad (5.3.16)$$

### Scheme 3 for scalar equations ( $N = 1$ ) with non-negative velocity with a discontinuous flux

We will also consider scalar conservation laws of the form

$$\phi_t + f(\gamma(x), \phi)_x = 0, \quad f(\gamma(x), \phi) = \phi v(\gamma(x), \phi), \quad v(\gamma, \phi) \geq 0, \quad (5.3.17)$$

where the spatially varying coefficient vector  $\gamma$  may have jump discontinuities. For the traffic flow model, the coefficient  $\gamma$  modulates the velocity function, and provides a way to model spatially varying road conditions. For the conservation law

(5.3.17), our numerical flux becomes

$$h(\gamma_{j+1}, \phi_{j+1}, \phi_j) = \phi_j v(\gamma_{j+1}, \phi_{j+1}), \quad \gamma_{j+1} := \gamma(x_{j+1}^+). \quad (5.3.18)$$

For the scheme defined by (5.3.18), Scheme 3, we cannot derive CFL conditions by enforcing a maximum principle like (5.3.13) or TVD property like (5.3.14). Nevertheless, we demonstrate in Section 5.4 that at least in one important case the scheme is stable and convergent if the following CFL conditions are satisfied:

$$\lambda \max_{j \in \mathbb{Z}_{\mathcal{J}}} v(\phi_j, \gamma_j) \leq \alpha, \quad \lambda \max_{j \in \mathbb{Z}_{\mathcal{J}}} \phi_j \cdot \max_{j \in \mathbb{Z}_{\mathcal{J}}} |\partial_{\phi} v(\gamma_j, \phi_j)| \leq \alpha, \quad \alpha = 1/2.$$

### 5.3.3 Numerical flux for systems of conservation laws

When generalizing the numerical flux to multi-species kinematic flows governed by (5.1.1) one should observe that only for the traffic and dispersion models, the velocities  $v_i(\Phi)$  are always nonnegative; for the sedimentation model, the velocities  $v_i(\Phi)$  are defined by (5.2.3) and may become negative due to buoyancy effects. This also occurs in the special case that all particles have the same density, and the velocities  $v_i(\Phi)$  are defined by (5.2.9).

#### Scheme 4 for systems ( $N \geq 1$ ) with non-negative velocities

In light of the above observation, for the multi-class traffic and the dispersion models a reasonable generalization of the scalar flux (5.3.8) is

$$h_{i,j+1/2} = h_i(\Phi_{j+1}, \Phi_j) = \phi_{i,j} v_i(\Phi_{j+1}), \quad i = 1, \dots, N. \quad (5.3.19)$$

We refer to the corresponding scheme as Scheme 4.

#### Scheme 5 for systems ( $N \geq 1$ ) with non-negative velocities and discontinuous flux

As mentioned previously, for the multi-class traffic model, we are also interested in spatially varying velocities of the form (5.2.4). In that case we replace the numer-

ical flux (5.3.19) by

$$\begin{aligned} h_{i,j+1/2} &= h_i(k_{i,j+1}, \Phi_{j+1}, \Phi_j) = \phi_{i,j} v_{\max,j+1}^i V(\phi_{j+1}/\phi_{\max,j+1}), \\ v_{\max,j+1}^i &:= v_{\max}^i(x_{j+1}^+), \quad \phi_{\max,j+1} := \phi_{\max}(x_{j+1}^+), \quad i = 1, \dots, N \end{aligned} \quad (5.3.20)$$

(Scheme 5).

### Schemes 6, 7 and 8 for systems ( $N \geq 1$ ) with velocities of variable sign

For the sedimentation model, where the velocities may become negative, a potential generalization of the scalar numerical flux (5.3.9) is

$$h_i(\Phi_{j+1}, \Phi_j) = \phi_{i,j} \max\{0, v_i(\Phi_{j+1})\} + \phi_{i,j+1} \min\{0, v_i(\Phi_{j+1})\}, \quad i = 1, \dots, N \quad (5.3.21)$$

(Scheme 6), and for this flux, the numerical viscosity coefficients are given by

$$Q_i(\Phi_{j+1}, \Phi_j) = \lambda |v_i(\Phi_{j+1})| + \lambda \phi_{i,j} \frac{v_i(\Phi_j) - v_i(\Phi_{j+1})}{\phi_{i,j+1} - \phi_{i,j}}. \quad (5.3.22)$$

Our numerical experiments with (5.3.19) give satisfactory results, and this is the first-order version of the flux that we use for systems where there are no negative velocities. When negative velocities are present, numerical experiments with (5.3.21) produce sharply resolved interfaces, but with overshoot in certain situations. To devise a numerical flux which overcomes this shortcoming, we return to the viscous formulation (5.3.10), (5.3.11) of the scalar numerical flux and observe that due to our assumption that  $v(\cdot)$  is non-increasing, both terms on the right-hand side of (5.3.11) are nonnegative. In fact, we can rewrite (5.3.11) in the equivalent form

$$\begin{aligned} Q(\phi_{j+1}, \phi_j) &= \lambda |v(\phi_{j+1})| + \lambda \phi_j \left| \frac{v(\phi_j) - v(\phi_{j+1})}{\phi_{j+1} - \phi_j} \right| \\ &= \lambda |v(\phi_{j+1})| + \lambda \phi_j \frac{|v(\phi_j) - v(\phi_{j+1})|}{\phi_{j+1} - \phi_j} \operatorname{sgn}(\phi_{j+1} - \phi_j). \end{aligned}$$

Inserting this into (5.3.10) yields the following form of the scalar numerical flux (5.3.9):

$$\begin{aligned} h(\phi_{j+1}, \phi_j) &= \frac{1}{2}(f(\phi_{j+1}) + f(\phi_j)) - \frac{1}{2}|v(\phi_{j+1})|(\phi_{j+1} - \phi_j) \\ &\quad - \frac{\phi_j}{2}|v(\phi_j) - v(\phi_{j+1})| \operatorname{sgn}(\phi_{j+1} - \phi_j), \end{aligned} \quad (5.3.23)$$

and this is the formulation that we generalize to systems when the velocities can become negative. In light of (5.3.23), a natural candidate for systems with velocities of both signs is

$$h_i(\Phi_{j+1}, \Phi_j) = \frac{1}{2}(\phi_{i,j+1}v_i(\Phi_{j+1}) + \phi_{i,j}v_i(\Phi_j)) - \frac{|v_i(\Phi_{j+1})|}{2}(\phi_{i,j+1} - \phi_{i,j}) - \frac{\phi_{i,j}}{2}|v_i(\Phi_j) - v_i(\Phi_{j+1})|\operatorname{sgn}(\phi_{i,j+1} - \phi_{i,j}), \quad i = 1, \dots, N, \quad (5.3.24)$$

which defines Scheme 7. For this flux the numerical viscosity coefficient is

$$Q_i(\Phi_{j+1}, \Phi_j) = \lambda|v_i(\Phi_{j+1})| + \lambda\phi_{i,j}\left|\frac{v_i(\Phi_j) - v_i(\Phi_{j+1})}{\phi_{i,j+1} - \phi_{i,j}}\right|.$$

Our modification (5.3.24) to the numerical flux (5.3.19) consists in forcing the second term in the viscosity coefficient (5.3.22) to be positive. For scalar equations, this term is always positive, but this is not always true for systems. This modification is also potentially applicable to systems where all of the velocities are nonnegative, but we have found that the original flux (5.3.19) is satisfactory for such systems.

For polydisperse settling problems we find that (5.3.24) is an improvement over (5.3.21) but still sometimes gives non-physical overshoots at the interfaces between beds of sediment. For these problems we propose a slightly more viscous version of (5.3.24) that provides a good compromise between sharply resolved interfaces and suppression of overshoots:

$$h_i(\Phi_{j+1}, \Phi_j) = \frac{1}{2}(\phi_{i,j+1}v_i(\Phi_{j+1}) + \phi_{i,j}v_i(\Phi_j)) - \frac{E_{j+1}}{2}(\phi_{i,j+1} - \phi_{i,j}) - \frac{\phi_{i,j}}{2}|v_i(\Phi_j) - v_i(\Phi_{j+1})|\operatorname{sgn}(\phi_{i,j+1} - \phi_{i,j}), \quad i = 1, \dots, N,$$

which defines Scheme 8, and where  $E_{j+1} := \max\{|v_1(\Phi_{j+1})|, \dots, |v_N(\Phi_{j+1})|\}$ .

### 5.3.4 Invariant regions and CFL conditions for systems

In Section 5.3.2 we derived CFL conditions by enforcing the TVD property and a very strong maximum principle. Both of these regularity properties are satisfied by

the true solutions of the scalar conservation laws being approximated, but not generally for systems of conservation laws. In this section we derive CFL conditions for systems. We first derive the form of these CFL conditions by requiring that a certain invariant region be preserved. Once we have the form of the CFL conditions, we determine the constants on the right sides by referring to our scalar CFL conditions.

As discussed in Section 5.1.1, the problems of interest to us have a natural invariant region  $\mathcal{D}_{\phi_{\max}}$  defined by (5.1.3). It is possible to show that our first-order scheme preserves this invariant region if we place some restrictions upon the velocity functions  $v_i(\Phi)$ . Since we also wish to allow for spatially varying coefficients, we generalize the definition (5.1.3), allowing it to vary spatially:

$$\begin{aligned} \mathcal{D}_{\phi_{\max,j}} := \{ \Phi = (\phi_1, \dots, \phi_N)^T \in \mathbb{R}^N : \\ \phi_1 \geq 0, \dots, \phi_N \geq 0, \phi := \phi_1 + \dots + \phi_N \leq \phi_{\max,j} \}. \end{aligned} \quad (5.3.25)$$

The following theorem applies to the multi-class traffic flow model discussed in Section 5.2.1.

**Theorem 5.3.1** *Consider Scheme 5 defined by (5.3.2) with numerical flux (5.3.20), and either type of boundary conditions, (5.3.4) or (5.3.5). Assume that all velocity functions  $v_i$  are of the form (5.2.4), where  $0 \leq v_{\max}^i(x) \leq \bar{v}_{\max}^i \leq \bar{v}_{\max}$  and  $0 < \underline{\phi}_{\max} \leq \phi_{\max}(x) \leq \bar{\phi}_{\max}$ , and that the hindrance factor  $V(z)$  satisfies*

$$0 \leq V(z) \leq V_{\max}, \quad V'(z) \leq 0, \quad |V'(z)| \leq |V'|_{\max}, \quad z \in [0, 1]; \quad V(1) = 0. \quad (5.3.26)$$

Then if  $\Phi_j^n \in \mathcal{D}_{\phi_{\max,j}}$  and the CFL conditions

$$\lambda \bar{v}_{\max} V_{\max} \leq \alpha, \quad \lambda (\bar{\phi}_{\max} / \underline{\phi}_{\max}) \bar{v}_{\max} |V'|_{\max} \leq \alpha, \quad \alpha = 1 \quad (5.3.27)$$

are satisfied at time level  $n$ , we will also have  $\Phi_j^{n+1} \in \mathcal{D}_{\phi_{\max,j}}$ .

**Proof.** Assume for now that the boundary conditions are periodic. The marching formula takes the form

$$\begin{aligned} \phi_{i,j}^{n+1} = \phi_{i,j}^n - \lambda \phi_{i,j}^n v_{\max,j+1}^i V \left( \frac{\phi_{j+1}^n}{\phi_{\max,j+1}} \right) \\ + \lambda \phi_{i,j-1}^n v_{\max,j}^i V \left( \frac{\phi_j^n}{\phi_{\max,j}} \right), \quad i = 1, \dots, N. \end{aligned} \quad (5.3.28)$$

From this expression, it is clear that

$$\phi_{i,j}^{n+1} \geq \phi_{i,j}^n - \lambda \phi_{i,j}^n v_{\max,j+1}^i V\left(\frac{\phi_{j+1}^n}{\phi_{\max,j+1}}\right) = \left[1 - \lambda v_{\max,j+1}^i V\left(\frac{\phi_{j+1}^n}{\phi_{\max,j+1}}\right)\right] \phi_{i,j}^n$$

for  $i = 1, \dots, N$ . This inequality implies that if  $\Phi_j^n \in \mathcal{D}_{\phi_{\max,j}}$  for all  $j \in \mathbb{Z}_{\mathcal{J}}$  we will have  $\phi_{i,j}^{n+1} \geq 0$  if the first CFL condition appearing in (5.3.27) is satisfied.

Returning to the marching formula (5.3.28), we obtain that

$$\phi_{i,j}^{n+1} \leq \phi_{i,j}^n + \lambda \phi_{i,j-1}^n v_{\max,j}^i V\left(\frac{\phi_j^n}{\phi_{\max,j}}\right) \leq \phi_{i,j}^n + \lambda \phi_{i,j-1}^n \bar{v}_{\max} V\left(\frac{\phi_j^n}{\phi_{\max,j}}\right).$$

Summing over  $i$  gives

$$\phi_j^{n+1} \leq \phi_j^n + \lambda \sum_{i=1}^N \phi_{i,j-1}^n \bar{v}_{\max} V\left(\frac{\phi_j^n}{\phi_{\max,j}}\right) =: G(\phi_j^n).$$

Assumption (5.3.26) implies that  $G(\phi_{\max,j}) = \phi_{\max,j}$ . Moreover,

$$G'(\phi_j^n) = 1 + \lambda \sum_{i=1}^N \frac{\phi_{i,j-1}^n \bar{v}_{\max}}{\phi_{\max,j}} V'\left(\frac{\phi_j^n}{\phi_{\max,j}}\right).$$

From this expression we deduce that if the second of the CFL conditions appearing in (5.3.27) is satisfied, the function  $G$  will be a nondecreasing function of  $\phi_j^n$ . Thus,

$$\max_{\phi_j^n \in [0, \phi_{\max,j}]} G(\phi_j^n) = G(\phi_{\max,j}) = \phi_{\max,j},$$

implying that  $\phi_j^{n+1} \leq \phi_{\max,j}$ . Finally, if the boundary conditions are of the zero-flux type, we only have to modify the proof at the two mesh points  $j = 0$  and  $j = \mathcal{J}$ , where one of the flux contributions in (5.3.28) will be zero. Retracing the steps of the proof, we see that all inequalities remain valid.  $\square$

It is common in traffic modeling to use a linear version of  $V$ , i.e.,  $V(z) = 1 - z$ . In that case the CFL conditions (5.3.27) can be reduced to the single condition

$$\lambda(\bar{\phi}_{\max}/\underline{\phi}_{\max})\bar{v}_{\max} \leq \alpha, \quad \alpha = 1, \quad (5.3.29)$$

and if  $\phi_{\max}$  does not depend on  $x$ , i.e.,  $\phi_{\max}(x) \equiv \phi_{\max}$ , this can be simplified even further to

$$\lambda \bar{v}_{\max} \leq \alpha, \quad \alpha = 1. \quad (5.3.30)$$

The oil-in-water dispersion model of Section 5.2.3 does not quite fit the hypotheses of the previous theorem, but it is still possible to prove that the scheme preserves the invariant region  $\mathcal{D}_{\phi_{\max}}$  if appropriate CFL conditions are enforced.

**Theorem 5.3.2** *Consider Scheme 4 defined by (5.3.2) with numerical flux functions defined by (5.3.19), and the zero-flux boundary conditions (5.3.5). With the form of the velocities  $v_i$  for the oil-in-water dispersion model specified in Section 5.2.3, if  $\Phi_j^n \in \mathcal{D}_{\phi_{\max}}$  (here  $\phi_{\max} = 1$ ) and the CFL conditions*

$$\begin{aligned} \lambda v_i(\Phi_j^n) &\leq \alpha, \quad i = 1, \dots, N, \quad j \in \mathbb{Z}_{\mathcal{J}}; \\ \lambda \frac{c}{\mu_d(\Phi_j^n)} \sum_{i=1}^N \phi_{i,j-1}^n \mathcal{V}_i^{2/3} &\leq \alpha, \quad \alpha = 1, \quad j \in \mathbb{Z}_{\mathcal{J}} \end{aligned} \quad (5.3.31)$$

are satisfied, then  $\Phi_j^{n+1} \in \mathcal{D}_{\phi_{\max}}$ .

**Proof.** First take the case where the boundary condition is not involved,  $0 < j < \mathcal{J}$  (an interior point). The marching formula then takes the form

$$\phi_{i,j}^{n+1} = \phi_{i,j}^n - \lambda \phi_{i,j}^n v_i(\Phi_{j+1}^n) + \lambda \phi_{i,j-1}^n v_i(\Phi_j^n), \quad i = 1, \dots, N. \quad (5.3.32)$$

This expression implies that

$$\phi_{i,j}^{n+1} \geq \phi_{i,j}^n - \lambda \phi_{i,j}^n v_i(\Phi_{j+1}^n) = (1 - \lambda v_i(\Phi_{j+1}^n)) \phi_{i,j}^n, \quad i = 1, \dots, N.$$

Using this inequality, along with the first CFL condition in (5.3.31), we conclude that if  $\phi_{i,j}^{n+1} \geq 0$ . The marching formula (5.3.32) also implies that  $\phi_{i,j}^{n+1} \leq \phi_{i,j}^n + \lambda \phi_{i,j-1}^n v_i(\Phi_j^n)$ . Summing over  $i$  gives

$$\phi_j^{n+1} \leq \phi_j^n + \lambda \sum_{i=1}^N \phi_{i,j-1}^n v_i(\Phi_j^n) =: G(\Phi_j^n).$$

To simplify notation, we write  $G$  as

$$G(\Phi) = \phi + \lambda \sum_{i=1}^N \psi_i v_i(\Phi), \quad \Phi = \Phi_j^n, \quad \phi = \phi_j^n, \quad \psi_i = \phi_{i,j-1}^n.$$

Recalling that for this model  $\phi_{\max} = 1$ , we complete the proof by showing that

$$\max_{\Phi \in \mathcal{D}_{\phi_{\max}}} G(\Phi) \leq 1. \quad (5.3.33)$$

From (5.2.10), we obtain that

$$G(\Phi) = \phi + \lambda B \cdot \frac{1 - \phi}{\mu_d(\Phi)}, \quad B := c \sum_{i=1}^N \psi_i \mathcal{V}_i^{2/3}. \quad (5.3.34)$$

Rearranging (5.3.34) and using  $\phi \leq \phi_{\max} = 1$  yields

$$G(\Phi) = \left(1 - \lambda \frac{B}{\mu_d(\Phi)}\right) \phi + \lambda \frac{B}{\mu_d(\Phi)} \leq 1.$$

To obtain the last inequality, we have used the second CFL condition appearing in (5.3.31). Thus, (5.3.33) is valid, and the proof is complete for each interior point. To complete the proof, we must deal with the remaining mesh points  $x_0$  and  $x_{\mathcal{J}}$ . At  $x_0$ , the marching formula (5.3.32) simplifies to

$$\phi_{i,0}^{n+1} = \phi_{i,0}^n - \lambda \phi_{i,0}^n v_i(\Phi_1^n), \quad i = 1, \dots, N. \quad (5.3.35)$$

That  $\phi_{i,0}^{n+1} \geq 0$  now follows from the CFL condition exactly as in the case of an interior point. For the upper bound, it is immediate by summing over  $i$  in (5.3.35) that  $\phi_0^{n+1} \leq \phi_0^n$ , and thus  $\Phi_0^{n+1} \in \mathcal{D}_{\phi_{\max}}$ . At  $x_{\mathcal{J}}$ , the marching formula (5.3.32) becomes

$$\phi_{i,\mathcal{J}}^{n+1} = \phi_{i,\mathcal{J}}^n + \lambda \phi_{i,\mathcal{J}-1}^n v_i(\Phi_{\mathcal{J}}^n), \quad i = 1, \dots, N. \quad (5.3.36)$$

Now the proof that  $\phi_{i,\mathcal{J}} \geq 0$  is clear from (5.3.36), and the upper bound  $\phi_{\mathcal{J}}^{n+1} \in \mathcal{D}_{\phi_{\max}}$  follows exactly as in the proof above for an interior point.  $\square$

In light of (5.2.10), the maximum velocities are given by  $v_{\max}^i = c \mathcal{V}_i^{2/3} / \mu_f$ . Using these maximum velocities, it is possible to combine the CFL conditions (5.3.31) for

the oil-in-water dispersion model into the single and simplified, but possibly more restrictive, condition

$$\lambda \max_{i=1,\dots,N} v_{\max}^i \leq \alpha, \quad \alpha = 1. \quad (5.3.37)$$

In the scalar case ( $N = 1$ ), the CFL conditions (5.3.27) and (5.3.31) are essentially the CFL conditions (5.3.16), except with Courant number  $\alpha = 1$  instead of  $1/2$ . The smaller  $\alpha = 1/2$  on the right side of (5.3.16) can be explained by the fact that those conditions were derived in order to enforce both a TVD property and a more restrictive local maximum principle. The non-oscillatory property of our scalar scheme is due to the TVD property. Since we wish to extend this property to the systems version of our scheme, in practice we use the more restrictive Courant number  $\alpha = 1/2$  in (5.3.27) for the multi-class traffic model. Similarly, we use  $\alpha = 1/2$  in the CFL condition (5.3.31) for the scheme as it applies to the oil-in-water dispersion model. Finally, we replace Courant number  $\alpha = 1$  by  $\alpha = 1/2$  in the simplified single CFL conditions (5.3.29) and (5.3.30) and the simplified single CFL condition (5.3.37) for the oil-in-water model.

For the multi-class traffic model and the oil-in-water dispersion model, we have found the form that CFL conditions should take by enforcing certain invariant regions, and then modifying the parameter on the right side of the CFL inequalities by referring back to simpler scalar conservation laws. For the polydisperse sedimentation model, we do not currently have a proof that our scheme preserves the invariant region  $\mathcal{D}_{\phi_{\max}}$ , so we can not directly carry out such a program. However, based on our analysis of the simpler multi-class traffic and oil-in-water dispersion models, the CFL condition of the following type seems reasonable for the polydisperse sedimentation model:

$$\lambda \max_{i=1,\dots,N} |v^i|_{\max} \leq \alpha, \quad \alpha = 1/2, \quad |v^i|_{\max} := \max_{\Phi \in \mathcal{D}_{\phi_{\max}}} |v_i(\Phi)|. \quad (5.3.38)$$

Due to the complicated form of the velocities  $v_i$  for the polydisperse sedimentation model, these maximum velocities may be difficult to calculate. As an alternative, we can replace the CFL condition (5.3.38) by

$$\lambda_n \max_{j \in \mathbb{Z}_{\mathcal{J}}} \max_{i=1,\dots,N} |v_i(\Phi_j^n)| \leq \alpha, \quad \alpha = 1/2.$$

We enforce this CFL condition by computing at each time level

$$\lambda_n = \frac{1}{2 \max_{j \in \mathbb{Z}_J} \max_{i=1, \dots, N} |v_i(\Phi_j^n)|},$$

and then computing the time step via  $\Delta t_n = \lambda_n \Delta x$ . Our numerical experiments indicate that this approach works well.

### 5.3.5 Higher-order versions (Schemes 9 and 10)

Schemes 1 to 8 are only first-order accurate, meaning that a very fine mesh is required in order to accurately resolve some features of the solution. To improve on this situation, we propose a formally second-order scheme, constructed by using MUSCL [124] spatial differencing, and Runge-Kutta temporal differencing. The MUSCL version of the  $i$ th flux component reads

$$h_i^m(\gamma_{i,j+1}, \Phi_{j+2}, \Phi_{j+1}, \Phi_j, \Phi_{j-1}) = h_i \left( \gamma_{i,j+1}, \Phi_{j+1} - \frac{1}{2} \sigma_{j+1}, \Phi_j + \frac{1}{2} \sigma_j \right), \quad (5.3.39)$$

$$\gamma_{i,j+1} := \gamma_i(x_{j+1}^+), \quad i = 1, \dots, N, \quad (5.3.40)$$

where  $h_i$  is the first-order version of the flux, and we define the slope vector  $\sigma_j := (\sigma_{1,j}, \dots, \sigma_{N,j})^T$  with

$$\sigma_{i,j} = \begin{cases} \text{minmod}\{\phi_{i,j+1} - \phi_{i,j}, \phi_{i,j} - \phi_{i,j-1}\} & \text{if } j = 1, \dots, J-1, \\ 0 & \text{if } j = 0 \text{ or } j = J, \end{cases} \quad (5.3.41)$$

$$i = 1, \dots, N,$$

where, as usual,  $\text{minmod}\{a, b\} := (\text{sgn}(a) + \text{sgn}(b)) \min\{|a|, |b|\}/2$ , or the less dissipative Van Leer limiter

$$\sigma_{i,j} = \begin{cases} \Theta_{i,j} & \text{if } j = 1, \dots, J-1, \\ 0 & \text{if } j = 0 \text{ or } j = J, \end{cases} \quad i = 1, \dots, N, \quad (5.3.42)$$

$$\Theta_{i,j} := \frac{|\phi_{i,j} - \phi_{i,j-1}|(\phi_{i,j+1} - \phi_{i,j}) + |\phi_{i,j+1} - \phi_{i,j}|(\phi_{i,j} - \phi_{i,j-1})}{|\phi_{i,j} - \phi_{i,j-1}| + |\phi_{i,j+1} - \phi_{i,j}|}.$$

When the boundary conditions are of the zero-flux type, we simply set  $\sigma_j = 0$  when  $j = 0, \mathcal{J}$ . In the scalar case, this avoids non-physical overshoot that can occur otherwise.

In all examples in this paper, the parameter  $\gamma$  is piecewise constant. If  $\gamma$  is piecewise smooth, it is necessary to use  $\gamma_{i,j+1/2} := \gamma_i(x_{j+1/2}^+)$  in (5.3.39) instead of  $\gamma_{i,j+1}$  in order to achieve second-order accuracy. Some care is required here in order to avoid non-physical overshoots at jumps in  $\gamma$ . A simple way to avoid such overshoots is to use  $\gamma_{j+1}$  instead of  $\gamma_{j+1/2}$  when there is a jump in  $\gamma$  between  $x_j$  and  $x_{j+1}$ . Note that in any case we are not attempting to achieve higher than first-order accuracy at the location of jumps in  $\gamma$ .

Consequently, away from the boundaries, the MUSCL scheme is formally second-order accurate in space, but not in time. To achieve formal second-order accuracy in time also, we use second-order Runge-Kutta (RK) time stepping. More specifically, if we write our scheme with first-order Euler time differencing and second-order spatial differencing abstractly as

$$\Phi_j^{n+1} = \Phi_j^n - \Gamma_j(\Phi_{j+2}^n, \Phi_{j+1}^n, \Phi_j^n, \Phi_{j-1}^n, \Phi_{j-2}^n), \quad (5.3.43)$$

then the RK version takes the following two-step form

$$\begin{aligned} \tilde{\Phi}_j^{n+1} &= \Phi_j^n - \Gamma_j(\Phi_{j+2}^n, \Phi_{j+1}^n, \Phi_j^n, \Phi_{j-1}^n, \Phi_{j-2}^n), \\ \Phi_j^{n+1} &= \frac{1}{2}\Phi_j^n + \frac{1}{2}\tilde{\Phi}_j^{n+1} - \frac{1}{2}\Gamma_j(\tilde{\Phi}_{j+2}^{n+1}, \tilde{\Phi}_{j+1}^{n+1}, \tilde{\Phi}_j^{n+1}, \tilde{\Phi}_{j-1}^{n+1}, \tilde{\Phi}_{j-2}^{n+1}). \end{aligned} \quad (5.3.44)$$

This type of time discretization is formally second-order accurate in time, Strong Stability Preserving (SSP), see [84], and does not require any additional reduction of the allowable time step. We refer to the scheme based on the first-order flux (5.3.8) and extended to second-order in space and time accuracy by (5.3.39), (5.3.41) and (5.3.43), (5.3.44), respectively, as Scheme 9, while the variant that uses the Van Leer limiter (5.3.42) (instead of (5.3.41)) as Scheme 10.

**Theorem 5.3.3** *Consider the scalar initial value problem with flux (5.3.6) and periodic boundary conditions. Assume that  $v'(\phi) \leq 0$ ,  $v(\phi) \geq 0$ ,  $v(\phi_{\max}) = 0$ ,  $v(0) = v_{\max}$ . Assume*

that the initial data satisfies  $\phi_0(x) \in [0, \phi_{\max}]$ ,  $TV(\phi_0) < \infty$ . Then Schemes 9 and 10 produce approximations that satisfy the maximum principle (5.3.13) and TVD property (5.3.14) if the CFL condition (5.3.16) is satisfied and the slopes  $\sigma_j$  satisfy

$$0 \leq \frac{\sigma_j}{2\Delta_+\phi_j} \leq 1, \quad 0 \leq \frac{\sigma_j}{2\Delta_-\phi_j} \leq 1. \quad (5.3.45)$$

**Remark 5.3.1** The main point of the preceding theorem is that we do not have to reduce the allowable time step when using the second-order scheme. Also, note that both the minmod limiter and the Van Leer limiter enforce the inequalities (5.3.45).

**Proof.** Since the RK processing does not affect the stability properties, we carry out the proof for the scheme where only the MUSCL processing is included. Following [140], we write the scheme in incremental form

$$\phi_j^{n+1} = \phi_j^n + C_{j+1/2}^n \Delta_+ \phi_j^n - D_{j-1/2}^n \Delta_- \phi_j^n,$$

where

$$C_{j+1/2}^n = \frac{-\lambda}{\Delta_+ \phi_j^n} \left[ \left( \phi_j^n + \frac{\sigma_j^n}{2} \right) v \left( \phi_{j+1}^n - \frac{\sigma_{j+1}^n}{2} \right) - \left( \phi_j^n + \frac{\sigma_j^n}{2} \right) v \left( \phi_j^n - \frac{\sigma_j^n}{2} \right) \right],$$

$$D_{j-1/2}^n = \frac{\lambda}{\Delta_- \phi_j^n} \left[ \left( \phi_j^n + \frac{\sigma_j^n}{2} \right) v \left( \phi_j^n - \frac{\sigma_j^n}{2} \right) - \left( \phi_{j-1}^n + \frac{\sigma_{j-1}^n}{2} \right) v \left( \phi_j^n - \frac{\sigma_j^n}{2} \right) \right].$$

A straightforward calculation gives

$$C_{j+1/2}^n = -\lambda \left( \phi_j^n + \frac{\sigma_j^n}{2} \right) v'(\xi_{j+1/2}^n) \left[ 1 - \frac{\sigma_{j+1}^n}{2\Delta_+ \phi_j^n} + \frac{\sigma_j^n}{2\Delta_+ \phi_j^n} \right], \quad (5.3.46)$$

$$D_{j-1/2}^n = \lambda v \left( \phi_j^n - \frac{\sigma_j^n}{2} \right) \left[ 1 + \frac{\sigma_j^n}{2\Delta_- \phi_j^n} - \frac{\sigma_{j-1}^n}{2\Delta_- \phi_j^n} \right]. \quad (5.3.47)$$

The assumptions on  $\phi_0$  imply  $\phi_j^0 \in [0, \phi_{\max}]$  and  $TV(\phi^0) < \infty$ . Assume that  $\phi_j^n \in [0, \phi_{\max}]$  and  $TV(\phi^n) < \infty$  also hold. Thanks to (5.3.45), the bracketed terms in (5.3.46) and (5.3.47) are nonnegative. The requirement (5.3.45) also implies that the quantities  $\phi_j^n \pm \sigma_j^n/2$  are contained in the interval  $[0, \phi_{\max}]$ . With these observations, it is clear that  $C_{j+1/2}^n \geq 0$  and  $D_{j-1/2}^n \geq 0$ .

Finally, (5.3.45) implies that the bracketed terms in (5.3.46) and (5.3.47) do not exceed 2. Combining this fact with the CFL condition (5.3.16), it is clear that  $C_{j+1/2}^n \leq$

$1/2$  and  $D_{j-1/2}^n \leq 1/2$ . Thus  $C_{j+1/2}^n + D_{j+1/2}^n \leq 1$  and  $C_{j+1/2}^n + D_{j-1/2}^n \leq 1$ . Combining these inequalities with the non-negativity of  $C_{j+1/2}^n$  and  $D_{j+1/2}^n$  proves that  $\phi_j^{n+1} \in [0, \phi_{\max}]$ , and  $TV(\phi^{n+1}) < \infty$ , and thus the proof is complete by induction on  $n$ .  $\square$

## 5.4 Convergence analysis

In this section we focus on the scalar initial value problem with periodic boundary conditions:

$$\begin{aligned} \phi_t + (k(x)\phi V(\phi/\phi_{\max}))_x &= 0, & (x, t) \in [0, L] \times (0, T) &=: \Pi_T \\ \phi(x, 0) &= \phi_0(x), \\ \phi(0, t) &= \phi(L, t), \end{aligned} \tag{5.4.1}$$

with the initial datum  $\phi_0$  satisfying

$$\phi_0 \in BV([0, L]) \cap L^1([0, L]) \cap L^\infty([0, L]), \quad \phi_0(x) \in [0, \phi_{\max}] \text{ for all } x \in [0, L]. \tag{5.4.2}$$

We assume that the coefficient  $k$  is positive, bounded, and piecewise constant:

$$0 < k_{\min} \leq k(x) \leq k_{\max}, \quad \exists \xi_1, \dots, \xi_M \in (0, L) : k|_{(\xi_m, \xi_{m+1})} \equiv k_m. \tag{5.4.3}$$

Note that the coefficient  $k$  has jumps at the points  $\xi_m$ .

Let  $f(\phi) := \phi V(\phi/\phi_{\max})$ . We assume that  $V : [0, 1] \mapsto [0, V_{\max}]$  is  $C^1$ , satisfies (5.3.26), and that

$$\exists \phi^* \in (0, \phi_{\max}) : f'(\phi) > 0 \text{ for } \phi \in (0, \phi^*) \text{ and } f'(\phi) < 0 \text{ for } \phi \in (\phi^*, \phi_{\max}). \tag{5.4.4}$$

This last condition is satisfied if for example,  $V(z) = (1 - z)^n$ , where  $n \geq 1$ .

This is a simple scalar model of traffic flow discussed in Section 5.2.1. Relating this to (5.2.2)–(5.2.4), we obtain the scalar velocity  $v(x, \phi) = k(x)V(\phi/\phi_{\max})$ . The parameter  $k(x)$  is playing the role of  $v_{\max}^1(x)$ ; we make this change to simplify the notation in this section. Also, we take  $\phi_{\max}$  to be constant in this section. With this simplification, along with the other assumptions stated above, the problem is a well-studied one.

**Definition 5.4.1** ( $BV_t$  entropy solution) *A measurable function  $\phi : \Pi_T \rightarrow \mathbb{R}$  is a  $BV_t$  entropy solution of the initial value problem (5.4.1) if*

$$\begin{aligned} \phi &\in L^1(\Pi_T) \cap BV_t(\Pi_T) \cap L^\infty(\Pi_T), \\ \phi(x, t) &\in [0, \phi_{\max}] \quad \text{for a.e. } (x, t) \in \Pi_T; \end{aligned} \quad (5.4.5)$$

the following Kruřkov-type entropy inequality holds for any  $\psi \in \mathcal{D}(\Pi_T)$ ,  $\psi \geq 0$ ,  $\psi(0, t) = \psi(L, t)$ :

$$\begin{aligned} &\iint_{\Pi_T} \left( |\phi - c| \partial_t \psi + \text{sgn}(\phi - c) (k(x)f(\phi) - k(x)f(c)) \partial_x \psi \right) \Delta t \Delta x \\ &+ \int_0^T \sum_{m=0}^M |k(\xi_m^+) - k(\xi_m^-)| f(c) \psi(\xi_m, t) \Delta t \geq 0 \quad \forall c \in \mathbb{R}; \end{aligned}$$

and the initial condition is satisfied in the following strong  $L^1$  sense:

$$\text{ess lim}_{t \downarrow 0} \int_{\mathbb{R}} |\phi(x, t) - \phi_0(x)| \Delta x = 0. \quad (5.4.6)$$

Due to our assumptions on the flux  $f$  and the coefficient  $k$ , there is a well-developed uniqueness and existence theory for the problem (5.4.1). In particular, by combining the results of [104] and [105], we have

**Theorem 5.4.2** *Problem (5.4.1) with assumptions (5.4.2)–(5.4.4) has a unique  $BV_t$  entropy solution in the sense of Definition 5.4.1.*

To construct approximate solutions to the initial value problem (5.4.1) we discretize  $\Pi_T$  as in Section 5.3.1, and use the marching formula

$$\phi_j^{n+1} = \phi_j^n - \lambda (h_{j+1/2}^n - h_{j-1/2}^n), \quad h_{j+1/2}^n := k_{j+1} \phi_j^n V(\phi_{j+1}^n / \phi_{\max}). \quad (5.4.7)$$

Here the flux  $h_{j+1/2}^n$  is defined by (5.3.18) (Scheme 3), as applied to the assumptions of this section.

To simplify the analysis, we choose a uniform time step  $\Delta t_n = \Delta t$  such that the CFL condition

$$\lambda k_{\max} V_{\max} \leq \alpha, \quad \lambda k_{\max} |V'|_{\max} \leq \alpha, \quad \alpha = 1/2 \quad (5.4.8)$$

is satisfied. This is the version of (5.3.27) that applies to the present situation. We extend the grid function  $\phi_j^n$  so that it is defined on all of  $\Pi_T$  via

$$\phi^\Delta(x, t) = \sum_{n=0}^{\mathcal{N}} \sum_{j=0}^{\mathcal{J}} \phi_j^n \chi_j(x) \chi_n(t),$$

where  $\chi_j(x)$  is the characteristic function for the spatial interval  $[x_j - \Delta x/2, x_j + \Delta x/2)$  and  $\chi_n(t)$  is the characteristic function for the temporal interval  $[t_n, t_n + \Delta t)$ .

**Lemma 5.4.1** *Scheme 3 is monotone in the sense that if  $\{\phi_j^n\}$  and  $\{\psi_j^n\}$  are two approximate solutions lying in the interval  $[0, \phi_{\max}]$  such that  $\phi_j^n \leq \psi_j^n$  for all  $j \in \mathbb{Z}_{\mathcal{J}}$ , then  $\phi_j^{n+1} \leq \psi_j^{n+1}$  for all  $j \in \mathbb{Z}_{\mathcal{J}}$ . Furthermore, if the initial data  $\phi_0(x)$  lies in the interval  $[0, \phi_{\max}]$  for all  $x \in [0, L]$ , then the computed approximation also satisfies  $\phi_j^n \in [0, \phi_{\max}]$  for all  $n \geq 0$  and all  $j \in \mathbb{Z}_{\mathcal{J}}$ . In addition, we have the discrete time continuity estimate*

$$\sum_{j=0}^{\mathcal{J}} |\phi_j^{n+1} - \phi_j^n| \leq C, \quad n = 0, 1, \dots, \mathcal{N}, \quad (5.4.9)$$

where the constant  $C$  is independent of the mesh size  $\Delta$  and the time level  $n$ .

**Proof.** Substituting the formula for the numerical flux into the marching formula (5.4.7) and then taking partial derivatives yields

$$\begin{aligned} \frac{\partial \phi_j^{n+1}}{\partial \phi_{j+1}^n} &= -\frac{\lambda k_{j+1} \phi_j^n}{\phi_{\max}} V' \left( \frac{\phi_{j+1}^n}{\phi_{\max}} \right), & \frac{\partial \phi_j^{n+1}}{\partial \phi_{j-1}^n} &= \lambda k_j V(\phi_j^n / \phi_{\max}), \\ \frac{\partial \phi_j^{n+1}}{\partial \phi_j^n} &= 1 - \lambda k_{j+1} V \left( \frac{\phi_{j+1}^n}{\phi_{\max}} \right) + \frac{\lambda k_j \phi_{j-1}^n}{\phi_{\max}} V' \left( \frac{\phi_j^n}{\phi_{\max}} \right). \end{aligned}$$

That the first two partial derivatives are nonnegative is obvious. The third one is nonnegative thanks to the CFL condition. The first assertion is now an immediate consequence of the non-negativity of these partial derivatives. For the second assertion, note that if we apply the scheme to the constant data  $p_j^0 \equiv 0$  and  $q_j^0 \equiv \phi_{\max}$ , the result is  $p_j^1 \equiv 0$  and  $q_j^1 \equiv \phi_{\max}$ . Since  $0 = p_j^0 \leq \phi_j^0 \leq q_j^0 \leq \phi_{\max}$ , we will have  $0 = p_j^1 \leq \phi_j^1 \leq q_j^1 \leq \phi_{\max}$ ; this follows from the monotonicity. Continuing this way by induction completes the proof of the second assertion. The third assertion (5.4.9)

is basically a consequence of the Crandall-Tartar lemma [45], along with the boundedness of the variation of the initial data. The proof is very similar to that of [104, Lemma 3.3], so we omit the details.  $\square$

In order to establish compactness, we need a spatial variation bound, which is provided by the following lemma. Let  $V_a^b(z)$  denote the total variation of the function  $x \mapsto z(x)$  over the interval  $[a, b]$ .

**Lemma 5.4.2** *For any interval  $[a, b]$  such that  $\{\xi_1, \dots, \xi_M\} \cap [a, b] = \emptyset$ , and any  $t \in [0, T]$  we have a spatial variation bound of the form  $V_a^b(\phi^\Delta(\cdot, t)) \leq C(a, b)$ , where  $C(a, b)$  is independent of  $\Delta$  and  $t$  for  $t \in [0, T]$ .*

**Proof.** Due to our time continuity estimate (5.4.9), there is a constant  $K$  such that

$$\Delta x \sum_{j=0}^{\mathcal{J}} \sum_{n=0}^{\mathcal{N}} |\phi_j^{n+1} - \phi_j^n| \leq K. \quad (5.4.10)$$

Since  $\{\xi_1, \dots, \xi_M\} \cap [a, b] = \emptyset$ , we can assume that there is an index  $m$  such that  $\xi_m < a < b < \xi_{m+1}$ . Fix  $r > 0$  satisfying  $2r < \min\{\text{dist}(\xi_m, [a, b]), \text{dist}(\xi_{m+1}, [a, b])\}$ , and without loss of generality, assume that  $r > \Delta x$  for all mesh sizes  $\Delta x$  of interest. Let

$$\mathcal{A} := \mathcal{A}(\Delta) := \{j | x_j \in [a - r - \Delta x, a]\}, \quad \mathcal{B} := \mathcal{B}(\Delta) := \{j | x_j \in [b, b + r + \Delta x]\},$$

and observe that  $|\mathcal{A}|\Delta x \geq r$ ,  $|\mathcal{B}|\Delta x \geq r$ . It is then clear from (5.4.10) that

$$\Delta x \sum_{j \in \mathcal{A}} \sum_{n=0}^{\mathcal{N}} |\phi_j^{n+1} - \phi_j^n| \leq K, \quad \Delta x \sum_{j \in \mathcal{B}} \sum_{n=0}^{\mathcal{N}} |\phi_j^{n+1} - \phi_j^n| \leq K. \quad (5.4.11)$$

We can choose  $j_a = j_a(\Delta)$ ,  $j_b = j_b(\Delta)$  with  $j_a \in \mathcal{A}$ ,  $j_b + 1 \in \mathcal{B}$  such that

$$\sum_{n=0}^{\mathcal{N}} |\phi_{j_a}^{n+1} - \phi_{j_a}^n| = \min_{j \in \mathcal{A}} \sum_{n=0}^{\mathcal{N}} |\phi_j^{n+1} - \phi_j^n|, \quad \sum_{n=0}^{\mathcal{N}} |\phi_{j_b+1}^{n+1} - \phi_{j_b+1}^n| = \min_{j \in \mathcal{B}} \sum_{n=0}^{\mathcal{N}} |\phi_j^{n+1} - \phi_j^n|.$$

It follows from (5.4.11) that

$$\sum_{n=0}^{\mathcal{N}} |\phi_{j_a}^{n+1} - \phi_{j_a}^n| \leq \frac{K}{|\mathcal{A}|\Delta x} \leq \frac{K}{r}, \quad \sum_{n=0}^{\mathcal{N}} |\phi_{j_b+1}^{n+1} - \phi_{j_b+1}^n| \leq \frac{K}{|\mathcal{B}|\Delta x} \leq \frac{K}{r}. \quad (5.4.12)$$

Due to the way that we selected  $j_a$  and  $j_b$ , for  $j_a \leq j \leq j_b$  we can write the scheme as

$$\phi_j^{n+1} = \phi_j^n - k_m \lambda \Delta_- \bar{f}(\phi_{j+1}^n, \phi_j^n), \quad \bar{f}(\phi_{j+1}^n, \phi_j^n) := \phi_j^n V(\phi_{j+1}^n / \phi_{\max}). \quad (5.4.13)$$

The formula (5.4.13) can also be written in incremental form

$$\phi_j^{n+1} = \phi_j^n + C_{j+1/2}^n \Delta_+ \phi_j^n - D_{j-1/2}^n \Delta_- \phi_j^n, \quad (5.4.14)$$

where

$$C_{j+1/2}^n = \lambda k_m \frac{f(\phi_j^n) - \bar{f}(\phi_{j+1}^n, \phi_j^n)}{\Delta_+ \phi_j^n}, \quad D_{j-1/2}^n = \lambda k_m \frac{f(\phi_j^n) - \bar{f}(\phi_j^n, \phi_{j-1}^n)}{\Delta_- \phi_j^n}.$$

Using the definitions of  $f$  and  $\bar{f}$ , and invoking the CFL condition (5.4.8), it is easy to check that

$$C_{j+1/2}^n \geq 0, \quad D_{j+1/2}^n \geq 0, \quad C_{j+1/2}^n + D_{j+1/2}^n \leq 1. \quad (5.4.15)$$

The incremental form (5.4.14) implies that the differences evolve according to

$$\begin{aligned} \Delta_+ \phi_j^{n+1} &= \Delta_+ \phi_j^n + C_{j+3/2}^n \Delta_+ \phi_{j+1}^n - C_{j+1/2}^n \Delta_+ \phi_j^n \\ &\quad - D_{j+1/2}^n \Delta_+ \phi_j^n + D_{j-1/2}^n \Delta_- \phi_j^n. \end{aligned} \quad (5.4.16)$$

Note that when  $j = j_a$ , we can write (5.4.16) as

$$\Delta_+ \phi_{j_a}^{n+1} = \Delta_+ \phi_{j_a}^n + C_{j_a+3/2}^n \Delta_+ \phi_{j_a+1}^n - D_{j_a+1/2}^n \Delta_+ \phi_{j_a}^n - (\phi_{j_a}^{n+1} - \phi_{j_a}^n). \quad (5.4.17)$$

Similarly, when  $j = j_b$ , (5.4.16) takes the form

$$\Delta_+ \phi_{j_b}^{n+1} = \Delta_+ \phi_{j_b}^n - C_{j_b+1/2}^n \Delta_+ \phi_{j_b}^n + D_{j_b-1/2}^n \Delta_- \phi_{j_b}^n + (\phi_{j_b+1}^{n+1} - \phi_{j_b+1}^n). \quad (5.4.18)$$

Taking absolute values and summing over  $j$  in (5.4.16), we use the properties (5.4.15) to proceed as in the proof of Harten's lemma (Lemma 2.2 of [88]). To deal

with the boundary contributions, we use (5.4.17) and (5.4.18). This calculation yields

$$\begin{aligned}
\sum_{j=j_a}^{j_b} |\Delta_+ \phi_j^{n+1}| &\leq (1 - D_{j_a+1/2}^n) |\Delta_+ \phi_{j_a}^n| + C_{j_a+3/2}^n |\Delta_+ \phi_{j_a+1}^n| + |\phi_{j_a}^{n+1} - \phi_{j_a}^n| \\
&\quad + \sum_{j=j_a+1}^{j_b-1} (1 - C_{j+1/2}^n - D_{j+1/2}^n) |\Delta_+ \phi_j^n| + \sum_{j=j_a+1}^{j_b-1} C_{j+3/2}^n |\Delta_+ \phi_{j+1}^n| \\
&\quad + \sum_{j=j_a+1}^{j_b-1} D_{j-1/2}^n |\Delta_- \phi_j^n| + (1 - C_{j_b+1/2}^n) |\Delta_+ \phi_{j_b}^n| \\
&\quad + D_{j_b-1/2}^n |\Delta_- \phi_{j_b}^n| + |\phi_{j_a}^{n+1} - \phi_{j_a}^n| \\
&\leq \sum_{j=j_a}^{j_b} |\Delta_+ \phi_j^n| + |\phi_{j_a}^{n+1} - \phi_{j_a}^n| + |\phi_{j_b+1}^{n+1} - \phi_{j_b+1}^n|.
\end{aligned}$$

Proceeding by induction, and then using (5.4.12), we find that for  $1 \leq n \leq \mathcal{N}$

$$\begin{aligned}
\sum_{j=j_a}^{j_b} |\Delta_+ \phi_j^n| &\leq \sum_{j=j_a}^{j_b} |\Delta_+ \phi_j^0| + \sum_{\nu=1}^n (|\phi_{j_a}^\nu - \phi_{j_a}^{\nu-1}| + |\phi_{j_b+1}^\nu - \phi_{j_b+1}^{\nu-1}|) \\
&\leq \sum_{j=j_a}^{j_b} |\Delta_+ \phi_j^0| + \frac{2K}{r}.
\end{aligned} \tag{5.4.19}$$

The proof is completed with the observation that  $[a, b] \subseteq [x_{j_a}, x_{j_b+1}]$ , along with the assumption that  $u_0$  has bounded variation.  $\square$

**Remark 5.4.1** Note that the spatial variation bound provided by Lemma 5.4.2 is only local, and due to the term  $2K/r$  appearing in (5.4.19), it blows up if the distance from one of the endpoints of the interval  $[a, b]$  to one of the jump points  $\xi_m$  or  $\xi_{m+1}$  approaches zero. This is consistent with the fact that there is currently no known global spatial variation bound for conservation laws of this type (i.e., with a discontinuous coefficient). This has made it necessary to use alternative approaches to prove compactness, including the singular mapping approach, and the compensated compactness approach. The local variation bound established above provides one more analytical tool for such problems.

We state the following lemma without proof; it follows from the monotonicity property (Lemma 5.4.1), and is based on a discrete entropy inequality due to Crandall and Majda [45] which was later adapted to the situation where there are discontinuous coefficients, see [104] or [105].

**Lemma 5.4.3** *For any  $c \in \mathbb{R}$ , the following cell entropy inequality is satisfied by approximate solutions  $\phi_j^n$  generated by the scheme (5.4.7) (Scheme 3):*

$$|\phi_j^{n+1} - c| \leq |\phi_j^n - c| - \lambda \Delta_- H_{j+1/2}^n + \lambda |k_{j+1} - k_j| f(c),$$

where the numerical entropy flux  $H_{j+1/2}^n$  is defined by

$$H_{j+1/2}^n = k_{j+1} \bar{f}(\phi_{j+1}^n \vee c, \phi_j^n \vee c) - k_{j+1} \bar{f}(\phi_{j+1}^n \wedge c, \phi_j^n \wedge c),$$

and  $\bar{f}$  is defined in (5.4.13).

**Theorem 5.4.3** *Let the function  $\phi^\Delta$  be defined by (5.4.7) (Scheme 3). Assume that  $\Delta := (\Delta x, \Delta t) \rightarrow 0$  with the ratio  $\lambda$  fixed and satisfying the CFL condition (5.4.8). Then  $\phi^\Delta \rightarrow \phi$  boundedly a.e. and in  $L^1(\Pi_T)$ , where  $\phi$  is the unique  $BV_t$  entropy solution to the initial value problem (5.4.1) in the sense of Definition 5.4.1.*

**Proof.** For our approximate solutions  $\phi^\Delta$ , Lemma 5.4.1 gives us an  $L^\infty$  bound and a time continuity bound. Since our spatial domain  $[0, L]$  is compact, a uniform  $L^1$  bound follows immediately from our  $L^\infty$  bound. We also have a bound on the spatial variation in any interval  $[a, b]$  not containing any of the points  $\xi_1, \dots, \xi_M$ .

By standard compactness results, for any set  $\mathcal{S}$  of the form

$$\mathcal{S} = \bigcup_{p=1}^P [a_p, b_p], \quad \mathcal{S} \cap \{\xi_1, \dots, \xi_M\} = \emptyset, \quad (5.4.20)$$

there is a subsequence (which we do not bother to relabel) such that  $\phi^\Delta$  converges in  $L^1(\mathcal{S} \times [0, T])$ . Taking a countable sequence of intervals  $\mathcal{S}_\nu$  satisfying (5.4.20) and

$$\bigcup_{\nu=1}^{\infty} \mathcal{S}_\nu = [0, L] \setminus \{\xi_1, \dots, \xi_M\},$$

and employing a standard diagonal process we can extract a subsequence (which we again do not relabel) such that  $\phi^\Delta$  converges in  $L^1(\Pi_T)$  and also a.e. in  $\Pi_T$  to some  $\phi \in L^1(\Pi_T) \cap L^\infty(\Pi_T)$ . That the limit  $\phi$  is also in  $BV_t(\Pi_T)$  is a consequence of the time continuity estimate (5.4.9). We have verified that the limit  $\phi$  satisfies (5.4.5) of Definition 5.4.1.

That the limit  $\phi$  satisfies the entropy inequality is a consequence of a Lax-Wendroff type calculation, which we omit since it is similar to the proof Lemma 4.1 of [104], see also the proof of Theorem 3.1 of [31]. A proof of (5.4.6), i.e., that the initial values are assumed in the strong  $L^1$  sense, can be found in [105], specifically, the proofs of Theorem 5.1 and Lemma B.1.

Finally, by the uniqueness portion of Theorem 5.4.2, the entire computed sequence  $\phi^\Delta$  (not just a subsequence) converges to  $\phi$  in  $L^1(\Pi_T)$  and boundedly a.e. in  $\Pi_T$ .  $\square$

## 5.5 Numerical examples

### 5.5.1 Example 5.1: Scalar equation without spatially varying parameters

To study the scalar scheme in the simplest possible setting, we apply Scheme 1 and the Lax-Friedrichs (LxF) flux

$$h_{j+1/2}^{\text{LxF}} := \frac{1}{2} (\phi_{j+1} v_{j+1} + \phi_j v_j) - \frac{q}{2\lambda} (\phi_{j+1} - \phi_j) \quad (5.5.1)$$

to the initial value problem

$$\phi_t + (\phi(1 - \phi)^\nu)_x = 0, \quad \phi_0(x) = \begin{cases} 0.85 & \text{if } |x| > 1, \\ 0.1 & \text{if } |x| < 1. \end{cases} \quad (5.5.2)$$

For the parameter  $q$  appearing in (5.5.1), we take  $q = 1/2$  because this ensures that the resulting scheme satisfies the maximum principle (5.3.13) and TVD property

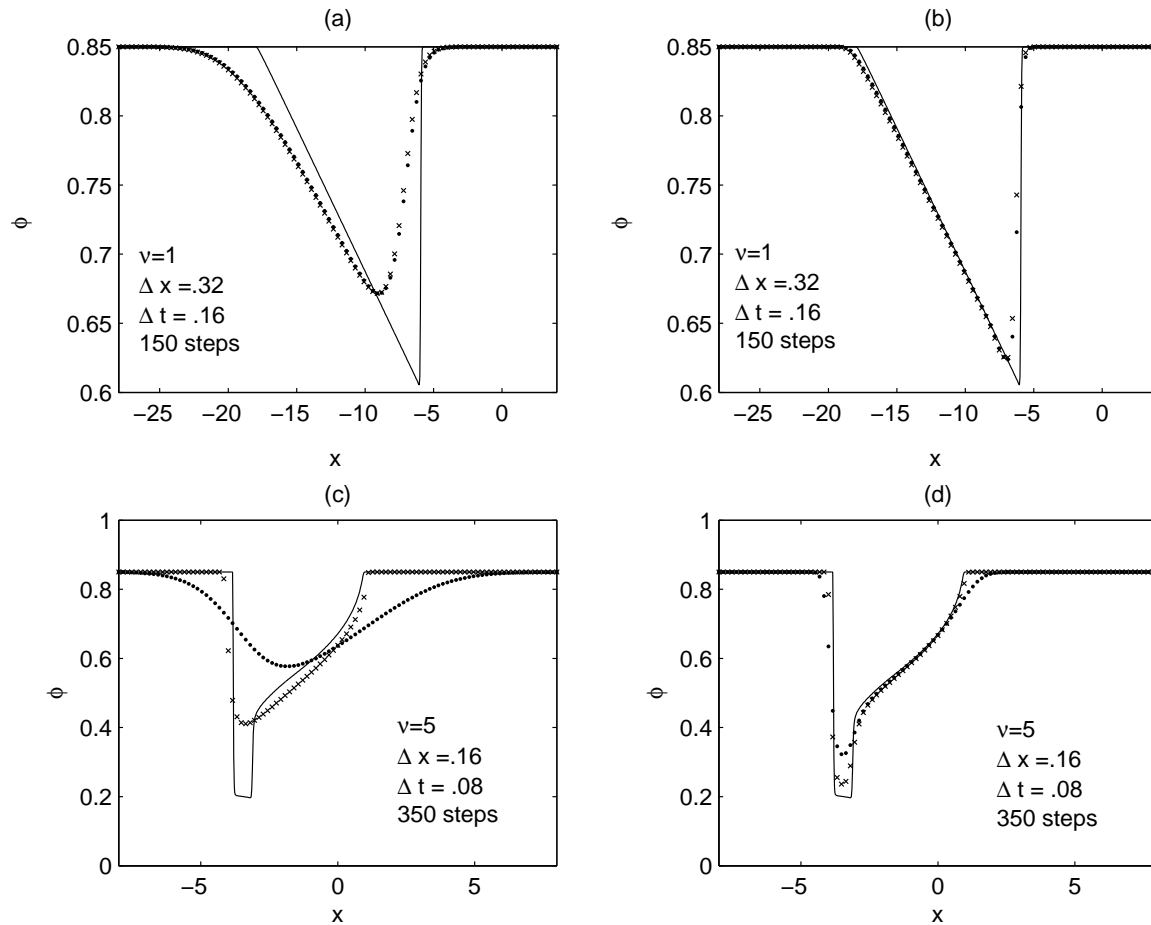


Figure 5.1: Example 5.1 (scalar case, problem (5.5.2)): Scheme 1 ( $\times$ ) (a, c), Scheme 10 ( $\times$ ) (b, d) and LxF flux ( $\cdot$ ). Plot (a): first-order schemes,  $\nu = 1$ . Plot (b): second-order schemes,  $\nu = 1$ . Plot (c): first-order schemes,  $\nu = 5$ . Plot (d): second-order schemes,  $\nu = 5$ . The solid line is the reference solution.

(5.3.14). Plots (a) and (b) of Figure 5.1 show that for  $\nu = 1$ , both schemes give similar results. Plots (c) and (d) illustrate that for  $\nu = 5$ , the schemes based on (5.3.8) (both first-order and second-order versions, Schemes 1 and 10) give better resolution than the schemes based on the LxF flux. The solid line in all plots of Figure 5.1 is a reference solution, computed using Scheme 10, and the discretization parame-

ters reduced by a factor of 8.

### 5.5.2 Example 5.2: Scalar equation with spatially varying coefficients

We next apply the variant of Scheme 1 that applies to conservation laws with discontinuous flux, namely Scheme 3, and Scheme 10 to scalar conservation laws with discontinuous flux of the form (5.2.2). The equation considered is

$$\phi_t + (v_{\max}(x)\phi(1 - \phi/\phi_{\max}(x)))_x = 0.$$

In Figures 5.2 (a) and (b) we use

$$\phi_{\max} = 1, \quad \phi_0(x) = \begin{cases} 0.8 & \text{for } x < 0, \\ 0.1 & \text{for } x > 0, \end{cases}, \quad v_{\max}(x) = \begin{cases} 1.0 & \text{for } x < 0, \\ 0.5 & \text{for } x > 0. \end{cases} \quad (5.5.3)$$

In Figures 5.2 (c) and (d) we set

$$\phi_{\max}(x) = \begin{cases} 1.0 & \text{for } x < 0, \\ 0.5 & \text{for } x > 0, \end{cases}, \quad \phi_0(x) = \begin{cases} 0.3 & \text{for } x < 0, \\ 0.7 & \text{for } x > 0, \end{cases}, \quad v_{\max} = 1. \quad (5.5.4)$$

The solid line visible in all plots is a reference solution, computed using Scheme 10, and the discretization parameters reduced by a factor of 16.

In each case, the new scheme (Scheme 3 or 10) gives better resolution than the corresponding scheme based on the LxF flux. Note that there is some overshoot visible in plots (a) and (b). This overshoot originates at the location of the jump in  $v_{\max}$ , and then propagates as a traveling wave (a bump). As the mesh size approaches zero, the magnitude and width of the bump approaches zero. Clearly, this non-physical feature is more pronounced for the LxF scheme.

### 5.5.3 Example 5.3: Clarifier-thickener model

We now adapt our scheme to the clarifier-thickener model with constant cross-sectional area studied in [31], specifically Example 2 of that paper. In this case the

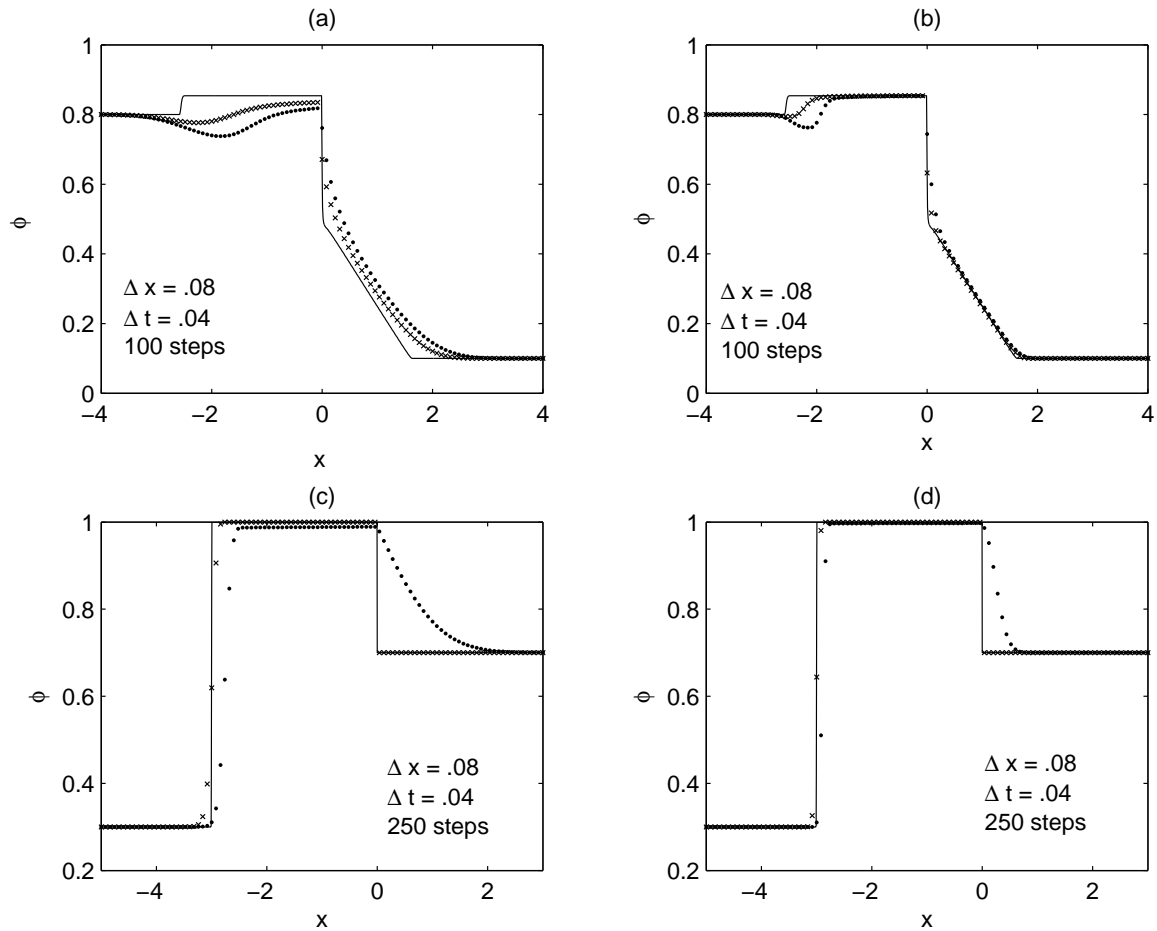


Figure 5.2: Example 5.2 (scalar case with discontinuous flux, see (5.5.2)): Scheme 3 ( $\times$ ) (a, c), Scheme 10 ( $\times$ ) (b, d) and LxF flux ( $\cdot$ ). Plot (a): coefficients (5.5.3), first-order schemes. Plot (b): coefficients (5.5.3), second-order schemes. Plot (c): coefficients (5.5.4), first-order schemes. Plot (d): coefficients (5.5.4), second-order schemes. The solid line is the reference solution.

conservation law is of the form

$$\phi_t + (\phi[a(x)\mathcal{S}(\phi) + c(x)] + b(x))_x = 0, \quad x \in \mathbb{R}, \quad t > 0, \quad (5.5.5)$$

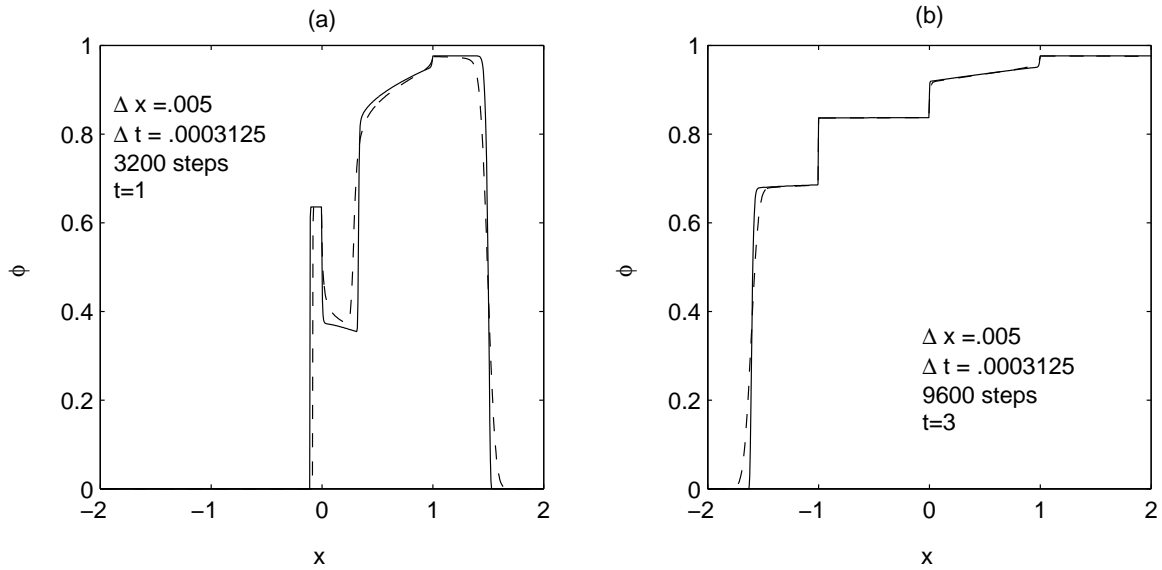


Figure 5.3: Example 5.3 (clarifier-thickener model (5.5.5)): (first-order) Scheme 2 (dashed line) and second-order Scheme 10 (solid line). Plot (a) shows  $t = 1$ , plot (b) shows  $t = 3$ .

where  $\mathcal{S}(\phi) = \phi_\infty(1 - \phi)^2$  and

$$a(x) = \begin{cases} 1 & \text{for } x \in (-1, 1), \\ 0 & \text{for } x \notin (-1, 1), \end{cases} \quad b(x) = \begin{cases} -q_L \phi_F & \text{for } x < 0, \\ -q_R \phi_F & \text{for } x > 0, \end{cases} \quad c(x) = \begin{cases} q_L & \text{for } x < 0, \\ q_R & \text{for } x > 0. \end{cases}$$

Except for the term  $b(x)$  which we discretize separately, this problem fits into the framework of (5.3.1) with  $N = 1$ , and the velocity  $v(\phi, x) = a(x)\mathcal{S}(\phi) + c(x)$ , which may assume either sign. Consequently, and following (5.3.9), the appropriate first-order scheme is Scheme 2, whose numerical flux is defined by

$$h_{j+1/2} = \phi_j \max\{0, v_{j+1}\} + \phi_{j+1} \min\{0, v_{j+1}\} + b_{j+1}, \quad v_j := a_j \mathcal{S}(\phi_j) + c_j. \quad (5.5.6)$$

Note that we use  $b_{j+1}$ , as opposed to  $b_j$  (or some average of the two values) for the first-order version of the scheme. Indeed, this biased discretization of the parameter  $b$  can be motivated by the requirement that if  $\mathcal{S} \equiv 0$ , then  $\phi \equiv \phi_F$  should be a stationary solution of (5.5.5).

For the second-order version of the scheme, we discretize  $\gamma(x) := (a(x), c(x))$  as in (5.3.40), and continue to use  $b_{j+1}$  in (5.5.6); this discretization of  $b(x)$  preserves the steady solution  $\phi \equiv \phi_F$  if  $\mathcal{S} \equiv 0$ . We use the Van Leer limiter (5.3.42), so the scheme in question is Scheme 10.

For our experiments, we used the same parameters as for Example 2 of [31], namely  $q_L = -1$ ,  $q_R = 0.6$ ,  $\phi_F = 0.8$  and  $\phi_\infty = 27/4$ . For discretization parameters, we used  $\Delta x = 5 \times 10^{-3}$ ,  $\Delta t = 3.125 \times 10^{-4}$ , implying  $\lambda = 1/16$ ; this value of  $\lambda$  was chosen to agree with Example 2 of [31]. We started with initial data  $\phi_0 \equiv 0$ . Plot (a) of Figure 5.3 shows the solution at  $t = 1$ , and plot (b) shows the solution at  $t = 3$ . These approximations are in good agreement with the solutions obtained in Example 2 of [31]. Scheme 2 provides a somewhat less accurate solution than the one provided by the Engquist-Osher scheme proposed in [31]. However, Scheme 2 is much easier to code, and at least with our implementation, runs significantly faster.

#### 5.5.4 Example 5.4: Multi-species traffic model

Zhang et al. [176] present numerical simulations of a traffic flow model with  $N = 9$  species (classes) of vehicles with the maximum velocities  $v_{\max}^i = (52.5 + i \cdot 7.5)$  km/h,  $i = 1, \dots, 9$ . We consider here Case 2 simulated in [176], where the function  $V(\phi) = \exp(-(\phi/\phi_*)^2/2)$  with the parameter  $\phi_* = 50$  cars/km is used. This case, which forms our Example 5.4, consists of the evolution of an isolated initial traffic “platoon” given by  $\Phi^0(x) = p(x)0.04\phi^0(1, 2, 3, 4, 5, 4, 3, 2, 1)^T$ , where

$$p(x) := \begin{cases} 10x & \text{for } 0 < x \leq 0.1, \\ 1 & \text{for } 0.1 < x \leq 0.9, \\ -10(x - 1) & \text{for } 0.9 < x \leq 1, \\ 0 & \text{otherwise} \end{cases}$$

is the platoon “shape function”, where  $x$  denotes distance measured in kilometers and  $\phi^0 = 120$  cars/km. We here use this example to compare the performance of Scheme 4, which is the first-order version of the scheme that applies to systems with

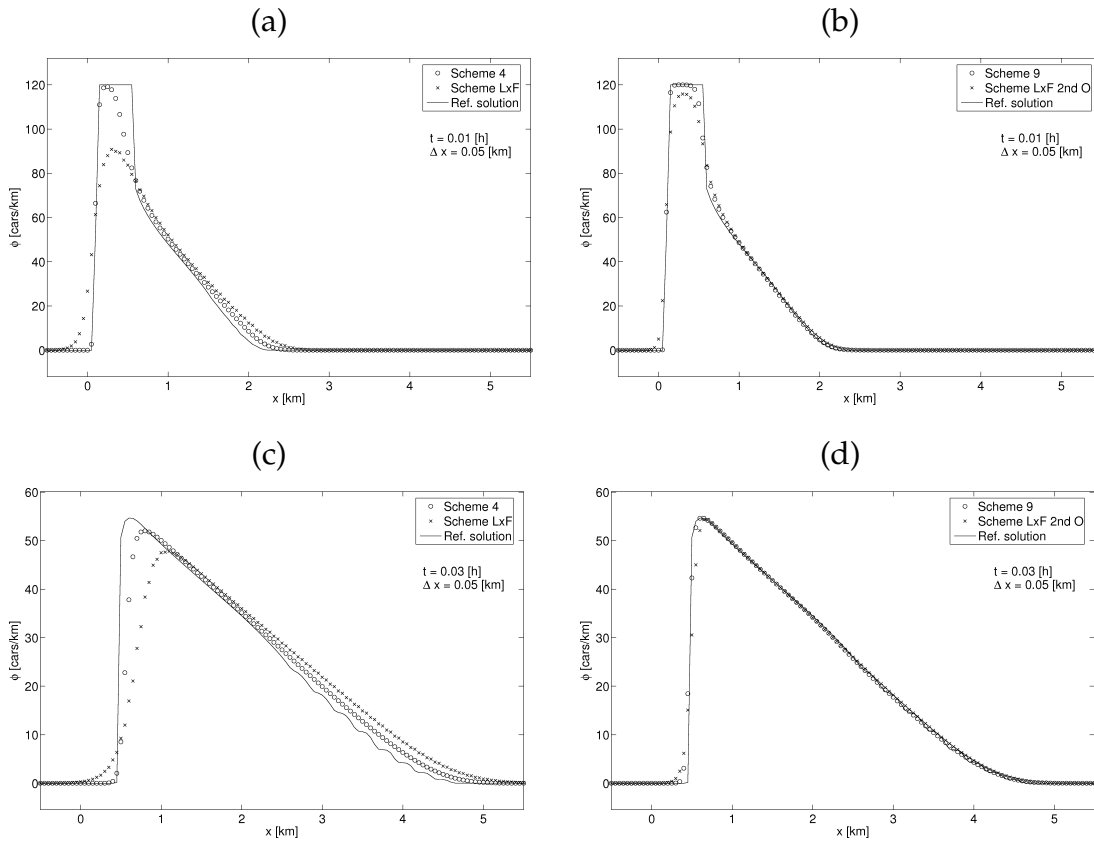


Figure 5.4: Example 5.4 (traffic model,  $N = 9$ ): simulated total car density. Plots (a, c): first-order schemes (LxF and Scheme 4). Plots (b, d): second-order schemes (LxF MM/RK and Scheme 9). Plots (a, b) show  $t = 0.01$  h, and plots (c, d) show  $t = 0.03$  h.

non-negative velocities only, with the standard first-order LxF scheme; and that of Scheme 9, which is the second-order version of Scheme 4 generated by spatial MUSCL extrapolation in combination with a second-order RK type discretization, with that of a second-order version of the LxF scheme generated by the analogous MUSCL/RK “upgrades”. The reference solution was calculated using Scheme 9 with the discretization parameters  $\Delta x = 1/480$  km. The reference solution and all numerical solutions of this example have been calculated with  $\lambda = 1/240$  h/km.

In Examples 5.4 and 5.6, we record an approximate  $L^1$  error defined with respect

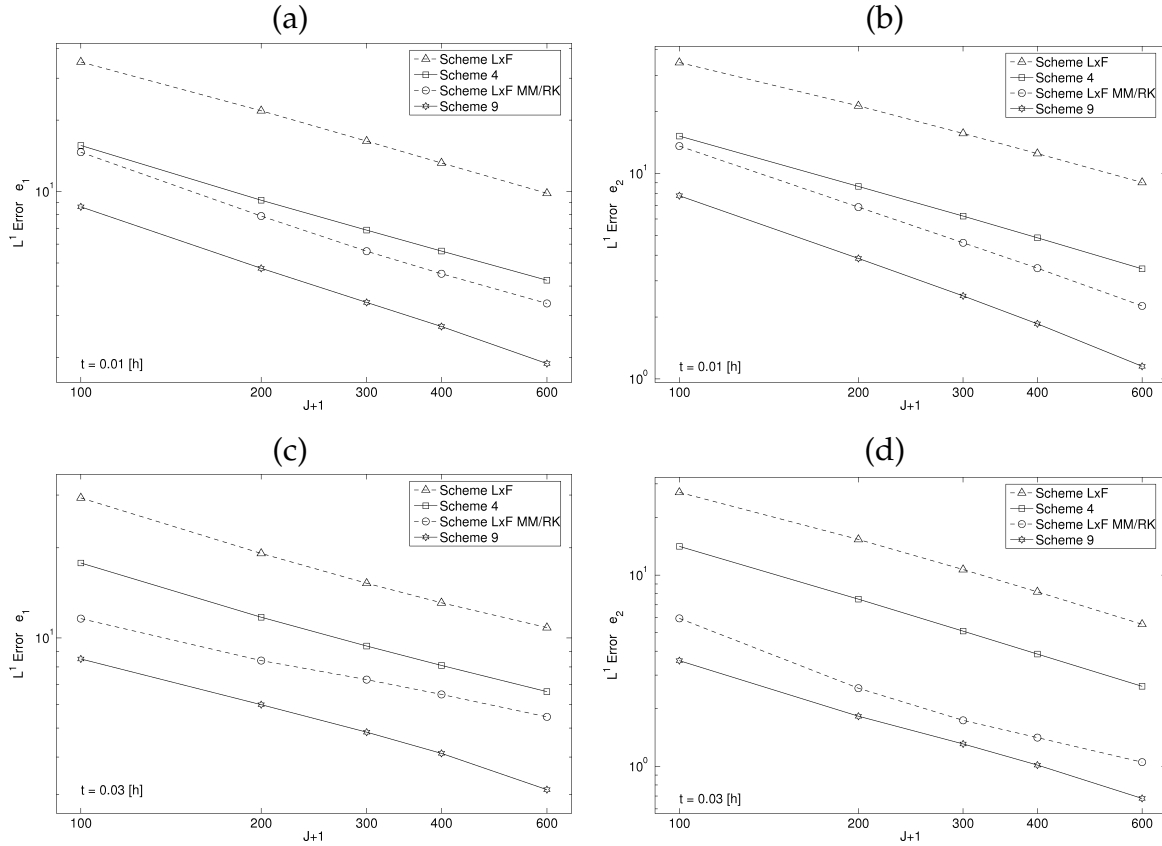


Figure 5.5: Example 5.4 (traffic model,  $N = 9$ ): approximate  $L^1$  errors (a, c)  $e_1$  and (b, d)  $e_2$ , measured at (a, b)  $t = 0.01$  h and (c, d)  $t = 0.03$  h.

to the reference solution, to evaluate the performance of some of the new schemes. We introduce two types of  $L^1$  error, denoted  $e_1$  and  $e_2$ , which are defined by

$$e_1 := \widetilde{\Delta}x \sum_{i=M_L}^{M_R} \sum_{j=1}^m \sum_{k=1}^N |\tilde{\phi}_{k,m(i-1)+j}^n - \phi_{k,i}^n|, \quad e_2 := \widetilde{\Delta}x \sum_{i=M_L}^{M_R} \sum_{j=1}^m \left| \sum_{k=1}^N (\tilde{\phi}_{k,m(i-1)+j}^n - \phi_{k,i}^n) \right|,$$

where  $\tilde{\phi}_{k,\tilde{l}}^n$  and  $\phi_{k,l}^n$  are the reference solution at  $x = x_{\tilde{l}}$  and the approximate solution at  $x = x_l$ , respectively, both for species  $k$  at  $t = t_n$ ;  $m$  is the value of  $\Delta x$  of the approximate solution divided by that of the reference solution;  $M_L$  and  $M_R$  are the indices of the positions between which we calculate the errors of the numerical approxima-

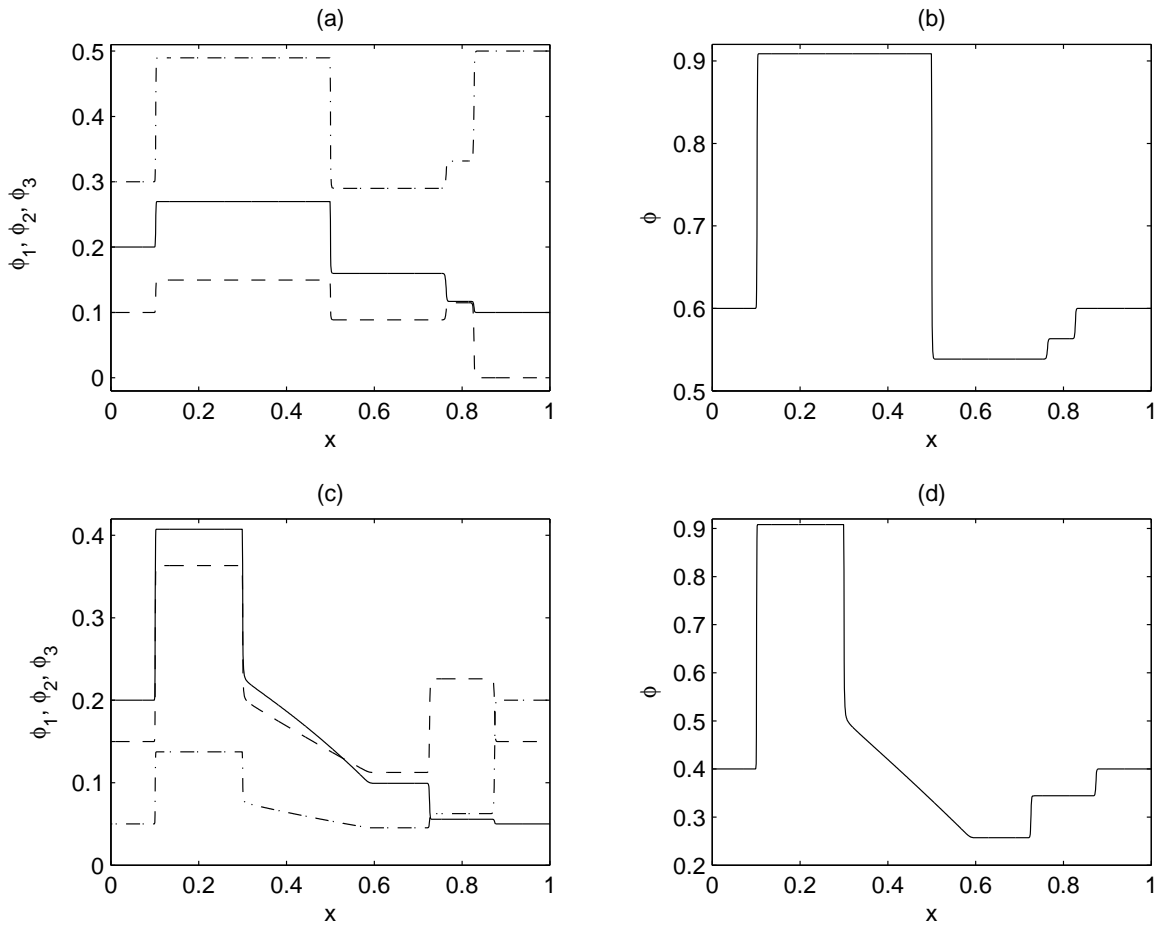


Figure 5.6: Examples 5.5.1 (a, b) and 5.2 (c, d) (traffic model with spatially varying  $\phi_{\max}$ ,  $N = 3$ ): plots (a, c) show  $\phi_1/\phi_{\max}$  (solid line),  $\phi_2/\phi_{\max}$  (dashed line),  $\phi_3/\phi_{\max}$  (dash-dotted line). Plots (b, d) show  $(\phi_1 + \phi_2 + \phi_3)/\phi_{\max}$ . Solutions are obtained by Scheme 9.

tion; and  $\tilde{\Delta x}$  is the spatial discretization parameter of the reference solution.

For Example 5.4, Figure 5.4 shows the simulated total car density at two times produced by the LxF scheme, Scheme 4, the second-order version of the LxF scheme using the minmod limiter, and Scheme 9, while Figure 5.5 displays the approximate  $L^1$  errors for this example, measured over the interval  $[-1 \text{ km}, 6 \text{ km}]$ . Both Figures 5.4

and 5.5 indicate the superiority of Scheme 4 over the LxF scheme, and of Scheme 9 over the second-order MM/RK upgrade of the LxF scheme, respectively.

### 5.5.5 Example 5.5: Multiclass traffic model with spatially varying $\phi_{\max}$

As an example where the flux has a spatially varying parameter, we also present two simulations (Examples 5.5.1 and 5.5.2) that can be compared with numerical results by Zhang et al. [178]. The model is the multi-class traffic model of Section 5.2.1, whose flux is given by (5.2.4). Both examples are Riemann problems, and  $N = 3$ . The (normalized [178]) maximum velocities are constant:  $v_{\max}^1 = 0.50$ ,  $v_{\max}^2 = 0.75$  and  $v_{\max}^3 = 1.00$ . We use the second-order scheme of Section 5.3.5 with the minmod limiter (5.3.41) (Scheme 9). The mesh size for both problems is  $\Delta x = 6.25 \times 10^{-4}$ ,  $\Delta t = 1.25 \times 10^{-4}$ . We march the solution forward in time for 8000 steps, arriving at  $t = 1$ . The initial data  $\Phi^0$  and maximum density  $\phi_{\max}$  are constant except for a jump at  $x_0 \in (0, 1)$ ,

$$\phi_{\max}(x) = \begin{cases} 3 & \text{for } x < x_0, \\ 1 & \text{for } x > x_0, \end{cases}, \quad \Phi^0(x) = \begin{cases} \Phi_L^0 & \text{for } x < x_0, \\ \Phi_R^0 & \text{for } x > x_0. \end{cases}$$

For Examples 5.5.1 and 5.5.2, we choose  $x_0 = 0.5$ ,  $\Phi_L^0 = (0.6, 0.3, 0.9)^T$  and  $\Phi_R^0 = (0.1, 0.0, 0.5)^T$ , and  $x_0 = 0.3$ ,  $\Phi_L^0 = (0.6, 0.45, 0.15)^T$  and  $\Phi_R^0 = (0.05, 0.15, 0.2)^T$ , respectively. As shown in Figure 5.6, for both problems, the various waves are well resolved, and there is good agreement with the results obtained by Zhang et al. in [178] (see Figures 4 and 7 of that paper).

### 5.5.6 Example 5.6: Settling of a bidisperse suspension of equal-density spheres

In this example, the parameters are  $N = 2$ ,  $\varrho_1 = \varrho_2 = \varrho_s = 2790 \text{ kg/m}^3$ ,  $d_1 = 4.96 \times 10^{-4} \text{ m}$ ,  $d_2 = 1.25 \times 10^{-4} \text{ m}$ ,  $\varrho_f = 1208 \text{ kg/m}^3$  and  $\mu_f = 0.02416 \text{ Pa}\cdot\text{s}$ . Here, we

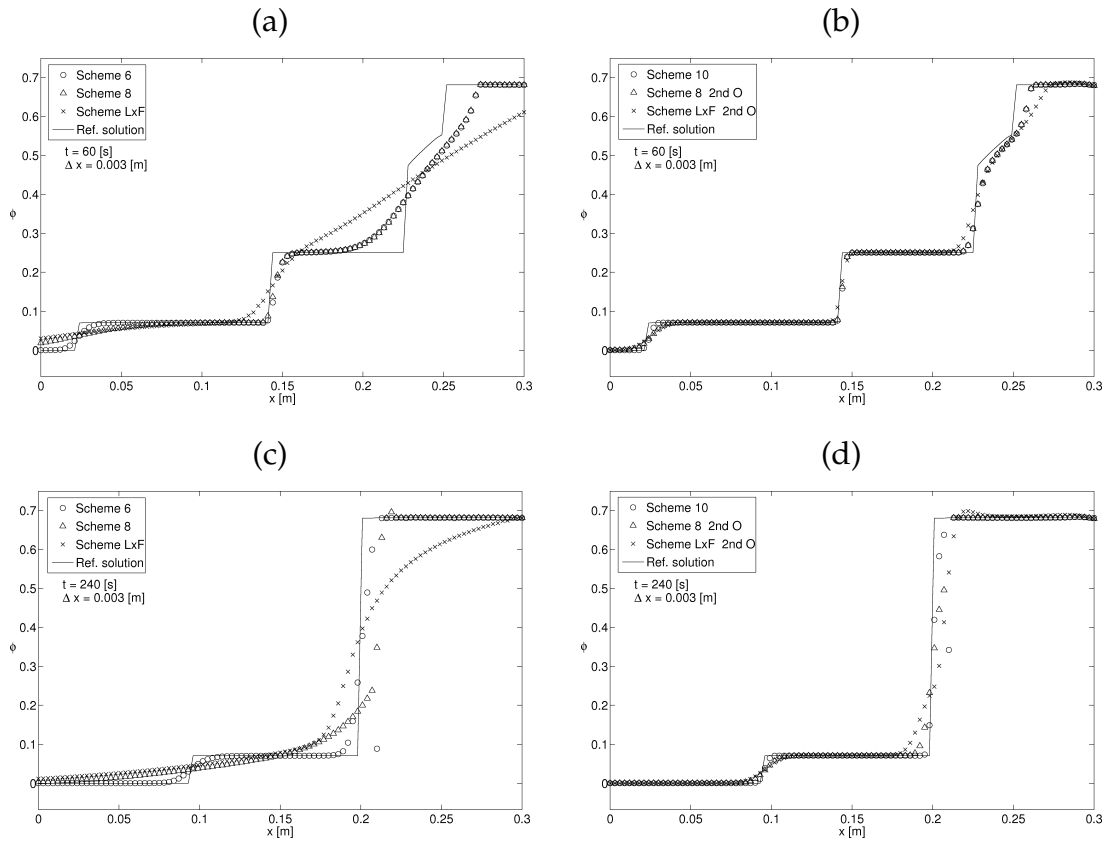


Figure 5.7: Example 5.6 (settling of a suspension of equal-density spheres,  $N = 2$ ): simulated total solids concentration. Plots (a, c): first-order schemes (LxF, Schemes 6 and 8). Plots (b, d): second-order schemes (LxF VL/RK, Scheme 8 VL/RK and Scheme 9). Plots (a, b) show solutions at  $t = 60$  s, and plots (c, d) show solutions at  $t = 240$  s.

have  $\delta_1 = 1$  and  $\delta_2 = d_2^2/d_1^2 = 0.06351213$ . For this mixture, we select the phase space  $\mathcal{D}_{0.68}$  [22] and the function  $V(\phi)$  given by (5.2.6) with the exponent  $n = 4.7$ ; all these parameters correspond to experimental data by Schneider et al. [151]. As in [151], we consider an initially homogeneous suspension with  $\Phi^0 = (\phi_1^0, \phi_2^0)^T = (0.2, 0.05)$  in a vessel of height  $L = 0.3$  m.

The reference solution was calculated using the Scheme 10 with the discretization

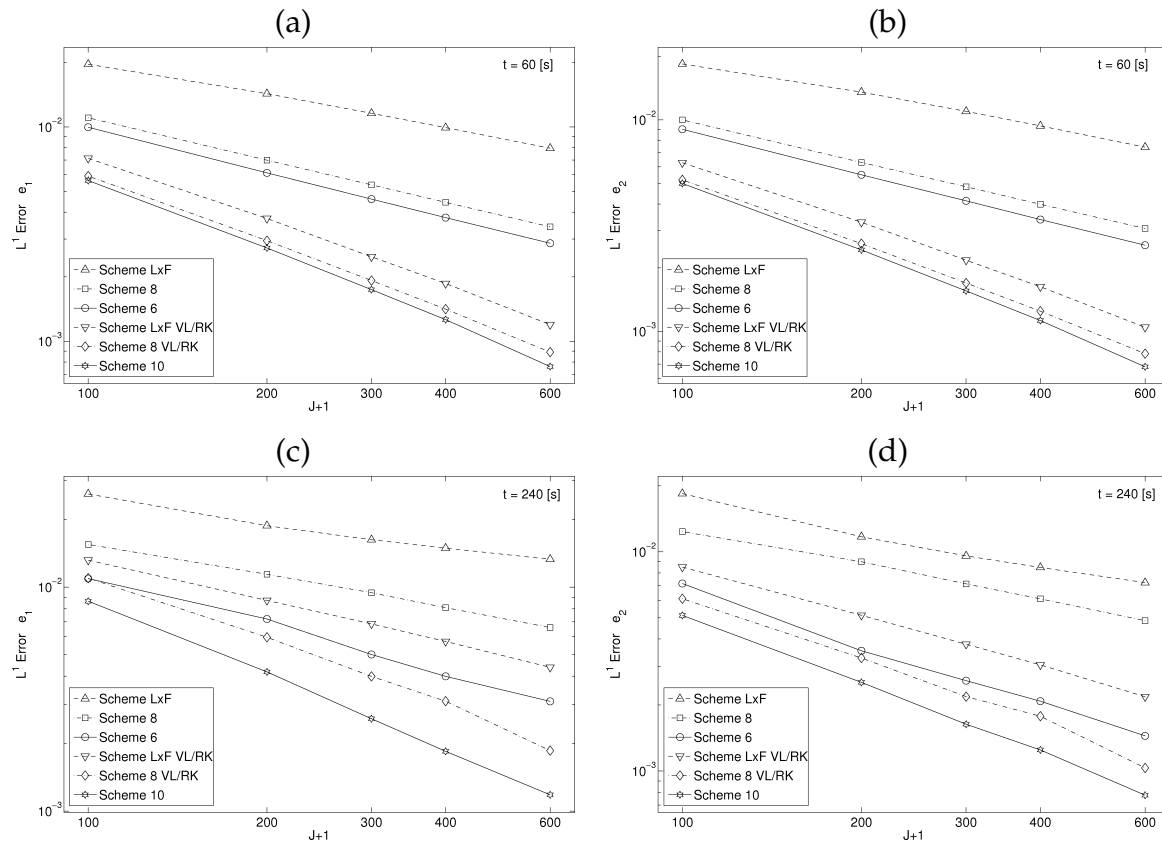


Figure 5.8: Example 5.6 (settling of a suspension of equal-density spheres,  $N = 2$ ): approximate  $L^1$  errors (a, c)  $e_1$  and (b, d)  $e_2$ , measured at (a, b)  $t = 60$  s and (c, d)  $t = 240$  s.

parameter  $\Delta x = 1/8000$  m. For the reference solution and all other computations of this example, we use  $\lambda = 56.95$  s/m. For Example 5.6, Figure 5.7 shows the numerical solution of the total solids concentration for  $t = 60$  s and  $t = 240$  s, produced by the first-order LxF scheme, Schemes 6 and 8, the second-order version of the LxF scheme involving the Van Leer limiter function, Scheme 8 with the Van Leer limiter function, and Scheme 10, while Figure 5.8 displays the approximate  $L^1$  errors for this example, measured over the interval  $[0 \text{ m}, 0.3 \text{ m}]$ . (Again, all second-order schemes utilize RK time stepping.)

$i$	$d_i [10^{-5} \text{ m}]$	$\delta_i$	$\phi_i^0$
1	8.769	1.0000	0.000435
2	8.345	0.9056	0.003747
3	7.921	0.8159	0.014420
4	7.497	0.7309	0.032603
5	7.073	0.6506	0.047912
6	6.649	0.5749	0.047762
7	6.225	0.5039	0.032663
8	5.801	0.4376	0.015104
9	5.377	0.3760	0.004511
10	4.953	0.3190	0.000783
11	4.529	0.2668	0.000060

Table 5.1: Example 5.7: Parameters for the settling of a suspension with  $N = 11$  particle sizes.

It is clear from Figure 5.7 that Schemes 6 and 8 and their second order versions are less dissipative than their counterparts based on the LxF flux. In plots (c) and (d), there is a spurious “kink” and a small overshoot in the solution created by Schemes 6 and 10. These artifacts are diminished by using instead the more viscous Scheme 8, and its second order version. In the reference solution, which is computed using a very fine mesh, these features are not visible at all. Figure 5.8 corroborates what we see in the plots, specifically, smaller errors and faster rates of convergence for Schemes 6 and 8 and their second order versions than the LxF based schemes. It is interesting that Scheme 6, which is formally first order accurate, has smaller errors at  $t = 240 \text{ s}$  than the formally second order accurate version of the LxF scheme.

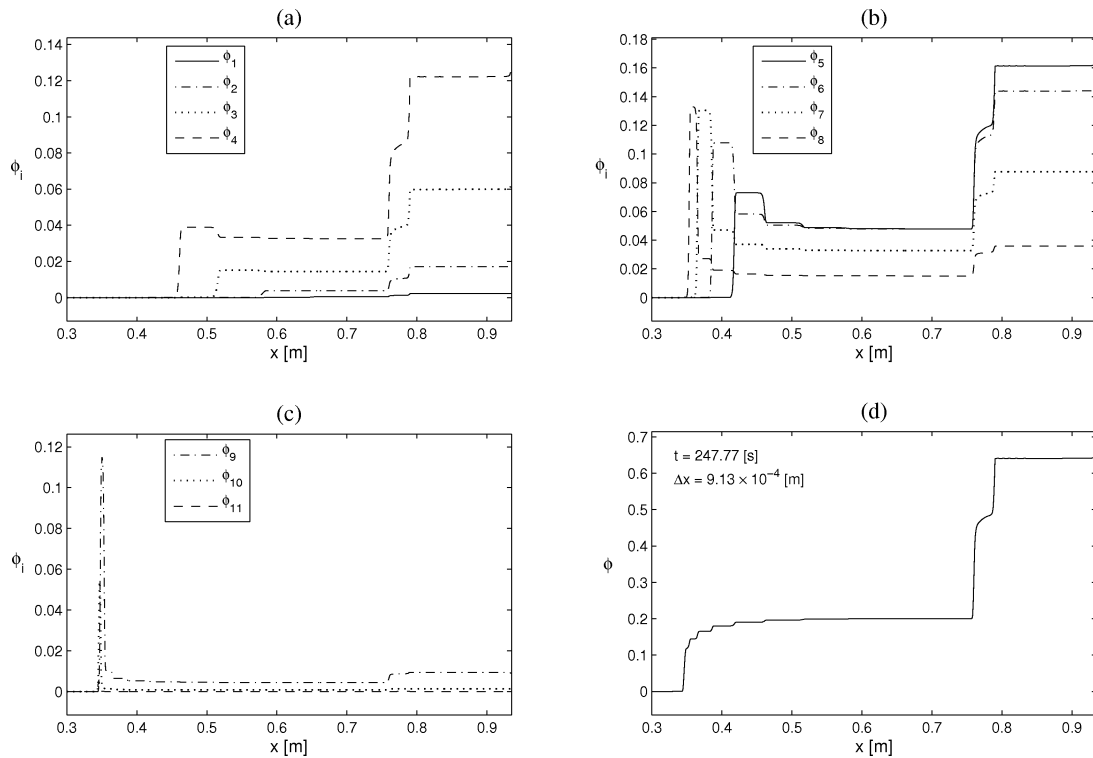


Figure 5.9: Example 5.7 (settling of a suspension with particles of  $N = 11$  different sizes): solids concentrations at  $t = 247.77$  s simulated by Scheme 10.

### 5.5.7 Example 5.7: Settling of a suspension with particles of 11 different sizes

To illustrate that the new method handles systems with a large number of particle species, we consider a suspension of equal-density particles of  $N = 11$  different sizes. The parameters and initial concentrations of these size classes are displayed in Table 5.1. This size distribution was determined by Tory et al. [158] as a discrete approximation for a suspension of closely-sized spherical particles with continuously, roughly normally distributed particle sizes [152]. Following [152], we consider a settling column of height  $L = 0.935$  m. The hindered settling factor found suitable

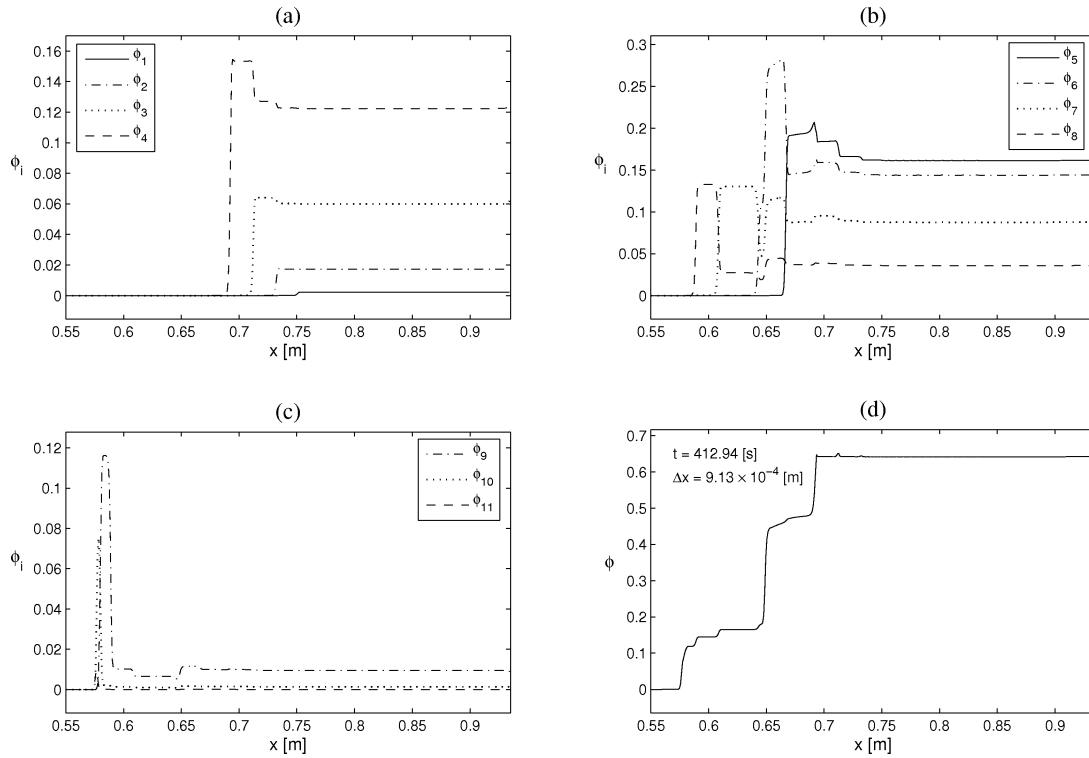


Figure 5.10: Example 5.7 (settling of a suspension with particles of  $N = 11$  different sizes): solids concentrations at  $t = 412.94$  s simulated by Scheme 10.

is (5.2.6) with  $n = 4.65$  and  $\phi_{\max} = 0.641$ . According to [152], a single sphere with diameter  $6.694 \times 10^{-5}$  m has a Stokes velocity of  $\tilde{v}_{\infty} = 0.00392$  m/s, so we here use (5.2.9) with  $v_{\infty} = (8.769/6.694)^2 \tilde{v}_{\infty} = 0.00673$  m/s. We calculate the numerical solution at the times  $t = t_1 = 247.77$  s,  $t = t_2 = 412.94$  s and  $t_3 = 578.15$  s, using Scheme 10 with the discretization parameters  $\Delta x = 9.13 \times 10^{-4}$  m =  $L/1024$  and  $\Delta t = \lambda \Delta x$ , where  $\lambda = 74.29$  s/m. The values of  $\Delta x$  and  $t_1$ ,  $t_2$  and  $t_3$  have been chosen such that results can be compared with the numerical solution of the same example by the multiresolution WENO scheme done by Bürger and Kozakevicius [36].

Figures 5.9, 5.10 and 5.11 show the numerical solutions of each species concentration and the total solids concentration for  $t = 247.77$  s,  $t = 412.94$  s, and  $t = 578.15$  s,

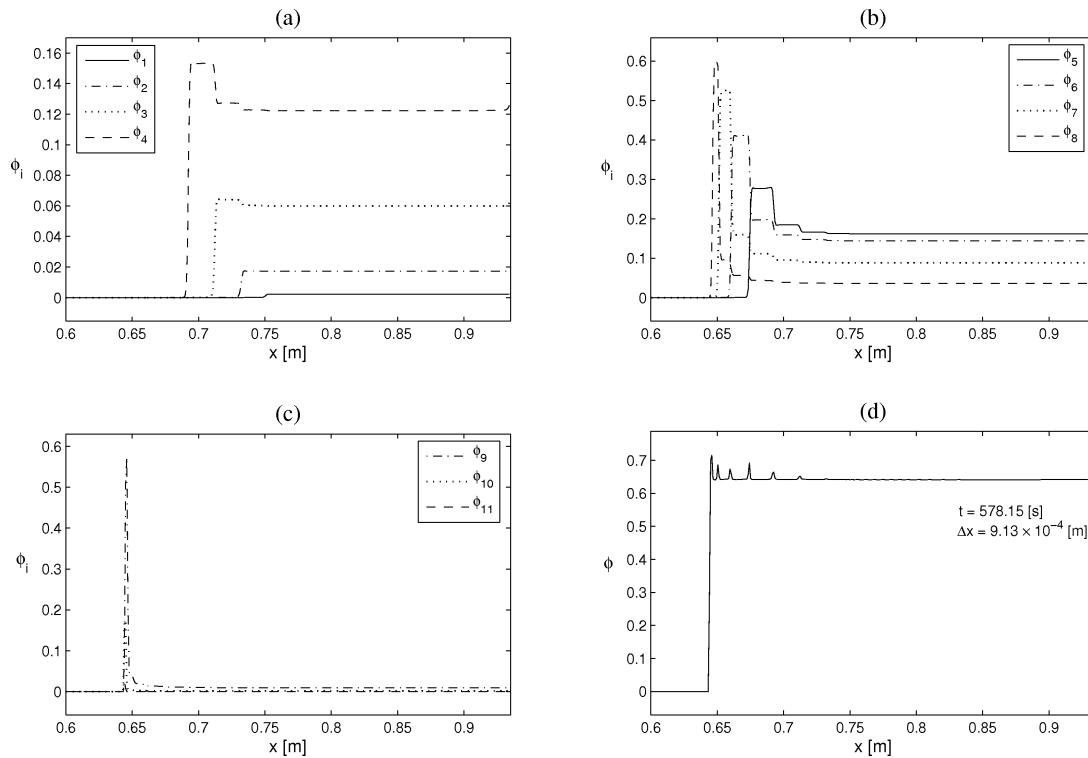


Figure 5.11: Example 5.7 (settling of a suspension with particles of  $N = 11$  different sizes): solids concentrations at  $t = 578.15$  s simulated by Scheme 10.

respectively, over intervals where the solutions are different from zero. By comparing these figures with Figures 18, 19, and 20 of [36], it is clear that Scheme 10 captures the same solution as the multiresolution scheme of that paper.

In all figures we notice that larger species settle first and fill the lower layers of the vessel. In Figure 5.10 we can see spurious tips in the solutions of the species 4 to 9, which do not appear in Figures 5.9 and 5.11. There are also peaks in the simulated total concentration in Figures 5.10 and 5.11. It is clear that this does not have physical sense and therefore is a numerical artefact.

$i$	$D_i [10^{-6} \text{ m}]$	$\mathcal{V}_i [10^{-18} \text{ m}^3]$	$\theta_i$	$\phi_i^0 / \phi^0$	$\phi_i^0$
1	5	65.4	0.019	$6.654 \times 10^{-5}$	$3.327 \times 10^{-6}$
2	10	523.6	0.050	$1.401 \times 10^{-3}$	$7.004 \times 10^{-5}$
3	15	1767.1	0.047	$4.444 \times 10^{-3}$	$2.222 \times 10^{-4}$
4	20	4188.8	0.081	$1.815 \times 10^{-2}$	$9.077 \times 10^{-4}$
5	25	8181.2	0.148	$6.479 \times 10^{-2}$	$3.239 \times 10^{-3}$
6	30	14137.2	0.207	$1.566 \times 10^{-1}$	$7.829 \times 10^{-3}$
7	35	22449.3	0.202	$2.426 \times 10^{-1}$	$1.213 \times 10^{-2}$
8	40	33510.3	0.169	$3.030 \times 10^{-1}$	$1.515 \times 10^{-2}$
9	45	47712.9	0.064	$1.634 \times 10^{-1}$	$8.169 \times 10^{-3}$
10	50	65449.8	0.013	$4.553 \times 10^{-2}$	$2.276 \times 10^{-3}$

Table 5.2: Example 5.8: Droplet sizes and initial volume fractions for a dispersion of diesel oil in water according to [50].

### 5.5.8 Example 5.8: Oil-in-water dispersion model: Creaming of a dispersion with 10 different droplet sizes

We consider the settling of a dispersion of droplets of diesel oil in water. We utilize the droplet size distribution with  $N = 10$  given by Figure 2 of Das and Biswas [50], a histogram of relative frequencies, which is converted into the initial vector  $\Phi^0$  in Table 5.2. We use here the viscosity function  $\mu_d(\Phi) = \mu_d(\phi) = \mu_f(1 - \phi/\phi_{\max})^{-2}$ , with  $\phi_{\max} = 0.9$ , and consider the creaming of the mixture characterized by Table 5.2 in three different vessels of height  $L = 1$  m and with the bottom located in  $x = 0$ : Vessel 1 (Example 5.8.1), a settling column of unit cross-sectional area, Vessel 2 (Example 5.8.2), which is defined by the cross-sectional area function

$$S_2(x) = \begin{cases} 0.0025 \text{ m}^2 & \text{for } 0 \text{ m} \leq x \leq 0.5 \text{ m}, \\ 0.01 \text{ m}^2 & \text{for } 0.5 \text{ m} < x \leq 1.0 \text{ m}, \end{cases}$$

and Vessel 3 (Example 5.8.3), which is just Vessel 2 turned “upside-down”, and is characterized by the cross-sectional area function  $S_3(x) := S_2(1.0 \text{ m} - x)$ . Thus, in Examples 5.8.2 and 5.8.3, we have a system of conservation laws whose flux depends discontinuously on  $x$ . Namely, we have the initial value problem

$$\begin{aligned} S(x)\partial_t\phi_i + \partial_x f_i(S(x), \Phi) &= 0, \quad (x, t) \in (0, L) \times (0, T) =: \Pi_T, \quad i = 1, \dots, N, \\ f_i(S(x), \Phi) &= S(x)\phi_i v_i(\Phi), \quad \Phi(x, 0) = \Phi^0(x), \quad x \in (0, L), \end{aligned}$$

which is supplemented by the zero-flux boundary conditions  $f_i(S(0), \Phi) = f_i(S(L), \Phi) = 0$  for  $i = 1, \dots, N$ , where the cross-sectional area function  $S$  equals  $S_2$  and  $S_3$  for Vessels 2 and 3, respectively.

For Examples 5.8.2 and 5.8.3, in the numerical scheme we multiply  $\lambda$  by  $1/S_j$  with  $S_j = S(x_j^+)$ , and in the CFL conditions (5.3.31), multiply the Courant number  $\alpha$  by  $S_{\min}/S_{\max}$ , where  $S_{\min}$  and  $S_{\max}$  denote the minimum and the maximum cross-sectional areas of the vessel, respectively.

For Example 5.8.1, we present the solution at three different times plus a plot of the cumulate density  $\phi$ , while for Examples 5.8.2 and 5.8.3 we consider plots of  $\phi$  only. In Example 5.8.1, we compare the performances of Schemes 4 and 9, while in Examples 5.8.2 and 5.8.3, we use Scheme 9 only. We set  $\Delta x = 1/512 \text{ m}$  in all cases,  $\lambda = 738.9 \text{ s/m}$  for Example 5.8.1, and  $\lambda = 184.725 \text{ s/m}$  for Examples 5.8.2 and 5.8.3.

Figure 5.12 shows the simulated total oil concentration  $\phi$  of Example 5.8.1 for  $t = 1000 \text{ s}$ ,  $t = 10000 \text{ s}$ , and  $t = 150000 \text{ s}$ , with a zoom into a zone where the solution exhibits strong variation. In Figures 5.13, 5.14 and 5.15 we show the numerical solutions of the concentration of each species and the total oil concentration of the Example 5.8.1 for  $t = 1000 \text{ s}$ ,  $t = 10000 \text{ s}$ , and  $t = 150000 \text{ s}$ , respectively, over intervals where the solutions are different from zero. Clearly, the larger species settle first and fill the upper layers of the vessel.

Figures 5.16 (a), (c) and (e) show the numerical solutions of the total oil concentration of Example 5.8.2 (creaming of a oil-in-water dispersion with 10 different droplet sizes in Vessel 2) at three different times, with a zoom in a zone with many changes in the solution, while Figures 5.16 (b), (d) and (f) display the corresponding

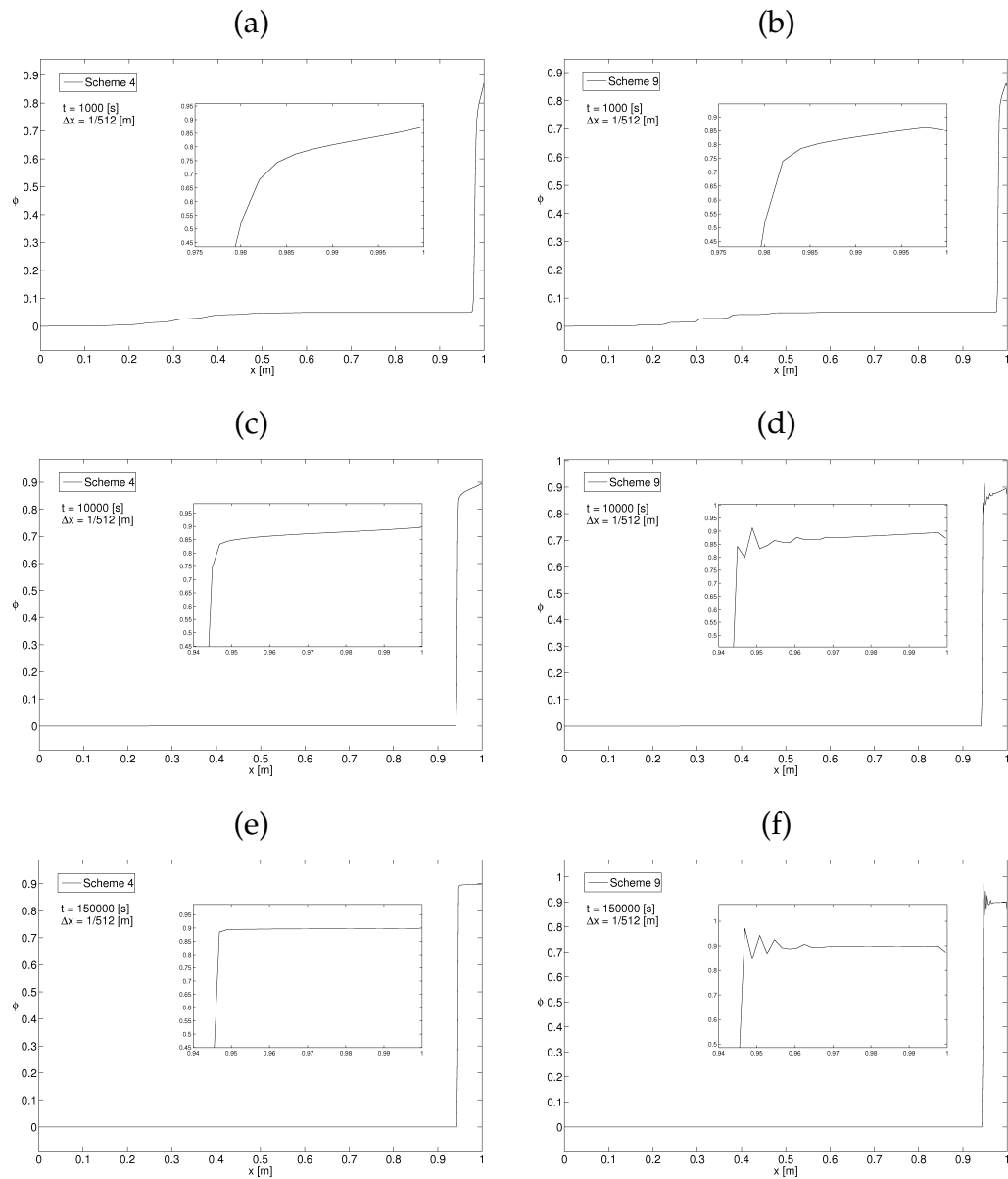


Figure 5.12: Example 5.8.1 (creaming of a oil-in-water dispersion with  $N = 10$  droplet sizes in Vessel 1): simulated total oil concentration with Schemes 4 and 9: (a, b) at  $t = 1000$  s, (c, d) at  $t = 10000$  s, and (e, f) at  $t = 150000$  s.

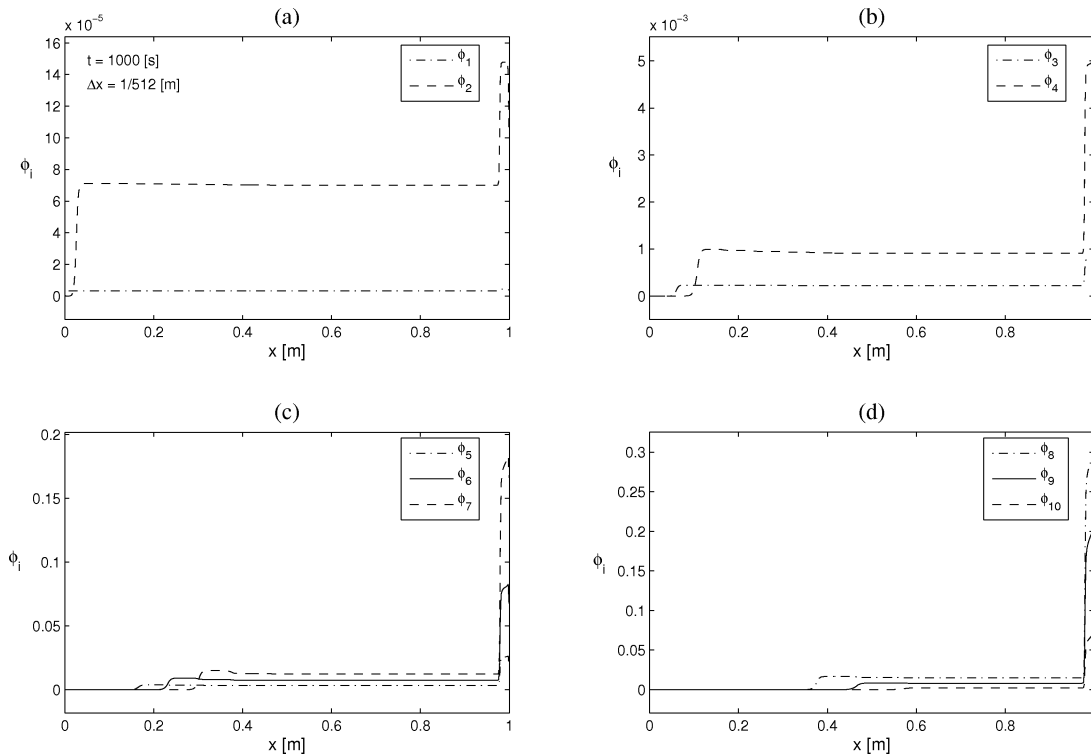


Figure 5.13: Example 5.8.1 (creaming of an oil-in-water dispersion with  $N = 10$  droplet sizes in Vessel 1): concentrations at  $t = 1000$  s simulated by Scheme 9.

results of Example 5.8.3.

We notice the effect of the geometry of Vessels 2 and 3 on the concentration profile. In the case of Vessel 2, for  $t = 1000$  s, the expansion of the area produces an instantaneous decrease of the total concentration at  $x = 0.5$  m. In the case of Vessel 3, for  $t = 1000$  s, due to the contraction of the area, the total concentration increases instantaneously just below  $x = 0.5$  m, decreases strongly in  $x = 0.5$  m, and then decreases smoothly. Moreover, near steady state, for example at  $t = 150000$  s, the thickness of the sediment in Vessel 2 is smaller than that in Vessel 3. We see that in general that there is some oscillation in the solution using Scheme 9 at the location of a large jump in  $\phi$ ; this does not seem to be present with the first order version of

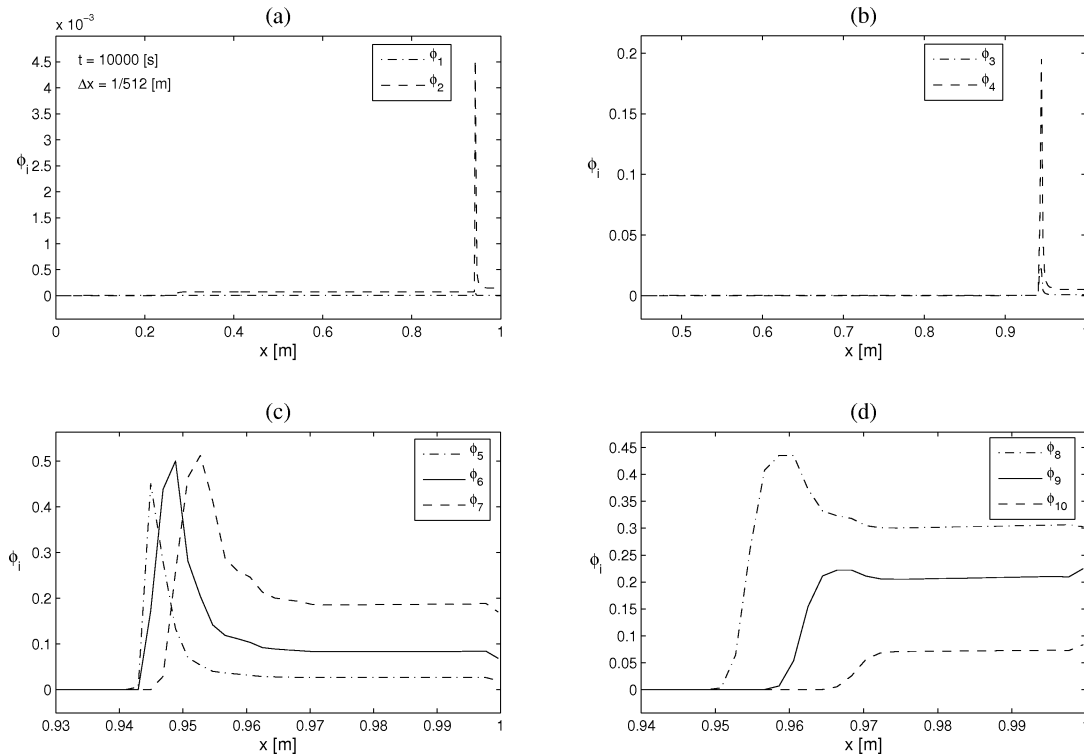


Figure 5.14: Example 5.8.1 (creaming of a oil-in-water dispersion with  $N = 10$  droplet sizes in Vessel 1): concentrations at  $t = 10000$  s simulated by Scheme 9.

the scheme (Scheme 4). This is left as a problem for future investigation.

## 5.6 Conclusions

In this paper, we have presented a family of working numerical schemes for kinematic flows with discontinuous flux. The basic design principle of the schemes, and the analysis of some of them, is based on the explicit “concentration times velocity” structure of the flux of each species. Our Example 5.1 shows that the simple Scheme 1 exhibits noticeably smaller numerical viscosity than the LxF scheme, but has the same monotonicity property as the LxF scheme. This property is crucial for

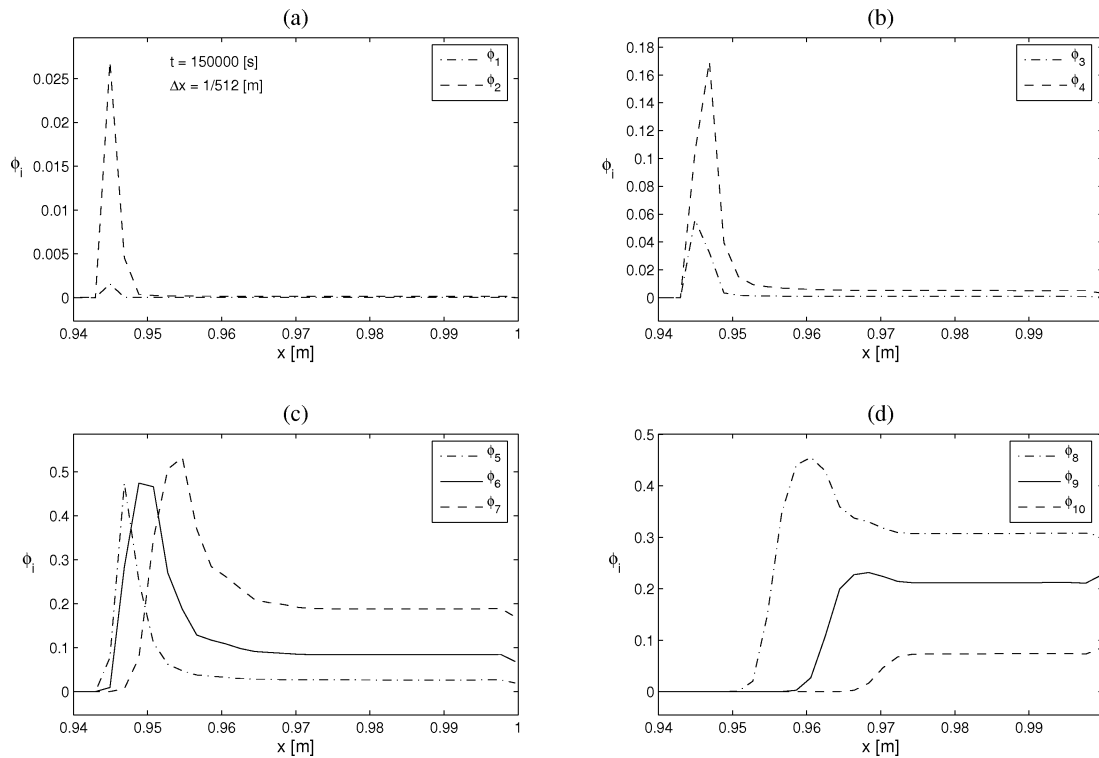


Figure 5.15: Example 5.8.1 (creaming of a oil-in-water dispersion with  $N = 10$  droplet sizes in Vessel 1): concentrations at  $t = 150000$  s simulated by Scheme 9.

the convergence analysis for Scheme 3 conducted in Section 5.4. The marching formula (5.3.2) combined with the numerical flux of Scheme 1, (5.3.8), also forms the core of a discrete traffic model proposed by Hilliges and Weidlich [93] (see also [91]). Interestingly, they do not view their discrete model as a method to approximate solutions of a first-order conservation law, and therefore do not discuss, for example, whether the scheme satisfies a discrete entropy condition; rather, they focus on the second-order, diffusive modified equation associated with a semi-discrete version of their model, and show by a linear stability analysis that the model is always stable. Consequently, our analysis complements that of [93].

The kinematic models studied herein are algebraically very similar, but belong

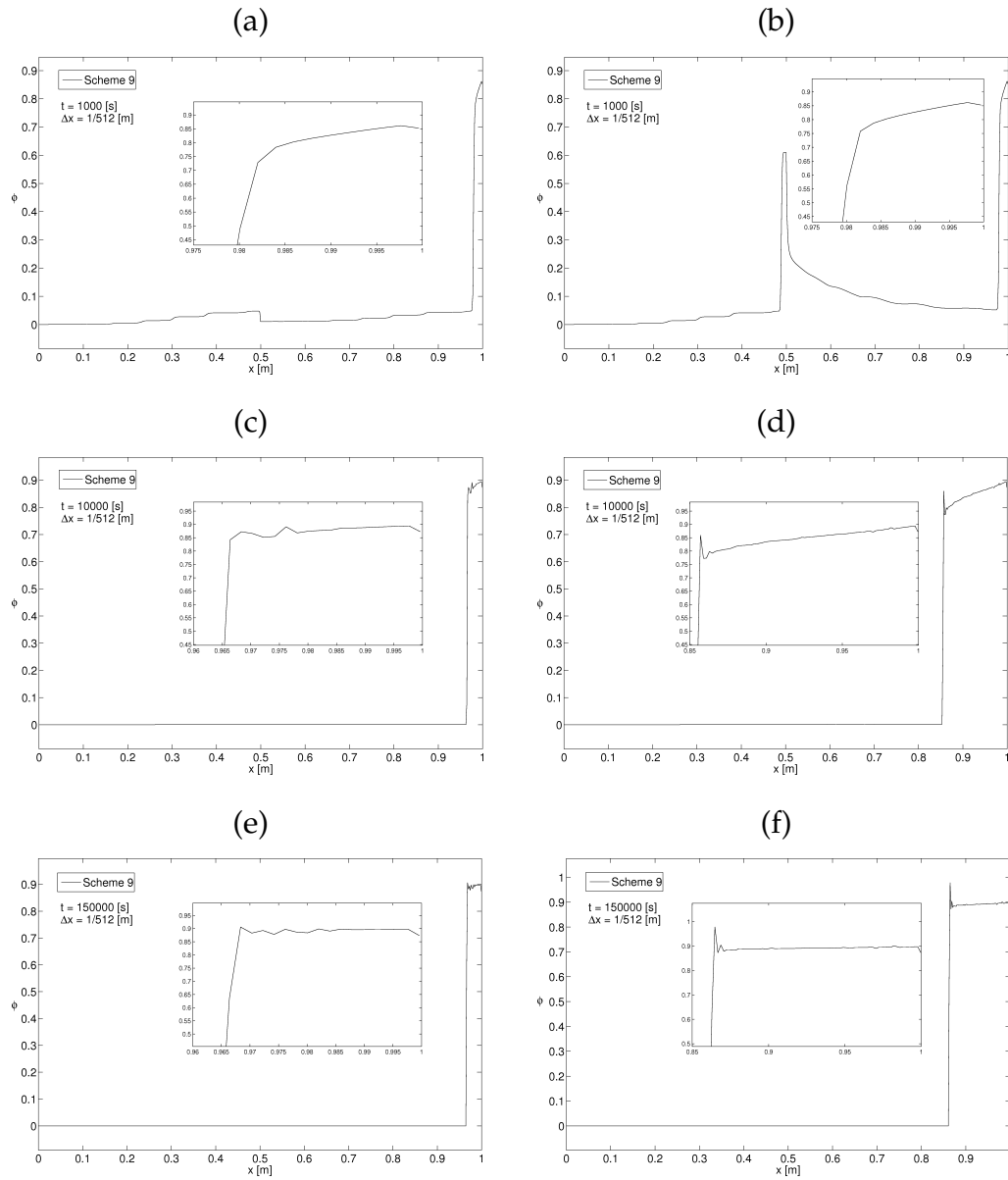


Figure 5.16: Examples 5.8.2 and 5.8.3 (creaming of a oil-in-water dispersion with  $N = 10$  droplet sizes in Vessels 2 (a, c, e) and 3 (b, d, f)): total oil concentration simulated by Scheme 9 at (a, b)  $t = 1000$  s, (c, d)  $t = 10000$  s and (e, f)  $t = 150000$  s.

to two groups, one formed by the traffic and the oil-in-water dispersion model, for which all velocities are nonnegative, and another including the polydisperse sedimentation model, which for  $N \geq 2$  includes velocities of either sign. It has been shown that although the basic scheme, Scheme 1, can be adapted to accommodate multi-species models of both groups (Schemes 4–8), only in the case of non-negative velocities it is possible to establish an invariant region principle (Theorems 5.3.1 and 5.3.2). This principle represents a very desirable property in multiphase and traffic flow modeling. It is not clear whether this principle can also be possibly established for the polydisperse sedimentation model. Furthermore, our Example 5.8.1, for instance (see Figure 5.12), illustrates that for  $N \geq 2$  our second-order schemes do not seem to obey an invariance principle. The oscillatory numerical behaviour visible in Figures 5.12 (d) and (f) (and others) is, however, more distracting than it questions the principal soundness of the second-order upgrade, since our Figures 5.5 and 5.8 illustrate that all second-order schemes converge with consistently smaller errors in the  $L^1$  sense, and at slightly better rates than their first-order versions, even in the systems case that is not backed up by a convergence analysis.

Let us now comment on a few aspects of our treatment that are more related to the discontinuity of the numerical flux. Of course, the formulation of Scheme 3, for example, and the first part of the analysis of Section 5.4 are strongly based on the authors' previous works on conservation laws with discontinuous flux, for example [31, 104, 105]. However, the local variation bound established in Lemma 5.4.2 is genuinely new. To put this result in the proper perspective, we mention that the local variation bound is one more analytical tool that can be used for establishing compactness of conservation laws with discontinuous coefficients. The main technical challenge in establishing convergence of an approximating sequence for such problems is somehow controlling the spatial variation. Up until now this has been done either via the singular mapping approach [3, 31, 113], or by compensated compactness (using weak  $L^2$  bounds on the spatial derivatives) [106]. The singular mapping approach quickly becomes unwieldy in the absence of convexity. The compensated compactness approach is probably the most powerful in that it is applicable even for

coefficients that are discontinuous both space and time, but has the drawback that the flux is required to be genuinely nonlinear. The local variation bound developed here only applies to spatial discontinuities, but does not become any more complicated if the flux is nonconvex, and does not require any assumptions about genuine nonlinearity.

Finally, the reader may have noted that our definition (5.3.25) and the invariance principle for Scheme 5, Theorem 5.3.1, explicitly include the case of a spatially (possibly discontinuously) varying maximum density  $\phi_{\max} = \phi_{\max}(x)$ , and that this case also appears in Examples 5.2 and 5.5 of Section 5.5, but that the convergence analysis of Section 5.4 is limited to the case of constant  $\phi_{\max}$ . As we state in Section 5.4, this simplification is made so that problem (5.4.1) reduces to the well-studied case of an initial value problem for a conservation law with a multiplicative discontinuous coefficient (in this case,  $k(x)$ ). Meanwhile, in another paper [26] we have made further advances in analyzing the problem (5.4.1), where we consider  $k(x)$  constant, but allow  $\phi_{\max}(x)$  to vary discontinuously, and prove uniqueness of properly defined entropy solutions and convergence of a slightly modified version of Scheme 3, as well as of variants of the Godunov and Engquist-Osher schemes. The solution concept adopted in [26] is a novel one, which is based on the concept of so-called adapted entropies [6].



## Chapter 6

# A Difference Scheme and Entropy Solutions for an Inhomogeneous Kinematic Traffic Flow Model

The well-known Lighthill-Whitham-Richards kinematic traffic model is extended to a unidirectional road on which the maximum density  $a(x)$  represents road inhomogeneities, such as variable numbers of lanes, and is allowed to vary discontinuously. The evolution of the car density  $\phi = \phi(x, t)$  can then be described by the initial value problem

$$\phi_t + (\phi v(\phi/a(x)))_x = 0, \quad (x, t) \in \mathbb{R} \times (0, T); \quad \phi(x, 0) = \phi_0(x), \quad x \in \mathbb{R}. \quad (*)$$

Here  $z \mapsto v(z)$  is the velocity function, where it is assumed that  $v(z) \geq 0$ , and  $z \mapsto v(z)$  is nonincreasing. Since  $a(x)$  is allowed to have a jump discontinuity, (\*) is a scalar conservation law with a spatially discontinuous flux. Conservation laws having flux discontinuities have received a good deal of attention in recent years. The authors of the present paper recently proposed a simple finite difference scheme for conservation laws like (\*) [25]. In this contribution, the design and analysis of that scheme is improved, while its simplicity is maintained. In particular, small spurious overshoots that can occur with the original version are reduced. A novel version of the Engquist-Osher scheme that applies

to the problem (\*) is also proposed. Furthermore, a solution concept involving Kružkov-type entropy inequalities is proposed, and it is proved that these entropy inequalities imply uniqueness. This concept includes an adapted entropy similar to the type recently proposed by Audusse and Perthame [6]. It is proved that both difference schemes and the improved Godunov scheme used by Daganzo [49] converge to the unique entropy solution. To establish compactness of the approximating sequence, a new local bound on the spatial variation is utilized [25]. The solution concept necessarily agrees with the one that follows from regarding the present problem as a resonant hyperbolic system. This follows from the uniqueness theorem presented herein, along with the convergence theorem as it applies to their Godunov scheme. Results of numerical experiments and an  $L^1$  error study are presented both for the first order schemes, and for the MUSCL/Runge-Kutta versions that are formally second order accurate.

## 6.1 Introduction

### 6.1.1 Scope

The well-known LWR kinematic model (Lighthill & Whitham [125]; Richards [146]) for traffic flow on a single-lane, uniform highway starts from the principle of conservation of cars,  $\phi_t + (\phi v)_x = 0$ , where  $x \in \mathbb{R}$  is position,  $t$  is time,  $\phi = \phi(x, t)$  is the local density of cars at position  $x$  at time  $t$ , and  $v = v(x, t)$  is the velocity of the car located at  $(x, t)$ . It is then assumed that each driver immediately adjusts his velocity to the local density, which means that  $v(x, t) = v(\phi(x, t))$ . This leads to the scalar conservation law

$$\phi_t + (\phi v(\phi))_x = 0, \quad x \in \mathbb{R}, \quad t > 0. \quad (6.1.1)$$

We may assume that  $v(0) = v_{\max}$ , where  $v_{\max}$  is a maximum freeway velocity that without loss of generality we assume to equal one, and  $v(a) = 0$  if  $a$  denotes the maximum car density, corresponding to a bumper-to-bumper situation. The simplest relationship satisfying these assumptions is  $v(\phi) = 1 - \phi/a$ . For the remainder

of the paper, we assume that  $v$  depends on  $\phi/a$ , so that (6.1.1) turns into

$$\phi_t + (\phi v(\phi/a))_x = 0, \quad x \in \mathbb{R}, \quad t > 0. \quad (6.1.2)$$

In recent years, numerous extensions of the LWR model were proposed and analyzed, including traffic flow with heterogeneous road surface conditions [27, 101, 132], multi-species traffic models [10, 36, 168, 176], and traffic flow on networks [49, 74, 75, 93, 95]. These extensions lead to conservation laws with a flux that depends (possibly discontinuously) on  $x$ , strongly coupled systems of conservation laws, and weakly coupled systems of conservation laws, respectively; combinations of these ingredients have also been considered [25, 92, 178]. There are, of course, numerous further extensions to second-order traffic models with diffusive terms and velocity balance equations; however, we herein limit the discussion to first-order kinematic models.

In this paper, we advance a well-posedness and numerical analysis for the initial value problem

$$\phi_t + (\phi v(\phi/a(x)))_x = 0, \quad x \in \mathbb{R}, \quad 0 < t \leq T; \quad \phi(x, 0) = \phi_0(x), \quad x \in \mathbb{R}, \quad (6.1.3)$$

which is the variant of (6.1.2) that arises if the maximum density  $a$  is allowed to depend on the position  $x$ . Here,  $a(x)$  is allowed to have discontinuities, which models changes in the number of lanes. In particular, we present an entropy solution concept, a new uniqueness result including jump conditions, a convergence result for the adaptation of three known schemes for (6.1.1) to the conservation law (6.1.3), and numerical experiments. For each scheme, this adaptation consists the definition of a numerical interface flux that handles the flux discontinuities. For two of the schemes, these interface versions are new. A further novelty of our approach is the application of so-called connections between fluxes adjacent to a flux discontinuity, see e.g. [2], in combination with the recent, related concept of adapted entropies for discontinuous flux problems due to Audusse and Perthame [6].

To put this paper in the proper mathematical context, let us recall that solutions of the conservation law

$$u_t + f(u)_x = 0, \quad x \in \mathbb{R}, \quad t > 0; \quad u(x, 0) = u_0(x), \quad x \in \mathbb{R} \quad (6.1.4)$$

are in general discontinuous if  $f(u)$  is nonlinear, even if  $u_0$  is smooth. (This already occurs with  $f(u) = uv(u)$  in (6.1.1) if the function  $v$  is linear.) This requires that a solution of (6.1.4) be defined as an entropy solution, that is, as a weak solution that satisfies an entropy condition to ensure uniqueness. Within the common framework due to Kruřkov [114], a function  $u$  is defined to be to an entropy solution of (6.1.4) if

$$\forall c \in \mathbb{R} : \quad \partial_t |u - c| + \partial_x (\text{sgn}(u - c)(f(u) - f(c))) \leq 0 \quad (6.1.5)$$

in the sense of distributions. The entropy inequality (6.1.5) also decides which jumps of a solution of (6.1.4) are admissible. Its justification is usually based on the vanishing viscosity limit of the parabolic regularization of (6.1.4). The viscosity approach considers (6.1.4) in an abstract sense and is based on interpreting this equation as a model of continuum mechanics. The Kruřkov entropy solution concept is adopted in most analyses of traffic flow problems based on (6.1.1), see e.g. [27, 42, 74, 121, 155], and also forms the basis of this work. However, in traffic modeling the rationale for an admissible jump is occasionally based on a slightly different criterion, namely the driver's ride impulse of Ansorge [5]. As pointed out by Gasser [76], in the case of a non-convex function  $f(u)$ , this principle admits certain discontinuous solutions that violate (6.1.5).

We will sometimes write the flux of (6.1.3) as  $f(a(x), \phi) = \phi v(\phi/a(x))$  in order to simplify notation. Thus, the problem under study is a special case of conservation laws with discontinuous flux of the type

$$u_t + f(\mathbf{a}(x), u)_x = 0, \quad (6.1.6)$$

where  $\mathbf{a}(x)$  is a vector of discontinuous parameters. We briefly recall some known results for (6.1.6). The basic difficulty is that its well-posedness does not emerge as a straightforward limit case of the standard theory for conservation laws with a flux that depends smoothly on  $x$ . In fact, several extensions of the entropy solution concept of Kruřkov [114] to conservation laws with a discontinuous flux have been proposed [3, 6, 7, 80, 82, 103, 105, 106, 113, 130, 150, 159, 160]. Each of these concepts is supported by a convergence analysis of a numerical scheme; the differences between them appear in the respective admissibility conditions for stationary jumps

of the solution across the discontinuities of  $a$ . There has been particular interest in (6.1.6) in the context of so-called clarifier-thickener models, see [31, 34, 59] and the references cited in these papers. We may also write (6.1.3) as a non-strictly hyperbolic system

$$\begin{aligned} a_t = 0, \quad u_t + f(a, u)_x = 0, \quad x \in \mathbb{R}, \quad t > 0; \\ (a, u)(0, x) = (a_0(x), u_0(x)), \quad x \in \mathbb{R}, \end{aligned} \tag{6.1.7}$$

where we define  $a_0(x) := a(x)$ . This triangular hyperbolic system has been the starting point of several analyses of the initial-value problem for (6.1.6) [28, 54, 61, 80, 82, 112, 113, 157]. Godunov-type numerical schemes for (6.1.7) were analyzed by Lin *et al.* [126, 127]. Of particular importance for our study is the paper by Jin & Zhang [101], who studied (6.1.3) in the traffic context as a resonant hyperbolic system (6.1.7), resulting in an enumeration of the types of waves that are generated by Riemann problems. Based on their solution of the Riemann problem, Jin & Zhang [101] constructed a Godunov scheme for this problem.

Several authors including Daganzo [49] and Lebacque [123] proposed discrete models for the traffic problem that are ultimately equivalent to the Godunov scheme for a scalar conservation law. It is well known that the Godunov scheme converges to the classical entropy solution as the discretization parameters converge to zero. For our inhomogeneous problem (6.1.3), both Daganzo [49] and Lebacque [123] used the behavioral principles from their discrete models and extended them to the inhomogeneous case. On the other hand, the approach by Jin & Zhang [101] leads to the same solution concept. Jin & Zhang [101] showed that, at least for Riemann problems, all of those solution concepts are the same. In addition, the solution to the Riemann problem given by Jin & Zhang [101] is essentially the one given by Gimse [80], Gimse & Risebro [82] and Klingenberg & Risebro [113].

### 6.1.2 Outline of the paper

The remainder of this paper is organized as follows. In Section 6.2 we precisely state the problem under consideration and introduce the entropy solution concept.

In particular, we specify in Section 6.2.1 the discontinuous coefficient  $a(x)$ , which is assumed to be piecewise constant with just one discontinuity located at  $x = 0$ . It will become clear that our numerical scheme and analysis are readily extended to the case where  $a(x)$  is piecewise constant with finitely many jumps. Section 6.2.2 recalls the concept of connections between two fluxes adjacent to a flux discontinuity, that is in our case, between the two fluxes adjacent to the jump of  $a(x)$ . Roughly speaking, a connection is a pair  $(A, B)$  of  $u$ -arguments for which equality of fluxes to either side of a jump in  $a(x)$  holds, and which is subject to a characteristic condition that ensures that characteristics lead backward toward the  $x$ -axis on at least one side of the jump. Obviously, valid connections  $(A, B)$  form a one-parameter family, and each choice of  $(A, B)$  leads to a different solution concept. For the traffic model, however, we limit ourselves to such connections where either  $A$  or  $B$  coincides with the maximum (with respect to  $\phi$ ) of the adjacent fluxes. If  $H$  denotes the Heaviside function, then each connection  $(A, B)$  is associated with the function  $\hat{c}^{AB}(x) := H(x)B + (1 - H(x))A$ , which assumes the role of  $c$  in (6.1.5). This yields an integral inequality with so-called adapted entropies that eventually defines which jumps of the solution across  $x = 0$  are admissible. The adapted entropy concept is the core of our definition of entropy solutions of (6.1.3), which we introduce in Section 6.2.3.

In Section 6.3, we prove uniqueness of entropy solutions. A result by Vasseur [165] ensures the existence of strong traces of the solution from either sides at  $x = 0$ . We then establish the Rankine-Hugoniot condition and, exploiting our choice of the connection, adapted entropy jump conditions across  $x = 0$ . Then, in light of arguments similar to those of Bürger *et al.* [23] (Chapter 3 of this thesis), [31], we prove  $L^1$  stability and uniqueness of entropy solutions. When compared with these two papers, this analysis is simpler due to the adapted entropy.

In Section 6.4, we interpret our entropy theory (specifically, the jump requirements at the interface  $x = 0$ ) in terms of traffic flow. We argue that the entropy condition is consistent with the condition of driver's ride impulse (Ansorge [5]), which states that drivers speed up where possible, i.e., if they see that conditions ahead of

them allow for a higher driving speed. The decisive point is that our “behavioristic” approach for the condition that singles out admissible jumps across  $x = 0$  does not depend on a viscous regularization, in contrast e.g. to a model of flow in heterogeneous media and a clarifier-thickener model (see [29] for further discussion).

In Section 6.5, we introduce the numerical schemes for the approximation of (6.1.3). The basic discretization is a simple explicit conservative marching formula on a rectangular grid, where the numerical flux for all cells may be given by a known scheme for conservation laws, with the exception for the cell interface that is associated with the flux discontinuity, and for which an interface numerical flux  $\bar{f}_{\text{int}}$  has to be devised. This flux must be monotone and preserve certain steady-state solutions. In Section 6.5.1, we construct interface fluxes based on three different schemes, namely those of Hilliges & Weidlich [93], Godunov (Jin & Zhang [101]), and Engquist & Osher [65]. The numerical schemes described in Section 6.5.1 are only first-order accurate, meaning that a very fine mesh is required in order to accurately resolve some features of the solution. To improve on this situation, we propose in Section 6.5.2 a formally second order scheme, constructed by using MUSCL [124] spatial differencing, and Runge-Kutta temporal differencing.

In Section 6.6, we show that all three schemes of Section 6.5.1 converge to entropy solutions. By our uniqueness theorem (Theorem 6.3.1), all of these schemes converge to the same solution, and moreover, for the Riemann problems considered by Daganzo [49], Lebacque [123] and Jin & Zhang [101], all of these solution concepts are the same. Our solution concept is somewhat more general than that of these authors, because it is valid for more general types of initial data  $\phi_0$ .

Finally, we present in Section 6.7 five numerical examples and compare the numerical schemes. These examples in part been adapted from [101] and [75]. It turns out that the version of the Hilliges-Weidlich scheme introduced in Section 6.5.1 produces less overshoots than the unmodified version introduced by Bürger *et al.* [25]. In general, the Hilliges-Weidlich scheme is more diffusive than the Godunov or Engquist-Osher scheme, but easier to implement. An  $L^1$  error record confirms that the second-order MUSCL/RK versions of the schemes produce consistently smaller

errors than the first-order versions.

## 6.2 Preliminaries

### 6.2.1 Assumptions on the flux function

We assume that the parameter  $a$  is piecewise constant with a single jump located at the origin  $x = 0$ , i.e.,

$$a(x) = a_L \quad \text{for } x < 0, \quad a(x) = a_R \quad \text{for } x > 0, \quad (6.2.1)$$

where we assume that  $0 < \min\{a_L, a_R\} =: \underline{a} \leq a(x) \leq \bar{a} := \max\{a_L, a_R\}$ . We also assume that the flux is genuinely nonlinear in the following sense, where  $\mathcal{L}$  denotes Lebesgue measure:

$$\mathcal{L}(\{\phi \mid \partial_{\phi\phi}^2 f(a, \phi) = 0\}) = 0 \quad \text{for } a = a_L, a_R. \quad (6.2.2)$$

We assume that the velocity  $v : [0, 1] \rightarrow [0, v_{\max}]$  is Lipschitz continuous, strictly decreasing, and  $v(0) = v_{\max}$ ,  $v(1) = 0$ . This implies that the flux  $f(a, \phi)$  is nonnegative for  $\phi \in [0, a]$ , and  $f(a, 0) = f(a, a) = 0$ .

We assume that there is a unique  $\phi_L^* \in (0, a_L)$  such that  $f_\phi(a_L, \phi_L^*) = 0$ , and the mapping  $\phi \mapsto f(a_L, \phi)$  is strictly increasing for  $\phi \in (0, \phi_L^*)$  and strictly decreasing for  $\phi \in (\phi_L^*, a_L)$ . Similarly, we assume that there is a unique  $\phi_R^* \in (0, a_R)$  such that  $f_\phi(a_R, \phi_R^*) = 0$ , and the mapping  $\phi \mapsto f(a_R, \phi)$  is strictly increasing for  $\phi \in (0, \phi_R^*)$  and strictly decreasing for  $\phi \in (\phi_R^*, a_R)$ . From the relationship  $f_\phi(a, \phi) = (\phi/a)v'(\phi/a) + v(\phi/a)$ , it is clear that  $\phi_L^*/a_L = \phi_R^*/a_R$ , and thus  $\text{sgn}(\phi_R^* - \phi_L^*) = \text{sgn}(a_R - a_L)$ . Another useful relationship is

$$\text{sgn}(f(a_R, \phi) - f(a_L, \phi)) = \text{sgn}(a_R - a_L) \quad \text{for } \phi \in (0, \underline{a}). \quad (6.2.3)$$

To verify this, suppose for example that  $0 < \phi \leq a_L < a_R$ . Then  $v(\phi/a_L) < v(\phi/a_R)$ , and thus  $\phi v(\phi/a_L) < \phi v(\phi/a_R)$ .

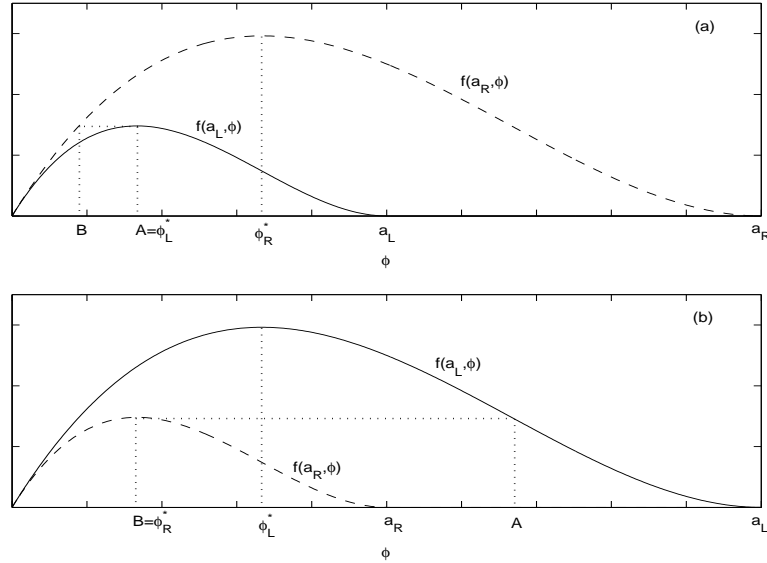


Figure 6.1: The flux functions  $f(a_L, \phi)$  and  $f(a_R, \phi)$ . The case  $a_L < a_R$  is shown in (a), and the case  $a_R < a_L$  is shown in (b).

## 6.2.2 Connections

Referring to Figure 6.1, we distinguish two states  $A \in [0, a_L]$  and  $B \in [0, a_R]$ , which we define as follows:

**Definition 6.2.1 (Definition of the states  $A$  and  $B$ )** *If  $a_L < a_R$ , then  $A = \phi_L^*$ , and  $B$  is the solution of the equation  $f(a_R, B) = f(a_L, A)$  satisfying  $B < \phi_R^*$ . In the reverse situation, i.e.,  $a_L < a_R$ , then  $B = \phi_R^*$ , and  $A$  is the solution of the equation  $f(a_R, B) = f(a_L, A)$  satisfying  $A > \phi_L^*$ .*

Note that we always have  $f(a_R, B) = f(a_L, A)$  and  $B < A$ . The first of these relationships follows directly from Definition 6.2.1, and the second follows from the same definition,  $\text{sgn}(\phi_R^* - \phi_L^*) = \text{sgn}(a_R - a_L)$  and (6.2.3).

Fixing a time  $t \in (0, T)$ , let  $\phi_{\pm} := \phi(0_{\pm}, t)$ . Any weak solution will satisfy the Rankine-Hugoniot condition

$$f(a_L, \phi_-) = f(a_R, \phi_+). \quad (6.2.4)$$

It is well known that this condition is not sufficient to guarantee uniqueness, and so additional conditions are required. Karlsen *et al.* [105] and Karlsen & Towers [106] required that, in addition, the following characteristic condition must hold:

**Definition 6.2.2 (Strong characteristic condition)** *The flux pair of states  $(\phi_-, \phi_+)$  is said to satisfy the strong characteristic condition if*

$$\min\{0, f_\phi(a_L, \phi_-)\} \cdot \max\{0, f_\phi(a_R, \phi_+)\} = 0. \quad (6.2.5)$$

This says that the characteristics must lead backward toward the  $x$ -axis on at least one side of the jump, unless  $\phi_- = \phi_+$ . The strong characteristic condition, when supplemented by the classical characteristic conditions that hold away from the jump in  $a$ , are sufficient for uniqueness, and result in a  $L^1$  contraction semigroup of solutions.

The distinguished states  $A$  and  $B$  defined in Definition 6.2.1 comprise an example of a so-called *connection*. The concept of connections goes back to Adimurthi *et al.* [2].

**Definition 6.2.3 (Connection  $(A, B)$ , after Adimurthi *et al.* [2])** *A pair of states  $(A, B) \in [0, a_L] \times [0, a_R]$  is called a connection if*

$$f(a_L, A) = f(a_R, B), \quad A \geq \phi_L^*, \quad B \leq \phi_R^*. \quad (6.2.6)$$

There is an entropy jump condition associated with such a connection, which may be stated as follows.

**Definition 6.2.4 (Characteristic condition)** *Assume that the pair  $(A, B)$  is a connection in the sense of Definition 6.2.3. We say that  $(A, B)$  satisfies the characteristic condition if*

$$\min\{0, f_\phi(a_L, \phi_-)\} \cdot \max\{0, f_\phi(a_R, \phi_+)\} = 0 \quad \text{if } (\phi_-, \phi_+) \neq (A, B). \quad (6.2.7)$$

This says that the characteristics must lead backward toward the  $x$ -axis on at least one side of the jump, unless  $\phi_- = A$  and  $\phi_+ = B$ , in which case there is no restriction on the characteristics.

It is clear that Definition 6.2.3 admits other  $(A, B)$  connections in addition to the one given by Definition 6.2.1. Adimurthi *et al.* [2] show that each of these connections, when associated with its  $(A, B)$  characteristic condition, leads to a different solution concept, and a different  $L^1$  contraction semigroup of solutions.

### 6.2.3 The entropy solution concept

We single out the particular connection  $(A, B)$  of Definition 6.2.1 because it leads to solutions in agreement with those generally accepted as being relevant for traffic modeling. In order to state our concept of entropy solution, we use  $\hat{c}^{AB}(x)$  to form the function  $V^{AB}(x, \phi) := |\phi - \hat{c}^{AB}(x)|$ , which is an example of what Audusse and Perthame [6] call an *adapted entropy*.

**Definition 6.2.5 (Entropy solution)** *A measurable function  $\phi : \Pi_T \rightarrow \mathbb{R}$  is an entropy solution of the initial value problem (6.1.3) if it satisfies the following conditions:*

(D.1)  $\phi \in L^1(\Pi_T) \cap L^\infty(\Pi_T) \cap C(0, T; L^1(\mathbb{R})),$

(D.2)

$$\phi(x, t) \in \begin{cases} [0, a_L] & \text{for a.e. } (x, t) \in (-\infty, 0) \times (0, T), \\ [0, a_R] & \text{for a.e. } (x, t) \in (0, \infty) \times (0, T). \end{cases} \quad (6.2.8)$$

(D.3) *For all test functions  $\psi \in \mathcal{D}(\mathbb{R} \times [0, T))$*

$$\iint_{\Pi_T} (\phi \psi_t + f(a(x), \phi) \psi_x) dx dt + \int_{\mathbb{R}} \phi_0(x) \psi(x, 0) dx = 0. \quad (6.2.9)$$

(D.4) *For all test functions  $0 \leq \psi \in \mathcal{D}(\Pi_T)$  which vanish for  $x \geq 0$*

$$\iint_{\Pi_T} (|\phi - c| \psi_t + \text{sgn}(\phi - c) (f(a_L, \phi) - f(a_L, c)) \psi_x) dx dt \geq 0 \quad \forall c \in \mathbb{R}, \quad (6.2.10)$$

*and for all test functions  $0 \leq \psi \in \mathcal{D}(\Pi_T)$  which vanish for  $x \leq 0$*

$$\iint_{\Pi_T} (|\phi - c| \psi_t + \text{sgn}(\phi - c) (f(a_R, \phi) - f(a_R, c)) \psi_x) dx dt \geq 0 \quad \forall c \in \mathbb{R}, \quad (6.2.11)$$

(D.5) The following Kružkov-type entropy inequality holds for all test functions  $0 \leq \psi \in \mathcal{D}(\Pi_T)$ :

$$\iint_{\Pi_T} \left\{ |\phi - \hat{c}^{AB}(x)| \psi_t + \operatorname{sgn}(\phi - \hat{c}^{AB}(x)) \left( f(a(x), \phi) - f(a(x), \hat{c}^{AB}(x)) \right) \psi_x \right\} dx dt \geq 0. \quad (6.2.12)$$

A function  $u : \Pi_T \rightarrow \mathbb{R}$  satisfying (D.1)–(D.3) is called a weak solution of the initial value problem (6.1.3).

### 6.3 Uniqueness

**Lemma 6.3.1** Let  $\phi$  be an entropy solution of (6.1.3). For a.e.  $t \in (0, T)$ , the function  $\phi(\cdot, t)$  has strong traces from the left and right at  $x = 0$ , i.e., the following limits exist for a.e.  $t \in (0, T)$ :

$$\phi(0-, t) := \operatorname{ess\,lim}_{x \uparrow 0} \phi(x, t), \quad \phi(0+, t) := \operatorname{ess\,lim}_{x \downarrow 0} \phi(x, t),$$

**Proof.** Condition (6.2.10) guarantees that  $\phi$  is an entropy solution of the conservation law  $\phi_t + f(a_L, \phi)_x = 0$  in the domain  $(-\infty, 0) \times (0, T]$ . This fact, along with the genuine nonlinearity assumption (6.2.2) ensures the existence of a strong trace from the left – this is due to a result of Vasseur [165]. The existence of a strong trace from the right follows from in a similar way from (6.2.11).  $\square$

With the existence of strong traces guaranteed, it is possible to describe the behavior of solutions at  $x = 0$  (where the interface is located), which is the subject of the following lemma.

**Lemma 6.3.2** Let  $\phi_{\pm} = \phi_{\pm}(t) = \phi(0_{\pm}, t)$ .

**J1.** The following Rankine-Hugoniot condition holds for a.e.  $t \in (0, T)$ :

$$f(a_R, \phi_+(t)) = f(a_L, \phi_-(t)). \quad (6.3.1)$$

**J2.** The following entropy jump condition holds for a.e.  $t \in (0, T)$ :

$$\begin{aligned} & \operatorname{sgn}(\phi_+(t) - B) (f(a_R, \phi_+(t)) - f(a_R, B)) \\ & - \operatorname{sgn}(\phi_-(t) - A) (f(a_L, \phi_-(t)) - f(a_L, A)) \leq 0. \end{aligned} \quad (6.3.2)$$

**J3.** For a.e.  $t \in (0, T)$ , the following characteristic condition is satisfied:

$$\min\{0, f_\phi(a_L, \phi_-(t))\} \cdot \max\{0, f_\phi(a_R, \phi_+(t))\} = 0. \quad (6.3.3)$$

**Remark 6.3.1** The characteristic condition (6.3.3) says that the characteristics must lead backward toward the  $x$ -axis on at least one side of the jump at the location of the jump in the parameter  $a$ .

**Proof.** The Rankine-Hugoniot condition (6.3.1) is a consequence of the weak formulation (6.2.9), while the entropy jump condition (6.3.2) follows from (6.2.12). We omit the details of the proofs of these facts; they can be found (with slight modifications where necessary) in Lemmas 2.4 and 2.6 of [105].

In what follows, we write  $\phi_\pm := \phi_\pm(t)$ , wherever there is no danger of confusion. To prove (6.3.3), it suffices to show that  $\phi_- > A$  while  $\phi_+ < B$  is impossible (see Figure 6.1). By way of contradiction, assume that  $\phi_- > A$  while  $\phi_+ < B$ . Combining this assumption with the entropy inequality (6.3.2), we have

$$(f(a_R, B) - f(a_R, \phi_+)) + (f(a_L, A) - f(a_L, \phi_-)) \leq 0. \quad (6.3.4)$$

However, from  $\phi_- > A$  and  $\phi_+ < B$ , it is clear that  $f(a_R, B) > f(a_R, \phi_+)$  and  $f(a_L, A) > f(a_L, \phi_-)$  (see Figure 6.1). Combining these inequalities with (6.3.4) gives the desired contradiction.  $\square$

**Theorem 6.3.1 ( $L^1$  stability and uniqueness)** Let  $\phi$  and  $\hat{\phi}$  be two entropy solutions in the sense of Definition 6.2.5 of the initial value problem (6.1.3) with initial data  $\phi_0$  and  $\hat{\phi}_0$ , respectively. Then

$$\int_{\mathbb{R}} |\phi(x, t) - \hat{\phi}(x, t)| dx \leq \int_{\mathbb{R}} |\phi_0(x) - \hat{\phi}_0(x)| dx \quad \text{for a.e. } t \in (0, T).$$

In particular, there exists at most one entropy solution of the initial value problem (6.1.3).

**Proof.** We only sketch the proof. Following [105], we can prove for any  $0 \leq \phi \in \mathcal{D}(\Pi_T)$

$$- \iint_{\Pi_T} \left( |\phi - \hat{\phi}| \psi_t + \operatorname{sgn}(\phi - \hat{\phi}) (f(a(x), \phi) - f(a(x), \hat{\phi})) \psi_x \right) dt dx \leq E, \quad (6.3.5)$$

$$E := \int_0^T \left[ \operatorname{sgn}(\phi - \hat{\phi}) (f(a(x), \phi) - f(a(x), \hat{\phi})) \right]_{x=0-}^{x=0+} \psi(0, t) dt, \quad (6.3.6)$$

where the notation  $[\cdot]_{x=0-}^{x=0+}$  indicates the limit from the right minus the limit from the left at  $x = 0$ . Recall that Lemma 6.3.1 ensures the existence of these limits.

For almost every  $t \in (0, T)$ , the contribution to  $E$  at the jump  $x = 0$  is

$$S := \left[ \operatorname{sgn}(\phi - \hat{\phi}) (f(a(x), \phi) - f(a(x), \hat{\phi})) \right]_{x=0-}^{x=0+}. \quad (6.3.7)$$

Let us fix  $t \in (0, T)$ , and use the notation  $\phi_{\pm}(t) = \phi_{\pm}$ . Then

$$S = \operatorname{sgn}(\phi_+ - \hat{\phi}_+) (f(a_R, \phi_+) - f(a_R, \hat{\phi}_+)) - \operatorname{sgn}(\phi_- - \hat{\phi}_-) (f(a_L, \phi_-) - f(a_L, \hat{\phi}_-)).$$

Our goal at this point is to show that  $S \leq 0$ , which implies that  $E \leq 0$  holds since  $t$  is arbitrary. It is then standard to conclude from (6.3.5) that the theorem holds, see [105].

If  $f(a_R, \phi_+) - f(a_R, \hat{\phi}_+) = 0$ , then by the Rankine-Hugoniot condition,  $f(a_L, \phi_-) - f(a_L, \hat{\phi}_-)$  also vanishes, yielding  $S = 0$ . So assume without loss of generality that

$$f(a_R, \phi_+) > f(a_R, \hat{\phi}_+). \quad (6.3.8)$$

By the Rankine-Hugoniot condition again, we also have

$$f(a_L, \phi_-) > f(a_L, \hat{\phi}_-). \quad (6.3.9)$$

By way of contradiction, assume that  $S > 0$ . Then due to (6.3.8) and (6.3.9), we must have

$$\operatorname{sgn}(\phi_+ - \hat{\phi}_+) > 0, \quad \operatorname{sgn}(\phi_- - \hat{\phi}_-) < 0. \quad (6.3.10)$$

Combining the inequalities (6.3.8), (6.3.9), (6.3.10), we must have at least one of  $\phi_+ < B$ ,  $\hat{\phi}_+ < B$ , and we must also have at least one of  $\phi_- > A$ ,  $\hat{\phi}_- > A$ . In fact, since

$\text{sgn}(\phi_+ - \hat{\phi}_+) > 0$ , it must be that  $\hat{\phi}_+ < B$ , and since  $\text{sgn}(\phi_- - \hat{\phi}_-) < 0$ , it must be that  $\hat{\phi}_- > A$ . Combining these last two inequalities, we conclude that the pair of states  $(\hat{\phi}_-, \hat{\phi}_+)$  violates the entropy jump condition (6.3.2), and we have the desired contradiction.  $\square$

**Remark 6.3.2** With the large set of adapted entropies used by Audusse and Perthame the quantity  $E$  in (6.3.6) vanishes. Note that since we are not using such a large set of adapted entropies, we still must deal with this residue term, and thus we still have an interface condition (entropy jump conditions) and must establish the existence of traces.

## 6.4 Relationship between interface entropy conditions and traffic flow

We make the following assumptions:

**K1.** Drivers approaching the interface will attempt to speed up if

$$v(\phi_L^0/a_L) < v(\phi_R^0/a_R), \quad (6.4.1)$$

i.e., if they see that conditions immediately ahead of them allow for a higher driving speed. Whether or not they are actually able to speed up is constrained by **K2** and **K3** below.

**K2.** Any such speedup will create a decrease in density immediately to the left of  $x = 0$  and an increase in density immediately to the right of  $x = 0$ .

**K3.** Cars are conserved, i.e., the Rankine-Hugoniot condition must remain in effect across the interface at  $x = 0$ .

**Remark 6.4.1** Due to the Rankine-Hugoniot condition, the condition (6.4.1) expressing higher velocity directly ahead is equivalent to  $\phi_L > \phi_R$ , i.e., lower density directly ahead. We focus on the velocity comparison (as opposed to density comparison) because it is perhaps more directly related to the behavior of a single driver,

who easily detects the condition (6.4.1) when the distance between his car and the one in front of him is increasing. It is not so clear how he would compare the two densities appearing in the inequality  $\phi_L > \phi_R$ .

Referring to Lemma 6.3.2, particularly the entropy jump condition 6.3.3 and Remark 6.3.1, we see that among two-state solutions  $(\phi_L, \phi_R)$  of the form

$$\phi(x, t) = \phi_L \text{ for } x < 0, \quad \phi(x, t) = \phi_R \text{ for } x > 0, \quad (6.4.2)$$

such that the Rankine-Hugoniot condition  $f(a_L, \phi_L) = f(a_R, \phi_R)$  is satisfied, the only ones that are excluded by our entropy theory are ones where  $a_L > A$  and  $a_R < B$ .

In Figure 6.2 (a), the pair  $(\phi_L^0, \phi_R^0)$  shows such an inadmissible two state solution for the case when  $a_L < a_R$ , while Figure 6.2 (b) shows such a  $(\phi_L^0, \phi_R^0)$  when  $a_L > a_R$ . In either case, the state  $(\phi_L^0, \phi_R^0)$  is unstable. Drivers immediately to the left of  $x = 0$  will speed up (corresponding to the left-facing arrow on the  $f(a_L, \phi)$  graph) because they see that the allowable velocity  $v(\phi_R^0/a_R)$  immediately ahead of them exceeds their current velocity  $v(\phi_L^0/a_L)$ . According to **K2**, this speedup has two effects - first it decreases the density immediately to the left of  $x = 0$ , and second it increases the density to the right of  $x = 0$  (corresponding to the right-facing arrow on the  $f(a_R, \phi)$  graph). This results in both forward and backward facing rarefaction waves. This evolution will continue until the state  $(\phi(x-, t), \phi(x+, t)) = (\phi_L^1, \phi_R^1)$  shown in Figure 6.2 is achieved. That this is the terminal state makes sense if we think not of individual cars (which would still like to speed up), but of a group of cars passing through  $x = 0$ . The maximum allowable flux is  $f(a_L, \phi_L^*)$  for (a) and  $f(a_R, \phi_R^*)$  for (b); this constraint keeps the cars immediately to the left of  $x = 0$  from speeding up beyond this point.

In contrast to Figure 6.2, Figure 6.3 shows a type of two state solution  $(\phi_L^0, \phi_R^0)$  that is admissible under our entropy theory. To see why these solutions are stable, note that in spite of the fact that drivers immediately to the left of  $x = 0$  might want to speed up because  $v(\phi_R^0/a_R) > v(\phi_L^0/a_L)$  (such a speedup corresponds to the left-facing arrow near the graph of  $f(a_L, \phi)$ ), any such speedup will cause an increase of density immediately to the right of  $x = 0$ , corresponding to the right-facing arrow

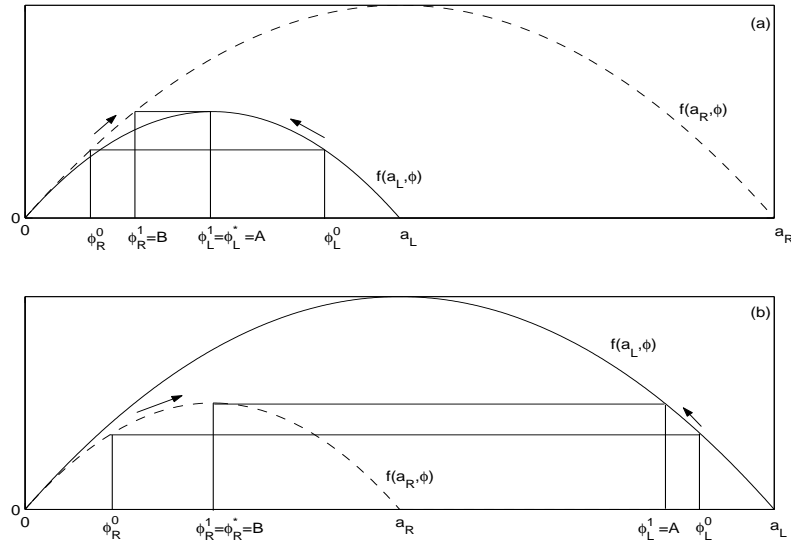


Figure 6.2: Inadmissible two-state solutions  $(\phi_L^0, \phi_R^0)$  for the cases (a)  $a_L < a_R$  and (b)  $a_L > a_R$ .

on the graph of  $f(a_R, \phi)$ . From the figure it is clear that this would lead to a violation of the Rankine-Hugoniot condition (conservation of cars).

Figure 6.4 shows another type of admissible two-state solution  $(\phi_L^0, \phi_R^0)$ . In Figure 6.4 (a), we have the situation described in the previous paragraph. In Figure 6.4 (b), the solution is stable because cars immediately to the left of  $x = 0$  do not attempt to speed up since  $v(\phi_R^0/a_R) < v(\phi_L^0/a_L)$ .

Figure 6.5 shows the final type of admissible two state solution  $(\phi_L^0, \phi_R^0)$ . In this case, cars immediately to the left of  $x = 0$  do not attempt to speed up because  $v(\phi_R^0/a_R) < v(\phi_L^0/a_L)$ .

Assuming that the mapping  $\phi \mapsto f(a, \phi)$  is concave and that the parameter  $a$  is constant, it is also possible to understand the classical Oleinik/Lax/Kružkov entropy condition for an admissible jump in terms of traffic flow. Now we consider two-state solutions of the form

$$\phi(x, t) = \phi_L \quad \text{for } x < st, \quad \phi(x, t) = \phi_R \quad \text{for } x > st, \quad (6.4.3)$$

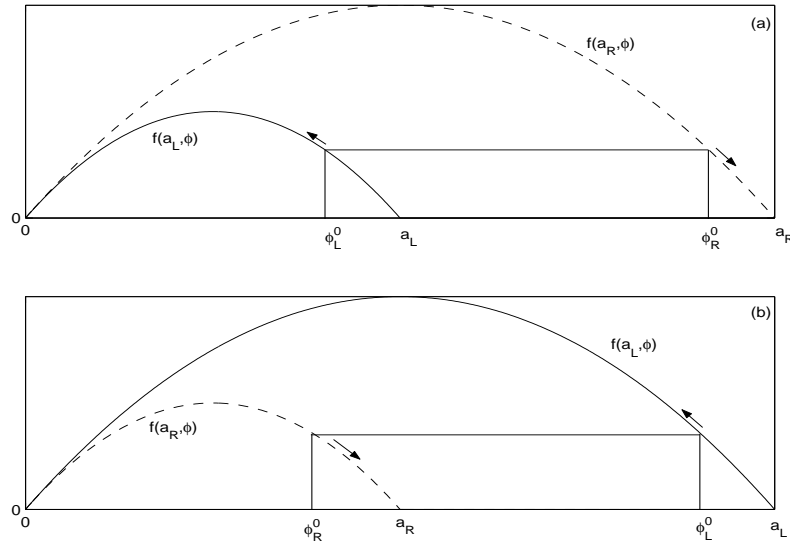


Figure 6.3: Admissible two-state solutions  $(\phi_L^0, \phi_R^0)$  for the cases (a)  $a_L < a_R$  and (b)  $a_L > a_R$ .

and in this situation the Rankine-Hugoniot condition is

$$\frac{f(a, \phi_R) - f(a, \phi_L)}{\phi_R - \phi_L} = s. \quad (6.4.4)$$

The speed  $s$  of the discontinuity can be written as

$$s = v(\phi_L/a) + \phi_R \frac{v(\phi_R/a) - v(\phi_L/a)}{\phi_R - \phi_L} = v(\phi_R/a) + \phi_L \frac{v(\phi_R/a) - v(\phi_L/a)}{\phi_R - \phi_L},$$

from which it is clear that cars immediately to the left and right of the discontinuity are traveling faster than the discontinuity. As a consequence, cars drive through the discontinuity, instantaneously changing their velocities as they do so. Our assumption in this setting is that drivers immediately to the left of such a discontinuity will speed up if they detect that conditions ahead of them allow it, ie. if  $v(\phi_R/a) > v(\phi_L/a)$ .

Recall that according to the classical theory (we are still assuming that the flux is strictly concave), a solution of the form (6.4.3) is admissible if  $\phi_L < \phi_R$  and inadmissible if  $\phi_L > \phi_R$ . In Figure 6.6 (a), the two-state solution  $(\phi_L^0, \phi_R^0)$  is inadmissible. To

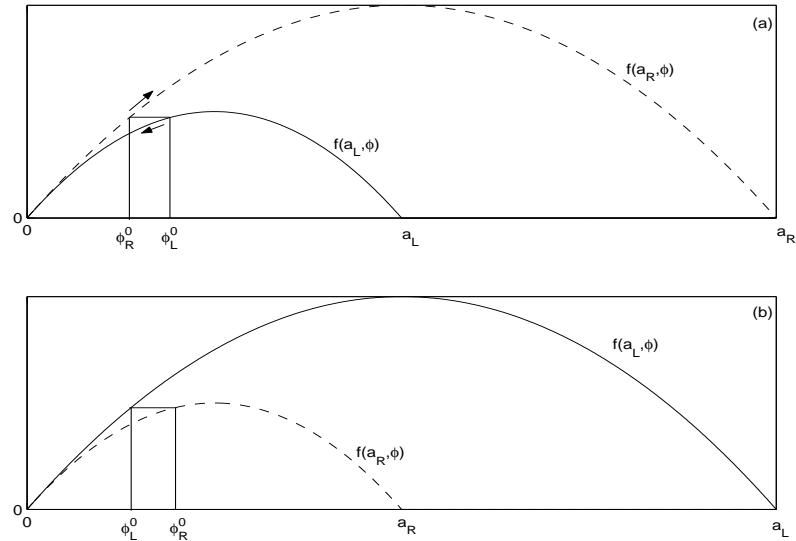


Figure 6.4: Admissible two-state solutions  $(\phi_L^0, \phi_R^0)$  for the cases (a)  $a_L < a_R$  and (b)  $a_L > a_R$ .

see why this solution is unstable, note that drivers on the left side of the jump will see that  $v(\phi_L^0/a) < v(\phi_R^0/a)$ , and thus will speed up, corresponding to the left facing arrow in Figure 6.6 (a). As these higher velocity cars pass through the discontinuity from the left, they create an increase in density on the right side of the discontinuity, corresponding to the right facing arrow in (a) of Figure 6.6. This process will continue until the two adjacent states meet at some point  $\phi_R^1 = \phi_L^1$ . At that point, a stable situation exists because there is no longer a discontinuity in the solution. From the driver's point of view, the opportunity to speed up afforded by a density jump no longer exists.

**Remark 6.4.2** In the case where  $a(x)$  is constant (no interface), our motivation for admissible discontinuities gives the same jump conditions as the so-called driver's ride impulse of Ansorge [5], which states that drivers smooth a discontinuous solution to a continuous one if  $\phi_L > \phi_R$ , but not if  $\phi_L < \phi_R$ . In other words, the admissible discontinuities under the driver's ride impulse are exactly those with  $\phi_L < \phi_R$ ,

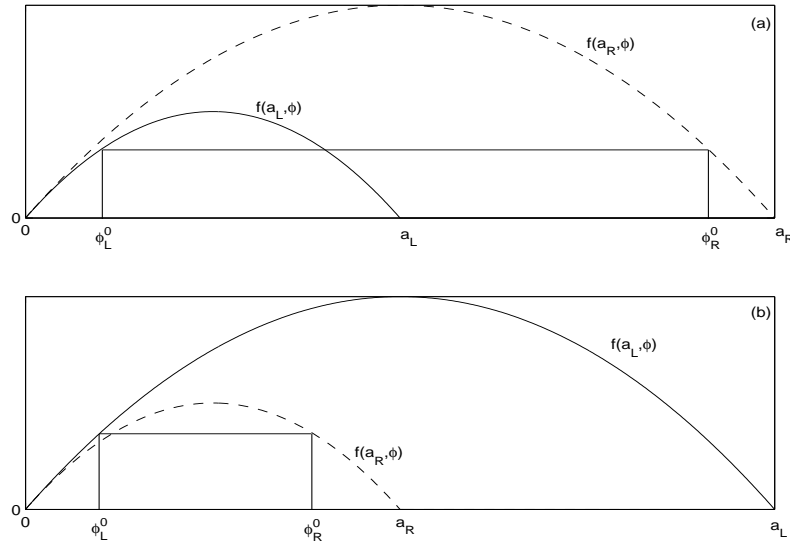


Figure 6.5: Admissible two-state solutions  $(\phi_L^0, \phi_R^0)$  for the cases (a)  $a_L < a_R$  and (b)  $a_L > a_R$ .

which are also the admissible ones under our motivation, and also under the classical Lax/Oleinik/Kružkov theory if the flux  $f$  is strictly concave.

In the more general situation considered in this paper, the driver's ride impulse does not apply to the jump at the discontinuity in  $a$ . This is because it is not possible to smooth the discontinuity at  $x = 0$  - there will always be a discontinuity there unless  $\phi_L = \phi_R = 0$ . This is why we have introduced the rationale proposed here, i.e., that drivers will try to speed up if they detect that the velocity directly ahead is greater than their own velocity. This also seems more directly related to driver behavior than the driver's ride impulse, since drivers can detect a difference in speed much more easily than they can detect a difference in density. Moreover, in contrast to the driver's ride impulse, our concept of driver behavior does not require that drivers try to smooth a jump in the density, or even that they have any awareness of a such a jump.

Finally, still concentrating on the situation away from the interface (where  $a$  is

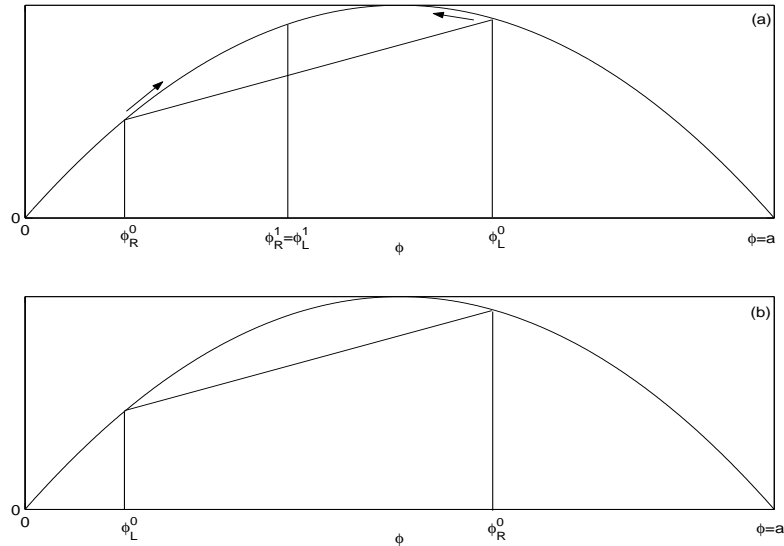


Figure 6.6: (a) Inadmissible, (b) admissible two-state solution  $(\Phi_L^0, \Phi_R^0)$  for  $a = \text{const.}$

constant) both the driver's ride impulse and our rationale give a jump condition that is different from that dictated by the classical Lax/Oleinik/Kružkov theory *if the flux is not strictly concave*. In the case of the driver's ride impulse, this was pointed out by Gasser [76]. Note that away from the jump in  $a$ , the entropy solutions of the present paper satisfy the classical jump conditions, and so if the flux is not strictly concave (we are allowing for this in our setup), our entropy theory will give jumps that may not be completely in agreement with our motivation in terms of traffic flow. The question of how to modify the definition of entropy solution, and also the difference schemes described below, so that the entropy theory completely agrees with our notion of driver behavior is an interesting open problem.

## 6.5 Definition of difference schemes

We discretize the spatial domain  $\mathbb{R}$  into cells  $I_j := [x_{j-1/2}, x_{j+1/2})$ ,  $j \in \mathbb{Z}$ , where  $x_{j \pm 1/2} = (j \pm 1/2)\Delta x$ . The centers of these cells are located at  $x_j = j\Delta x$ . Similarly,

the time interval  $(0, T)$  is discretized via  $t^n = n\Delta t$  for  $n = 0, \dots, N$ , where  $N = \lfloor T/\Delta t \rfloor + 1$ , which results in the time strips  $I^n := [t^n, t^{n+1})$ ,  $n = 0, \dots, N - 1$ . Here  $\Delta x > 0$  and  $\Delta t > 0$  denote the spatial and temporal discretization parameters, respectively. When sending  $\Delta \downarrow 0$  we will do so with the ratio  $\lambda := \Delta t/\Delta x$  kept constant. Let  $\chi_j(x)$  and  $\chi^n(t)$  be the characteristic functions for the intervals  $I_j$  and  $I^n$ , respectively. Define  $\chi_j^n(x, t) := \chi_j(x)\chi^n(t)$  to be the characteristic function for the rectangle  $R_j^n := I_j \times I^n$ . We denote by  $\Phi_j^n$  the finite difference approximation of  $\phi(x_j, t^n)$ . We discretize the initial data in a pointwise manner:

$$\Phi_j^0 := \phi_0(x_j-), \quad (6.5.1)$$

and the parameter  $a(x)$  according to

$$a_j = a_L \text{ for } j \leq 0, \quad a_j = a_R \text{ for } j > 0. \quad (6.5.2)$$

We then define

$$\phi^\Delta(x, t) := \sum_{n=0}^{\mathcal{N}} \sum_{j \in \mathbb{Z}} \Phi_j^n \chi_j^n(x, t). \quad (6.5.3)$$

Our difference scheme is an explicit time-marching algorithm of the type

$$\Phi_j^{n+1} = \Phi_j^n - \lambda \Delta_- h_{j+1/2}^n, \quad (6.5.4)$$

where we define the difference operators  $\Delta_- V_j := V_j - V_{j-1}$  and  $\Delta_+ V_j := V_{j+1} - V_j$ , and the numerical flux has the form

$$h_{j+1/2}^n := h_{j+1/2}(\Phi_{j+1}^n, \Phi_j^n) = \begin{cases} \bar{f}(a_L, \Phi_{j+1}^n, \Phi_j^n) & \text{for } j < 0, \\ \bar{f}_{\text{int}}(a_R, a_L, \Phi_{j+1}^n, \Phi_j^n) & \text{for } j = 0, \\ \bar{f}(a_R, \Phi_{j+1}^n, \Phi_j^n) & \text{for } j > 0. \end{cases} \quad (6.5.5)$$

Next, we study three variants of the scheme, based on the numerical flux  $\bar{f}(a, q, p)$ , and an associated interface version  $\bar{f}_{\text{int}}(a_R, a_L, q, p)$ . In each case the numerical flux  $\bar{f}(a, q, p)$  is a two-point monotone flux (the mapping  $p \mapsto \bar{f}(a, q, p)$  is nondecreasing, and the mapping  $q \mapsto \bar{f}(a, q, p)$  is nonincreasing), Lipschitz continuous, and consistent in the sense that  $\bar{f}(a, p, p) = f(a, p)$ . Similarly, the interface flux  $\bar{f}_{\text{int}}(a_R, a_L, q, p)$  is monotone with respect to the variables  $p$  and  $q$  as described above, and is designed to preserve certain discrete steady state solutions, see Lemma 6.5.1.

### 6.5.1 Numerical fluxes and first-order schemes

We next specify the three numerical fluxes:

#### Flux I: Hilliges-Weidlich flux

Away from the interface, the numerical flux in this case is defined by

$$\bar{f}^{\text{HW}}(a, q, p) := pv(q/a). \quad (6.5.6)$$

This flux was originally proposed by Hilliges & Weidlich [93] (see also [25] and [91]) for the purpose of constructing discrete traffic flow models. We define the interface flux as

$$\bar{f}_{\text{int}}^{\text{HW}}(a_{\text{R}}, a_{\text{L}}, q, p) := \min\{pv(q/a_{\text{R}}), f(a_{\text{L}}, A)\} = \min\{pv(q/a_{\text{R}}), f(a_{\text{R}}, B)\}. \quad (6.5.7)$$

That  $\bar{f}^{\text{HW}}$  is monotone and consistent is readily verified by inspection of (6.5.6), keeping in mind our assumptions about the mapping  $z \mapsto v(z)$ . To verify monotonicity of  $\bar{f}_{\text{int}}^{\text{HW}}$ , we start with the fact that the mapping  $(q, p) \mapsto pv(q/a_{\text{R}})$  is monotone in the sense defined above, and then observe that taking the min with  $f(a_{\text{R}}, B)$  preserves this property.

In [25] we proposed a scheme using this flux, but without special processing for the interface. More specifically, we proposed using the flux

$$\tilde{h}_{j+1/2}^n = \Phi_j^n v(\Phi_{j+1}^n / a_{j+1}), \quad (6.5.8)$$

which defines the same scheme as the one being proposed in this paper, *except at the interface*. We will not analyze the scheme appearing in [25] in this paper. The advantages of the scheme proposed above over the simpler scheme of Bürger *et al.* [25] are twofold. First, the special processing at the interface (the interface flux) greatly diminishes, and many cases removes entirely, certain small spurious traveling overshoots that occur with the scheme of Bürger *et al.* [25]. Second, the fact that the interface flux preserves the steady solution  $P_j^0$  defined below allows for a simpler entropy theory.

The scheme that results by combining (6.5.6) away from the interface and (6.5.7) at the interface is easily combined into a simple modified version of (6.5.8) that can be applied globally, i.e., without requiring logic to detect interface points:

$$h_{j+1/2}^n = \min\{\Phi_j^n v(\Phi_{j+1}^n/a_{j+1}), f_j^*, f_{j+1}^*\}, \quad f_j^* := \max_{\phi \in [0, a_j]} f(a_j, \phi). \quad (6.5.9)$$

Although we will concentrate on the case where  $a(x)$  is piecewise constant with a single jump, the scheme defined by (6.5.9) is readily applied to the case where the coefficient is a piecewise continuous function.

From the expression (6.5.9), we see that for the HW numerical flux, the partial derivatives satisfy

$$0 \leq \frac{\partial h_{j+1/2}^n}{\partial \Phi_j^n} \leq v(\Phi_{j+1}^n/a_{j+1}), \quad (6.5.10)$$

$$0 \geq \frac{\partial h_{j+1/2}^n}{\partial \Phi_{j+1}^n} \geq \frac{\Phi_j^n}{a_{j+1}} v'(\Phi_{j+1}^n/a_{j+1}) \geq \alpha v'(\Phi_{j+1}^n/a_{j+1}), \quad \alpha := \bar{a}/\underline{a}. \quad (6.5.11)$$

## Flux II: Godunov flux

In this case  $\bar{f}$  is the well-known Godunov flux

$$\bar{f}^G(a, q, p) = \begin{cases} \min_{r \in [p, q]} f(a, r) & \text{for } p \leq q, \\ \max_{r \in [q, p]} f(a, r) & \text{for } q \leq p, \end{cases} \quad (6.5.12)$$

and the interface flux is

$$\bar{f}_{\text{int}}^G = \min\{f(a_L, \min\{p, \phi_L^*\}), f(a_R, \max\{q, \phi_R^*\})\}. \quad (6.5.13)$$

This formula for  $\bar{f}_{\text{int}}^G$  is given by Jin & Zhang [101], see Eqns. (27)–(29) of their paper, who observe that this interface flux was already used by Daganzo [49] and Lebacque [123]. Adimurthi *et al.* [1] also proposed an interface flux of Godunov type. Although they use slightly different assumptions about the fluxes at the endpoints, the interface flux given above can also be found in at least one of their formulations, see Eq. (3.3) of [1].

Both numerical fluxes  $\bar{f}^G$  and  $\bar{f}_{\text{int}}^G$  are Lipschitz continuous. That  $\bar{f}^G(a, q, p)$  is monotone is well known and readily verified, in fact

$$\begin{aligned} 0 &\leq \partial_p \bar{f}^G(a, p, q) \leq \max\{0, \partial_p f(a, p)\}, \\ 0 &\geq \partial_q \bar{f}^G(a, q, p) \geq \min\{0, \partial_q f(a, q)\}. \end{aligned} \quad (6.5.14)$$

To see that the interface flux  $\bar{f}_{\text{int}}^G$  is monotone, note that the mapping  $p \mapsto f(a_L, \min\{p, \phi_L^*\})$  is nondecreasing and the mapping  $q \mapsto f(a_R, \max\{q, \phi_R^*\})$  is non-increasing, and finally that these relationships remain true when we take the minimum to form  $\bar{f}_{\text{int}}^G$ . The partial derivatives of the interface flux satisfy

$$0 \leq \partial_p \bar{f}_{\text{int}}^G \leq \max\{0, \partial_p f(a_L, p)\}, \quad 0 \geq \partial_q \bar{f}_{\text{int}}^G \geq \min\{0, \partial_q f(a_R, q)\}. \quad (6.5.15)$$

As we did for the HW flux, we can define a global version of the flux via

$$h_{j+1/2}^n = \min\left\{f(a_j, \min\{\Phi_j^n, \phi_j^*\}), f(a_{j+1}, \max\{\Phi_{j+1}^n, \phi_{j+1}^*\})\right\}, \quad (6.5.16)$$

and in this form the partial derivatives satisfy

$$\begin{aligned} 0 &\leq \frac{\partial h_{j+1/2}^n}{\partial \Phi_j^n} \leq \max\left\{0, \frac{\partial f(a_j, \Phi_j^n)}{\partial \Phi_j^n}\right\}, \\ 0 &\geq \frac{\partial h_{j+1/2}^n}{\partial \Phi_{j+1}^n} \geq \min\left\{0, \frac{\partial f(a_{j+1}, \Phi_{j+1}^n)}{\partial \Phi_{j+1}^n}\right\}. \end{aligned} \quad (6.5.17)$$

### Flux III: Engquist-Osher flux

For this scheme, we use the standard Engquist-Osher flux [65]

$$\bar{f}^{\text{EO}}(a, q, p) = \frac{1}{2}(f(a, p) + f(a, q)) - \frac{1}{2} \int_p^q |f_\phi(a, \phi)| d\phi \quad (6.5.18)$$

away from the interface. For the interface flux, we use

$$\begin{aligned} \bar{f}_{\text{int}}^{\text{EO}}(a_R, a_L, q, p) &= \frac{1}{2}(\tilde{f}(a_R, q) + \tilde{f}(a_L, p)) \\ &\quad - \frac{1}{2} \left[ \int_B^q |\tilde{f}_\phi(a_R, \phi)| d\phi - \int_A^p |\tilde{f}_\phi(a_L, \phi)| d\phi \right], \\ \tilde{f}(a_L, p) &:= \min\{f(a_L, p), f(a_L, A)\}, \\ \tilde{f}(a_R, q) &:= \min\{f(a_R, q), f(a_R, B)\}. \end{aligned} \quad (6.5.19)$$

The flux  $\bar{f}^{\text{EO}}$  is a standard monotone flux, with partial derivatives satisfying

$$\begin{aligned} 0 &\leq \partial_p \bar{f}^{\text{EO}}(a, q, p) = \max\{0, \partial_p f(a, p)\}, \\ 0 &\geq \partial_q \bar{f}^{\text{EO}}(a, q, p) = \min\{0, \partial_q f(a, q)\}. \end{aligned} \quad (6.5.20)$$

To verify that the interface flux  $\bar{f}_{\text{int}}^{\text{EO}}$  is monotone, note that

$$\begin{aligned} \partial_p \bar{f}_{\text{int}}^{\text{EO}} &= \frac{1}{2} \tilde{f}_\phi(a_L, p) + \frac{1}{2} |\tilde{f}_\phi(a_L, p)| \geq 0, \\ \partial_q \bar{f}_{\text{int}}^{\text{EO}} &= \frac{1}{2} \tilde{f}_\phi(a_R, q) - \frac{1}{2} |\tilde{f}_\phi(a_R, q)| \leq 0. \end{aligned} \quad (6.5.21)$$

It is clear from these relationships that the partial derivatives EO interface flux satisfy the same type of inequalities (6.5.15) as for the Godunov interface flux:

$$0 \leq \partial_p \bar{f}_{\text{int}}^{\text{EO}} \leq \max\{0, \partial_p f(a_L, p)\}, \quad 0 \geq \partial_q \bar{f}_{\text{int}}^{\text{EO}} \geq \min\{0, \partial_q f(a_R, q)\}. \quad (6.5.22)$$

The EO version of the flux also has a global version  $h_{j+1/2}$  like (6.5.9) and (6.5.16), which we will not explicitly display. We merely remark that relationship (6.5.17) also holds for the partial derivatives of the EO flux.

When letting  $(\Delta x, \Delta t) \rightarrow (0, 0)$ , we will do so with the ratio  $\lambda := \Delta t / \Delta x$  fixed and satisfying the CFL condition for the HW version

$$\lambda v(z) \leq 1/2, \quad \alpha \lambda |v'(z)| \leq 1/2, \quad z \in [0, 1] \quad (6.5.23)$$

or the CFL condition for the Godunov and EO version

$$\lambda |v(z) + z v'(z)| \leq 1, \quad z \in [0, 1], \quad (6.5.24)$$

respectively. Note that in contrast to (6.5.23), the CFL condition for the Godunov and EO schemes, (6.5.24), does *not* depend on  $a(x)$ .

For a numerical approximation at time level  $n$ ,  $\{\Phi_j^n\}_{j \in \mathbb{Z}}$ , we denote the time advance operator that applies one timestep of our scheme by  $\Gamma_j$ , i.e.  $\Gamma_j(\Phi^n) = \Phi_j^{n+1}$ .

**Lemma 6.5.1** *Each of the interface fluxes  $\bar{f}_{\text{int}} = \bar{f}_{\text{int}}^{\text{HW}}, \bar{f}_{\text{int}}^{\text{G}}, \bar{f}_{\text{int}}^{\text{EO}}$  satisfies*

$$\begin{aligned} \bar{f}_{\text{int}}(a_R, a_L, B, A) &= f(a_L, A) = f(a_R, B), \\ \bar{f}_{\text{int}}(a_R, a_L, a_R, a_L) &= 0, \quad \bar{f}_{\text{int}}(a_R, a_L, 0, 0) = 0. \end{aligned} \quad (6.5.25)$$

Moreover, if we define

$$P_j^0 = \begin{cases} A & \text{for } j \leq 0, \\ B & \text{for } j > 0, \end{cases} \quad Q_j^0 = \begin{cases} a_L & \text{for } j \leq 0, \\ a_R & \text{for } j > 0, \end{cases} \quad R_j^0 = 0, \quad j \in \mathbb{Z}, \quad (6.5.26)$$

then the scheme (6.5.4), (6.5.5) using any of the three variants leaves each of these grid functions fixed, i.e.,

$$\Gamma_j(P^0) = P_j^0, \quad \Gamma_j(Q^0) = Q_j^0, \quad \Gamma_j(R^0) = R_j^0, \quad j \in \mathbb{Z}. \quad (6.5.27)$$

**Proof.** The proof of (6.5.25) in each case is a straightforward calculation starting from the definition of the specific interface flux, and using the fact that  $A \geq \phi_L^*$ ,  $B \leq \phi_R^*$ . We omit the details.

For the proof of (6.5.27), the first condition in (6.5.25) implies that  $j \in \mathbb{Z}$ ,  $\Gamma_j(P^0) = P_j^0$ , the second condition implies that  $\Gamma_j(Q^0) = Q_j^0$ , and the third condition implies that  $\Gamma_j(R^0) = R_j^0$ .  $\square$

**Proposition 6.5.1** *Each of the interface fluxes  $\bar{f}_{\text{int}} = \bar{f}_{\text{int}}^{\text{HW}}, \bar{f}_{\text{int}}^{\text{G}}, \bar{f}_{\text{int}}^{\text{EO}}$  satisfies*

$$\bar{f}_{\text{int}} \leq f(a_L, A) = f(a_R, B) = \min\{f(a_L, \phi_L^*), f(a_R, \phi_R^*)\}. \quad (6.5.28)$$

**Proof.** For  $\bar{f}_{\text{int}}^{\text{HW}}$  and  $\bar{f}_{\text{int}}^{\text{G}}$  this is readily verified from the respective definitions (6.5.7) and (6.5.13). For the EO interface flux, starting from the monotonicity of the flux, the maximum value of  $\bar{f}_{\text{int}}^{\text{EO}}$  over  $(q, p) \in [0, a_R] \times [0, a_L]$  must occur at  $(q, p) = (0, a_L)$ , and so from the definition (6.5.19) we have

$$\begin{aligned} \bar{f}_{\text{int}}^{\text{EO}} &\leq \bar{f}_{\text{int}}(a_R, a_L, 0, a_L) = \frac{1}{2}(\tilde{f}(a_R, 0) + \tilde{f}(a_L, a_L)) \\ &\quad - \frac{1}{2} \left[ \int_B^0 |\tilde{f}_\phi(a_R, \phi)| d\phi - \int_A^{a_L} |\tilde{f}_\phi(a_L, \phi)| d\phi \right] \\ &= -\frac{1}{2} \left[ \int_B^0 |\tilde{f}_\phi(a_R, \phi)| d\phi - \int_A^{a_L} |\tilde{f}_\phi(a_L, \phi)| d\phi \right] \\ &= \frac{1}{2}(f(a_R, B) + f(a_L, A)). \end{aligned}$$

□

Proposition 6.5.1 is not required for our subsequent analysis, but shows that each interface flux simulates an important property of the continuous solution, namely that the flux across the interface cannot exceed  $\min\{f(a_L, \phi_L^*), f(a_R, \phi_R^*)\}$ ; this is a consequence of the Rankine-Hugoniot condition (6.2.4). In the case of the HW flux, the version (6.5.8) that we used in [25] does not always satisfy this constraint. Indeed, our interface flux  $\bar{f}_{\text{int}}^{\text{HW}}$  can be seen as simply a means of enforcing this constraint.

Figure 6.7 shows contour plots of the three interface fluxes  $(q, p) \mapsto \bar{f}_{\text{int}}(a_R, a_L, q, p)$  for  $f(a, \phi) = \phi(1 - \phi/a)$ . The first row shows  $\bar{f}_{\text{int}}^{\text{HW}}$  with  $(a_R, a_L) = (2, 1)$  on the left and  $(a_R, a_L) = (1, 2)$  on the right. The second and third rows are  $\bar{f}_{\text{int}}^{\text{G}}$  and  $\bar{f}_{\text{int}}^{\text{EO}}$ . The 0.25 contour which is labelled in each plot is the maximum value of the numerical flux, which agrees with Proposition 6.5.1, since for this example  $\max\{f(a_L, \phi_L^*), f(a_R, \phi_R^*)\} = 0.25$ . Both the HW and Godunov flux vanish along the left boundary ( $p = 0$ ) and the upper boundary ( $a = a_R$ ). The EO flux vanishes along portions of those boundaries but actually takes on negative values (the minimum value being 0.25) near the upper left corner  $(p, q) = (0, a_R)$ . Finally, it is clear from the plots that in each case the mapping  $p \mapsto \bar{f}_{\text{int}}(a_R, a_L, q, p)$  is nondecreasing, and  $q \mapsto \bar{f}_{\text{int}}(a_R, a_L, q, p)$  is nonincreasing.

## 6.5.2 A MUSCL/Runge-Kutta extension of the schemes

The MUSCL version of the flux  $h_{j+1/2}$  reads

$$h_{j+1/2}^{\text{m}}(\Phi_{j+2}, \Phi_{j+1}, \Phi_j, \Phi_{j-1}) = h_{j+1/2} \left( \Phi_{j+1} - \frac{1}{2}\sigma_{j+1}, \Phi_j + \frac{1}{2}\sigma_j \right), \quad (6.5.29)$$

where  $h$  is the first order version of the flux, and we define the slope  $\sigma_j$  by the VanLeer limiter

$$\sigma_j := \frac{|\phi_j - \phi_{j-1}|(\phi_{j+1} - \phi_j) + |\phi_{j+1} - \phi_j|(\phi_j - \phi_{j-1})}{|\phi_j - \phi_{j-1}| + |\phi_{j+1} - \phi_j|}. \quad (6.5.30)$$

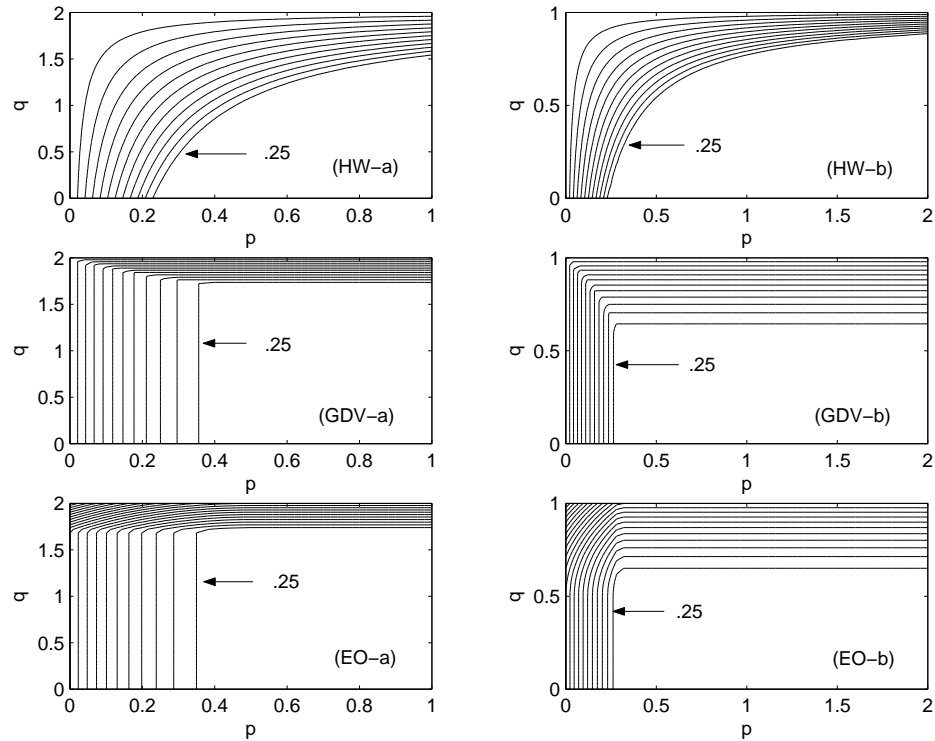


Figure 6.7: The numerical flux  $\bar{f}_{\text{int}}(a_R, a_L, q, p)$  as a function of  $(q, p)$ . In the left column  $(a_R, a_L) = (2, 1)$ , and in the right column  $(a_R, a_L) = (1, 2)$ . First row:  $\bar{f}_{\text{int}} = \bar{f}_{\text{int}}^{\text{HW}}$ , second row:  $\bar{f}_{\text{int}} = \bar{f}_{\text{int}}^{\text{G}}$ , third row:  $\bar{f}_{\text{int}} = \bar{f}_{\text{int}}^{\text{EO}}$ .

This MUSCL scheme is formally second-order accurate in space, but not in time. To achieve formal second order accuracy in time also, we use second order Runge-Kutta time stepping. More specifically, if we write our scheme with first order Euler time differencing and second order spatial differencing abstractly as

$$\Phi_j^{n+1} = \Phi_j^n - \Gamma_j(\Phi_{j+2}^n, \Phi_{j+1}^n, \Phi_j^n, \Phi_{j-1}^n, \Phi_{j-2}^n), \quad (6.5.31)$$

then the Runge-Kutta version takes the two-step form

$$\begin{aligned} \tilde{\Phi}_j^{n+1} &= \Phi_j^n - \Gamma_j(\Phi_{j+2}^n, \Phi_{j+1}^n, \Phi_j^n, \Phi_{j-1}^n, \Phi_{j-2}^n), \\ \Phi_j^{n+1} &= \frac{1}{2}\Phi_j^n + \frac{1}{2}\tilde{\Phi}_j^{n+1} - \frac{1}{2}\Gamma_j(\tilde{\Phi}_{j+2}^{n+1}, \tilde{\Phi}_{j+1}^{n+1}, \tilde{\Phi}_j^{n+1}, \tilde{\Phi}_{j-1}^{n+1}, \tilde{\Phi}_{j-2}^{n+1}). \end{aligned} \quad (6.5.32)$$

For the Godunov and EO versions, we halve the timestep allowed by the CFL condition (6.5.24). For the HW version, we can use the timestep allowed by the CFL condition (6.5.23).

## 6.6 Convergence analysis

Recall that the difference scheme (6.5.4) is monotone [45, 87] if

$$\Phi_j^n \leq \Psi_j^n \quad \forall j \in \mathbb{Z} \quad \implies \quad \Gamma_j(\Phi^n) \leq \Gamma_j(\Psi^n) \quad \forall j \in \mathbb{Z}. \quad (6.6.1)$$

**Lemma 6.6.1** *Assume that  $\phi_0(x) \in [0, a_L]$  for  $x < 0$  and  $\phi_0(x) \in [0, a_R]$  for  $x > 0$ , and that  $\Phi_j^n$  is generated by any of the three variants of the difference scheme (6.5.4), (6.5.5). Then for  $n \geq 0$*

$$\Phi_j^n \in [0, a_L] \quad \text{for } j \leq 0, \quad \Phi_j^n \in [0, a_R] \quad \text{for } j > 0. \quad (6.6.2)$$

Moreover, the difference scheme is monotone.

In addition, we have the following discrete time continuity estimate:

$$\sum_{j \in \mathbb{Z}} |\Phi_j^{n+1} - \Phi_j^n| \leq C, \quad n = 0, 1, \dots, N \quad (6.6.3)$$

where the constant  $C$  is independent of the mesh size  $\Delta$  and the time level  $n$ .

**Proof.** To prove the monotonicity assertion, it suffices to show that

$$\frac{\partial \Phi_j^{n+1}}{\partial \Phi_{j+i}^n} \geq 0, \quad i = -1, 0, 1. \quad (6.6.4)$$

From (6.5.4), it is clear that

$$\frac{\partial \Phi_j^{n+1}}{\partial \Phi_{j-1}^n} = \lambda \frac{\partial h_{j-1/2}}{\partial \Phi_{j-1}^n}, \quad \frac{\partial \Phi_j^{n+1}}{\partial \Phi_{j+1}^n} = -\lambda \frac{\partial h_{j+1/2}}{\partial \Phi_{j+1}^n} \quad (6.6.5)$$

$$\frac{\partial \Phi_j^{n+1}}{\partial \Phi_j^n} = 1 - \lambda \frac{\partial h_{j+1/2}}{\partial \Phi_j^n} + \lambda \frac{\partial h_{j-1/2}}{\partial \Phi_j^n}. \quad (6.6.6)$$

That the inequalities in (6.6.4) for  $i = -1, 1$  hold for the HW version is clear from (6.5.10) and (6.5.11), and for the Godunov and EO version, this is evident from (6.5.17).

To prove (6.6.4) for  $i = 0$  for the HW version, we use (6.6.6), along with (6.5.10) and (6.5.11) to compute

$$\frac{\partial \Phi_j^{n+1}}{\partial \Phi_j^n} \geq 1 - \lambda v(\Phi_{j+1}^n/a_{j+1}) + \alpha \lambda v'(\Phi_j^n/a_j), \quad (6.6.7)$$

and this last quantity is nonnegative thanks to the CFL condition (6.5.23).

To prove (6.6.4) for  $i = 0$  for the Godunov and EO versions, we use (6.6.6) and (6.5.17) to compute

$$\frac{\partial \Phi_j^{n+1}}{\partial \Phi_j^n} \geq 1 - \lambda \min \left\{ 0, \frac{\partial f(a_j, \Phi_j^n)}{\partial \Phi_j^n} \right\} + \lambda \max \left\{ 0, \frac{\partial f(a_j, \Phi_j^n)}{\partial \Phi_j^n} \right\} = 1 - \lambda \left| \frac{\partial f(a_j, \Phi_j^n)}{\partial \Phi_j^n} \right|,$$

and this last quantity is nonnegative thanks to the CFL condition (6.5.24).

Due to our method of discretizing the initial data, we will have

$$R_j^0 \leq \Phi_j^0 \leq Q_j^0, \quad j \in \mathbb{Z}. \quad (6.6.8)$$

Since each of the three schemes is a monotone function of the data at the lower time level, i.e.,  $\Phi_j^1 = \Gamma_j(\Phi_{j+1}^0, \Phi_j^0, \Phi_{j-1}^0)$  is a nondecreasing function of the arguments  $\Phi_{j+1}^0$ ,  $\Phi_j^0$  and  $\Phi_{j-1}^0$ , the ordering in (6.6.8) will be preserved when we apply  $\Gamma_j$ . Recalling that  $\Gamma_j$  leaves  $Q^0$  and  $R^0$  fixed (Lemma 6.5.1), we see that  $R_j^0 \leq \Phi_j^1 \leq Q_j^0$  for  $j \in \mathbb{Z}$ . Continuing this way by induction, we may complete the proof of (6.6.2).

For the proof of (6.6.3), we combine the conservativity of the scheme,

$$\sum_{j \in \mathbb{Z}} \Phi_j^{n+1} = \sum_{j \in \mathbb{Z}} \Phi_j^n,$$

the monotonicity of the time advance operator  $\Phi^n \mapsto \Phi^{n+1}$ , and the boundedness of the variation of the initial data. This allows us to apply the Crandall-Tartar lemma [45]. The proof is very similar to that of Lemma 3.3 of [104], so we omit the details.

□

Let  $V_a^b(z)$  denote the total variation of the function  $x \mapsto z(x)$  over the interval  $[a, b]$ . The following lemma is essentially Lemma 4.2 of [25], where a proof can be found.

**Lemma 6.6.2** *Let  $\{\xi_1, \dots, \xi_M\}$  be a finite set of real numbers. Suppose that  $\Phi_j^n$  is generated by an algorithm which can be written in incremental form*

$$\Phi_j^{n+1} = \Phi_j^n + C_{j+1/2}^n \Delta_+ \Phi_j^n - D_{j-1/2}^n \Delta_- \Phi_j^n, \quad (6.6.9)$$

*except at finitely many indices  $j$  such that  $|x_j - \xi_m| \leq \rho \Delta x$  for some  $m = 1, \dots, M$ , where  $\rho > 0$ . Assume that the incremental coefficients satisfy*

$$C_{j+1/2}^n \geq 0, \quad D_{j+1/2}^n \geq 0, \quad C_{j+1/2}^n + D_{j+1/2}^n \leq 1. \quad (6.6.10)$$

*Finally, assume that the approximations  $\Phi_j^n$  satisfy the time-continuity estimate (6.6.3). Then for any interval  $[a, b]$  such that  $\{\xi_1, \dots, \xi_M\} \cap [a, b] = \emptyset$ , and any  $t \in [0, T]$  we have a spatial variation bound of the form*

$$V_a^b(\phi^\Delta(\cdot, t)) \leq C(a, b), \quad (6.6.11)$$

*where  $C(a, b)$  is independent of  $\Delta$  and  $t$  for  $t \in [0, T]$ .*

The following lemma provides a spatial variation bound that holds in any interval not containing the origin, where the jump in  $a(x)$  occurs.

**Lemma 6.6.3** *For any interval  $[a, b]$  such that  $0 \notin [a, b]$ , and any  $t \in [0, T]$  we have a spatial variation bound of the form (6.6.11), where  $C(a, b)$  is independent of  $\Delta$  and  $t$  for  $t \in [0, T]$ .*

**Proof.** Lemma 6.6.2 is readily applicable here. We only need to verify that for  $j \neq 0, 1$  it is possible to write the scheme in the incremental form (6.6.9), where the coefficients satisfy (6.6.10).

For  $j < 0$ , the incremental coefficients are given by Harten [88]:

$$\begin{aligned} C_{j+1/2}^n &= \lambda \frac{\bar{f}(a_L, \Phi_j^n, \Phi_j^n) - \bar{f}(a_L, \Phi_{j+1}^n, \Phi_j^n)}{\Delta_+ \Phi_j^n}, \\ D_{j+1/2}^n &= \lambda \frac{\bar{f}(a_L, \Phi_{j+1}^n, \Phi_{j+1}^n) - \bar{f}(a_L, \Phi_{j+1}^n, \Phi_j^n)}{\Delta_+ \Phi_j^n}. \end{aligned} \quad (6.6.12)$$

The first two inequalities in (6.6.10) are immediate since the flux  $\bar{f}(a_L, \Phi_{j+1}^n, \Phi_j^n)$  is monotone, i.e., nondecreasing with respect to  $\Phi_j^n$  and nonincreasing with respect to  $\Phi_{j+1}^n$ .

For  $\bar{f}^G$  and  $\bar{f}^{EO}$ , in order to verify the third inequality (6.6.10), we use (6.5.14), (6.5.20) and (6.6.12) to find that

$$C_{j+1/2}^n + D_{j+1/2}^n \leq \lambda \int_0^1 \left| \partial_\phi f(a_L, \Phi_j^n + \theta(\Phi_{j+1}^n - \Phi_j^n)) \right| d\theta.$$

It is clear from this last inequality, along with the CFL condition (6.5.24), that the desired inequality holds.

Still assuming that  $j < 0$ , the incremental coefficients for  $\bar{f}^{HW}$  are given by

$$C_{j+1/2}^n = \lambda \Phi_j^n \frac{v(\Phi_j^n/a_L) - v(\Phi_{j+1}^n/a_L)}{\Phi_{j+1}^n - \Phi_j^n}, \quad D_{j+1/2}^n = \lambda v(\Phi_{j+1}^n/a_L). \quad (6.6.13)$$

The first two inequalities in (6.6.10) follow from the fact that  $\Phi_j^n \geq 0$ ,  $\Phi_{j+1}^n \geq 0$ , and the mapping  $z \mapsto v(z)$  is nonincreasing. It is clear that the third inequality in (6.6.10) will hold if we force  $C_{j+1/2}^n \leq 1/2$ ,  $D_{j+1/2}^n \leq 1/2$ . Note that for some  $\theta$  between  $\Phi_j^n$  and  $\Phi_{j+1}^n$ ,  $C_{j+1/2}^n = -\lambda(\Phi_j^n/a_L)v'(\theta/a_L)$ , and that  $\Phi_j^n/a_L \in [0, 1]$ . Thus the third inequality in (6.6.10) is verified due to (6.5.23).

We can then repeat these calculations for  $j > 1$ , replacing  $a_L$  by  $a_R$ .  $\square$

The following lemma provides a discrete version of the adapted entropy inequality (6.2.12). Before stating it, we need to discretize the function  $\hat{c}^{AB}(x)$ , and we do so according to

$$c_j = A \quad \text{for } j \leq 0, \quad c_j = B \quad \text{for } j > 0. \quad (6.6.14)$$

**Lemma 6.6.4** *With  $c_j$  defined by (6.6.14), the following cell entropy inequality is satisfied by approximate solutions  $\Phi_j^n$  generated by the scheme (6.5.4):*

$$\left| \Phi_j^{n+1} - c_j \right| \leq \left| \Phi_j^n - c_j \right| - \lambda \Delta_- \mathcal{H}_{j+1/2}^n, \quad (6.6.15)$$

where the numerical entropy flux  $\mathcal{H}_{j-1/2}^n$  is defined by

$$\mathcal{H}_{j-1/2}^n = h_{j-1/2} \left( \Phi_j^n \vee c_j, \Phi_{j-1}^n \vee c_{j-1} \right) - h_{j-1/2} \left( \Phi_j^n \wedge c_j, \Phi_{j-1}^n \wedge c_{j-1} \right). \quad (6.6.16)$$

**Proof.** We adapt the proof by Crandall & Majda [45] to the situation at hand. Recalling that  $\Phi_j^{n+1}$  depends on the values at the three neighboring cells at the lower time level, we write (6.5.4) as  $\Phi_j^{n+1} = \Gamma_j(\Phi_{j+1}^n, \Phi_j^n, \Phi_{j-1}^n)$ . According to Lemma 6.6.1,  $\Gamma_j$  is a nondecreasing function of each of its three arguments, implying that

$$\Phi_j^{n+1} \vee \Gamma_j(c_{j+1}, c_j, c_{j-1}) \leq \Gamma_j(\Phi_{j+1}^n \vee c_{j+1}, \Phi_j^n \vee c_j, \Phi_{j-1}^n \vee c_{j-1}), \quad (6.6.17)$$

$$\Phi_j^{n+1} \wedge \Gamma_j(c_{j+1}, c_j, c_{j-1}) \geq \Gamma_j(\Phi_{j+1}^n \wedge c_{j+1}, \Phi_j^n \wedge c_j, \Phi_{j-1}^n \wedge c_{j-1}). \quad (6.6.18)$$

Subtracting (6.6.18) from (6.6.17), and using the identity  $\rho \vee \sigma - \rho \wedge \sigma = |\rho - \sigma|$ , yields

$$\begin{aligned} |\Phi_j^{n+1} - \Gamma_j(c_{j+1}, c_j, c_{j-1})| &\leq \Gamma_j(\Phi_{j+1}^n \vee c_{j+1}, \Phi_j^n \vee c_j, \Phi_{j-1}^n \vee c_{j-1}) \\ &\quad - \Gamma_j(\Phi_{j+1}^n \wedge c_{j+1}, \Phi_j^n \wedge c_j, \Phi_{j-1}^n \wedge c_{j-1}). \end{aligned} \quad (6.6.19)$$

Now  $\Gamma_j(c_{j+1}, c_j, c_{j-1}) = c_j$ ; this follows from Lemma 6.5.1, once we identify  $c_j = P_j^0$ . Thus the left-hand side of (6.6.19) simplifies to  $|\Phi_j^{n+1} - c_j|$  for all  $j$ . It is easy to check from the definitions that the right-hand side of (6.6.19) agrees with the right-hand side of (6.6.15).  $\square$

**Theorem 6.6.1** *Let the function  $\phi^\Delta$  be defined by (6.5.1)–(6.5.5) and (6.5.6), (6.5.7) for the HW version, or (6.5.12), (6.5.13) for the Godunov version, or (6.5.18), (6.5.19) for the EO version. Assume that  $\Delta := (\Delta x, \Delta t) \rightarrow 0$  with the ratio  $\lambda$  fixed and satisfying the appropriate CFL condition (6.5.23) or (6.5.24). Then  $\phi^\Delta \rightarrow \phi$  boundedly a.e. and in  $L^1(\Pi_T)$ , where  $\phi$  is the unique entropy solution to the initial value problem (6.1.3) in the sense of Definition 6.2.5.*

**Proof.** The portion of the proof concerning convergence to a limit function  $\phi \in L^1(\Pi_T) \cap L^\infty(\Pi_T) \cap C(0, T; L^1(\mathbb{R}))$  (i.e., satisfying (D.1)) is very similar to the corresponding portion of the proof of Theorem 4.2 of [25], and so we will omit it. It is clear that any limit function  $\phi$  must satisfy property 6.2.8; this is a direct consequence of Lemma 6.6.1. That the limit solution  $\phi$  satisfies the weak form of the conservation law (D.3) follows from a standard Lax-Wendroff type of calculation that we omit, see the proof of Lemma 4.2 [105]. To verify that the limit solution satisfies the entropy inequalities (6.2.10) and (6.2.11), note that if the interface flux is not involved

each version of the scheme is a standard three-point monotone scheme, and thus satisfies a discrete entropy inequality [45]. Thus two more (standard) Lax-Wendroff calculations yield (6.2.10) and (6.2.11).

It only remains to prove that the limit solution  $\phi$  satisfies (D.5), i.e. the entropy inequality (6.2.12). Let  $0 \leq \psi \in \mathcal{D}(\Pi_T)$ , and  $\psi_j^n = \psi(x_j, t^n)$ . Proceeding as in the proof of the Lax-Wendroff theorem, we move all of the terms in (6.6.15) to the left side of the inequality, multiply by  $\psi_j^n \Delta x$ , and sum over  $j \in \mathbb{Z}$ ,  $n \geq 0$ , and finally sum by parts to get

$$\Delta x \Delta t \sum_{j \in \mathbb{Z}} \sum_{n \geq 0} |\Phi_j^{n+1} - c_j| \frac{\psi_j^{n+1} - \psi_j^n}{\Delta t} + \Delta x \Delta t \sum_{j \in \mathbb{Z}} \sum_{n \geq 0} \mathcal{H}_{j+1/2}^n \frac{\Delta_+ \psi_j^n}{\Delta x} \geq 0. \quad (6.6.20)$$

By the bounded convergence theorem, the first sum converges to

$$\iint_{\Pi_T} |\phi - \hat{c}^{AB}(x)| \psi_t dx dt.$$

For the second sum, note that the interface flux is only involved on a set whose measure will approach zero when we let  $\Delta \downarrow 0$ . Thus we can ignore the interface contribution, and consider separately the contribution for  $x_j$  to the left of the interface (where the discrete entropy flux will be  $\bar{f}(a_L, \Phi_j^n \vee A, \Phi_{j-1}^n \vee A) - \bar{f}(a_L, \Phi_j^n \wedge A, \Phi_{j-1}^n \wedge A)$ ) and the contribution for  $x_j$  to the right of the interface (where the discrete entropy flux will be  $\bar{f}(a_R, \Phi_j^n \vee B, \Phi_{j-1}^n \vee B) - \bar{f}(a_R, \Phi_j^n \wedge B, \Phi_{j-1}^n \wedge B)$ ). With this observation, and the bounded convergence theorem again, we find that the second sum converges to

$$\begin{aligned} & \iint_{\Pi_T \cap \{x < 0\}} \operatorname{sgn}(\phi - A) (f(a_L, \phi) - f(a_L, A)) \psi_x dx dt \\ & + \iint_{\Pi_T \cap \{x > 0\}} \operatorname{sgn}(\phi - B) (f(a_R, \phi) - f(a_R, B)) \psi_x dx dt, \end{aligned} \quad (6.6.21)$$

and this quantity is equal to

$$\iint_{\Pi_T} \operatorname{sgn}(\phi - \hat{c}^{AB}(x)) \left( f(a(x), \phi) - f(a(x), \hat{c}^{AB}(x)) \right) \psi_x dx dt,$$

thus completing the verification of the entropy condition (D.5).

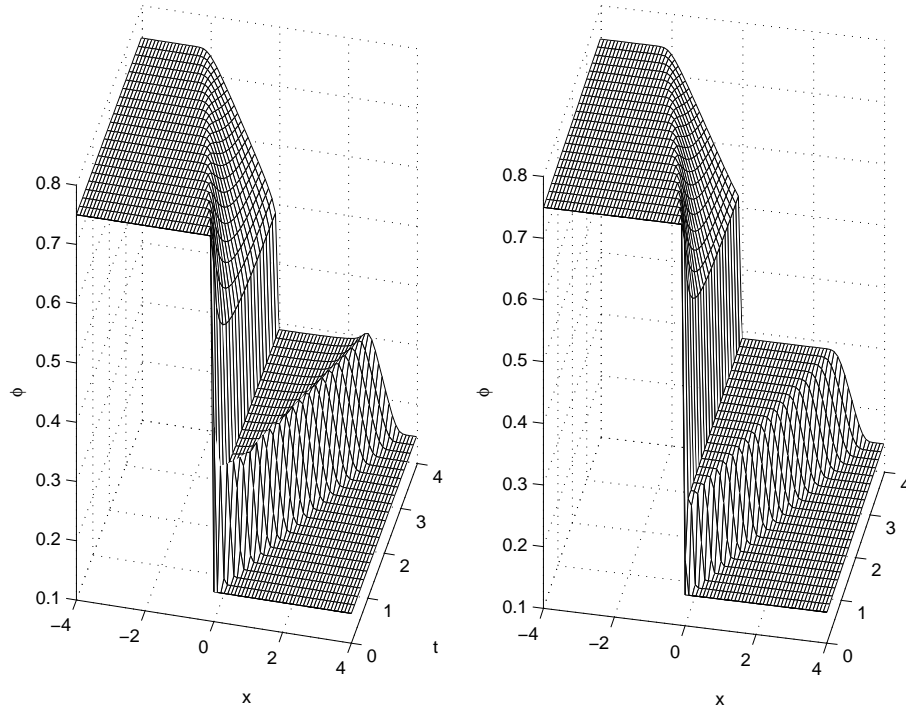


Figure 6.8: Example 6.1 (Riemann problem: HW flux): (a) HW scheme without interface fix, (b) HW scheme with interface fix.

Finally, by Theorem 6.3.1 the entire computed sequence  $\phi^\Delta$  (not just a subsequence) converges to  $\phi$  in  $L^1(\Pi_T)$  and boundedly a.e. in  $\Pi_T$ .  $\square$

## 6.7 Numerical Examples

### 6.7.1 Example 6.1 (Riemann problem: HW flux)

In Example 6.1, we apply the first-order HW flux to the Riemann problem

$$\phi_0(x) = \begin{cases} 0.75 & \text{for } x < 0, \\ 0.15 & \text{for } x > 0, \end{cases} \quad a(x) = \begin{cases} 1 & \text{for } x < 0, \\ 2 & \text{for } x > 0. \end{cases} \quad (6.7.1)$$

The velocity is linear,  $v(z) = 1 - z$ , so the flux is  $f(a, \phi) = \phi(1 - \phi/a)$ . We used  $\Delta x = 0.005$ ,  $\Delta t = 0.0025$ , and ran both versions of the scheme for 1600 steps. Figure 6.8 (a) shows the numerical result of the unmodified version (6.5.8) of the HW interface flux used in our previous paper [25], while Figure 6.8 (b) shows the result produced by the new modified version (6.5.7). The unmodified version shows a small spurious overshoot that occurs at the shock. Overshoots like these are observed on some (not all) Riemann problems. With the modified version of the flux, the overshoot is not present. The modified flux seems to fix most overshoots of this type, with a few remaining cases where there are very small overshoots of the same type that occur when the left and right states of the initial data  $\phi_0$  are close to a steady state solution.

### 6.7.2 Example 6.2 (Riemann problem: comparison of schemes)

For Example 6.2, we again use the flux  $f(a, \phi) = \phi(1 - \phi/a)$ . This time the data are defined by the Riemann problem

$$\phi_0(x) = \begin{cases} 0.45 & \text{for } x < 0, \\ 0.15 & \text{for } x > 0, \end{cases} \quad a(x) = \begin{cases} 2 & \text{for } x < 0, \\ 1 & \text{for } x > 0. \end{cases} \quad (6.7.2)$$

Figure 6.9 (a) shows both the fixed version of the HW scheme, and its formally second order MUSCL/RK version. Figure 6.9 (b) shows the Godunov scheme and its MUSCL/RK version, and plot (c) shows the EO and its MUSCL/RK version. The HW scheme is somewhat more diffusive than the Godunov and EO schemes. Its main advantage is that it is simpler to implement. We used  $\Delta x = 0.16$ ,  $\Delta t = 0.08$ ,

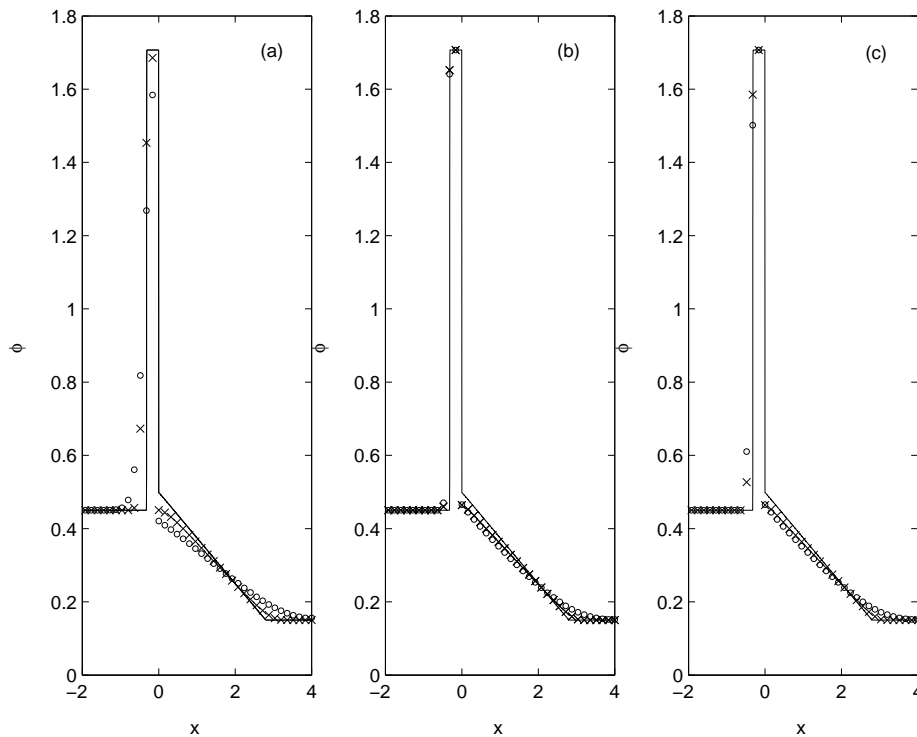


Figure 6.9: Example 6.2 (Riemann problem: comparison of schemes): (a) HW scheme, (b) Godunov scheme, (c) EO scheme. First-order schemes (o) and second-order MUSCL/RK versions ( $\times$ ). The solid line is the reference solution.

and ran the schemes for 50 steps. The thin solid line in Figures 6.9 (a)–(c) is the reference solution, which was calculated with the parameters  $\Delta x = 0.0025$ ,  $\Delta t = 0.00125$ .

### 6.7.3 Example 6.3 (bottleneck problem, after Jin & Zhang [101])

Example 6.3 is the bottleneck problem studied by Jin & Zhang [101]. A circular road of length  $L = 22.4$  km is supposed to have two lanes for most of its length, but reduces to one lane over a small interval. The so-called jam density (where the

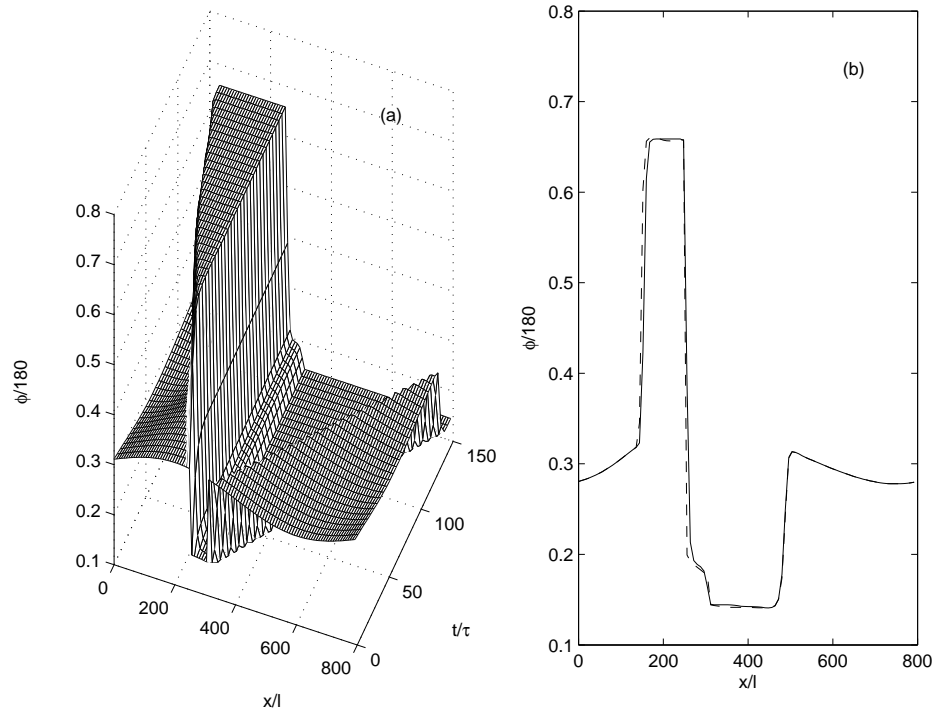


Figure 6.10: Example 6.3 (bottleneck problem, after Jin & Zhang [101]): (a) mesh plot using MUSCL/RK version of HW scheme, (b) MUSCL/RK versions of Godunov (dashed line) and HW (solid line) schemes after 50 time steps.

velocity is zero) is 180 vehicles per kilometer and lane. The flux is defined by

$$f(a, \phi) = \phi v(\phi/a),$$

$$v(\phi/a) = 5.0461 \left[ \left( 1 + \exp \left\{ \frac{[\phi/a - 0.25]}{0.06} \right\} \right)^{-1} - 3.72 \times 10^{-6} \right]. \quad (6.7.3)$$

Note that for  $a \equiv 1$ , this is the velocity function due to Kerner & Konhäuser [109]. In our case, the parameter  $a(x)$  is given by

$$a(x) = \begin{cases} 180 \text{ cars/km} & \text{for } x \in [320l, 400l], \\ 360 \text{ cars/km} & \text{otherwise.} \end{cases} \quad (6.7.4)$$

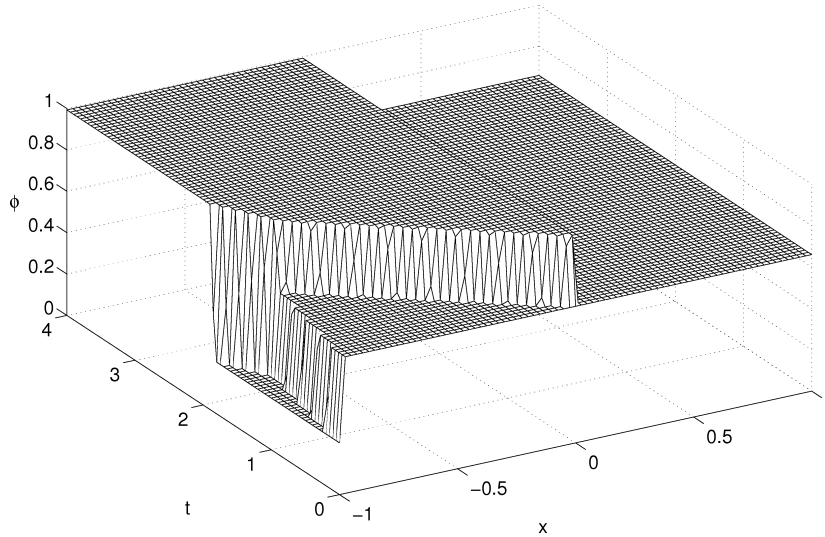


Figure 6.11: Example 6.4 (bottleneck problem, after Garavello & Piccoli [75]): simulated car density using MUSCL/RK version of Godunov scheme for  $\Delta x = 1/160$ .

The initial datum is

$$\phi_0(x) = \frac{a(x)}{180} \left( 28 + 3 \sin \frac{2\pi x}{L} \right). \quad (6.7.5)$$

Following [101], we take  $L = 800l = 22.4$  km,  $l = 0.028$  km,  $\tau = 5$  s,  $\Delta x = 0.224$  km and  $\Delta t = \tau$ . We enforce periodic boundary conditions modeling a circular road of length  $L$ . Figure 6.10 (a) shows a plot of the solution computed over 150 time steps, using the MUSCL/RK version of the HW scheme, while Figure 6.10 (b) shows the solution after 50 time steps. In Figure 6.10 (b), we see that the HW version is more diffusive than the Godunov version. The advantage of the HW version is that it is much easier to implement.

#### 6.7.4 Example 6.4 (bottleneck problem: comparison of schemes, after Garavello & Piccoli [75])

Example 6.4 is a bottleneck problem studied by Garavello & Piccoli [75]. The original example is tackled as an initial and boundary problem, but here we treat it

as a Riemann problem. We use the flux  $f(a, \phi) = \phi(1 - \phi/a)$  and

$$\phi_0(x) = \begin{cases} 0.25 & \text{for } x < -1, \\ 0.66 & \text{for } x > -1, \end{cases} \quad a(x) = \begin{cases} 1 & \text{for } x < 0, \\ 2/3 & \text{for } x > 0. \end{cases} \quad (6.7.6)$$

In this example, we record approximate  $L^1$  errors defined with respect to a reference solution, and convergence rates to study the performance of the numerical schemes. The  $L^1$  error is defined by

$$e_1 := \widetilde{\Delta x} \sum_{j=M_L}^{M_R} \sum_{i=1}^m |\tilde{\phi}_{m(j-1)+i}^n - \phi_j^n|,$$

where  $\tilde{\phi}_l^n$  and  $\phi_l^n$  are the reference solution at  $x = x_l$  and the approximate solution at  $x = x_l$ , respectively, at  $t = t_n$ ;  $m$  is the value of  $\Delta x$  of the approximate solution divided by that of the reference solution;  $M_L$  and  $M_R$  are the indices of the positions between which we calculate the errors of the numerical approximation; and  $\widetilde{\Delta x}$  is the spatial discretization parameter of the reference solution.

Here and in Example 6.5, the reference solution was calculated using the MUSCL/RK versions of the Godunov scheme with the discretization parameter  $\widetilde{\Delta x} = 1/960$ . For the reference solution and all other computations of this example, we use  $\lambda = 1/3$ .

Figure 6.11 shows the plot of the reference solution computed until  $t = 4$ , using the MUSCL/RK version of the Godunov scheme. Since for  $x \in [-1, 0]$ ,  $f(a_L, \phi_0(x)) = 0.2244 > 1/6 = \max_{\phi \in [0, 2/3]} f(a_R, \phi)$ , a formation of traffic jam from  $t = 0$  can be observed.

Figures 6.12 and 6.13 show the numerical simulation of the car density at  $t = 0.1$ ,  $t = 0.5$ , and  $t = 1, t = 4$ , respectively, produced by the first-order HW, Godunov and EO schemes, and the MUSCL/RK version of the HW, Godunov and EO schemes. Tables 6.1 and 6.2 displays the approximate  $L^1$  errors for this example, measured over the interval  $[-1, 1]$ .

It is clear from Figures 6.12 and 6.13 that Godunov and EO schemes and their second order versions are less dissipative than their counterparts based on the HW

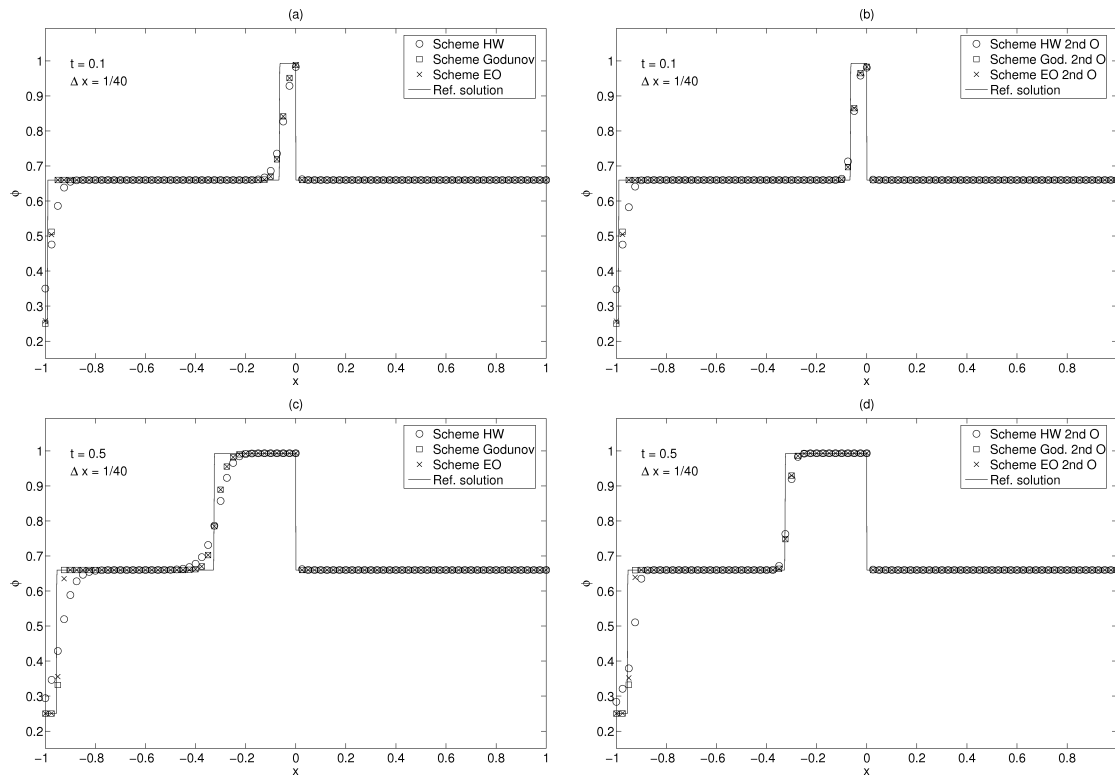


Figure 6.12: Example 6.4 (bottleneck problem, after Garavello & Piccoli [75]): simulated car density. Plots (a, c): first-order schemes (HW, Godunov and EO). Plots (b, d): second-order schemes (MUSCL/RK versions of HW, Godunov and EO). Plots (a, b) show solutions at  $t = 0.1$ , and plots (c, d) show solutions at  $t = 0.5$ .

flux. Tables 6.1 and 6.2 corroborates what we see in the plots, specifically, smaller errors and faster rates of convergence for Godunov and EO schemes and their second order versions than the HW flux based schemes. Moreover, we observe that at  $t = 4$  Godunov and EO schemes give the same results, the same for their second order versions. It is interesting that for  $t = 0.1$  and  $t = 4$  the Godunov scheme, which is formally first order accurate, has smaller errors than the second order accurate version of the HW scheme.

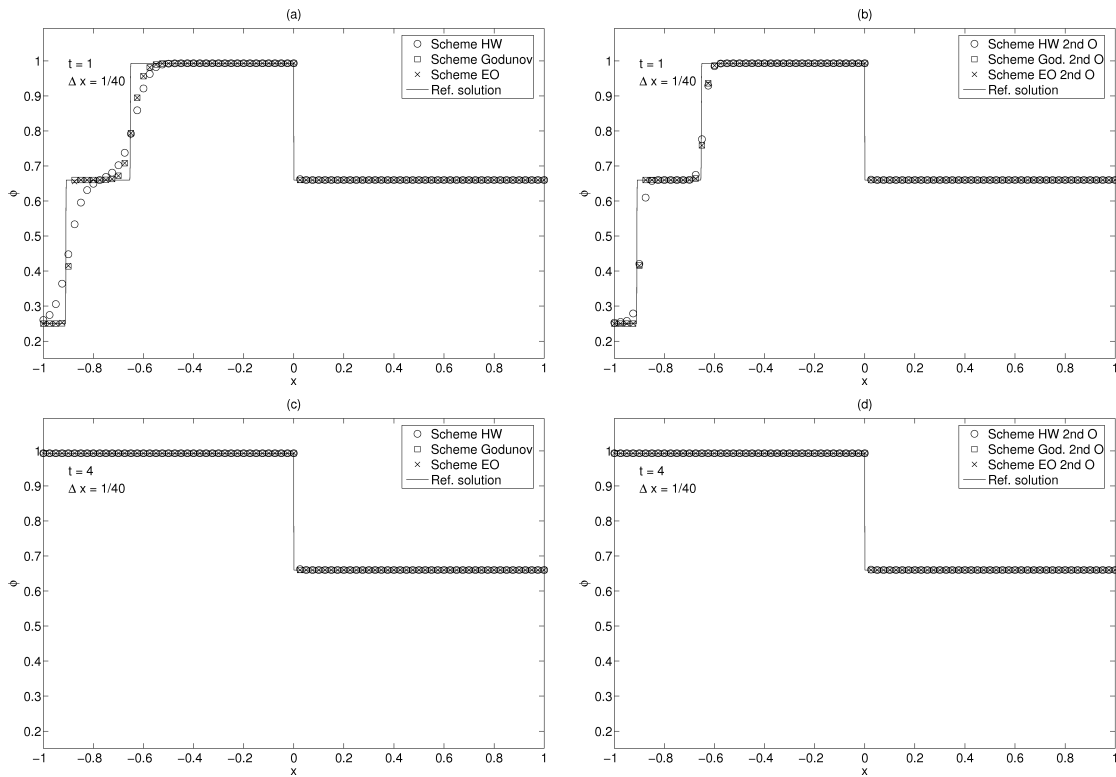


Figure 6.13: Example 6.4 (bottleneck problem, after Garavello & Piccoli [75]): simulated car density. Plots (a, c): first-order schemes (HW, Godunov and EO). Plots (b, d): second-order schemes (MUSCL/RK versions of HW, Godunov and EO). Plots (a, b) show solutions at  $t = 1$ , and plots (c, d) show solutions at  $t = 4$ .

### 6.7.5 Example 6.5 (bottleneck problem with zero initial condition, after Garavello & Piccoli [75])

Example 6.5 is another bottleneck problem studied by Garavello & Piccoli [75]. As in Example 6.4, the original problem is considered as an initial and boundary problem, but here we treat it as a Riemann problem. We use the flux  $f(a, \phi) = \phi(1 - \phi/a)$  with the same parameter  $a(x)$  as in Example 4, but now our initial condition is  $\phi_0(x) = 0.4$  for  $x < -1$  and  $\phi_0(x) = 0$  for  $x > -1$ . Figure 6.14 shows the plot of the reference solution computed until  $t = 10$ , using the MUSCL/RK version of the

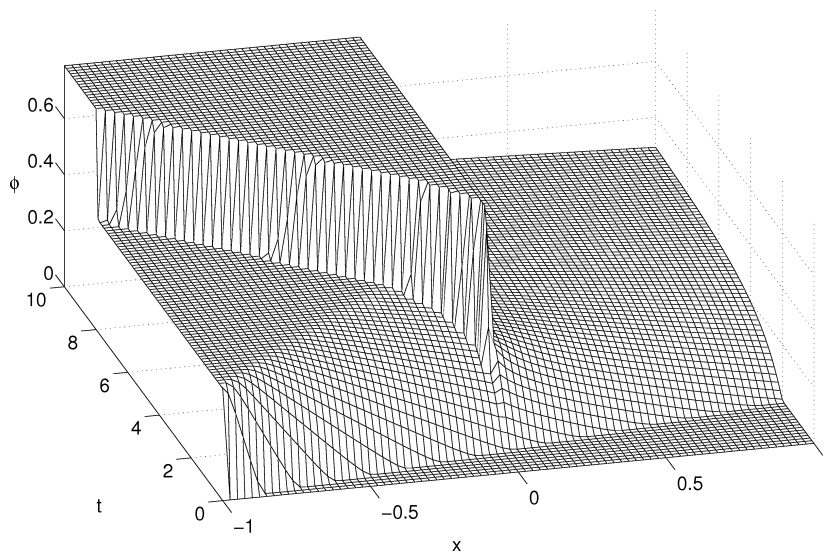


Figure 6.14: Example 6.5 (bottleneck problem with zero initial condition, after Garavello & Piccoli [75]): simulated car density using MUSCL/RK version of Godunov scheme for  $\Delta x = 1/160$ .

Godunov scheme. Since for  $x < -1$ ,  $f(a_L, \phi_0(x)) = 0.24 > 1/6 = \max_{\phi \in [0, 2/3]} f(a_R, \phi)$ , also in this case there is a formation of traffic jam from  $t = 2$  approximately. Figures 6.15 and 6.16 shows the numerical simulation of the car density at  $t = 0.1$ ,  $t = 2$ , and  $t = 4$ ,  $t = 10$ , respectively, produced by the first-order HW, Godunov and EO schemes, and the MUSCL/RK version of the HW, Godunov and EO schemes.

It is clear from Figures 6.15 and 6.16 that Godunov and EO schemes and their second order versions are more accurate than those based on the HG flux.

$\mathcal{J}$ $= L/\Delta x$	$t = 0.1$		$t = 0.5$		$t = 1$		$t = 4$	
	$e_1$ $10^{-3}$	Conv. rate	$e_1$ $10^{-3}$	Conv. rate	$e_1$ $10^{-3}$	Conv. rate	$e_1$ $10^{-3}$	Conv. rate
	HW							
20	80.617		131.992		128.608		33.215	
40	52.017	0.632	73.557	0.844	72.633	0.824	16.434	1.015
80	31.472	0.725	39.635	0.892	41.159	0.819	8.044	1.031
160	17.052	0.884	20.509	0.951	20.745	0.988	3.850	1.063
240	11.779	0.913	13.556	1.021	13.511	1.058	2.453	1.112
320	9.031	0.923	9.974	1.067	10.006	1.044	1.755	1.164
	Godunov							
20	79.916		113.196		115.266		32.989	
40	49.387	0.694	57.937	0.966	57.914	0.993	16.321	1.015
80	27.255	0.858	28.418	1.028	28.628	1.016	7.988	1.031
160	13.412	1.023	13.770	1.045	13.878	1.045	3.822	1.063
240	8.805	1.038	8.850	1.090	8.901	1.095	2.434	1.113
320	6.367	1.127	6.394	1.130	6.446	1.122	1.741	1.165
	EO							
20	80.222		113.617		112.981		32.989	
40	49.705	0.691	57.965	0.971	57.926	0.964	16.321	1.015
80	27.407	0.859	28.444	1.027	28.695	1.013	7.988	1.031
160	13.429	1.029	13.802	1.043	14.005	1.035	3.822	1.063
240	8.867	1.024	8.904	1.081	8.910	1.116	2.434	1.113
320	6.403	1.132	6.479	1.106	6.491	1.101	1.741	1.165

Table 6.1: Example 6.4 (bottleneck problem, after Garavello & Piccoli [75]): approximate  $L^1$  errors for first-order schemes.

$\mathcal{J}$ $= L/\Delta x$	$t = 0.1$		$t = 0.5$		$t = 1$		$t = 4$	
	$e_1$ $10^{-3}$	Conv. rate	$e_1$ $10^{-3}$	Conv. rate	$e_1$ $10^{-3}$	Conv. rate	$e_1$ $10^{-3}$	Conv. rate
HW MUSCL/RK								
20	79.118		122.294		123.847		33.101	
40	49.852	0.666	63.638	0.942	63.955	0.953	16.377	1.015
80	29.141	0.775	31.380	1.020	27.794	1.202	8.015	1.031
160	14.827	0.975	13.346	1.233	12.888	1.109	3.834	1.064
240	9.844	1.010	8.290	1.174	8.031	1.166	2.440	1.114
320	7.213	1.081	5.942	1.158	5.842	1.106	1.743	1.169
Godunov MUSCL/RK								
20	78.168		107.400		108.829		32.988	
40	47.304	0.725	53.818	0.997	53.107	1.035	16.321	1.015
80	26.029	0.862	25.989	1.050	26.019	1.029	7.987	1.031
160	12.483	1.060	12.444	1.062	12.492	1.059	3.820	1.064
240	8.067	1.077	7.931	1.111	7.979	1.105	2.431	1.115
320	5.732	1.188	5.677	1.162	5.722	1.156	1.736	1.170
EO MUSCL/RK								
20	78.452		107.840		109.870		32.988	
40	47.597	0.721	53.874	1.001	53.196	1.046	16.321	1.015
80	26.176	0.863	26.034	1.049	26.040	1.031	7.987	1.031
160	12.506	1.066	12.454	1.064	12.542	1.054	3.820	1.064
240	8.131	1.062	7.944	1.109	7.996	1.110	2.431	1.115
320	5.772	1.191	5.700	1.154	5.742	1.151	1.736	1.170

Table 6.2: Example 6.4 (bottleneck problem, after Garavello & Piccoli [75]): approximate  $L^1$  errors for second-order MUSCL/RK schemes.

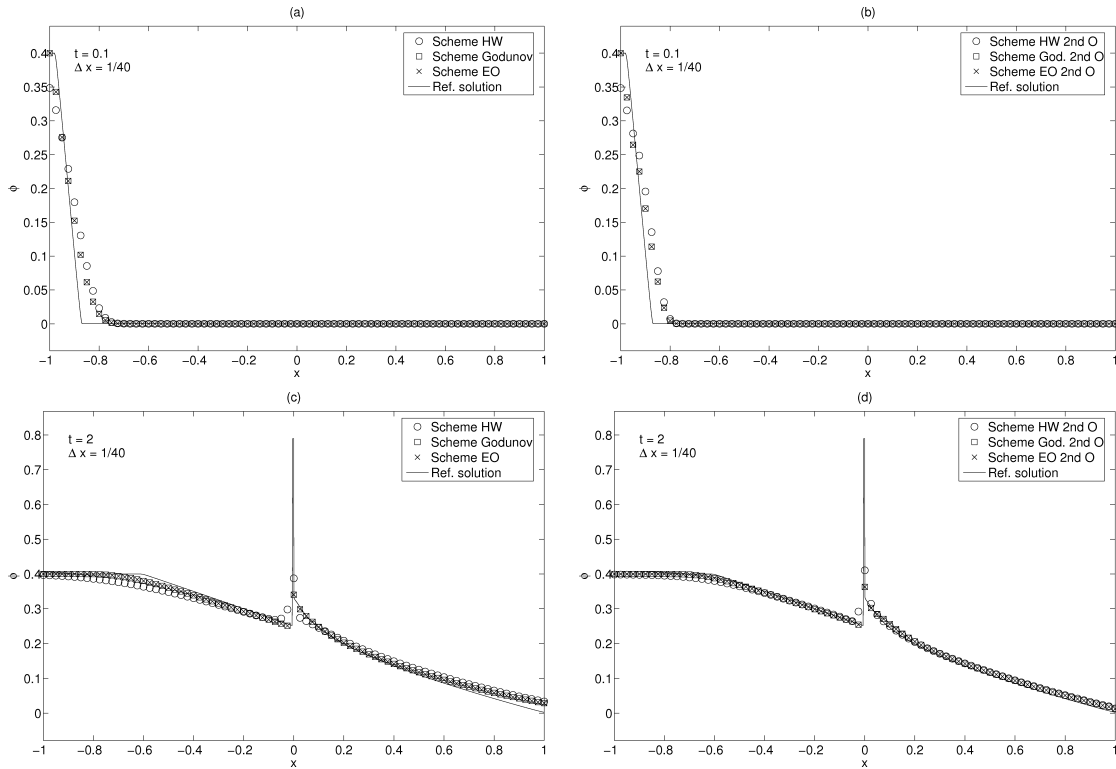


Figure 6.15: Example 6.5 (bottleneck problem with zero initial condition, after Garavello & Piccoli [75]): simulated car density. Plots (a, c): first-order schemes (HW, Godunov and EO). Plots (b, d): second-order schemes (MUSCL/RK versions of HW, Godunov and EO). Plots (a, b) show solutions at  $t = 0.1$ , and plots (c, d) show solutions at  $t = 2$ .

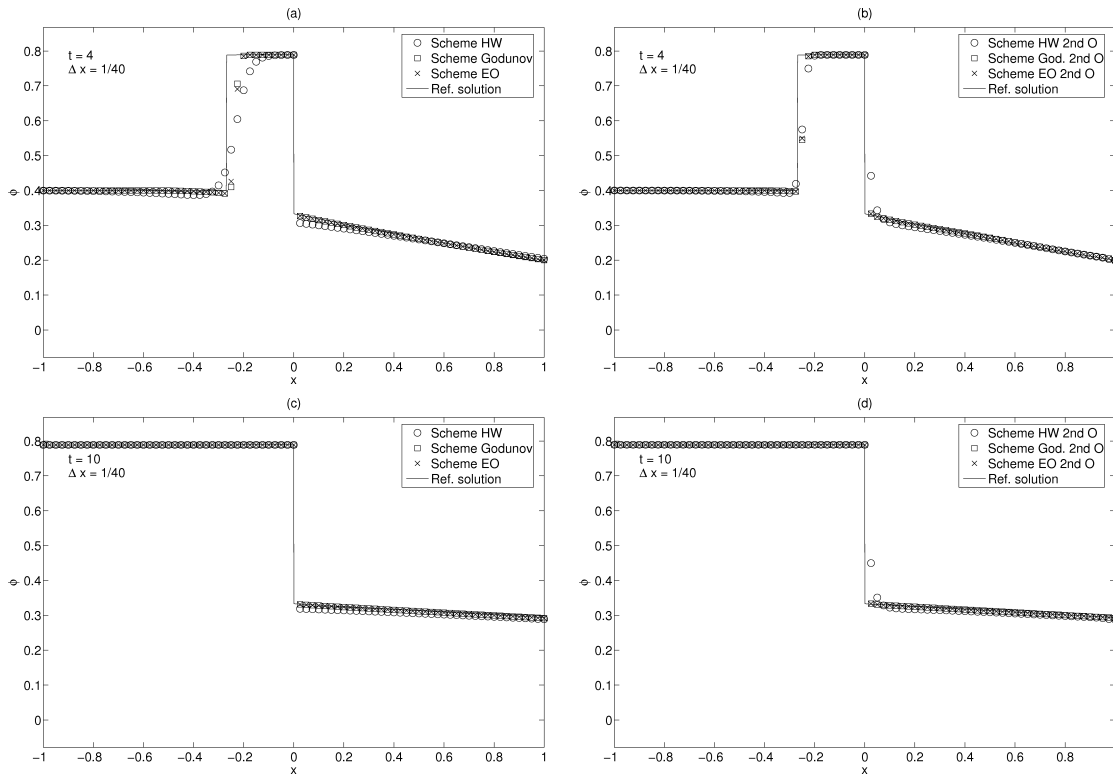


Figure 6.16: Example 6.5 (bottleneck problem with zero initial condition, after Garavello & Piccoli [75]): simulated car density. Plots (a, c): first-order schemes (HW, Godunov and EO). Plots (b, d): second-order schemes (MUSCL/RK versions of HW, Godunov and EO). Plots (a, b) show solutions at  $t = 4$ , and plots (c, d) show solutions at  $t = 10$ .

## Chapter 7

# Sedimentation of Polydisperse Suspensions with a Continuous Particle Size Distribution

Polydisperse suspensions with particles of  $N$  distinct size classes have been mainly utilized in laboratory experiments. However, in most real-world applications, for example in mineral processing, the sizes of particles are continuously distributed. In this paper, the one-dimensional kinematic model for batch sedimentation of polydisperse suspensions of small equal-density spheres is extended to suspensions with a continuous particle size distribution. For this purpose, the so-called phase density function  $\Phi = \Phi(t, x, \xi)$ , where  $\xi \in [0, 1]$  is the normalized squared size of the particles, is introduced, whose integral with respect to  $\xi$  on a interval  $[\xi_1, \xi_2]$ , is equivalent to the volume fraction at  $(t, x)$  occupied by the particles in that size range. The resulting mathematical model, obtained by combining the Masliyah-Lockett-Bassoon (MLB) model for the solid-fluid relative velocity for each solids species with the concept of phase density function, is a scalar first-order kinetic equation for  $\Phi$ . Three numerical schemes for the solution of this equation are introduced, and a numerical example and an  $L^1$  error study show that one of these schemes introduces not

much numerical diffusion and without spurious oscillations near discontinuities. Several numerical examples illustrate the simulated behaviour of this kind of suspensions.

## 7.1 Introduction

Numerous engineering applications involve the sedimentation of small solid particles dispersed in a viscous fluid. In so-called polydisperse suspensions, the particles belong to several species that differ in size or density, and usually segregate and create areas of different composition. This differential movement is frequently described by spatially one-dimensional models. In most circumstances, the diameter of the particles is small compared to that of the flow duct, which justifies identifying each species with a continuous phase. In general, we distinguish between  $N$  different species that give rise to  $N$  superimposed continuous phases, where particles of species  $i$ , associated with volume fraction  $\phi_i$ , have size  $d_i$  and density  $\rho_i$ , and  $d_i \neq d_j$  or  $\rho_i \neq \rho_j$  for  $i \neq j$ . If  $v_i$  is the phase velocity of species  $i$ , then the continuity equations of the  $N$  species in differential form are  $\partial_t \phi_i + \partial_x(\phi_i v_i) = 0$  for  $i = 1, \dots, N$ , where  $t$  is time and  $x$  is depth. The velocities  $v_1, \dots, v_N$  are assumed to be given functions of the vector  $\Phi := \Phi(x, t) := (\phi_1(x, t), \dots, \phi_N(x, t))^T$  of local concentrations. This yields systems of conservation laws of the type

$$\begin{aligned} \partial_t \Phi + \partial_x \mathbf{f}(\Phi) &= 0, & \mathbf{f}(\Phi) &= (f_1(\Phi), \dots, f_N(\Phi))^T, \\ f_i(\Phi) &= \phi_i v_i(\Phi), & i &= 1, \dots, N. \end{aligned} \tag{7.1.1}$$

One-dimensional multi-species flow models given by (7.1.1), which involve no unknown flow variables other than the concentrations, are called *kinematic*. Similar models describe multi-species traffic flow [10, 168, 176, 177, 178] and the settling of oil-in-water emulsions [149], see [25, 36] for overviews. We recall that for a given vector  $\Phi$ , (7.1.1) is called *hyperbolic* if the Jacobian  $\mathbf{J}_f(\Phi) := (\partial f_i(\Phi) / \partial \phi_j)_{i,j=1,\dots,N}$  has real eigenvalues only, and *strictly hyperbolic* if these are moreover pairwise distinct. The significance of hyperbolicity for polydisperse sedimentation models will be dis-

cussed further below. Hyperbolicity ensures that concentration changes, and solution information in general, propagate at finite speed.

## 7.2 The mathematical model

### 7.2.1 Polydisperse suspensions with a discrete particle size distribution

We consider a suspension of particles made of the same material, and therefore having the same density  $\rho_s$ , which are dispersed in a viscous fluid of density  $\rho_f$  and having the dynamic viscosity  $\mu_f$ . We assume that the particles can be subdivided into  $N$  size classes or species, where particles of the  $i$ -th species have size  $d_i$ , and we assume that  $d_1 > d_2 > \dots > d_N$ . According to the Masliyah-Lockett-Bassoon (MLB) model [32], the one-dimensional sedimentation of this mixture is modeled by the first-order system of  $N$  conservation laws

$$\partial_t \phi_i + \partial_x \left( \phi_i \left[ q + u_i - \sum_{m=1}^N \phi_m u_m \right] \right) = 0, \quad i = 1, \dots, N, \quad (7.2.1)$$

where  $t$  is time,  $x$  is depth,  $\phi_i$  is the volume fraction of particle species  $i$ ,  $u_i$  is the solid-fluid relative velocity (or slip velocity) of particle species  $i$ , and  $q$  is the volume average velocity of the mixture, which can be controlled externally. We limit ourselves to the simple case of a settling column that is closed at its bottom, for which  $q = 0$ . For small equal-density spheres, the MLB model postulates the equation

$$u_i = \frac{\bar{\rho}_s g}{18\mu_f} d_i^2 \tilde{V}(\phi)(1 - \phi), \quad (7.2.2)$$

where  $\bar{\rho}_s = \rho_s - \rho_f$ ,  $g$  is the acceleration of gravity,  $\mu_f$  is the viscosity of the fluid, and  $\phi = \phi_1 + \dots + \phi_N$  is the total solids volume fraction. The function  $V(\phi) := \tilde{V}(\phi)(1 - \phi)$

is the hindered settling factor. We choose the continuous function

$$\tilde{V}(\phi) = \begin{cases} (1 - \phi)^\gamma & \text{for } \phi \in [0, \phi_q), \\ (1 - \phi_q)^\gamma \frac{\phi_{\max} - \phi}{\phi_{\max} - \phi_q} & \text{for } \phi \in [\phi_q, \phi_{\max}], \\ 0 & \text{otherwise,} \end{cases} \quad (7.2.3)$$

with  $\gamma \geq 1$ ,  $\phi_q \in (0, \phi_{\max})$ , and the maximum solid concentration  $\phi_{\max} \in (0, 1]$ . To further simplify the model, let  $v_1 := \bar{\rho}_s g d_1^2 / (18\mu_f)$  be the settling velocity of the largest species. We consider a settling column of height  $L$  and introduce the dimensionless space variable  $\tilde{x} = x/L$ , the time variable  $\tilde{t} = (v_1/L)t$ , and the parameters  $\delta_i := d_i^2/d_1^2$ ,  $i = 1, \dots, N$ . Inserting (7.2.2) into (7.2.1) for  $q = 0$ . Using the vector  $\phi = (\phi_1, \dots, \phi_N)^\top$ , we obtain the governing system of conservation laws

$$\partial_t \phi + \partial_x \mathbf{f}(\phi) = 0, \quad (7.2.4)$$

where the components  $f_1(\phi), \dots, f_N(\phi)$  of the flux vector  $\mathbf{f}(\phi)$  are defined by

$$f_i(\phi) = \phi_i \left( \delta_i - \sum_{m=1}^N \delta_m \phi_m \right) V(\phi), \quad i = 1, \dots, N. \quad (7.2.5)$$

The zero-flux boundary conditions relevant to a closed column can then be stated as

$$f_i|_{x=0} = f_i|_{x=1} = 0, \quad i = 1, \dots, N. \quad (7.2.6)$$

Finally, one assumes that an initial concentration distribution  $\phi^0(x) = (\phi_1^0(x), \dots, \phi_N^0(x))^\top$  is given, i.e.

$$\phi_i(t, x)|_{t=0} = \phi_i^0(x), \quad x \in [0, 1], \quad i = 1, \dots, N, \quad (7.2.7)$$

such that

$$\phi^0(x) \in \mathcal{D} := \left\{ \Phi = (\phi_1, \dots, \phi_N)^\top \in \mathbb{R}^N \mid \begin{array}{l} \phi_1 \geq 0, \dots, \phi_N \geq 0, \\ \phi_1 + \dots + \phi_N \leq \phi_{\max} \end{array} \text{ for } x \in [0, 1] \right\}$$

## 7.2.2 Properties of the model for a finite number of particle species

In [12] it was proved that the system (7.2.5) is strictly hyperbolic for arbitrary  $N \in \mathbb{N}$ , size distributions  $\delta_1 = 1 > \delta_2 > \dots > \delta_N$ , hindered settling functions  $\tilde{V}(\phi)$  with  $\tilde{V}(\phi) > 0$  and  $\tilde{V}'(\phi) < 0$  for  $\phi \in [0, \phi_{\max})$ , and vectors  $\phi$  with  $\phi_i > 0$  for  $i = 1, \dots, N$  and  $\phi < \phi_{\max}$ . More precisely, the following theorem was proved in [12].

**Theorem 7.2.1 ([12])** *For any vector  $\phi = (\phi_1, \dots, \phi_N)^T \in \mathcal{D}$  we recall the abbreviation  $\bar{\phi} = \phi_1 + \dots + \phi_N$  and define the quantities*

$$\bar{\delta} := \sum_{i=1}^N \delta_i \phi_i, \quad \lambda_\infty := -2\bar{\delta}V(\phi) + V(\phi)'(\bar{\delta} + \phi). \quad (7.2.8)$$

*If  $\delta_1 = 1 > \delta_2 > \dots > \delta_N$  and the vector  $\phi$  is chosen from the interior of  $\mathcal{D}$ , then the eigenvalues  $\lambda_N(\phi) \leq \lambda_{N-1}(\phi) \leq \dots \leq \lambda_1(\phi)$  of the Jacobian  $\mathbf{J}_f(\phi)$  satisfy*

$$\lambda_i(\phi) \in (V(\phi)(\delta_{i+1} - \bar{\delta}), V(\phi)(\delta_i - \bar{\delta})), \quad i = 1, \dots, N-1, \quad (7.2.9)$$

$$\lambda_N(\phi) \in (\lambda_\infty, V(\phi)(\delta_N - \bar{\delta})). \quad (7.2.10)$$

**Remark:** Note that  $V(\phi) > 0$  is guaranteed in the previous theorem due to (7.2.3) since we have assumed that  $\phi \in \mathcal{D}$ . Thus the first  $N-1$  eigenvalues  $\lambda_i(\phi)$  in (7.2.9) indicate a continuous distribution in the limit  $N \rightarrow \infty$ , whereas the last eigenvalue  $\lambda_N(\phi)$  plays an extra role in the theory.

Simulations of the settling of polydisperse suspensions with a finite number of size classes based on numerical solution of (7.2.5), (7.2.6), (7.2.7) are presented in [12, 20, 22, 170].

## 7.2.3 Polydisperse suspensions with a continuous particle size distribution

Polydisperse suspensions with particles of  $N$  distinct size classes have been utilized in many laboratory experiments. However, in most applications, for example in mineral processing, the sizes of particles are continuously distributed. Since

most real suspensions have passed through a sieve with a determined mesh-width, we can assume that there exists a maximum particle size, which is normalized to one as in the discrete case. Consequently, the local composition of the polydisperse suspension as a function of time  $t$  and depth  $x$  is no longer determined by a vector  $\phi = \phi(t, x)$ , but by a density function  $\Phi = \Phi(t, x, \xi)$ ,  $\xi \in [0, 1]$ , where  $\int_{\xi_1}^{\xi_2} \Phi(t, x, \xi) d\xi$  denotes the volume fraction at  $(t, x)$  occupied by all particles with normalized squared size  $\xi_1 < \xi < \xi_2$ .

To derive a kinetic equation for the evolution of  $\Phi$ , we may approximate the continuous size distribution by a discrete one, multiply the  $i$ -th equation in (7.2.5) by  $\delta_i - \delta_{i-1}$ , sum the equations from  $i_1$  to  $i_2$ , and then require that the summed equation holds for all choices  $1 \leq i_1 \leq i_2 \leq N$ . Passing to  $N \rightarrow \infty$  and replacing the sum in the flux in (7.2.5) by an integration, we obtain that the following equation holds for all  $0 \leq \xi_1 < \xi_2 \leq 1$ :

$$\int_{\xi_1}^{\xi_2} \left\{ \partial_t \Phi(t, x, \xi) + \partial_x \left( \Phi(t, x, \xi) V(\bar{\Phi}(t, x)) [\xi - \bar{\xi}(t, x)] \right) \right\} d\xi = 0, \quad (7.2.11)$$

where the total volume fraction  $\bar{\Phi}$  and the local average value  $\bar{\xi}$  of  $\xi$  with respect to  $\Phi$  are given by the respective expressions

$$\bar{\Phi}(t, x) := \int_0^1 \Phi(t, x, \xi) d\xi, \quad \bar{\xi}(t, x) := \int_0^1 \xi \Phi(t, x, \xi) d\xi. \quad (7.2.12)$$

Since (7.2.11) is assumed to hold for all suitable  $\xi_1 < \xi_2$ , the integrand should vanish, which leads to the following kinetic equation, written down in a compact form by dropping the arguments  $t, x$  and  $\xi$  of the functions  $\Phi, \bar{\Phi}$  and  $\bar{\xi}$ :

$$\partial_t \Phi + \partial_x (\Phi V(\bar{\Phi})(\xi - \bar{\xi})) = 0. \quad (7.2.13)$$

## 7.2.4 Kinetic problem in final form

For easy reference, we collect here the ingredients of the kinetic model in final form. For a given final time  $T > 0$ , we seek a function

$$\Phi : [0, T] \times [0, 1] \times [0, 1] \rightarrow [0, \infty)$$

which satisfies the kinetic equation

$$\begin{aligned} \partial_t \Phi(t, x, \xi) + \partial_x (\Phi(t, x, \xi) V(\bar{\Phi}(t, x)) [\xi - \bar{\xi}(t, x)]) &= 0, \\ t \in (0, T], \quad x \in (0, 1) \end{aligned} \quad (7.2.14)$$

subject to the initial condition

$$\Phi(0, x, \xi) = \Phi_0(x, \xi), \quad x \in [0, 1], \quad \Phi_0 : [0, 1] \times [0, 1] \rightarrow [0, \infty) \quad (7.2.15)$$

and zero-flux boundary conditions, i.e.

$$F(t, 0, \xi) = F(t, 1, \xi) = 0 \quad \text{for all } \xi \in [0, 1] \text{ and all } t \in [0, T] \quad (7.2.16)$$

with the “kinetic flux function”

$$F(t, x, \xi) := \Phi(t, x, \xi) V(\bar{\Phi}(t, x)) [\xi - \bar{\xi}(t, x)]. \quad (7.2.17)$$

Recall that we have put  $L = 1$  in the dimensionless form. However, this is not an important restriction in the sequel.

### 7.2.5 Cumulative quantities for the conservation of mass

This subsection is presented for two purposes. First, we introduce a concept that will be important for the eigenvalue analysis of the hyperbolic system (7.2.14) in the asymptotic case  $N \rightarrow \infty$  of infinitely many species which will be presented next. On the other hand, we provide a very simple numerical test for the conservation of mass with respect to the continuum of all species. We first define the primitive  $\Phi^*$  of the phase density  $\Phi$  with respect to the kinetic parameter  $\xi$  by

$$\Phi^*(t, x, \xi) := \int_0^\xi \Phi(t, x, \xi') d\xi'. \quad (7.2.18)$$

Note that

$$\Phi^*(t, x, \xi_2) - \Phi^*(t, x, \xi_1) = \int_{\xi_1}^{\xi_2} \Phi(t, x, \xi') d\xi' \quad (7.2.19)$$

determines the volumetric concentration at  $(t, x)$  occupied by all particles with dimensionless size  $0 \leq \xi_1 \leq \xi_2 \leq 1$ . Then we can also rewrite the moments (7.2.12) of  $\Phi$  in terms of  $\Phi^*$  as

$$\bar{\Phi}(t, x) = \Phi^*(t, x, 1), \quad \bar{\xi}(t, x) = \Phi^*(t, x, 1) - \int_0^1 \Phi^*(t, x, \xi) d\xi, \quad (7.2.20)$$

where we have applied integration by parts for  $\bar{\xi}(t, x)$ . We also obtain from (7.2.14) by using integration by parts the conservation law of mass with respect to all species for all  $t \in (0, T]$  and  $x \in (0, L)$ :

$$\begin{aligned} & \partial_t \Phi^*(t, x, \xi) \\ & + \partial_x \left( V(\Phi^*(t, x, 1)) \left[ \Phi^*(t, x, \xi)(\xi - \bar{\xi}(t, x)) - \int_0^\xi \Phi^*(t, x, \xi) d\xi \right] \right) = 0. \end{aligned} \quad (7.2.21)$$

This may be regarded as a separate kinetic equation for the so-called cumulative phase density  $\Phi^*$ , but we will not use (7.2.20) and (7.2.21) for numerical purposes. Equation (7.2.21) contains exactly the same information as the original kinetic equation, but has two major advantages: The quantity  $\Phi^*$  is a standard volume fraction, and thus has a direct physical meaning. The second advantage is important for the eigenvalue analysis in the asymptotic case  $N \rightarrow \infty$ , namely the fact that the cumulative quantity  $\Phi^*$  has better regularity properties in the case that  $\Phi$  is a distributional or singular solution, which cannot be excluded a priori.

## 7.3 The eigenvalue problem for the kinetic equation

### 7.3.1 Introduction to the eigenvalue problem and formulation of the basic integral equation

Next we will pass from the eigenvalue problems of the hyperbolic systems with finitely many particle species to the eigenvalue problem corresponding to the cumulative kinetic phase density  $\Phi^*(t, x, \xi)$  describing the continuous distribution of particle sizes with the kinetic variable  $\xi \in [0, 1]$ . For this analysis, the arguments  $t$

and  $x$  in  $\Phi^*$  are fixed parameters, which will be omitted in the sequel by writing simply  $\Phi^* = \Phi^*(\xi)$  instead of  $\Phi^*(t, x, \xi)$ .

We start with the hyperbolic system (7.2.5) corresponding to  $N$  different particle species, but with a slight change of notation which is better adapted for the continuum limit  $N \rightarrow \infty$ . We introduce for simplicity the  $N$  equidistant numbers

$$\xi_i := i/N, \quad i = 1, \dots, N, \quad (7.3.1)$$

where  $\xi_i = \delta_{N+1-i}$ , since the finite sequence of the  $\delta_i$  is starting with  $\delta_1 = \xi_N = 1$  and decreasing. Adapted to the definition of the quantities  $\xi_i$ , we will also reverse the numbering of the basic variables  $\phi_i$  in the hyperbolic system (7.2.5) by introducing the new basic variables  $\Phi_i := \phi_{N+1-i}$ . Now we may rewrite (7.2.5) as

$$\partial_t \Phi_i + \partial_x F_i = 0, \quad i = 1, \dots, N, \quad (7.3.2)$$

where the fluxes  $F_i$  are given functions of the new basic variables  $\Phi_i$  according to

$$F_i := \Phi_i \left( \xi_i - \sum_{n=1}^N \Phi_n \xi_n \right) V \left( \sum_{n=1}^N \Phi_n \right), \quad i = 1, \dots, N. \quad (7.3.3)$$

Next, we pass to the cumulative volume fractions  $\Phi_n^*$  and the corresponding cumulative fluxes  $F_n^*$  defined by

$$\Phi_n^* := \sum_{i=1}^n \Phi_i, \quad F_n^* := \sum_{i=1}^n F_i, \quad n = 1, \dots, N. \quad (7.3.4)$$

By using the identities

$$\sum_{i=1}^n \Phi_i \xi_i = \Phi_n^* \xi_n - \sum_{i=1}^{n-1} \Phi_i^* (\xi_{i+1} - \xi_i), \quad n = 1, \dots, N, \quad (7.3.5)$$

we can also express the cumulative fluxes in terms of the cumulative volume fractions as

$$F_n^* = - \left[ \Phi_n^* \left( \Phi_n^* \xi_N - \sum_{i=1}^{N-1} \Phi_i^* (\xi_{i+1} - \xi_i) \right) - \left( \Phi_n^* \xi_n - \sum_{i=1}^{n-1} \Phi_i^* (\xi_{i+1} - \xi_i) \right) \right] V(\Phi_N^*), \quad n = 1, \dots, N. \quad (7.3.6)$$

From these fluxes we form for  $n, k = 1, \dots, N$  the Jacobian  $N \times N$  matrix with the coefficients

$$\frac{\partial F_n^*}{\partial \Phi_k^*} = \frac{\partial F_n^*}{\partial \Phi_k^*}(\Phi_1^*, \dots, \Phi_N^*),$$

and obtain

$$\begin{aligned} & \frac{\partial F_n^*}{\partial \Phi_k^*} \\ &= -\delta_{nk} \left( \Phi_N^* \xi_N - \sum_{i=1}^{N-1} \Phi_i^* (\xi_{i+1} - \xi_i) \right) V(\Phi_N^*) \\ & \quad - \left( \delta_{Nk} \xi_N - (\xi_{k+1} - \xi_k) \sum_{i=k}^N \delta_{i(N-1)} \right) \Phi_n^* V(\Phi_N^*) \\ & \quad + \left( \delta_{nk} \xi_n - (\xi_{k+1} - \xi_k) \sum_{i=k}^N \delta_{i(n-1)} \right) V(\Phi_N^*) \\ & \quad - \delta_{Nk} \left[ \Phi_n^* \left( \Phi_N^* \xi_N - \sum_{i=1}^{N-1} \Phi_i^* (\xi_{i+1} - \xi_i) \right) - \left( \Phi_n^* \xi_n - \sum_{i=1}^{n-1} \Phi_i^* (\xi_{i+1} - \xi_i) \right) \right] V'(\Phi_N^*). \end{aligned} \tag{7.3.7}$$

Next we prescribe a vector with  $N$  real components  $\Psi_1^*, \dots, \Psi_N^*$  and apply the Jacobian matrix in (7.3.7) on it to obtain the resulting vector with components

$$\begin{aligned} & \sum_{k=1}^N \frac{\partial F_n^*}{\partial \Phi_k^*} \Psi_k^* \\ &= -\Psi_n^* \left( \Phi_N^* \xi_N - \sum_{i=1}^{N-1} \Phi_i^* (\xi_{i+1} - \xi_i) \right) V(\Phi_N^*) \\ & \quad - \left( \Psi_N^* \xi_N - \sum_{k=1}^{N-1} (\xi_{k+1} - \xi_k) \Psi_k^* \right) \Phi_n^* V(\Phi_N^*) + \left( \Psi_n^* \xi_n - \sum_{k=1}^{n-1} (\xi_{k+1} - \xi_k) \Psi_k^* \right) V(\Phi_N^*) \\ & \quad - \Psi_N^* \left[ \Phi_n^* \left( \Phi_N^* \xi_N - \sum_{i=1}^{N-1} \Phi_i^* (\xi_{i+1} - \xi_i) \right) - \left( \Phi_n^* \xi_n - \sum_{i=1}^{n-1} \Phi_i^* (\xi_{i+1} - \xi_i) \right) \right] V'(\Phi_N^*). \end{aligned} \tag{7.3.8}$$

The eigenvalue problem for the cumulative  $N \times N$  hyperbolic system

$$\partial_t \Phi_n^* + \partial_x F_n^* = 0, \quad n = 1, \dots, N, \tag{7.3.9}$$

with an eigenvalue  $\lambda$  and an eigenvector  $(\Psi_1^*, \dots, \Psi_N^*)^T$  is

$$\sum_{k=1}^N \frac{\partial F_n^*}{\partial \Phi_k^*} \Psi_k^* = \lambda \Psi_n^*, \quad n = 1, \dots, N, \quad (7.3.10)$$

whereas the eigenvalue problem for the original system reads

$$\sum_{k=1}^N \frac{\partial F_n}{\partial \Phi_k} \Psi_k = \lambda \Psi_n, \quad n = 1, \dots, N. \quad (7.3.11)$$

The relation between (7.3.10) and (7.3.11) is explained in the following lemma.

**Lemma 7.3.1** *For a given vector  $\Phi = (\Phi_1, \dots, \Phi_N)^T \in \mathbb{R}^N$ , let  $\Psi = (\Psi_1, \dots, \Psi_N)^T \in \mathbb{R}^N$  be an eigenvector for the real eigenvalue  $\lambda$  such that (7.3.11) is satisfied. Define the cumulative quantities*

$$\Psi_n^* := \sum_{i=1}^n \Psi_i, \quad n = 1, \dots, N.$$

Then  $\Psi^* = (\Psi_1^*, \dots, \Psi_N^*)^T$  is eigenvector of (7.3.10) with the same eigenvalue  $\lambda$ .

**Proof.** We define for  $n, k = 1, \dots, N$  the Jacobian  $N \times N$  matrix  $\nabla_* F^*$  with the coefficients

$$\frac{\partial F_n^*}{\partial \Phi_k^*} = \frac{\partial F_n^*}{\partial \Phi_k^*}(\Phi_1^*, \dots, \Phi_N^*),$$

the Jacobian  $N \times N$  matrix  $\nabla F$  with the coefficients

$$\frac{\partial F_n}{\partial \Phi_k} = \frac{\partial F_n}{\partial \Phi_k}(\Phi_1, \dots, \Phi_N),$$

and the regular  $N \times N$  matrix

$$\mathbf{T} = \begin{pmatrix} 1 & 0 & \dots & 0 \\ 1 & 1 & \ddots & \vdots \\ \vdots & & \ddots & 0 \\ 1 & \dots & \dots & 1 \end{pmatrix}$$

such that  $\Psi^* = \mathbf{T}\Psi$ . Then we have

$$(\nabla F)\Psi = \lambda\Psi$$

$$\begin{aligned}
&\Leftrightarrow (\nabla F)\mathbf{T}^{-1}(\mathbf{T}\Psi) = \mathbf{T}^{-1}(\lambda\mathbf{T}\Psi) \\
&\Leftrightarrow (\nabla F)\mathbf{T}^{-1}\Psi^* = \mathbf{T}^{-1}(\lambda\Psi^*) \\
&\Leftrightarrow (\mathbf{T}(\nabla F)\mathbf{T}^{-1})\Psi^* = \lambda\Psi^*, \\
&\Leftrightarrow (\nabla_* F^*)\Psi^* = \lambda\Psi^*,
\end{aligned}$$

which is the statement of the lemma.  $\square$

**Corollar 1** Consider a vector  $\Phi^* = (\Phi_1^*, \dots, \Phi_N^*)^\top \in \mathcal{D}$  and define the quantities

$$\bar{\xi} := \sum_{i=1}^N \xi_i \Phi_i, \quad \lambda_\infty := -2\bar{\xi}V(\Phi_N^*) + V(\Phi_N^*)'(\bar{\xi} + \Phi_N^*). \quad (7.3.12)$$

Then the eigenvalues  $\lambda_1(\Phi^*) \geq \lambda_2(\Phi^*) \geq \dots \geq \lambda_N(\Phi^*)$  of the eigenvalue problem (7.3.10) satisfy

$$\bar{\xi} + \frac{\lambda_i(\Phi^*)}{V(\Phi_N^*)} \in (\xi_{i-1}, \xi_i), \quad i = 2, \dots, N, \quad (7.3.13)$$

$$\bar{\xi} + \frac{\lambda_1(\Phi^*)}{V(\Phi_N^*)} \in \left( \bar{\xi} + \frac{\lambda_\infty}{V(\Phi_N^*)}, \xi_1 \right) = \left( \frac{V(\Phi_N^*)'}{V(\Phi_N^*)}(\bar{\xi} + \Phi_N^*) - \bar{\xi}, \xi_1 \right) \quad (7.3.14)$$

**Proof.** The corollary is a direct consequence of Theorem 7.2.1 and Lemma 7.3.1.  $\square$

Lemma 7.3.1 motivates why we consider the cumulative problem (7.3.10) instead of the original problem (7.3.11), because in the limit  $N \rightarrow \infty$  the cumulative eigenvectors will be replaced by integrals.

Let  $\Phi^* : [0, 1] \rightarrow [0, \phi_{\max}]$  be any continuously differentiable and monotone function such that  $\Phi^*(0) = 0$  and  $\Phi^*(1) \leq \phi_{\max}$ . As in (7.2.20), we put

$$\bar{\Phi} = \Phi^*(1), \quad \bar{\xi} = \bar{\Phi} - \int_0^1 \Phi^*(\xi) d\xi, \quad (7.3.15)$$

and require that

$$V(\bar{\Phi}) \neq 0 \quad \text{and} \quad \bar{\Phi} < \phi_{\max}. \quad (7.3.16)$$

The first condition in (7.3.16) implies the second one because of the constitutive law for  $\tilde{V}$  given in (7.2.3). We define for the limit  $N \rightarrow \infty$  the integral operator

$A^* : C^1[0, 1] \rightarrow C^1[0, 1]$  for any continuously differentiable function  $\Psi^* : [0, 1] \rightarrow \mathbb{R}$ , according to (7.3.8) by

$$\begin{aligned} (A^*\Psi^*)(\xi) &:= -\Psi^*(\xi)\bar{\xi}V(\bar{\Phi}) - \left(\Psi^*(1) - \int_0^1 \Psi^*(\eta) d\eta\right)\Phi^*(\xi)V(\bar{\Phi}) \\ &+ \left(\Psi^*(\xi)\xi - \int_0^\xi \Psi^*(\eta) d\eta\right)V(\bar{\Phi}) \\ &- \Psi^*(1) \left[\Phi^*(\xi)\bar{\xi} - \left(\Phi^*(\xi)\xi - \int_0^\xi \Phi^*(\eta) d\eta\right)\right]V'(\bar{\Phi}). \end{aligned} \quad (7.3.17)$$

The analogue of the discrete eigenvalue problem (7.3.10) will now be considered in the limit  $N \rightarrow \infty$  and reads  $A^*\Psi^* = \lambda\Psi^*$ , where we put

$$\xi_\lambda = \bar{\xi} + \frac{\lambda}{V(\bar{\Phi})} \quad (7.3.18)$$

and have to require for all  $\xi \in [0, 1]$  that

$$\begin{aligned} (\xi - \xi_\lambda)\Psi^*(\xi) &= \int_0^\xi \Psi^*(\eta) d\eta + \left(\Psi^*(1) - \int_0^1 \Psi^*(\eta) d\eta\right)\Phi^*(\xi) \\ &+ \Psi^*(1) \frac{V'(\bar{\Phi})}{V(\bar{\Phi})} \left[\Phi^*(\xi)(\bar{\xi} - \xi) + \int_0^\xi \Phi^*(\eta) d\eta\right]. \end{aligned} \quad (7.3.19)$$

### 7.3.2 Solution of the eigenvalue problem

For the solution we distinguish two cases.

**Case A:**  $\Psi^*(1) = 0$ .

This case is important for the discussion of the uniqueness problem of the eigenfunctions corresponding to a given eigenvalue  $\lambda$ . We put  $\xi := 1$  in (7.3.19) to obtain first with (7.3.16)

$$\int_0^1 \Psi^*(\eta) d\eta = 0.$$

Here the eigenvalue problem reduces to

$$(\xi - \xi_\lambda)\Psi^*(\xi) = \int_0^\xi \Psi^*(\eta) d\eta. \quad (7.3.20)$$

We first assume that  $\xi_\lambda \notin [0, 1]$  and obtain from (7.3.20) that  $\Psi^*$  is arbitrarily smooth with zero-derivative, such that  $\Psi^*(\xi) = 0$  for all  $\xi \in [0, 1]$ . Next we assume that  $\xi_\lambda \in [0, 1]$  and obtain from (7.3.20) in the limit  $\xi \rightarrow \xi_\lambda$

$$\int_0^{\xi_\lambda} \Psi^*(\eta) d\eta = 0,$$

which implies

$$(\xi - \xi_\lambda)\Psi^*(\xi) = \int_{\xi_\lambda}^{\xi} \Psi^*(\eta) d\eta.$$

Thus also in this subcase we have that  $\Psi^*$  is arbitrarily smooth with zero-derivative and hence zero for all  $\xi \in [0, 1]$ . We finally conclude that in the case A we have only the zero- solution for  $\Psi^*$ , which is not an eigensolution.

**Case B:**  $\Psi^*(1) = 1$ .

This is a normalization condition for the eigenfunctions which can be assumed without loss of generality if the first case does not hold. Assume first that we have two eigenfunctions  $\Psi_1^*$  and  $\Psi_2^*$  with the same real eigenvalue  $\lambda$ , which both satisfy the normalization condition  $\Psi_1^*(1) = \Psi_2^*(1) = 1$ . Then we conclude that  $\Psi^* = \Psi_1^* - \Psi_2^*$  satisfies equation (7.3.20) in case A with  $\Psi^*(1) = 0$ , such that  $\Psi^*$  is identically zero and hence  $\Psi_1^* = \Psi_2^*$ . This means that in case B, the eigenvalue problem admits at most one eigenfunction with respect to a fixed eigenvalue  $\lambda$ . If we put  $\xi := 1$  in (7.3.19), then we can calculate from (7.3.15) that

$$1 - \int_0^1 \Psi^*(\eta) d\eta = \frac{\xi_\lambda}{1 - \bar{\Phi}} - \bar{\xi} \frac{V'(\bar{\Phi})}{V(\bar{\Phi})}. \quad (7.3.21)$$

Thus the eigenvalue problem may be rewritten in the form

$$\begin{aligned} (\xi - \xi_\lambda)\Psi^*(\xi) &= \int_0^{\xi} \Psi^*(\eta) d\eta + F(\xi) \quad \text{with} \\ F(\xi) &= \frac{\xi_\lambda}{1 - \bar{\Phi}}\Phi^*(\xi) - \frac{V'(\bar{\Phi})}{V(\bar{\Phi})} \left[ \xi\Phi^*(\xi) - \int_0^{\xi} \Phi^*(\eta) d\eta \right]. \end{aligned} \quad (7.3.22)$$

But  $F$  is continuously differentiable on  $\xi \in (0, 1)$  due to our assumptions, and therefore so is the expression  $\Psi^*(\xi)$  on the left-hand side of (7.3.22), except at most for  $\xi = \xi_\lambda \in (0, 1)$ . Thus we define at least for  $\xi \in (0, 1)$ ,  $\xi \neq \xi_\lambda$ , the quantities

$$\Phi(\xi) := \frac{d\Phi^*}{d\xi}(\xi), \quad \Psi(\xi) := \frac{d\Psi^*}{d\xi}(\xi), \quad (7.3.23)$$

and obtain from the first equation in (7.3.22) for  $\xi \in (0, 1)$ ,  $\xi \neq \xi_\lambda$ , the necessary condition

$$\Psi(\xi) = \frac{\Phi(\xi)}{\xi - \xi_\lambda} \left[ \frac{\xi_\lambda}{1 - \bar{\Phi}} - \frac{V'(\bar{\Phi})}{V(\bar{\Phi})} \xi \right]. \quad (7.3.24)$$

In order to obtain a solution of the eigenvalue problem, also the condition (7.3.21) has to be satisfied. This requires that the right-hand side in (7.3.24) is continuous for  $0 \leq \xi \leq 1$  and hence integrable. We summarize our results and interpret equation (7.3.24) as an eigensolution of the original eigenvalue problem (7.3.11) in the continuum limit  $N \rightarrow \infty$ , provided that

a) in the case  $\xi_\lambda \in [0, 1]$  there exists for  $\xi \in [0, 1] \setminus \{\xi_\lambda\}$  the limit

$$\Psi(\xi_\lambda) := \lim_{\xi \rightarrow \xi_\lambda} \frac{\Phi(\xi)}{\xi - \xi_\lambda} \left[ \frac{\xi_\lambda}{1 - \bar{\Phi}} - \frac{V'(\bar{\Phi})}{V(\bar{\Phi})} \xi \right], \quad (7.3.25)$$

b) the integration constant  $C \in \mathbb{R}$  of the primitive function

$$\Psi^*(\xi) := C + \int_0^\xi \frac{\Phi(\eta)}{\eta - \xi_\lambda} \left[ \frac{\xi_\lambda}{1 - \bar{\Phi}} - \frac{V'(\bar{\Phi})}{V(\bar{\Phi})} \eta \right] d\eta, \quad \xi \in [0, 1], \quad (7.3.26)$$

is chosen such that the normalization condition  $\Psi^*(1) = 1$  is satisfied.

If  $\Psi^*$  is a normalized eigensolution of the eigenvalue problem (7.3.19) with eigenvalue  $\xi_\lambda$ , then it is necessarily given by (7.3.26).

In numerical tests it is very important to decide whether the values of  $\xi_\lambda$  in (7.3.18) for the discrete eigenvalue problem are in the interval  $[0, 1]$  or not. For this purpose we have done extensive numerical studies which show that the discrete values for  $\xi_\lambda$  are in general in the interval  $[0, 1]$ .

## 7.4 Numerical scheme

### 7.4.1 Discretization parameters and boundary conditions

We discretize time by setting  $t_m := m\delta_t$  for  $m = 0, \dots, M$ , where  $\delta_t := T/M$  with  $M \in \mathbb{N}$ . The phase space is discretized by  $x_k := k\delta_x$  for  $k = 0, \dots, \mathcal{K}$ , where  $\delta_x := L/\mathcal{K}$  and  $\mathcal{K} \in \mathbb{N}$  is given. We set  $\xi_n := n\delta_\xi$  for  $n = 0, \dots, \mathcal{N}$ , where  $\mathcal{N} \in \mathbb{N}$  and  $\delta_\xi := 1/\mathcal{N}$ . The numbers  $M$ ,  $\mathcal{K}$  and  $\mathcal{N}$  are given discretization parameters. Finally, we denote by  $\phi_{k,n}^m$  the finite difference approximation of  $\Phi(t_m, x_{k-1/2}, \xi)$  for  $\xi_{n-1} \leq \xi < \xi_n$ . At a fixed time  $t = t_m$ , we discretize  $\Phi = \Phi(t_m, x, \xi)$  in the  $x$ - $\xi$  phase space by the piecewise constant function  $\Phi_D(t_m, x, \xi)$ , where  $\Phi_D(t_m, x, \xi) = \phi_{k,n}^m$  on the phase space cell

$$\Omega_{k,n} := \{(x, \xi) \mid x_{k-1} \leq x < x_k, \xi_{n-1} \leq \xi < \xi_n\}, \quad k = 1, \dots, \mathcal{K}, \quad n = 1, \dots, \mathcal{N}.$$

Thus,  $\Phi_D(t_m, \cdot, \cdot)$  is given by a  $\mathcal{K} \times \mathcal{N}$  matrix. However, for the numerical computation we only store the updated current initial data, starting at the current time step with the initial matrix  $(\Phi_{k,n}^0) \in \mathbb{R}^{\mathcal{K} \times \mathcal{N}}$ .

Formulating boundary conditions for a kinetic scheme is in general a subtle issue. Below we will discuss two cases for numerical boundary conditions, which can be sufficiently described in every time step  $t_m$  by two given vectors

$$\Phi_-^m := (\phi_{0,1}^m, \phi_{0,2}^m, \dots, \phi_{0,\mathcal{N}}^m), \quad \Phi_+^m := (\phi_{\mathcal{K}+1,1}^m, \phi_{\mathcal{K}+1,2}^m, \dots, \phi_{\mathcal{K}+1,\mathcal{N}}^m) \in \mathbb{R}^{\mathcal{N}}.$$

They describe essentially initial value problems, but from the numerical point of view they are still important, since the computation can only be performed on a finite domain.

#### Case 1: Boundary data for Riemann initial data.

This is the simplest case, where we can choose the boundary data as

$$\phi_{0,n}^m = \phi_{1,n}^m, \quad \phi_{\mathcal{K}+1,n}^m = \phi_{\mathcal{K},n}^m, \quad n = 1, \dots, \mathcal{N}. \quad (7.4.1)$$

This is sufficient for the numerical study of certain Riemann initial value problems on the spatial computational domain  $[0, L]$ , provided that up to the final time  $t = T$ , no signal coming from the interior of the spatial domain has reached the boundaries.

**Case 2: Periodic boundary conditions.**

If we have a periodic initial phase density which satisfies the condition

$$\Phi(0, x, \xi) = \Phi(0, x + L, \xi) \quad \text{for all } x \in \mathbb{R} \text{ and all } \xi \in [0, 1],$$

then we can just put boundary data

$$\phi_{0,n}^m = \phi_{\mathcal{K},n}^m, \quad \phi_{\mathcal{K}+1,n}^m = \phi_{1,n}^m, \quad n = 1, \dots, \mathcal{N}. \quad (7.4.2)$$

In these two cases described above, we define the boundary phase cells

$$\begin{aligned} \Omega_{0,n} &:= \{(x, \xi) \mid -\delta_x \leq x < 0, \xi_{n-1} \leq \xi < \xi_n\}, \\ \Omega_{\mathcal{K}+1,n} &:= \{(x, \xi) \mid L \leq x < L + \delta_x, \xi_{n-1} \leq \xi < \xi_n\}, \end{aligned}$$

on which  $\Phi_D(t_m, x, \xi)$  assumes the piecewise constant boundary values of (7.4.1) or (7.4.2). Thus,  $\Phi_D(t_m, x, \xi)$  is given on the extended domain  $-\delta_x \leq x \leq L + \delta_x$ ,  $0 \leq \xi \leq 1$  in a piecewise constant manner by the extended matrix  $(\phi_{k,n}^m)_{k=0,\dots,\mathcal{K}+1, n=1,\dots,\mathcal{N}}$ . Finally, we define for  $k = -1, \dots, \mathcal{K}$  the quantities  $x_{k+1/2} := (k + 1/2)\delta_x$ . For  $k = 0, \dots, \mathcal{K}$  and  $n = 1, \dots, \mathcal{N}$ , we define the intervals  $\tilde{J}_k := [x_{k-1/2}, x_{k+1/2}]$  and the rectangles, also-called dual phase space cells,  $\tilde{\Omega}_{k,n} := \tilde{J}_k \times [\xi_{n-1}, \xi_n]$ . The latter have the area  $|\tilde{\Omega}_{k,n}| = \delta_x \delta_\xi$ , as have the cells  $\Omega_{k,n}$ . However, for the sedimentation process in a closed vessels we need the so-called zero-flux boundary condition, which cannot be captured appropriate by this approach presented below. This boundary condition has to supplement the discretization of the kinetic equation which will be described now.

### 7.4.2 Discretization of the kinetic equation

Using the kinetic equation (7.2.14), we can exactly calculate at time  $t = t_m$  the time derivative of the integral average

$$\tilde{\phi}_{k,n}(t) := \frac{1}{\delta_x \delta_\xi} \iint_{\tilde{\Omega}_{k,n}} \Phi_D(t, x, \xi) dx d\xi, \quad k = 0, \dots, \mathcal{K}, \quad n = 1, \dots, \mathcal{N}. \quad (7.4.3)$$

To this end, we consider for  $\xi_{n-1} < \xi < \xi_n$  the relationships

$$\Phi_D(t_m, x_{k-1/2}, \xi) = \phi_{k,n}^m, \quad k = 0, \dots, \mathcal{K} + 1, \quad n = 1, \dots, \mathcal{N}. \quad (7.4.4)$$

Using the following definitions, which are valid for every  $x$  with  $x_{k-1} < x < x_k$ ,

$$A_k^m := \int_0^1 \Phi_D(t_m, x, \xi) d\xi = \delta_\xi \sum_{n=1}^{\mathcal{N}} \phi_{k,n}^m,$$

$$B_k^m := \int_0^1 \xi \Phi_D(t_m, x, \xi) d\xi = \delta_\xi \sum_{n=1}^{\mathcal{N}} \phi_{k,n}^m \frac{\xi_n + \xi_{n-1}}{2},$$

we obtain by taking the integral average of (7.2.14) with respect to the phase space cell  $\tilde{\Omega}_{k,n}$ :

$$\begin{aligned} & \frac{d\tilde{\phi}_{k,n}}{dt}(t_m) \\ & + \frac{1}{\delta_x \delta_\xi} \int_{\xi_{n-1}}^{\xi_n} (\phi_{k+1,n}^m V(A_{k+1}^m)(\xi - B_{k+1}^m) - \phi_{k,n}^m V(A_k^m)(\xi - B_k^m)) d\xi = 0, \end{aligned} \quad (7.4.5)$$

which implies

$$\begin{aligned} \delta_x \frac{d\tilde{\phi}_{k,n}}{dt}(t_m) &= -\phi_{k+1,n}^m V(A_{k+1}^m) \left( \frac{\xi_n + \xi_{n-1}}{2} - B_{k+1}^m \right) + \phi_{k,n}^m V(A_k^m) \left( \frac{\xi_n + \xi_{n-1}}{2} - B_k^m \right), \\ k &= 0, \dots, \mathcal{K}, \quad n = 1, \dots, \mathcal{N}. \end{aligned}$$

Note that for the integration with respect to  $x$ , we have used here the fundamental theorem of infinitesimal calculus, and the integration with respect to  $\xi$  has been performed exactly as well, so conservativity is ensured. Consequently, for the time evolution, the first proposed numerical scheme (Scheme 1) is the following:

$$\phi_{k,n}^{m+1} = \frac{1}{2} (\phi_{k+1,n}^m + \phi_{k-1,n}^m) - \frac{\delta_t}{2} \left( \frac{d\tilde{\phi}_{k,n}}{dt} + \frac{d\tilde{\phi}_{k-1,n}}{dt} \right)$$

$$\begin{aligned}
&= \frac{1}{2}(\phi_{k+1,n}^m + \phi_{k-1,n}^m) - \frac{1}{2} \frac{\delta_t}{\delta_x} \left[ \phi_{k+1,n}^m V(A_{k+1}^m) \left( \frac{\xi_n + \xi_{n-1}}{2} - B_{k+1}^m \right) \right. \\
&\quad \left. - \phi_{k-1,n}^m V(A_{k-1}^m) \left( \frac{\xi_n + \xi_{n-1}}{2} - B_{k-1}^m \right) \right], \quad k = 1, \dots, \mathcal{K}, \quad n = 1, \dots, \mathcal{N}.
\end{aligned}$$

If we use the following marching formula in conservation form:

$$\begin{aligned}
\phi_{k,n}^{m+1} &= \phi_{k,n}^m - \lambda (h_{k+1/2,n}^m - h_{k-1/2,n}^m), \quad \lambda := \frac{\delta_t}{\delta_x}, \\
k &= 1, \dots, \mathcal{K}, \quad n = 1, \dots, \mathcal{N},
\end{aligned} \tag{7.4.6}$$

where  $h_{k+1/2,n}^m$  represents the numerical flux, Scheme 1 is the well-known conservative first-order central difference scheme of Lax-Friedrichs with numerical fluxes

$$\begin{aligned}
h_{k+1/2,n}^m &= h_n(\Phi_k^m, \Phi_{k+1}^m) = \frac{1}{2\lambda} (\phi_{k,n}^m - \phi_{k+1,n}^m) + \frac{1}{2} (\bar{f}_n(\Phi_k^m) + \bar{f}_n(\Phi_{k+1}^m)), \\
k &= 0, \dots, \mathcal{K}, \quad n = 1, \dots, \mathcal{N},
\end{aligned}$$

with  $\Phi_k^m := (\phi_{k,1}^m, \dots, \phi_{k,\mathcal{N}}^m)$  and  $\bar{f}_n(\Phi_k^m) := \phi_{k,n}^m v_n(\Phi_k^m)$ , where  $v_n(\Phi_k^m)$  is defined by

$$v_n(\Phi_k^m) := V(A_k^m) \left( \frac{1}{2} (\xi_n + \xi_{n-1}) - B_k^m \right). \tag{7.4.7}$$

We also define the vector  $\bar{\mathbf{f}}(\Phi_k^m) := (\bar{f}_1(\Phi_k^m), \dots, \bar{f}_{\mathcal{N}}(\Phi_k^m))^T$ . This scheme is stable provided the following CFL condition holds

$$\lambda \max \rho(\mathbf{J}_{\bar{\mathbf{f}}}(\Phi_k^m)) \leq 1, \tag{7.4.8}$$

where  $\rho(\cdot)$  denotes the spectral radius, and  $\mathbf{J}_{\bar{\mathbf{f}}}(\Phi_k^m)$  the  $\mathcal{N} \times \mathcal{N}$  Jacobian of  $\bar{\mathbf{f}}(\Phi_k^m)$ . We approximate  $\max \rho(\mathbf{J}_{\bar{\mathbf{f}}}(\Phi_k^m))$  by

$$\alpha := \max_{k,m,n} |v_n(\Phi_k^m)|.$$

The second proposed numerical scheme (Scheme 2), which is introduced in [25], is given by (7.4.6) with the following numerical fluxes, where  $v_n(\Phi_k^m)$  is defined by (7.4.7):

$$\begin{aligned}
h_{k+1/2,n}^m &= \phi_{k,n}^m \max\{0, v_n(\Phi_{k+1}^m)\} + \phi_{k+1,n}^m \min\{0, v_n(\Phi_{k+1}^m)\}, \\
k &= 0, \dots, \mathcal{K}, \quad n = 1, \dots, \mathcal{N}.
\end{aligned} \tag{7.4.9}$$

When negative velocities are present, which is possible in our model, numerical experiments with Scheme 2 produce sharply resolved interfaces, but with overshoot or oscillations in certain situations. To overcome this shortcoming we propose a more viscous version of Scheme 2 that provides a good compromise between sharply resolved interfaces and suppression of overshoots. Scheme 3 is the conservative formula (7.4.6) with numerical fluxes

$$h_{k+1/2,n}^m = \frac{1}{2} \left\{ \phi_{k+1,n}^m v_n(\Phi_{k+1}^m) + \phi_{k,n}^m v_n(\Phi_k^m) \right\} - \frac{E_{k+1}^m}{2} (\phi_{k+1,n}^m - \phi_{k,n}^m) \\ - \frac{\phi_{k,n}^m}{2} |v_n(\Phi_k^m) - v_n(\Phi_{k+1}^m)| \operatorname{sgn}(\phi_{k+1,n}^m - \phi_{k,n}^m), \\ k = 0, \dots, \mathcal{K}, \quad n = 1, \dots, \mathcal{N},$$

where  $E_{k+1}^m := \max\{|v_1(\Phi_{k+1}^m)|, \dots, |v_{\mathcal{N}}(\Phi_{k+1}^m)|\}$ , and which is also introduced in [25].

For Schemes 2 and 3, according to [25], there is not a proof of stability, but based on an analysis of a model with non-negative velocities, the following CFL condition is given

$$\lambda \max_{k,m,n} |v_n(\Phi_k^m)| =: \lambda \alpha \leq \frac{1}{2}. \quad (7.4.10)$$

It is easy to prove that for our model  $\alpha = 1$ .

To compute  $\phi_{0,n}^m$  and  $\phi_{\mathcal{K}+1,n}^m$  we utilize (7.4.1) or (7.4.2) for the Riemann or the periodic initial value problem, respectively. However, for the description of a sedimentation process in a closed vessel, we have to formulate zero-flux boundary conditions and to modify the scheme as described below.

### Case 3: Zero-flux boundary conditions.

When dealing with zero-flux boundary conditions, we always set in the conservative formula (7.4.6)

$$h_{1/2,n}^m = h_{\mathcal{K}+1/2,n}^m = 0, \quad m = 0, \dots, M, \quad n = 1, \dots, \mathcal{N}. \quad (7.4.11)$$

### 7.4.3 Numerical test of mass conservation

From the numerical point of view, we compute the original phase density  $\Phi$  in terms of the matrix with coefficients  $\phi_{k,n}^m$  according to the numerical scheme described above. In order to justify the numerical mass conservation for a sedimentation process in a closed vessel, we only have to check that the ‘species vector’ with components

$$S_n^m := \sum_{k=1}^{\mathcal{K}} \phi_{k,n}^m, \quad n = 1, \dots, \mathcal{N}, \quad (7.4.12)$$

is approximatively conserved in time, i.e. independent on the time step  $t_m$ . If we define at the current time step  $t_m$  the cumulative  $\mathcal{K} \times \mathcal{N}$  phase density matrix with coefficients

$$\phi_{k,n}^{*m} := \sum_{\nu=1}^n \phi_{k,\nu}^m, \quad (7.4.13)$$

then we can also compute at each time step  $t_m$  the cumulative  $\mathcal{N}$ -vector with coefficients

$$S_n^{*m} := \sum_{k=1}^{\mathcal{K}} \phi_{k,n}^{*m} = \sum_{k=1}^{\mathcal{K}} \sum_{\nu=1}^n \phi_{k,\nu}^m \quad (7.4.14)$$

for the indices  $n = 1, \dots, \mathcal{N}$ . Instead of using (7.4.12), we can also check numerically whether this cumulative vector is independent on the time step  $t_m$  in order to justify mass conservation for the batch sedimentation process. Of course, for the implementation we need not calculate and store the cumulative matrix with the coefficients given in (7.4.13) because we can directly calculate the double sum on the right hand side of (7.4.14). The conservation property of  $S_k^m$  may now be interpreted as the fact that none of the species will exchange mass with other species or with the fluid, so that the total mass of each species is conserved during the sedimentation process.

## 7.5 Numerical examples

Recall that the equi-distribution of particle size is represented by the distribution function

$$\mathcal{F}_{\text{eq}}(\xi) := \xi, \quad \xi \in [0, 1]. \quad (7.5.1)$$

On the other hand, the Rosin-Rammler distribution function is given by

$$\mathcal{F}_{\text{RR}}(\xi) := 1 - \exp\left(-\left[\frac{d_1\sqrt{\xi}}{l}\right]^m\right), \quad \xi \in [0, 1], \quad (7.5.2)$$

where  $l$  is a characteristic size,  $m$  is a uniformity coefficient, and  $d_1$  is the diameter of the largest species. Since  $\mathcal{F}_{\text{RR}}(1) < 1$ , we use the normalized version

$$\mathcal{F}_{\text{RRn}}(\xi) := \mathcal{F}_{\text{RR}}(\xi)/\mathcal{F}_{\text{RR}}(1), \quad \xi \in [0, 1]. \quad (7.5.3)$$

If  $\phi_{\text{tot}}(x)$  denotes the initial profile of total solids volume fraction, then the initial condition of the solids phase density of a suspension with particle size distribution  $\mathcal{F}(\xi)$  is

$$\Phi_0(x, \xi) = \phi_{\text{tot}}(x)\mathcal{F}'(\xi), \quad x \in [0, L], \quad \xi \in [0, 1], \quad \mathcal{F}'(\xi) := \frac{d}{d\xi}\mathcal{F}(\xi). \quad (7.5.4)$$

In all examples, we employ  $\tilde{V}(\phi)$  given by (7.2.3) with  $\gamma = 2.7$ ,  $\phi_{\text{max}} = 0.8$  and  $\phi_{\text{q}} = (\gamma\phi_{\text{max}} - 1)/(\gamma - 1) = 0.6824$ , so the transition between the linear and non-linear portions of  $\tilde{V}(\phi)$  is smooth.

### 7.5.1 Examples with zero-flux boundary conditions

**Example 7.1: Sedimentation of a suspension with equi-distribution of particle size**

As an example where the boundary conditions are of zero-flux type, we present the simulation of a sedimentation of a suspension with equi-distributed particle sizes in a closed vessel. The normalized material parameters are  $L = 1$ ,  $v_1 = 1$ , and

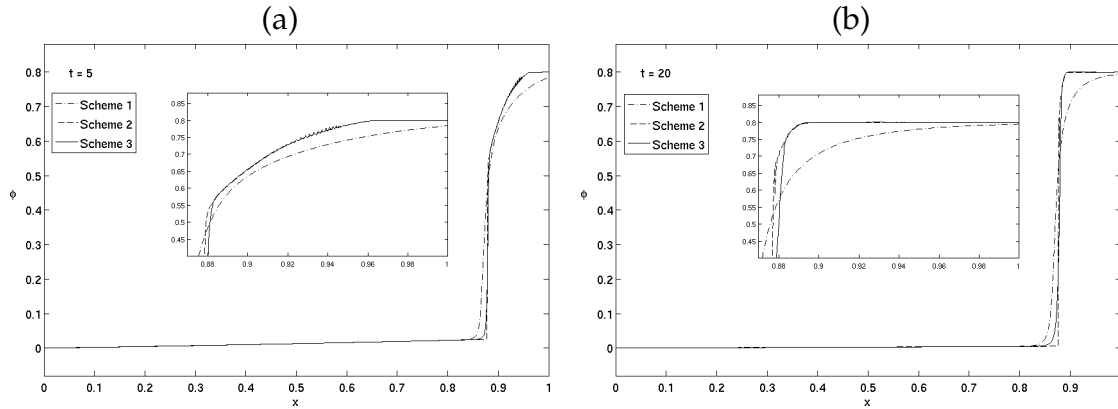


Figure 7.1: Example 7.1: Comparison of numerical schemes for the simulated total solids volume fraction as a function of the spatial position. (a)  $t = 5$ , (b)  $t = 20$ .

the initial total solids volume fraction  $\phi_{\text{tot}}(x) = 0.1$ ,  $x \in [0, L]$ ; and the discretization parameters are  $\delta_x = 1/3600$ ,  $\lambda = 0.5$  and  $\delta_\xi = 1/128$ . (Note that with these parameters, we measure time in multiples of the time a particle of the largest species needs to settle through the vessel in pure fluid.)

In this example, we record approximate  $L^1$  errors defined with respect to the reference solution. We introduce two types of  $L^1$  error, denoted  $e_1$  and  $e_2$ , which are defined by

$$e_1 := \tilde{\delta}_\xi \delta_x \sum_{n=1}^{\mathcal{N}} \sum_{j=1}^{\mu} \sum_{k=M_L}^{M_R} |\tilde{\phi}_{\mu(n-1)+j,k}^m - \phi_{n,k}^m|, \quad e_2 := \tilde{\delta}_\xi \delta_x \sum_{n=1}^{\mathcal{N}} \sum_{j=1}^{\mu} \left| \sum_{k=M_L}^{M_R} (\tilde{\phi}_{\mu(n-1)+j,k}^m - \phi_{n,k}^m) \right|,$$

where  $\tilde{\phi}_{\tilde{n},l}^m$  and  $\phi_{n,l}^m$  are the reference solution for  $\xi = \xi_{\tilde{n}}$  and the approximate solution for  $\xi = \xi_n$ , respectively, both at  $x = x_l$  and  $t = t_m$ ;  $\mu$  is the value of  $\mathcal{N}$  of the reference solution divided by that of the approximate solution;  $M_L$  and  $M_R$  are the indices of the positions between which we calculate the errors of the numerical approximation; and  $\tilde{\delta}_\xi$  is the size discretization parameter of the reference solution. The error study of the numerical schemes is made using a reference solution calculated with Scheme 3 with the size discretization parameter  $\tilde{\delta}_\xi = 1/128$ .

Figures 7.1 and 7.2 show the simulated total solids volume fraction as a function

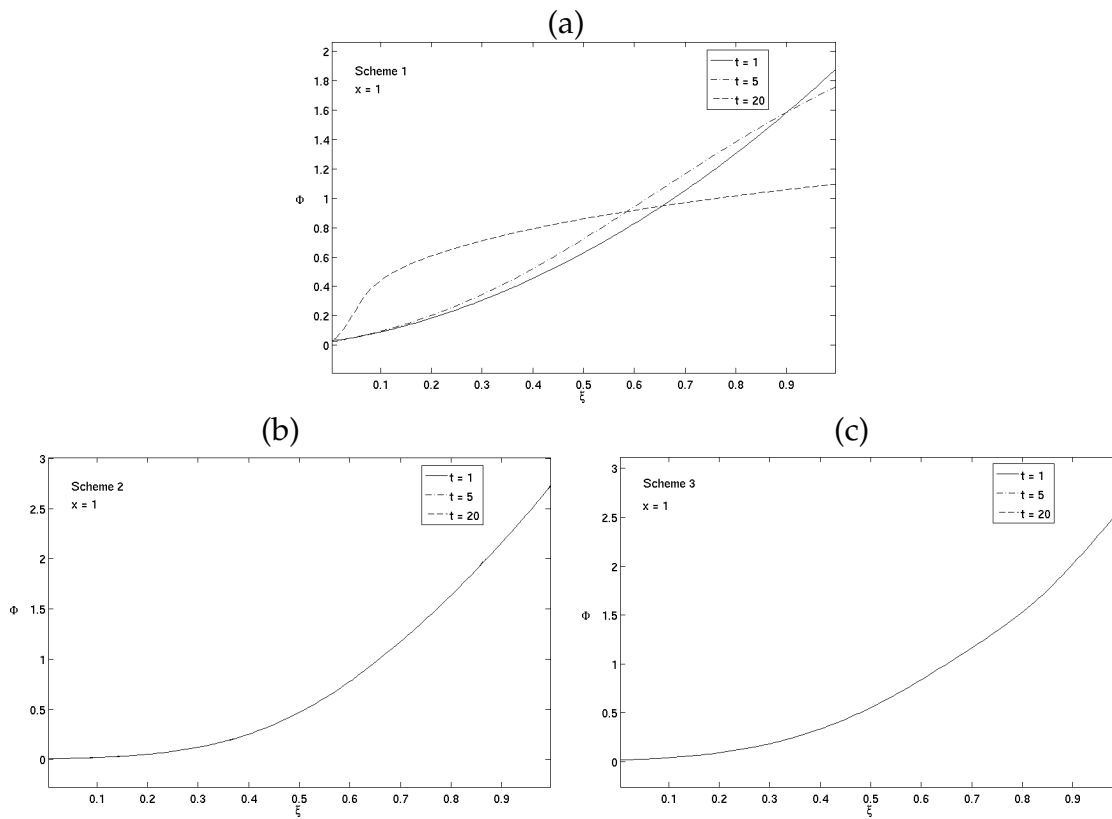


Figure 7.2: Example 7.1: Comparison of numerical schemes for the simulated solids phase density as a function of the normalized squared size at  $x = 1$  for three different times. (a) Scheme 1, (b) Scheme 2, (c) Scheme 3.

of the spatial position for  $t = 5$  and  $t = 20$ , and the simulated solids phase density in function of the normalized squared size for  $t = 1$ ,  $t = 5$  and  $t = 20$ , respectively, produced by Schemes 1, 2 and 3, while Tables 7.1 and 7.2 display the approximate  $L^1$  errors for, the solids phase density and the solids volume fraction, respectively, measured over the domain  $[0, 1] \times [0, 1]$ .

Figure 7.1 shows that Scheme 2 introduces less numerical diffusion than Scheme 1 and Scheme 3 do, but with spurious oscillations, while both tables indicate that Scheme 3 yields solutions with less  $L^1$  error and greater convergence rate. Moreover, Figure 7.2 shows the increasing numerical viscosity of the Scheme 1 as

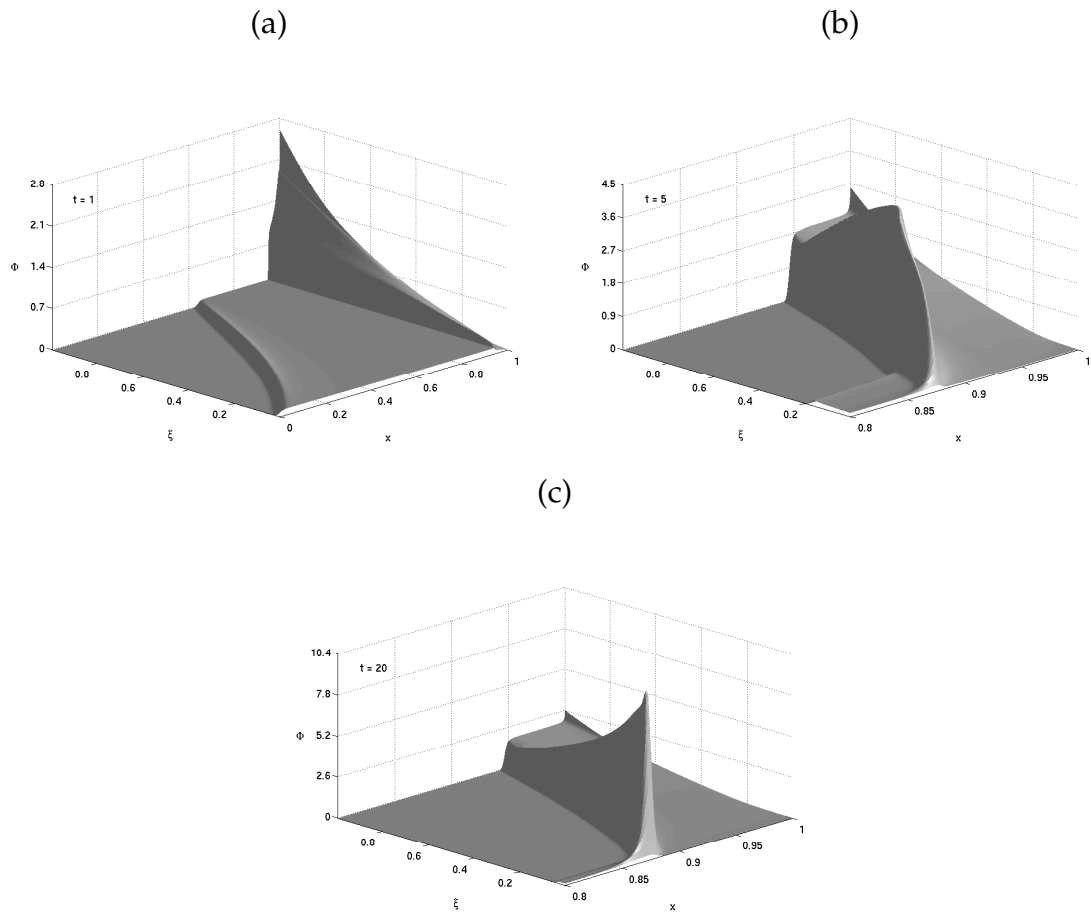


Figure 7.3: Example 7.1: Simulated solids phase density at (a)  $t = 1$ , (b)  $t = 5$ , (c)  $t = 20$ .

the time advances, while solutions at  $x = 1$  generated by Scheme 2 and Scheme 3 do not change. Therefore, we choose the Scheme 3 for simulating all the examples of this work.

Figure 7.3 shows the simulated solids phase density as a function of the normalized squared size and the spatial position, at  $t = 1$ ,  $t = 5$  and  $t = 20$ , produced by Scheme 3.

In Figures 7.3 (a) and (b) we observe that the larger particles settle faster than the smaller ones, and therefore the larger ones fill the bottom of the vessel and form

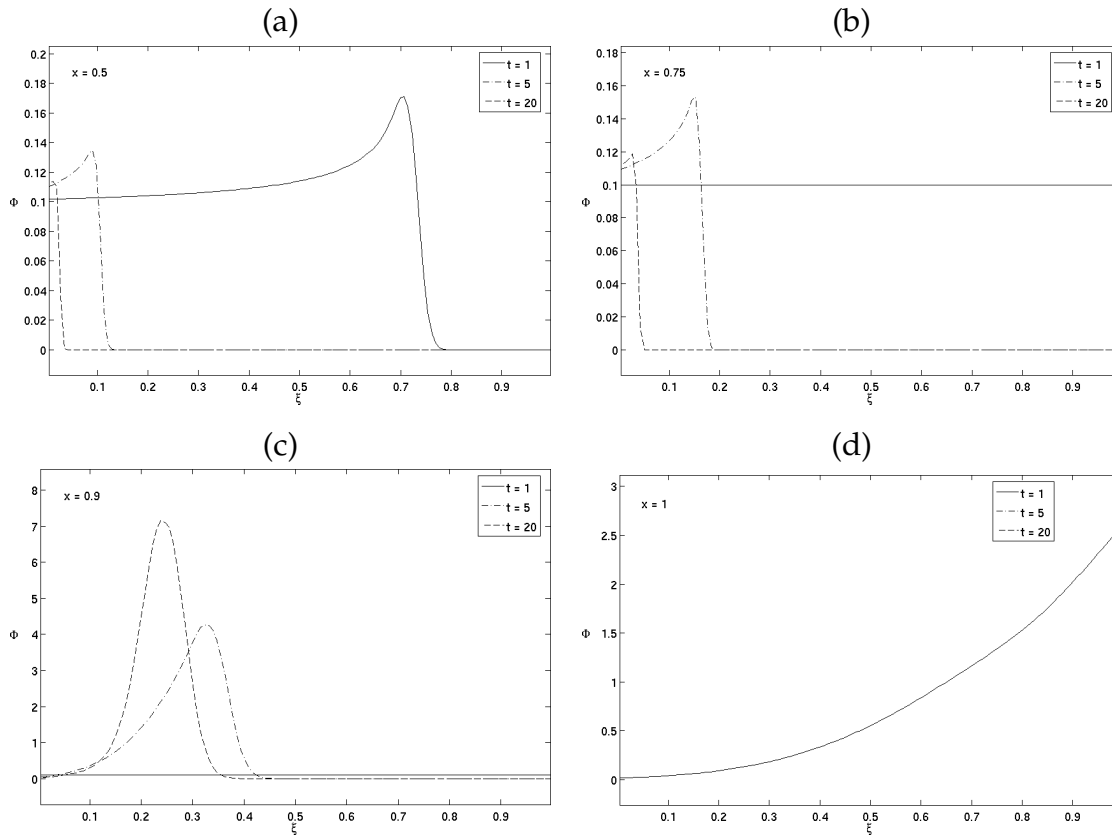


Figure 7.4: Example 7. 1: Simulated solids phase density as a function of the normalized squared size for three different times. (a)  $x = 0.5$ , (b)  $x = 0.75$ , (c)  $x = 0.9$ , (d)  $x = 1.0$ .

a thick sediment layer. We also see that the smaller particles are partially removed from the bottom and with those in suspension form a very thin and concentrated sediment layer above the larger ones.

The formation of the concentrated sediment upper layer is explained by the form of the flux function (7.2.17). We observe, for fixed  $x$ , that if the normalized squared size,  $\xi$ , of a particle is smaller than the average size  $\bar{\xi}$ , then the particle will move upwards due to the negative value of the flux, yielding an accumulation of particles of the same size in the upper zone of the suspension.

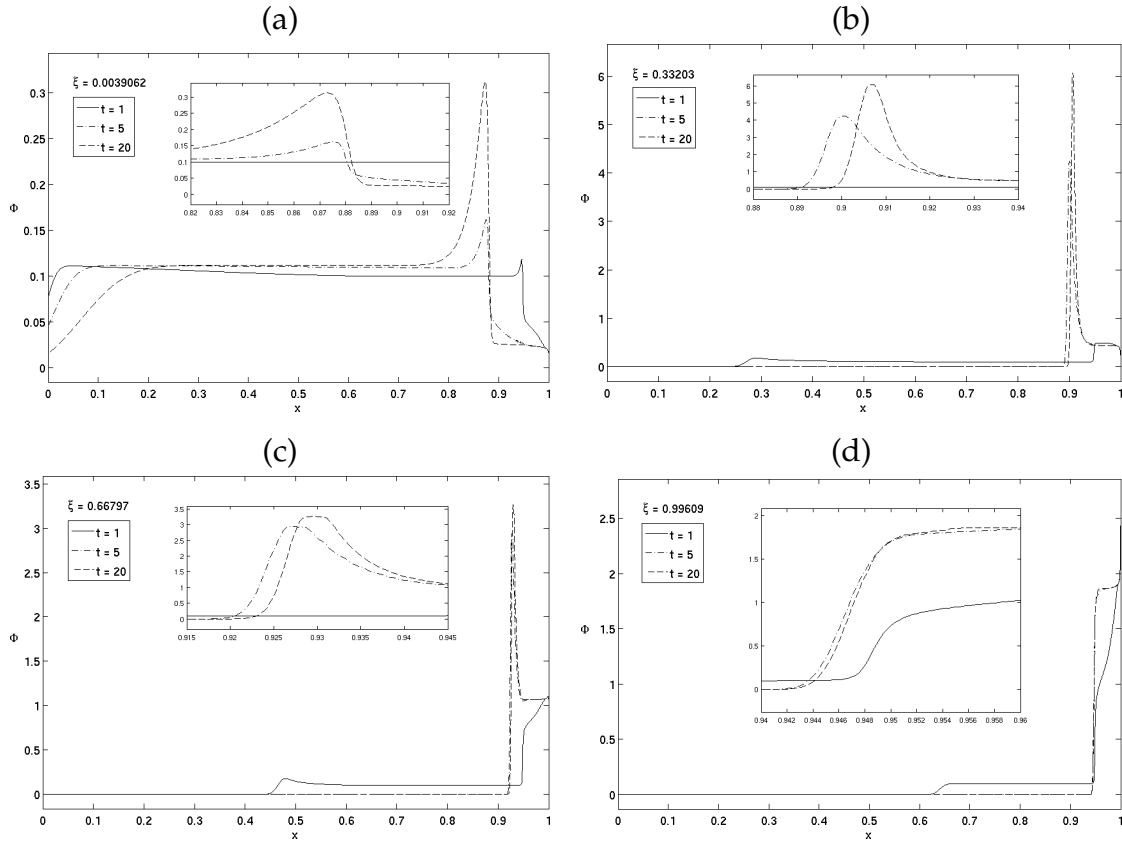


Figure 7.5: Example 7.1: Simulated solids phase density as a function of the spatial position for three different times. (a)  $\xi = 0.0039062$ , (b)  $\xi = 0.33203$ , (c)  $\xi = 0.66797$ , (d)  $\xi = 0.99609$ .

Figure 7.4 shows the simulated solids phase density as a function of the normalized squared size at  $x = 0.5$ ,  $x = 0.75$ ,  $x = 0.9$  and  $x = 1.0$ , for the times  $t = 1$ ,  $t = 5$  and  $t = 20$ , produced by Scheme 3.

In Figures 7.4 (a) and 7.4 (b) we observe that at  $x = 0.5$  and  $x = 0.75$  the total volume fraction  $\bar{\Phi}$ , the average normalized squared size  $\bar{\xi}$  and the width of the size range  $w_r$  decrease as the time advances. Moreover,  $\bar{\xi}$  is on the right half of the size range. In Figure 7.4 (c) we see that at  $x = 0.9$   $\bar{\xi}$  and  $w_r$  decrease as the time advances, while the evolution of  $\bar{\Phi}$  is not evident, but from Figure 7.1 we can see that  $\bar{\Phi}$  in-

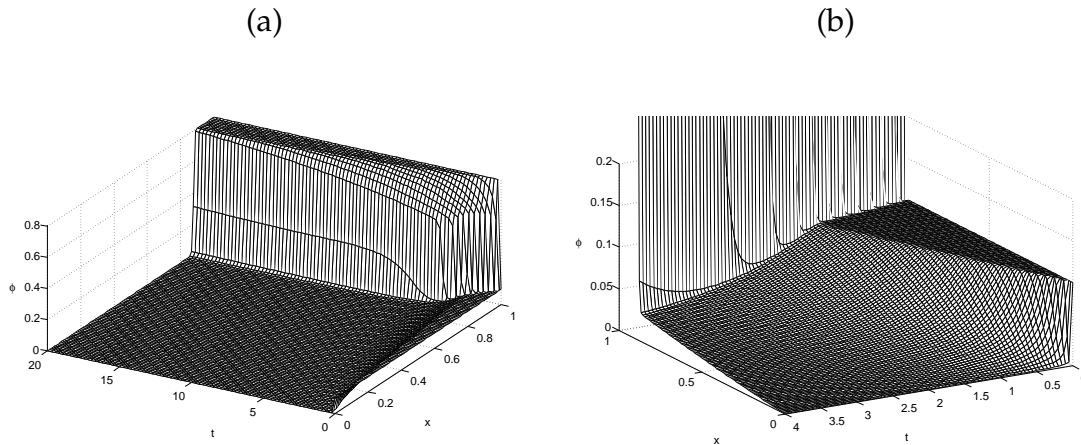


Figure 7.6: Example 7.1: Simulated total solids volume fraction until (a)  $t = 20$ , (b)  $t = 4$ .

crease. Likewise,  $\bar{\xi}$  is on the right half of the size range. In Figure 7.4 (d) we observe that at the bottom of the vessel  $\bar{\Phi}$ ,  $\bar{\xi}$  and  $w_r$  do not change, and  $\bar{\xi}$  is on the right half of the size range.

Figure 7.5 shows the simulated solids phase density as a function of the spatial position for  $\xi = 0.0039602$ ,  $\xi = 0.33203$ ,  $\xi = 0.66797$ , and  $\xi = 0.99609$ , for the times  $t = 1$ ,  $t = 5$  and  $t = 20$ , produced by Scheme 3.

In Figure 7.5 (a) we see that for the smallest species the peak of concentration moves upwards. In Figures 7.5 (b) and 7.5 (c) we observe that the peak of concentration for  $\xi = 0.33203$  and  $\xi = 0.66797$  moves downwards, and at  $t = 1$  there is a peak of concentration at the upper part of the suspension. In Figure 7.5 (d) we see that for the largest species there is a peak of concentration at the bottom, and at  $t = 1$  there is a smooth change of concentration at the upper part of the suspension.

Figure 7.6 shows the simulated total solids volume fraction until  $t = 20$ , and a zoom between  $t = 0$  and  $t = 4$  to see this zone in great detail.

$\mathcal{N}$ $= 1/\delta_\xi$	$t = 1$				$t = 20$			
	$e_1$ $10^{-3}$	Conv. rate	$e_2$ $10^{-6}$	Conv. rate	$e_1$ $10^{-3}$	Conv. rate	$e_2$ $10^{-6}$	Conv. rate
	Scheme 1							
2	24.020		0.1082		91.733		69.424	
4	14.686	0.710	0.4834	-2.160	89.446	0.0364	69.513	-0.0018
8	9.922	0.566	0.1678	1.526	88.188	0.0204	69.189	0.0067
16	7.935	0.322	0.2264	-0.432	85.811	0.0394	67.669	0.0320
32	7.163	0.148	0.1965	0.204	84.528	0.0217	67.739	-0.0015
	Scheme 2							
2	20.946		0.1893		73.260		189.835	
4	11.506	0.864	0.3310	-0.807	49.957	0.552	91.324	1.056
8	6.284	0.873	0.2335	0.503	31.725	0.655	65.466	0.480
16	3.461	0.861	0.1050	1.153	26.695	0.249	39.736	0.720
32	2.089	0.728	0.0795	0.402	24.806	1.059	21.648	0.876
	Scheme 3							
2	20.909		0.1907		73.140		186.852	
4	11.506	0.862	0.3310	-0.796	49.957	0.550	91.324	1.033
8	6.037	0.930	0.0824	2.007	29.633	0.754	36.368	1.328
16	3.087	0.968	0.0358	1.204	16.386	0.855	14.537	1.323
32	1.554	0.990	0.0197	0.864	8.172	1.004	6.722	1.113

Table 7.1: Example 7.1: Approximate  $L^1$  errors for the solids phase density.

### Example 7.2: Steady state of a sedimentation of a suspension with equi-distribution of particle size

Here we present the simulation of the steady state of a sedimentation of a suspension with particle size equi-distribution in a closed vessel. The material parameters are  $L = 1$ ,  $v_1 = 1$ , and the initial total solids volume fraction  $\phi_{\text{tot}}(x) = 0.1$ ,  $x \in [0, L]$ .

$\mathcal{N}$ $= 1/\delta_\xi$	$t = 1$				$t = 20$			
	$e_1$ $10^{-3}$	Conv. rate	$e_2$ $10^{-3}$	Conv. rate	$e_1$ $10^{-3}$	Conv. rate	$e_2$ $10^{-3}$	Conv. rate
	Scheme 1							
2	49.281		49.232		49.265		49.231	
4	24.240	1.0236	24.226	1.0231	24.259	1.0221	24.225	1.0230
8	11.723	1.0481	11.722	1.0473	11.754	1.0453	11.722	1.0472
16	5.470	1.0996	5.470	1.0995	5.491	1.0979	5.471	1.0995
32	2.344	1.2224	2.344	1.2224	2.492	1.1397	2.345	1.2223
	Scheme 2							
2	49.292		49.232		49.194		49.118	
4	24.257	1.0230	24.225	1.0231	24.281	1.0187	24.194	1.0216
8	11.737	1.0474	11.722	1.0473	11.810	1.0398	11.709	1.0470
16	5.476	1.0998	5.470	1.0995	5.559	1.0872	5.466	1.0992
32	2.348	1.2219	2.344	1.2224	2.439	1.1886	2.343	1.2222
	Scheme 3							
2	49.290		49.232		49.189		49.119	
4	24.257	1.0229	24.225	1.0231	24.281	1.0185	24.194	1.0217
8	11.730	1.0482	11.722	1.0473	11.757	1.0463	11.713	1.0465
16	5.471	1.1002	5.470	1.0995	5.479	1.1016	5.467	1.0992
32	2.344	1.2226	2.344	1.2224	2.347	1.2228	2.343	1.2223

Table 7.2: Example 7.1: Approximate  $L^1$  errors for the solids volume fraction.

For saving computing time we use the discretization parameters  $\delta_x = 1/1800$ ,  $\lambda = 0.5$  and  $\delta_\xi = 1/32$ .

Figure 7.7 shows the simulated solids phase density as a function of the normalized squared size and the spatial position, at a long enough time ( $t = 200$ ), which represents the steady state. We observe that the steady state consists of a thick layer

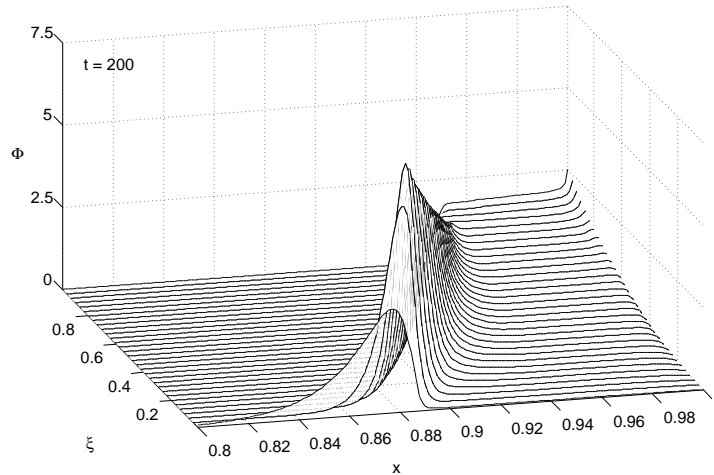


Figure 7.7: Example 7.2: Sediment composition near steady state ( $t = 200$ ): simulated solids phase density for all species.

of large particles with a little amount of small particles above the bottom of the vessel, and a very thin and concentrated layer of small particles above the layer of large ones.

Figures 7.8 (a) and (b) show the simulated solids phase density as a function of the normalized squared size at  $x = 0.8$ ,  $x = 0.9$ , and  $x = 1.0$ , and the simulated solids phase density as a function of the spatial position for  $\xi = 0.015625$ ,  $\xi = 0.49219$ , and  $\xi = 0.98438$ , at steady state, respectively.

Figure 7.8 (c) shows the simulated total solids volume fraction as a function of the spatial position at the steady state ( $t = 200$ ). In Figure 7.8 (c) we clearly observe that at steady state the total solids volume fraction is divided into two parts. Above around  $x = 0.875$ , it has the value 0, and below this position, it has the value of  $\phi_{\max}$ . Also in Figure 7.8 (c) we can deduce that there is conservation of mass or volume because the area between the graph and  $\phi = 0$  is approximately  $0.8(1 - 0.875) = 0.1$ , which is the same value of the area under the graph at  $t = 0$  (initial volume of the solids). Figure 7.9 shows the simulated total solids volume fraction until the steady

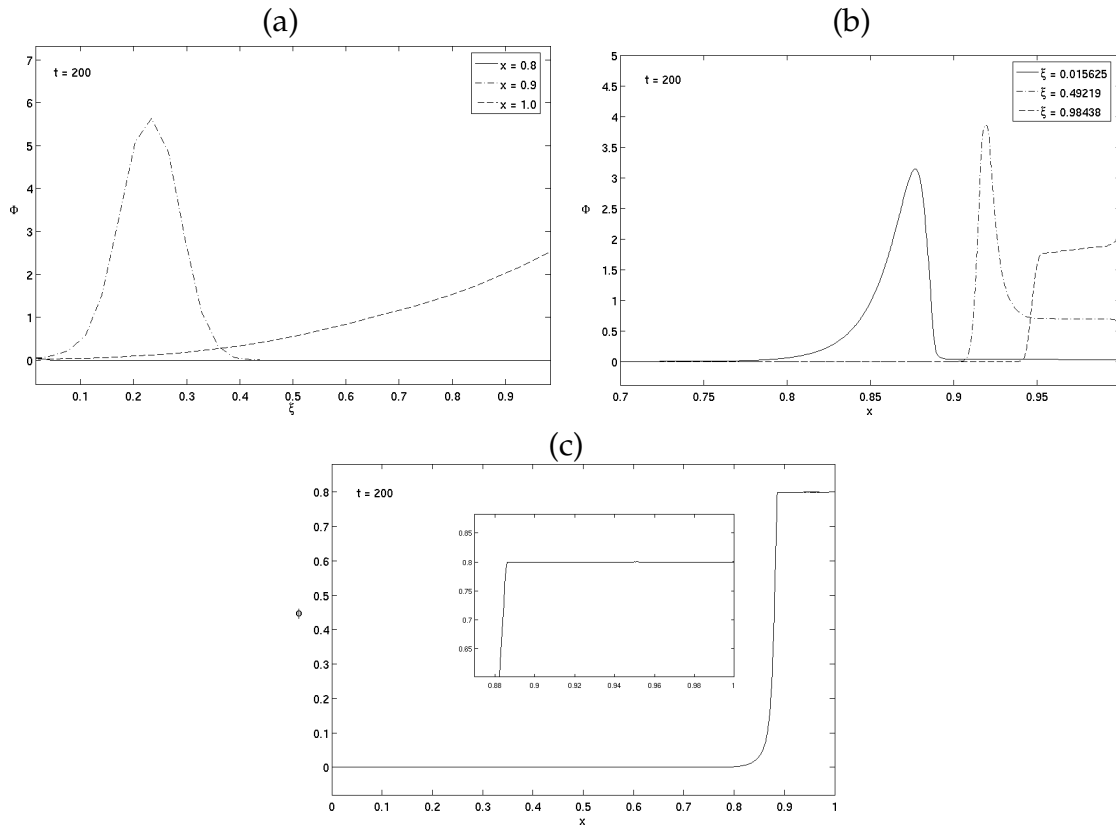


Figure 7.8: Example 7.2: Sediment composition near steady state ( $t = 200$ ): simulated solids phase density (a) as a function of the normalized squared size for three different positions, (b) as a function of the spatial position for three different normalized squared sizes, (c) total solids volume fraction.

state ( $t = 200$ ).

### Example 7.3: Comparison between sedimentation of suspensions with equi-distribution and Rosin-Rammler distribution of particle size

In this example we present the simulation of sedimentation of suspensions with equi-distribution and Rosin-Rammler distribution of particle size in a closed vessel. The material parameters are  $L = 1$ ,  $v_1 = 1$ , the initial total solids volume fraction

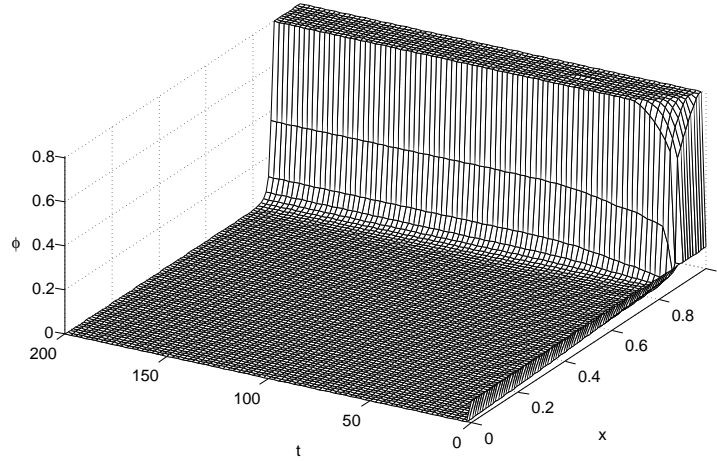


Figure 7.9: Example 7.2: Simulated total solids volume fraction.

$\phi_{\text{tot}}(x) = 0.1$ ,  $x \in [0, L]$ ; the Rosin-Rammler distribution parameters are  $m = 2.0$  and  $l = d_1/2$ , with  $d_1 = 1.0689 \times 10^{-3}$  m ; and the discretization parameters are  $\delta_x = 1/3600$ ,  $\lambda = 0.5$  and  $\delta_\xi = 1/32$ .

Figure 7.10 shows the simulated solids phase density for suspensions with equi-distribution and Rosin-Rammler distribution of particle size, at  $t = 1$  and  $t = 20$ . In Figure 7.10 we observe the effect of a greater ratio small particles to large particles of the Rosin-Rammler distribution with respect to the equi-distribution. Figure 7.11 shows the simulated total solids volume fraction for suspensions with equi-distribution and Rosin-Rammler distribution of particle size, at  $t = 1$  and  $t = 20$ . In Figure 7.11 we observe that the suspension with Rosin-Rammler distribution of particle size settles more slowly than the suspension with equi-distribution of particle size does, due to the greater ratio small particles to large particles of the Rosin-Rammler distribution with respect to the equi-distribution. Figure 7.12 shows the simulated total solids volume fraction of suspensions with equi-distribution and Rosin-Rammler distribution of particle size.

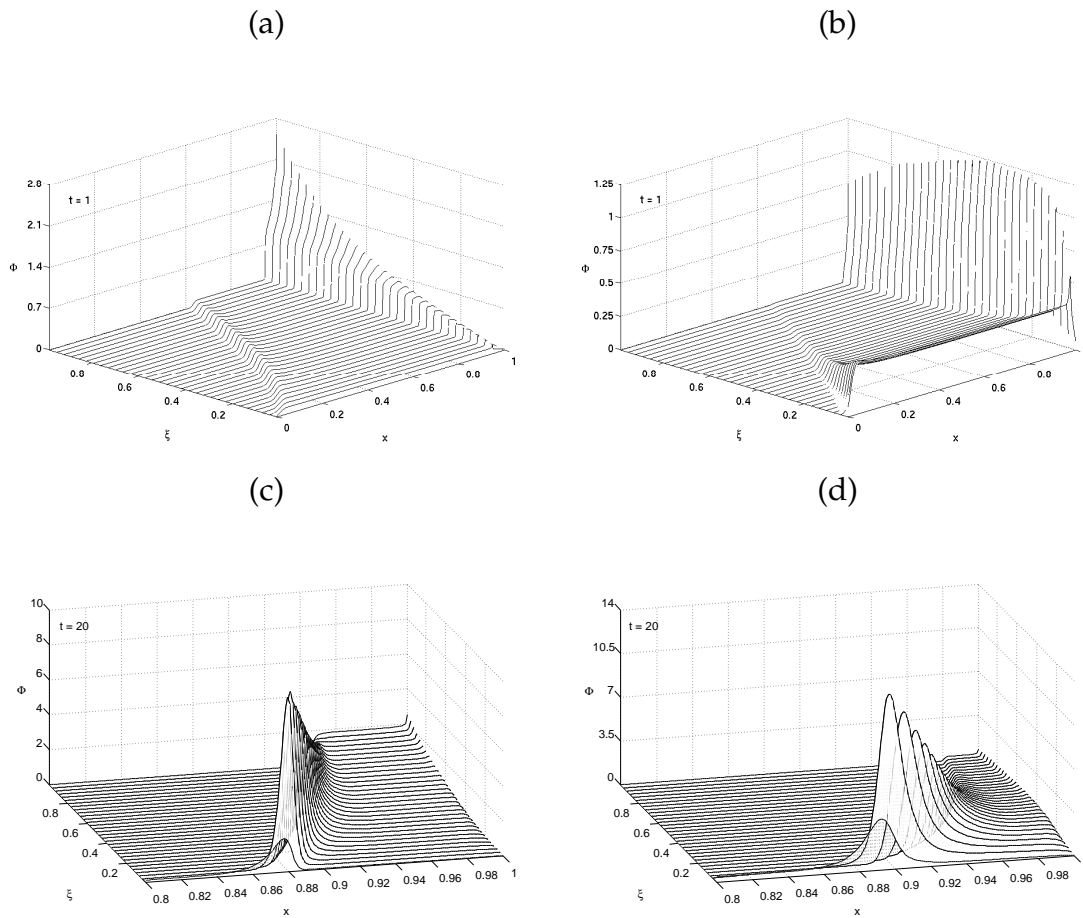


Figure 7.10: Example 7.3: Simulated solids phase density at  $t = 1$  and  $t = 20$ , of suspensions with two particle size distributions. (a, c) equi-distribution, (b, d) Rosin-Rammler distribution.

### 7.5.2 Example 7.4: Sedimentation of a suspension with periodic boundary conditions

Here we present the simulation of a sedimentation with periodic boundary conditions of a suspension with particle size equi-distribution. The material parameters

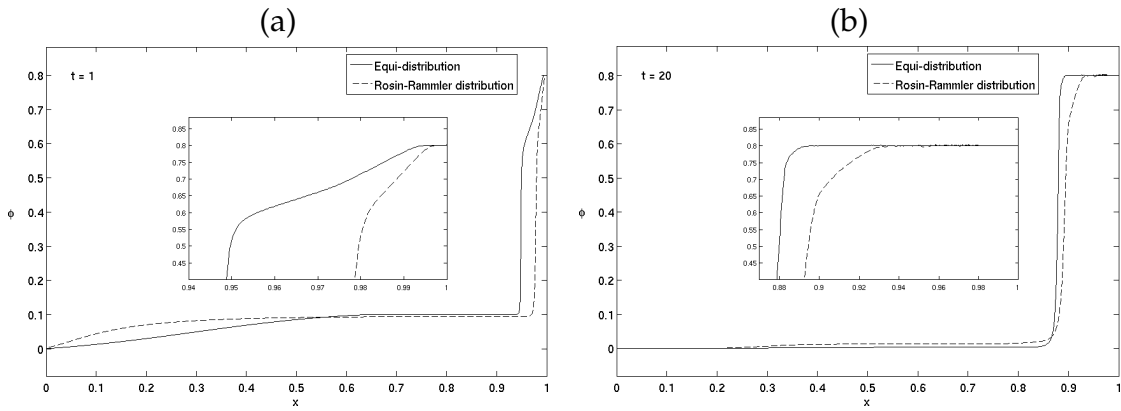


Figure 7.11: Example 7.3: Simulated total solids volume fraction of suspensions with equi-distribution and Rosin-Rammler distribution of particle size. (a)  $t = 1$ , (b)  $t = 20$ .

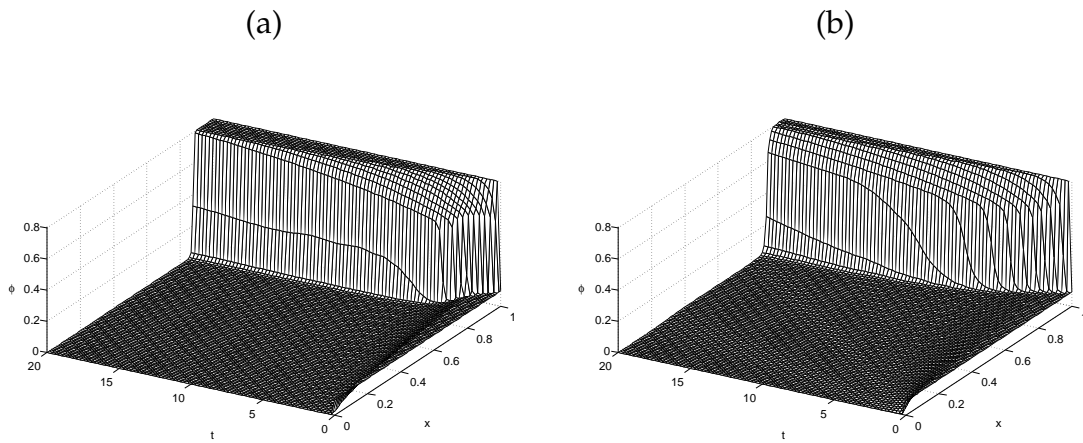


Figure 7.12: Example 7.3: Simulated total solids volume fraction of suspensions with (a) equi-distribution, (b) Rosin-Rammler distribution.

are the period  $L = 1$ ,  $v_1 = 1$ , and the initial total solids volume fraction

$$\phi_{\text{tot}}(x) = \begin{cases} 0 & \text{for } x \in [0, 1/2), \\ 0.1 & \text{for } x \in [1/2, 1]. \end{cases}$$

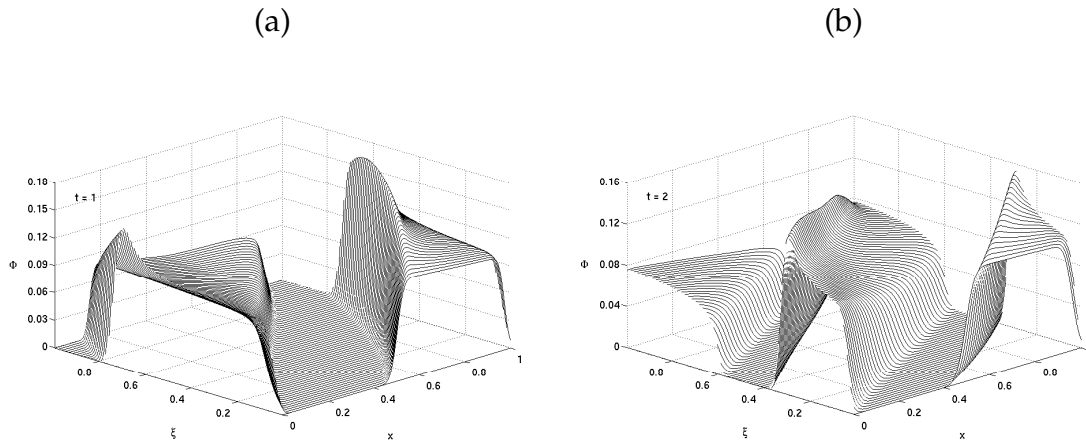


Figure 7.13: Example 7.4: Simulated solids phase density at (a)  $t = 1$ , (b)  $t = 2$ .

The discretization parameters are  $\delta_x = 1/1800$ ,  $\lambda = 0.5$ , and  $\delta_\xi = 1/64$ .

Figure 7.13 shows the simulated solids phase density as a function of the normalized squared size and the spatial position, at  $t = 1$  and  $t = 2$ .

In Figure 7.13 we observe that the mean value of the phase density of larger particles decrease in time but they cover greater spatial interval.

Figure 7.14 shows the simulated solids phase density as a function of the normalized squared size at  $x = 0.25$ ,  $x = 0.5$ ,  $x = 0.75$  and  $x = 0.9$ , for the times  $t = 1$ ,  $t = 2$  and  $t = 100$ .

Figure 7.15 shows the simulated solids phase density as a function of the spatial position for  $\xi = 0.0078125$  and  $\xi = 0.32031$ , and,  $\xi = 0.64844$  and  $\xi = 0.99219$ , respectively, for the times  $t = 1$ ,  $t = 2$  and  $t = 100$ . In Figure 7.15 we see that the amplitude of the solids concentration waves decreased with the time, especially for the largest species (large  $\xi$ ). Figure 7.16 shows the simulated total solids volume fraction as a function of the spatial position at  $t = 2$ ,  $t = 10$  and  $t = 100$ . In Figure 7.16 we observe that the amplitude of the curve of the total solids volume fraction decreases with time and the numerical solution tends to the constant value of  $\phi = 0.05$ . Figure 7.17 shows the simulated total solids volume fraction until  $t = 100$ . We observe that the graph has singular structures at approximately  $t = 27$ ,  $t = 40$  and  $t = 80$ .

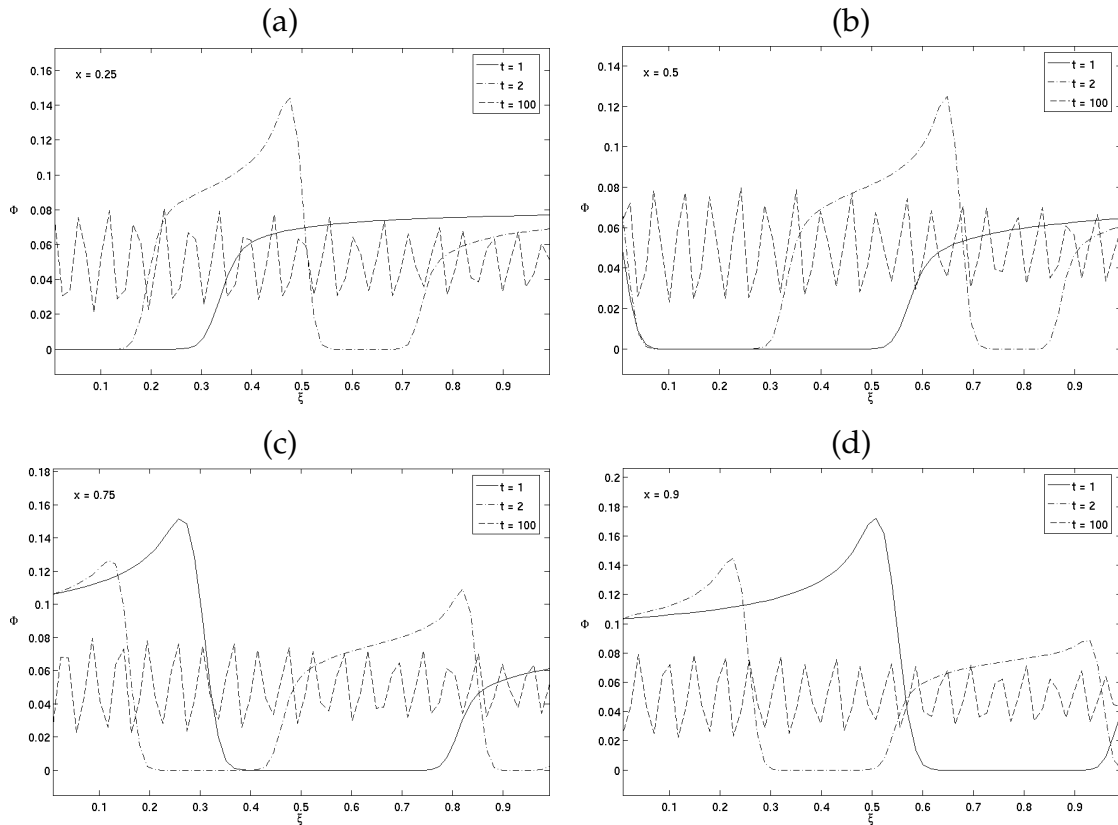


Figure 7.14: Example 7.4: Simulated solids phase density as a function of the normalized squared size for three different times. (a)  $x = 0.25$ , (b)  $x = 0.5$ , (c)  $x = 0.75$ , (d)  $x = 0.9$ .

We leave the explanation of this occurrence as an open problem.

### 7.5.3 Examples 7.5 and 7.6: Sedimentation of a suspension with Riemann initial data

In this pair of examples, we show the simulation of a sedimentation with Riemann initial data of a suspension with particle size equi-distribution. The material

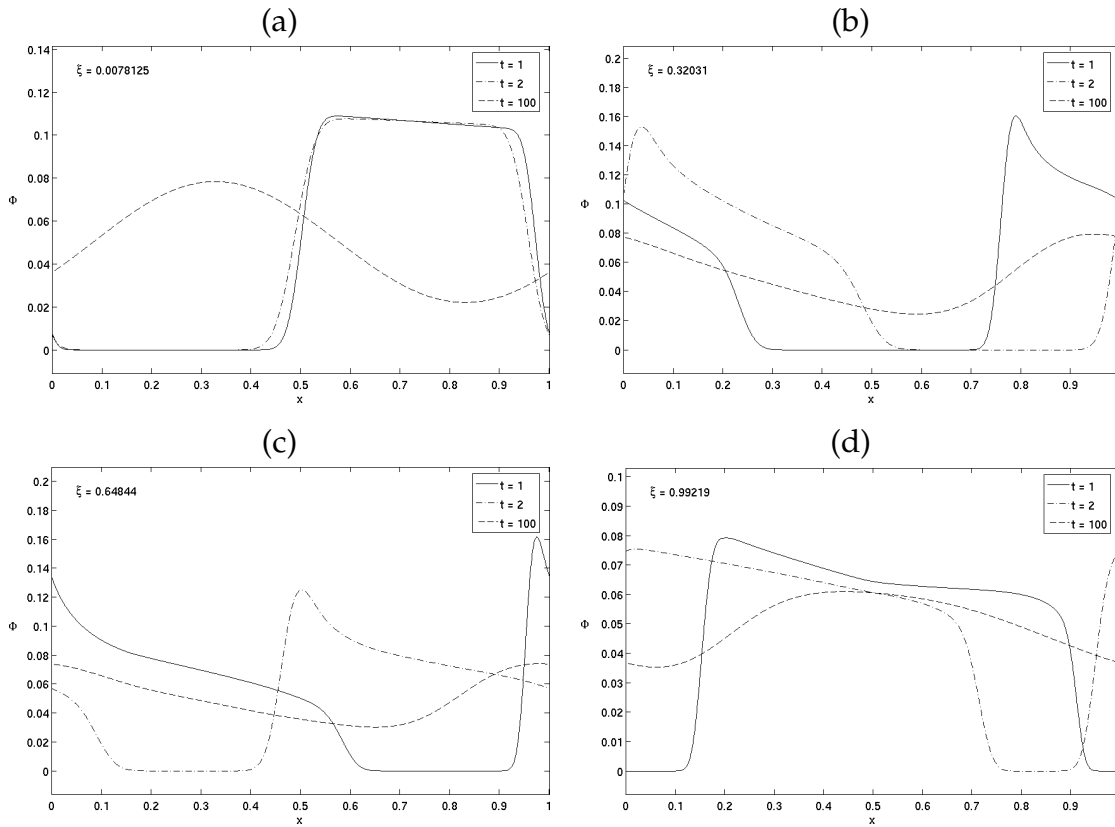


Figure 7.15: Example 7.4: Simulated solids phase density as a function of the spatial position for three different times. (a)  $\xi = 0.0078125$ , (b)  $\xi = 0.32031$ , (c)  $\xi = 0.64844$ , (d)  $\xi = 0.99219$ .

parameters are  $v_1 = 1$ , and for Example 7.5, the initial total solids volume fraction is

$$\phi_{\text{tot}}(x) = \begin{cases} 0 & \text{for } x < 0, \\ 0.1 & \text{for } x \geq 0, \end{cases}$$

while for Example 7.6, the initial datum is

$$\phi_{\text{tot}}(x) = \begin{cases} 0.3 & \text{for } x < 0, \\ 0 & \text{for } x \geq 0, \end{cases}$$

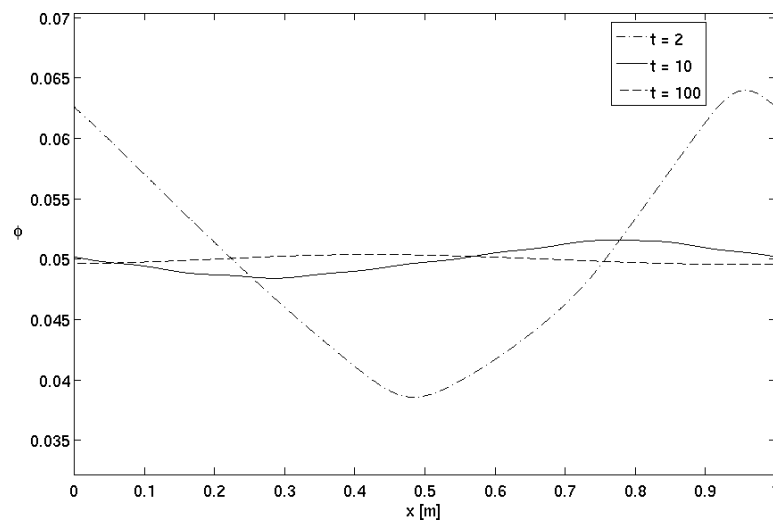


Figure 7.16: Example 7.4: Simulated total solids volume fraction for three different times.

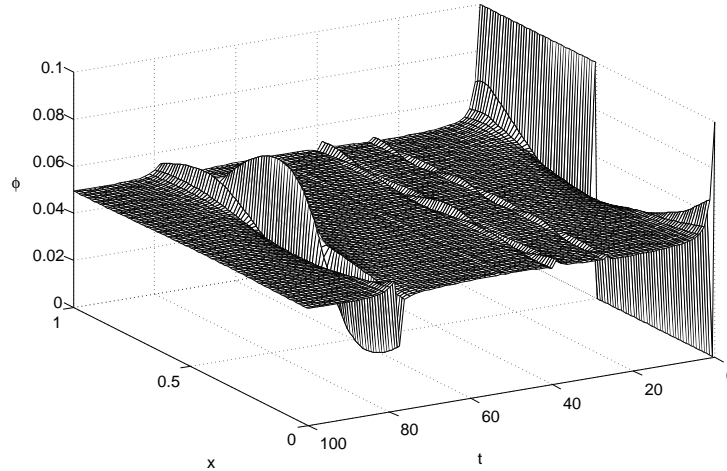


Figure 7.17: Example 7.4: Simulated total solids volume fraction.

We use the discretization parameters  $\delta_x = 1/3600$ ,  $\lambda = 0.5$  and  $\delta_\xi = 1/32$ .

Figure 7.18 shows the simulated solids phase density as a function of the normalized squared size and the spatial position, at  $t = 2$ . We see, as in Figure 7.5 (b,c) of

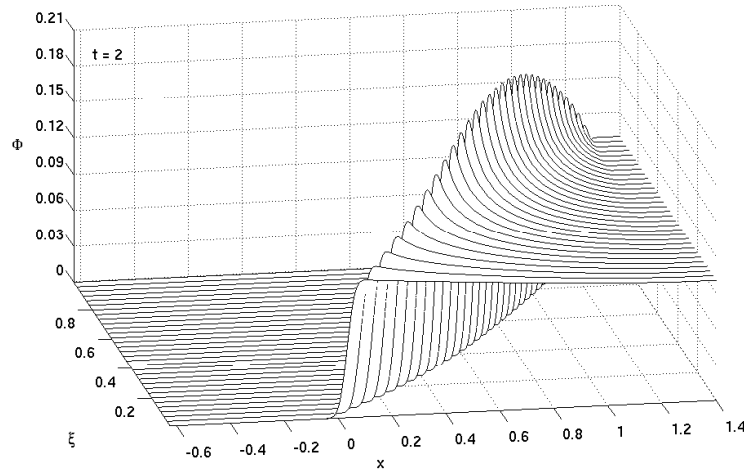


Figure 7.18: Example 7.5: Simulated solids phase density at  $t = 2$ .

the Example 7.1, that there is a considerable accumulation of medium size particles on the back of the wave of solid particles. The explanation of this phenomenon is given in the Example 7.1. Moreover, it is clear that the larger particles move faster than the smaller ones. Figures 7.19 (a) and (b) show the simulated solids phase density as a function of the normalized squared size at  $x = 0.75$  and  $x = 1.0$ , for the times  $t = 1, t = 2$  and  $t = 20$ . Figure 7.19 (c) and (d) show the simulated solids phase density as a function of the spatial position for  $\xi = 0.015625$  and  $\xi = 0.32812$ , for the times  $t = 1, t = 2$  and  $t = 20$ . Figure 7.20 shows the simulated total solids volume fraction as a function of the spatial position, at  $t = 1, t = 2$  and  $t = 20$ . Figure 7.21 (a) shows the simulated total solids volume fraction until  $t = 20$ . The “steps” in the graph are consequence of the discretization size of the  $\xi$ -axis. Figure 7.21 (b) shows the corresponding result for Example 7.6.

In addition, we use this example, and Example 7.6, to analyze the behaviour of the eigenvalues as the number of species  $N$  is increased. To this end, we recall first that the exact solution of Example 7.5 depends on  $\omega := x/t$  only, so it is sufficient to calculate the solution for one fixed time. We chose the cases  $N = 2, 4, 8$  and  $32$

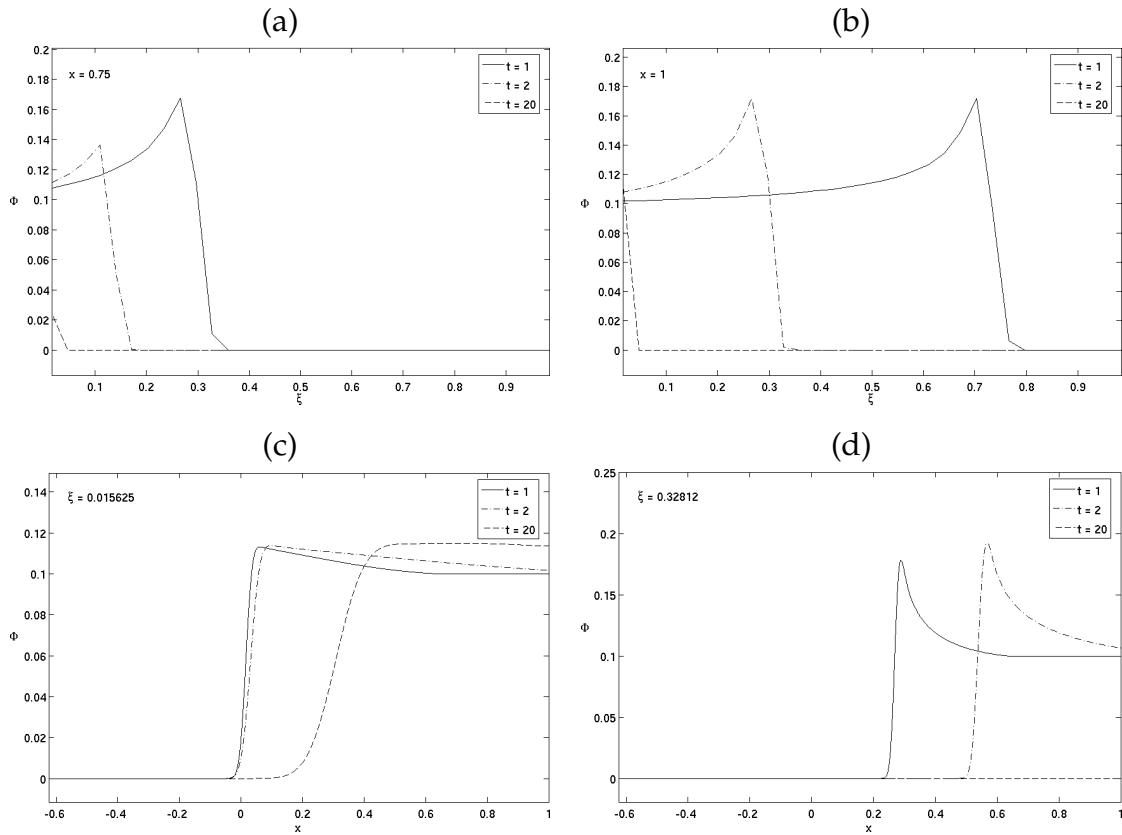


Figure 7.19: Example 7.5: Simulated solids phase density (a, b) as a function of the normalized squared size for three different times: (a)  $x = 0.75$ , (b)  $x = 1$ ; and (c, d) as a function of the spatial position for three different times: (c)  $\xi = 0.015625$ , (d)  $\xi = 0.32812$ .

for close inspection, and plotted the eigenvalues  $\lambda_1 \geq \lambda_2 \geq \dots \geq \lambda_N$  of Corollary 1 as a function of  $\omega$ ; according to Proposition 7.3.1, these eigenvalues coincide with that of the Jacobian  $\mathbf{J}_f$  (see Theorem 7.2.1) if both are evaluated at corresponding vectors  $\phi$  and  $\Phi$ , respectively. For Example 7.5, Figures 7.22 and 7.23 display the eigenvalues  $\lambda_1, \dots, \lambda_N$  (solid lines) and corresponding transformed eigenvalues  $\xi_{\lambda_1}, \dots, \xi_{\lambda_N}$  (dashed lines) for (a, b)  $N = 2, N = 4$  and  $N = 8$  (Figure 7.22) and  $N = 32$  (Figure 7.23). The dashed lines are the bounds established by (7.2.9) and (7.2.10) for

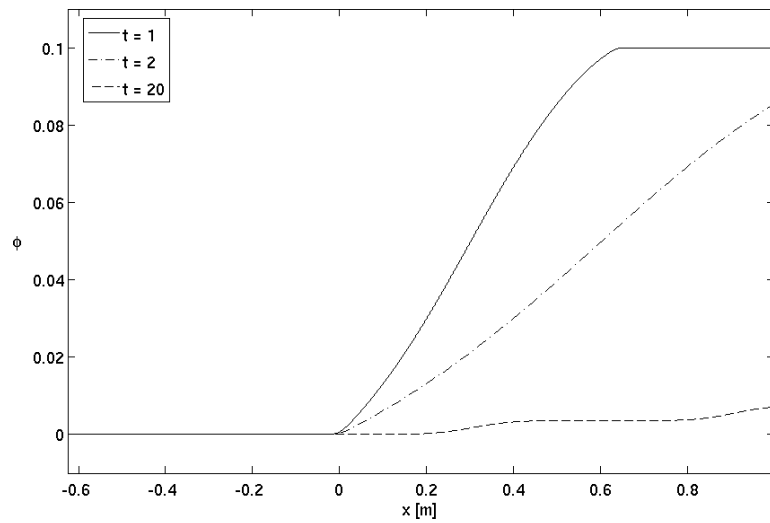


Figure 7.20: Example 7.5: Simulated total solids volume fraction at  $t = 1$ ,  $t = 2$  and  $t = 20$ .

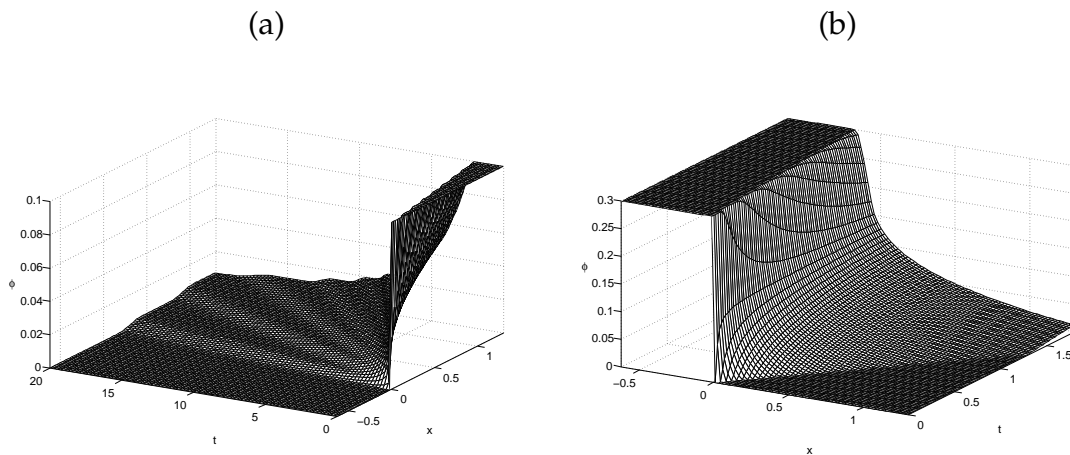


Figure 7.21: Example 7.5 (a) and Example 7.6 (b): simulated total solids volume fraction.

$\lambda_1, \dots, \lambda_N$  and (7.3.13) and (7.3.14) for  $\xi_{\lambda_1}, \dots, \xi_{\lambda_N}$ , respectively. Figures 7.24 and 7.25 show the analogous results for Example 7.6.

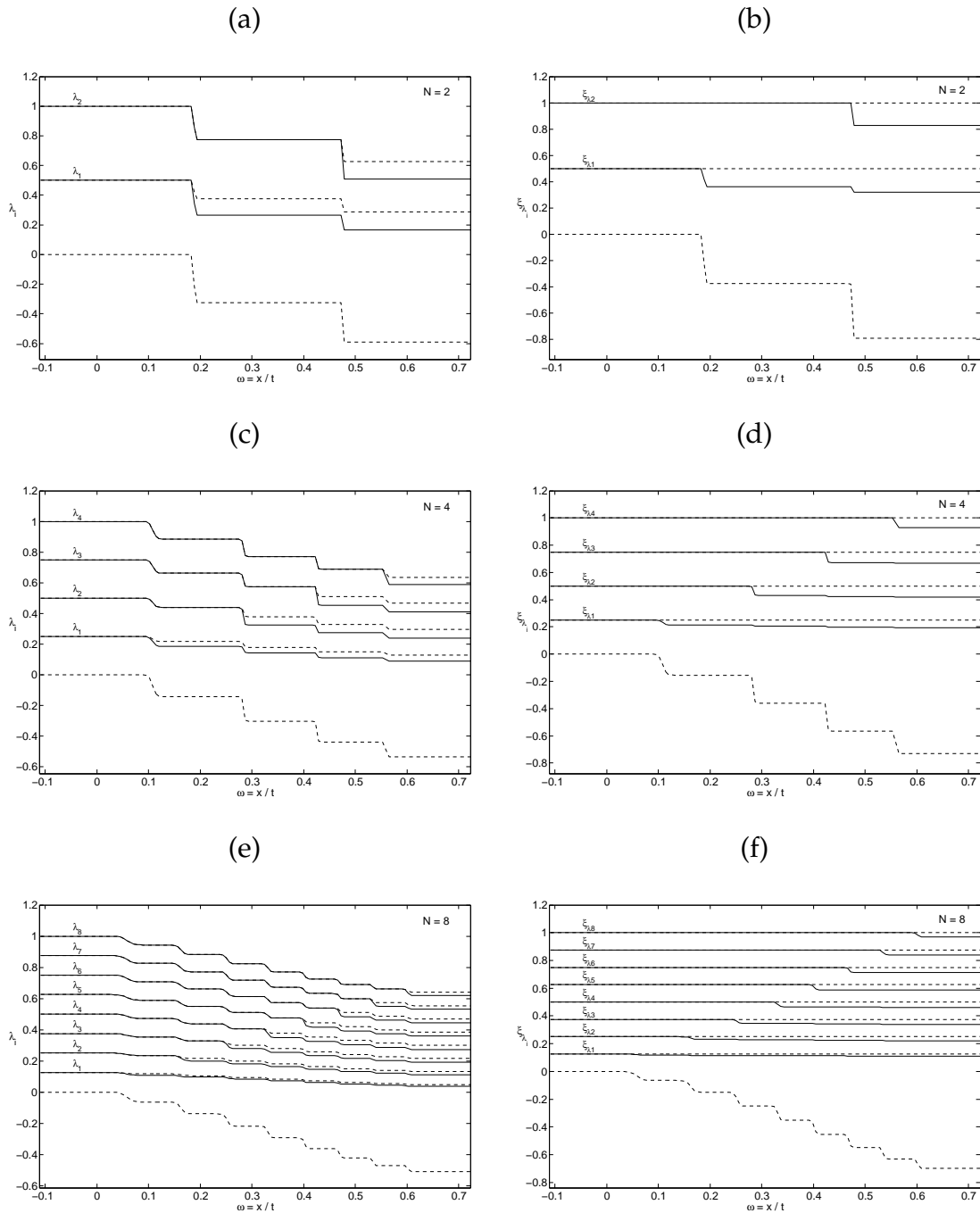


Figure 7.22: Example 7.5: (a, c, e) eigenvalues  $\lambda_1, \dots, \lambda_N$  (solid lines) and (b, d, f) corresponding transformed eigenvalues  $\xi_{\lambda_1}, \dots, \xi_{\lambda_N}$  (solid lines) for (a, b)  $N = 2$ , (c, d)  $N = 4$  and (e, f)  $N = 8$ . The dotted lines are the bounds established by (a, c, e) (7.2.9), (7.2.10) and (b, d, f) (7.3.13), (7.3.14).

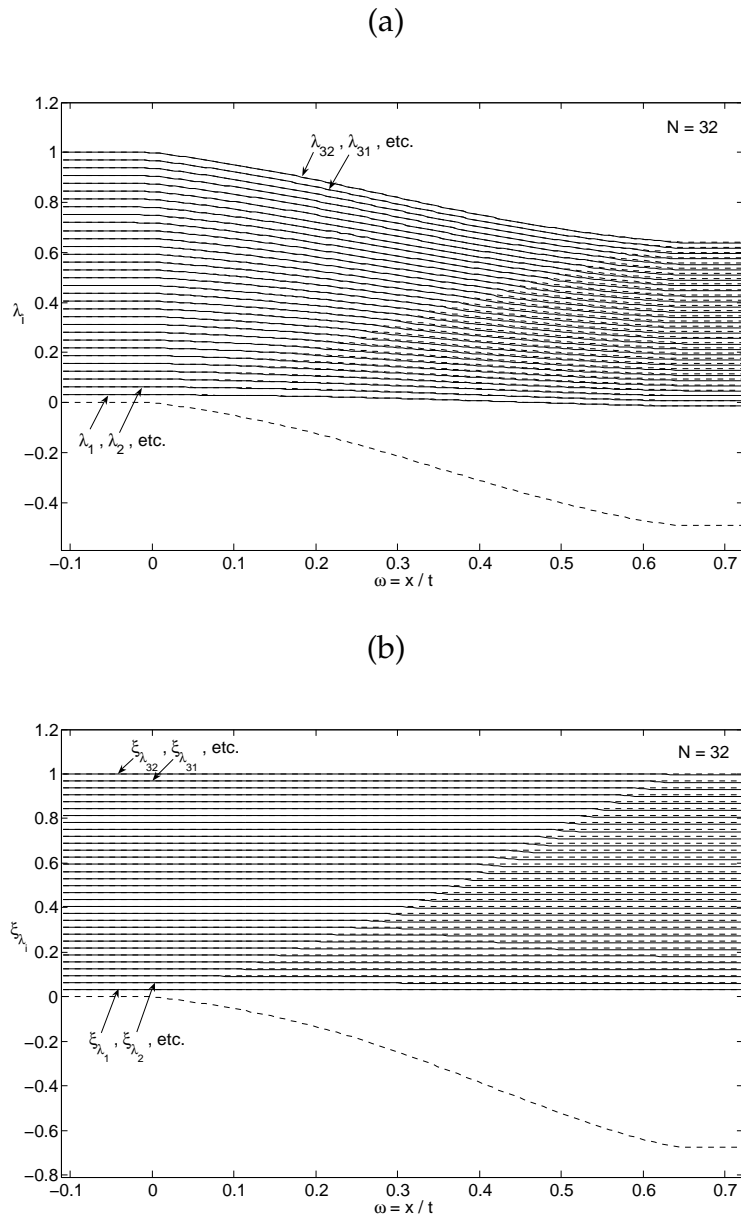


Figure 7.23: Example 7.5: (a) eigenvalues  $\lambda_1, \dots, \lambda_{32}$  (solid lines) and (b) corresponding transformed eigenvalues  $\xi_{\lambda_1}, \dots, \xi_{\lambda_{32}}$  (solid lines) for  $N = 32$ . The dotted lines are the bounds established by (a) (7.2.9), (7.2.10) and (b) (7.3.13), (7.3.14).

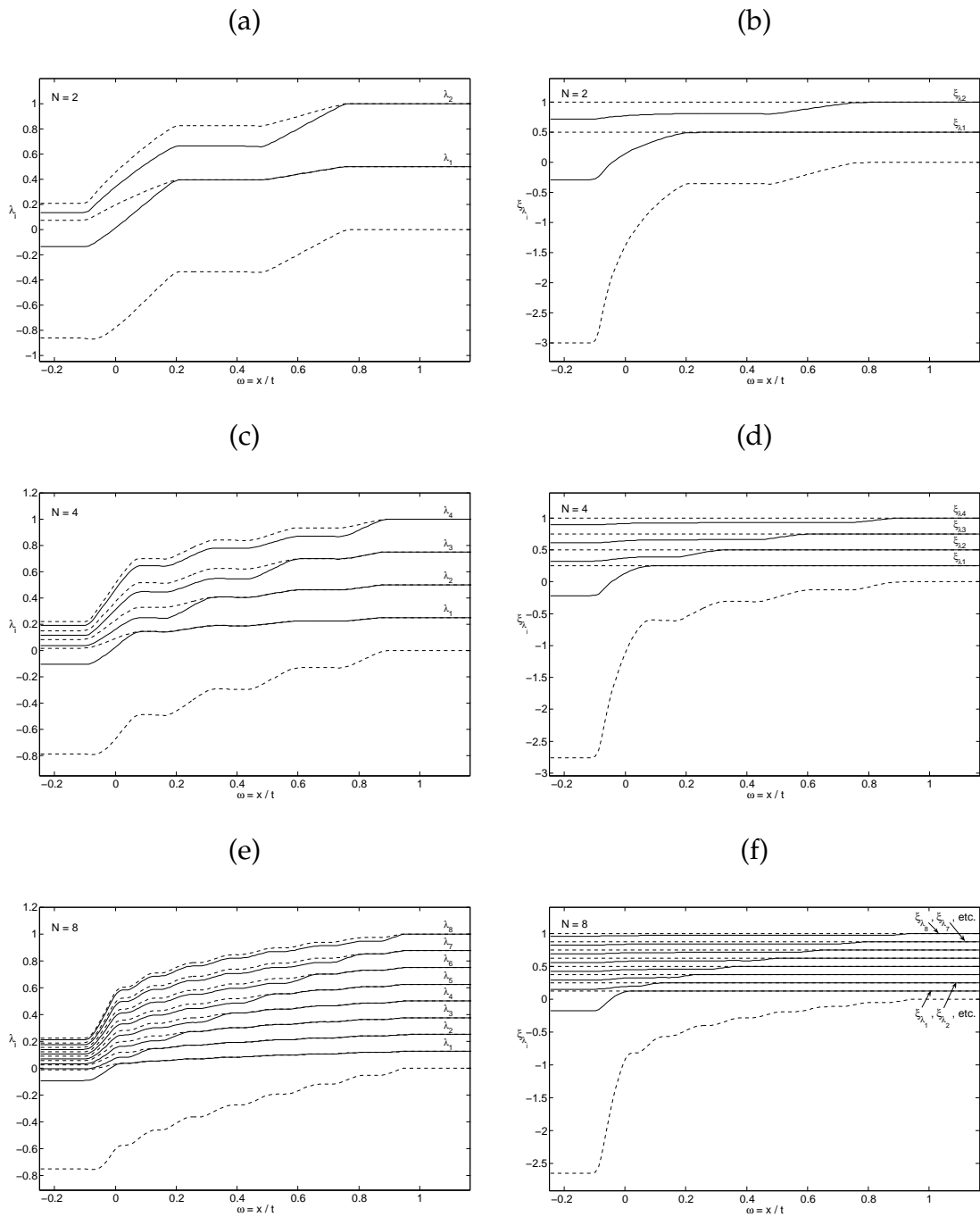


Figure 7.24: Example 7.6: (a, c, e) eigenvalues  $\lambda_1, \dots, \lambda_N$  (solid lines) and (b, d, f) corresponding transformed eigenvalues  $\xi_{\lambda_1}, \dots, \xi_{\lambda_N}$  (solid lines) for (a, b)  $N = 2$ , (c, d)  $N = 4$  and (e, f)  $N = 8$ . The dotted lines are the bounds established by (a, c, e) (7.2.9), (7.2.10) and (b, d, f) (7.3.13), (7.3.14).

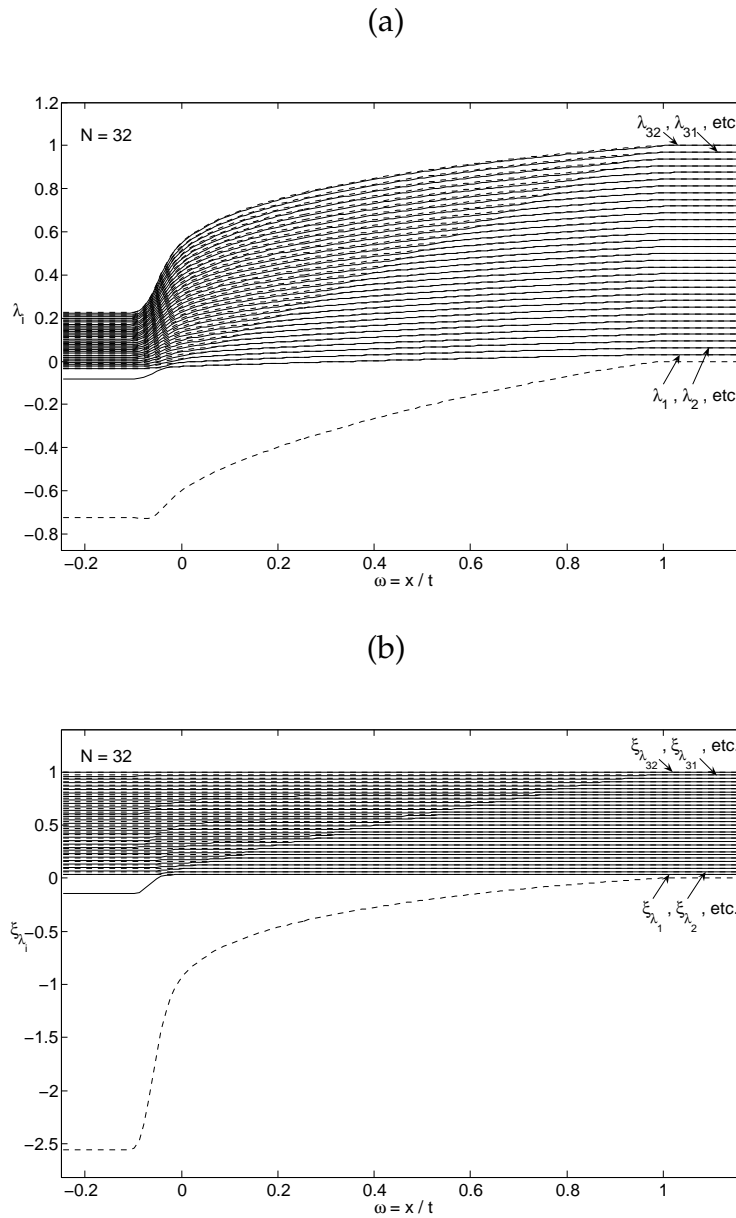


Figure 7.25: Example 7.6: (a) eigenvalues  $\lambda_1, \dots, \lambda_{32}$  (solid lines) and (b) corresponding transformed eigenvalues  $\xi_{\lambda_1}, \dots, \xi_{\lambda_{32}}$  (solid lines) for  $N = 32$ . The dotted lines are the bounds established by (a) (7.2.9), (7.2.10) and (b) (7.3.13), (7.3.14).

# Chapter 8

## Conclusions

This thesis is concerned with the well-posedness analysis and numerical methods for kinematic models consisting of continuity (or balance) equations of different species, which involve flux functions that are discontinuous with respect to the spatial variable, that is, we consider systems of equations of the type  $\Phi_t + \mathbf{f}(\boldsymbol{\gamma}(x), \Phi)_x = \eta(x)\Phi_x$ , where  $\Phi = (\phi_1, \dots, \phi_N)^T$  is the vector of concentrations of species  $1, \dots, N$ ,  $\boldsymbol{\gamma}$  is a vector of parameters, which is a discontinuous function of the spatial position  $x$ , and the possibly discontinuous function  $\eta(x)$  is the transport coefficient of the non-conservative term  $\eta(x)\Phi_x$ .

In **Chapter 3**, the clarifier-thickener model studied in [31] is extended by a singular sink through which material is extracted from the unit.

The injection of material of given concentration at a fixed location leads to a homogeneous conservation law with discontinuous flux. On the other hand, the extraction of suspension at a fixed location leads to a balance equation with discontinuous flux, and which has a new non-conservative transport term. This difference justified studying the sink term problem in its own right.

Schemes 2 and 3 proposed for the full problem have the slight inconvenience that to evaluate the Engquist-Osher numerical flux, one has to determine numerically the extrema of the composite flux function, which for the Scheme 2 is  $q(u - u_F) + b(u)$

for  $q \in \{q_L, \tilde{q}_R\}$ . This is a drawback to the development of methodologies of control.

The numerical examples illustrate that the sink term may give rise to a variety of stationary discontinuities across the sink level  $x = x_D$  (decreasing or increasing in the direction of increasing  $x$ ). The parameters can be chosen in such a way that either the solid material flowing into the clarifier zone is fully absorbed by the singular sink, or material is extracted through the sink without affecting the solution in the clarifier zone. The existence of a discontinuity across the sink level in some cases can be determined if we look at the jump condition (3.3.9) of the associated reduced problem for the parameters given in those cases.

Because of the fact that the formation of a jump of concentration across the sink level  $x = x_D$  is possible, the value  $u(x_D, t)$  becomes indeterminate, and therefore, it is necessary to develop a method to calculate the solids concentration of the suspension extracted through the sink. We leave the devise and analysis of that method as open problem.

In **Chapter 4**, a new model for continuous separation and classification of poly-disperse suspensions is presented. To this end, the discontinuous-flux CT model for the continuous solid-liquid separation of suspensions is extended to a generalized clarifier-thickener model (GCT), in which an arbitrary number of discharge streams is described by singular sink terms. This feature allows us to describe the continuous extraction of products of different composition.

Some simplifications are made in the formulation of the flux functions with the purpose of facilitating easy the calculation, and to be consistent with previous works, in particular, with the stability analysis of Bürger et al. [32]. For example, an explicit formula for the solid-fluid relative velocity of each species is derived from the implicit formulation defined by Masliyah [129], and an average Richardson-Zaki exponent for all species is used in the hindered settling factor  $V(\phi)$ .

In Chapter 3 [23] we prove that, for the case of a monodisperse suspension in a vessel with constant cross-sectional area and one sink, the model is well-posed, and show that a monotone numerical scheme converges to the entropy solution. These

---

results along with those of [31] were a motivation to formulate our GCT model.

A numerical method to calculate the solids concentration in the sinks is proposed, from mass balances of solids and based on the finite speed of propagation of the concentration waves. We leave the analysis of this method as open problem.

In Examples 4.2 and 4.3 we adopt experimental data given by Chen et al. in [40], and our simulations fit reasonably well the results of their experiments.

It is clear that the GCT model is subject to some limitations. First, the model applies only to units that are (at least approximately) one-dimensional, and where lateral concentration or velocity gradients are negligible. This means, for example, that particles should be reasonably small, so that wall effects are unimportant, and that strong changes in the cross-sectional area must be excluded. It also presumed that the parameters for the MLB model for the solid-fluid relative velocity are known, for example from batch settling experiment. The MLB model actually presumes that particles are small rigid spheres. While sphericity can be considered as a useful approximation for particles of slightly more general geometry, the rigidity of particles is essential.

In **Chapter 5**, a family of numerical schemes for kinematic flows with discontinuous flux is presented. The basic design principle of the schemes, and the analysis of some of them, is based on the explicit “concentration times velocity” structure of the flux of each species.

One of the main advantages of these new schemes is that (other than an estimate of the spectral radius for the CFL condition) they do not require any calculation of eigenvalues, eigenvectors, field-by-field decomposition, flux vector splitting, etc., that are usually required for an upwind scheme. In this sense they are like a central scheme.

The kinematic models studied are algebraically very similar, but belong to two groups, one formed by the traffic and the oil-in-water dispersion model, for which all velocities are nonnegative, and another including the polydisperse sedimentation model, which for  $N \geq 2$  includes velocities of either sign.

Formally, almost every system of conservation laws  $\partial_t \phi_i + \partial_x (f_i(\Phi)) = 0$ ,  $i = 1, \dots, N$ , can be written as a “kinematic system”  $\partial_t \phi_i + \partial_x (\phi_i v_i(\Phi)) = 0$ ,  $i = 1, \dots, N$ , if we define  $v_i(\Phi) = f_i(\Phi)/\phi_i$  (presuming that this quotient remains bounded when  $\phi_i \rightarrow 0$ ). Consequently, the schemes could be applied to nearly arbitrary systems of conservation laws. However, the properties that are specific to scalar kinematic models and essential for our analysis are that the velocity  $v(\phi)$  is given by a positive default coefficient multiplying a hindrance function, such that  $v(\phi) \geq 0$  and  $v'(\phi) \leq 0$ . On the other hand, some of the desirable properties, for example, that  $\Phi$  belongs to a bounded phase space  $\mathcal{D}_{\phi_{\max}}$ , are typical for multi-species models, but of course, are not meaningful for systems that represent balances of different physical quantities such as mass, linear momentum and energy.

Although the basic scheme, Scheme 1, can be adapted to accommodate multi-species models of both groups (Schemes 4–8), only in the case of non-negative velocities it was possible to establish a very desirable invariant region principle (Theorems 5.3.1 and 5.3.2). It is not clear whether this principle can also be possibly established for the polydisperse sedimentation model.

Furthermore, our Example 5.8.1, for instance (see Figure 5.12 (d) and (f)), illustrates that for  $N \geq 2$  our second-order schemes do not seem to obey an invariance principle. However, our Figures 5.5 and 5.8 illustrate that all second-order schemes converge with consistently smaller errors in the  $L^1$  sense, and at slightly better rates than their first-order versions, even in the systems case that is not backed up by a convergence analysis.

In regard to aspects that are more related to the discontinuity of the numerical flux, the main technical challenge in establishing convergence of an approximating sequence for conservation laws with discontinuous coefficients is somehow controlling the spatial variation of the solution. The local variation bound developed here only applies to spatial discontinuities, does not become any more complicated if the flux is nonconvex, and does not require any assumptions about genuine nonlinearity.

Finally, our definition (5.3.25) and the invariance principle for Scheme 5, Theo-

rem 5.3.1, explicitly include the case of a spatially (possibly discontinuously) varying maximum density  $\phi_{\max} = \phi_{\max}(x)$ , which appears in Examples 5.2 and 5.5, but the convergence analysis of Section 5.4 is limited to the case of constant  $\phi_{\max}$ . Meanwhile, in Chapter 6 we have made further advances in analyzing the problem where we allow  $\phi_{\max}(x)$  to vary discontinuously.

In **Chapter 6**, the well-known Lighthill-Whitham-Richards (LWR) kinematic traffic model was extended to a unidirectional road on which the maximum density  $a(x)$  represents road inhomogeneities, such as variable numbers of lanes, and is allowed to vary discontinuously.

In the case where  $a(x)$  is constant (no interface), our motivation for admissible discontinuities gives the same jump conditions as the so-called driver's ride impulse of Ansorge [5], which states that drivers smooth a discontinuous solution if  $\phi_L > \phi_R$ , but not if  $\phi_L < \phi_R$ . This point of view also coincides with the classical Lax/Oleinik/Kružkov theory if the flux  $f$  is strictly concave. If the flux is not strictly concave, both the driver's ride impulse and our rationale give a jump condition that is different from that dictated by the classical Lax/Oleinik/Kružkov theory. In the case of the driver's ride impulse, this was pointed out by Gasser [76].

In the more general situation considered in Chapter 6, the driver's ride impulse does not apply to the jump at the discontinuity in  $a$ . This is because it is not possible to smooth the discontinuity at  $x = 0$ , i.e., there will always be a discontinuity there unless  $\phi_L = \phi_R = 0$ . This is why we have introduced the rationale proposed here, i.e., that the driver will try to speed up if he/she detects that the velocity directly ahead is greater than his/her own velocity (when the distance between his/her car and the one in front of him/her is increasing). This also seems more directly related to driver behavior than the driver's ride impulse, since drivers can detect a difference in speed much more easily than they can detect a difference in density.

In **Chapter 7**, the one-dimensional kinematic model for batch sedimentation

of polydisperse suspensions of small equal-density spheres was extended to suspensions with a continuous particle size distribution. The resulting mathematical model, obtained by using the Masliyah-Lockett-Bassoon (MLB) model for the solid-fluid relative velocity for each solids species and the concept of phase density function  $\Phi$ , is a scalar first-order kinetic equation for  $\Phi$ .

According to Chapter 5 [25], there is not a proof of stability for the numerical scheme utilized (Scheme 3), but based on an analysis of a model with non-negative velocities, a CFL condition is given. However, Figures 7.1 and 7.2, and Tables 5.1 and 5.2 indicate the superiority of Scheme 3 over Schemes 1 and 2. In particular, Figure 7.1 shows that Scheme 2 introduces spurious oscillations near discontinuities, and Figure 7.2 (a) illustrates the increasing numerical viscosity of the Scheme 1 as the time advances.

Several numerical examples allow us to know more about the behaviour of this kind of suspensions. In particular:

In Example 7.1 (sedimentation of a suspension with equi-distribution of particle size), Figure 7.3 illustrates that the larger particles settle faster than the smaller ones, and therefore the larger ones fill the lower layers of the vessel and form thick sediment layers, and, the smaller particles are partially removed from the bottom and with those in suspension form very thin sediment layers above the larger ones.

In Example 7.3 (comparison between sedimentation of suspensions with equi-distribution and Rosin-Rammler distribution of particle size), Figure 7.12 indicates that the suspension with Rosin-Rammler distribution of particle size settles more slowly than the suspension with equi-distribution of particle size does, due to the greater ratio small particles to large particles of the Rosin-Rammler distribution with respect to the equi-distribution.

In Example 7.5 (sedimentation of a suspension with Riemann initial data), Figure 7.18 illustrates that there is a considerable accumulation of medium size particles on the back of the wave of solid particles.

# Appendix A

## Additional numerical examples

### A.1 Additional numerical examples of Chapter 4

Here, we show numerical examples that were part of earlier versions of the article “A kinematic model of continuous separation and classification of polydisperse suspensions” (Chapter 4 of this work). The choice of examples of the final version of that paper is based on comments we received in the reviews of that. Nevertheless, we decided to include the earlier examples in this thesis, since they represent other interesting cases, such as classification in vessels with rectangular cross-sectional area, classifier operated in clarifier-thickener mode, and classification with changes in the control variables.

#### A.1.1 Preliminary remarks

We consider four units for separation or classification: three of them are operated in the FC mode and have constant (Vessel 1, see Figure A.1) or variable varying interior cross-sectional area (Vessels 3 and 4, see Figures A.11 and A.16), while Vessel 2 is operated in the CT mode and has variable interior cross-sectional area (see Figure A.6). In all of them, the outer pipes are cylinders. Associated to Vessels 1, 2, 3, and 4 are Examples A.1, A.2, A.3, and A.4, respectively. The parameters used

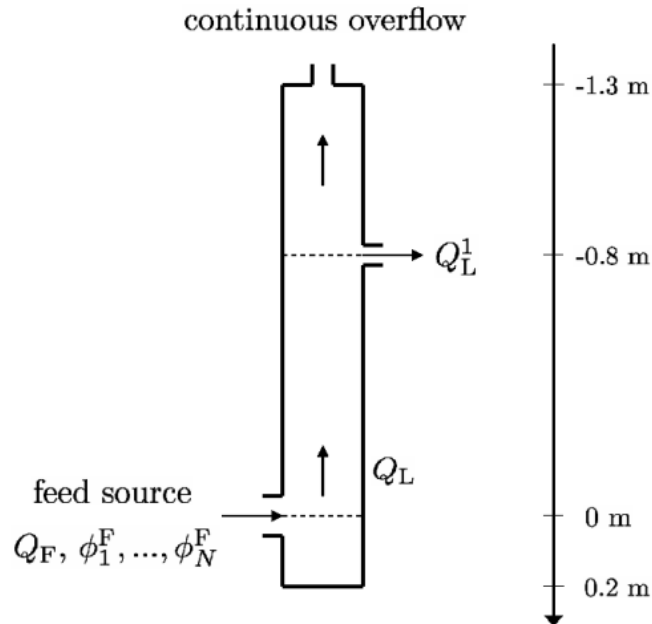


Figure A.1: Vessel 1: A fluidization column with constant interior area.

in each example are given in Table A.1. For all the examples, we use the equation (4.6.1) with  $\phi_q = 0.63$  and  $\phi_{\max} = 0.68$ , and use the first alternative of (4.3.8).

### A.1.2 Example A.1: Continuous separation of a bidisperse suspension in a closed-bottom CT with sink

We simulate the continuous separation of a bidisperse suspension in Vessel 1, for which

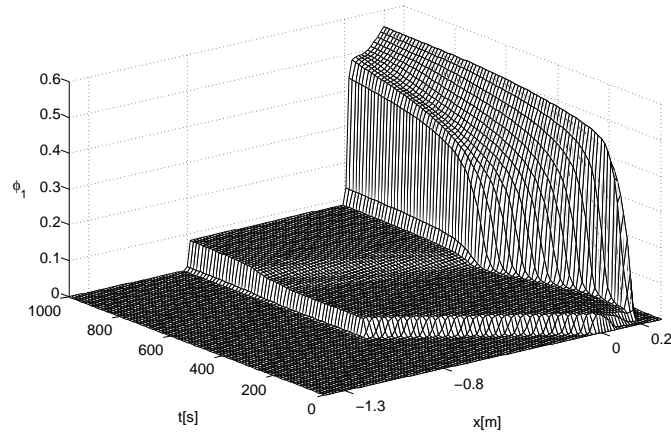
$$S(x) = \begin{cases} 4.9 \times 10^{-4} \text{ m}^2 & \text{for } x \leq -1.3 \text{ m,} \\ 0.1 \text{ m}^2 & \text{for } x > -1.3 \text{ m.} \end{cases}$$

A suspension of ballotini spheres with the density and viscosity parameters given in Table A.1 and a continuous particle size distribution centered in the range between  $d_1$  and  $d_2$  was considered by Galvin and Nguyentranlam in [73].

	Example A.1	Example A.2	Example A.3	Example A.4
$N$	2	2	2	3
$d_1$ [m]	$9.00 \times 10^{-5}$	$3.90 \times 10^{-4}$	$9.00 \times 10^{-4}$	$1.5 \times 10^{-3}$
$d_2$ [m]	$5.70 \times 10^{-5}$	$1.37 \times 10^{-4}$	$5.50 \times 10^{-4}$	$9.0 \times 10^{-4}$
$d_3$ [m]	—	—	—	$5.5 \times 10^{-4}$
$\delta_2$	0.4011	0.1234	0.3735	0.3600
$\delta_3$	—	—	—	0.1344
$\rho_1$ [kg/m <sup>3</sup> ]	2403	1050	2470	2470
$\rho_2$ [kg/m <sup>3</sup> ]	2403	2850	2470	2470
$\rho_3$ [kg/m <sup>3</sup> ]	—	—	—	2470
$\rho_f$ [kg/m <sup>3</sup> ]	998.2	1120	998.2	998.2
$\mu_f$ [10 <sup>-3</sup> Pas]	1.005	1.410	1.005	1.005
$n$	4.700	5.765	2.58	2.51
$\phi_1^F$	0.05	0.065	0.0676	0.0728
$\phi_2^F$	0.05	0.067	0.0624	0.0676
$\phi_3^F$	—	—	—	0.0624
$Q_F$ [m <sup>3</sup> /s]	$6.40 \times 10^{-4}$	$4.40 \times 10^{-6}$	$5.773 \times 10^{-3}$	$5.773 \times 10^{-3}$
$Q_R$ [m <sup>3</sup> /s]	0	$3.30 \times 10^{-6}$	See *	$-1.450 \times 10^{-3}$
$Q_L^1$ [m <sup>3</sup> /s]	$-3.84 \times 10^{-4}$	0	0	$-1.834 \times 10^{-3}$
$Q_L$ [m <sup>3</sup> /s]	$-6.40 \times 10^{-4}$	$-1.10 \times 10^{-6}$	See *	$-7.223 \times 10^{-3}$
$Q_R^1$ [m <sup>3</sup> /s]	0	$-1.32 \times 10^{-6}$	See *	$-3.668 \times 10^{-4}$
$\Delta x$ [cm]	0.3167	0.1068	0.5	0.745
$\Delta t$ [10 <sup>-3</sup> s]	14.01	0.2960	0.04883	0.1267

Table A.1: Parameters for the numerical simulations. \* In Example A.3, the value of  $Q_L$  is changed at  $t = 120$  s from  $-7.223 \times 10^{-3}$  to  $-5.389 \times 10^{-3}$ , and at  $t = 165$  s from this last value to  $-3.210 \times 10^{-3}$ , while that of  $Q_R^1$  is changed at  $t = 120$  s from  $-3.668 \times 10^{-4}$  to  $-2.201 \times 10^{-3}$ .  $Q_R$  is calculated from the formula  $Q_R = Q_F + Q_L$ .

(a)



(b)

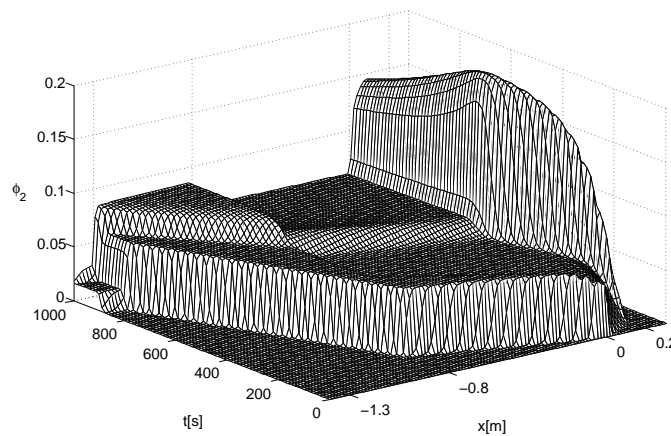
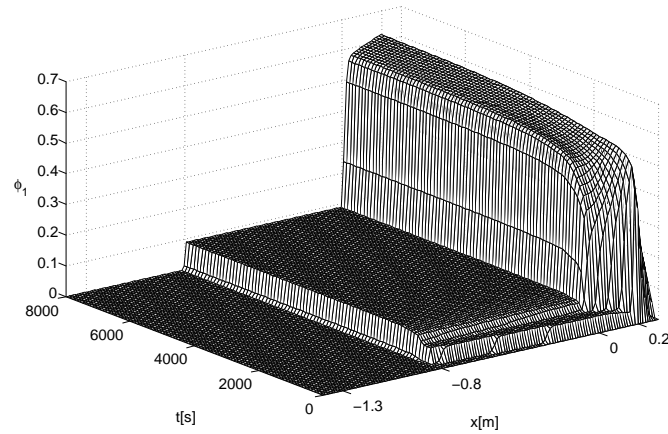


Figure A.2: Example A.1: Simulated concentrations (a)  $\phi_1$  (large particles), (b)  $\phi_2$  (small particles). Startup phase ( $T = 1000$  s).

We see in Figures A.2 and A.3 (a) that species 1 enters both the clarification and settling zones. It accumulates at the bottom and forms a rising sediment, and exhibits an increasing jump of concentration at feed source level. (Here and in the sequel, spatially “increasing” and “decreasing” behaviour is always meant “downwards”, i.e. in the direction of increasing  $x$ ). Species 2 also enters both zones, accu-

(a)



(b)

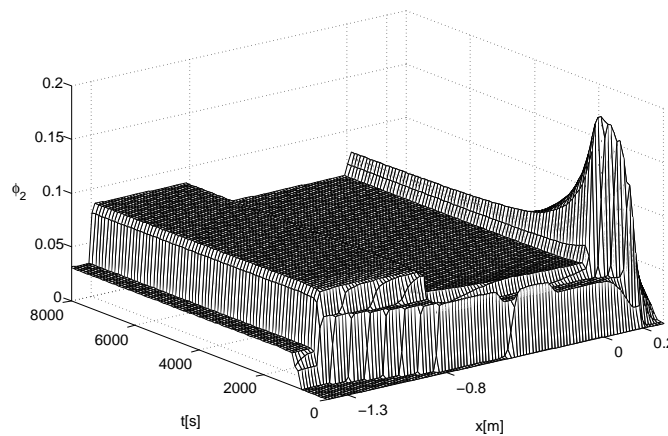


Figure A.3: Example A.1: Simulated concentrations (a)  $\phi_1$  (large particles), (b)  $\phi_2$  (small particles). Long-time behaviour ( $T = 8000$  s).

mulates on the bottom above species 1, and forms a rising sediment. Towards the end of our simulation, it has a small increasing jump of concentration at feed source level, a small decreasing jump at sink level, and a small increasing jump of concentration at overflow level. Furthermore, we observe in Figure A.5 that species 1 leaves the unit by the sink only, whereas species 2 leaves the unit by the sink and

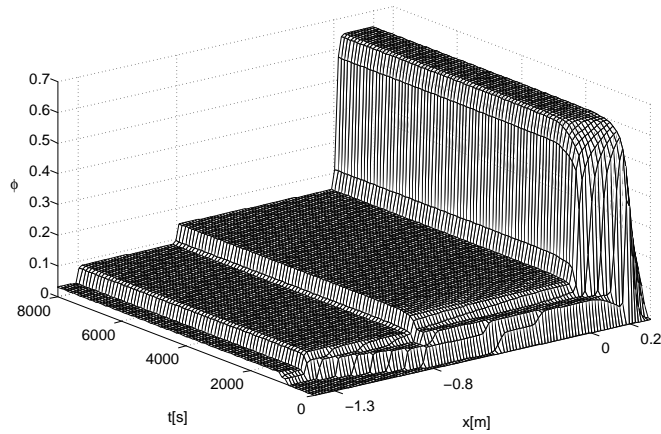


Figure A.4: Example A.1: Simulated total solids concentration  $\phi$ .

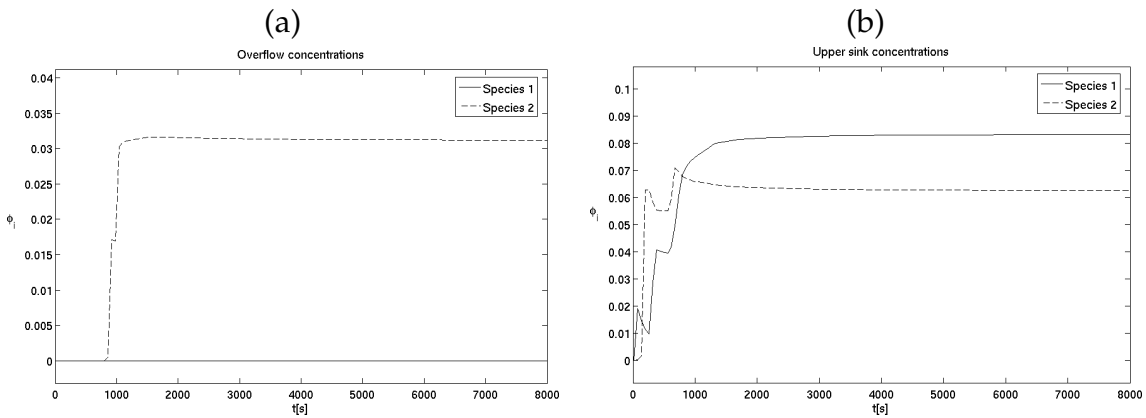


Figure A.5: Example A.1: (a) Overflow, (b) sink concentrations.

the overflow. Then, we can deduce that full separation is attained in the overflow, but with a decrease of the concentration of species 1 in relation to feed concentration, whereas in the sink, concentrations of both species increase in relation to feed. In fact, Figure A.5 illustrates that according to our simulation, the system has nearly attained steady state at  $t = 8000$  s, since at steady state the entire influx of

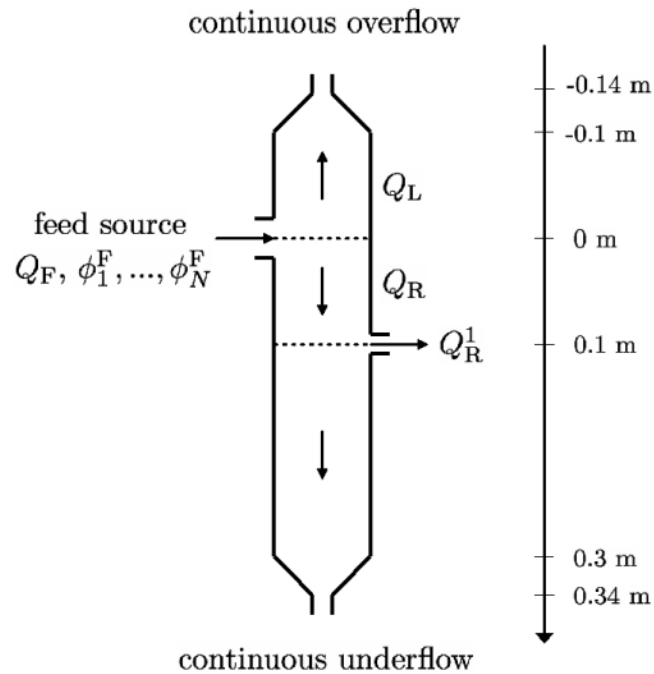


Figure A.6: Vessel 2: Classifier-type CT with varying interior area.

species 1 should leave the unit through the sink, causing a sink stream concentration of  $(Q_F/|Q_L^1|)\phi_1^F = 0.0833$ . This value is practically attained by  $t = 8000$  s.

In Figure A.4 we can observe the evolution of the total volume fraction of solids, which seems to reach steady state before each species does.

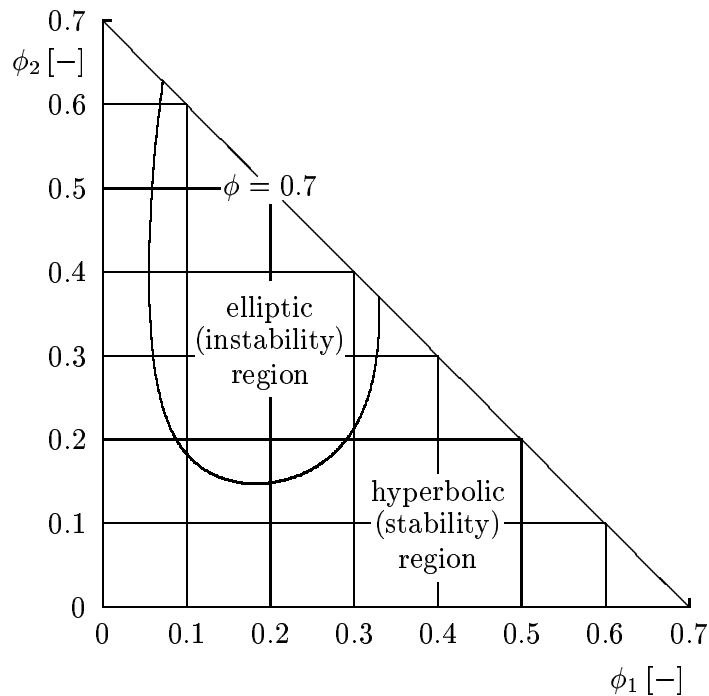
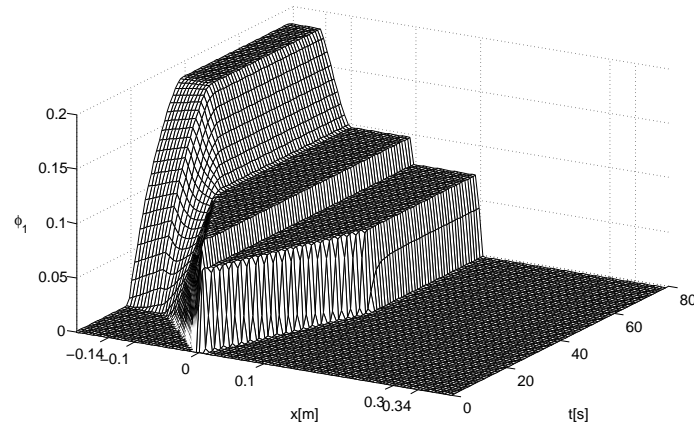


Figure A.7: Example A.2: Stability and instability regions.

### A.1.3 Example A.2: Separation of a bidisperse suspension in a continuous CT with sink

Nasr-El-Din et al. in [136, 134, 135] consider bidisperse suspensions with buoyant and heavy species, and we here take the parameters of the experimental data indicated by Nasr-el-Din et al. in [135]. For this heavy-buoyant system, the model equations are no longer uniformly hyperbolic (stable); rather, an appreciable ellipticity (instability) region in phase space emerges, see Figure A.7. It can be shown that in regions where  $S(x) > 0$ , the governing equation (4.4.7) is stable (hyperbolic) for a given vector  $\Phi \in \mathcal{D}_{\phi_{\max}}$  if and only if the equation for batch settling in (4.2.2) is.

(a)



(b)

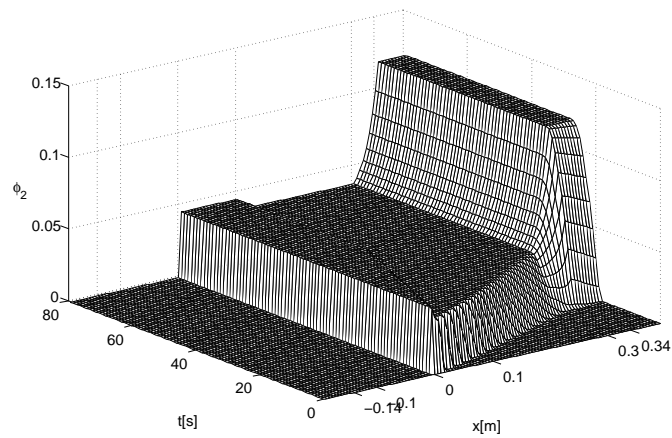


Figure A.8: Example A.2: Simulated concentrations (a)  $\phi_1$  (buoyant particles), (b)  $\phi_2$  (heavy particles).

We work here with Vessel 2, whose cross-sectional area function is given by

$$S(x) = \begin{cases} 2.2 \times 10^{-5} \text{ m}^2 & \text{for } x \leq -0.14 \text{ m and } x > 0.34 \text{ m,} \\ S_1(x) & \text{for } -0.14 \text{ m} < x \leq -0.1 \text{ m,} \\ 4.24 \times 10^{-4} \text{ m}^2 & \text{for } -0.1 \text{ m} < x \leq 0.3 \text{ m,} \\ S_2(x) & \text{for } 0.3 \text{ m} < x \leq 0.34 \text{ m.} \end{cases}$$

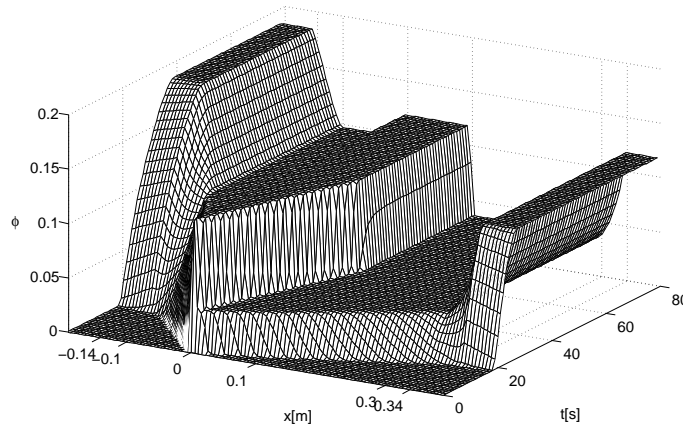


Figure A.9: Example A.2: Simulated total solids concentration  $\phi$ .

Following Nasr-el-Din et al. [135], we assume that Vessel 2 has a rectangular cross section, and that one side of the rectangle (the “thickness” of the equipment) is constant for  $-0.14 \text{ m} \leq x \leq 0.34 \text{ m}$ . In the zones  $[-0.14 \text{ m}, -0.1 \text{ m}]$  and  $[0.3 \text{ m}, 0.34 \text{ m}]$ , which appear in Figure A.6 as “roof-shaped” segments, the cross-sectional area varies linearly with  $x$ , and is defined by

$$S_1(x) := 9.898 \times 10^{-3} \text{ m} \times (x - 0.14 \text{ m}) + 2.809 \times 10^{-5} \text{ m}^2,$$

$$S_2(x) := -9.898 \times 10^{-3} \text{ m} \times (x - 0.3 \text{ m}) + 4.24 \times 10^{-4} \text{ m}^2.$$

The material, model and flow parameters for this case given in Table A.1 are based on experimental from Nasr-el-Din et al. [135]. The particle parameters correspond to polystyrene particles (species 1) and glass beads (species 2), while the fluid parameters come from a salt solution at  $20^\circ\text{C}$ . For monodisperse suspensions of each particle species, the suitable exponents of the Richardson and Zaki hindered settling function are  $n = n_1 = 5.705$  and  $n = n_2 = 5.826$ , respectively. For this bidisperse suspension we utilize  $n = (n_1 + n_2)/2 = 5.765$ .

We observe in Figure A.8 that species 1 enters both the clarification and settling zones. Near steady state, its concentration has a small increasing jump at feed source

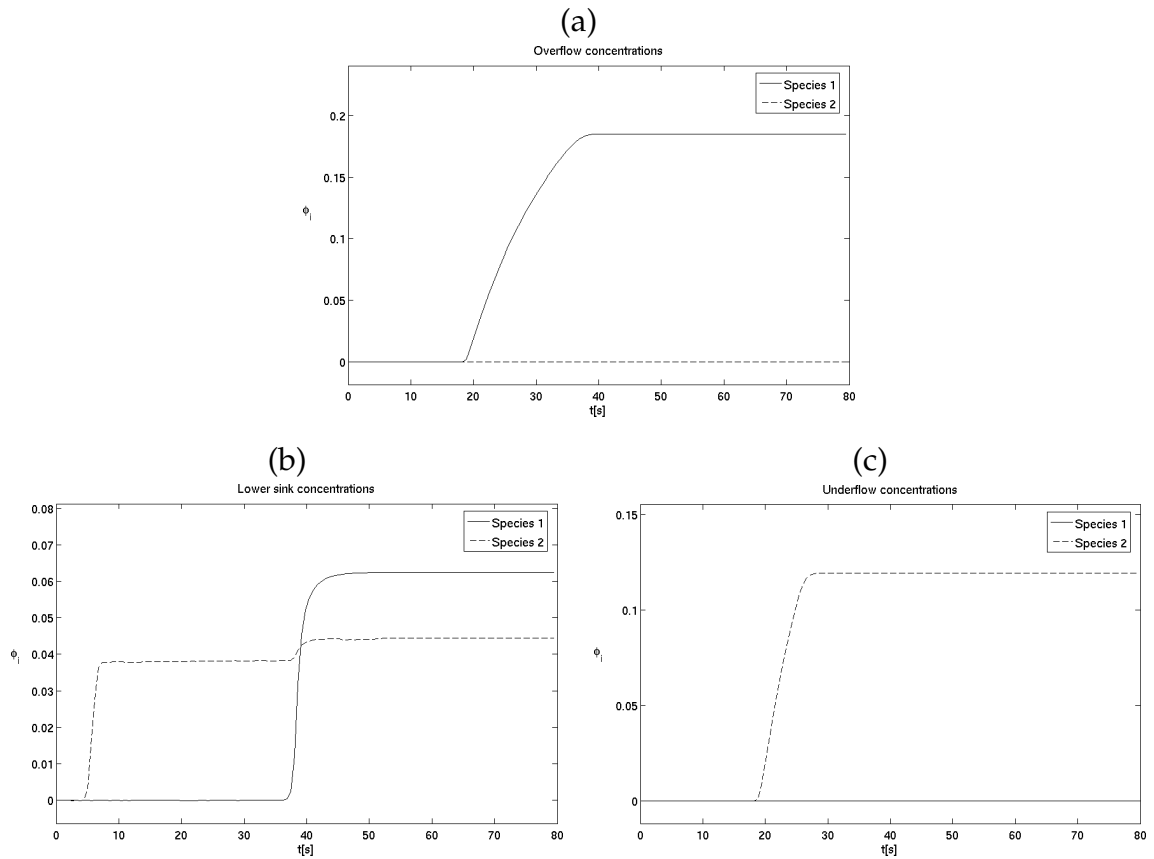


Figure A.10: Example A.2: (a) Overflow, (b) lower sink, (c) underflow concentrations.

level, gradually increases near the overflow level, and has a decreasing jump at sink level. Species 2 only enters the settling zone. At steady state, the concentration of  $\phi_2$  shows a small decreasing jump at sink level, and a big gradual increase of concentration near the underflow level. Moreover, we see in Figure A.10 that species 1 leaves the clarification zone by the overflow and the settling zone by the sink, whereas species 2 leaves the settling zone by the sink and underflow. Then we can conclude that full separation is attained in the overflow and underflow, with a significant increase of the concentration of species 1 and species 2 in relation to feed concentration, respectively. In the sink, species 1 does not change much its concentration,

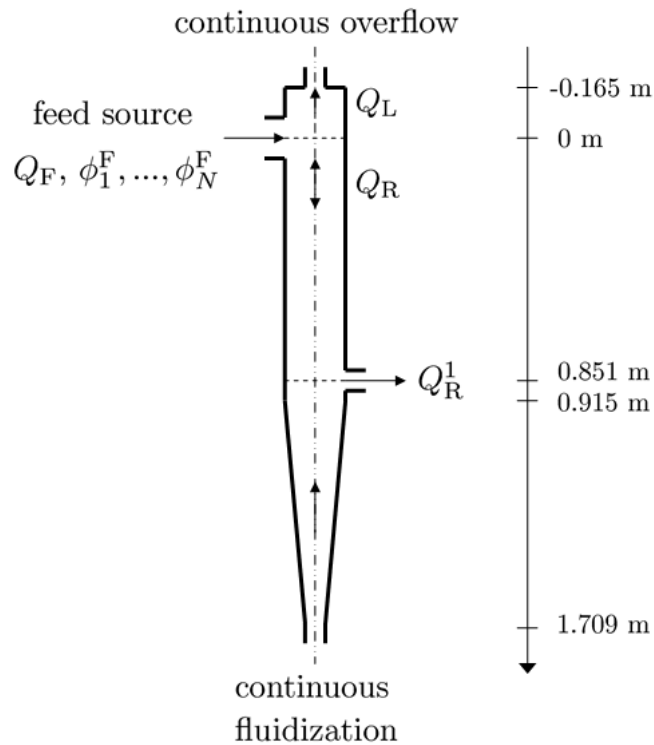


Figure A.11: Vessel 3: Classifier-type liquid fluidized bed with varying interior area.

and species 2 has a drop in its concentration, both in relation to feed. Figure A.9 illustrates that for this particular example, the total solids concentration for this example remains below 0.2. This indicates that here the numerical solution completely sojourns in the region of stability shown in Figure A.7.

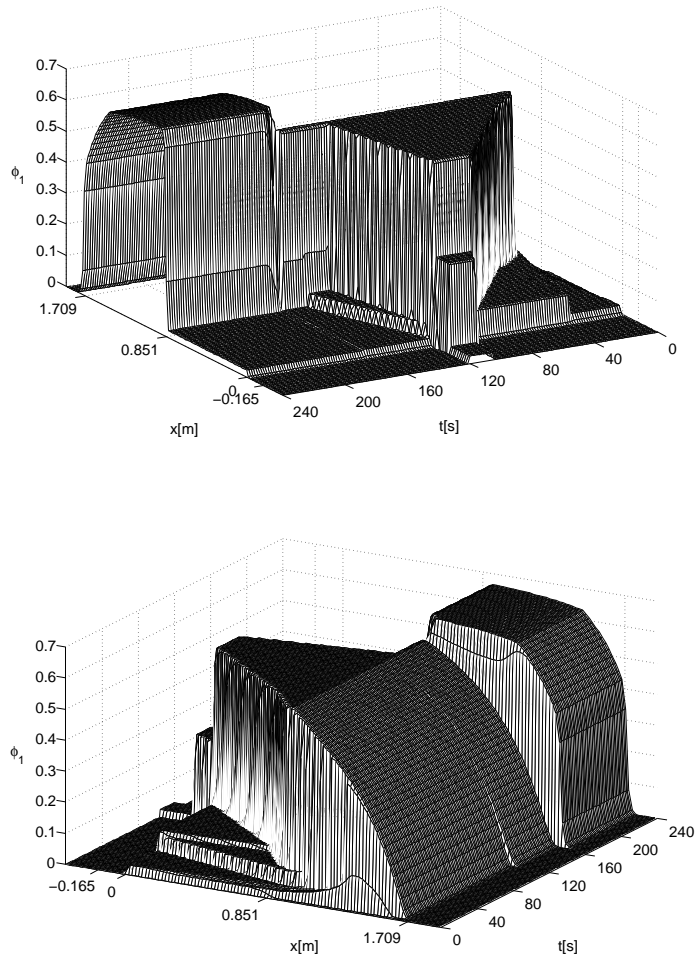


Figure A.12: Example A.3: Simulated concentration  $\phi_1$  (large particles; two views).

#### A.1.4 Example A.3: Continuous separation of a bidisperse suspension in a liquid fluidized bed classifier with variable control functions

Chen et al. in [40] report a hydrodynamic model for a liquid-solid classifier applied to the steady state separation of monodisperse, bidisperse and multi-sized

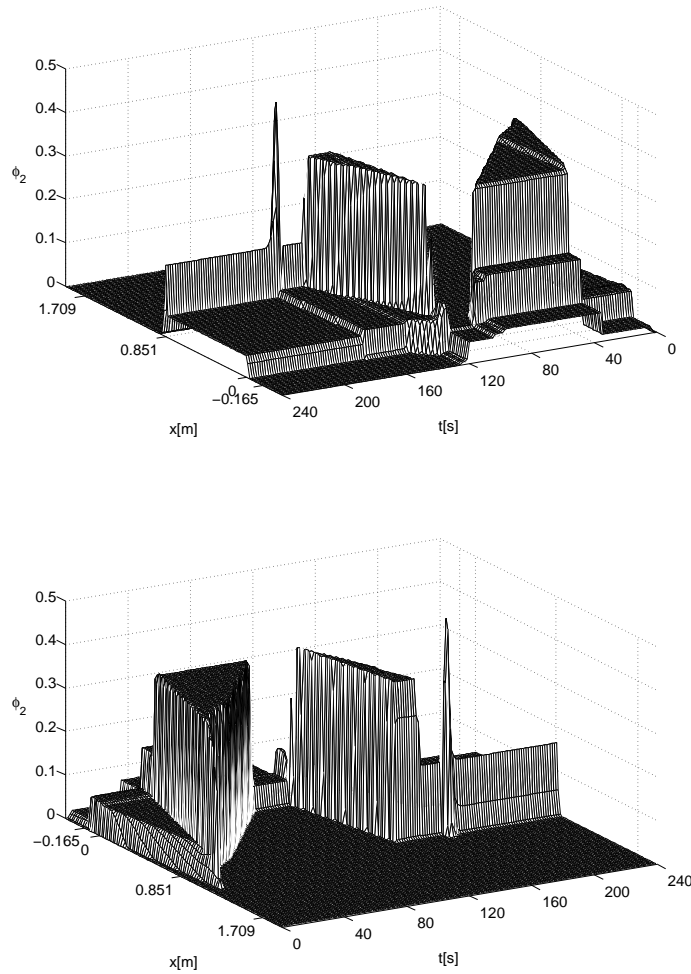


Figure A.13: Example A.3: Simulated concentration  $\phi_2$  (small particles; two views).

suspensions in a liquid fluidized bed classifier, and we here take the parameters of the experimental data described there. We consider Vessel 3, corresponding to

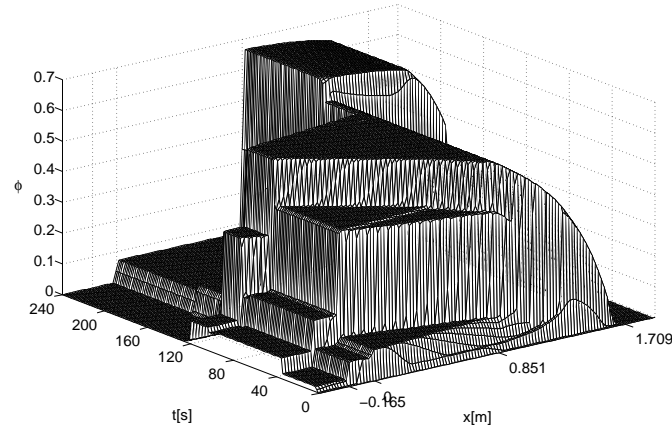


Figure A.14: Example A.3: Simulated total solids concentration  $\phi$ .

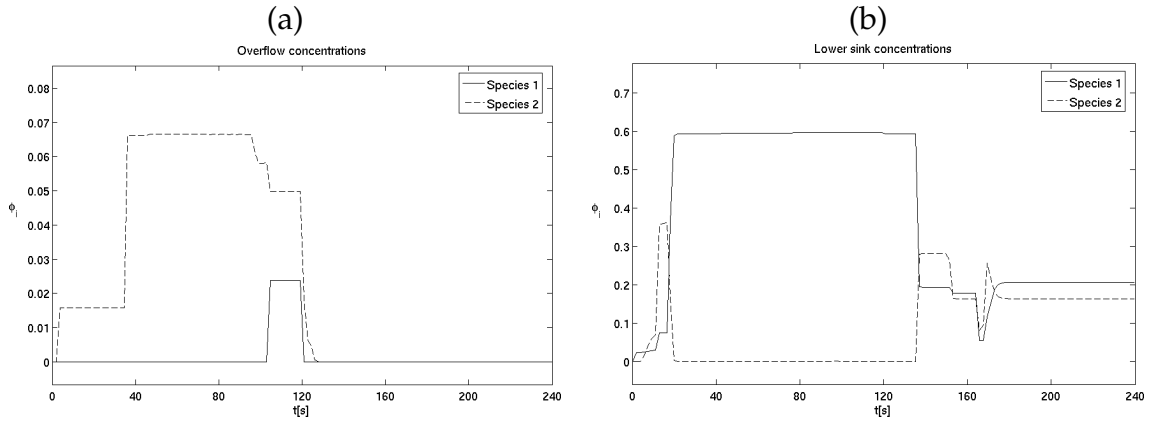


Figure A.15: Example A.3: (a) Overflow, (b) Sink concentrations.

equipment “T-2” used by Chen et al. in [40], which is described by the function

$$S(x) = \begin{cases} 4.54 \times 10^{-3} \text{ m}^2 & \text{for } x \leq -0.165 \text{ m,} \\ 0.0287 \text{ m}^2 & \text{for } -0.165 \text{ m} < x \leq 0.915 \text{ m,} \\ S_3(x) & \text{for } 0.915 \text{ m} < x \leq 1.709 \text{ m,} \\ 2.04 \times 10^{-3} \text{ m}^2 & \text{for } x > 1.709 \text{ m,} \end{cases}$$

including a conical segment defined by

$$S_3(x) := 0.7854(0.191\text{m} - 0.1763(x - 0.915\text{ m}))^2.$$

The material parameters indicated in Table A.1 correspond to glass beads of two different sizes and water at 20 °C. In this simulation, the values of  $Q_L$  and  $Q_R^1$  are chosen as piecewise constant functions of  $t$  as indicated in Table A.1. For monodisperse suspensions of spherical particles, we calculate the exponents of the Richardson and Zaki hindered settling function for each species  $n = n_1$  and  $n = n_2$ , respectively, with the formulas given by Richardson and Zaki in [147]. Then, for this bidisperse suspension we utilize  $n = (n_1 + n_2)/2 = 2.58$ .

We see in Figure A.12 that between  $t = 0$  and  $t = 120\text{ s}$ , species 1 enters the settling zone and forms a rising sediment. At steady state, the concentration of species 1 increases continuously in the conical zone and has decreasing jumps across the overflow and feed source levels. On the other hand, we observe in Figure A.13 that species 2 enters both zones and forms a rising sediment above the sediment of species 1, but it does not reach the conical zone. At steady state, the concentration of species 2 has small increasing jumps at the feed source and near the overflow level, and a small decreasing jump at overflow level. Moreover, we observe in Figure A.15 that at steady state, species 1 leaves the vessel by the sink stream and overflow, whereas species 2 leaves the vessel only by the overflow. Then we can deduce that a full separation is attained in the sink, with an increase of the concentration of species 1 in relation to feed concentration, whereas in the overflow, concentrations of both species are smaller in relation to feed.

Between  $t = 120\text{ s}$  and  $t = 165\text{ s}$ , we observe that species 1 and 2 disappear from the clarification zone, leaving the vessel only by the sink, and their concentrations reach a new steady state with jumps at sink level. After  $t = 165\text{ s}$ , species 1 has a big and rapid rise of its concentration in the settling zone rapidly and leaves the unit only by the sink, meanwhile species 2 does not enter the settling zone, has a small drop of its concentration and leaves the vessel by the sink. Note the jump of concentration of species 2 at sink level. In Figure A.14 we show the total concentration of solids for this simulation.

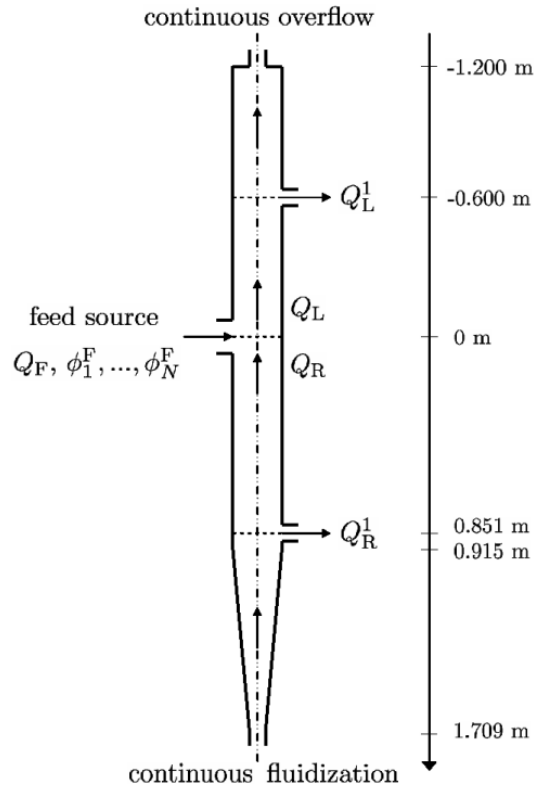


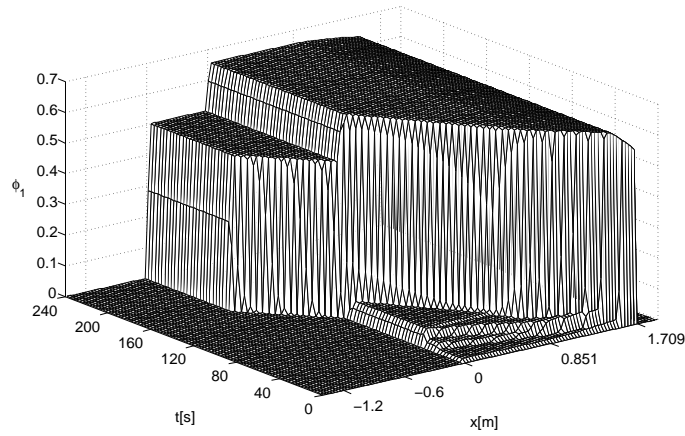
Figure A.16: Vessel 4: Classifier-type liquid fluidized bed with varying interior area and two sinks.

### A.1.5 Example A.4: Continuous separation of a tridisperse suspension in a liquid fluidized bed classifier

We here take the parameters of the experimental data described by Chen et al. in [40] with some few changes. We consider Vessel 4 with the function

$$S(x) = \begin{cases} 0.01815 \text{ m}^2 & \text{for } x \leq -1.200 \text{ m}, \\ 0.0287 \text{ m}^2 & \text{for } -1.200 \text{ m} < x \leq 0.915 \text{ m}, \\ S_4(x) & \text{for } 0.915 \text{ m} < x \leq 1.709 \text{ m}, \\ 8.17 \times 10^{-3} \text{ m}^2 & \text{for } x > 1.709 \text{ m}, \end{cases}$$

(a)



(b)

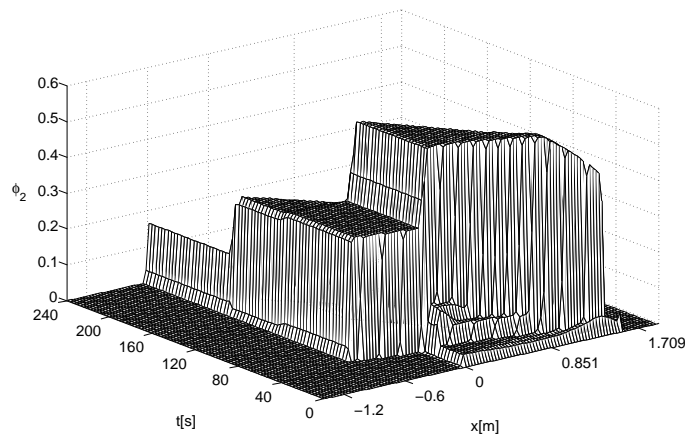


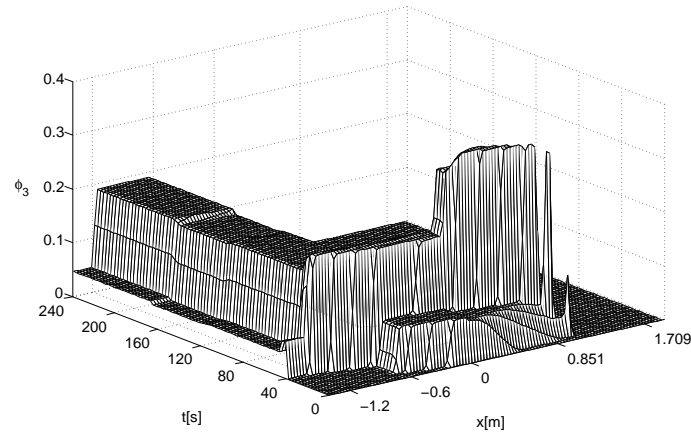
Figure A.17: Example A.4: Simulated concentrations (a)  $\phi_1$  (large particles), (b)  $\phi_2$  (medium particles).

where the conical segment is described by

$$S_4(x) := 0.7854(0.191 \text{ m} - 0.1121(x - 0.915 \text{ m}))^2.$$

The solid and fluid materials are, as in Example 3, glass beads and water at room temperature.

(a)



(b)

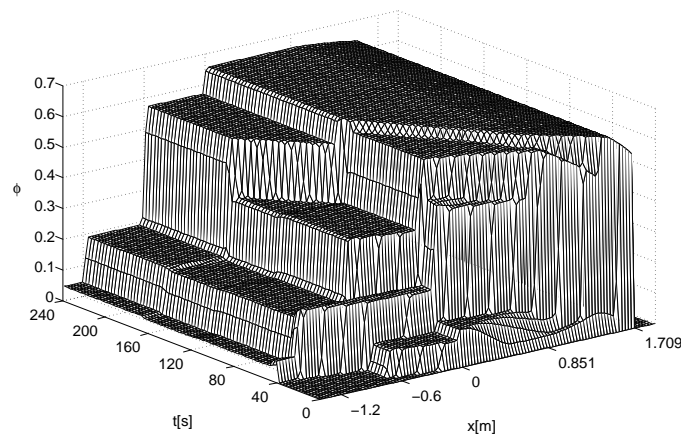


Figure A.18: Example A.4: Simulated concentrations (a)  $\phi_3$  (small particles), (b)  $\phi$  (total solids).

We see in Figure A.17 that species 1 enters the settling zone and forms a rising sediment. At steady state, the concentration of species 1 has an increasing jump at underflow level, increases continuously in the conical zone, and has decreasing jumps across the feed source and upper sink levels. On the other hand, species 2 enters the settling zone and forms a rising sediment above the sediment of species 1.

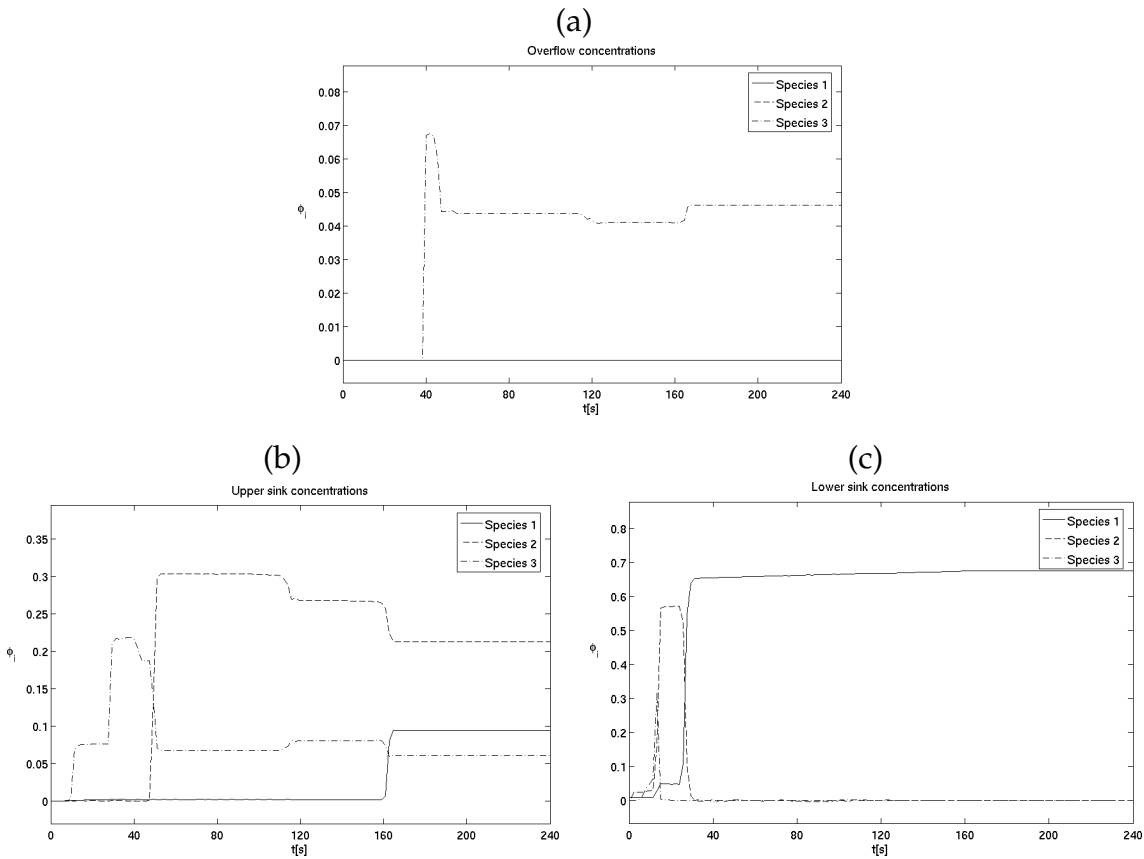


Figure A.19: Example A.4: (a) Overflow, (b) upper sink, (c) lower sink concentrations.

At steady state, the concentration of species 2 has small increasing jumps across the feed source and below the upper sink levels, and a decreasing jump at the upper sink level. Finally, we see in Figure A.18 (a) that species 3 enters both zones and forms a rising sediment above the sediment of species 2, but does not reach the conical zone. At steady state, the concentration of species 3 has a small increasing jump at feed source level, an increasing jump at upper sink level, and a decreasing jump at overflow level. Moreover, we observe in Figure A.19 that species 1 leaves the vessel by the lower and upper sinks, species 2 leaves the vessel by the upper sink, and species 3 leaves the vessel by the upper sink and overflow. Then we can

deduce that a full separation of species 1 is attained in the lower sink, with a big increase of the concentration of species 1 in relation to feed; also a full separation of species 3 is attained in the overflow, with a small decrease of the concentration of species 3 in relation to feed. In the upper sink, the concentration of species 2 increases much, but concentrations of species 1 and 3 almost do not change, in relation to feed. Figure A.18 (b) shows the total volume fraction of solids for this example.



# Bibliography

- [1] Adimurthi, Jaffré, J. & Veerappa Gowda, G.D. (2004) Godunov-type methods for conservation laws with a flux function discontinuous in space. *SIAM J. Numer. Anal.*, **42**, 179–208.
- [2] Adimurthi, Mishra, S. & Veerappa Gowda, G.D. (2005) Optimal entropy solutions for conservation laws with discontinuous flux-functions. *J. Hyp. Diff. Eqns.*, **2**, 783–837.
- [3] Adimurthi & Veerappa Gowda, G.D. (2002) Conservation law with discontinuous flux. *J. Math. Kyoto Univ.*, **42**, 27–70.
- [4] Amadori, D., Gosse, L. & Guerra G. (2004) Godunov-type approximation for a general resonant balance law with large data. *J. Differential Equations*, **198**, 233–274.
- [5] Ansorge, R. (1990) What does the entropy condition mean in traffic flow theory? *Transp. Res. B*, **24**, 133–143.
- [6] Audusse, E. & Perthame, B. (2005) Uniqueness for a scalar conservation law with discontinuous flux via adapted entropies. *Proc. Royal Soc. Edinburgh Sect. A*, **135**, 253–265.
- [7] Bachmann, F. & Vovelle, J. (2006) Existence and uniqueness of entropy solution of scalar conservation laws with a flux function involving discontinuous coefficients. *Comm. Partial Differential Equations*, **31**, 371–395.

- 
- [8] Batchelor, G.K. & Janse van Rensburg, R.W. (1986) Structure formation in bidisperse sedimentation. *J. Fluid Mech.*, **166**, 379–407.
- [9] Bellomo, N., Marasco, A. & Romano, A. (2002) From the modelling of driver's behavior to hydrodynamic models and problems of traffic flow. *Nonlin. Anal. Real. World Appl.*, **3**, 339–363.
- [10] Benzoni-Gavage, S. & Colombo, R.M. (2003) An  $n$ -populations model for traffic flow. *Eur. J. Appl. Math.*, **14**, 587–612.
- [11] Berres, S. (2006) *Modeling, analysis and numerical simulation of polydisperse suspensions*, Doctoral Thesis, University of Stuttgart.
- [12] Berres, S., Bürger, R., Karlsen, K.H. & Tory, E.M. (2003) Strongly degenerate parabolic-hyperbolic systems modeling polydisperse sedimentation with compression. *SIAM J. Appl. Math.*, **64**, 41–80.
- [13] Berres, S., Bürger, R. & Karlsen, K.H. (2004) Central schemes and systems of conservation laws with discontinuous coefficients modeling gravity separation of polydisperse suspensions. *J. Comp. Appl. Math.*, **164-165**, 53–80.
- [14] Biesheuvel, P.M. (2000) Particle segregation during pressure filtration for cast formation. *Chem. Eng. Sci.*, **55**, 2595–2606.
- [15] Biesheuvel, P.M., Verweij, H. & Breedveld, V. (2001) Evaluation of instability criterion for bidisperse sedimentation. *AIChE Journal*, **47**, 45–52.
- [16] Bonzani, I. (2000) Hydrodynamic models of traffic flow: drivers' behaviour and nonlinear diffusion. *Math. Comp. Modelling*, **31**, 1–8.
- [17] Bouchut, F. & James, F. (1998) One-dimensional transport equations with discontinuous coefficients. *Nonlinear Anal.*, **32**, 891–933.
- [18] Braun, J. (2001) Segregation of granular media by diffusion and convection. *Phys. Rev. E*, **64**, paper 011307.

- 
- [19] Brennen, C.E. (2005) *Fundamentals of Multiphase Flow*, Cambridge University Press, Cambridge, UK.
- [20] Bürger, R., Concha, F., Fjelde, K.K. & Karlsen, K.H. (2000) Numerical simulation of the settling of polydisperse suspensions of spheres. *Powder Technol.*, **113**, 30–54.
- [21] Bürger, R., Concha, F., Karlsen, K.H. & Narváez, A. (2006) Numerical simulation of clarifier-thickener units treating ideal suspensions with a flux density function having two inflection points. *Math. Comp. Modelling*, **44**, 255–275.
- [22] Bürger, R., Fjelde, K.K., Höfler, K. & Karlsen, K.H. (2001) Central difference solutions of the kinematic model of settling of polydisperse suspensions and three-dimensional particle-scale simulations. *J. Eng. Math.*, **41**, 167–187.
- [23] Bürger, R., García, A., Karlsen, K.H. & Towers, J.D. (2006) On an extended clarifier-thickener model with singular source and sink terms. *Eur. J. Appl. Math.*, **17**, 257–292.
- [24] Bürger, R., García, A., Karlsen, K.H. & Towers, J.D. (2007) A kinematic model of continuous separation and classification of polydisperse suspensions. *Comput. Chem. Eng.*, to appear.
- [25] Bürger, R., García, A., Karlsen, K.H. & Towers, J.D. (2007) A family of schemes for kinematic flows with discontinuous flux. *J. Eng. Math.*, to appear.
- [26] Bürger, R., García, A., Karlsen, K.H. & Towers, J.D. (2007) A difference scheme and entropy solutions for an inhomogeneous kinematic traffic model. In preparation.
- [27] Bürger, R. & Karlsen, K.H. (2003) On a diffusively corrected kinematic-wave traffic flow model with changing road surface conditions. *Math. Models Methods Appl. Sci.*, **13**, 1767–1799.

- [28] Bürger, R., Karlsen, K.H., Klingenberg, C. & Risebro, N.H. (2003) A front tracking approach to a model of continuous sedimentation in ideal clarifier-thickener units. *Nonlin. Anal. Real World Appl.*, **4**, 457–481.
- [29] Bürger, R., Karlsen, K.H., Mishra, S. & Towers, J.D. (2005) On conservation laws with discontinuous flux. *Trends in Applications of Mathematics to Mechanics* (Y. Wang & K. Hutter eds.). Aachen: Shaker Verlag, pp. 75–84.
- [30] Bürger, R., Karlsen, K.H., Risebro, N.H. & Towers, J.D. (2004) Numerical methods for the simulation of continuous sedimentation in ideal clarifier-thickener units. *Int. J. Mineral Process.*, **73**, 209–228.
- [31] Bürger, R., Karlsen, K.H., Risebro, N.H. & Towers, J.D. (2004) Well-posedness in  $BV_t$  and convergence of a difference scheme for continuous sedimentation in ideal clarifier-thickener units. *Numer. Math.*, **97**, 25–65.
- [32] Bürger, R., Karlsen, K.H., Tory, E.M. & Wendland, W.L. (2002) Model equations and instability regions for the sedimentation of polydisperse suspensions of spheres. *ZAMM Z. Angew. Math. Mech.*, **82**, 699–722.
- [33] Bürger, R., Karlsen, K.H. & Towers, J.D. (2005) Closed-form and finite difference solutions to a population balance model of grinding mills. *J. Eng. Math.*, **51**, 165–195.
- [34] Bürger, R., Karlsen, K.H. & Towers, J.D. (2005) A model of continuous sedimentation of flocculated suspensions in clarifier-thickener units. *SIAM J. Appl. Math.*, **65**, 882–940.
- [35] Bürger, R., Karlsen, K.H. & Towers, J.D. (2005) Mathematical model and numerical simulation of the dynamics of flocculated suspensions in clarifier-thickeners. *Chem. Eng. J.*, **111**, 119–134.
- [36] Bürger, R. & Kozakevicius, A. (2007) Adaptive multiresolution WENO schemes for multi-species kinematic flow models. *J. Comput. Phys.*, **224**, 1190–1222.

- [37] Bustos, M.C., Concha, F. (1999) Settling velocities of particulate systems: 10. A numerical method for solving Kynch sedimentation processes. *Int. J. Miner. Process.* **57**, 185-203.
- [38] Bustos, M.C., Concha, F., Bürger, R. & Tory, E.M. (1999) *Sedimentation and Thickening*. Kluwer Academic Publishers, Dordrecht, The Netherlands.
- [39] Čanić, S. & Mirković, D. (2001) A hyperbolic system of conservation laws in modeling endovascular treatment of abdominal aortic aneurysm. *Hyperbolic Problems: Theory, Numerics, Applications. Eighth International Conference in Magdeburg, February/March 2000, Volume I. International Series of Numerical Mathematics* **140** (Freistühler, H. & Warnecke, G. eds.). Basel: Birkhäuser Verlag, pp. 227–236.
- [40] Chen, A., Grace, J.R., Epstein, N. & Lim, C.J. (2002) Steady state dispersion of mono-size, binary and multi-size particles in a liquid fluidized bed classifier. *Chem. Eng. Sci.*, **57**, 991–1002.
- [41] Chen, A., Grace, J.R., Epstein, N. & Lim, C.J. (2002) Unsteady state hydrodynamic model and dynamic behaviour of a liquid fluidized-bed classifier. *Chem. Eng. Sci.*, **57**, 1003–1010.
- [42] Chitour, Y. & Piccoli, B. (2005) Traffic circles and timing of traffic lights for cars flow. *Discr. Cont. Dyn. Syst. Ser. B*, **5**, 599–630.
- [43] Chodavarapu, P., Munukutla, S.S. & Peddieson, J. (1995) A comprehensive model of batch sedimentation. *Fluid/Particle Sep. J.*, **8**, 54–57.
- [44] Coclite, G.M., Garavello, M. & Piccoli, B. (2005) Traffic flow on a road network. *SIAM J. Math. Anal.*, **36**, 1862–1886.
- [45] Crandall, M.G. & Majda, A. (1980) Monotone difference approximations for scalar conservation laws. *Math. Comp.*, **34**, 1–21.

- [46] Crowe, C., Sommerfeld, M. & Tsuji, Y. (1998) *Multiphase Flows with Droplets and Particles*, CRC Press, Boca Raton, FL, USA.
- [47] Dafermos, C.M. (1972) Polygonal approximation of solutions of the initial value problem for a scalar conservation law. *J. Math. Anal. Appl.*, **38**, 33–41.
- [48] Dafermos, C.M. (2005) *Hyperbolic Conservation Laws in Continuum Physics*, Second Ed., Springer-Verlag, Berlin.
- [49] Daganzo, C.F. (1995) The cell transmission model, part II: network traffic. *Transp. Res. B*, **29**, 79–93.
- [50] Das, S.K. & Biswas, M.N. (2003) Separation of oil-water mixture in tank. *Chem. Eng. Comm.*, **190**, 116–127
- [51] Deen, N.G., Van Sint Annaland, M., Van der Hoef, M.A., & Kuipers, J.A.M. (2007) Review of discrete particle modelling of fluidized beds. *Chem. Eng. Sci.*, **62**, 28–44.
- [52] Diehl, S. (1995) On scalar conservation laws with point source and discontinuous flux function. *SIAM J. Math. Anal.*, **26**, 1425–1451.
- [53] Diehl, S. (1996) A conservation law with point source and discontinuous flux function modelling continuous sedimentation. *SIAM J. Appl. Math.*, **56**, 388–419.
- [54] Diehl, S. (1996) Scalar conservation laws with discontinuous flux function: I. The viscous profile condition. *Commun. Math. Phys.*, **176**, 23–44.
- [55] Diehl, S. (1997) Dynamic and steady-state behaviour of continuous sedimentation. *SIAM J. Appl. Math.*, **57**, 991–1018.
- [56] Diehl, S. (2000) On boundary conditions and solutions for ideal clarifier-thickener units. *Chem. Eng. J.*, **80**, 119–133.

- [57] Diehl, S. (2001) Operating charts for continuous sedimentation I: Control of steady states. *J. Eng. Math.*, **41**, 117–144.
- [58] Diehl, S. (2005) Operating charts for continuous sedimentation II: Step responses. *J. Eng. Math.*, **53**, 139–185.
- [59] Diehl, S. (2006) Operating charts for continuous sedimentation III: Control of step inputs. *J. Eng. Math.*, **54**, 225–259.
- [60] Diehl, S. (2007) Operating charts for continuous sedimentation IV. *J. Eng. Math.*, to appear.
- [61] Diehl, S. & Wallin, N.-O. (1996) Scalar conservation laws with discontinuous flux function: II. On the stability of the viscous profiles. *Commun. Math. Phys.*, **176**, 45–71.
- [62] Drew, D.A. & Passman, S.L. (1999) *Theory of Multicomponent Fluids*, Springer-Verlag, New York.
- [63] El-Genk, M.S., Kim, S.H. & Erickson, D. (1985) Sedimentation of binary mixtures of particles of unequal densities and of different sizes. *Chem. Eng. Commun.*, **36**, 99–119.
- [64] Engquist, B. & Osher, S. (1980) Stable and entropy satisfying approximations for transonic flow calculations. *Math. Comp.*, **34**, 45–75.
- [65] Engquist, B. & Osher, S. (1981) One-sided difference approximations for nonlinear conservation laws. *Math. Comp.*, **36**, 321–351.
- [66] Enwald, H., Peirano, E. & Almstedt, A.E. (1996) Eulerian two-phase flow theory applied to fluidization. *Int. J. Multiphase Flow*, **22** (Suppl.), 21–66.
- [67] Esipov, S.E. (1995) Coupled Burgers equations: a model of polydisperse sedimentation. *Phys. Rev. E*, **52**, 3711–3718.

- [68] Falk, V. & D'Ortona, U. (2002) A polydisperse sedimentation and polydisperse packing model. *Powder Technol.*, **128**, 229–335.
- [69] Fried, E. & Roy, B.C. (2003) Gravity-induced segregation of cohesionless granular mixtures. *Dynamic Response of Granular and Porous Materials Under Large and Catastrophic Deformations* (K. Hutter, N. Kirchner eds.). Berlin: Springer-Verlag, pp. 393–421.
- [70] Frising, T., Noik, C. & Dalmazzone, C. (2006) The liquid/liquid sedimentation process: From droplet coalescence to technologically enhanced water/oil emulsion gravity separators: A review. *J. Disp. Sci. Technol.*, **27**, 1035–1057
- [71] Galvin, K.P., Callen, A., Zhou, J. & Doroodchi, E. (2005) Performance of the reflux classifier for gravity separation at full scale. *Minerals Eng.*, **18**, 19–24.
- [72] Galvin, K.P., Doroodchi, E., Callen, A.M., Lambert, N. & Pratten, S.J. (2002) Pilot plant trial of the reflux classifier. *Minerals Eng.*, **15**, 19–25.
- [73] Galvin, K.P. & Nguyentrannam, G. (2002) Influence of parallel plates in a liquid fluidized bed system. *Chem. Eng. Sci.*, **57**, 1231–1234.
- [74] Garavello, M. & Piccoli, B. (2005) Source-destination flow on a road network. *Comm. Math. Sci.*, **3**, 261–283.
- [75] Garavello, M. & Piccoli, B. (2006) *Traffic Flow on Networks*, American Institute of Mathematical Sciences, Springfield, MO, USA.
- [76] Gasser, I. (2003) On non-entropy solutions of scalar conservation laws for traffic flow. *ZAMM Z. Angew. Math. Mech.*, **83**, 137–143.
- [77] Gera, D., Gautam, M., Tsuji, Y., Kawaguchi, T. & Tanaka, T. (1998). Computer simulation of bubbles in large-particle fluidized beds. *Powder Technol.*, **98**, 38–47.
- [78] Gibilaro, L.G. (2001). *Fluidization-dynamics*, Butterworth-Heinmann, Jordan Hill, UK.

- [79] Gidaspow, D. (1994). *Multiphase Flow and Fluidization*, Academic Press, San Diego, CA, USA.
- [80] Gimse, T. (1993) Conservation laws with discontinuous flux functions. *SIAM J. Math. Anal.*, **24**, 279–289.
- [81] Gimse, T. & Risebro, N.H. (1990) Riemman problems with a discontinuous flux function. *Proc. 3rd Conf. Hyp. Problems, Uppsala, Sweden*.
- [82] Gimse, T. & Risebro, N.H. (1992) Solution of the Cauchy problem for a conservation law with a discontinuous flux function. *SIAM J. Math. Anal.*, **23**, 635–648.
- [83] Glowinski, R., Pan, T.W., Hesla, T.I., Joseph, D.D. & Périaux, J. (2001). A fictitious domain approach to the direct numerical simulation of incompressible viscous flow past moving rigid bodies: application to particulate flow. *J. Comput. Phys.*, **169**, 363–426.
- [84] Gottlieb, S., Shu, C.W. & Tadmor, E. (2001) Strong stability preserving high-order time discretization methods. *SIAM Review*, **43**, 89–112.
- [85] Greenspan, H.P. & Ungarish, M. (1982) On hindered settling of particles of different sizes. *Int. J. Multiphase Flow*, **8**, 587–604.
- [86] Ha, Z. & Liu, S. (2002) Settling velocities of polydisperse concentrated suspensions. *Canad. J. Chem. Eng.*, **80**, 783–790.
- [87] Harten, A., Hyman, J.M. & Lax, P.D. (1976) On finite difference approximations and entropy conditions for shocks. *Comm. Pure Appl. Math.*, **29**, 297–322.
- [88] Harten, A. (1983) High resolution schemes for hyperbolic conservation laws. *J. Comput. Phys.*, **49**, 357–393.
- [89] Hartland, S. & Jeelani, S.A.K. (1987) Choice of model for predicting the dispersion height in liquid/liquid gravity settlers from batch settling data. *Chem. Eng. Sci.*, **42** 1927–1938.

- [90] Hartland, S. & Jeelani, S.A.K. (1988) Prediction of sedimentation and coalescence profiles in a decaying batch dispersion. *Chem. Eng. Sci.*, **43**, 2421–2429
- [91] Helbing, D. (1997) *Verkehrsdynamik*, Springer-Verlag, Berlin.
- [92] Herty, M., Kirchner, C. & Moutari, S. (2006) Multi-class traffic models on road networks. *Comm. Math. Sci.*, **4**, 591–608.
- [93] Hilliges, M. & Weidlich, W. (1995) A phenomenological model for dynamic traffic flow in networks. *Transp. Res. B*, **29**, 407–431.
- [94] Holden, H., Holden, L. & Høegh-Krohn, R. (1988) A numerical method for first order nonlinear scalar conservation laws in one dimension. *Comput. Math. Appl.*, **15**, 595–602.
- [95] Holden, H. & Risebro, N.H. (1995) A mathematical model of traffic flow on a network of unidirectional roads. *SIAM J. Math. Anal.*, **26**, 999–1017.
- [96] Holden, H. & Risebro, N.H., 2002. *Front Tracking For Conservation Laws*, Springer-Verlag, New York.
- [97] Jackson, R. (2000) *The Dynamics of Fluidized Particles*, Cambridge University Press, Cambridge, UK.
- [98] Jeelani, S.A.K. & Hartland, S. (1988) Dynamic response of gravity settlers to changes in dispersion throughput. *AIChE J.*, **34**, 335–340
- [99] Jeelani, S.A.K. & Hartland, S. (1993) The continuous separation of liquid/liquid dispersions. *Chem. Eng. Sci.*, **48**, 239–254.
- [100] Jeelani, S.A.K., Pandit, A. & Hartland, S. (1990) Factors affecting the decay of batch liquid-liquid dispersions. *Canad. J. Chem. Eng.*, **68**, 924–931.
- [101] Jin, W. & Zhang, H. (2003) The inhomogeneous kinematic wave traffic flow model as a resonant nonlinear system. *Transp. Sci.*, **37**, 294–311.

- [102] Kaasschieter, E.F. (1999) Solving the Buckley-Leverett equation with gravity in a heterogeneous porous medium. *Comput. Geosci.*, **3**, 23–48.
- [103] Karlsen, K.H., Klingenberg, C. & Risebro, N.H. (2003) A relaxation scheme for conservation laws with a discontinuous coefficient. *Math. Comp.*, **73**, 1235–1259.
- [104] Karlsen, K.H., Risebro, N.H. & Towers, J.D. (2002) Upwind difference approximations for degenerate parabolic convection-diffusion equations with a discontinuous coefficient. *IMA J. Numer. Anal.*, **22**, 623–664.
- [105] Karlsen, K.H., Risebro, N.H. & Towers, J.D. (2003)  $L^1$  stability for entropy solutions of nonlinear degenerate parabolic convection-diffusion equations with discontinuous coefficients. *Skr. K. Nor. Vid. Selsk.*, 49 pp.
- [106] Karlsen, K.H. & Towers, J.D. (2004) Convergence of the Lax-Friedrichs scheme and stability for conservation laws with a discontinuous space-time dependent flux. *Chin. Ann. Math.*, **25B**, 287–318.
- [107] Kawaguchi, T., Tanaka, T. & Tsuji, Y. (1998) Numerical simulation of two-dimensional fluidized beds using the discrete element method (comparison between the two- and three-dimensional models). *Powder Technol.*, **96**, 129–138.
- [108] Kawaguchi, T., Sakamoto, M., Tanaka, T., & Tsuji, Y. (2000) Quasi-three-dimensional numerical simulation of spouted beds in cylinder. *Powder Technol.*, **109**, 3–12.
- [109] Kerner, B.S. & Konhäuser, P. (1993) Cluster effect in initially homogeneous traffic flow. *Phys. Rev. E*, **48**, R2335–R2338.
- [110] Kim, B.H. & Klima, M.S. (2004) Development and application of a dynamic model for hindered-settling column separations. *Minerals Eng.*, **17**, 403–410.
- [111] Klar, A., Kühne, R.D. & Wegener, R. (1996) Mathematical models for vehicular traffic. *Surv. Math. Ind.*, **6**, 215–239.

- [112] Klausen, R.A. & Risebro, N.H. (1999) Stability of conservation laws with discontinuous coefficients. *J. Diff. Eqns.*, **157**, 41–60.
- [113] Klingenberg, C. & Risebro, N.H. (1995) Convex conservation laws with discontinuous coefficients. *Comm. PDE*, **20**, 1959–1990.
- [114] Kružkov, S.N. (1970) First order quasilinear equations in several independent variables. *Math. USSR Sb.*, **10**, 217–243.
- [115] Kunii, D. & Levenspiel, O. (1991) *Fluidization Engineering*, 2nd edition, Butterworth-Heinemann, Jordan Hill, UK.
- [116] Kunik, M. (1992) A numerical method for some initial-value problems of one scalar hyperbolic conservation law. *Math. Methods Appl. Sci.*, **15**, 495–509.
- [117] Kunik, M. (1993) A solution formula for a non-convex scalar hyperbolic conservation law with monotone initial data. *Math. Methods Appl. Sci.*, **16**, 895–902.
- [118] Kunik, M., Wendland, W.L., Paiva, F. & Bustos, M.C. (1993) The polygonal approximation in the Kynch theory of sedimentation. *Technical Report 93-07, Department of Mathematical Engineering, University of Concepcion, Chile.*
- [119] Kurganov, A. & Tadmor, E. (2000) New high resolution central schemes for nonlinear conservation laws and convection-diffusion equations. *J. Comput. Phys.*, **160**, 241–282.
- [120] Kynch, G.J. (1952) A theory of sedimentation. *Trans. Faraday Soc.*, **48**, 166–176.
- [121] Lattanzio, C. & Marcati, P. (1997) The zero relaxation limit for the hydrodynamic Whitham traffic flow model. *J. Diff. Eqns.*, **141**, 150–178.
- [122] Law, H.S., Masliyah, J.H., MacTaggart, R.S. & Nandakumar, K. (1987) Gravity separation of bidisperse suspensions: light and heavy particle species. *Chem. Eng. Sci.*, **42**, 1527–1538.

- [123] Lebacque, J.P. (1996) The Godunov scheme and what it means for first order traffic flow models. *Transportation and Traffic Theory, Proceedings of the 13th ISTTT* (J.B. Lesort ed.). Oxford: Pergamon Press, pp. 647–677.
- [124] Le Veque, R.J. (1992) *Numerical Methods for Conservation Laws*, Birkhauser Verlag, Basel, Switzerland.
- [125] Lighthill, M.J. & Whitham, G.B. (1955) On kinematic waves. II. A theory of traffic flow on long crowded roads. *Proc. Roy. Soc. London Ser. A*, **229**, 317–345.
- [126] Lin, L., Temple, J.B. & Wang, J. (1995) A comparison of convergence rates for Godunov's method and Glimm's method in resonant nonlinear systems of conservation laws. *SIAM J. Numer. Anal.*, **32**, 824–840.
- [127] Lin, L., Temple, J.B. & Wang, J. (1995) Suppression of oscillations in Godunov's method for a resonant non-strictly hyperbolic system. *SIAM J. Numer. Anal.*, **32**, 841–864.
- [128] Lockett, M.J. & Bassoon, K.S. (1979) Sedimentation of binary particle mixtures. *Powder Technol.*, **24**, 1–7.
- [129] Masliyah, J.H. (1979) Hindered settling in a multiple-species particle system. *Chem. Eng. Sci.*, **34**, 1166–1168.
- [130] Mishra, S. (2005) Convergence of upwind finite difference schemes for a scalar conservation law with indefinite discontinuities in the flux function. *SIAM J. Numer. Anal.*, **43**, 559–577.
- [131] Mitsutani, K., Grace, J.R. & Lim, C.J. (2005) Residence time distribution of particles in a continuous liquid-solid classifier. *Chem. Eng. Sci.*, **60**, 2703–2713.
- [132] Mochon, S. (1987) An analysis of the traffic on highways with changing road surface conditions. *Math. Modelling*, **9**, 1–11.
- [133] Nadiv, C. & Semiat, R. (1995) Batch settling of liquid-liquid dispersion. *Ind. Eng. Chem. Res.*, **34**, 2427–2435.

- [134] Nasr-El-Din, H., Masliyah, J.H. & Nandakumar, K. (1990) Continuous gravity separation of concentrated bidisperse suspensions in a vertical column. *Chem. Eng. Sci.*, **45**, 849–857.
- [135] Nasr-El-Din, H., Masliyah, J.H. & Nandakumar, K. (1999) Continuous separation of suspensions containing light and heavy particle species. *Canad. J. Chem. Eng.*, **77**, 1003–1012.
- [136] Nasr-El-Din, H., Masliyah, J.H., Nandakumar, K. & Law, D.H.-S. (1988) Continuous gravity separation of a bidisperse suspension in a vertical column. *Chem. Eng. Sci.*, **43**, 3225–3234.
- [137] Nelson, P. (2002) Traveling-wave solutions of the diffusively corrected kinematic-wave model. *Math. Comp. Modelling*, **35**, 561–579.
- [138] Nessyahu, H. & Tadmor, E. (1990) Non-oscillatory central differencing for hyperbolic conservation laws. *J. Comput. Phys.*, **87**, 408–463.
- [139] Nguyentranlam, G. & Galvin, K.P. (2001) Particle classification in the reflux classifier. *Minerals Eng.*, **14**, 1081–1091.
- [140] Osher, S. (1985) Convergence of generalized MUSCL schemes. *SIAM J. Numer. Anal.*, **22**, 947–961.
- [141] Ostrov, D. (2002) Solutions of Hamilton-Jacobi equations and scalar conservation laws with discontinuous space-time dependence. *J. Diff. Eqns.*, **182**, 51–77.
- [142] Pan, T.W., Joseph, D.D., Bai, R., Glowinski, R. & Sarin, V. (2002) Fluidization of 1204 spheres: simulation and experiment. *J. Fluid Mech.*, **451**, 169–191.
- [143] Panoussopoulos, K. (1998) *Separation of Crude Oil-Water Emulsions: Experimental Techniques and Models. Dissertation*, ETH Zürich, Switzerland.
- [144] Patwardhan, V.S. & Tien, C. (1985) Sedimentation and liquid fluidization of solid particles of different sizes and densities. *Chem. Eng. Sci.*, **40**, 1051–1060.

- [145] Qian, S., Bürger, R. & Bau, H.H. (2005) Analysis of sedimentation biodetectors. *Chem. Eng. Sci.*, **60**, 2585–2598.
- [146] Richards, P.I. (1956) Shock waves on the highway. *Oper. Res.*, **4**, 42–51.
- [147] Richardson, J.F. & Zaki, W.N. (1954) Sedimentation and fluidization: Part I. *Trans. Instn. Chem. Engrs. (London)*, **32**, 35–53.
- [148] Ross, D.S. (1988) Two new moving boundary problems for scalar conservation laws. *Comm. Pure Appl. Math.*, **41**, 725–737.
- [149] Rosso, F. & Sona, G. (2001) Gravity-driven separation of oil-water dispersions. *Adv. Math. Sci. Appl.*, **11**, 127–151.
- [150] Seguin, N. & Vovelle, J. (2003) Analysis and approximation of a scalar conservation law with a flux function with discontinuous coefficients. *Math. Models Meth. Appl. Sci.*, **13**, 221–257.
- [151] Schneider, W., Anestis, G. & Schaflinger, U. (1985) Sediment composition due to settling of particles of different sizes. *Int. J. Multiphase Flow*, **11**, 419–423.
- [152] Shannon, P.T., Stroupe, E. & Tory, E.M. (1963) Batch and continuous thickening. *Ind. Eng. Chem. Fund.*, **2**, 203–211.
- [153] Simura, R. & Ozawa, K. (2006) Mechanism of crystal redistribution in a sheet-like magma body: Constraints from the Nosappumisaki and other Shoshonite intrusions in the Nemuro peninsula, Northern Japan. *J. Petrology*, **47**, 1809–1851.
- [154] Spannenberg, A., Galvin, K., Raven, J. & Scarboro, M. (1996) Continuous differential sedimentation of a binary suspension. *Chem. Eng. in Australia*, **21**, 7–11.
- [155] Strub, I.S. & Bayen, A.M. (2006) Weak formulation of boundary conditions for scalar conservation laws: an application to highway traffic modelling. *Int. J. Robust Nonlinear Control*, **16**, 733–748.

- [156] Tadmor, E. (1984) Numerical viscosity and the entropy condition for conservative difference schemes. *Math. Comp.*, **43**, 369–381.
- [157] Temple, B. (1982) Global solution of the Cauchy problem for a class of  $2 \times 2$  nonstrictly hyperbolic conservation laws. *Adv. Appl. Math.*, **3**, 335–375.
- [158] Tory, E.M., Ford, R.A. & Bargieł, M. (2003) Simulation of the sedimentation of monodisperse and polydisperse suspensions. *Analysis and Simulation of Multi-field Problems* (Wendland, W.L., Efendiev, M. eds.). Berlin: Springer-Verlag, pp. 343–348.
- [159] Towers, J.D. (2000) Convergence of a difference scheme for conservation laws with a discontinuous flux. *SIAM J. Numer. Anal.*, **38**, 681–698.
- [160] Towers, J.D. (2001) A difference scheme for conservation laws with a discontinuous flux: The nonconvex case. *SIAM J. Numer. Anal.*, **39**, 1197–1218.
- [161] Tsuji, Y., Kawaguchi, T. & Tanaka, T. (1993) Discrete particle simulation of two-dimensional fluidized bed. *Powder Technol.*, **77**, 79–87.
- [162] Tsuji, Y., Tanaka, T. & Yonemura, S. (1998) Cluster patterns in circulating fluidized beds predicted by numerical simulation (discrete particle model versus two-fluid model). *Powder Technol.*, **95**, 254–264.
- [163] Ungarish, M. (1993) *Hydrodynamics of Suspensions*, Springer-Verlag, Berlin.
- [164] Van Duijn, C.J., De Neef, M.J. & Molenaar, J. (1995) Effects of capillary forces on immiscible two-phase flow in strongly heterogeneous porous media. *Transp. Porous Media*, **21**, 71–93.
- [165] Vasseur, A. (2001) Strong traces of multidimensional scalar conservation laws. *Arch. Rat. Mech. Anal.*, **160**, 181–193.
- [166] Weiland, R.H., Fessas, Y.P. & Ramarao, B.V. (1984). On instabilities arising during sedimentation of two-component mixtures of solids. *J. Fluid Mech.*, **142**, 383–389.

- [167] Wang, X., Miles, N.J. & Kingman, S. (2006) Numerical study of centrifugal fluidized bed separation. *Minerals Eng.*, **19**, 1109–1114.
- [168] Wong, G.C.K. & Wong, S.C. (2002) A multi-class traffic flow model—an extension of LWR model with heterogeneous drivers. *Transp. Res. A*, **36**, 827–841.
- [169] Wong, S.C. & Wong, G.C.K. (2002) An analytical shock-fitting algorithm for LWR kinematic wave model embedded with linear speed-density relationship. *Transp. Res. B*, **36**, 683–706.
- [170] Xue, B. & Sun, Y. (2003) Modeling of sedimentation of polydisperse spherical beads with a broad size distribution. *Chem. Eng. Sci.*, **58**, 1531–1543.
- [171] Yamamoto, Y., Potthoff, M., Tanaka, T., Kajishama, T. & Tsuji, Y. (2001). Large-eddy simulation of turbulent gas-particle flow in a vertical channel: effect of considering inter-particle collisions. *J. Fluid Mech.*, **442**, 303–334.
- [172] Yan, Y. & Masliyah, J.H. (1993) Sedimentation of solid particles in oil-in-water emulsions. *Int. J. Multiphase Flow*, **19**, 875–886.
- [173] Young, M.L. & Klima, M.S. (2000). Evaluation of a hindered-settling column for size/density separations. *Minerals & Metallurgical Processing*, **17**, 194–197.
- [174] Zeidan, A., Rohani, S. & Bassi, A. (2004) Dynamic and steady-state sedimentation of polydisperse suspension and prediction of outlets particle-size distribution. *Chem. Eng. Sci.*, **59**, 2619–2632.
- [175] Zeidan, A., Rohani, A., Bassi, A. & Whiting, P. (2003) Review and comparison of solids settling velocity models. *Reviews in Chemical Engrg.*, **19**, 473–530.
- [176] Zhang, M., Shu, C.W., Wong, G.C.K. & Wong, S.C. (2003) A weighted essentially non-oscillatory numerical scheme for a multi-class Lighthill-Whitham-Richards traffic flow model. *J. Comput. Phys.*, **191**, 639–659

- [177] Zhang, P., Liu, R.X., Wong, S.C. & Dai, S.Q. (2006) Hyperbolicity and kinematic waves of a class of multi-population partial differential equations. *Eur. J. Appl. Math.*, **17**, 171–200.
- [178] Zhang, P., Wong, S.C. & Shu, C.W. (2006) A weighted essentially non-oscillatory numerical scheme for a multi-class traffic flow model on an inhomogeneous highway. *J. Comput. Phys.*, **212**, 739–756.